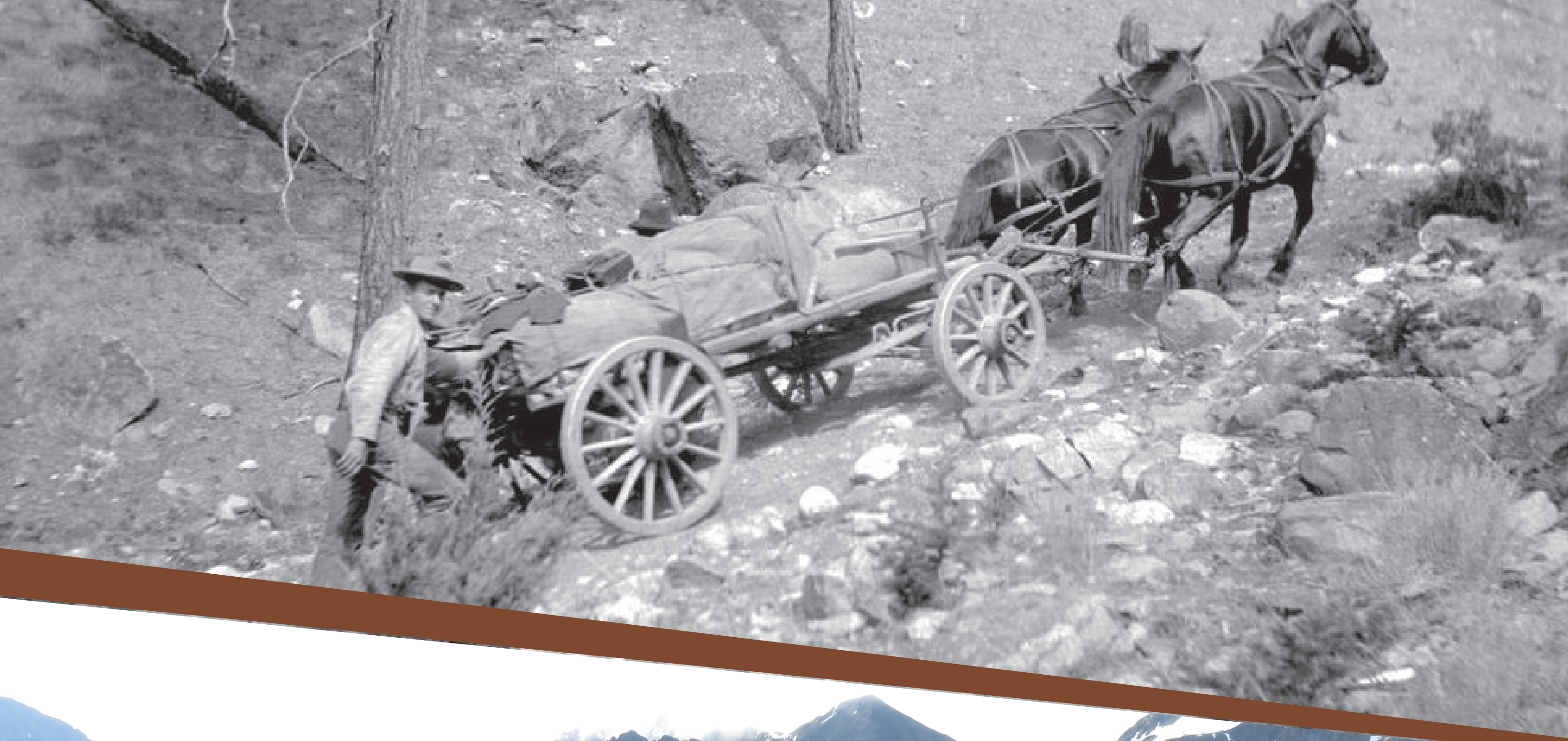

British Columbia Geological Survey
est. 125 1895

Geological Fieldwork 2019

A Summary of Field Activities and Current Research

British Columbia
Ministry of Energy, Mines and Petroleum Resources

Paper 2020-01

BRITISH COLUMBIA

Ministry of
Energy, Mines and
Petroleum Resources

BRITISH COLUMBIA
est. 125 1895
GEOLOGICAL SURVEY

Ministry of Energy, Mines and Petroleum Resources

Geological Fieldwork 2019

A Summary of Field Activities and Current Research

Ministry of Energy, Mines and Petroleum Resources
British Columbia Geological Survey

Paper 2020-01

Ministry of Energy, Mines and Petroleum Resources
Mines and Mineral Resources Division
British Columbia Geological Survey

Recommended citation format for individual papers:

Nixon, G.T., Friedman, R.M., and Creaser, R.A., 2020. Late Neogene porphyry Cu-Mo(±Au-Ag) mineralization in British Columbia: the Klaskish Plutonic Suite, northern Vancouver Island. In: Geological Fieldwork 2019, British Columbia Ministry of Energy, Mines and Petroleum Resources, British Columbia Geological Survey Paper 2020-01, pp. 119-132.

Front Cover:
Top. Camp move to Highland Valley, 1910. **Photo by Frank Cyril Swannell.**
From Royal BC Museum Archives, reference code I-33680.

Bottom. Camp move, eastern Hogem batholith, 2018. In background are diorites of the Thane Creek plutonic suite.
See Ootes, L., Bergen, A.L., Milidragovic, D., Jones, G.O., Camacho, A., and Friedman, R., 2020. An update on the geology of northern Hogem batholith and its surroundings, north-central British Columbia, this volume. **Photo by Dejan Milidragovic.**

Back Cover:
Moderately dipping interstratified siltstones (grey) and slates (recessive, brown) of the Dewar Formation, Takla Group (Upper Triassic), Stikine terrane. Individual beds are 2 to 4 cm thick and bedsets are 10 to 15 m thick. The photograph was taken west of Omineca River; view to the northwest.
See Ootes, L., Bergen, A.L., Milidragovic, D., Jones, G.O., Camacho, A., and Friedman, R., 2020. An update on the geology of northern Hogem batholith and its surroundings, north-central British Columbia, this volume. **Photo by Anika Bergen.**

This publication is available, free of charge, from the British Columbia Geological Survey website:
https://www2.gov.bc.ca/gov/content/industry/mineral-exploration-mining/british-columbia-geological-survey/publications

British Columbia Cataloguing in Publication Data

Main entry under title:

Geological Fieldwork: - 1974 -

Annual.

Issuing body varies

Vols. for 1978-1996 issued in series: Paper / British Columbia. Ministry of Energy, Mines and Petroleum Resources; vols. for 1997 - 1998, Paper / British Columbia. Ministry of Employment and Investment; vols. for 1999-2004, Paper / British Columbia. Ministry of Energy and Mines; vols. for 2005-2009, Paper / British Columbia. Ministry of Energy, Mines and Petroleum Resources; vols. for 2010, Paper / British Columbia. Ministry of Forests, Mines and Lands; vols. for 2011, Paper / British Columbia. Ministry of Energy and Mines; vols. for 2012- , Paper / British Columbia. Ministry of Energy, Mines and Natural Gas; vols. for 2014- , Paper / British Columbia. Ministry of Energy and Mines.

Includes Bibliographical references.

ISSN 0381-243X=Geological Fieldwork

1. Geology - British Columbia - Periodicals. 2. Mines and mineral resources - British Columbia - Periodicals. 3. Geology - Fieldwork - Periodicals. 4. Geology, Economic - British Columbia - Periodicals. 5. British Columbia. Geological Survey Branch - Periodicals. I. British Columbia. Geological Division. II. British Columbia. Geological Survey Branch. III. British Columbia. Geological Survey Branch. IV. British Columbia. Dept. of Mines and Petroleum Resources. V. British Columbia. Ministry of Energy, Mines and Petroleum Resources. VI. British Columbia. Ministry of Employment and Investment. VII. British Columbia Ministry of Energy and Mines. VIII. Series: Paper (British Columbia. Ministry of Energy, Mines and Petroleum Resources). IX. Series: Paper (British Columbia. Ministry of Employment and Investment). X. Series: Paper (British Columbia Ministry of Energy and Mines). XI. Series: Paper (British Columbia Ministry of Energy, Mines and Petroleum Resources). XII. Series: Paper (British Columbia Ministry of Forests, Mines and Lands). XIII. Series: Paper (British Columbia Ministry of Energy and Mines). XIV. Series: Paper (British Columbia Ministry of Energy, Mines and Natural Gas). XV. Series: Paper (British Columbia Ministry of Energy and Mines).

QE187.46 622.1’09711 C76-083084-3 (Rev.)

Victoria
British Columbia
Canada

January 2020

Preface

Geological Fieldwork 2019

Geological Fieldwork 2019 is the forty-fifth edition of an annual volume that presents peer-reviewed papers detailing the results of geoscience research by the British Columbia Geological Survey (BCGS) and its partners. This volume, the Provincial Overview of Exploration and Mining in British Columbia, and the Coal Industry Overview are published each year in January. The Survey also disseminates its data through Open Files, GeoFiles, Geoscience Maps, and databases, all of which are freely accessed through the BCGS website or through MapPlace, the BCGS interactive web service. Additionally, BCGS staff contribute to external publications including journals (see Appendix). In 2019, the Survey released or contributed to 49 publications.

Geological Fieldwork 2019 highlights BCGS field activities. Hunter et al. report on the first year of a multi-year mapping and geochronological study in northwestern British Columbia. This study, along with Miller et al., is in the most active mineral exploration district in the province, colloquially known as the Golden Triangle. Ootes et al. present results from the second year of bedrock mapping at the Hogem batholith in east-central British Columbia. New geochronologic data from an area in southern British Columbia east of the Coast Belt are presented by Schiarizza et al. As detailed in a study by Nixon et al., Neogene mineralization on northern Vancouver Island constitutes a well-defined but underexplored metallotect. Reporting on a project conducted in partnership with University of British Columbia (UBC) and the Geological Survey of Canada, Nott et al. mapped the Polaris ultramafic-mafic Alaskan-type intrusion in north-central British Columbia. BCGS is also a contributing partner of UBC's Bradshaw Research Initiative for Minerals and Mining (BRIMM)-Natural Resources Canada's Clean Growth project that is evaluating the feasibility of sequestering atmospheric CO_2 using serpentinized ultramafic rocks, and Steinthorsdottir et al. report on the extent and controls of alteration at the Decar prospect in the Trembleur ultramafite. BCGS is developing new exploration methods to help in the search for buried deposits; Rukhlov et al. describe treatments of samples collected for geochemical analysis from drainages on Vancouver Island, and Shewchuk et al. evaluate the use of major oxides and pathfinder elements in till samples collected from near Highland Valley mine in the Interior Plateau. The Survey has invested in a remotely piloted aircraft (RPA) and Elia et al. report on optical surveys that enhance mapping in remote settings.

As a result of recommendations made by the Minister's appointment of a Mining Jobs Task Force, delivery of geoscience in British Columbia was the subject of a formal review in 2019. The report has been foundational in prioritizing BCGS's ongoing activities. Framework geoscience (geological mapping) and delivering data were identified as the most important priorities for the Survey. Resources have been focussed primarily on new mapping and updating BC digital geology. The Survey has made advances in this area through its internationally recognized Geospatial Framework Data (GFD) model approach. Ongoing digital capture has intensively targeted recovering and digitizing Assessment Report data. Updating and modernizing geological databases remains critical in making British Columbia a competitive mineral exploration jurisdiction. This modernization also underpins new province-wide mineral potential assessments needed for land management initiatives that are being reinvigorated.

The British Columbia Geological Survey is the oldest science agency in the province and is proud to be celebrating its 125th anniversary in 2020. The Survey continues to evolve through renewal, building on its tradition of advancing geoscience knowledge.

Adrian S. Hickin
Chief Geologist and Executive Director
British Columbia Geological Survey

Table of Contents

British Columbia Geological Survey annual program review 2019-2020

Filippo Ferri[1, a], Larry D. Jones[1], Gordon Clarke[2], and Adrian S. Hickin[1]

[1] British Columbia Geological Survey, Ministry of Energy, Mines and Petroleum Resources, Victoria, BC, V8W 9N3
[2] British Columbia Geological Survey, Ministry of Energy, Mines and Petroleum Resources, Vancouver, BC, V6Z 2G3
[a] corresponding author: Fil.Ferri@gov.bc.ca

Recommended citation: Ferri, F., Jones, L.D., Clarke, G., and Hickin, A.S., 2020. British Columbia Geological Survey annual program review 2019-2020. In: Geological Fieldwork 2019, Ministry of Energy, Mines and Petroleum Resources, British Columbia Geological Survey Paper 2020-01, pp. 1-12.

1. Introduction

Founded in 1895, the British Columbia Geological Survey (BCGS) is the oldest scientific agency in the province. Throughout its history, the BCGS has conducted research (Fig. 1) and published information (Fig. 2) defining the geological evolution and natural resources of the province. The BCGS generates, disseminates, and archives British Columbia's geoscience information to make the province a competitive jurisdiction for mineral exploration and provide knowledge to guide land use and resource management decisions that balance the economy, the environment, and community interests. Survey maps, reports, and databases are freely available online, connecting the public, First Nations, local communities, the minerals industry, public safety agencies, environmental scientists, other research organizations, and government to the provinces' geology and mineral resources.

The BCGS is part of the Mines and Minerals Resource Division in the British Columbia Ministry of Energy, Mines and Petroleum Resources. The Survey is headquartered in Victoria and operates the Mineral Development Office (MDO) as its representative in Vancouver. Staffed by 29 people (Fig. 3), the BCGS consists of three sections: 1) Cordilleran Geoscience; 2) Resource Information and 3) the Mineral Development Office. The Cordilleran Geoscience Section is responsible for generating new geoscience knowledge through field-based bedrock and surficial geology mapping programs, regional geochemical surveys, and targeted mineral deposit studies. It also manages the Survey's laboratory, curates the provincial sample archive, and trains the next generation of field geoscientists. The Resource Information Section is responsible for maintaining and developing provincial geoscience databases and disseminating data online through MapPlace, the BCGS geospatial web service. The Resource Information Section is also responsible for collecting, evaluating, approving, and archiving mineral and coal exploration assessment reports submitted by industry to maintain titles in good standing. As the steward of mineral and coal resources in the province, the Survey has an important role in stimulating activity, attracting investment, and providing continuous research based on a corporate memory that extends back more than 125 years. The Mineral Development Office provides investment intelligence to government and global business. It also produces the annual Provincial Overview of Exploration and Mining in British Columbia volume (e.g., Clarke et al., 2020).

We are proud to announce that Emeritus Scientist JoAnne Nelson (Fig. 4) was awarded the 2019-2020 Howard Street Robinson Medal by the Geological Association of Canada. Regarded as the leading expert on the tectonics and metallogeny of the Cordillera, JoAnne's career as a field geologist spans more than 30 years. JoAnne continues to be generous with her energies, supporting new and old colleagues, and nurturing the next generation of field geologists. In 2017, JoAnne was awarded the Provincial and Territorial Geologists Medal by the Committee of Provincial and Territorial Geologists. The Survey is delighted that she is receiving the recognition she rightfully deserves.

The BCGS continues to renew itself. In 2019, the Survey welcomed Rebecca Hunter as a Senior Minerals Geologist and Pierre Landry as a Mineral Assessment Geoscientist. At the end of January 2020, Fil Ferri will retire after 32 years with the Ministry of Energy, Mines and Petroleum Resources. His position as the Director of Cordilleran Geoscience will be filled by Neil Wildgust. Other key geoscientist positions will be filled in 2020 as the Survey celebrates its 125th anniversary.

2. Partnerships

The British Columbia Geological Survey works to optimize resources through collaborative projects, and partnerships are important. The BCGS and the Geological Survey of Canada (GSC) are traditional partners and continue to work together in delivering projects through the second iteration of the Geo-mapping for Energy and Minerals (GEM 2) program and through three Targeted Geoscience Initiative 5 (TGI-5) projects.

In 2013, the Government of Canada renewed support for the second phase of the GEM program aimed at advancing geological knowledge and further developing modern geological maps and datasets. The BCGS collaborated with the GSC and the Yukon Geological Survey (YGS) through the

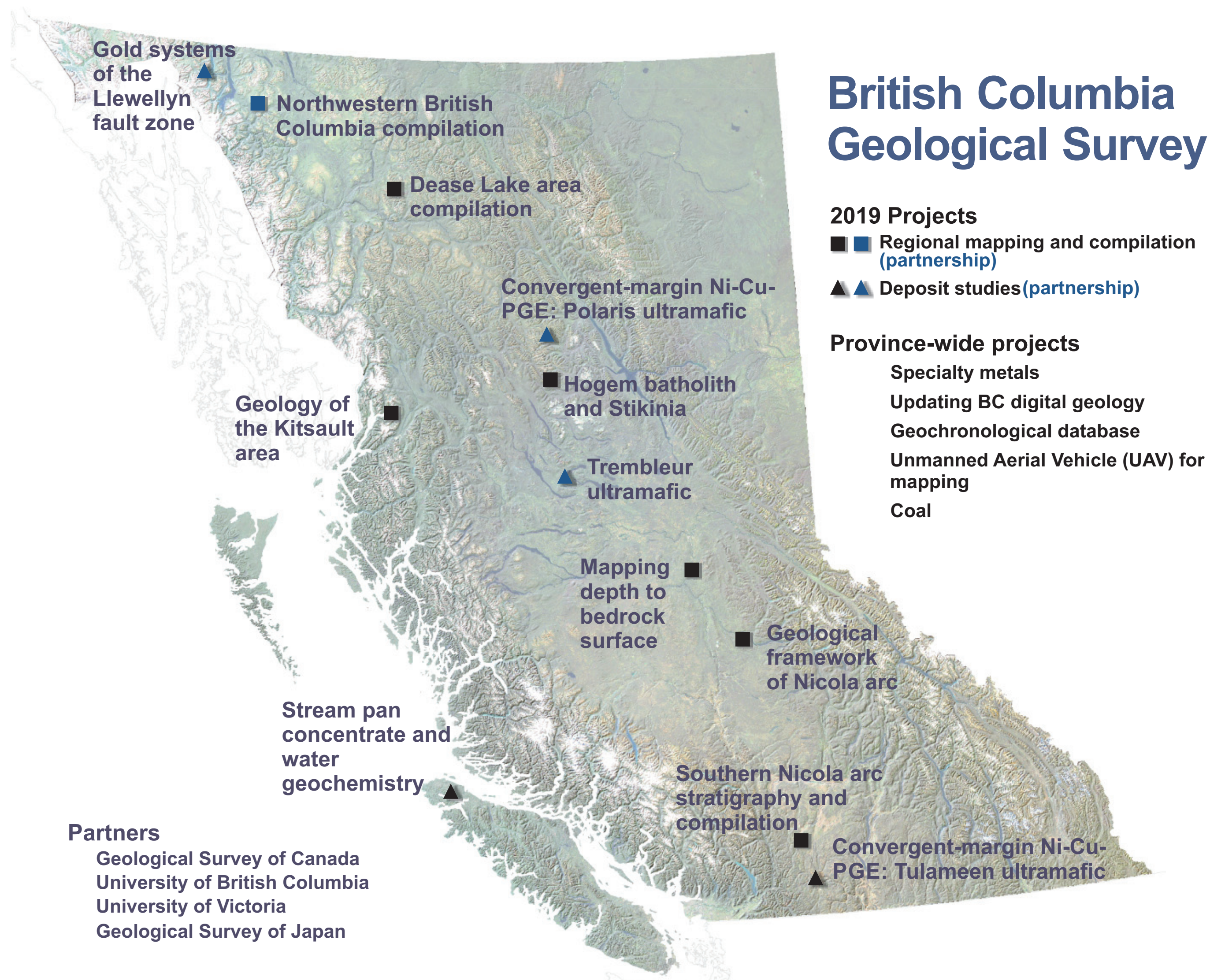

Fig. 1. British Columbia Geological Survey projects in 2019.

Cordilleran Activity, in which the British Columbia component focussed on the Cache Creek and Stikine terranes near Atlin. The GEM program will wrap up in 2020 and produce a summary volume and associated bedrock maps. In late March, the GSC, BCGS, and YGS, in conjunction with the Pacific Section of the Geological Association of Canada, will be holding a two-day workshop (Cordilleran Geoscience: A 2020 perspective) in Vancouver.

TGI-5 is directed at building knowledge and developing methods to more effectively target buried mineral deposits. The program aims to better understand the geological processes responsible for liberating ore metals from their source regions and to establish the controls on metals transport and deposition. The current iteration of TGI-5 is expected to conclude in 2020. BCGS projects include: 1) assessing gold deposits spatially related to the Llewellyn fault and Tally Ho shear zone in northwest British Columbia and southern Yukon; 2) examining specialty metal deposits that host rare earth elements, lithium, tantalum, and niobium (also in partnership with the Geological Survey of Japan); and 3) defining a new mineral deposit model for orogenic Ni-Cu-PGE mineralization in Alaskan-type ultramafic-mafic intrusions.

3. Cordilleran Geoscience Section

Geologists with the Cordilleran Geoscience Section collect fundamental geoscience data through single and multi-year field-based programs, including regional-scale mapping, mineral deposit studies, and developing new exploration methods. Collectively, these researchers provide a wide range of expertise that includes regional mapping, metallogeny, coal, tectonics, surficial and Quaternary geology, geochemistry, petrology, and mineral exploration methods.

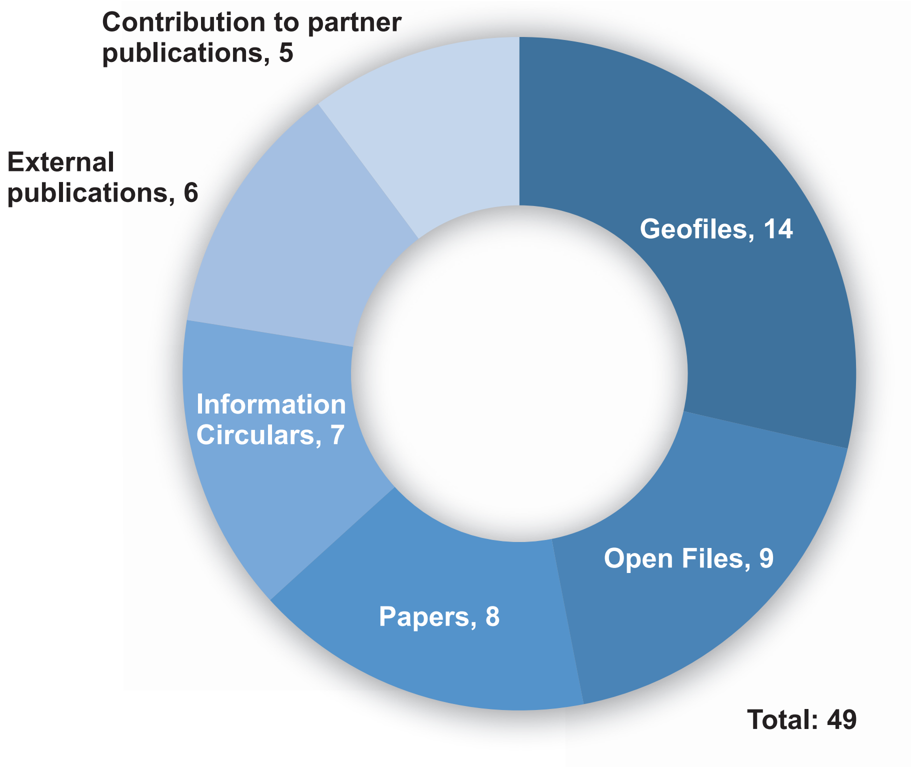

Papers*: This series is reserved for reviews and final thematic or regional works. Geological Fieldwork, our annual review of field activities and current research, is released as the first Paper of each year.

Geoscience Maps: This series is the BCGS vehicle for publishing final maps.

Open Files: These maps and reports present the interim results of ongoing research, particularly mapping projects.

GeoFiles: These publications enable rapid release of extensive data tables from ongoing geochemical, geochronologic, and geophysical work. As such, they serve the same function as data repositories provided by many journals, providing immediate access to raw data from specific projects.

Information Circulars: These publications provide accessible geoscience information to a broad audience in government, industry, and the general public. Included in the Information Circular series are the annual Provincial Overview of Mining and Exploration, **Exploration and Mining in British Columbia, and the Coal Industry Overview.

Contributions to partner publications: This category includes reports, maps, and other products published by another agency such as the Geological Survey of Canada or Geoscience BC, but have received contributions from British Columbia Geological Survey staff.

External publications: These are contributions to the peer reviewed literature and published in a recognized national or international scientific journal.

*The count refers to the total number of articles authored by BCGS personnel in a volume.

**Although five articles are included in Exploration and Mining in British Columbia, it is counted as a single volume.

Fig. 2. Types and numbers of publications produced by the British Columbia Geological Survey in 2019.

In addition to ongoing work, this volume presents results from a previous project in which Schiarizza et al. (2020) report new U-Pb detrital zircon ages from the Gun Lake unit (Noel Formation) in the Bridge River area of southwestern British Columbia. They show that certain sections previously considered to be equivalent to the lower Relay Mountain Group are correlative to the middle part of this group and the younger Paradise Formation. Elia and Ferbey (2020) describe the use of

Fig. 3. Members of the British Columbia Geological Survey, 2019.

Fig. 4. JoAnne Nelson mapping in the Iskut area.

remotely piloted aircraft systems to generate photogrammetric digital elevation models. These models are easy to acquire, affordable, and immediately accessible, providing field crews with geologic details in near real-time that otherwise might not have been gained.

3.1. Mapping, regional synthesis and compilation

3.1.1. Porphyry transitions (BCGS–GSC)

This project, a collaboration with the Geological Survey of Canada through the Geo-mapping for Energy and Minerals (GEM 2), was initiated in 2016 to test the continuity of prospective Triassic-Jurassic magmatic rocks into northern Stikinia and assess their porphyry potential. With the GEM 2 wrap up in 2020, the project will produce a final report and map compilations.

3.1.2. Stratigraphic architecture of the Nicola arc

Although the field component of the Nicola arc project was completed (Schiarizza, 2019), the project continued with synthesis of earlier mapping (Schiarizza, 2016, 2017, 2018) and compilation of work in the Merritt and Princeton areas (Mihalynuk et al., 2014, 2015, 2016) to produce a coherent stratigraphic framework for this important metallotect. This compilation will be incorporated into the British Columbia digital geological database.

3.1.3. Regional mapping in the Dease Lake area

Major field activities for this project finished in 2018. This mapping program focussed on Upper Triassic to Middle Jurassic arc-related volcanic and sedimentary rocks encircling the Hotailuh batholith in order to refine the tectonic and metallogenic history of northern Stikinia (van Straaten et al., 2012, 2017; van Straaten and Bichlmaier, 2018; van Straaten and Wearmouth, 2019). A very limited field program took place in 2019 to further refine unconformable relationships between the Stuhini Group (Upper Triassic) and the Horn Mountain Formation (Lower Jurassic). Field data from 2019 will be incorporated with work from previous years, compiled into a 1:100,000 Geoscience Map, and incorporated into the British Columbia digital geology database. In addition, all geochronology, paleontology, petrography, lithogeochemistry, structural, and petrophysical data will be released in a GeoFile publication.

3.1.4. Northern Hogem batholith, Stikine and Cache Creek terranes

A multi-year bedrock and surficial mapping project was initiated in 2018 targeting northern Hogem batholith and adjacent intrusive, volcanic and sedimentary rocks of the Stikine and Cache Creek terranes (Ootes et al., 2019 a, b; Fig. 5). The main objectives of this project are to update the bedrock and surficial maps of the area and incorporate new geochronological and lithogeochemical data to better understand the timing of intrusive events and relationship to mineralization.

Mapping in 2019 (Ootes et al., 2020a, b) further refined the distribution and relationships of plutonic rocks in northern Hogem batholith. The Hogem batholith is a composite body consisting of: ca. 197 Ma hornblendite and diorite of the Thane Creek suite; 182 to 178 Ma biotite pyroxenite and syenite of the Duckling Creek suite; ca.160 Ma granite of the Osilinka suite; and ca. 174 Ma tonalite and 140 to 135 Ma granodiorite and granite of the Mesilinka suite. All units contain a penetrative foliation, and $^{40}Ar/^{39}Ar$ biotite ages indicate post-deformation cooling and uplift after ca. 124 Ma. Mafic to ultramafic

Fig. 5. Looking north at the rugged terrane of northern Hogem batholith; see Ootes et al. (2020a).

intrusions (Abraham Creek and Dortatelle Creek complexes) were also mapped in the Quesnel terrane. The Hogem batholith is bounded to the north and east by volcanic and sedimentary rocks of the Nicola Group (Triassic) along fault and intrusive contacts. To the west, Hogem batholith and Nicola Group are separated from the Cache Creek and Stikine terranes along the Pinchi-Ingenika dextral strike-slip fault system; farther west, an unexposed thrust fault juxtaposes Cache Creek rocks above Stikine terrane rocks. The Stikine terrane in the study area includes the Asitka Group (Carboniferous to Permian) volcano-sedimentary basement that is overlain by immature siliciclastic sedimentary rocks of the Dewar Formation (Takla Group; Triassic), and which is overlain by the Telkwa Formation (Hazelton Group; Jurassic). Uppermost Hazelton Group rocks pass upwards into Jurassic and Cretaceous siliciclastic rocks of the Bowser and Sustut groups, which constitute overlap assemblages deposited after the terranes amalgamated. Cache Creek terrane encompasses metamorphic rocks of the Sitlika assemblage (Lower Jurassic), which have sedimentary and volcanic protoliths, serpentinites of the Trembleur ultramafic complex (Permian to Upper Triassic), mixed volcanic and metasedimentary rocks of the Sowchea succession (Upper Pennsylvanian to Lower Jurassic), and Cretaceous intrusive rocks of the Axelgold layered mafic intrusion. About 88 mineral occurrences in the area are documented in MINFILE. Seven new occurrences were discovered in 2019. When combined with results of 2018 mapping, 24 new mineral occurrences have been documented in the study area. Porphyry Cu±Mo, Au in Hogem batholith is the predominant type followed by quartz-carbonate vein-hosted base and precious metals in Quesnel and Stikine terranes, and volcanic/sediment-hosted Cu in the Telkwa Formation of the Stikine terrane.

3.1.5. Hazelton Group stratigraphy and associated mineralization in the Kitsault area

In 2019, the BCGS initiated a new regional mapping program in the Kitsault area of northwestern British Columbia, in the southern part of a region popularly referred to as the Golden Triangle (Hunter and van Straaten, 2020; Fig. 6). This region is well known for its significant porphyry Cu-Au, epithermal Au, and volcanogenic massive sulphide (VMS), and precious and base metal deposits. Although this area was mapped by Alldrick et al. (1986), it lacked modern geochronology and lithogeochemistry. In addition, our knowledge of Stuhini Group (Triassic) and Hazelton Group (latest Triassic to Middle Jurassic) stratigraphy has significantly advanced since this original work (e.g., Nelson et al., 2018). This project builds on concurrent research nearby at Kinskuch Lake by Miller et al. (2020; see below).

Mapping focussed on facies analysis of Hazleton Group volcanosedimentary rocks. New U-Pb geochronology from detrital zircons indicates a maximum depositional age of ca. 206 Ma (Rhaetian) for the onset of Hazelton Group volcanism. A monzonite dike near the Homestake Ridge deposit yielded a U-Pb age of ca. 191 Ma suggesting that this Cu-Au

Fig. 6. Maroon volcanic breccia in the lower part of the Hazelton Group in the Kitsault area; see Hunter et al. (2020).

mineralization is Early Jurassic. Felsic lapilli tuff in underlying the Wolf deposit contain zircons with crystallization ages of ca. 178 Ma indicating that this VMS related mineralization is in the upper part of the Hazelton Group, and a volcanic-derived sandstone sample from the southern shore of Kitsault Lake returned a detrital zircon maximum depositional age of ca. 169 Ma. These upper Hazelton Group units differ from those in the Eskay rift and at the Anyox deposit, which contain abundant bimodal felsic and mafic volcanic rocks. Nonetheless, these coeval syngenetic mineralizing systems are likely related and VMS mineralization in the Kitsault River area may reflect hydro-magmatic fluids flowing along syndepositional faults to near-surface levels. Extensional processes that operated at Eskay may have extended into in the Kitsault River area but without producing a large rift basin.

3.1.6. Geology of the Kinskuch Lake area

Mapping by Miller et al. (2020) in the Kinskuch Lake area during the last two summers has focussed on the depositional and structural history of the Stuhini and Hazleton groups and related Cu mineralization at the Big Bulk prospect. This work indicates that syndepositional faulting in the Rhaetian (latest Triassic) strongly influenced the transition from Stuhini Group to Hazelton Group deposition. Conglomerates, informally referred as the Kinskuch conglomerates, containing Stuhini Group-derived megaclasts (up to 120 m) at the base of the Hazelton Group (Fig. 7) signify a high-relief, fault-generated paleotopography and mark a fundamental break in the tectonic history of the region. This tectonism also appears to be related to emplacement of Cu mineralization in the Big Bulk porphyry system, which returned a U-Pb zircon age of 204.61 ±0.18 Ma. Like other areas in northwestern Stikinia, latest Triassic to Early Jurassic sedimentation, magmatism, and porphyry mineralization appear to have had a strong structural control.

Fig. 7. Dark grey-weathered Stuhini Group-derived megaclast in Kinskuch conglomerate, basal Hazelton Group near Kinskuch Lake; see Miller et al. (2020).

3.2. Deposit studies and exploration methods

3.2.1. Late Neogene porphyry Cu-Mo(±Au-Ag) mineralization, northern Vancouver Island

In northern Vancouver Island, recent high-precision dating (U-Pb zircon and Re-Os molybdenite) of mineralized stocks of the Klaskish Plutonic Suite (ca. 7 to 4.6 Ma) show that porphyry Cu-Mo magmatic-hydrothermal systems are genetically linked to pluton emplacement and crystallization. This dating also confirms that the emplacement of these plutons was coeval with older phases of Alert Bay volcanism (8-2.5 Ma). Nixon et al. (2020) formally name the Klaskish Plutonic Suite and show that these plutons, which are in the forearc of the Cascadia subduction zone, define the northeast trending late Neogene Brooks-Haddington tract that extends for 65 km across the island, from the Pacific Coast to Queen Charlotte Strait. Previous to this work, Neogene Mo/Cu-Mo mineralization elsewhere in British Columbia was thought to have been restricted to the Pemberton arc along the southeastern Coast Mountains. Dating is key in distinguishing these Neogene plutons from Early to Middle Jurassic intrusions of the Island Plutonic Suite which host major porphyry Cu-Mo-Au-Ag deposits on the island. These young plutons in northern Vancouver Island define an extensive and underexplored Cu-Mo porphyry metallotect.

3.2.2. Specialty metals

Part of the TGI-5 program, the specialty metals project is a BCGS collaboration with the GSC and Geological Survey of Japan. Specialty metals are elements that are essential to the growth of the electronics and green-energy sector, and critical or strategic for technologically advanced devices and industrial processes. They include rare earth elements (REE), Li, Ta, Nb, Ga, Ge, In, Co, W, Mg, Cs, Rb, Rh, Be, Zr, Hf, V, Sb and Sc.

Work in 2019 focussed on laboratory analyses of carbonatite samples collected in the last six years, compilation, and publication. Akam et al. (2019) published a paper about selecting analytical procedures and reference materials for evaluating REE-bearing deposits and a paper documenting mineral control on chemical zoning in the main mineralized zone at the Rock Canyon Creek REE-Ba-F deposit is in progress. In addition, rare earth element concentrations were acquired from dolomite and calcite hosted by various deposits and deposit-types, including: 1) Mississippi Valley-type deposits; 2) the Rock Canyon Creek deposit (Paradis and Simandl, 2019); 3) the Mount Brussilof magnesite deposit (Simandl et al., 2019) and 4) carbonatites in general. The concentration and pattern of these elements will be described in external papers that focus on each deposit or deposit-type.

3.2.3. Polaris: towards a new mineral deposit model for convergent margin Ni-Cu-PGE (BCGS–TGI-5)

This is the second year of a TGI-5 project that builds on our current understanding of high-tenor Ni-Cu-PGE-bearing Alaskan-type ultramafic-mafic intrusions. The primary objective of this project is to establish the temporal and magmatic evolution of the Polaris intrusion that will have implications on the nature and timing of sulphide mineralization. This new work will ultimately feed into the development of a new mineral deposit model encompassing the temporal evolution and ore system processes involved in the genesis of Ni-Cu-PGE-rich sulphides in Alaskan-type ultramafic bodies in the Cordillera.

Work in 2019 (Nott et al., 2020) focussed on delineating the main phases of the Polaris ultramafite, showing it to be an elongate, 14 km long, sill-like body with rock types distributed asymmetrically. Dunite is predominant in the east, wehrlite, clinopyroxenite, and mixed zones in the central parts, and gabbro-diorite to hornblende clinopyroxenite in the west. Chromitite layers, hosted primarily by dunite, occur as schlieren and Ni-Cu-platinum group element sulphides are mainly hosted by clinopyroxenite. Future work will focus on the emplacement history of the various phases based on detailed geochronological analyses.

3.2.4. Serpentinized ultramafic rocks and CO_2 sequestration

The BCGS continues to work on projects aimed at a low-carbon economy. This is primarily through a partnership with the University of British Columbia under Natural Resources Canada Clean Growth Program that will determine the feasibility of ultramafic rock tailings to sequester CO_2 from the atmosphere. BCGS researchers will also compile the distribution of serpentinized ultramafic rocks in the province that have the potential to sequester CO_2.

Fieldwork in the Trembleur Lake area (Steinthorsdottir et al., 2020) focussed on serpentinized ultramafic rocks in the Cache Creek terrane that are part of the Decar Ni prospect. Here, Ni-bearing awaruite is associated with brucite, which can sequester CO_2 from the atmosphere. Work in 2019 focussed on the protoliths and alteration of the Trembleur ultramafite and resulted in recognizing that the primary ultramafite composition likely controlled fluid pathways and the extent of serpentinizing fluids and the abundance and distribution of awaruite and brucite. The heterogeneity in the Trembleur ultramafite protolith, together with the extent of alteration will have implications on the abundance and distribution of brucite and awaruite and, ultimately, the nickel and carbon sequestration potential of this occurrence.

3.2.5. Rapid, inexpensive and effective drainage geochemical surveys for mineral exploration

Typically, heavy mineral surveys use extensive laboratory processing of bulk samples to recover heavy mineral concentrates and indicator minerals. This process is expensive and beyond the affordability for most prospectors. In this volume, Rukhlov et al. (2020), describe a method for collecting heavy mineral separates in the field using a portable sluice, and panning, that is both effective and inexpensive (Fig. 8). This pilot study was undertaken in northern Vancouver Island where it confidently identified known mineralization in stream drainages that conventional stream and moss-captured sediments commonly failed to detect, even where close to known mineralization. In addition, Rukhlov et al. (2020) describe the use of Pb isotopic data and show that they are effective at fingerprinting different mineralizing systems. They propose a three-stage survey consisting of reconnaissance, exploration and detailed steps. Reconnaissance-level work targets 3rd order and higher drainages leading to exploration-level sampling at the mouths of tributaries within basins identified as being anomalous. This part of the survey will identify the single drainage containing the anomaly leading to focussed prospecting and detailed geochemical and geophysical surveys.

Fig. 8. Photomicrographs of panned sluice heavy mineral concentrate with abundant pink euhedral Mn-rich almandine in 1-2 mm fraction; see Rukhlov et al. (2020).

3.2.6. Exploration in drift-covered areas of the Interior Plateau

Abundances of major oxides and pathfinder elements are not typically used in drift prospecting. Using analytical data from subglacial till samples collected in the Highland Valley mine area by Ferbey et al. (2016) and principal component analysis, Shewchuk et al. (2020) demonstrate that major oxide concentrations can detect drift-covered porphyry Cu-Mo mineralization. Furthermore, the pathfinder elements Pb, Zn, As and Sb also delineate local dispersal fields. This analysis can also outline specific rock types in the area. This method offers a potentially new exploration and mapping tool in heavily drift covered areas.

To help steer future exploration efforts, the BCGS is currently undertaking a regional depth-to-bedrock study in the drift-covered area of the Quesnel terrane between the Mount Polley and Mount Milligan Cu-Au porphyry deposits. This project will use publically available data, including drill hole, bedrock, and surficial maps to establish the geometry of the bedrock-drift interface.

3.3. Geochemical and geochronological databases

BCGS field activities generate voluminous geochemical data, primarily in the form of rock, till, stream-sediment, and coal analyses. This information is currently contained in individual representative databases. A current project is developing a skeleton data model (Han et al., 2019) capable of capturing and representing the commonalities of these different data sets. Establishing a reliable method for managing BCGS geochemical data, this skeleton data model will update current databases and streamline data handling. In addition, an effort is underway to update and modernize the current geochronological database for the province.

4. Resource Information Section

The British Columbia Geological Survey is the custodian of all provincial public geoscience data. Since its inception, the main activities of the BCGS have been targeted at enhancing the province's geological knowledge base and making it a competitive jurisdiction for mineral exploration. This entails constantly upgrading databases and making this information, and its derivatives, easily accessible through web portals. BCGS geoscientists collect fundamental geoscience information that is funneled into these online databases and used by industry to develop projects and assist with the search for new discoveries. This information includes traditional geological maps together with thematic studies and reports, geochemical, geophysical, and geological databases, plus archived information such as MINFILE, COALFILE, and Property File.

4.1. MapPlace

MapPlace is the BCGS geospatial web service to efficiently visualize, search, report, and generate custom results and maps from all province-wide geoscience databases (Fig. 9). Some of the advanced applications and user interfaces are specifically designed to enable research and analysis in mineral exploration and prospecting. Easy access to, and analysis of, geoscience data and maps are fundamental for informing decisions about mineral exploration, mining, environmental protection, and land use management. MapPlace 2 provides a platform to facilitate the discovery, display, search, and analysis of geoscience in the context of all other relevant data such as mineral titles, assessment reports, linear infrastructure, aquifers, topography and satellite imagery. After 25 years of webservice, the original MapPlace will be retired this year.

4.2. ARIS reports and database

ARIS (Assessment Report Index System) is a database linking to a collection of mineral exploration assessment reports submitted in compliance with the Mineral Tenure Act Regulation. The ARIS library of more than 37,600 PDF reports dating from 1947 describes exploration work valued at more $2.8 billion. After a one-year confidentiality period, the reports become an open resource for planning mineral exploration, investment, research, land use, and resource management. All reports are available online as PDF documents through the Survey website. Digital data from 545 assessment reports are available for download through the ARIS search application and monthly tables. The ARIS database records metadata about the location, mineral occurrences, commodities, claims, general and specific work types, and expenditures in the reports. A version of the ARIS database is available in Microsoft Access format (.mdb) from the BCGS digital geoscience data webpage.

Extracting data in assessment reports from the Interior Plateau, Norris and Fortin (2019) generated a surface sediment geochemical database with a total of more than 1.45 million determinations from about 34,000 samples. This work has continued, and more data have been added to the database and incorporated into MapPlace 2. In another project that harvests data from assessment reports, the BCGS has begun to develop a drill hole database.

4.2.1. ARIS digital data submission

Traditionally, data in assessment reports have been embedded in paper or non-digital electronic files, such as PDF, making them difficult to extract and use. To resolve this problem, the Survey has embarked on a program to encourage digital data submission. Explorationists will benefit because digital data can be easily retrieved, integrated, processed, recalculated, and recast for specific needs. Digital submission will also enable the Survey to better maintain province-wide databases and create derivative products that use past results to guide future exploration.

The BCGS requests the submission of digital data files such as spreadsheets, databases, maps, grids describing technical work in an assessment report. Data can be uploaded through the ARIS data submission page (http://ardata.bcgeologicalsurvey.ca), submitted by CD/DVD/USB when a report is filed, or e-mailed to ARIS.digital@gov.bc.ca.

4.3. Other databases

COALFILE includes a collection of 1020 coal assessment reports dating from 1900. Associated data include

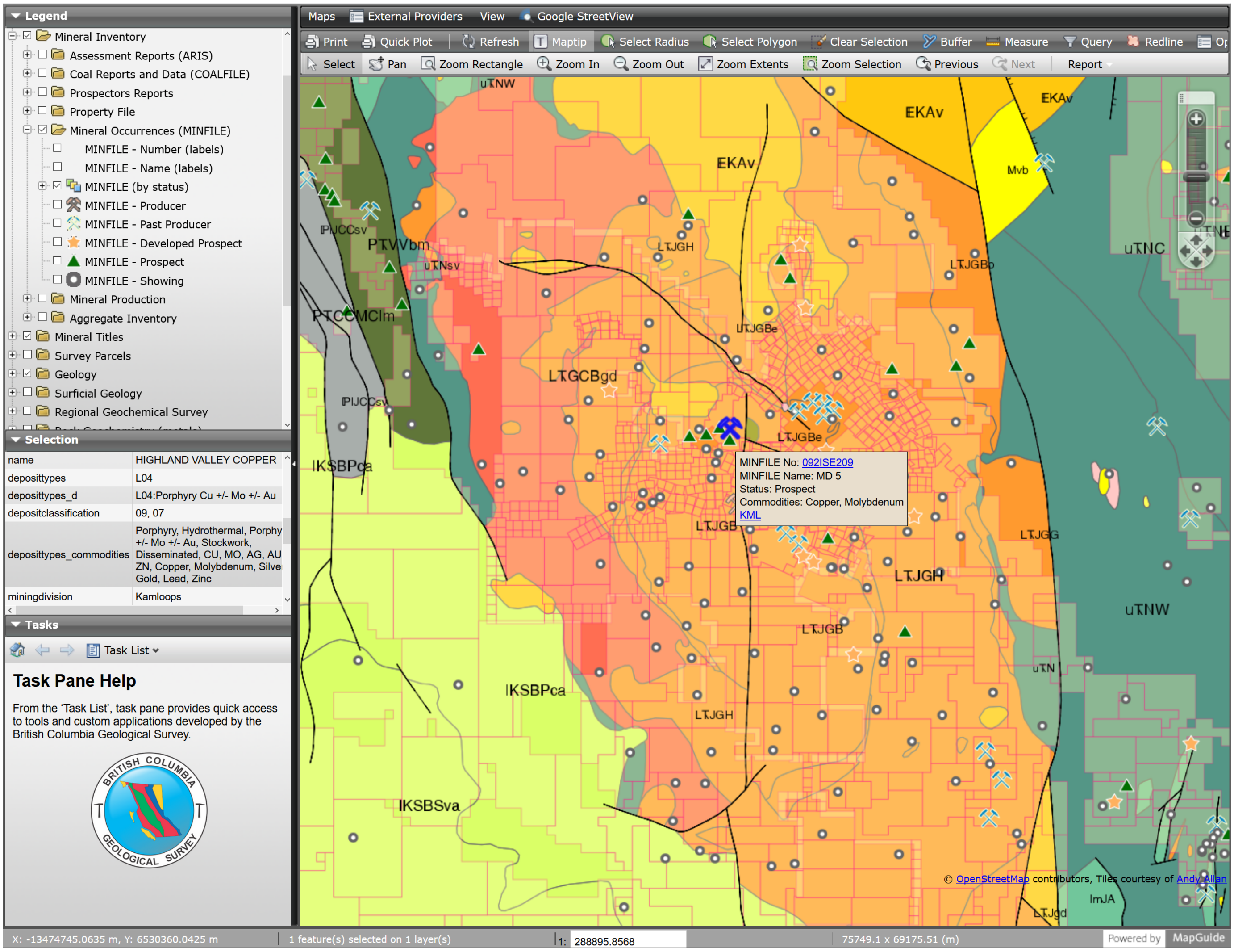

Fig. 9. MapPlace interface with the geology of the Highland Valley mine area and data from MINFILE, and Mineral Titles Online.

15,900 boreholes, 550 bulk samples, 5500 maps, 3650 trenches, 484 coal ash chemistry analyses and links to MINFILE. COALFILE data are integrated with MapPlace.

MINFILE is a database for mineral, coal, and industrial mineral occurrences and associated details on geology and economic information for more than 15,000 records. In the last year, more than 200 new occurrences and 480 updates were added to the database. The web-enabled MINFILE search application interacts with MapPlace, ARIS and Property File. The BCGS implemented the open geoscience standard EarthResourceML and developed interoperable connections of the Survey's mineral inventory databases for the OneGeology portal.

Property File is a collection of more than 82,400 archived reports, maps, photos, and technical notes documenting mineral exploration activities in British Columbia from the late 1800s. These documents are accessible in a full-text, searchable, online database. Recent additions include 1400 documents from Albert Reeves, 1900 documents from Gerry Carlson, and the complete collection of George Cross Newsletters. The records are spatially linked to MINFILE. The Survey accepts donations to Property File.

The provincial geochemical databases hold field and geochemical data from multi-media surveys by the Geological Survey of Canada, the BCGS, and Geoscience BC. The databases are updated regularly and contain results from: 1) the Regional Geochemical Survey program (RGS) including analyses from more than 65,000 stream-sediment, lake-sediment, moss, and water samples; 2) 10,500 till surveys; and 3) 11,000 lithogeochemical samples.

4.4. British Columbia digital geology map

The BCGS offers province-wide integrated digital coverage of bedrock geology, including details from compilation of field mapping at scales from 1:50,000 to 1:250,000. The British Columbia digital geology continuously integrates new regional compilations. The bedrock geology is standardized with consistent stratigraphic coding, ages, and rock types to enable computations. The digital geology is available for download in GeoPackage and Esri shapefile formats. Customized bedrock geological maps and legends can be explored and data downloaded as KML by spatial and non-spatial queries via MapPlace. The Survey is using vocabularies adopted by the Commission for the Management and Application of Geoscience Information, which enables the access to the digital geology on the OneGeology portal and allows interoperable connections of Survey databases to the exploration and mining industry.

5. Mineral Development Office

The Mineral Development Office is the Vancouver base of the British Columbia Geological Survey. It links the more than 800 exploration and mining companies headquartered in Vancouver to provincial mineral and coal information. The MDO distributes Survey data and provides technical information and expertise about mineral opportunities to the domestic and international investment community. The MDO monitors the activities of the mining and exploration sectors and co-ordinates production of the 'Provincial Overview of Exploration and Mining in British Columbia', an annual volume that summarizes activities in the different regions of the province and written by the Regional Geologists and the MDO (see e.g., Clarke et al., 2020).

6. Regional Geologists

The British Columbia Regional Geologists (Table 1) represent the provincial government on geological matters at a regional level and capture information on industry activity in their jurisdictions. Within their communities, they provide information on exploration trends, possible investment opportunities, land use processes, First Nation capacity building, and public outreach. We welcome Sean Tombe as the new Regional Geologist for the Northwest Region.

Table 1. British Columbia Regional Geologists.

Regional Geologist	Office	Region
Sean Tombe	Smithers	Northwest
Vacant	Prince George	Northeast and North Central
Vacant	Kamloops	South Central
Fiona Katay	Cranbrook	Southeast
Bruce Northcote	Vancouver	Southwest

Acknowledgment

We thank George Owsiacki of Total Earth Science Services (Victoria) for the desktop publishing of this volume.

References cited

Akam, C., Simandl, G.J., Let, R., Paradis, P., Hoshino, M., Kon,Y., Araoka, D., Green, C., Kodama, S., Takagi, T., and Chaudhry, M., 2019. Comparison of methods for the geochemical determination of rare earth elements: Rock Canyon Creek REE–F–Ba deposit case study, SE British Columbia, Canada. Geochemistry: Exploration, Environment, Analysis 19, 414-430. https://doi.org/10.1144/geochem2018-044.

Alldrick, D.J., Dawson, G.L., Bosher, J.A., and Webster, I.C.L., 1986. Geology of the Kitsault River Area (NTS 103P), British Columbia British Columbia Ministry of Energy and Mines, British Columbia Geological Survey Open File 1986-02, scale 1:50,000.

Clarke, G., Northcote, B., Katay, F., and Tombe, S.P., 2020. Exploration and Mining in British Columbia, 2019: A summary. In: Provincial Overview of Exploration and Mining in British Columbia, 2019. British Columbia Ministry of Energy, Mines and Petroleum Resources, British Columbia Geological Survey Information Circular 2020-01, in press.

Elia, E.A., and Ferbey, T., 2020. Generating photogrammetric DEMs in the field from remotely piloted aircraft systems. In: Geological Fieldwork 2019, British Columbia Ministry of Energy, Mines and Petroleum Resources, British Columbia Geological Survey Paper 2020-01, pp. 189-200.

Ferbey, T., Plouffe, A., and Bustard, A.L., 2016. Geochemical, mineralogical, and textural data from tills in the Highland Valley Copper mine area, south-central British Columbia. British Columbia Ministry of Energy, Mines and Petroleum Resources, British Columbia Geological Survey GeoFile 2016-11, 15 p.

Han, T., Rukhlov, A.S., Riddell, J.M., and Ferbey, T., 2019. A skeleton data model for geochemical databases at the British Columbia Geological Survey. In: Geological Fieldwork 2018, British Columbia Ministry of Energy, Mines and Petroleum Resources, British Columbia Geological Survey Paper 2019-01, pp. 125-135.

Hunter, R.C., and van Straaten, B.I., 2020. Preliminary stratigraphy and geochronology of the Hazelton Group, Kitsault River area, Stikine terrane, northwest British Columbia. In: Geological Fieldwork 2019, British Columbia Ministry of Energy, Mines and Petroleum Resources, British Columbia Geological Survey Paper 2020-01, pp. 101-118.

Mihalynuk, M.G., Logan, J.M., Diakow, L.J., Henderson, M.A., Jacob, J., and Watson, A.K.G., 2014. Allison Creek area preliminary geology (NTS 92H/9W and 10E) (and parts of adjacent sheets north and south), British Columbia Ministry of Energy, Mines and Petroleum Resources, British Columbia Geological Survey Open File 2014-05, scale 1:50,000.

Mihalynuk, M.G., Diakow, L.J., Logan, J.M, and Friedman, R.M., 2015. Preliminary geology of the Shrimpton Creek area (NTS 092H/15E, 16W) Southern Nicola Arc Project. In: Geological Fieldwork 2014, British Columbia Ministry of Energy, Mines and Petroleum Resources, British Columbia Geological Survey Paper 2015-1, pp. 129-163.

Mihalynuk, M.G., Diakow, L.J., Friedman, R.M., and Logan, J.M., 2016. Chronology of southern Nicola arc stratigraphy and deformation. In: Geological Fieldwork 2015, British Columbia Ministry of Energy and Mines, British Columbia Geological Survey Paper 2016-1, pp. 31-63.

Miller, E.A., Kennedy, L.A., and van Straaten, B.I., 2020. Geology of the Kinskuch Lake area and Big Bulk porphyry prospect, northwestern British Columbia: Syndepositional faulting and basin formation during the Rhaetian (latest Triassic) transition from the Stuhini to the Hazelton Group. In: Geological Fieldwork 2019, British Columbia Ministry of Energy, Mines and Petroleum Resources, British Columbia Geological Survey Paper 2020-01, pp. 77-99.

Nelson, J., Waldron, J., van Straaten, B., Zagorevski, A., and Rees, C., 2018. Revised stratigraphy of the Hazelton Group in the Iskut River region, northwestern British Columbia. In: Geological Fieldwork 2017, British Columbia Ministry of Energy, Mines and Petroleum Resources, British Columbia Geological Survey Paper 2018-1, pp. 15-38.

Nixon, G.T., Friedman, R.M., and Creaser, R.A., 2020. Late Neogene porphyry Cu-Mo(±Au-Ag) mineralization in British Columbia: the Klaskish Plutonic Suite, northern Vancouver Island. In: Geological Fieldwork 2019, British Columbia Ministry of Energy, Mines and

Petroleum Resources, British Columbia Geological Survey Paper 2020-01, pp. 119-132.

Norris, J., and Fortin, G., 2019. Assessment report-sourced surface sediment geochemical database: Development and initial data release from the Interior Plateau. British Columbia Ministry of Energy, Mines and Petroleum Resources, British Columbia Geological Survey GeoFile 2019-04, 10 p.

Nott, J., Milidragovic, D., Nixon, G., and Scoates, J., 2020. New geological investigations of the Polaris ultramafic-mafic Alaskan-type intrusion (Early Jurassic), north-central British Columbia. In: Geological Fieldwork 2019, British Columbia Ministry of Energy, Mines and Petroleum Resources, British Columbia Geological Survey Paper 2020-01, pp. 59-76.

Ootes, L., Bergen, A., Milidragovic, D., Graham, B., and Simmonds, R., 2019a. Preliminary geology of northern Hogem batholith, Quesnel terrane, north-central British Columbia. In: Geological Fieldwork 2018, British Columbia Ministry of Energy, Mines and Petroleum Resources, British Columbia Geological Survey Paper 2019-01, pp. 31-53.

Ootes, L., Bergen, A.L., Milidragovic, D., and Graham, B., 2019b. Preliminary bedrock geology of Notch Peak and Ogden Creek (parts of NT S 094C/04 and 093N/13), northern Hogem batholith, Quesnel terrane, north-central British Columbia, British Columbia Ministry of Energy, Mines and Petroleum Resources, British Columbia Geological Survey Open File 2019-02, scale 1:50,000.

Ootes, L., Bergen, A.L., Milidragovic, D., Jones, G.O., Camacho, A., and Friedman, R., 2020a. An update on the geology of northern Hogem batholith and its surroundings, north-central British Columbia. In: Geological Fieldwork 2019, British Columbia Ministry of Energy, Mines and Petroleum Resources, British Columbia Geological Survey Paper 2020-01, pp. 25-47.

Ootes, L., Bergen, A.L., Milidragovic, D., and Jones, G.O., 2020b. Preliminary geology of the northern Hogem batholith and its surroundings, north-central British Columbia. British Columbia Ministry of Energy, Mines and Petroleum Resources, British Columbia Geological Survey Open File 2020-02, scale 1:50,000.

Paradis, S., and Simandl, G.J., 2019. Preliminary carbon and oxygen isotope analyses of hydrothermal carbonates from Mississippi Valley-type and REE-F-Ba deposits of the southern Canadian Rocky Mountains–a comparison. In: Rogers, N., (Ed.), Targeted Geoscience Initiative: 2018 Report of Activities, Geological Survey of Canada Open File 8549, pp. 205-216. https://doi.org/10.4095/313652.

Rukhlov, A.S., Fortin, G., Kaplenkov, G.N., Lett, R.E., Lai, V. W.-M., and Weis, D., 2020. Multi-media geochemical and Pb isotopic evaluation of modern drainages on Vancouver Island. In: Geological Fieldwork 2019, British Columbia Ministry of Energy, Mines and Petroleum Resources, British Columbia Geological Survey Paper 2020-01, pp. 133-167.

Schiarizza, P., 2016. Toward a regional stratigraphic framework for the Nicola Group: Preliminary results from the Bridge Lake-Quesnel River area. In: Geological Fieldwork 2015, British Columbia Ministry of Energy, Mines and Petroleum Resources, British Columbia Geological Survey Paper 2016-1, pp. 13-30.

Schiarizza, P., 2017. Ongoing stratigraphic studies in the Nicola Group: Stump Lake-Salmon River area, southcentral British Columbia. In: Geological Fieldwork 2016, British Columbia Ministry of Energy, Mines and Petroleum Resources, British Columbia Geological Survey Paper 2017-1, pp. 17-33.

Schiarizza, P., 2018. Geology of the Spanish Lake area, south-central British Columbia. In: Geological Fieldwork 2017, British Columbia Ministry of Energy, Mines and Petroleum Resources, British Columbia Geological Survey Paper 2018-1, pp. 143-156.

Schiarizza, P., 2019. Geology of the Nicola Group in the Bridge Lake-Quesnel River area, south-central British Columbia. In: Geological Fieldwork 2018, British Columbia Ministry of Energy, Mines and Petroleum Resources, British Columbia Geological Survey Paper 2019-01, pp. 15-30.

Schiarizza, P., Monger, J.W.H., Friedman, R.M., and Northcote, B., 2020. Detrital zircons from the Gun Lake unit, Gold Bridge area, southwestern British Columbia. In: Geological Fieldwork 2019, British Columbia Ministry of Energy, Mines and Petroleum Resources, British Columbia Geological Survey Paper 2020-01, pp. 13-24.

Shewchuk, C., Ferbey, T., and Lian, O.B., 2020. Detecting porphyry Cu-Mo mineralization using major oxides and pathfinder elements in subglacial till, Highland Valley mine area, south-central British Columbia. In: Geological Fieldwork 2019, British Columbia Ministry of Energy, Mines and Petroleum Resources, British Columbia Geological Survey Paper 2020-01, pp. 169-187.

Steinthorsdottir, K., Cutts, J., Dipple, G., Milidragovic, D., and Jones, F., 2020. Origin and serpentinization of ultramafic rocks in dismembered ophiolite north of Trembleur Lake, central British Columbia. In: Geological Fieldwork 2019, British Columbia Ministry of Energy, Mines and Petroleum Resources, British Columbia Geological Survey Paper 2020-01, pp. 49-58.

Simandl, G.J., Petrus, J.A., Leybourne, M.I., Paradis, S., and Akam, C., 2019. Characterization of primary fersmite from the Mount Brussilof magnesite deposit, southeastern British Columbia. In: Geological Fieldwork 2018, British Columbia Ministry of Energy, Mines and Petroleum Resources, British Columbia Geological Survey Paper 2019-01, pp. 113-123.

van Straaten, B.I., Logan, J.M., and Diakow, L.J., 2012. Mesozoic magmatism and metallogeny of the Hotailuh batholith, northwestern British Columbia. British Columbia Ministry of Energy, Mines and Petroleum Resources, British Columbia Geological Survey Open File 2012-06, 58 p.

van Straaten, B.I., and Bichlmaier, S.J., 2018. Preliminary bedrock geology of the McBride River area, British Columbia, British Columbia Ministry of Energy, Mines and Petroleum Resources, British Columbia Geological Survey Open File 2018-03, scale 1:50,000.

van Straaten, B.I., Gibson, R., and Nelson, J., 2017. Preliminary bedrock geology of the Tanzilla and McBride area, British Columbia Ministry of Energy, Mines and Petroleum Resources, British Columbia Geological Survey Open File 2017-09, scale 1:50,000.

van Straaten, B.I., and Wearmouth, C.D., 2019. Preliminary bedrock geology of the Latham and Pallen Creek area, British Columbia Ministry of Energy, Mines and Petroleum Resources, British Columbia Geological Survey Open File 2019-05, scale 1:50,000.

In memoriam
Dr. Victor M. Levson (1956-2019)

Victor M. Levson passed away on 31 March 2019, at the age of 62. Vic was a Quaternary geologist and spent most of his professional career at the British Columbia Ministry of Energy, Mines and Petroleum Resources in Victoria. He first worked as a Quaternary geologist with the British Columbia Geological Survey (1989 to 2002) and then moved to the Oil and Gas Division where he started as a Quaternary geologist, moved to Director of Petroleum Geoscience and then went on to head the Resource Development and Geoscience Branch (2002 to 2009).

Vic was a pioneer of drift prospecting in the Canadian Cordillera. He made significant contributions to the discipline and provided important insights into the Quaternary history of British Columbia, and the effect of complex ice-flow histories (including ice-flow reversals) on the clastic dispersal of mineralized bedrock in subglacial tills. Vic also wrote important papers on the stratigraphy and geologic settings of gold placers in the Cariboo and Atlin regions of British Columbia.

Vic's M.Sc. and Ph.D. work focussed on the Quaternary sedimentology, stratigraphy, and history of the Jasper area under the supervision of Nat Rutter at the University of Alberta. He joined the British Columbia Geological Survey in 1989 and completed his Ph.D. in 1995. Upon leaving government in 2009, he formed his own consultancy, Quaternary Geosciences Inc. Throughout his career Vic was keenly interested in applied aspects of Quaternary geology, across a diverse range of research topics. He is best known for his contributions to Canadian Quaternary stratigraphy, sedimentology, and ice-flow histories, seismic hazard maps for parts of southwest British Columbia, and drift prospecting method development for the Canadian Cordillera. Vic authored or co-authored more than 150 scientific papers, reports and maps, and wrote countless conference abstracts and presentations. Known for his astute observations and attention to detail, his till geochemical datasets continue to guide mineral exploration in central British Columbia.

Vic was also an Adjunct Professor in the School of Earth and Ocean Sciences, University of Victoria, where he supervised 10 graduate students. He served as an external examiner for many theses at University of Victoria and other Canadian schools. For 18 years Vic taught a fourth-year applied Quaternary geology course at the University of Victoria. A highlight of the undergraduate program, this course inspired many students to pursue careers in Quaternary geology. His annual four-day field trip through Washington State, with stops at the Channeled Scablands and Mount Baker, became legend. Vic also lectured in the Department of Geography (University of Victoria) and the Department of Chemistry and Geoscience (Camosun College).

Perhaps Vic's greatest contribution was how he treated people. Not only was Vic a respected geoscientist and gifted teacher, he was a selfless mentor and friend. Vic taught all of us fortunate to have worked with him how 'to do the right thing', a legacy that will endure. He led by example and passed on a set of core values that have continued to guide us well.

Cherished by his family, Vic squeezed the most out of every day. We will miss his infectious laugh, ingenious practical jokes, and unwavering friendship.

Detrital zircons from the Gun Lake unit, Gold Bridge area, southwestern British Columbia

Paul Schiarizza[1, a], James W.H. Monger[2], Richard M. Friedman[3], and Bruce Northcote[1]

[1] British Columbia Geological Survey, Ministry of Energy, Mines and Petroleum Resources, 300-865 Hornby Street, Vancouver, BC, V6Z 2G3
[2] Geological Survey of Canada, 1500-605 Robson Street, Vancouver, BC, V5A 1S6
[3] Pacific Centre for Isotopic and Geochemical Research, The University of British Columbia, Vancouver, BC, V6T 1Z4
[a] corresponding author: Paul.Schiarizza@gov.bc.ca

Recommended citation: Schiarizza, P., Monger, J.W.H., Friedman, R.M., and Northcote, B., 2020. Detrital zircons from the Gun Lake unit, Gold Bridge area, southwestern British Columbia. In: Geological Fieldwork 2019, British Columbia Ministry of Energy, Mines and Petroleum Resources, British Columbia Geological Survey Paper 2020-01, pp. 13-24.

Abstract

Undated siliciclastic rocks that rest above the Bridge River complex (Mississippian-Jurassic) at several localities near Gold Bridge were previously assigned to the Gun Lake unit and thought to correlate with the basal Callovian-early Oxfordian unit of the Relay Mountain Group (lower Tyaughton basin). Detrital zircons analyzed from two of these localities show that the sampled rocks represent two different units, both younger than the basal unit of the Relay Mountain Group. The Gun Lake unit near Downton Lake contains detrital zircons ranging from 180 to 118 Ma. We now correlate these rocks with the Paradise Formation (Aptian-early Albian) of the Taylor Creek Group (upper part of the Tyaughton basin). Our results are consistent with previous interpretations of a western source in the southwest part of the Coast belt. The Gun Lake unit near Truax Creek contains detrital zircons that mostly fall within a restricted time span between 165 and 142 Ma, with a much smaller population of Late Triassic (214-208 Ma) grains. These rocks, and the adjacent Truax Creek conglomerate, are here correlated with the middle (upper Oxfordian-Valanginian) unit of the Relay Mountain Group. A likely source area to the northeast includes Cadwallader terrane and a Late Jurassic volcanic-plutonic belt that cuts across it.

Keywords: Gun Lake unit, Bridge River complex, Tyaughton basin, Relay Mountain Group, Taylor Creek Group, Paradise Formation, Cayoosh assemblage

1. Introduction

Bridge River terrane is a tract of oceanic rocks exposed in the eastern Coast Mountains of southwestern British Columbia (Fig. 1), where it forms the boundary between markedly different geologic domains. To the west are assemblages of the southwestern Coast belt (Monger and Journeay, 1994), including the Harrison arc terrane (Triassic-Jurassic), Early Cretaceous arc volcanic and sedimentary rocks of the Gambier Group, and voluminous Middle Jurassic to Late Cretaceous granitic intrusions. To the east are Cadwallader, Cache Creek and Quesnel terranes (late Paleozoic-Middle Jurassic), the Methow basin (Jurassic-Cretaceous), and belts of Late Jurassic and Early Cretaceous volcanic and plutonic rocks that cut across the older terrane boundaries (Monger, 1989; Monger and McMillan, 1989; Mahoney et al., 2013; Schiarizza, 2013).

Bridge River terrane consists mainly of Paleozoic-Mesozoic assemblages of predominantly chert and basalt that Monger and Journeay (1994) considered part of a subduction-related accretionary wedge. The Bridge River complex is the predominant component; correlative rocks of the Hozameen Group form the southeast part of the terrane, and rocks of the Cogburn Group, metamorphosed to amphibolite grade, form the southwestern part (Monger, 1989). Siliciclastic sedimentary and metasedimentary rocks are distributed along the full length of the terrane and include the Cayoosh assemblage (above the Bridge River complex), and the correlative(?) Settler schist, which is spatially associated with the Cogburn Group in the

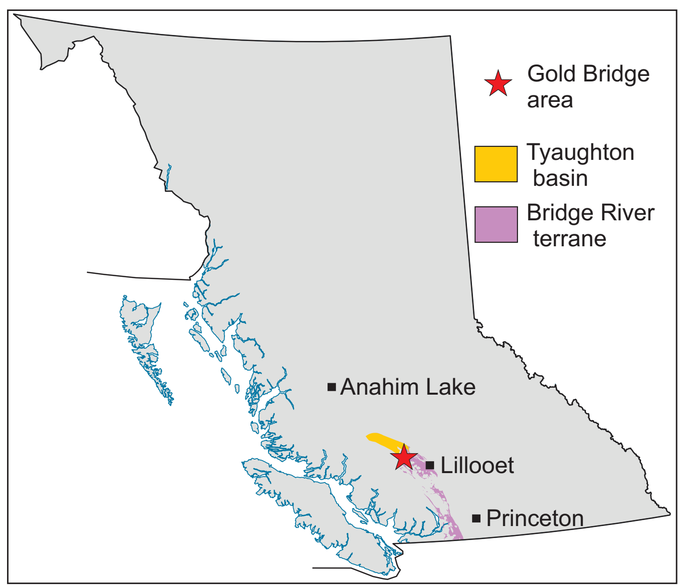

Fig. 1. Location of the Gold Bridge area and the main exposures of the Bridge River terrane and Tyaughton basin.

southwest part of the terrane (Monger, 1989, 1991; Journeay and Mahoney, 1994). These siliciclastic rocks are commonly included in Bridge River terrane, but it is generally unclear if they are an integral part or represent an overlying overlap assemblage (Monger and Journeay, 1994).

The Bridge River complex is best understood near the northern limit of Bridge River terrane, near Gold Bridge, where Cordey and Schiarizza (1993) interpreted it as an accretionary complex because of its lithologic components (radiolarian chert, basalt, glaucophane schist), wide age range (Mississippian to late Middle Jurassic), and lack of a coherent stratigraphy. Siliciclastic rocks inferred to rest depositionally above the Bridge River complex at several localities in this area were mapped as the Gun Lake unit by Schiarizza et al. (1997). Undated, these rocks were thought to correlate with the Relay Mountain Group (lower part of Tyaughton basin) exposed to the north and/or to parts of the Cayoosh assemblage overlying the Bridge River complex to the south. In this study we analyzed detrital zircons from two samples of the Gun Lake unit, to establish maximum depositional ages, provenance, and possible correlations with strata of the Tyaughton basin.

2. Geology of the Gold Bridge area

The community of Gold Bridge, 180 km north of Vancouver, is in the valley of the Bridge River, now occupied by Downton and Carpenter lakes, which cuts through rugged terrain of the southeastern Coast Mountains (Fig. 2). The area around Gold Bridge is underlain predominantly by chert, basalt and related rocks of the Bridge River complex (Mississippian to Jurassic). It is also underlain by Jura-Cretaceous siliciclastic rocks of the Tyaughton basin, undated siliciclastic rocks that rest stratigraphically above the Bridge River complex south of the Tyaughton basin (Gun Lake unit and Cayoosh assemblage), fault panels containing late Paleozoic and Mesozoic rocks of the Cadwallader arc terrane, and Late Cretaceous and Tertiary granitoid intrusions (Fig. 2). Structures in the area include several generations of southwest-directed thrusts (mid- to Late Cretaceous), slightly younger northeast-vergent thrusts and folds, and an array of northwest-trending dextral strike-slip faults and related structures that are part of the latest Cretaceous and early Tertiary Yalakom fault system (Umhoefer and Schiarizza, 1996; Schiarizza et al., 1997). Within the Bridge River complex these map-scale structures are superimposed on older structures attributed to deformation in an accretionary complex.

The Bridge River complex comprises rocks previously referred to as Bridge River Series (McCann, 1922), Fergusson Series (Cairnes, 1937, 1943) and Bridge River Group (Woodsworth, 1977). It is a heterogeneous assemblage of rocks lacking a coherent map-scale stratigraphy and with many outcrop-scale faults and folds (Schiarizza et al., 1997). Radiolarian chert and basalt are the predominant components, but it also includes argillite, limestone, gabbro, diabase, serpentinite, sandstone, siltstone, and conglomerate. Cherts dated with radiolarians range from Mississippian to late Middle Jurassic (Cordey and Schiarizza, 1993), limestones dated with conodonts are mainly Late Triassic, and a belt of blueschist-facies rocks, traced for 14 km near Tyaughton Lake (Fig. 2) has yielded Late Triassic Ar-Ar ages on white mica (Schiarizza et al., 1997).

The Tyaughton basin, exposed mainly north and northwest of the Gold Bridge area, includes a lower component (late Middle Jurassic to Early Cretaceous) represented by sandstone, siltstone, shale, and conglomerate of the Relay Mountain Group (Umhoefer et al., 2002), and an upper component (mid-Cretaceous) represented by the Taylor Creek Group and Silverquick Formation (Garver, 1989, 1992). The Relay Mountain Group is subdivided into lower (Callovian-lower Oxfordian), middle (upper Oxfordian-Valanginian), and upper (Hauterivian) units. The base of the group is not exposed, but it is inferred to have been deposited, at least in part, on the Bridge River complex (Schiarizza et al., 1997; Umhoefer et al., 2002). The Taylor Creek Group comprises synorogenic conglomerates, sandstones, and shales that were deposited unconformably above the Relay Mountain Group and, locally, the Bridge River complex. It includes three main compositionally distinct units (Garver, 1989, 1992): one derived from volcanic rocks to the west (Paradise Formation); one derived mainly from the Bridge River complex (Dash Formation); and one consisting of arkoses derived from the east (Lizard Formation).

The Relay Mountain Group crops out only in the northwest corner of the Gold Bridge area, where it is structurally overlain to the east by fault panels of Cadwallader terrane and is truncated to the south by Late Cretaceous granodiorite (Fig. 2). However, a narrow fault-bounded lens in the Bridge River complex on the south side of Carpenter Lake, 11 km NE of Gold Bridge, may be correlative. This lens (Truax Creek conglomerate on Fig. 2) comprises unstratified pebble to cobble conglomerate containing mainly felsic to intermediate volcanic clasts, with a smaller but significant number of clasts derived from mafic volcanic rocks, granitic to gabbroic plutonic rocks, shale, and siltstone. Church and MacLean (1987) reported that fossils collected from a small siltstone lens in the conglomerate were identified as *Buchia* sp. (latest Jurassic?), making it the same age as the middle part of the Relay Mountain Group.

The upper part of the Tyaughton basin is represented by a well-exposed section of mid-Cretaceous (Albian-Cenomanian) rocks that crosses Tyaughton Lake in the north-central part of the Gold Bridge area (Fig. 2; Garver, 1989, 1992). This section, from bottom to top, consists of chert-rich conglomerates of the Dash Formation, mica-bearing quartzofeldspathic sandstones of the Lizard Formation, and polymictic conglomerates of the Silverquick Formation. The latter unit is locally overlain by volcanic and volcaniclastic rocks included in the Powell Creek Formation, a unit of subaerial arc volcanic rocks that makes extensive exposures northwest of the Gold Bridge area. The Dash Formation is the oldest unit of the Taylor Creek Group exposed in the Tyaughton Lake area, where it rests unconformably above the Bridge River complex, including blueschist facies metamorphic rocks (Fig. 2). However, Taylor Creek Group exposures to the northwest include an older unit

(Paradise Formation) that rests stratigraphically beneath the Dash Formation.

Cadwallader terrane, represented mainly by exposures east, northeast, and northwest of Bridge River terrane (Schiarizza, 2013) forms a number of composite fault panels across the full width of the Gold Bridge area (Fig. 2). The Cadwallader Group, including Late Triassic arc basalts of the Pioneer Formation and overlying Late Triassic arc-derived sandstone and conglomerate of the Hurley Formation (Rusmore, 1987) is the predominant component in all these fault panels. The panels invariably contain slices of the Bralorne-East Liza complex (Early Permian), which includes diorite, gabbro, metabasalt and serpentinized ultramafic rocks. These plutonic and volcanic rocks are correlated with crustal components of the Shulaps ophiolite complex, which is exposed east and northeast of the Gold Bridge area and is juxtaposed above the Cadwallader Group across west-directed thrusts (Calon et al., 1990; Schiarizza et al., 1997). Fault panels of Cadwallader Group and Bralorne-East Liza complex in the Gold Bridge area are interpreted as remnants of mid-Cretaceous sheets that were thrust westward over the Bridge River complex and Tyaughton basin then cut and segmented by younger structures (Schiarizza et al., 1997).

2.1. Gun Lake unit

Schiarizza et al. (1997) introduced the term Gun Lake unit for undated siliciclastic rocks they mapped at five different localities near Gold Bridge (Fig. 2) in the southern part of the Taseko-Bridge River map area. At each locality, the rocks are known or inferred to be in depositional contact with underlying rocks of the Bridge River complex and consist mainly of argillite, siltstone, and feldspathic volcanic-lithic sandstone. Two northwest-trending belts near Downton and Gun lakes had previously been mapped as Noel Formation by Cairnes (1937, 1943), who recognized that they were in depositional contact above the Bridge River complex (his Fergusson Series). The three small belts assigned to the Gun Lake unit farther east had previously been included in undifferentiated Bridge River Group (Woodsworth, 1977). Schiarizza et al. (1997) correlated the Gun Lake unit with the lower part of the Cayoosh assemblage to the south (Mahoney and Journeay, 1993; Journeay and Mahoney, 1994) and with the lower unit of the Relay Mountain Group to the north, but also noted that the Gun Lake sandstones are lithologically similar to narrow lenses of volcanic-rich sandstone, none of mappable extent, that are included in the Bridge River complex.

2.2. Cayoosh assemblage

The Cayoosh assemblage comprises undated siliciclastic rocks, mainly phyllitic argillite, siltstone and sandstone, that overlie the Bridge River complex over large areas mainly to the south of the Gold Bridge area (Mahoney and Journeay, 1993; Journeay and Mahoney, 1994). The assemblage was traced into the southern part of the Gold Bridge area (Fig. 2) by Journeay and Mahoney (1994) and Monger and Journeay (1994). These Cayoosh exposures were inferred to correlate with the Gun Lake unit (Monger and Journeay, 1994; Schiarizza et al., 1997) and, like the Gun Lake unit, included rocks that had been mapped as Noel Formation by Cairnes (1937, 1943).

3. Detrital zircon geochronology

Here we present the results from isotopic analyses of detrital zircons extracted from two samples from the Gun Lake unit. The samples were collected in September 2015, from outcrops that had previously been mapped by Schiarizza et al. (1997). Sample preparation and analytical work (LA-ICP-MS) was conducted at the Pacific Centre for Isotopic and Geochemical Research (PCIGR), the Department of Earth, Ocean and Atmospheric Sciences, the University of British Columbia. Sample 15PSC-185 was processed in 2016, using a New Wave UP-213 laser ablation system, and techniques summarized by Mihalynuk et al. (2016). Sample 15PSC-183 was processed in 2017 using a Resonetics RESOlution M-50-LR, with procedures summarized here.

Following mineral separation by standard procedures, zircons were handpicked in alcohol and mounted in epoxy, along with reference materials. Grain mounts were then wet ground with carbide abrasive paper and polished with diamond paste. Next, cathodoluminescence (CL) imaging was carried out on a Philips XL-30 scanning electron microscope (SEM) equipped with a Bruker Quanta 200 energy-dispersion X-ray microanalysis system at the Electron Microbeam/X-Ray Diffraction Facility (EMXDF). An operating voltage of 15 kV was used, with a spot diameter of 6 µm and peak count time of 30 seconds. After removal of the carbon coat, the grain mount surface was washed with mild soap and rinsed with high-purity water. Before analysis, the grain mount surface was cleaned with 3 N HNO_3 acid and again rinsed with high-purity water to remove any surficial Pb contamination that could interfere with the early portions of the spot analyses.

Analyses were conducted using a Resonetics RESOlution M-50-LR, which contains a Class I laser device equipped with a UV excimer laser source (Coherent COMPex Pro 110, 193 nm, pulse width of 4 ns) and a two-volume cell designed and developed by Laurin Technic Pty. Ltd. (Australia). This sample chamber allowed us to investigate several grain mounts in one analytical session. The laser path was fluxed by N_2 to ensure better stability. Ablation was carried out in a cell with a volume of approximately 20 cm^3 and a He gas stream that ensured better signal stability and lower U-Pb fractionation (Eggins et al., 1998). The laser cell was connected via a Teflon squid to an Agilent 7700x quadrupole ICP-MS housed at PCIGR. A pre-ablation shot was used to ensure that the spot area on grain surface was free of contamination. Samples and reference materials were analyzed for 36 isotopes, including Pb (^{204}Pb, ^{206}Pb, ^{207}Pb, ^{208}Pb), ^{232}Th, and U (^{235}U, ^{238}U) with a dwell time of 0.02 seconds for each isotope. Pb/U and Pb/Pb ratios were determined on the same spots along with trace element concentrations. The settings for the laser were: spot size of 34 µm with a total ablation time of 30 seconds, frequency of

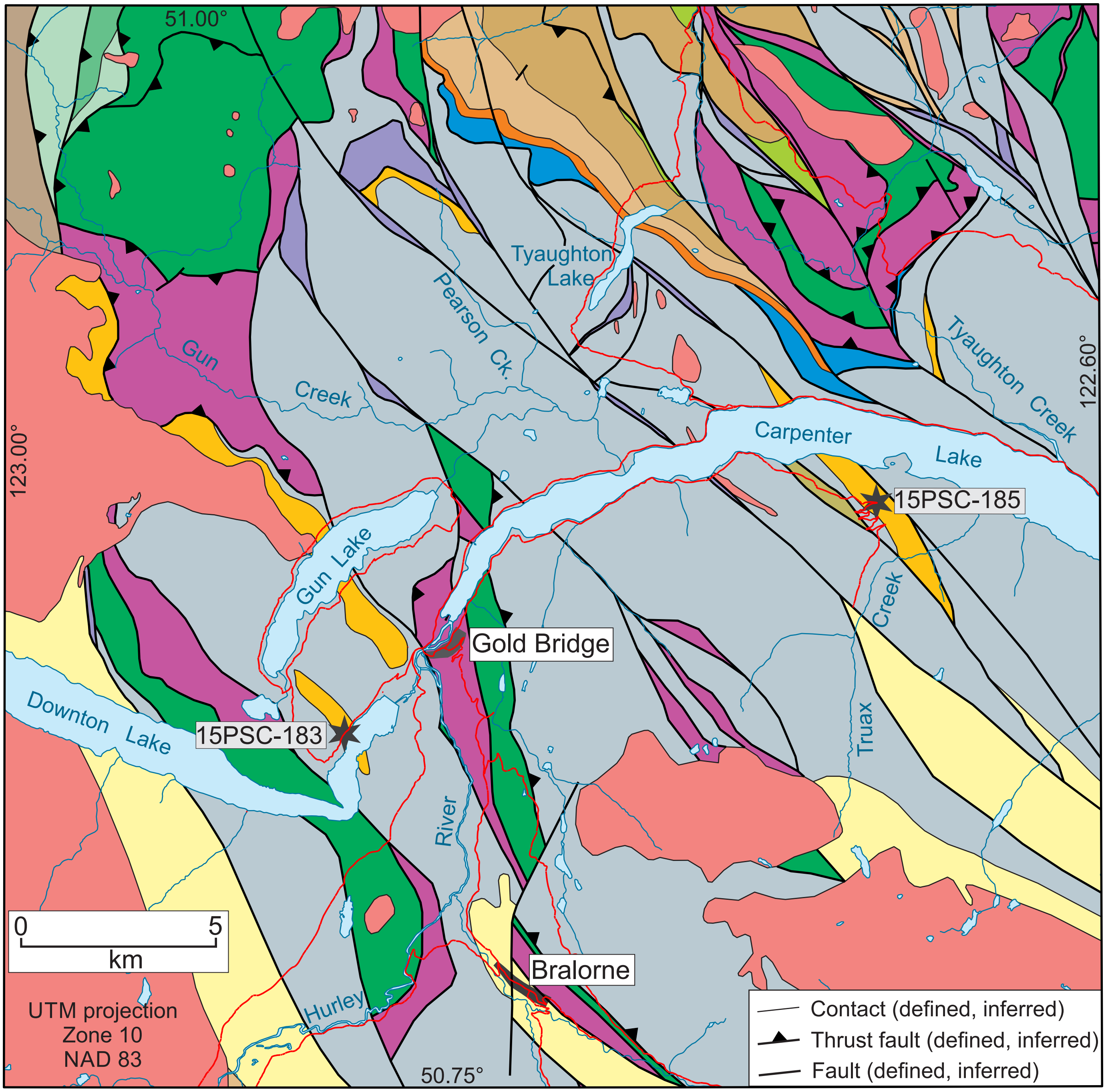

Fig. 2. Geologic map of the Gold Bridge area showing locations of the two samples discussed in this report. Geology mainly from Schiarizza et al. (1997) and Monger and Journeay (1994).

5 Hz, fluence of 5 J/cm^2, power of 7.8 mJ after attenuation, pit depths of approximately 15 µm, He flow rate of 800 mL/min, N_2 flow rate of 2 mL/min, and a carrier gas (Ar) flow rate of 0.57 L/min.

Reference materials were analyzed throughout the sequence to allow for drift correction and to characterize downhole fractionation for Pb/U and Pb/Pb isotopic ratios. For U-Pb analyses, natural zircon reference materials were used, including Plešovice (Sláma et al., 2008) or 91500 (Wiedenbeck et al., 1995, 2004) as the internal reference material, and both Temora2 (Black et al., 2004) and Plešovice and/or 91500 as monitoring reference materials; the zircon reference materials were placed between the unknowns. Raw data were reduced using the Iolite 3.4 extension (Paton et al., 2011) for Igor Pro™ yielding U/Pb ages, and their respective uncertainties. Final interpretation and plotting of the analytical results employed the ISOPLOT software of Ludwig (2003).

Fig. 2. Continued.

3.1. Sample 15PSC-183, Downton Lake

Sample 15PSC-183 was collected from a roadside outcrop (508736E, 5631125N, UTM Zone 10, NAD 83) on the north side of Downton Lake, 1.5 km southwest of the Lajoie dam at the northeast end of the lake. Here, the Gun Lake unit forms a narrow northwest-trending outlier that was mapped as Noel Formation by Cairnes (1937) and inferred to form the core of a minor synform. The surrounding Bridge River complex is mostly undated, but chert exposed about 800 m southwest of the sample site yielded Late Triassic (Late Norian) radiolarians (F. Cordey in Schiarizza et al., 1997). The sampled outcrop (Fig. 3) consists of medium to dark grey, medium- to coarse-grained sandstone, locally intercalated with lenses (2-30 cm) of dark grey slaty argillite. Sample 15PSC-183 is a medium-gained sandstone that consists mainly of feldspathic volcanic lithic grains and plagioclase. It also contains about 10% monocrystalline quartz grains, some with markedly angular outlines, and uncommon grains of fine-grained sedimentary rock, polycrystalline quartz, and quartz-plagioclase (tonalite?) aggregates. Epidote alteration is conspicuous in some of the volcanic lithic grains, and some grains (rare) are almost entirely epidote.

The $^{206}Pb/^{238}U$ ages for most of the analyzed zircons (N=65) range from 117.6 ±4.3 Ma to 179.6 ±6.2 Ma, with a strong peak at 141 Ma on the probability density curve (Fig. 4, Table 1). Two older grains have ages of 211.3 ±6.5 Ma and 242 ±13 Ma.

Fig. 3. Downton Lake outcrop of Gun Lake unit from which sample 15PSC-183 was collected. View is northwest.

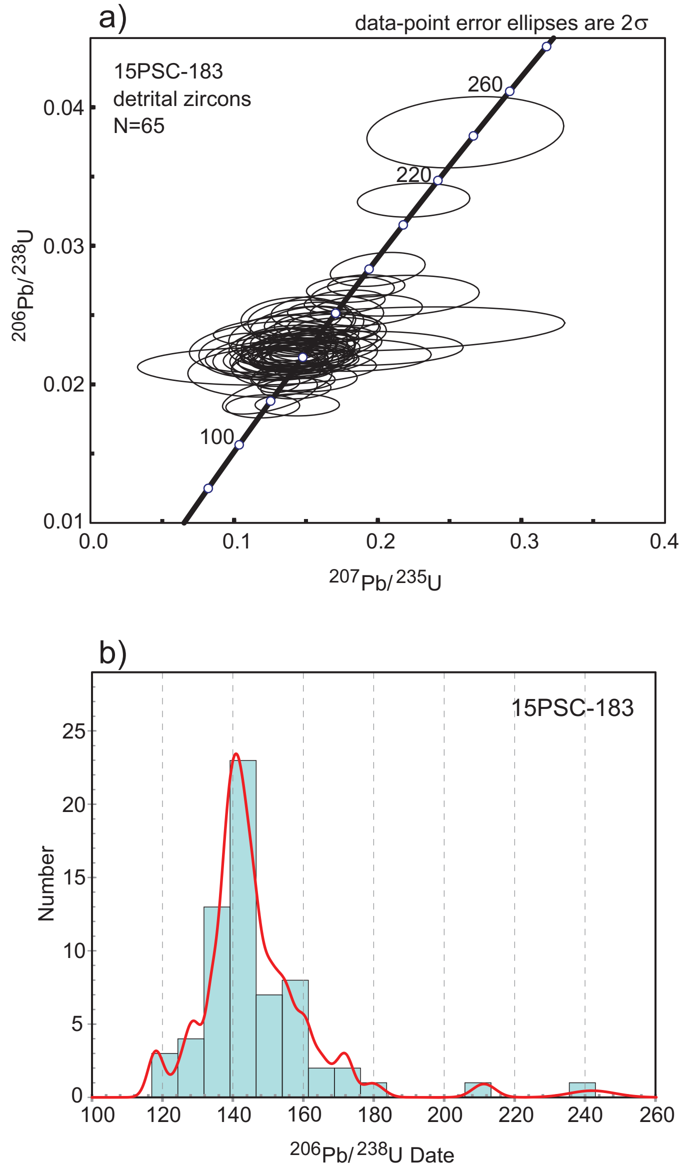

Fig. 4. a) Concordia plot of all detrital zircons analyzed from sample 15PSC-183. **b)** Histogram of detrital zircon ages and superimposed probability density curve.

The youngest grains (117.6 ±4.3 Ma, 118.3 ±4.1 Ma, 122.5 ±7.1 Ma, 125.7 ±3.9 Ma) suggest a maximum depositional age of around 120 Ma (Aptian).

3.2. Sample 15PSC-185, Truax Creek

Sample 15PSC-185 is from a panel of siliciclastic sedimentary rocks first mapped as Gun Lake unit by Schiarizza et al. (1993) that outcrops on the south side of Carpenter Lake, about 12 km east-northeast of Gold Bridge. Here, the Gun Lake unit comprises medium to dark grey slaty siltstone intercalated with grey to green fine- to coarse-grained sandstone. These rocks dip to the west or southwest but are overturned, as indicated by graded beds and cross stratification at several localities (Schiarizza et al., 1997). They are truncated to the northeast by a major strand of the Castle Pass dextral strike-slip fault system and pass southwestward, across an indistinct contact in a zone of slaty argillite with lenses of sandstone and chert, into the Bridge River complex, represented by structurally interleaved chert, argillite, sandstone, basalt, limestone and serpentinite. This panel of Bridge River rocks is juxtaposed against an extensive belt of Bridge River complex farther west by southwest-dipping thrust(?) faults that enclose the Truax Creek conglomerate lens (Fig. 2).

Sample 15PSC-185 was collected from an outcrop on the south side of the road at the first major switchback on the Truax Creek logging road (522380E, 5637101N, UTM Zone 10, NAD 83). The outcrop is predominantly medium grey, medium- to coarse-grained sandstone that forms thin to thick beds and rare boudinaged lenses, intercalated with dark grey slaty siltstone (Fig. 5). The sample, comprising coarse-grained sandstone from a thick bed at the east end of the outcrop, consists mainly of plagioclase and plagioclase-rich volcanic lithic grains, but also includes a substantial amount of monocrystalline quartz (10%), and minor amounts of polycrystalline quartz, and fine-grained sedimentary lithic grains.

The $^{206}Pb/^{238}U$ ages for most of the analyzed zircons (N=59) fall between 142.2 ±2.8 Ma and 164.7 ±3.7 Ma, with a strong peak at 151 Ma on the probability density curve (Fig. 6, Table 2) Five older grains have ages ranging from 207.8 ±8.1 Ma to 214.2 ±5.9 Ma. The youngest grains (17 grains between 142.2 ±2.8 Ma and, 149.8 ±3.4 Ma) indicate a maximum depositional age near the Jurassic-Cretaceous boundary (145 Ma).

4. Discussion

Schiarizza et al. (1997) suggested that the Gun Lake unit correlates with the lower unit of the Relay Mountain Group. However, the detrital zircon data presented here show that the Gun Lake unit includes at least two separate subunits, both younger than the lower unit of the Relay Mountain Group, which necessitates revised correlations. We now correlate Gun

Table 1. Zircon U-Pb laser ablation analytical data for sample 15PSC-183, Downton Lake outcrop.

Sample no.	**Isotopic Ratios**							**Isotopic Ages**					
Analysis ID	$^{207}Pb/^{235}U$	2σ (abs)	$^{206}Pb/^{238}U$	2σ (abs)	ρ	$^{207}Pb/^{206}Pb$	2σ (abs)	$^{207}Pb/^{235}U$	2σ (Ma)	$^{206}Pb/^{238}U$	2σ (Ma)	$^{207}Pb/^{206}Pb$	2σ (Ma)
X15PSC_183_1	0.1410	0.0240	0.02033	0.00064	0.018	0.0487	0.0082	136	20	129.7	4.0	130	320
X15PSC_183_2	0.1200	0.0210	0.01841	0.00068	0.080	0.0463	0.0078	118	19	117.6	4.3	-10	290
X15PSC_183_3	0.1450	0.0320	0.02286	0.00096	0.031	0.0463	0.0100	133	28	145.7	6.1	-90	390
X15PSC_183_4	0.1440	0.0320	0.02470	0.00130	0.069	0.0408	0.0093	133	28	157.3	7.9	-260	380
X15PSC_183_5	0.1540	0.0400	0.02260	0.00110	0.371	0.0500	0.0120	140	36	143.7	7.0	-40	450
X15PSC_183_6	0.1440	0.0240	0.01852	0.00065	0.005	0.0548	0.0096	138	20	118.3	4.1	310	330
X15PSC_183_7	0.1180	0.0410	0.02080	0.00140	0.006	0.0410	0.0140	107	36	132.8	8.5	-300	520
X15PSC_183_8	0.1310	0.0230	0.02169	0.00082	0.068	0.0446	0.0082	127	21	138.3	5.2	-60	330
X15PSC_183_9	0.1410	0.0350	0.02150	0.00100	0.357	0.0460	0.0110	130	31	137.2	6.4	-100	450
X15PSC_183_11	0.1430	0.0200	0.01970	0.00061	0.097	0.0531	0.0079	135	18	125.7	3.9	190	270
X15PSC_183_12	0.1400	0.0210	0.02176	0.00068	0.165	0.0471	0.0071	132	18	138.7	4.3	30	290
X15PSC_183_13	0.1330	0.0300	0.02330	0.00140	0.127	0.0430	0.0098	124	27	148.4	8.6	-140	410
X15PSC_183_14	0.1650	0.0320	0.02510	0.00110	0.048	0.0464	0.0120	153	28	159.9	6.8	0	370
X15PSC_183_15	0.1300	0.0260	0.02120	0.00110	0.065	0.0453	0.0090	121	23	134.9	6.8	-90	360
X15PSC_183_16	0.2080	0.1000	0.02400	0.00130	0.273	0.0670	0.0260	186	71	153.1	7.9	390	550
X15PSC_183_19	0.1380	0.0230	0.02239	0.00078	0.143	0.0434	0.0073	133	20	142.7	4.9	-20	310
X15PSC_183_20	0.1440	0.0320	0.02213	0.00097	0.062	0.0470	0.0110	133	29	141.1	6.1	-110	410
X15PSC_183_21	0.1250	0.0270	0.01920	0.00110	0.584	0.0500	0.0099	116	26	122.5	7.1	-10	420
X15PSC_183_22	0.1480	0.0160	0.02097	0.00045	0.077	0.0520	0.0057	140	14	133.8	2.8	260	230
X15PSC_183_24	0.1700	0.0260	0.02391	0.00074	0.182	0.0531	0.0087	157	22	152.3	4.7	270	330
X15PSC_183_25	0.1490	0.0300	0.02047	0.00083	0.024	0.0504	0.0100	138	26	130.6	5.2	30	390
X15PSC_183_26	0.1240	0.0450	0.02270	0.00150	0.224	0.0440	0.0170	123	43	144.5	9.2	-280	600
X15PSC_183_27	0.1410	0.0230	0.02210	0.00092	0.003	0.0478	0.0084	132	20	140.7	5.8	30	300
X15PSC_183_29	0.1590	0.0230	0.02311	0.00069	0.199	0.0496	0.0074	148	20	147.3	4.3	120	290
X15PSC_183_30	0.1510	0.0300	0.02226	0.00090	0.366	0.0510	0.0110	140	26	141.9	5.7	30	370
X15PSC_183_31	0.2000	0.0270	0.02830	0.00100	0.288	0.0510	0.0077	182	22	179.6	6.2	320	230
X15PSC_183_32	0.1510	0.0260	0.02235	0.00068	0.152	0.0476	0.0081	141	23	142.5	4.3	140	320
X15PSC_183_33	0.2610	0.0560	0.03820	0.00210	0.175	0.0502	0.0110	238	42	242.0	13.0	160	390
X15PSC_183_34	0.1350	0.0310	0.02169	0.00110	0.048	0.0490	0.0120	126	27	138.3	6.7	-70	400
X15PSC_183_35	0.1310	0.0120	0.02006	0.00054	0.212	0.0443	0.0047	124	11	128.0	3.4	-50	190
X15PSC_183_36	0.1500	0.0330	0.02450	0.00130	0.045	0.0390	0.0098	136	30	156.0	7.9	-290	390
X15PSC_183_37	0.1110	0.0290	0.02210	0.00130	0.015	0.0380	0.0100	104	26	141.0	8.0	-330	420
X15PSC_183_38	0.1490	0.0310	0.02172	0.00073	0.129	0.0483	0.0099	138	27	138.5	4.6	60	380
X15PSC_183_39	0.1400	0.0490	0.02210	0.00130	0.201	0.0570	0.0180	125	42	141.0	8.2	-120	580
X15PSC_183_40	0.1550	0.0220	0.02426	0.00074	0.112	0.0480	0.0073	144	19	154.5	4.7	20	290
X15PSC_183_41	0.1380	0.0270	0.02260	0.00120	0.040	0.0490	0.0093	129	25	143.7	7.9	-40	400
X15PSC_183_42	0.1810	0.0250	0.02685	0.00076	0.123	0.0510	0.0071	171	22	170.8	4.8	210	260
X15PSC_183_43	0.1620	0.0360	0.02360	0.00120	0.205	0.0520	0.0120	148	31	150.1	7.3	20	430
X15PSC_183_44	0.2120	0.0480	0.02640	0.00120	0.162	0.0580	0.0140	188	39	167.9	7.2	360	460
X15PSC_183_45	0.1920	0.0220	0.02711	0.00065	0.068	0.0526	0.0063	180	19	172.5	4.1	220	240
X15PSC_183_46	0.1690	0.0260	0.02416	0.00088	0.055	0.0512	0.0076	156	22	153.9	5.5	190	310
X15PSC_183_47	0.1480	0.0220	0.02458	0.00084	0.376	0.0447	0.0066	138	19	156.5	5.3	-70	280
X15PSC_183_48	0.1480	0.0310	0.02194	0.00079	0.080	0.0515	0.0110	141	27	139.9	5.0	50	390
X15PSC_183_49	0.1480	0.0300	0.02430	0.00110	0.285	0.0430	0.0096	136	27	154.7	7.0	-140	390
X15PSC_183_50	0.1320	0.0290	0.02266	0.00110	0.168	0.0436	0.0094	123	26	144.4	6.8	-160	380
X15PSC_183_52	0.1420	0.0250	0.02301	0.00082	0.061	0.0452	0.0083	136	23	146.6	5.1	-20	340
X15PSC_183_53	0.1660	0.0170	0.02363	0.00055	0.095	0.0521	0.0057	155	15	150.5	3.5	220	230
X15PSC_183_54	0.1280	0.0290	0.02182	0.00095	0.098	0.0413	0.0092	120	26	139.1	6.0	-190	380
X15PSC_183_55	0.1220	0.0300	0.02170	0.00110	0.038	0.0415	0.0099	113	27	138.1	6.8	-310	390
X15PSC_183_56	0.1810	0.0460	0.02211	0.00095	0.031	0.0630	0.0160	170	40	141.0	6.0	370	490
X15PSC_183_57	0.1580	0.0170	0.02522	0.00058	0.042	0.0440	0.0049	148	15	160.6	3.6	-40	220
X15PSC_183_58	0.1480	0.0260	0.02249	0.00097	0.136	0.0520	0.0097	138	22	143.3	6.1	90	340
X15PSC_183_59	0.1450	0.0160	0.02220	0.00058	0.074	0.0465	0.0059	140	15	141.5	3.6	20	220
X15PSC_183_60	0.1460	0.0210	0.02280	0.00061	0.040	0.0449	0.0063	137	18	145.3	3.8	0	280
X15PSC_183_61	0.1510	0.0270	0.02260	0.00130	0.078	0.0513	0.0097	140	23	143.9	8.0	70	350
X15PSC_183_62	0.2250	0.0320	0.03330	0.00100	0.113	0.0492	0.0071	212	24	211.3	6.5	200	260
X15PSC_183_63	0.1410	0.0200	0.02161	0.00077	0.220	0.0480	0.0069	132	18	137.8	4.9	30	280
X15PSC_183_64	0.1500	0.0250	0.02195	0.00086	0.277	0.0556	0.0082	152	21	140.0	5.4	290	310
X15PSC_183_65	0.1770	0.0230	0.02595	0.00070	0.230	0.0506	0.0071	164	20	165.1	4.4	220	300
X15PSC_183_66	0.1920	0.0320	0.02535	0.00091	0.220	0.0548	0.0096	175	27	161.4	5.7	350	310
X15PSC_183_67	0.1160	0.0680	0.02130	0.00110	0.039	0.0360	0.0160	108	37	136.0	7.0	-350	490
X15PSC_183_68	0.1520	0.0390	0.02270	0.00120	0.462	0.0480	0.0130	141	37	144.5	7.7	120	480
X15PSC_183_69	0.1390	0.0310	0.02177	0.00087	0.013	0.0450	0.0100	134	28	138.8	5.5	-50	400
X15PSC_183_70	0.1910	0.0560	0.02260	0.00100	0.066	0.0630	0.0170	179	47	144.3	6.5	270	560
X15PSC_183_71	0.1430	0.0340	0.02280	0.00120	0.078	0.0470	0.0120	132	29	145.5	7.6	20	450

Table 2. Zircon U-Pb laser ablation analytical data for sample 15PSC-185, Truax Creek outcrop.

Sample no.	Isotopic Ratios							Isotopic Ages					
Analysis ID	$^{207}Pb/^{235}U$	2σ (abs)	$^{206}Pb/^{238}U$	2σ (abs)	ρ	$^{207}Pb/^{206}Pb$	2σ (abs)	$^{207}Pb/^{235}U$	2σ (Ma)	$^{206}Pb/^{238}U$	2σ (Ma)	$^{207}Pb/^{206}Pb$	2σ (Ma)
PSC185_6	0.1760	0.0110	0.02503	0.00060	0.077	0.0498	0.0033	160.4	9.6	159.3	3.8	140	110
PSC185_7	0.1660	0.0076	0.02414	0.00054	0.182	0.0494	0.0024	156.8	6.7	153.7	3.4	166	91
PSC185_8	0.1790	0.0120	0.02393	0.00080	0.000	0.0532	0.0038	166	10	152.4	5.0	300	140
PSC185_9	0.1621	0.0088	0.02347	0.00066	0.079	0.0487	0.0028	151.2	7.6	149.5	4.2	140	100
PSC185_10	0.2200	0.0130	0.03380	0.00094	0.107	0.0459	0.0028	200	11	214.2	5.9	20	110
PSC185_11	0.1681	0.0050	0.02469	0.00052	0.351	0.0489	0.0014	157.5	4.3	157.2	3.3	140	57
PSC185_12	0.1750	0.0130	0.02479	0.00082	0.156	0.0509	0.0040	162	11	157.7	5.1	220	140
PSC185_13	0.1541	0.0056	0.02287	0.00043	0.100	0.0492	0.0019	145.5	4.8	145.7	2.7	149	74
PSC185_14	0.1466	0.0049	0.02232	0.00044	0.220	0.0472	0.0017	138.9	4.4	142.2	2.8	84	67
PSC185_15	0.1674	0.0092	0.02493	0.00065	0.140	0.0482	0.0027	156.3	7.9	158.7	4.1	120	100
PSC185_16	0.1570	0.0060	0.02355	0.00061	0.259	0.0480	0.0020	147.4	5.3	150.0	3.9	106	79
PSC185_17	0.1726	0.0085	0.02394	0.00057	0.035	0.0516	0.0027	161.9	7.4	152.5	3.6	243	99
PSC185_18	0.1890	0.0099	0.02514	0.00071	0.006	0.0525	0.0032	175.9	8.4	160.0	4.4	320	120
PSC185_19	0.1746	0.0075	0.02584	0.00060	0.206	0.0499	0.0023	162.1	6.4	164.7	3.7	176	86
PSC185_20	0.1770	0.0120	0.02366	0.00069	0.057	0.0540	0.0038	165.7	9.6	150.7	4.3	340	130
PSC185_21	0.1599	0.0043	0.02386	0.00050	0.258	0.0472	0.0014	150.4	3.7	151.9	3.1	72	55
PSC185_22	0.1755	0.0071	0.02425	0.00055	0.266	0.0507	0.0022	163.0	6.1	154.4	3.5	211	83
PSC185_23	0.1684	0.0070	0.02459	0.00058	0.181	0.0484	0.0022	158.1	6.1	156.5	3.7	109	83
PSC185_24	0.1507	0.0092	0.02277	0.00059	0.140	0.0468	0.0030	141.4	8.1	145.1	3.7	70	110
PSC185_25	0.1700	0.0150	0.02589	0.00093	0.161	0.0462	0.0041	156	13	164.7	5.9	90	150
PSC185_26	0.1673	0.0059	0.02449	0.00055	0.353	0.0500	0.0018	156.4	5.2	155.9	3.5	192	71
PSC185_27	0.1564	0.0082	0.02378	0.00062	0.191	0.0492	0.0027	147.2	7.1	151.4	3.9	180	100
PSC185_28	0.1601	0.0047	0.02383	0.00047	0.328	0.0501	0.0015	150.9	4.1	151.8	2.9	197	60
PSC185_29	0.1684	0.0070	0.02490	0.00063	0.304	0.0503	0.0021	158.4	5.9	158.5	4.0	201	79
PSC185_30	0.1511	0.0074	0.02351	0.00053	0.119	0.0476	0.0025	144.0	6.5	149.8	3.4	103	92
PSC185_31	0.1840	0.0100	0.02527	0.00067	0.090	0.0541	0.0033	169.0	8.8	160.8	4.2	250	110
PSC185_32	0.1550	0.0088	0.02320	0.00078	0.113	0.0492	0.0031	147.0	7.6	147.8	4.9	130	110
PSC185_33	0.1663	0.0073	0.02373	0.00060	0.187	0.0500	0.0023	155.9	6.4	151.1	3.8	188	89
PSC185_34	0.1553	0.0059	0.02307	0.00055	0.236	0.0479	0.0019	145.9	5.2	147.0	3.5	102	74
PSC185_35	0.1762	0.0079	0.02457	0.00072	0.233	0.0525	0.0026	164.2	6.8	156.4	4.5	269	97
PSC185_36	0.1710	0.0090	0.02271	0.00061	0.286	0.0544	0.0028	162.0	7.9	144.7	3.9	350	100
PSC185_37	0.1650	0.0100	0.02355	0.00065	0.028	0.0514	0.0035	154.9	8.4	150.0	4.1	180	110
PSC185_38	0.2300	0.0120	0.03320	0.00100	0.271	0.0507	0.0027	211.4	9.7	210.3	6.3	230	100
PSC185_39	0.1544	0.0084	0.02363	0.00067	0.153	0.0474	0.0027	145.9	7.3	150.5	4.2	110	100
PSC185_40	0.2405	0.0070	0.03316	0.00060	0.249	0.0520	0.0016	218.2	5.8	210.2	3.7	263	60
PSC185_41	0.2361	0.0079	0.03369	0.00078	0.415	0.0517	0.0017	214.5	6.5	213.5	4.9	243	65
PSC185_42	0.1783	0.0077	0.02510	0.00070	0.434	0.0509	0.0021	165.6	6.7	159.7	4.4	224	84
PSC185_43	0.1680	0.0110	0.02449	0.00074	0.101	0.0510	0.0035	159.1	9.4	155.9	4.7	250	120
PSC185_44	0.1693	0.0045	0.02437	0.00063	0.546	0.0499	0.0013	159.3	3.9	155.1	4.0	180	53
PSC185_45	0.1501	0.0078	0.02251	0.00069	0.395	0.0493	0.0026	141.1	6.9	143.5	4.4	170	100
PSC185_47	0.1623	0.0055	0.02348	0.00051	0.306	0.0499	0.0018	152.0	4.8	149.8	3.2	184	69
PSC185_48	0.1680	0.0140	0.02450	0.00120	0.178	0.0518	0.0047	158	13	155.7	7.6	210	170
PSC185_49	0.1656	0.0090	0.02348	0.00058	0.181	0.0500	0.0027	154.8	7.8	149.5	3.7	210	100
PSC185_50	0.1561	0.0091	0.02311	0.00072	0.213	0.0481	0.0029	148.0	8.0	147.2	4.5	120	110
PSC185_51	0.1602	0.0034	0.02316	0.00046	0.488	0.0494	0.0010	150.6	2.9	147.6	2.9	178	44
PSC185_52	0.1716	0.0070	0.02504	0.00074	0.283	0.0497	0.0021	161.3	6.3	159.4	4.6	175	85
PSC185_53	0.1635	0.0068	0.02388	0.00059	0.328	0.0489	0.0020	153.4	5.9	152.1	3.7	139	77
PSC185_54	0.2230	0.0180	0.03260	0.00130	0.229	0.0488	0.0040	204	15	207.8	8.1	160	160
PSC185_55	0.1620	0.0081	0.02358	0.00067	0.244	0.0491	0.0024	152.2	7.0	150.2	4.2	199	95
PSC185_56	0.1800	0.0150	0.02530	0.00095	0.178	0.0527	0.0044	166	12	160.9	6.0	270	150
PSC185_57	0.1610	0.0100	0.02352	0.00077	0.166	0.0505	0.0034	151.2	8.7	149.8	4.8	210	120
PSC185_58	0.1618	0.0098	0.02468	0.00074	0.233	0.0499	0.0031	152.4	8.6	157.1	4.7	160	120
PSC185_59	0.1633	0.0082	0.02350	0.00074	0.138	0.0504	0.0027	153.1	7.0	149.6	4.7	200	100
PSC185_60	0.1601	0.0080	0.02324	0.00063	0.255	0.0502	0.0025	149.5	7.0	148.4	4.0	186	93
PSC185_61	0.1700	0.0180	0.02340	0.00120	0.140	0.0529	0.0057	160	16	148.9	7.3	280	200
PSC185_62	0.1644	0.0055	0.02364	0.00053	0.375	0.0503	0.0016	155.3	4.8	150.6	3.3	197	65
PSC185_63	0.1730	0.0130	0.02368	0.00088	0.146	0.0561	0.0044	161	11	150.8	5.5	350	150
PSC185_64	0.1594	0.0063	0.02309	0.00056	0.188	0.0502	0.0020	150.2	5.4	147.1	3.5	214	77
PSC185_65	0.1827	0.0095	0.02503	0.00079	0.404	0.0523	0.0026	171.5	8.2	159.3	5.0	282	99

Fig. 5. Truax Creek outcrop of Gun Lake unit from which sample 15PSC-185 was collected. View is south, rocks dip west but are overturned.

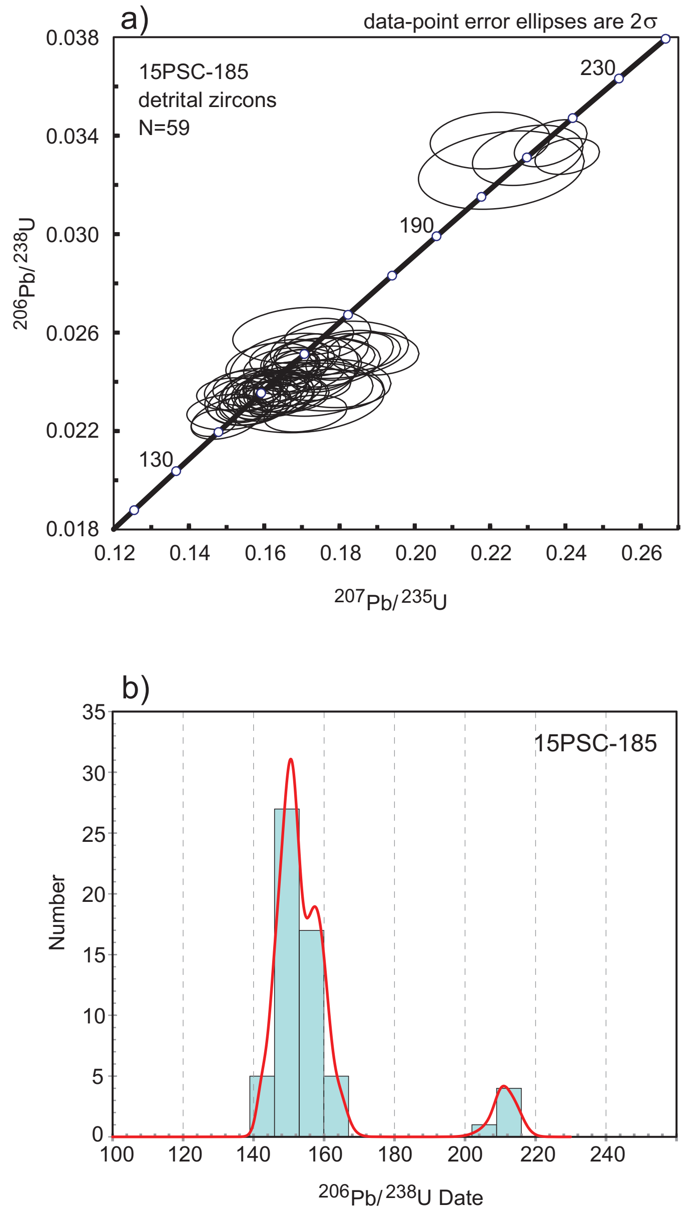

Fig. 6. a) Concordia plot of all detrital zircons analysed from sample 15PSC-185. **b)** Histogram of detrital zircon ages and superimposed probability density curve.

Lake unit exposures near Downton Lake with the Paradise Formation of the Taylor Creek Group, and those at Truax Creek with the middle unit of the Relay Mountain Group.

4.1. Downton Lake sample

The Gun Lake unit sampled at Downton Lake is a feldspathic volcanic-lithic sandstone with a maximum depositional age of about 120 Ma. The age and composition indicate that it correlates with the Paradise Formation (Taylor Creek Group), which is well exposed in the Relay Mountain area, 30 km north-northwest of the Downton Lake sample site (Garver, 1992; Schiarizza et al., 1997). Here, it forms that base of the Taylor Creek Group and is overlain by the Dash and Lizard formations which form the upper part of the group. The Paradise Formation is missing in the Tyaughton Lake area, 15 km north of Downton Lake, where the Dash Formation is directly above the Bridge River complex (Fig. 2).

The Paradise Formation is mostly shale and sandstone (consisting mainly of volcanic lithic grains and plagioclase), but also includes thick lenses of volcanic-pebble conglomerate (Garver, 1992). It is older than the mid-Albian Dash Formation which overlies it, and an Aptian to early Albian depositional age was inferred by Garver and Brandon (1994) based on a date of 113 ±6.5 Ma from the youngest detrital zircon fission-track peak. Paleocurrent indicators are sparse, but indicate sediment transport from the west (Garver, 1989). Garver (1989, 1992) suggested that the Paradise Formation was deposited as a submarine fan derived from an active volcanic source built on a substrate that included older metavolcanic and plutonic rocks. He also considered that sediment was likely derived from erosion of the southwestern Coast belt directly west of the Bridge River terrane and Tyaughton basin. The ages of detrital zircons from our Downton Lake sample (180 to 120 Ma) are entirely consistent with this interpretation. The zircons may have been derived from volcanic units within, or correlative with, the Lower to Middle Jurassic Harrison Lake Formation, the Upper Jurassic Billhook Creek Formation, and the Lower Cretaceous Gambier Group (Arthur et al., 1993; Monger and Journeay, 1994), as well as from the voluminous Middle Jurassic to Cretaceous plutons in this part of the Coast Mountains (Friedman and Armstrong, 1995).

4.2. Truax Creek sample

The Gun Lake unit sampled near Truax Creek is a feldspathic volcanic-lithic sandstone with a maximum depositional age of about 145 Ma. If this age is close to the actual depositional age then these exposures of Gun Lake unit are coeval with rocks in the middle unit of the Relay Mountain Group, which consists mainly of sandstones that are lithologically similar to those of the Gun Lake unit. Likewise, the nearby Truax Creek conglomerate (Late Jurassic) is similar, in age and lithology, to volcanic-clast conglomerates that occur locally in the middle unit of the Relay Mountain Group (Umhoefer et al., 2002). We therefore correlate the Gun Lake unit at Truax Creek, and the nearby Truax Creek conglomerate, with the middle unit of the Relay Mountain Group (lower Tyaughton basin). We infer that the two units were part of the same stratigraphic succession, which was deformed and segmented by northeast vergent thrust faults (including faults that bound the Truax Creek conglomerate) and associated overturned folds. This is essentially the interpretation of Schiarizza et al. (1997; their Figure 19b, section F), who correlated the structures near Truax Creek with the northeast-vergent North Cinnabar fold-fault system, which deforms rocks as young as the Late Cretaceous Powell Creek Formation and is along strike, just 12 km to the northwest (Fig. 2). However, Schiarizza et al. (1997) correlated the unit with the lower unit of the Relay Mountain Group (Callovian and early Oxfordian, ~166-160 Ma). Detrital zircons show that, at Truax Creek, Gun Lake rocks are no older than about 145 Ma, indicating that the entire lower unit and part of the middle unit of the Relay Mountain Group, as exposed in the type locality 30 km to the northwest, are missing. This implies that the base of the Tyaughton basin is highly diachronous. It also has implications for the age of the Bridge River complex, suspected by Schiarizza et al. (1997) to be late Middle Jurassic and older because this was the age of the youngest dated chert from the complex, and also the age of the basal Relay Mountain Group which was inferred to overlie it. It is likely that the Bridge River complex, like the base of the Tyaughton basin, is a diachronous unit that at some localities may include rocks that are younger than Middle Jurassic.

Most detrital zircons from sample 15PSC185 define a restricted population between 165 and 142 Ma. Zircons of this age are common in the broader (180-120 Ma) age distribution from the Downton Lake sample, conceivably suggesting that both had a common westerly source. However, the 165-142 Ma age range coincides almost exactly with the age of a Late Jurassic volcanic-plutonic belt to the east, northeast, and north of Bridge River terrane and the Tyaughton basin, suggesting that derivation from these sources is more likely. This Late Jurassic volcanic-plutonic belt stretches northwest-southeast for more than 500 km, from near Anahim Lake (Hotnarko volcanic rocks, U-Pb zircon age of 153.75 ±0.95 Ma, van der Heyden, 2004) to the international boundary south of Princeton (Eagle and Zoa plutonic complexes, U-Pb zircon ages from 148 ±6 to 157 ±4 Ma, Greig et al., 1992). The nearest exposures are at Piltz Peak, 70 km north of Gold Bridge, where the Piltz Peak complex includes volcanic rocks that have yielded a U-Pb zircon age of 164.3 ±1.0 Ma, and tonalitic intrusions with U-Pb zircon ages between 145.5 ±2.0 Ma and 151.1 ±1.0 Ma (Mahoney et al., 2013). The substrate to the Piltz Peak volcanic-plutonic complex is not exposed, but is inferred to be Cadwallader terrane (Schiarizza, 2013), which is a likely source for the secondary population of 208-214 Ma zircon grains in sample 15PSC-185. This interpretation is consistent with that of Umhoefer et al. (2002), who argued that the lower and middle units of the Relay Mountain Group were derived from sources to the northeast.

4.3. Correlation of other Gun Lake occurrences

The belt of Gun Lake rocks that crosses Gun Lake northwest of Gold Bridge is spatially associated with the Downton Lake occurrence, is lithologically most similar to the Downton Lake occurrence (less argillite and siltstone than the Gun Lake occurrences to the north and east), and, like the Downton Lake occurrence, has a sharp contact with the underlying Bridge River complex. These rocks are therefore, like the Downton Lake occurrence, correlated with the Paradise Formation of the Taylor Creek Group. Correlation of the other two occurrences, one that crosses lower Tyaughton Creek and the other near the head of Pearson Creek (Fig. 2), remains uncertain. Likewise, data are insufficient to attempt correlation of the several belts of Cayoosh assemblage in the southern part of the Gold Bridge area with either of the two Gun Lake occurrences analyzed here.

5. Conclusions

The two samples analyzed in this study, both mapped as Gun Lake unit by Schiarizza et al. (1997), represent two different units. The sandstones near Downton Lake are correlated with the mid-Cretaceous Paradise Formation of the Taylor Creek Group, and those near Truax Creek are correlated with the middle unit of the Jura-Cretaceous Relay Mountain Group.

The Gun Lake unit sampled at Downton Lake is a feldspathic volcanic-lithic sandstone with a maximum depositional age of about 120 Ma. Correlation with the Paradise Formation of the Taylor Creek Group is based on age and composition. The 180 to 118 Ma age range of most detrital zircons is consistent with derivation from the adjacent southwest Coast Mountains, as suggested for the Paradise Formation by Garver (1989, 1992).

The Gun Lake unit sampled near Truax Creek is a feldspathic volcanic-lithic sandstone with a maximum depositional age near the Jurassic-Cretaceous boundary (145 Ma). It is compositionally similar to sandstone in the Jura-Cretaceous Relay Mountain Group, and a nearby fault-bounded lens of Upper Jurassic volcanic-clast conglomerate (Truax Creek conglomerate) is likewise similar to age-equivalent rocks of the Relay Mountain Group. These two units are interpreted as different parts of a stratigraphic succession that correlates with part of the middle unit of the Relay Mountain Group but was deformed and segmented during Late Cretaceous northeast-vergent contractional deformation. The entire lower unit and part of the middle unit of the Relay Mountain Group, as exposed in its type locality 30 km to the northwest, are missing at Truax Creek, suggesting that the base of the Tyaughton basin is highly diachronous. Detrital zircons (mainly 165-142 Ma, but also 214-208 Ma) were likely derived from sources to the northeast, including the Cadwallader arc terrane and a Late Jurassic volcanic-plutonic belt that cuts across it.

Acknowledgments

We thank Marghaleray Amini, June Cho, Hai Lin, Dave Newton, and Taylor Ockerman for their contributions to mineral separation, sample preparation and analyses at PCIGR. Lawrence Aspler and Jim Logan reviewed the paper and made suggestions that improved it.

References cited

Arthur, A.J., Smith, P.L., Monger, J.W.H., and Tipper, H.W., 1993. Mesozoic stratigraphy and Jurassic paleontology west side of Harrison Lake, southwestern British Columbia. Geological Survey of Canada, Bulletin 441, 62 p.

Black, L.P., Kamo, S.L., Allen, C.M., Davis, D.W., Aleinikoff, J.N., Valley, J.W., Mundil, R., Campbell, I.H., Korsch, R.J., Williams, I.S., and Foudoulis, C., 2004. Improved $^{206}Pb/^{238}U$ microprobe geochronology by the monitoring of a trace-element-related matrix effect; SHRIMP, ID-TIMS, ELA-ICP-MS and oxygen isotope documentation for a series of zircon standards. Chemical Geology, 205, 115-140.

Cairnes, C.E., 1937. Geology and mineral deposits of the Bridge River mining camp, British Columbia. Geological Survey of Canada, Memoir 213, 140 p.

Cairnes, C. E., 1943. Geology and mineral deposits of Tyaughton Lake area, British Columbia. Geological Survey of Canada, Paper 43-15, 39 p.

Calon, T.J., Malpas, J.G., and Macdonald, R., 1990. The anatomy of the Shulaps ophiolite. In: Geological Fieldwork 1989, British Columbia Ministry of Energy, Mines and Petroleum Resources, British Columbia Geological Survey Paper 1990-1, pp. 375-386.

Church, B.N., and MacLean, M.E., 1987. Geology and mineralization in the vicinity of the Mary Mac mine. In: Exploration in British Columbia 1986, British Columbia Ministry of Energy, Mines and Petroleum Resources, pp. B33-B37.

Cordey, F., and Schiarizza, P., 1993. Long-lived panthalassic remnant: The Bridge River accretionary complex, Canadian Cordillera. Geology, 21, 263-266.

Eggins, S.M., Kinsley L., and Shelley J., 1998. Deposition and element fractionation processes during atmospheric pressure laser sampling for analysis by ICP-MS. Applied Surface Science, 127-129, 278-286.

Friedman, R.M., and Armstrong, R.L., 1995. Jurassic and Cretaceous geochronology of the southern Coast Belt, British Columbia, 49° to 51° N. In: Miller, D.M., and Busby, C., (Eds.), Jurassic magmatism and tectonics of the North American cordillera, Geological Society of America, Special Paper 299, pp. 95-139.

Garver, J.I., 1989. Basin evolution and source terranes of Albian-Cenomanian rocks in the Tyaughton basin, southern British Columbia: Implications for mid-Cretaceous tectonics in the Canadian Cordillera. Ph.D. thesis, The University of Washington, 227 p.

Garver, J.I., 1992. Provenance of Albian-Cenomanian rocks of the Methow and Tyaughton basins, southern British Columbia: a mid-Cretaceous link between North America and the Insular Terrane. Canadian Journal of Earth Sciences, 29, 1274-1295.

Garver, J.I., and Brandon, M.T., 1994. Fission-track ages of detrital zircons from Cretaceous strata, southern British Columbia: Implications for the Baja BC hypothesis. Tectonics, 13, 401-420.

Greig, C.J., Armstrong, R.L., Harakal, J.E., Runkle, D., and van der Heyden, P., 1992. Geochronometry of the Eagle Plutonic Complex and the Coquihalla area, southwestern British Columbia. Canadian Journal of Earth Sciences, 29, 812-829.

Journeay, J.M., and Mahoney, J.B., 1994. Cayoosh assemblage: Regional correlations and implications for terrane linkages in the southern Coast Belt, British Columbia. In: Current Research Part A, Geological Survey of Canada Paper1994-A, pp. 165-175.

Ludwig, K.R., 2003 Isoplot 3.09-A geochronological toolkit for Microsoft Excel. Berkeley Geochronology Center, The University of California at Berkeley, Special Publication No. 4.

Mahoney, J.B., and Journeay, J.M., 1993. The Cayoosh assemblage, southwestern British Columbia: Last vestige of the Bridge River ocean. In: Current Research, Part A, Geological Survey of Canada, Paper 93-1A, pp. 235-244.

Mahoney, J.B., Hickson, C.J., Haggart, J.W., Schiarizza, P., Read, P.B., Enkin, R.J., van der Heyden, P., and Israel, S., 2013. Geology, Taseko Lakes, British Columbia. Geological Survey of Canada, Open File 6150, scale 1:250,000.

McCann, W.S., 1922. Geology and mineral deposits of the Bridge River map-area, British Columbia. Geological Survey of Canada Memoir 130, 115 p.

Mihalynuk, M.G., Diakow, L.J., Friedman, R.M., and Logan, J.M., 2016. Chronology of southern Nicola arc stratigraphy and deformation. In: Geological Fieldwork 2015, British Columbia Ministry of Energy, Mines and Petroleum Resources, British Columbia Geological Survey Paper 2016-1, pp. 31-63.

Monger, J.W.H., 1989. Geology, Hope, British Columbia. Geological Survey of Canada, Map 41-1989, scale 1:250,000.

Monger, J.W.H., and McMillan, W.J., 1989. Geology, Ashcroft, British Columbia. Geological Survey of Canada, Map 42-1989, scale 1:250,000.

Monger, J.W.H., 1991. Correlation of Settler schist with Darrington phyllite and Shuksan greenschist and its tectonic implications, Coast and Cascade mountains, British Columbia and Washington. Canadian Journal of Earth Sciences, 28, 447-458.

Monger, J.W.H., and Journeay, J.M., 1994. Guide to the geology and tectonic evolution of the southern Coast Mountains. Geological Survey of Canada, Open File 2490, 77p.

Paton C., Hellstrom J., Paul, B., Woodhead J., and Hergt, J., 2011. Iolite: freeware for the visualisation and processing of mass spectrometric data. Journal of Analytical Atomic Spectrometry, 26, 2508-2518.

Rusmore, M.E., 1987. Geology of the Cadwallader Group and the Intermontane-Insular superterrane boundary, southwestern British Columbia. Canadian Journal of Earth Sciences, 24, 2279-2291.

Schiarizza, P., 2013. The Wineglass assemblage, lower Chilcotin River, south-central British Columbia: Late Permian volcanic and plutonic rocks that correlate with the Kutcho assemblage of northern British Columbia. In: Geological Fieldwork 2012, British Columbia Ministry of Energy, Mines and Natural Gas, British Columbia Geological Survey Paper 2013-1, pp. 53-70.

Schiarizza, P., Gaba, R.G., Garver, J.I., Glover, J.K., Macdonald, R.W.J., Archibald, D.A., Lynch, T., Safton, K.E., Sajgalik, P.P., Calon, T., Malpas, J., and Umhoefer, P.J., 1993. Geology of the Bralorne (north half) and northeastern Dickson Range map areas (92J/14, 15). British Columbia Ministry of Energy, Mines and Petroleum Resources, British Columbia Geological Survey Geoscience Map 1993-7, scale 1:50,000.

Schiarizza, P., Gaba, R.G., Glover, J.K., Garver, J.I., and Umhoefer, P.J., 1997. Geology and mineral occurrences of the Taseko-Bridge River area. British Columbia Ministry of Employment and Investment, British Columbia Geological Survey Bulletin 100, 291 p.

Sláma, J., Košler, J., Condon, D., and Crowley J., 2008. Plešovice zircon-a new natural reference material for U-Pb and Hf isotopic microanalysis. Chemical Geology, 249, 1-35.

Umhoefer, P.J., and Schiarizza, P., 1996. Latest Cretaceous to Early Tertiary dextral strike-slip faulting on the southeastern Yalakom fault system, southeastern Coast Belt, British Columbia.

Geological Society of America, Bulletin, 108, 768-785.
Umhoefer, P.J., Schiarizza, P., and Robinson, M., 2002. Relay Mountain Group, Tyaughton-Methow basin, southwest British Columbia: a major Middle Jurassic to Early Cretaceous terrane overlap assemblage. Canadian Journal of Earth Sciences, 39, 1143-1167.
van der Heyden, P., 2004. Uranium-lead and potassium-argon ages from eastern Bella Coola and adjacent parts of Anahim Lake and Mount Waddington map areas, west-central British Columbia. Geological Survey of Canada, Current Research 2004-A2, 14 p.
Wiedenbeck, M., Alle, P., Corfu, F., Griffin, W.L., Meier, M., Oberli, F., Quadt, A.V., Roddick, J.C., and Spiegel, W., 1995. Three natural zircon standards for U-Th-Pb, Lu-Hf, trace element and REE analyses. Geostandards Newsletter, 19, 1-23.
Wiedenbeck, M., Hanchar, J.M., Peck, W.H., Sylvester, P., Valley, J., Whitehouse, M., Kronz, A., Morishita, Y., Nasdala, L., Fiebig, F., Franchi, I., Girard, J.P., Greenwood, R.C., Hinton, R., Kita, N., Mason, P.R.D., Norman, M., Ogasawara, M., Piccoli, P.M., Rhede, D., Satoh, H., Schulz-Dobrick, B., Skår, Ø., Spicuzza, M.J., Terada, K., Tindle, K., Togashi, S., Vennemann, T., Xie, Q., and Zheng, Y.F., 2004. Further characterization of the 91500 zircon crystal. Geostandards and Geoanalytical Research, 28, 9-39.
Woodsworth, G.J., 1977. Geology, Pemberton (92J) map-area. Geological Survey of Canada, Open File 482, scale 1:250,000.

An update on the geology of northern Hogem batholith and its surroundings, north-central British Columbia

Luke Ootes[1, a], Anika L. Bergen[1], Dejan Milidragovic[1], Gabrielle O. Jones[1, 2], Alfredo Camacho[3], and Richard Friedman[4]

[1] British Columbia Geological Survey, Ministry of Energy, Mines and Petroleum Resources, Victoria, BC, V8W 9N3
[2] Department of Earth & Atmospheric Sciences, University of Alberta, Edmonton, AB, T6G 2E3
[3] Department of Geological Sciences, University of Manitoba, Winnipeg, MB, R3T 2N2
[4] Pacific Centre for Geochemical and Isotopic Research, University of British Columbia, Vancouver, BC, V6T 1Z4
[a] corresponding author: Luke.Ootes@gov.bc.ca

Recommended citation: Ootes, L., Bergen, A.L., Milidragovic, D., Jones, G.O., Camacho, A., and Friedman, R., 2020. An update on the geology of northern Hogem batholith and its surroundings, north-central British Columbia. In: Geological Fieldwork 2019, British Columbia Ministry of Energy, Mines and Petroleum Resources, British Columbia Geological Survey Paper 2020-01, pp. 25-47.

Abstract

New bedrock mapping refines the distribution and relationships of plutonic rocks in northern Hogem batholith and surrounding rocks in the Quesnel, Stikine, and Cache Creek terranes. Cutting the Quesnel terrane, the Hogem batholith is composed of ca. 197 Ma hornblendite and diorite of the Thane Creek suite, 182 to 178 Ma biotite pyroxenite and syenite of the Duckling Creek suite, ca. 160 Ma granite of the Osilinka suite, and ca. 174 Ma tonalite and 140 to 135 Ma granodiorite and granite of the Mesilinka suite. All units contain a penetrative foliation and $^{40}Ar/^{39}Ar$ biotite ages indicate post-deformation cooling and uplift after ca. 124 Ma. The Hogem batholith is bounded to the north and east by volcanic and sedimentary rocks of the Nicola Group (Triassic) along fault and intrusive contacts. To the west, Hogem batholith and Nicola Group are separated from the Cache Creek and Stikine terranes along the Pinchi-Ingenika dextral strike-slip fault system; farther west, an unexposed thrust fault juxtaposes Cache Creek rocks above Stikine terrane rocks. The Stikine terrane in the study area includes the Asitka Group (Carboniferous to Permian) volcano-sedimentary basement that is overlain by immature siliciclastic sedimentary rocks of the Dewar Formation (Takla Group; Triassic), and which is overlain by the Telkwa Formation (Hazelton Group; Jurassic). Cache Creek terrane encompasses metamorphic rocks of the Sitlika assemblage (Lower Jurassic), which have sedimentary and volcanic protoliths, serpentinites of the Trembleur ultramafic complex (Permian to Upper Triassic), mixed volcanic and metasedimentary rocks of the Sowchea succession (Upper Pennsylvanian to Lower Jurassic), and Cretaceous intrusive rocks of the Axelgold layered mafic intrusion. About 88 mineral occurrences in the area are documented in MINFILE. Seven new occurrences discovered in 2019; five of these close to previously recognized mineralization. When combined with results of 2018 mapping, 24 new mineral occurrences have been documented in the study area. Porphyry Cu ±Mo, Au in Hogem batholith is the predominant type followed by quartz-carbonate vein-hosted base and precious metals in Quesnel and Stikine terranes, and volcanic/sediment-hosted Cu in the Telkwa Formation of the Stikine terrane.

Keywords: Hogem batholith, Quesnel terrane, Stikine terrane, Cache Creek terrane, Cretaceous deformation, copper and gold, porphyry, veins, sediment-hosted

1. Introduction

In 2018, the British Columbia Geological Survey initiated a three-year mapping project in the Omineca Mountains of north-central British Columbia (Figs. 1, 2; Ootes et al., 2019a, b, 2020a). The project aims to better understand the bedrock and surficial geology and associated base- and precious-metal mineralization in the northern part of Hogem batholith. Detailed 1:50,000-scale mapping in 2019 included parts of NTS 93M/16, 93N/13, 94C/03, 04, 05, and 94D/01, 08 (Fig. 3; Ootes et al., 2020a). Herein we present the results of this mapping, which focussed on northern Hogem batholith and surrounding supracrustal, intrusive, and ultramafic rocks of the Quesnel, Stikine, and Cache Creek terranes; a companion full-scale map is presented elsewhere (Ootes et al., 2020a). We also present the preliminary results of new U-Pb zircon and $^{40}Ar/^{39}Ar$ biotite, hornblende, and muscovite geochronology and geochemical data, the details of which will also be presented elsewhere (Ootes et al., 2020b).

2. Geologic setting

The 2019 study area includes igneous intrusive rocks of northern Hogem batholith, metamorphosed volcanic and sedimentary rocks and less common intrusive rocks of the Quesnel and Stikine terranes, and metamorphic and ultramafic rocks of the Cache Creek terrane (Fig. 2). The Hogem batholith is bounded to the north and east by volcanic and sedimentary rocks of the Nicola Group (Triassic; Quesnel terrane) along fault and intrusive contacts (Figs. 2, 3). To the west, Hogem batholith and Nicola Group are juxtaposed against Cache Creek and Stikine terranes across the Pinchi-Ingenika dextral strike-slip fault system. The Stikine and Cache Creek terranes are separated by an unexposed thrust fault (Figs. 2, 3). To the

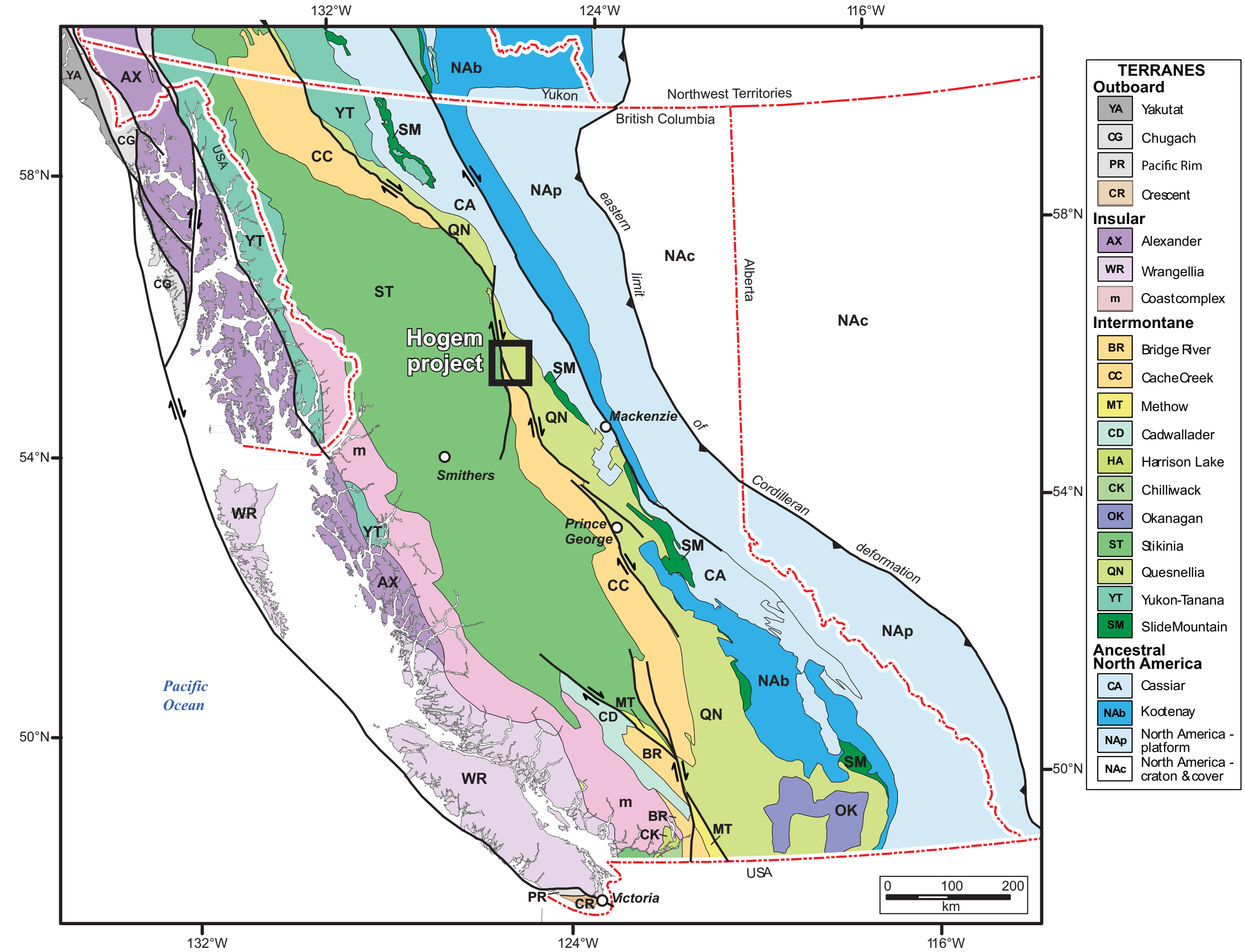

Fig. 1. Terrane map of British Columbia with location of study area. Modified after Nelson et al. (2013).

west, Stikine rocks are covered or are in fault contact with Bowser Lake and Sustut group sedimentary rocks (Jurassic to Cretaceous; Evenchick et al., 2007). CGG Canada Services Ltd. (2018) presented the results of an airborne geophysical survey that extends across much of the study area and includes both radiometric (K, U, Th) and magnetic data.

3. Quesnel terrane supracrustal rocks and northern Hogem batholith

Northern Hogem batholith was mapped by Armstrong (1946), Lord (1948, 1949), Armstrong and Roots (1948, 1954) and Roots (1954). Although Roots (1954) gave thorough descriptions of a wide variety of intrusive units, he grouped these units as 'undivided'. Woodsworth (1976) further subdivided northern Hogem batholith, and Irvine (1976) investigated ultramafic intrusions near northern Hogem batholith. In the south-central part of the study area, Nelson et al. (2003) updated mapping near the Hawk quartz vein-hosted gold prospect. Southern Hogem batholith was subdivided by Garnett (1972, 1978). Nixon and Peatfield (2003), Bath et al. (2014), and Devine et al. (2014) studied the Lorraine porphyry Cu-Au deposit southeast of the study area, providing isotopic ages for mineralization and the host rocks. Mapping by Ferri et al. (2001a, b), in areas to the east and northeast, focussed on the Takla Group (referred to herein as the Nicola Group; see below) and left the Hogem batholith largely undivided. Schiarizza and Tan (2005a, b) mapped the Nicola Group north of the study area, plotting preliminary isotopic ages for plutonic rocks at the northern tip of Hogem batholith.

3.1. Nicola Group (also referred to as Takla Group)

Previous mappers in the study area and in the general region used the term 'Takla Group' to refer to Triassic volcanic and sedimentary rocks of the Quesnel terrane (e.g., Armstrong, 1948; Lord, 1948, 1949; Armstrong and Roots, 1948; Monger, 1977; Ferri et al., 2001a, b; Schiarizza and Tan, 2005a, b). However, equivalent rocks in southern Quesnel terrane are referred to as 'Nicola Group' (see summaries in e.g., Schiarizza, 2016, 2019), which is the term we adopt here; for use in the Stikine terrane we retain 'Takla Group' (see section 4.2.). Ferri

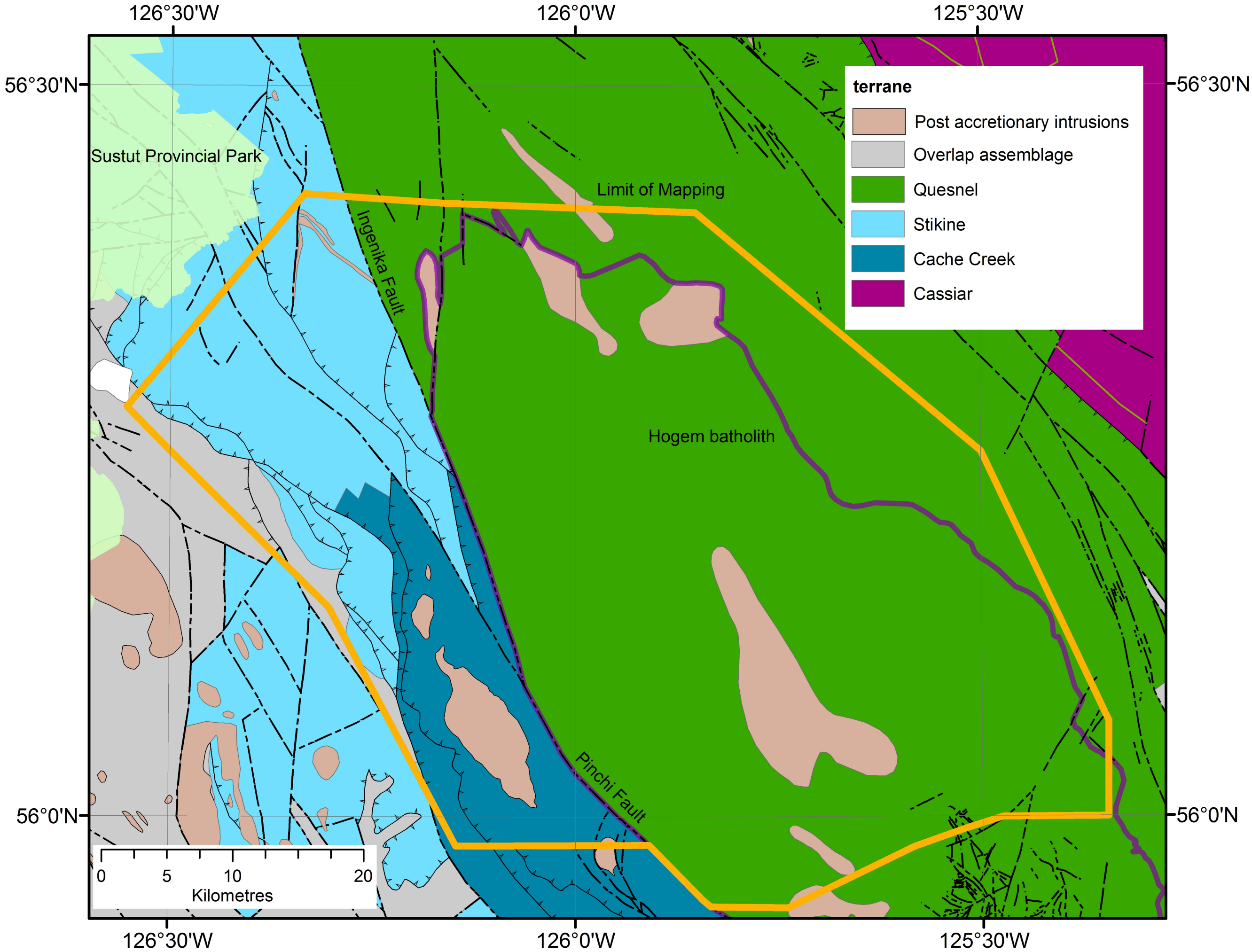

Fig. 2. Regional context of northern Hogem batholith and its surroundings. Orange line delimits the study area mapped during the 2018-2019 field seasons. Hogem batholith (purple outline) is in the Quesnel terrane, which is separated from the Cache Creek and Stikine terranes by the Pinchi-Ingenika fault (dextral strike-slip). Thrust faults on the map have teeth on the hanging wall side; dashed lines are undifferentiated strike-slip and normal faults.

et al. (2001a, b) divided these rocks into the Plughat Mountain (Late Triassic) and Vega Creek successions (Late Triassic-Early Jurassic). Only the Plughat Mountain succession is in the study area, where it consists of grey and green augite and augite-plagioclase phyric mafic tuffs and volcanic breccias with lesser volcanic flows, tuffaceous sedimentary rocks, argillites, and limestones. To the west and north, Schiarizza and Tan (2005a, b) divided the Nicola Group into the Goldway Peak unit, which consists mainly of pyroxene-bearing volcanic rocks, and the Kliyul unit, which consists mainly of volcaniclastic rocks. Both units are considered equivalent to the Plughat Mountain succession of Ferri et al. (2001a, b).

3.2. Hogem batholith

We organize the intrusive phases in northern Hogem batholith into four suites (Fig. 3) modified after Woodsworth (1976) and Woodsworth et al. (1991). The descriptions are modified and simplified from Ootes et al. (2019b). All major intrusive phases in Hogem batholith are deformed.

3.2.1. Thane Creek suite; Early Jurassic, ca. 197 to 196 Ma

The eastern and southwestern parts of the study area are underlain by diorite to quartz monzodiorite and lesser hornblendite of the Thane Creek suite, the oldest intrusive rocks in Hogem batholith (Ootes et al., 2019a, b). Diorite crosscuts and co-mingles with the hornblendite and where co-mingling is present, the rocks are texturally and compositionally heterogeneous in terms of amphibole, plagioclase, and magnetite concentrations. The diorite contains a penetrative ductile fabric defined by aligned hornblende and/or biotite. A hornblendite sample yielded a U-Pb zircon age of 197.55 ±0.11 Ma and a diorite sample yielded a $^{206}Pb/^{238}U$ zircon age of 196.61 ±0.19, both of which we interpreted as crystallization ages (see below). Biotite and hornblende from the diorite sample were also analyzed by laser step heating, yielding $^{40}Ar/^{39}Ar$ age ages of ca. 124 Ma, which we interpret to record the time of cooling through closure temperatures after regional deformation (see below).

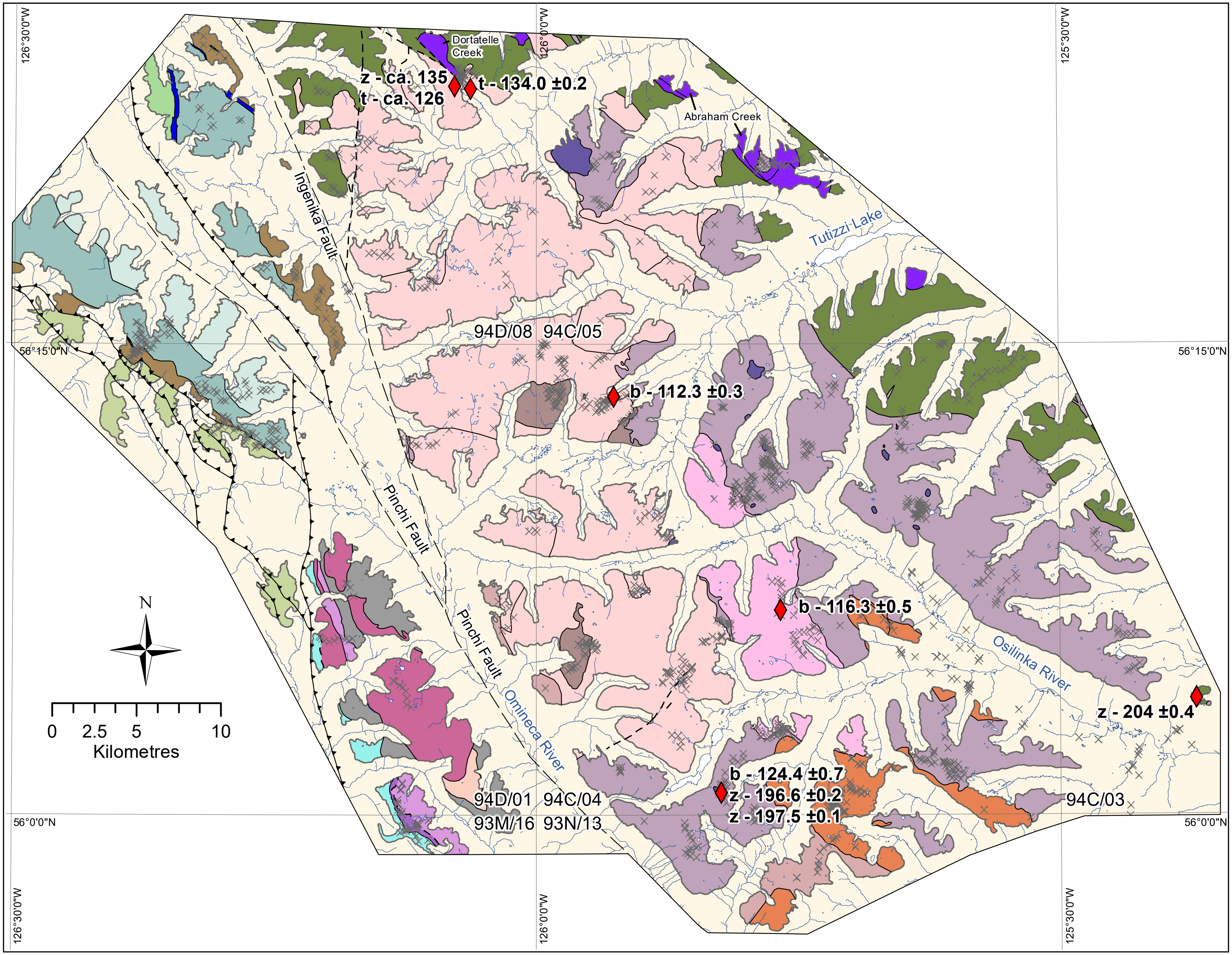

Fig. 3. Geology of northern Hogem batholith and surroundings, generalized from Ootes et al. (2020a) and modified after Lord (1949), Armstrong and Roots (1954), Richards (1976), Woodsworth (1976), Ferri et al. (2001a, b), Schiarizza and Tan (2005b), and Evenchick et al. (2007). Geochronologic data include results from this study, Mortensen et al. (1995), Schiarizza and Tan (2005b), and Ootes et al. (2020b).

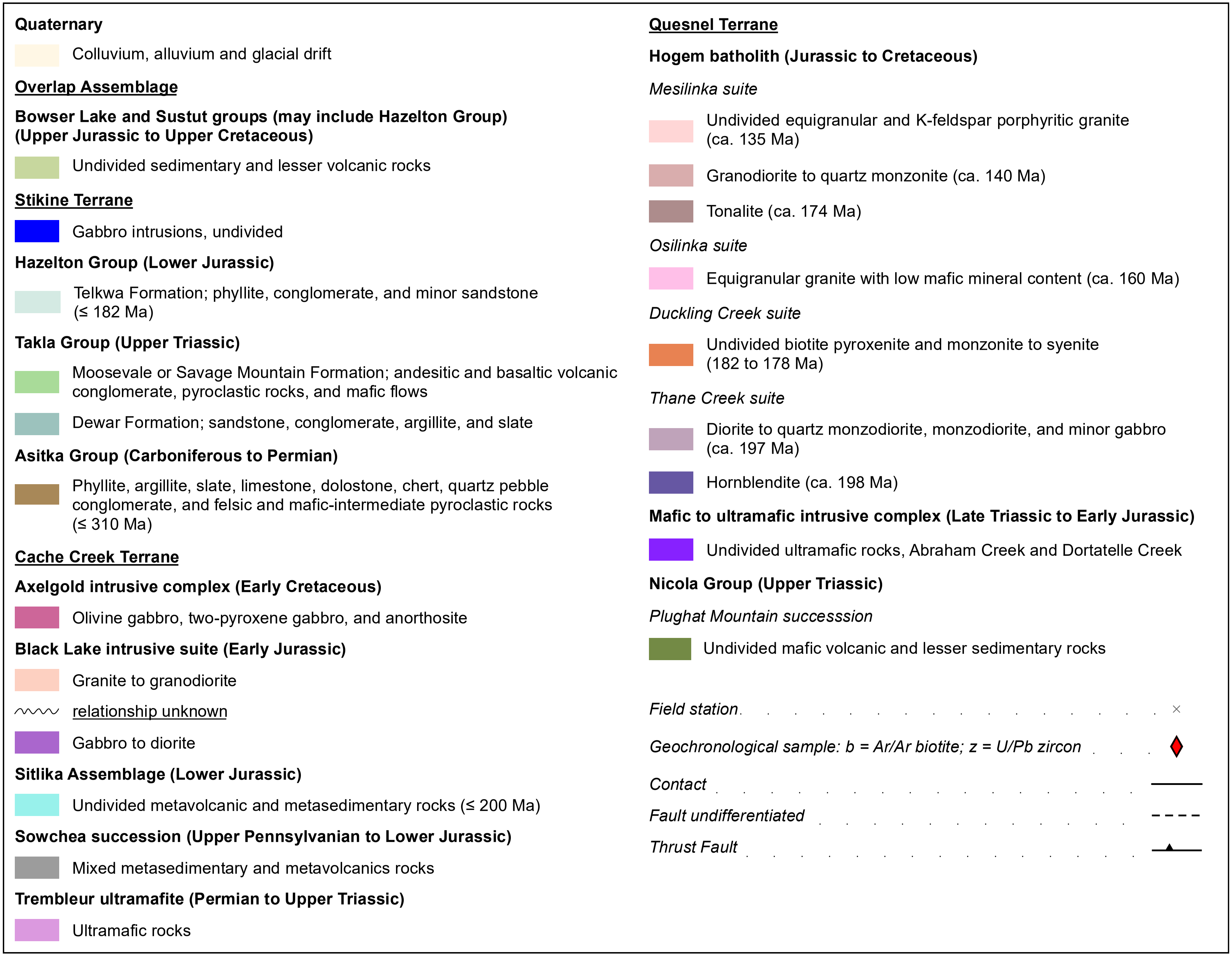

Fig. 3. Continued.

3.2.2. Duckling Creek suite; Early Jurassic, ca. 182 to 178 Ma

The south-southeast part of the study area is underlain by quartz-undersaturated rocks of the Duckling Creek suite (Fig. 3). South of the study area, Devine et al. (2014) identified three stages of the Duckling Creek suite and constrained the timing with U-Pb zircon ages: 1) biotite pyroxenite (ca. 182 to 178.5 Ma); 2) predominantly K-feldspar porphyritic syenite to monzonite (ca. 178.8 to 178.4 Ma); and 3) massive syenite and pegmatite (ca. 177 to 175 Ma). All three phases exist in the study area. The oldest phase is biotite pyroxenite, locally with megascopic phenocrysts (up to 0.5 cm) of white weathering apatite. Biotite pyroxenite is crosscut by syenite to monzonite, with lesser monzodiorite. These rocks range from equigranular to porphyritic to pegmatitic. Porphyritic varieties contain tabular, commonly zoned, K-feldspar phenocrysts (up to 5 cm long) that are set in a groundmass of equigranular green pyroxene and lesser plagioclase (possibly albite), hornblende, magnetite, titanite, and apatite. Rhythmic magmatic layering defined by varying felsic and mafic mineral ratios and alignment of K-feldspar phenocrysts is common. The entire unit has moderate to strong magnetism, with areas of highest magnetism spatially associated with biotite pyroxenite. The biotite pyroxenite zones are locally stained with malachite and have disseminated chalcopyrite.

Hornblende was separated from a K-feldspar porphyritic syenite sample and analyzed by laser step-heating, yielding an integrated $^{40}Ar/^{39}Ar$ age of a ca. 177.6 Ma (Ootes et al., 2020b). This result overlaps, within uncertainty, with a previously reported $^{40}Ar/^{39}Ar$ biotite age of 177.1 ±0.9 Ma for a similar syenite sample to the south (Devine et al., 2014). These ages are best interpreted as magmatic cooling through the closure temperature of hornblende (ca. 550°C).

3.2.3. Osilinka suite; Late Jurassic, ca. 160 Ma

The central part of the Hogem batholith is underlain by a unit of mafic-poor equigranular granite of the Osilinka suite. The scarcity of micaceous or mafic minerals in the granite likely hampered the development of a foliation and the granites appear massive, but mafic dykes within it contain penetrative foliation and shear fabrics (Ootes et al., 2019b).

Preliminary geochemical results indicate that this unit is an S-type granite and preliminary geochronology indicate that it contains significant zircon inherited from older crustal sources; the youngest zircons are ca. 160 Ma, providing a maximum crystallization age for the granite (Ootes et al., 2020b). This granite was previously thought to be the youngest mappable intrusive phase in Hogem batholith (Ootes et al., 2019a, b), but is now considered older than the granitic rocks of the Mesilinka suite (section 3.2.4.). Biotite and muscovite from an Osilinka granite sample were analyzed by laser step heating, yielding $^{40}Ar/^{39}Ar$ cooling ages between ca. 122 to 115 Ma (see below). These cooling ages are interpreted to post-date the peak of regional deformation.

3.2.4. Mesilinka suite; Early Cretaceous, ca. 140 Ma, but with mappable Middle Jurassic, ca. 174 Ma, enclaves

Throughout the western part of the study area the predominant rock type is equigranular and K-feldspar porphyritic granite (Fig. 3). These rocks contain elevated Th over K and are particularly evident on the Th/K radiometric maps (CGG Canada Services Ltd, 2018; Ootes et al., 2019a). The K-feldspar porphyritic granite crosscuts the equigranular granite and both contain a foliation that cuts the intrusive contacts. Both contain enclaves of tonalite and granodiorite. The tonalite enclaves form small mappable bodies in the western part of the study area (Fig. 3), and we previously considered them be part of the Thane Creek suite (Ootes et al., 2019a, b). However, the tonalite only occurs as enclaves within the younger Mesilinka granites and Schiarizza and Tan (2005b) reported a preliminary age of ca. 174 Ma age for similar tonalites in northern Hogem batholith. Thus, we now consider the tonalite as the oldest phase of the Mesilinka suite. Similarly, we now consider that the granodiorite enclaves in the southwest part of Hogem batholith that we previously assigned to Thane Creek suite (Ootes et al., 2019a, b) are part of the Mesilinka suite. In addition, preliminary geochemical data (Ootes et al., 2020b) indicate that these granodiorites have a kinship with their granitic hosts.

The Mesilinka granites are S-type and preliminary U-Pb zircon results indicate significant inheritance from older crustal sources, with the youngest zircons (ca. 135 Ma) providing a maximum crystallization age (Ootes et al., 2020b). Biotite from a Mesilinka K-feldspar porphyritic granite sample yielded an integrated $^{40}Ar/^{39}Ar$ age of 112.3 ±0.3 Ma (see below) and two separate aliquots of biotite from a tonalite sample yielded $^{40}Ar/^{39}Ar$ ages of ca. 112 and 109 Ma ages (Ootes et al., 2020b), which we consider related to post-deformation uplift. However, mineral separates from a granodiorite phase yielded an $^{40}Ar/^{39}Ar$ age for biotite of ca. 122.6 Ma and for hornblende of ca. 139 Ma (Ootes et al., 2020b), potentially indicating primary magmatic cooling before deformation.

3.3. Mafic-ultramafic intrusive complexes; Late Triassic to Early Jurassic

Mafic-ultramafic intrusive complexes are on the periphery of northern Hogem batholith and surrounding Nicola Group (Fig. 3; e.g., Irvine, 1976; Ferri et al., 2001a). They differ from the Thane Creek suite hornblendites by containing olivine and clinopyroxene-rich ultramafic rock types. The precise age of the mafic-ultramafic complexes remains unknown but are considered Late Triassic to Early Jurassic.

3.3.1. Abraham Creek intrusive complex

The Abraham Creek intrusive complex is an elongate (ca. 30 by 5 km) northeast-trending body that cuts the Nicola Group northeast of the Hogem batholith (Fig. 3; Ferri et al., 1993, 2001a). Also known as the Aiken Lake intrusive complex (Massey et al., 2005a, b), it consists of hornblende gabbro, diorite, and clinopyroxenite with lesser peridotite, hornblendite, and orthopyroxenite (Irvine, 1976; Ferri et al., 1993). The complex displays a strong aeromagnetic signature that contrasts with the weak to moderately magnetic host rocks. The most mafic rock type is dark grey-green, medium-grained olivine (<25%) clinopyroxenite (Fig. 4a) that is magnetite bearing and serpentinized. This grades into magnetite-hornblende clinopyroxenite with saussuritized interstitial plagioclase. Ubiquitous igneous breccias include fragments of dark green clinopyroxenite in a hornblende-rich gabbro to diorite groundmass (Fig. 4b). Northwest-striking, shallowly dipping, <30 cm wide quartz veins are associated with narrow (ca. 1 m) zones of rusty-weathering, malachite-stained clinopyroxenite, indicating local Cu-sulphide mineralization.

3.3.2. Dortatelle Creek ultramafic complex

The Dortatelle Creek ultramafic complex (Lord,1948; Irvine, 1976; Schiarizza and Tan, 2005b) is an elongate, northwest-trending ultramafic body in the northernmost part of the map area (Fig. 3). Its high aeromagnetic expression (CGG Canada Services Ltd., 2018) indicates dimensions of 5 by 1.5 km. The southwest flank of the complex is cut by weakly to moderately magnetic, high-Th granite of the Mesilinka suite with well-developed internal high-strain zones (Fig. 4d). To the northeast, the ultramafic rocks are in structural contact with highly strained rocks of the Nicola Group. Brown-weathering, fine- to medium-grained, fresh dunite is the predominant and most mafic lithology in the southeastern part of the complex (Fig. 4c). Trace amounts of chromite are homogeneously disseminated throughout the dunite. Dunite is crosscut by dikes of sugary, garnet±muscovite-bearing granite of the Mesilinka suite. Close to the granite are veins and stockworks of talc±carbonate. Green-weathering, variably magnetite-rich, olivine clinopyroxenite is also a main lithology.

4. Stikine terrane

Rocks assigned to the Stikine terrane in the study area were mapped by Lord (1948, 1949) and further subdivided by Richards (1976). Details of Permian (Asitka Group) and Triassic (Takla Group) units are summarized in Monger (1977) and the Jurassic section (Hazelton Group) is summarized in Tipper and Richards (1976). Evenchick et al. (2007) further refined Stikine geology focussing on Jurassic to Cretaceous overlap assemblages (e.g., Bowser Lake and Sustut groups).

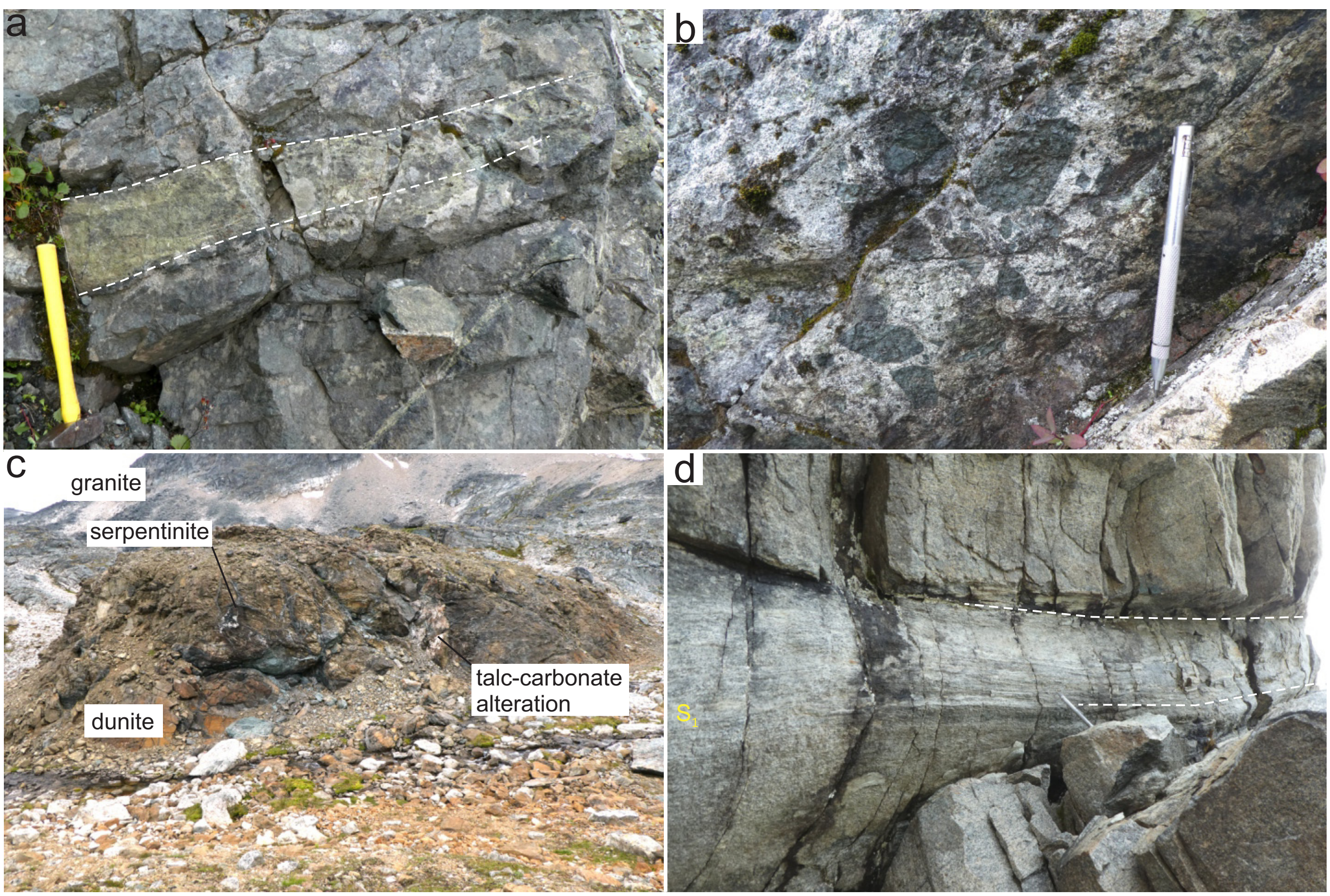

Fig. 4. a) Abraham Creek intrusive complex olivine clinopyroxenite (dark green), cut by a zone of hydrothermal epidote alteration (light green, bounded by white dashed lines). **b)** Abraham Creek intrusive complex intrusive breccia with olivine clinopyroxenite enclaves in a diorite groundmass. **c)** Dortatelle ultramafic complex rocks. Mesilinka suite granitic rocks are in the background. **d)** A high-strain zone (bounded by white dashed lines) in a strongly foliated, biotite-rich, equigranular granite of the Mesilinka suite.

4.1. Asitka Group

The Asitka Group (Carboniferous to Permian) represents a basement domain to the Stikine terrane. It is composed of felsic to intermediate flows and tuffs, argillites, slates, limestones, dolostones, and cherts (Fig. 5; Lord, 1948, 1949; Monger, 1977). A minimum thickness is estimated to be 2600 m, but the base is not exposed (Lord, 1948). Fossils, including fusulinids, corals, brachiopods, and bryozoan indicate it was deposited in the Lower Permian (Lord, 1948, 1949; Monger, 1977). Diakow (2001) reported a ca. 308 Ma U-Pb zircon crystallization age from a rhyolite about 80 km north of the study area. Although it was considered part of the Asitka Group, this rhyolite may be part of an older Carboniferous basement to the Stikine terrane (L. Diakow, personal communication 2019). Uranium-lead detrital zircon results from a quartz pebble conglomerate sample indicate provenance from Carboniferous sources, with the youngest zircons at ca. 310 Ma (Ootes et al., 2020b). Paleomagnetic data, acquired from volcanic rocks of the Asitka Group, indicate deposition at paleolatitudes of 21° to 23° N (Irving and Monger, 1987).

The Asitka Group underwent low-grade metamorphism and deformation, and many of the fine-grained siliciclastic units are best described as phyllites with a bedding-parallel foliation. Bedding (S_0) is best preserved in the chert units, where interbedded brown mudstone and chert are readily identifiable (Fig. 5b). In the phyllites and slates, bedding is transposed into a subparallel foliation (S_0 - S_1; Figs. 5c, d). Second generation structures are locally preserved as folds of S_0-S_1 and as a rare spaced crenulation cleavage (S_2; Figs. 5c, d). Second generation fold axes are moderately plunging, generally to the north-northeast. In the same outcrop however, the azimuth of fold axes in different folds can vary up to 90° (Fig. 6a), which may indicate that these folds are refolded.

4.2. Takla Group; Dewar Formation

The Asitka Group is unconformably overlain by the Takla Group (Fig. 3; Triassic; Lord, 1948; Monger, 1977). The basal unit of the Takla Group is the Dewar Formation, which comprises interbedded sandstone, siltstone, and argillite (Fig. 7). The Savage Mountain Formation is composed of mafic

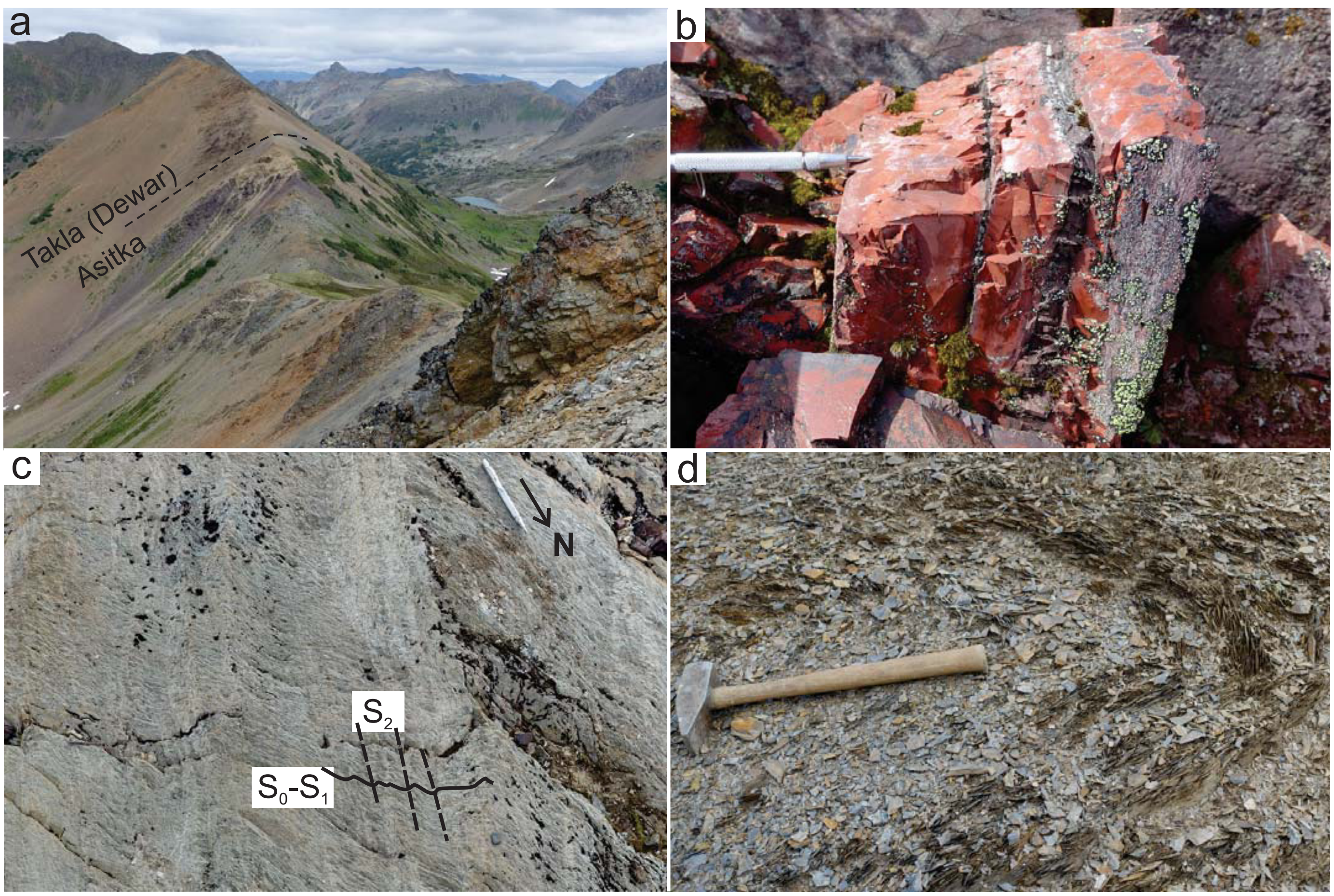

Fig. 5. Representative outcrop photographs of the Asitka Group. **a)** View looking up-section, showing the variable weathering colours of this unit. The resistant weathering outcrop in the immediate foreground (bottom right) is either feldspathic sandstone or felsic-intermediate volcanic flow. The upper contact with the Dewar Formation of the Takla Group is estimated. Photograph is from the western-most part of the study area, and the view is toward the northeast. **b)** Red-weathering chert with brown mudstone interbeds. **c)** Relationship between bedding and bedding parallel foliation (S_0-S_1) and a weakly developed spaced crenulation cleavage (S_2) in phyllite. **d)** Steeply northeast plunging F_2 fold of slaty bedding and cleavage.

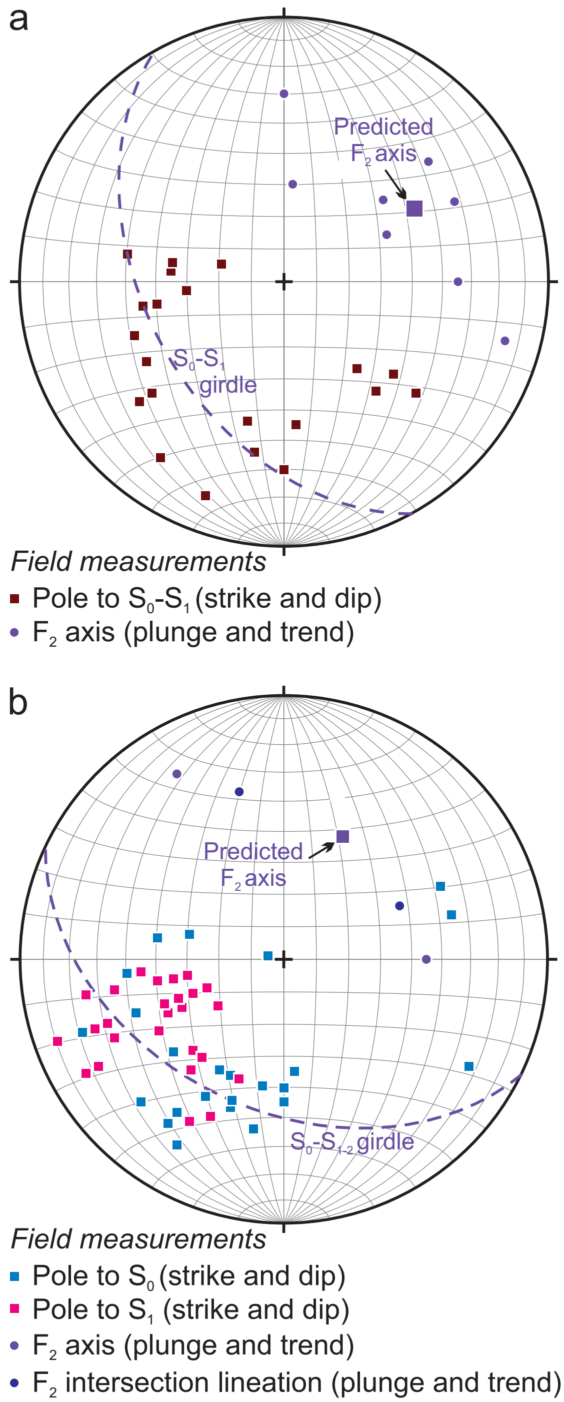

Fig. 6. Equal area stereonet lower hemisphere projections. **a)** Poles to Asitka Group bedding and bedding parallel foliation (S_0-S_1) define a best-fit great circle (S_0-S_1 girdle) with a pole that should predict the F_2 fold axis (purple square). **b)** Dewar Formation (Takla Group) and Telkwa Formation (Hazelton Group) structural measurements showing the same relationships as those depicted in a), but with S_0 and S_1 separated. Plots generated using Allmendinger software, available at: http://www.geo.cornell.edu/geology/faculty/RWA/programs/stereonet.html.

flows and pyroclastic rocks and overlies and is intercalated with the Dewar Formation. The uppermost Moosevale Formation is mostly coarse-grained volcaniclastic rocks (Monger, 1977). The Dewar Formation was examined at one location in the study area, where black, graphitic shale (slate) is above steel-grey phyllite and brown carbonate rocks of the Asitka Group (Fig. 7a). These rocks grade upsection into slate, then into thick-bedded (up to 1.5 m) feldspathic sandstone (±grains of clinopyroxene) with interbeds of argillite and lesser slate (Figs. 7a-c). Local cross beds in the sandstones and load casts and flame structures at sandstone-argillite contacts (Fig. 7b), indicate that bedding is upright and youngs to the east. Deformation in the Dewar Formation is similar to that of the Asitka Group and displayed as foliations that are sub-parallel to bedding and interpreted as S_1, and folds that are interpreted as F_2 (Fig. 6b).

4.3. Hazelton Group (latest Triassic to Middle Jurassic), Telkwa Formation

The Takla Group is overlain by the Hazelton Group. In the present map area, it includes three formations, from base to top: Telkwa, Nilkitkwa, and Smithers (Tipper and Richards, 1976; Monger, 1977). The Telkwa Formation is the main unit exposed in the study area (Fig. 3), although Evenchick et al. (2007) included other undivided Hazelton Group units. The Telkwa Formation consists of volcanic-derived siliciclastic rocks that are difficult to distinguish from the Moosevale Formation of the Takla Group, and commonly have similar weathering colours (maroon and green) to the Asitka Group (Monger, 1977). It includes clast-supported, monomictic (feldspar porphyry clasts) and polymictic (volcanic clasts) cobble conglomerates that are interbedded with purple well-sorted feldspathic sandstones, and purple, maroon, and green shales (Fig. 7d). Upsection are monomictic pebble conglomerates with intermediate volcanic clasts (Fig. 7e). Uranium-lead detrital zircon results from a volcanic-pebble conglomerate sample indicate provenance from Upper Triassic and Lower Jurassic sources, with the youngest zircons at ca. 182 Ma (Ootes et al., 2020b).

4.4. Overlap assemblages: Bowser Lake and Sustut groups

In the west-southwest part of the study area, the Bowser Lake (Jurassic-Cretaceous) and Sustut (Cretaceous) groups were mapped by Evenchick et al. (2007). These are undivided on Figure 3 where they are depicted in thrust contact with the structurally overlying Telkwa Formation and undivided Hazelton Group rocks and locally against the Asitka Group (Fig. 7a; Evenchick et al., 2007).

5. Cache Creek terrane

Rocks assigned to the Cache Creek terrane were mapped by Lord (1948, 1949) and further subdivided by Monger (1974), Paterson (1974), and Richards (1976), and Irvine (1974, 1976) mapped the Axelgold layered mafic intrusion. Immediately

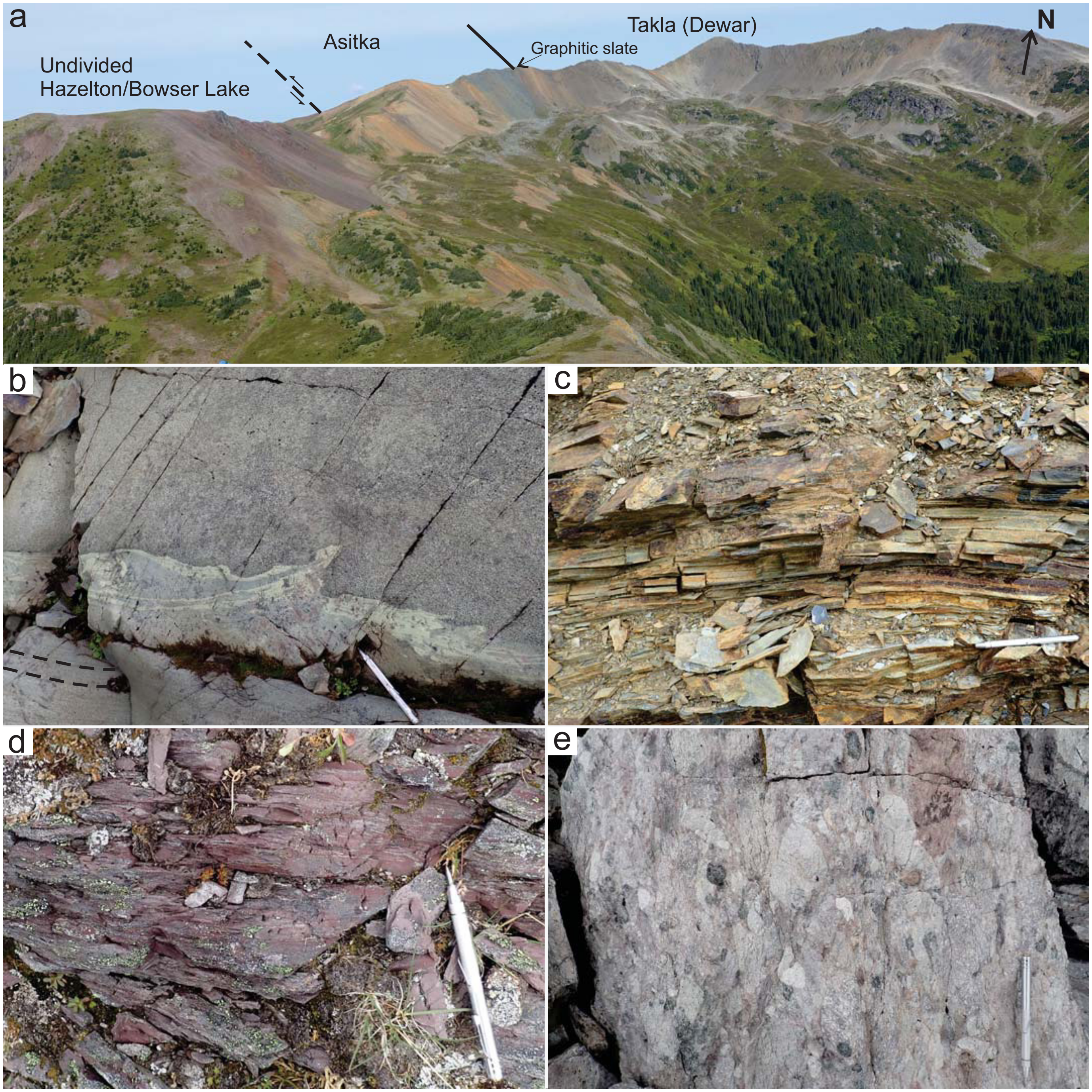

Fig. 7. Outcrop photographs of the Hazelton and Bowser Lake groups, Dewar Formation (Takla Group) and Telkwa Formation (Hazelton Group). **a)** A section of undivided Hazelton Group and Bowser Lake Group purple volcanic rocks that contain copper mineralization is structurally beneath the Asitka Group, which is overlain by the Dewar Formation, the base of which is marked by graphitic slates. View is to the north. **b)** Dewar Formation massive grey feldspathic cross-stratified sandstone with interbedded, fine-grained, green-grey argillite displaying flame structures. Beds are upright, younging is toward the top of the photograph. Dashed black lines mark subtle cross-beds in the lower sandstone bed. **c)** Dewar Formation slate. **d)** Telkwa Formation maroon mudstone. **e)** Telkwa Formation polymictic cobble conglomerate with volcanic clasts.

south of the study area, rocks of the Cache Creek terrane were mapped by Schiarizza (2000) and Evenchick et al. (2008).

5.1. Sowchea succession

The Sowchea succession (Upper Pennsylvanian to Upper Triassic; also referred to as Cache Creek Group; Paterson, 1974; Richards, 1976; Evenchick et al., 2007) includes phyllite chert, marble, greywacke, greenstone, amphibolite, and chlorite schist (Paterson, 1974; Schiarizza, 2000). A high-temperature contact metamorphic aureole is present around the Axelgold layered intrusion (Irvine, 1974).

5.2. Trembleur ultramafite serpentinite

Pervasively serpentinized ultramafic rocks form a narrow and discontinuous northwest-striking belt at least 25 km long, which follows the general structural and geophysical fabric of the area west of the Pinchi fault. The serpentinite weathers yellow-brown to dark brown and is dark green to dark grey on fresh surfaces. Warty textures on weathered surfaces indicate a harzburgitic or lherzolitic protolith that has been recrystallized to serpentine and magnetite±brucite, magnesite. Locally, metamorphic olivine and clinopyroxene indicate prograde metamorphism of serpentinite. In serpentine breccias, rounded fragments of light-weathering, medium-grained, massive serpentinite float in a darker, red and brown-weathering, fine-grained, foliated serpentinite matrix (Fig. 8a). The serpentinite has a high magnetic expression on the regional aeromagnetic map (CGG Canada Services Ltd., 2018). Sulphides are present in trace amounts in the serpentinized rocks.

In the southwest corner of the study area, strongly serpentinized peridotite is bordered to the west by gabbro to diorite of uncertain affinity. Near the contact, slivers of highly serpentinized rocks (Fig. 8b) may represent rafts of peridotite in diorite or fault slices.

5.3. Sitlika assemblage

The Sitlika assemblage (Upper Triassic to Lower Jurassic; Paterson, 1974) includes fine- to medium-grained, moderately to strongly foliated, greenschist-facies volcanic and sedimentary rocks. These rocks generally have a low to moderate aeromagnetic signature. In the southwest corner of the study area the unit forms two principal lithologic belts (Fig. 3). The western belt includes fine-grained brown to rusty argillaceous schist and medium-grained, calcareous clinozoisite-muscovite-biotite-quartz schist that are northwest-striking and moderately to steeply northeast dipping. The clinozoisite occurs as porphyroblasts that have corroded margins and are aligned along a muscovite and biotite-defined foliation (Fig. 8c). The eastern belt consists of fine-grained light green- to grey-weathering, moderately to strongly foliated chlorite-sericite schist that may have a volcanic protolith, similar to rocks interpreted by Logan et al. (2010) to have been derived from mafic to intermediate volcanic rocks. Locally, subparallel bedding and schistosity in argillaceous schists define broad open, nearly recumbent gently westward plunging folds (Fig. 8d). Paterson (1974) considered the age of the Sitlkika assemblage to be Upper to Triassic to Jurassic. Outside the study area, the Sitlika assemblage

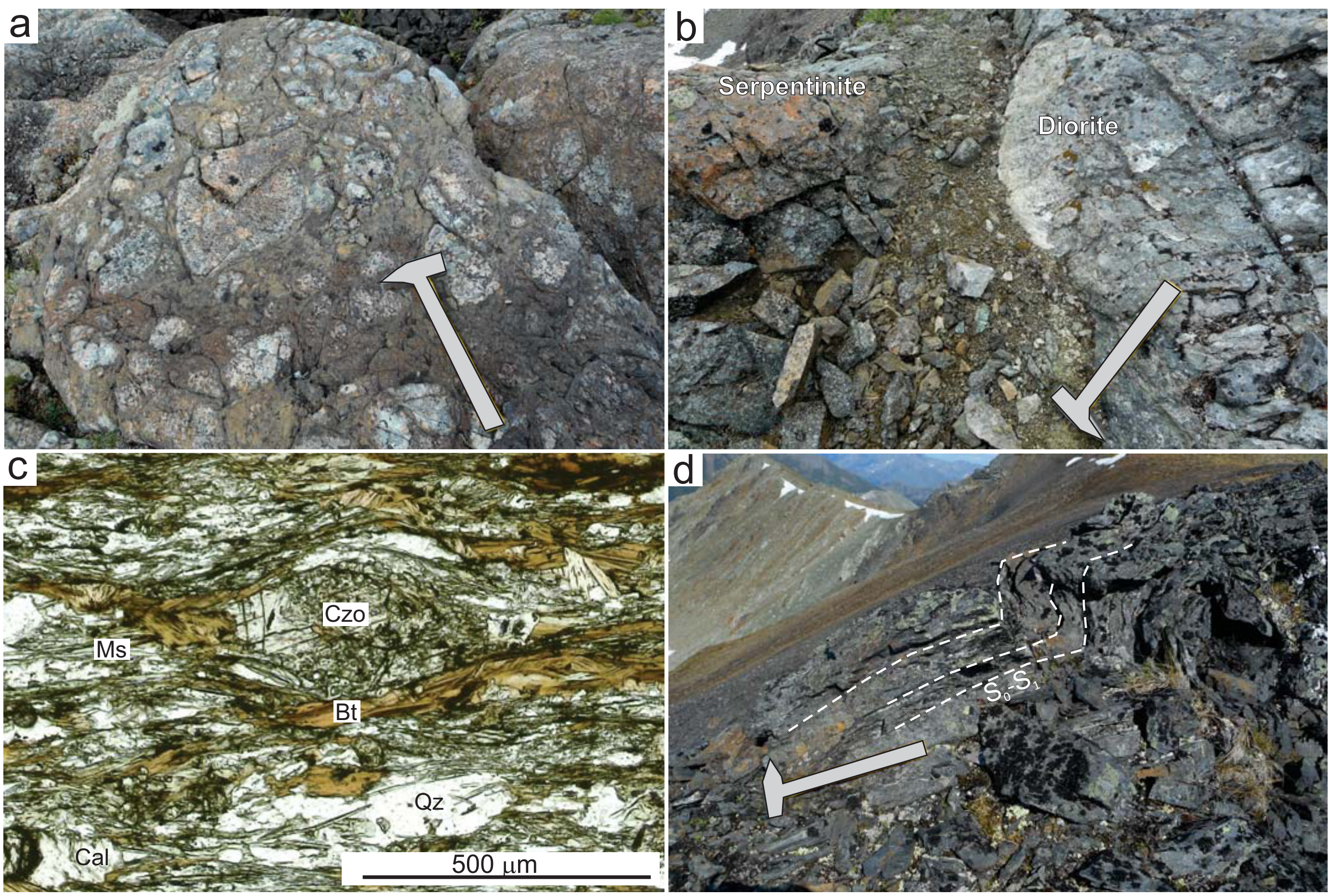

Fig. 8. a) Trembleur ultramafite serpentinite breccia. **b)** Trembleur ultramafite serpentinite adjacent to diorite (gabbro-diorite unit). **c)** Plane-polarized light photomicrograph of a strongly foliated (S_1), calcareous clinozoisite-muscovite-biotite-quartz schist from the western belt of the Sitlika assemblage. Bt=biotite; Cal=calcite; Czo=clinozoisite; Ms=muscovite; Qz=quartz. **d)** Sitlika assemblage argillaceous schists with broad open fold of subparallel bedding (S_0) and schistosity (S_1); hinge line plunges 20° toward 270°.

is considered to be Permian-Jurassic (Logan et al., 2010). Uranium-lead detrital zircon results from a sandstone sample indicate provenance from Carboniferous and Triassic sources, with the youngest zircons at ca. 200 Ma (Ootes et al., 2020b).

5.4. Gabbro to diorite

In the southwest part of the map area, mafic to intermediate intrusive rocks outcrop in a narrow sliver bounded by on the southwest by the Sitlika assemblage and the northeast by Trembleur ultramafic rocks. They display a mottled appearance defined by variable abundance and coarseness of the main minerals, plagioclase and hornblende. Other phases include apatite, alkali feldspar, quartz, and epidote. Fine-grained, sugary-textured, foliated intermediate to felsic quartz and/or feldspar phyric hypabyssal intrusive rocks are ubiquitous. Centimetre to metre-scale screens of well foliated Sitlika assemblage chlorite-sericite schist are in the intrusion, but the intrusive rocks lack a penetrative foliation and are considered to have intruded after development of the foliation.

5.5. Black Lake intrusive suite (Early Jurassic)

Cache Creek terrane rocks are cut by biotite-hornblende bearing granite to granodiorite that are assigned to the Black Lake intrusive suite (Jurassic; Evenchick et al., 2007). Only one pluton of this suite is in the study area (Fig. 3; Evenchick et al., 2007).

5.6. Axelgold layered gabbro intrusion (Early Cretaceous)

Rocks of the Axelgold intrusion are typically coarse-grained black to brown to green white weathering olivine gabbro, two-pyroxene gabbro, and anorthosite, and include lesser syenite phases. Magmatic layering is ubiquitous at the m-scale and consists of variable gabbroic compositions; overall the layering appears define a bowl shape (Irvine, 1975, 1976). A high-temperature metamorphic aureole is preserved in the Sowchea succession rocks. The pluton is undeformed, which led Irvine (1975) to estimate it was emplaced in the Cretaceous; subsequent K-Ar and Rb-Sr dating by Armstrong et al. (1985) yielded an age of 125 ±5 Ma.

6. Geochronology

Herein we present two results of U-Pb zircon chemical abrasion isotope dilution thermal ionization mass spectrometry (CA-ID-TIMS) conducted at the Pacific Centre for Isotopic and Geochemical Research (PCIGR), Department of Earth, Ocean and Atmospheric Sciences at the University of British Columbia (Fig. 9; Table 1). Unless otherwise noted, all errors are quoted at 2s (95% level of confidence). Isotopic ages were calculated with the decay constants l_{238}=1.55125^{-10} and l_{235}=9.8485^{-10} (Jaffey et al., 1971) and a ^{238}U/^{235}U ratio of 137.88. Uranium-lead zircon results presented without supporting data were analyzed by split-stream laser ablation inductively coupled plasma mass spectrometry at the University of Alberta. Methods, data, and interpretations are presented in Ootes et al. (2020b). We also present selected results from ^{40}Ar/^{39}Ar laser step heating, which

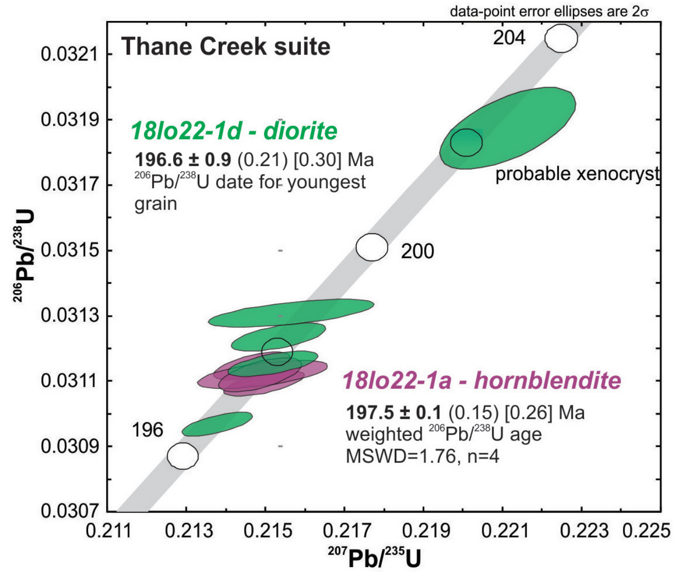

Fig. 9. Results of chemical abrasion ID-TIMS U-Pb zircon geochronology for Thane Creek diorite (18lo22-1d; green ellipses) and hornblendite (18lo22-1a; purple ellipses). MSWD=mean square of weighted deviation. Sample locations are in Figure 3, analytical results are in Table 1.

was performed at the University of Manitoba. A value of 295.5 was used for the atmospheric ^{40}Ar/^{36}Ar ratio (Steiger and Jaëger, 1977) and the decay constants were those recommended by Min et al. (2000). Each of the steps has relatively small errors, and the integrated ages are calculated from the average and uncertainty by standard deviation of the best analysis (Fig. 10; Table 2). Complete datasets and full methods are presented in Ootes et al. (2020b).

6.1. Thane Creek suite

6.1.1. Hornblendite sample 18lo22-1a

This sample was collected from a zone with pegmatitic plagioclase segregations in the hornblendite. It yielded good-quality igneous zircon. Four single grain zircon analyses yield concordant results that overlap within error at 197.55 ±0.11 Ma and have a narrow overlapping range of ^{206}Pb/^{238}U ages (Fig. 9; Table 1), interpreted as the time of crystallization of the hornblendite.

6.1.2. Diorite sample 18lo22-1d

This sample, consisting of homogeneous diorite, was collected ca. 30 m east of its intrusive contact with hornblendite of sample 18lo22-1a. It yielded good-quality igneous zircon; five single grain analyses are concordant but yield a spread of ages from ca. 202 to 196.5 Ma (Fig. 4) with a similar spread in the ^{206}Pb/^{238}U ages (Table 1). The youngest zircon analyzed yields a 196.61 ±0.19 ^{206}Pb/^{238}U age, interpreted as the time of crystallization of the diorite. The older zircons are interpreted as antecrysts or inherited (Fig. 9).

Biotite in the sample was analyzed by laser step heating. Nine release steps were conducted during the analysis. The biotite yielded an integrated ^{40}Ar/^{39}Ar age of 124.4 ±0.7 Ma,

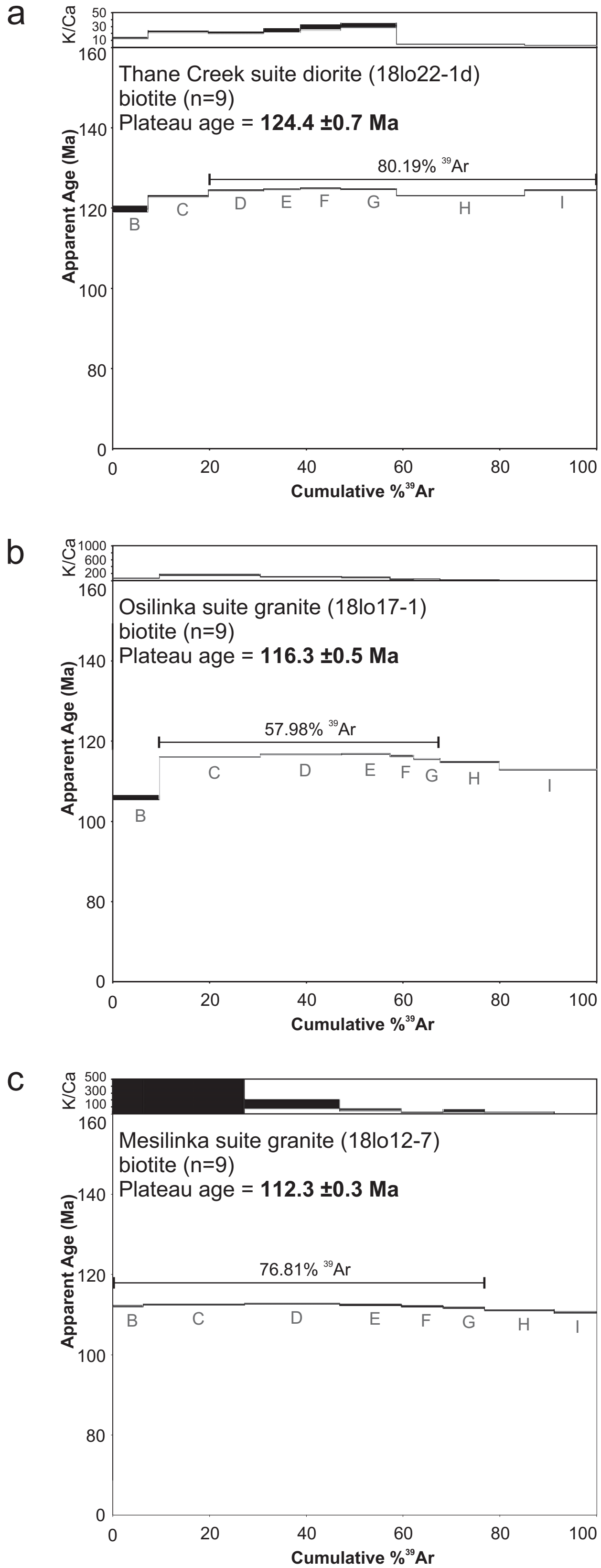

Fig. 10. Results of $^{40}Ar/^{39}Ar$ laser step heating for single biotite crystals. **a)** Thane Creek suite diorite (18lo22-1d). **b)** Osilinka suite granite (18lo17-1). **c)** Mesilinka suite K-feldspar porphyritic granite (18lo12-7). See text for description of plateau age determination.

representing 69.13% of ^{39}Ar released (steps D-I; Fig. 10a; Table 2). Hornblende was also analyzed and yielded a ca. 123 Ma integrated age (Ootes et al., 2020b). The results indicate the diorite cooled through the hornblende and biotite closure temperatures (ca. 550 to 300°C) at ca. 124 Ma, interpreted to post-date regional deformation.

6.2. Duckling Creek suite: K-feldspar porphyritic syenite

Hornblende from this sample yielded an integrated $^{40}Ar/^{39}Ar$ age of a ca. 177.6 Ma (Ootes et al., 2020b), best interpreted as a magmatic cooling age.

6.3. Osilinka suite

Many of the zircons analyzed are inherited from older crustal sources; the youngest zircons are ca. 160 Ma, providing a maximum crystallization age for the granite (Ootes et al., 2020b). Nine laser steps were conducted on biotite from an Osilinka granite sample (18lo17-1) and the results indicate a relatively well-behaved plateau, with an integrated $^{40}Ar/^{39}Ar$ age of 116.3 ±0.5 Ma, representing 57.98% of ^{39}Ar released (steps C-G; Fig. 10b; Table 2). Muscovite was also separated from the sample and two aliquots were analysed, yielding slightly more complicated plateaus with an integrated age of ca. 122 Ma (Ootes et al., 2020b). The results indicate the granite cooled through the muscovite and biotite closure temperatures (ca. 350 to 300°C) between ca. 122 to 115 Ma. These cooling ages are interpreted to post-date the peak of regional deformation.

6.4. Mesilinka suite

Preliminary U-Pb zircon results from a K-feldspar phenocrystic granite sample (ca. 135 Ma; Schiarizza and Tan, 2005b) indicate many zircons are inherited from older crustal sources and the youngest zircons are ca. 135 Ma, providing a maximum crystallization age (Ootes et al., 2020b). Nine laser steps were conducted of biotite from a K-feldspar porphyritic granite sample (18lo12-7) and the results indicate an integrated $^{40}Ar/^{39}Ar$ age of 112.3 ±0.3 Ma, representing 76.81% of ^{39}Ar released (steps B-G; Fig. 10c; Table 2). The results indicate the granite cooled through the biotite closure temperature (ca. 300°C) at ca. 112 Ma. This age is interpreted to post-date regional deformation.

Biotite from a tonalite sample (ca. 174 Ma; Schiarizza and Tan, 2005b) was also analyzed and two separate aliquots yielded ca. 112 and 109 Ma ages. Mineral separates from a granodiorite phase yielded older ages, including biotite with a ca. 122.6 Ma $^{40}Ar/^{39}Ar$ cooling age and hornblende with a ca. 139 Ma $^{40}Ar/^{39}Ar$ cooling age. The ca. 140 Ma age may record the time of primary magmatic cooling.

7. Mineralization

Eighty-eight mineral occurrences in the area are documented in MINFILE (Fig. 11). Most can be considered as part of four end-member styles of mineralization. First, syngenetic porphyry-style Cu (±Au, Ag, Mo) mineralization is typically represented by malachite staining or disseminated chalcopyrite

Table 1. U-Th-Pb isotopic data.

	Compositional Parameters								Radiogenic Isotopes									Isotopic Ages					
Sample	Wt. mg	U ppm	Pb ppm	Th/U	$^{206}Pb^*$ x10^{-13} mol	mol % $^{206}Pb^*$	Pb^*/Pb_c	Pb_c (pg)	$^{206}Pb/^{204}Pb$	$^{208}Pb/^{206}Pb$	$^{207}Pb/^{206}Pb$	% err	$^{207}Pb/^{235}U$	% err	$^{206}Pb/^{238}U$	% err	corr. coef.	$^{207}Pb/^{206}Pb$	±	$^{207}Pb/^{235}U$	±	$^{206}Pb/^{238}U$	±
(a)	(b)	(c)	(c)	(d)	(e)	(e)	(e)	(e)	(f)	(g)	(g)	(h)	(g)	(h)	(g)	(h)		(i)	(h)	(i)	(h)	(i)	(h)
18lo22-1a																							
A	0.0165	73	2.3	0.241	1.5655	99.12%	32	1.14	2111	0.077	0.05014	0.334	0.2150	0.390	0.03109	0.101	0.644	201.7	7.8	197.72	0.70	197.39	0.20
B	0.0125	67	2.1	0.262	1.0805	99.24%	37	0.68	2444	0.083	0.04999	0.307	0.2147	0.366	0.03115	0.111	0.642	194.3	7.1	197.46	0.66	197.73	0.22
C	0.0088	102	3.3	0.259	1.1718	98.53%	19	1.43	1261	0.083	0.05009	0.569	0.2149	0.628	0.03112	0.112	0.595	199	13	197.7	1.1	197.57	0.22
D	0.0099	157	4.9	0.243	2.0193	99.18%	34	1.37	2255	0.077	0.05008	0.334	0.2149	0.400	0.03112	0.135	0.616	198.7	7.8	197.64	0.72	197.56	0.26
18lo22-1d																							
A	0.0045	92	3.0	0.340	0.5343	98.14%	15	0.83	993	0.108	0.04996	0.733	0.2157	0.798	0.03131	0.114	0.620	193	17	198.3	1.4	198.74	0.22
B	0.0110	72	2.3	0.313	1.0364	99.02%	29	0.84	1897	0.099	0.05010	0.379	0.2152	0.434	0.03116	0.101	0.627	199.6	8.8	197.91	0.78	197.77	0.20
C	0.0107	123	3.9	0.346	1.7002	99.31%	42	0.97	2690	0.110	0.05007	0.284	0.2138	0.340	0.03097	0.097	0.673	198.2	6.6	196.73	0.61	196.61	0.19
D	0.0202	43	1.4	0.332	1.1321	99.02%	29	0.92	1893	0.106	0.05000	0.398	0.2153	0.455	0.03124	0.112	0.604	195.0	9.2	198.03	0.82	198.28	0.22
E	0.0291	30	1.0	0.421	1.1741	98.71%	23	1.26	1439	0.134	0.05032	0.508	0.2212	0.635	0.03188	0.323	0.609	210	12	202.9	1.2	202.28	0.64

(a) A, B etc. are labels for fractions composed of single zircon grains or fragments; all fractions annealed and chemically abraded after Mattinson (2005) and Scoates and Friedman (2008).
(b) Nominal fraction weights estimated from photomicrographic grain dimensions, adjusted for partial dissolution during chemical abrasion.
(c) Nominal U and total Pb concentrations subject to uncertainty in photomicrographic estimation of weight and partial dissolution during chemical abrasion.

(d) Model Th/U ratio calculated from radiogenic $^{208}Pb/^{206}Pb$ ratio and $^{206}Pb/^{238}U$ age.
(e) Pb* and Pbc represent radiogenic and common Pb, respectively; mol % $^{206}Pb^*$ with respect to radiogenic, blank and initial common Pb.
(f) Measured ratio corrected for spike and fractionation only. Mass discrimination of 0.25 ± 0.04%/amu based on analysis of NBS-982; all Daly analyses.
(g) Corrected for fractionation, spike, and common Pb; All common Pb was assumed to be procedural blank: $^{206}Pb/^{204}Pb$ = 18.50 ±1.0%; $^{207}Pb/^{204}Pb$ = 15.75 ±1.0%; $^{208}Pb/^{204}Pb$ = 38.40 ±1.0% (1σ errors).
(h) Errors are 2-sigma, propagated using the algorithms of Schmitz and Schoene (2007) and Crowley et al. (2007).
(i) Calculations are based on the decay constants of Jaffey et al. (1971). $^{206}Pb/^{238}U$ and $^{207}Pb/^{206}Pb$ ages corrected for initial disequilibrium in $^{230}Th/^{238}U$ using Th/U [magma] = 3.

Table 2a. Ar/Ar analytical data. Sample: 181o22-1d, biotite.

N		02A	02B	02C	02D	02E	02F	02G	02H	02I	**Age**
Power	%	0.2	1	1.3	1.6	1.9	2	2.3	3.5	6.5	
Age	(Ma)		119.7	122.9	124.4	124.7	124.9	124.7	123.1	124.5	**124.4**
±1σ	(Ma)		0.4	0.1	0.1	0.1	0.1	0.1	0.0	0.1	**0.7**
Ca/K			0.073	0.045	0.049	0.042	0.035	0.032	0.221	0.332	
±1σ			0.003	0.002	0.002	0.003	0.002	0.002	0.001	0.002	
Cl/K			0.000	0.000	0.000	0.000	0.000	0.000	0.000	0.000	
±1σ			0.001	0.000	0.000	0.001	0.001	0.000	0.000	0.000	
$\%^{40}Ar$	(%)		47.79	77.21	91.10	95.58	95.56	95.46	94.96	94.85	
$^{40}Ar^*/^{39}Ar_K$			3.639	3.739	3.786	3.795	3.801	3.794	3.744	3.788	
Corrected											
^{40}Ar	(fA)	0.34941	535.45794	583.88966	458.94563	289.97240	321.11499	441.30795	1008.52071	574.10785	
±1σ		0.03246	0.05814	0.06128	0.05701	0.04930	0.04787	0.04957	0.07328	0.06305	
^{39}Ar	(fA)	0.04913	70.26912	120.49689	110.37213	72.98369	80.67020	110.95525	255.62536	143.64570	
±1σ		0.01202	0.01726	0.02335	0.02268	0.01914	0.01842	0.02057	0.03411	0.02418	
^{38}Ar	(fA)	0.04955	1.02112	1.54145	1.33101	0.87092	0.96428	1.33507	3.10680	1.75978	
±1σ		0.01609	0.01637	0.01580	0.01485	0.01534	0.01704	0.01570	0.01602	0.01595	
^{37}Ar	(fA)	0.01008	0.35611	0.37455	0.37092	0.21077	0.19570	0.24391	3.86425	3.25987	
±1σ		0.01335	0.01359	0.01428	0.01390	0.01366	0.01375	0.01375	0.01396	0.01540	
^{36}Ar	(fA)	0.00042	0.94500	0.44815	0.13617	0.04194	0.04661	0.06550	0.17355	0.10313	
±1σ		0.00039	0.00263	0.00161	0.00100	0.00054	0.00063	0.00069	0.00109	0.00078	
Blanks											
^{40}Ar	(fA)	3.24651	2.77380	2.71458	3.88895	2.84610	3.26608	3.28220	2.81525	2.85239	
±1σ		0.02368	0.02392	0.02364	0.02288	0.02422	0.02121	0.02388	0.02112	0.02083	
^{39}Ar	(fA)	-0.00935	-0.00748	-0.00755	0.00598	0.02509	0.02232	0.02842	0.02756	0.05381	
±1σ		0.00885	0.00878	0.00887	0.00845	0.00904	0.00967	0.00836	0.00905	0.00922	
^{38}Ar	(fA)	-0.01959	0.01992	0.01535	0.02078	0.00748	0.00208	0.00520	0.00867	0.01629	
±1σ		0.01253	0.01134	0.01148	0.00996	0.01129	0.01130	0.01042	0.01012	0.01015	
^{37}Ar	(fA)	-0.01557	-0.02024	0.01072	0.00322	0.01013	0.02339	0.01371	0.00051	0.00699	
±1σ		0.00954	0.00952	0.00919	0.00931	0.01010	0.00975	0.00926	0.00947	0.01124	
^{36}Ar	(fA)	0.01083	0.00903	0.00926	0.01272	0.00885	0.01073	0.01030	0.00881	0.00822	
±1σ		0.00027	0.00022	0.00022	0.00026	0.00024	0.00028	0.00023	0.00023	0.00021	
IC^{CDD}		1.03104	1.03104	1.03104	1.03104	1.03104	1.03104	1.03104	1.03104	1.03104	
±1σ		0.00068	0.00068	0.00068	0.00068	0.00068	0.00068	0.00068	0.00068	0.00068	
Δt^3	(days)	112.55862	112.5891	112.61959	112.68424	112.71472	112.74524	112.81009	112.84072	112.87128	
J		0.0186	0.0186	0.0186	0.0186	0.0186	0.0186	0.0186	0.0186	0.0186	
±1σ		7.164E-05	7.164E-05	7.164E-05	7.164E-05	7.164E-05	7.164E-05	7.164E-05	7.164E-05	7.164E-05	
^{39}Ar Decay		1.000721	1.000721	1.000721	1.000721	1.000722	1.000722	1.000722	1.000723	1.000723	
^{37}Ar Decay		7.431369	7.435844	7.440325	7.449828	7.454315	7.458810	7.468369	7.472887	7.477401	
LambdaK		5.463E-10	5.463E-10	5.463E-10	5.463E-10	5.463E-10	5.463E-10	5.463E-10	5.463E-10	5.463E-10	
Irradiation		Can17E 6	Can17E 6	Can17E 6	Can17E 6	Can17E 6	Can17E 6	Can17E 6	Can17E 6	Can17E 6	

Table 2b. Ar/Ar analytical data. Sample: 181o17-1, biotite.

N		01A	01B	01C	01D	01E	01F	01G	01H	01I	**Age**
Power	%	0.2	1	1.3	1.6	1.9	2	2.3	3.5	6.5	
Age	(Ma)	133.6	105.9	116.1	116.7	116.9	116.3	115.6	114.8	112.9	**116.3**
±1σ	(Ma)	7.8	0.3	0.0	0.0	0.0	0.1	0.1	0.1	0.0	**0.5**
Ca/K		-0.028	0.016	0.006	0.009	0.012	0.024	0.022	0.047	0.193	
±1σ		0.322	0.001	0.000	0.001	0.001	0.002	0.001	0.001	0.000	
Cl/K		-0.003	0.000	0.000	0.000	0.000	-0.001	0.000	0.000	0.000	
±1σ		0.075	0.000	0.000	0.000	0.000	0.000	0.000	0.000	0.000	
$\%^{40}Ar$	(%)	46.89	58.17	95.13	92.56	96.04	93.19	90.07	87.53	93.65	
$^{40}Ar^{*}/^{39}Ar_K$		4.063	3.197	3.513	3.532	3.537	3.520	3.497	3.474	3.414	
Corrected											
^{40}Ar	(fA)	5.36295	1214.12544	1768.88282	1475.22441	850.40787	420.85736	487.08933	1123.30928	1684.08049	
±1σ		0.03467	0.07619	0.10459	0.09740	0.06660	0.05119	0.05548	0.08081	0.09826	
^{39}Ar	(fA)	0.61854	220.73267	478.65499	386.29563	230.74595	111.33094	125.38016	282.86170	461.61374	
±1σ		0.01318	0.02442	0.03636	0.03869	0.02868	0.01922	0.02267	0.03214	0.04008	
^{38}Ar	(fA)	0.00865	2.97674	5.78162	4.68674	2.74565	1.29959	1.53250	3.44122	5.59853	
±1σ		0.01592	0.01468	0.01598	0.01704	0.01588	0.01707	0.01619	0.01748	0.01543	
^{37}Ar	(fA)	-0.00127	0.26423	0.23014	0.27733	0.20579	0.20163	0.20782	0.97400	6.53509	
±1σ		0.01468	0.01447	0.01390	0.01427	0.01408	0.01400	0.01297	0.01319	0.01438	
^{36}Ar	(fA)	0.00962	1.71389	0.28033	0.36247	0.10853	0.09465	0.16094	0.46898	0.36280	
±1σ		0.00047	0.00585	0.00164	0.00174	0.00091	0.00086	0.00113	0.00211	0.00170	
Blanks											
^{40}Ar	(fA)	3.76014	3.50565	3.38754	4.06996	3.58692	3.57616	3.89730	3.85170	3.01199	
±1σ		0.02543	0.02276	0.02537	0.02123	0.02494	0.02217	0.02385	0.01965	0.02250	
^{39}Ar	(fA)	0.01603	0.00213	0.05272	0.04053	0.10374	0.06006	0.02596	0.05614	0.03263	
±1σ		0.00957	0.00863	0.00940	0.00948	0.00846	0.00885	0.00897	0.00892	0.00875	
^{38}Ar	(fA)	-0.01528	0.00089	0.00670	-0.00227	0.00561	0.02456	0.00888	-0.00034	-0.00849	
±1σ		0.01144	0.01045	0.01075	0.01082	0.01156	0.01215	0.01129	0.01170	0.01128	
^{37}Ar	(fA)	0.01475	0.01989	-0.00961	-0.01107	0.03367	-0.00072	0.00854	0.03253	0.03502	
±1σ		0.01033	0.01095	0.00980	0.01123	0.00936	0.01008	0.00867	0.00921	0.00921	
^{36}Ar	(fA)	0.01235	0.01140	0.01037	0.01268	0.01076	0.01147	0.01262	0.01229	0.00961	
±1σ		0.00024	0.00024	0.00024	0.00029	0.00025	0.00027	0.00025	0.00025	0.00023	
IC^{CDD}		1.03378	1.03378	1.03378	1.03378	1.03378	1.03378	1.03378	1.03378	1.03378	
±1σ		0.00305	0.00305	0.00305	0.00305	0.00305	0.00305	0.00305	0.00305	0.00305	
Δt^3	(days)	109.07263	109.10306	109.13353	109.19803	109.22852	109.25898	109.32353	109.35397	109.38443	
J		0.0186	0.0186	0.0186	0.0186	0.0186	0.0186	0.0186	0.0186	0.0186	
±1σ		5.216E-05	5.216E-05	5.216E-05	5.216E-05	5.216E-05	5.216E-05	5.216E-05	5.216E-05	5.216E-05	
^{39}Ar Decay		1.000696	1.000696	1.000696	1.000697	1.000697	1.000697	1.000698	1.000698	1.000698	
^{37}Ar Decay		6.936947	6.941117	6.945296	6.954149	6.958338	6.962526	6.971407	6.975600	6.979798	
LambdaK		5.463E-10	5.463E-10	5.463E-10	5.463E-10	5.463E-10	5.463E-10	5.463E-10	5.463E-10	5.463E-10	
Irradiation		Can17E 2	Can17E 2	Can17E 2	Can17E 2	Can17E 2	Can17E 2	Can17E 2	Can17E 2	Can17E 2	

Table 2c. Ar/Ar analytical data. Sample: 181o12-7, biotite.

N		01A	01B	01C	01D	01E	01F	01G	01H	01I	**Age**
Power	%	0.2	1	1.3	1.6	1.9	2	2.3	3.5	6.5	
Age	(Ma)		112.2	112.5	112.7	112.5	112.1	111.8	111.1	110.6	**112.3**
±1σ	(Ma)		0.1	0.0	0.0	0.1	0.1	0.1	0.1	0.1	**0.3**
Ca/K			0.002	0.003	0.007	0.017	0.040	0.021	0.039	0.703	
±1σ			0.006	0.002	0.002	0.003	0.004	0.004	0.002	0.004	
Cl/K			0.002	0.000	-0.001	0.000	-0.002	0.000	0.000	-0.002	
±1σ			0.001	0.000	0.000	0.001	0.001	0.001	0.001	0.001	
$\%^{40}Ar$	(%)		97.01	97.93	97.88	96.78	96.51	97.23	95.88	95.33	
$^{40}Ar^{*}/^{39}Ar_K$			3.402	3.413	3.420	3.412	3.402	3.391	3.370	3.353	
Corrected											
^{40}Ar	(fA)	-0.33672	120.01286	398.27269	375.34799	245.83222	165.52959	162.98629	276.99555	167.74530	
±1σ		0.03137	0.03876	0.05064	0.05105	0.04034	0.03963	0.03843	0.04652	0.04075	
^{39}Ar	(fA)	0.09558	34.19651	114.19719	107.35892	69.67365	46.92505	46.69984	78.75325	47.67372	
±1σ		0.01395	0.01675	0.02294	0.02123	0.01840	0.01831	0.01734	0.01871	0.01698	
^{38}Ar	(fA)	0.00157	0.42943	1.36798	1.26223	0.82778	0.53388	0.56433	0.95132	0.53801	
±1σ		0.01609	0.01614	0.01530	0.01534	0.01607	0.01619	0.01514	0.01455	0.01601	
^{37}Ar	(fA)	0.00245	0.00476	0.02562	0.05481	0.08191	0.12883	0.06799	0.21242	2.26442	
±1σ		0.01479	0.01302	0.01527	0.01297	0.01343	0.01405	0.01395	0.01256	0.01288	
^{36}Ar	(fA)	-0.00266	0.01129	0.02515	0.02433	0.02521	0.01865	0.01426	0.03710	0.02993	
±1σ		0.00036	0.00041	0.00051	0.00048	0.00051	0.00046	0.00047	0.00060	0.00061	
Blanks											
^{40}Ar	(fA)	3.54869	2.89735	2.62744	3.56355	2.99392	2.75601	3.27554	2.72820	2.71520	
±1σ		0.02261	0.02043	0.02104	0.02377	0.02186	0.02136	0.02180	0.02419	0.02014	
^{39}Ar	(fA)	0.02535	0.00934	0.03037	0.03164	0.04759	0.03647	0.02026	0.02436	-0.00792	
±1σ		0.01019	0.00988	0.01050	0.00780	0.00908	0.00939	0.00861	0.00884	0.00841	
^{38}Ar	(fA)	0.00212	-0.00449	0.00389	0.00368	-0.00130	0.00654	-0.01138	-0.00245	0.01255	
±1σ		0.01065	0.01130	0.01140	0.01013	0.01099	0.01169	0.01071	0.01055	0.01102	
^{37}Ar	(fA)	0.01665	0.00211	0.00169	0.00366	-0.00788	-0.00684	0.00220	-0.00154	0.00714	
±1σ		0.01003	0.00953	0.01105	0.00858	0.01020	0.00994	0.01015	0.00918	0.00894	
^{36}Ar	(fA)	0.01180	0.00904	0.00826	0.01196	0.00949	0.00851	0.01078	0.00940	0.00862	
±1σ		0.00025	0.00023	0.00022	0.00027	0.00023	0.00021	0.00024	0.00024	0.00020	
IC^{CDD}		1.03107	1.03107	1.03107	1.03107	1.03107	1.03107	1.03107	1.03107	1.03107	
±1σ		0.00198	0.00198	0.00198	0.00198	0.00198	0.00198	0.00198	0.00198	0.00198	
Δt^3	(days)	113.10171	113.13229	113.16282	113.22774	113.25829	113.28885	113.35378	113.38444	113.41507	
J		0.0186	0.0186	0.0186	0.0186	0.0186	0.0186	0.0186	0.0186	0.0186	
±1σ		5.219E-05	5.219E-05	5.219E-05	5.219E-05	5.219E-05	5.219E-05	5.219E-05	5.219E-05	5.219E-05	
^{39}Ar Decay		1.000724	1.000725	1.000725	1.000725	1.000725	1.000726	1.000726	1.000726	1.000727	
^{37}Ar Decay		7.511508	7.516046	7.520580	7.530227	7.534772	7.539322	7.548997	7.553569	7.558139	
LambdaK		5.463E-10	5.463E-10	5.463E-10	5.463E-10	5.463E-10	5.463E-10	5.463E-10	5.463E-10	5.463E-10	
Irradiation		Can17E 7	Can17E 7	Can17E 7	Can17E 7	Can17E 7	Can17E 7	Can17E 7	Can17E 7	Can17E 7	

Integrated age (steps 2-7)
Notes:
1Corrected: Isotopic intensities corrected for blank, baseline, radioactivity decay and detector intercalibration, not for interfering reactions.
3Time interval (days) between end of irradiation and beginning of analysis.
fA = femto amps
Ages calculated relative to FC-1 Fish Canyon Tuff sanidine interlaboratory standard at 28.201+/-0 Ma

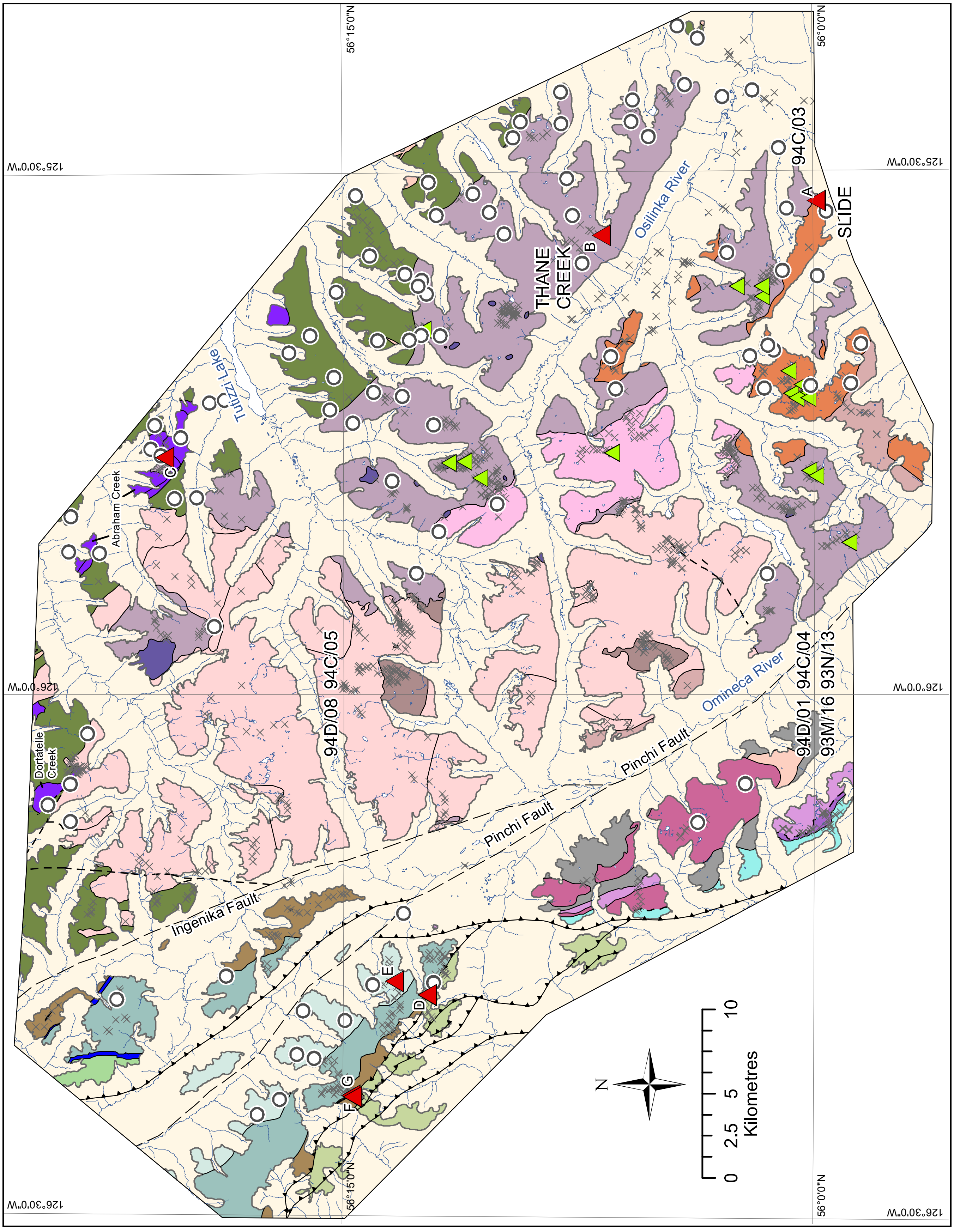

Fig. 11. Geology of northern Hogem batholith and surroundings with MINFILE and new mineral occurrences (see Table 3).

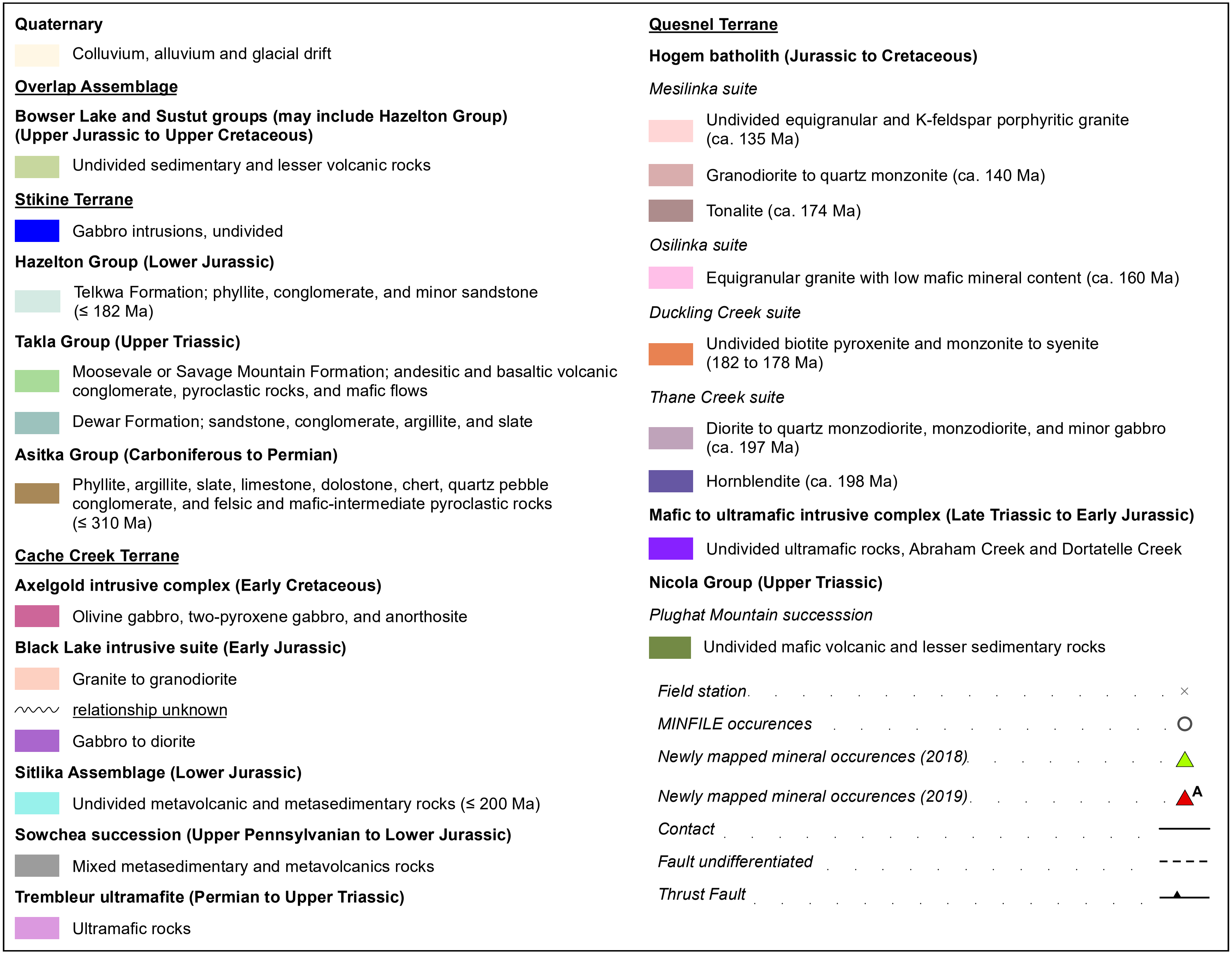

Fig. 11. Continued.

Table 3. Assay results from newly mapped mineral occurrences.

Label		**A**	**B**	**C**	**D**	**E**	**F**	**G**
station		GJO19-13-5b	GJO19-6-2	DMI19-24-3b	GJO19-19-5	GJO19-18-1	LOO19-4-2	LOO19-4-4
		^Known	^Known	^Known	^Known	^Known	New	New
MINFILE		SLIDE	THANE CREEK	WELT	LEISHMAN	ARP		
Longitude		-125.526168	-125.558130	-125.769215	-126.285185	-126.272182	-126.381604	-126.383056
Latitude		55.999451	56.113880	56.34665	56.206991	56.224369	56.247218	56.246246
Au	ppb	110	3330	16	< 2	15	< 2	22
Ag	ppm	1.8	11.4	2.3	1.1	28.5	0.4	44.3
Cu	ppm	7010	8980	3120	9990	> 10000	1750	> 10000
Cd	ppm	< 0.3	0.6	1.1	< 0.3	3.5	0.4	4.2
Mo	ppm	44	2	111	< 1	3	< 1	2
Pb	ppm	6	3	13	13	6	4	11
Ni	ppm	7	3	101	9	25	18	2
Zn	ppm	55	13	50	62	70	67	105
S	%	0.43	0.76	0.85	0.65	0.4	0.05	1.52
Al	%	7.93	0.48	5.85	4.86	8.47	4.58	0.38
As	ppm	2.2	3.1	< 0.5	3.8	7.4	2.8	12.1
Ba	ppm	2010	< 50	680	< 50	490	170	< 50
Be	ppm	1	< 1	< 1	< 1	< 1	< 1	< 1
Bi	ppm	5	< 2	< 2	< 2	3	< 2	< 2
Br	ppm	< 0.5	< 0.5	< 0.5	< 0.5	< 0.5	< 0.5	< 0.5
Ca	%	1.13	5.11	0.97	12.9	4.3	6.41	0.7
Co	ppm	11	3	60	14	25	25	4
Cr	ppm	12	31	331	34	62	55	34
Cs	ppm	< 1	< 1	1	< 1	< 1	< 1	< 1
Eu	ppm	0.2	0.2	< 0.2	0.6	0.5	0.8	< 0.2
Fe	%	3.27	2.36	24.4	4.19	4.49	5.78	2.57
Hf	ppm	3	< 1	< 1	1	2	3	< 1
Hg	ppm	< 1	< 1	< 1	< 1	< 1	< 1	< 1
Ir	ppb	< 5	< 5	< 5	< 5	< 5	< 5	< 5
K	%	4.96	0.07	1.27	0.06	1.21	0.28	0.05
Li	ppm	13	4	12	12	9	14	2
Mg	%	0.57	0.18	0.84	1.29	1.7	1.39	0.05
Mn	ppm	376	1170	503	1140	1140	1880	355
Na	%	2.24	0.05	3.23	2.72	1.99	2	0.11
P	%	0.078	0.005	0.002	0.07	0.105	0.088	0.012
Rb	ppm	127	< 15	< 15	< 15	< 15	< 15	< 15
Sb	ppm	0.3	1.3	0.2	0.4	0.8	< 0.1	3.7
Sc	ppm	4.3	1.1	4.8	10.4	18.8	19	1.1
Se	ppm	< 3	< 3	< 3	< 3	41	< 3	< 3
Sr	ppm	376	137	216	208	553	243	23
Ta	ppm	< 0.5	< 0.5	< 0.5	< 0.5	< 0.5	< 0.5	< 0.5
Ti	%	0.22	< 0.01	0.1	0.25	0.38	0.26	0.03
Th	ppm	4.9	< 0.2	< 0.2	1	2	0.8	0.2
U	ppm	1.9	< 0.5	< 0.5	< 0.5	< 0.5	1.4	< 0.5
V	ppm	79	9	607	135	209	84	9
W	ppm	7	< 1	< 1	< 1	< 1	< 1	< 1
Y	ppm	10	6	< 1	12	19	19	2
La	ppm	13.5	2.5	0.8	6.1	8.6	7.7	0.7
Ce	ppm	22	5	< 3	16	21	21	< 3
Nd	ppm	10	< 5	< 5	7	14	9	< 5
Sm	ppm	1.7	0.8	0.1	1.8	2.8	2.8	0.2
Sn	%	0.03	< 0.02	< 0.02	< 0.02	< 0.02	< 0.02	< 0.02
Tb	ppm	< 0.5	< 0.5	< 0.5	< 0.5	< 0.5	< 0.5	< 0.5
Yb	ppm	1.1	0.4	< 0.2	1	1.8	1.9	< 0.2
Lu	ppm	0.08	< 0.05	< 0.05	< 0.05	0.11	0.06	< 0.05
Mass	g	31.7	33.8	38.0	37.0	36.3	32.7	35.2

Labels correspond to locations plotted on Figure 11; underlined values are considered of interest; ^close to mineralization documented in MINFILE in the host-rock. The mineral showings of this type are hosted in the Thane Creek and Duckling Creek suites, or in Nicola Group adjacent to Hogem batholith. One porphyry Mo-showing is related to the Mesilinka granite and one to the Osilinka granite. The second style of mineralization is related to mafic and ultramafic intrusive rocks and includes Ni-Cu ±PGE in the Axelgold layered mafic intrusion, Alaskan-type chromite near the Dortatelle Creek mafic-ultramafic intrusion, and podiform chromite in a Cache Creek serpentinite. The third type is volcanic- and sediment-hosted Cu, which is typically stratabound in the Telkwa Formation of the Hazelton Group. The fourth style includes epigenetic quartz veins with local concentrations of precious and base metals (e.g., Hawk showing; Nelson et al., 2001). Other types of mineralization in the area are also reported in MINFILE (e.g., Besshi-type massive sulphides.

During mapping, we collected representative grab samples with metallic mineralization from outcrops. These samples were sent to Activation Laboratories (Ancaster, Ontario) where they were analyzed by a combination of instrumental neutron activation analysis (INAA) and acid dilution inductively coupled plasma-mass spectrometry (ICP-MS Table 3; Ootes et al., 2020b). To the 17 mineral occurrences discovered in 2018 (Ootes et al., 2019), we add seven new ones, five of which are close to previously documented mineralization (Fig. 11; Table 3).

All the documented occurrences are Cu-bearing, and one (B) contains ~3 ppm Au. On Figure 11, result A is close to the Slide showing in the Duckling Creek syenite and B is near the Thane Creek showing in the Thane Creek diorite, both of which are interpreted as alkalic porphyry Cu-type mineralization. Result C is adjacent to the Welt polymetallic vein showing, D is volcanic-hosted Cu, close to the Leishmann volcanic redbed Cu showing in undivided Bowser Lake and Sustut groups, and E is sediment-hosted Cu, close to the Arp volcanic redbed Cu showing in the Telkwa Formation. Results F and G are new Cu occurrences that are hosted in quartz veins that cut the Asitka Group.

8. Summary

This study provides a preliminary overview of the geology of the northern Hogem batholith and its surrounding rocks in the Quesnel, Stikine, and Cache Creek terranes. The first modern U-Pb zircon and Ar-Ar laser step heating results indicate the earliest intrusive phases in Hogem batholith are ca. 197 Ma hornblendite and diorite of the Thane Creek suite (Fig. 4). The Duckling Creek syenite was emplaced between 182 and 178 Ma, the Osilinka suite granite at ca. 160 Ma, or younger, and the Mesilinka suite tonalite at ca. 174 Ma, and granodiorite and granites at ca. 140 Ma. Foliation-defining biotite preserves 125 to 110 Ma ages, indicating post-deformation cooling and uplift. The results indicate that a regional contractional deformation event affected the Hogem batholith between 140 and 125 Ma.

The Thane Creek suite rocks in Hogem batholith have undergone at least two stages of deformation and the youngest, the rocks of the Mesilinka suite, are deformed (Ootes et al., 2019). Multigenerational fabrics are also developed in rocks of the Stikine and Cache Creek terranes; further evaluation of the structural relationship between these three terranes is ongoing.

Assay samples collected during bedrock mapping identify new mineralized horizons, five of which are close to documented occurrences and two occur as quartz vein-hosted Cu in the Asitka Group (Table 3). When combined with the results of 2018 mapping, the project has identified 24 mineral occurrences in addition to 88 previously documented. This supports that the study area is prospective for mineral resources.

Acknowledgments

Field assistance in 2019 was from Dylan Spence, Jade Lockie, Kristian Shortridge, and Moe Farhat, and 2018 field assistance was from Ben Graham, Dylan Spence, Silken Rauhala, and Reid Simmonds. We thank Silver King helicopters for air support, Cassiar Geoscience for expediting services, and the Abraham family for accommodations. Ongoing interest and support from the Tsay Keh Dene First Nation is appreciated. A field visit with Don Bragg and Jarrod Put helped improve our understanding of some parts of the southeastern Hogem batholith. Discussions with colleagues at the BC Geological Survey improved our understanding of the regional geology. Reviews by F. Ferri and L. Aspler helped improve the clarity of the manuscript.

References cited

Armstrong, J.E., 1946. Aiken Lake (south half), British Columbia. Geological Survey of Canada, Paper 46-11, 1 sheet, scale 1 inch:2 miles.

Armstrong, J.E., 1948. Fort St. James, British Columbia. Geological Survey of Canada, A Series Map 907A, scale 1inch:4 miles.

Armstrong, J.E., and Roots, E.F., 1948. Aiken Lake map-area, British Columbia. Geological Survey of Canada, Paper 48-5, 46 p.

Armstrong, J.E., and Roots, E.F., 1954. Aiken Lake, Cassiar District, British Columbia. Geological Survey of Canada, A Series Map 1030A, scale 1inch:4 miles.

Armstrong, R.L., Monger, J.W.H., and Irving, E., 1985. Age of magnetization of the Axelgold Gabbro, north-central British Columbia. Canadian Journal of Earth Sciences, 22, 1217-1222.

Bath, A.B., Cooke, D.R., Friedman, R.M., Faure, K., Kamenetsky, V.S., Tosdal, R.M., and Berry, R.F., 2014. Mineralization, U-Pb geochronology, stable isotope geochemistry of the Lower Main Zone of the Lorraine deposit, north-central British Columbia: A replacement-style alkalic Cu-Au porphyry. Economic Geology, 109, 979-1004.

CGG Canada Services Ltd., 2018. Geophysical survey report MIDAS high resolution magnetic and radiometric survey Search Project Phase III. Geoscience BC Report 2018-2.

Devine, F.A.M., Chamberlain, C.M., Davies, A.G.S., Friedman, R., and Baxter, P., 2014. Geology and district-scale setting of tilted alkalic porphyry Cu-Au mineralization at the Lorraine deposit, British Columbia. Economic Geology, 109, 939-977.

Evenchick, C.A., Mustard, P.S., McMechan, M., Ferri, F., Porter, S., Hadlari, T., and Jakobs, G., 2007. Geology, McConnell Creek, British Columbia. Geological Survey of Canada, Open File 5571, British Columbia Ministry of Energy, Mines and Petroleum Resources, Petroleum Geology Open File 2007-10, scale 1:125,000.

Evenchick, C.A., McMechan, M., Mustard, P.S., Ritcey, D.H., Smith, G.T., Ferri, F., and Waldron, JW.F., 2008. Geology, Hazelton, British Columbia. Geological Survey of Canada, Open File 5704, British Columbia Ministry of Energy, Mines and Petroleum Resources, Petroleum Geology Open File 2008-06, scale 1:125,000.

Ferri, F., Dudka, S, Rees, C., and Meldrum, D., 1993. Geology of the Aiken Lake area and Osilinka River areas, northern Quesnel Trough (NTS 94C/2, 3, 5, 6 & 12). British Columbia Ministry of Energy, Mines and Petroleum Resources, British Columbia Geological Survey Paper 1993-1, pp. 109-134.

Ferri, F., Dudka, S.F., Rees, C., and Meldrum, D., 2001a. Geology of the Aiken Lake area, north-central British Columbia, NTS 94C/5, 6 and 12. British Columbia Ministry of Energy, Mines and Petroleum Resources, British Columbia Geological Survey Geoscience Map 2001-10, scale 1:50,000.

Ferri, F., Dudka, S.F., Rees, C.J., Meldrum, D.G., and Willson, M.J., 2001b. Geology of the Uslika Lake Area, North-Central B.C. (NTS 94C/2, 3 & 4). British Columbia Ministry of Energy, Mines and Petroleum Resources, British Columbia Geological Survey Geoscience Map 2001-04, scale 1:50,000.

Garnett, J.A., 1972, Preliminary geological map of part of Hogem batholith, Duckling Creek area (parts of NTS 93N/13, 14; 94C/3, 4). British Columbia Ministry of Energy, Mines and Petroleum Resources, British Columbia Geological Survey Preliminary Map 09.

Garnett, J.A., 1978. Geology and mineral occurrences of the southern Hogem batholith. British Columbia Ministry of Energy, Mines and Petroleum Resources, British Columbia Geological Survey Bulletin 70, 75 p.

Irvine, T.N., 1975. Axelgold layered gabbro intrusion, McConnell Creekmap-area, British Columbia. Geological Survey of Canada Paper 75-1B, pp. 81-88.

Irvine, T.N., 1976. Studies of Cordilleran gabbroic and ultramafic intrusions, British Columbia. Geological Survey of Canada, Paper 76-1A, 75-81.

Irving, E., and Monger, J.W.H., 1987. Preliminary paleomagnetic results from the Permian Asitka Group, British Columbia. Canadian Journal of Earth Sciences, 24, 1490-1497.

Jaffey, A.H., Flynn, K.F., Glendenin, L.E., Bentley, W.C., and Essling, A.M., 1971. Precision measurement of half-lives and specific activities of ^{235}U and ^{238}U. Physical Review C, 4, 1889-1906.

Logan, J.M., Schiarizza, P., Struik, L.C., Barnett, C., Nelson, J.L., Kowalczyk, P., Ferri, F., Mihalynuk, M.G., Thomas, M.D., Gammon, P., Lett, R., Jackaman, W., and Ferbey, T., 2010. Bedrock Geology of the QUEST map area, central British Columbia. British Columbia Geological Survey Geoscience Map 2010-1, Geoscience BC Report 2010-5, Geological Survey of Canada Open File 6476, scale 1:500,000.

Lord, C.S., 1948. McConnell Creek map-area, Cassiar District, British Columbia. Geological Survey of Canada, Memoir 251, 82 p.

Lord, C.S., 1949. McConnell Creek, Cassiar District, British Columbia. Geological Survey of Canada, A Series Map 962A, scale 1inch:4 miles.

Massey, N.W.D., MacIntyre, D.J., Desjardins, P.J., and Cooney, R.T., 2005a. Digital geology map of British Columbia: whole province. British Columbia Ministry of Energy, Mines and Petroleum Resources, British Columbia Geological Survey GeoFile 2005-1, scale 1:250,000.

Massey, N.W.D., MacIntyre, D.G., Okulitch, A.V., Desjardins, P.J., and Cooney, R.T., 2005b. Digital geology map of British Columbia: Tile No10 northeast B.C., British Columbia Ministry of Energy, Mines and Petroleum Resources, British Columbia Geological Survey GeoFile 2005-10, scale 1:250,000.

Min K., Mundil R., Renne P.R. and Ludwig K.R., 2000. A test for systematic errors in $^{40}Ar/^{39}Ar$ geochronology through comparison with U-Pb analysis of a 1.1 Ga rhyolite. Geochimica et Cosmochimica Acta, 64, 73-98.

Monger, J.W.H., 1974. Upper Paleozoic and Lower Mesozoic rocks of the Omineca Mountains. Geological Survey of Canada, Paper 74-1A, pp. 19-20.

Monger, J.W.H., 1977. The Triassic Takla Group in McConnell Creek map-area, north-central British Columbia. Geological Survey of Canada, Paper 76-29, 45 p.

Mortensen, J.K., Ghosh, D.K., and Ferri, F., 1995. U-Pb geochronology of intrusive rocks associated with copper-gold porphyry deposits in the Canadian Cordillera. Canadian Institute of Mining, Metallurgy and Petroleum, Special Volume 46, pp. 142-158.

Nelson, J., Carmichael, B., and Gray, M., 2003. Innovative gold targets in the Pinchi Fault/Hogem Batholith area: The Hawk and Axelgold properties, central British Columbia (94C/4, 94N/13). British Columbia Ministry of Energy, Mines and Petroleum Resources, British Columbia Geological Survey Paper 2003-1, pp. 97-114.

Nelson, J.L., Colpron, M., and Israel, S., 2013. The Cordillera of British Columbia, Yukon, and Alaska: Tectonics and metallogeny. In: Colpron, M., Bissing, T., Rusk, B.G., and Thompson, J.F.H., (Eds.), Tectonics, Metallogeny, and Discovery: The North American Cordillera and similar accretionary settings. Society of Economic Geologists, Special Publication 17, pp. 53-109.

Nixon, G.T., and Peatfield, G.R., 2003. Geological setting of the Lorraine Cu-Au porphyry deposit, Duckling Creek syenite complex, north-central British Columbia. British Columbia Ministry of Energy, Mines and Petroleum Resources, British Columbia Geological Survey Open File 2003-4, 24 p.

Ootes, L., Bergen, A.L., Milidragovic, D., and Graham, B., 2019a. Bedrock geology of Notch Peak and Ogden Creek (parts of NTS 094C/04 and 093N/13), northern Hogem batholith, Quesnel terrane, north-central British Columbia. British Columbia Ministry of Energy, Mines and Petroleum Resources, British Columbia Geological Survey Open File 2019-02, scale 1:50,000.

Ootes, L., Bergen, A., Milidragovic, D., Graham, B., and Simmonds, R., 2019b. Preliminary geology of northern Hogem batholith, Quesnel terrane, north-central British Columbia. British Columbia Ministry of Energy, Mines and Petroleum Resources, British Columbia Geological Survey Paper 2019-01, pp. 31-53.

Ootes, L., Bergen, A.L., Milidragovic, D., and Jones, G.O., 2020a. Preliminary geology of the northern Hogem batholith and its surroundings, north-central British Columbia. British Columbia Ministry of Energy, Mines and Petroleum Resources, British Columbia Geological Survey Open File 2020-02, scale 1:50,000.

Ootes, L., Milidragovic, D., Camacho, A., Jones, G.O., Luo, Y., Pearson, G.D., and Friedman, R., 2020b. Geochronologic and geochemical data from northern Hogem batholith and its surroundings, north-central British Columbia. British Columbia Ministry of Energy, Mines and Petroleum Resources, British Columbia Geological Survey GeoFile, in prep.

Paterson, I.A., 1974. Geology of the Cache Creek Group and Mesozoic rocks at the northern end of the Stuart Lake belt, central British Columbia. Geological Survey of Canada, Paper 74-1B, 31-42.

Roots, E.F., 1954. Geology and mineral deposits of Aiken Lake map-area, British Columbia. Geological Survey of Canada, Memoir 274, 246 p.

Schiarizza, P., 2000. Old Hogem (western part), NTS 93N/11, 12, 13. British Columbia Ministry of Energy and Mines, British Columbia Geological Survey Open File 2000-33, scale 1:100,000.

Schiarizza, P., 2016. Toward a regional stratigraphic framework for the Nicola Group: Preliminary results from the Bridge Lake-

Quesnel River area. British Columbia Ministry of Energy and Mines, British Columbia Geological Survey Paper 2016-1, pp. 13-30.

Schiarizza, P., 2019. Geology of the Nicola Group in the Bridge Lake-Quesnel River area, south-central British Columbia. British Columbia Ministry of Energy, Mines and Petroleum Resources, British Columbia Geological Survey Paper 2019-01, pp. 15-30.

Schiarizza, P., and Tan, S.H., 2005a. Geology and mineral occurrences of the Quesnel Terrane between the Mesilinka River and Wrede Creek (NTS 94D/8, 9), north-central British Columbia. British Columbia Ministry of Energy and Mines, British Columbia Geological Survey Paper 2005-1, pp. 109-130.

Schiarizza, P., and Tan, S.H., 2005b. Geology of the Johanson Lake area, parts of NTS 94D/8 and 9. British Columbia Ministry of Energy, Mines and Petroleum Resources, British Columbia Geological Survey Open File 2005-4, scale 1:50,000.

Steiger R.H., and Jäger E., 1977. Subcommission on geochronology: convention on the use of decay constants in geo- and cosmochronology. Earth and Planetary Science Letters, 36, 359-362.

Tipper, H.W., and Richards, T.A., 1976. Jurassic stratigraphy and history of north-central British Columbia. Geological Survey of Canada, Bulletin 270, 73 p.

Woodsworth, G.J., 1976. Plutonic rocks of McConnell Creek (94 D west half) and Aiken Lake (94 C east half) map-areas, British Columbia. Geological Survey of Canada, Paper 76-1A, 69-73.

Woodsworth, G.J., Anderson, R.G., and Armstrong, R.L., 1991. Plutonic regimes, Chapter 15, In: Gabrielse, H., and Yorath, C.J., (Eds.), Geology of the Cordilleran Orogen in Canada, Geological Survey of Canada, Geology of Canada, no. 4, 491-531.

Origin and serpentinization of ultramafic rocks in dismembered ophiolite north of Trembleur Lake, central British Columbia

Katrin Steinthorsdottir[1, a], Jamie Cutts[1], Greg Dipple[1], Dejan Milidragovic[2], and Frances Jones[1]

[1] Bradshaw Research Initiative for Minerals and Mining, Department of Earth, Ocean and Atmospheric Sciences, University of British Columbia, Vancouver, BC, V6T 1Z4
[2] British Columbia Geological Survey, Ministry of Energy, Mines and Petroleum Resources, Victoria, BC, V8W 9N3
[a] corresponding author: ksteinth@eoas.ubc.ca

Recommended citation: Steinthorsdottir, K., Cutts, J., Dipple, G., Milidragovic, D., and Jones, F., 2020. Origin and serpentinization of ultramafic rocks in dismembered ophiolite north of Trembleur Lake, central British Columbia. In: Geological Fieldwork 2019, British Columbia Ministry of Energy, Mines and Petroleum Resources, British Columbia Geological Survey Paper 2020-01, pp. 49-58.

Abstract

Serpentinization of ultramafic rocks can produce alteration minerals such as brucite ($Mg(OH)_2$), which has the potential to sequester carbon dioxide, and awaruite (Ni_3Fe), a potential source of nickel. The Trembleur ultramafite is part of a dismembered ophiolite in central British Columbia. Field and petrographic data indicate that it is heterogeneous both in protolith and alteration. The protolith consists mainly of harzburgite, lherzolite, dunite, and lesser pyroxenite. Dunite, more abundant than previously recognized, could be a replacement of harzburgite (±lherzolite). All ultramafic rocks in the Decar area, north of Trembleur Lake, are altered to some extent (mainly partially to pervasively serpentinized) and locally contain higher temperature metamorphic assemblages. Carbonate alteration post-dated serpentinization, degrading minerals such as brucite and awaruite to locally produce ophicarbonates, soapstone, and listwanite. The primary olivine-pyroxene ratio of the protolith may have controlled fluid pathways and thus the extent of serpentinization and the abundance, distribution, and grain size of brucite and awaruite, which has implications for carbon sequestration and nickel potential in the Decar area.

Keywords: Trembleur ultramafite, Decar, Baptiste deposit, serpentinite, listwanite, CO_2 sequestration, brucite, awaruite, dunite, harzburgite, lherzolite, pyroxenite

1. Introduction

Alteration of ophiolitic rocks is common and includes hydration (e.g., serpentinization) and carbonation (e.g., formation of listwanite). Serpentinization produces minerals such as serpentine, magnetite, brucite ($Mg(OH)_2$), and awaruite (Ni_3Fe; O'Hanley, 1996). Brucite, along with serpentine, can react with and sequester atmospheric CO_2 in carbonate minerals (Power et al., 2013) and awaruite forms with serpentinization in reducing environments from primary olivine or sulphides and is a potential source of nickel (Eckstrand, 1975; Britten, 2017). Listwanite is formed by the dehydration and carbonate alteration of these hydrated minerals and is a natural analogue of CO_2 sequestration through mineral carbonation (Hansen et al., 2005). Characterizing the chemical, mineralogical, and textural variability of a protolith is key to constraining its variable alteration to serpentinite and listwanite (Hall and Zhao, 1995; Hansen et al., 2005; Milidragovic and Grundy, 2019).

The Trembleur ultramafite is in the southern segment of the Cache Creek terrane, which extends through British Columbia into southern Yukon (Fig. 1; e.g., Monger and Gibson, 2019). The Trembleur ultramafite in the Decar area form part of a dismembered supra-subduction zone ophiolite and is variably serpentinized and carbonate-altered (Britten, 2017; Milidragovic and Grundy, 2019). The ultramafic protoliths are heterogeneous and consists of diverse peridotites and lesser pyroxenites. The serpentinized ultramafic rocks in the Decar area contain brucite, of potential environmental value (e.g., Vanderzee et al., 2019) and awaruite (Ni_3Fe), of potential economic value (Britten, 2017). This contribution summarizes the field and petrographic results of a study designed to evaluate the protoliths and alteration of the Trembleur ultramafite in order to constrain the controls on the formation, distribution, and abundance of brucite and awaruite and to identify the extent of alteration in the field.

2. Geological setting

The Decar area is underlain by rocks of the Cache Creek terrane, a tectonostratigraphic unit that contains Late Devonian to Middle Jurassic oceanic rocks and extends from southern British Columbia to Yukon (Fig. 1a; Cordey et al., 1991; Golding et al., 2016). These oceanic rocks were deformed and metamorphosed by ca. 172 Ma, following collision with the Stikine terrane on its western flank (Mihalynuk et al., 1994; Struik et al., 2001; Mihalynuk et al., 2004; Monger and Gibson, 2019). Exposed in the area are: greenschist- to amphibolite-facies ultramafic to intermediate igneous rocks

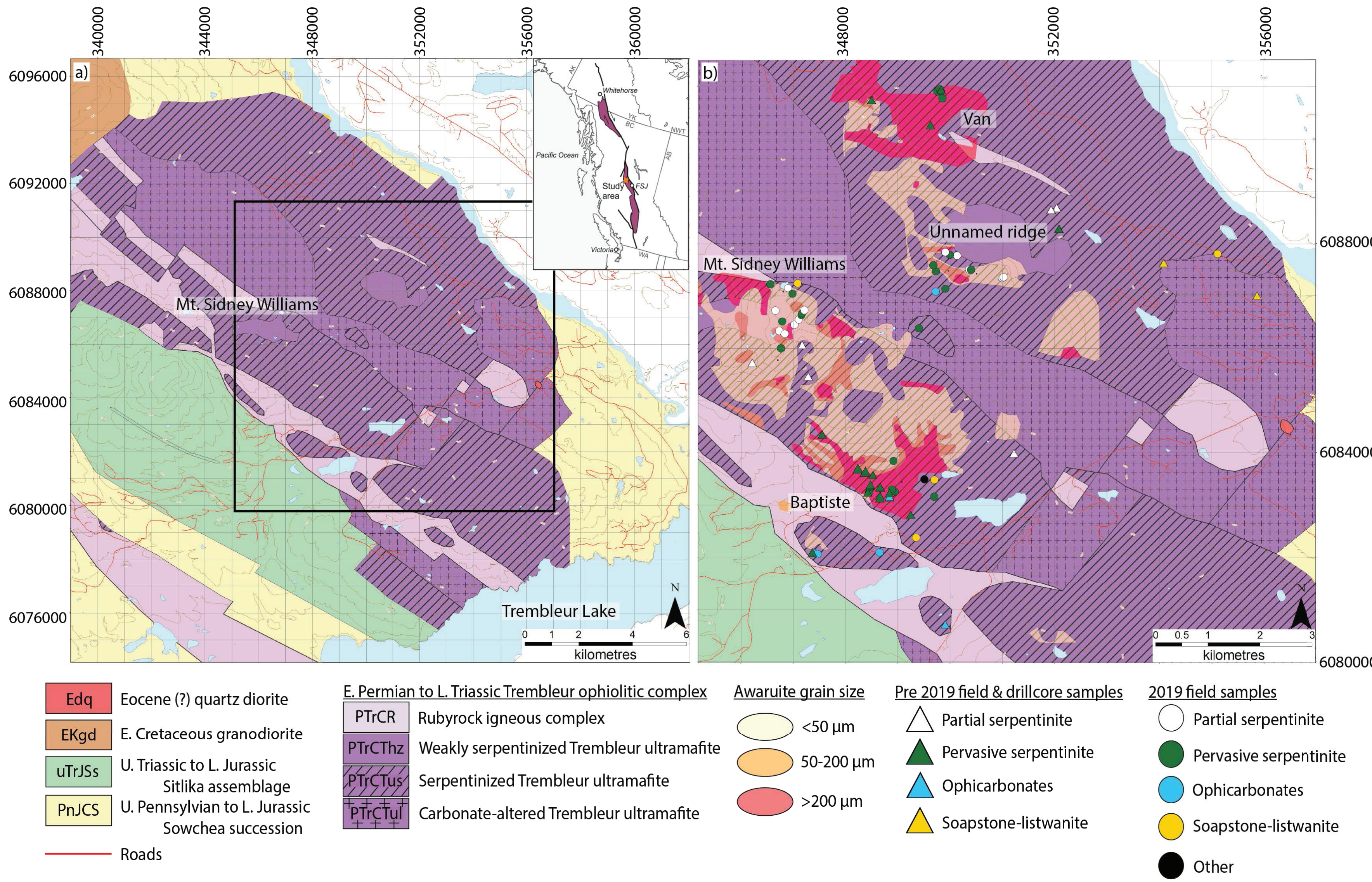

Fig. 1. **a)** Geological map of the area north of Trembleur Lake. **b)** Geological map of the Decar area with sample locations and mapped awaruite grain size. Modified from Britten (2017) and Milidragovic (2019).

and metasedimentary rocks of the Rubyrock igneous complex (early Permian to Late Triassic); altered ultramafic rocks of the Trembleur ultramafite (early Permian to Late Triassic); volcanic, siliciclastic, and carbonate rocks of the Sowchea succession (Upper Pennsylvanian to Lower Jurassic); and sedimentary and volcanic rocks of the Sitlika assemblage (Upper Triassic to Lower Jurassic; Fig. 1a; for details see Milidragovic et al., 2018; Milidragovic, 2019). The rocks are exposed in fault-bounded, northwest-trending belts that are dismembered by cross faults. The Sowchea succession and parts of the Sitlika assemblage are interpreted to record volcanism and sedimentation in an intraplate oceanic setting (Schiarizza and Massey, 2010; Milidragovic and Grundy, 2019). In contrast, the Rubyrock igneous complex and Trembleur ultramafite are interpreted to represent the crustal and mantle sections of a dismembered supra-subduction zone ophiolite (Schiarizza and MacIntyre, 1999; Struik et al., 2001; Schiarizza and Massey, 2010; Britten 2017; Milidragovic and Grundy, 2019). In this contribution, we focus on the Trembleur ultramafite.

The least serpentinized and carbonate-altered rocks of the Trembleur ultramafite outcrop in areas of relatively high elevation on Mount Sidney Williams (also known as Mount Sidney, Tselk'un or Red Rock) and an unnamed ridge ca. 3 km ENE of Mount Sidney Williams (Fig. 1b). In contrast, the most altered rocks occupy areas of low elevation. Highly serpentinized areas host awaruite, which is coarse grained at Baptiste and other places in the area (shown as irregular red polygons in Fig. 1b; Britten, 2017). Variable abundances of brucite have been documented in the highly serpentinized area in the Baptiste area (Vanderzee et al., 2019), but abundances are unknown in other parts of the Trembleur ultramafite. Ophicarbonate (serpentine-magnesite), soapstone (talc-magnesite), and listwanite (magnesite-quartz) assemblages are mainly in the southeastern and eastern part of the Trembleur ultramafite (Milidragovic et al., 2018).

3. Methods

A total of 89 hand samples of ultramafic rocks were selected for this study (Fig. 1b). Of these, 55 are surface samples collected during the 2019 field season, 15 are surface samples collected during the 2017 field season (Milidragovic and Grundy, 2019), and 19 are cores provided by FPX Nickel Corp. from drilling in nine holes at the Baptiste deposit. Hand samples were selected to represent the full range of alteration and textures of the serpentinized or carbonate-altered Trembleur ultramafite, whereas drill core samples were chosen at various depths (12 to 182 m), to include different rock types, bulk compositions, and mineral content based on Vanderzee et al. (2019).

4. Trembleur ultramafite protolith

The ultramafic rocks at Decar have all undergone some degree of serpentinization or carbonate alteration. Harzburgite (olivine and orthopyroxene-rich, <5% clinopyroxene) is the predominant rock type (Grundy, 2018; Milidragovic and Grundy, 2019), with lesser lherzolite (5-15% clinopyroxene), and dunite (>90% olivine). Relatively unaltered pyroxenite (>60% pyroxene) dikes and veins are a minor component. These rock types are distinguished in the field by the colour and texture of their weathered surfaces. Weathered surfaces of dunitic rocks are typically smooth and dun compared to more pyroxene-rich rocks, which weather rough and darker brown. The ultramafic rocks are not obviously strained, but shear zones and related folds are locally developed (Figs. 2a, b).

4.1. Harzburgite and lherzolite

Pyroxene-bearing peridotite, spanning the compositional spectrum between harzburgite and clinopyroxene-poor lherzolite, are the most common rocks at Decar. It is difficult to differentiate between the two rock types in the field because most are altered to some extent. Harzburgite (±lherzolite) is composed of olivine (≥60%), orthopyroxene (20-40%), and primary spinel. Orthopyroxene-poor harzburgite (ca. 20% pyroxene), which grades into dunite, is less common and occurs in layers or as pods. Orthopyroxene grains range from <0.5 to1.5 cm and are commonly altered to bastite. The colour of bastite varies in hand specimen from dark grey-green to light grey to white, and in thin section from brown to grey with increasing degree of serpentinization (Figs. 3c, d). Milidragovic et al. (2018) described relatively unaltered spinel harzburgite with coarse orthopyroxene, olivine, and rare finer grained clinopyroxene (Fig. 3c).

Lherzolite is distinguished from harzburgite by more abundant (5-13%) clinopyroxene that occurs as <0.5-1 mm-sized subhedral to euhedral prismatic grains (Fig. 3e). Clinopyroxene occurs as individual grains or as aggregates surrounded by orthopyroxene and/or olivine. Some clinopyroxene grains show lamellae of secondary spinel along cleavage planes. In both lherzolite and harzburgite samples, primary spinel grains vary from <0.3 to 2 mm, range from red to black, and typically show a vermicular or irregular habit, although some are equant. Chlorite and serpentine locally form haloes around spinel, thus spinel could be the source of aluminum for chlorite.

4.2. Dunite

Dunite comprises ca. 15% of all ultramafic rocks at Mt. Sidney and on the unnamed ridge to the east, where it is more abundant than was previously noted by Milidragovic and Grundy (2019). The dunite consists mostly of 1-6 mm equigranular olivine (Fig. 3a) and some samples contain rare brown or grey, fine-grained (<4 mm) bastite after orthopyroxene or clinopyroxene. Fine-grained (<1 mm) unaltered orthopyroxene and clinopyroxene grains are locally (<5%) preserved. Dunite typically occurs within harzburgite (±lherzolite) although it also forms massive uniform outcrops >20 m across. The contact between dunite and harzburgite is typically sharp although rare gradational contacts were also observed. Where dunite is hosted in harzburgite (±lherzolite) it forms sets of parallel to randomly oriented veins or dikes (0.5-50 cm wide), lone dikes, irregular- to lenticular-shaped pods or lenses <1 m wide, or as parallel, discontinuous layers 1-50 cm thick (Fig. 2; Fig. 4a).

Fig. 2. a) Dunite with thin pyroxenite veins and spinel (Spl) grains. **b)** Centimetre-scale shear zone cutting harzburgite (±lherzolite) and dunite layers. **c)** Dunite with spinel (Spl) as discontinuous layers and irregular pods in harzburgite (±lherzolite). **d)** Coarse spinel (Spl) grains with apparent long axes concordant to the walls of a dunite dike in harzburgite (±lherzolite). **e)** Pyroxenite vein concordant with dunite dike in harzburgite (±lherzolite). **f)** Pyroxenite dike crosscutting dunite and harzburgite (±lherzolite) layers.

Primary spinel is common in dunite and occurs as disseminated grains or multi-crystal aggregates. In plane-polarized light, spinel grains are red to black. Disseminated spinel grains range from <0.5 mm to 0.5 cm and characteristically have an equant habit (Fig. 3a). Apparent long axes of coarse disseminated spinel grains are typically aligned with the walls of the host dunite dikes. Spinel aggregates, which form 0.5-5 cm wide veins, are also aligned with host dunite dikes or layers (Fig. 2d). Less commonly, thin spinel veinlets are at an angle to dunite dikes and pyroxenite veins and pinch out in peridotite host rock (Fig. 2a).

4.3. Pyroxenite

Pyroxenite typically forms 0.5-5 cm wide veins in dunite layers (Figs. 2a, e) and ca. 10 cm-wide dikes that crosscut dunite and harzburgite (Fig. 2f). The modal abundance

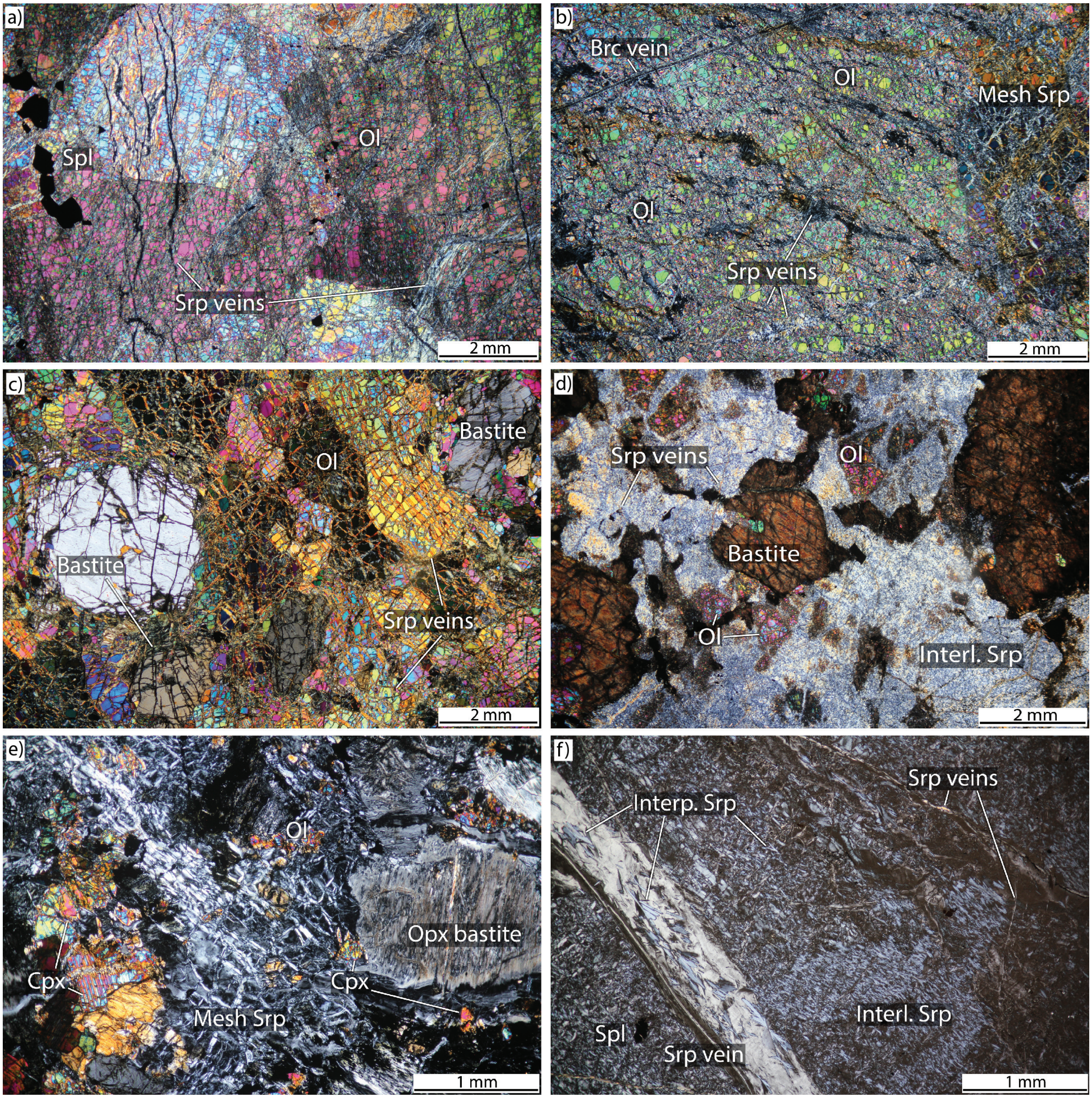

Fig. 3. Partial and pervasive serpentinites. **a)** Partially serpentinized dunite with olivine (Ol), serpentine (Srp) veins and primary spinel (Spl). **b)** Pervasively serpentinized dunite with olivine (Ol), serpentine (Srp) veins, mesh serpentine texture (Mesh Srp), and brucite (Brc) ±serpentine vein. **c)** Partially serpentinized harzburgite (±lherzolite) with bastite grains, olivine (Ol) and serpentine (Srp) veins. **d)** Pervasively serpentinized harzburgite with bastite, relict olivine (Ol), interlocking serpentine texture (Interl. Srp.) and serpentine (Srp) veins. **e)** Pervasively serpentinized lherzolite with clinopyroxene (Cpx), orthopyroxene (Opx) bastite, relict olivine, and mesh serpentine texture (Mesh Srp). **f)** Pervasive serpentinite with a coarse serpentine vein and interlocking serpentine texture (Interl. Srp.) overprinted by interpenetrating serpentine (Interp. Srp.) texture and secondary spinel (Spl). All images are in cross-polarized light.

of orthopyroxene and clinopyroxene in the pyroxenites is variable. In orthopyroxene-rich pyroxenite, the orthopyroxene grains are 4-6 mm with finer grained clinopyroxene, olivine, and red to black spinel of holly leaf texture. In clinopyroxene-rich pyroxenite, the clinopyroxene grains are >2 mm with finer olivine grains.

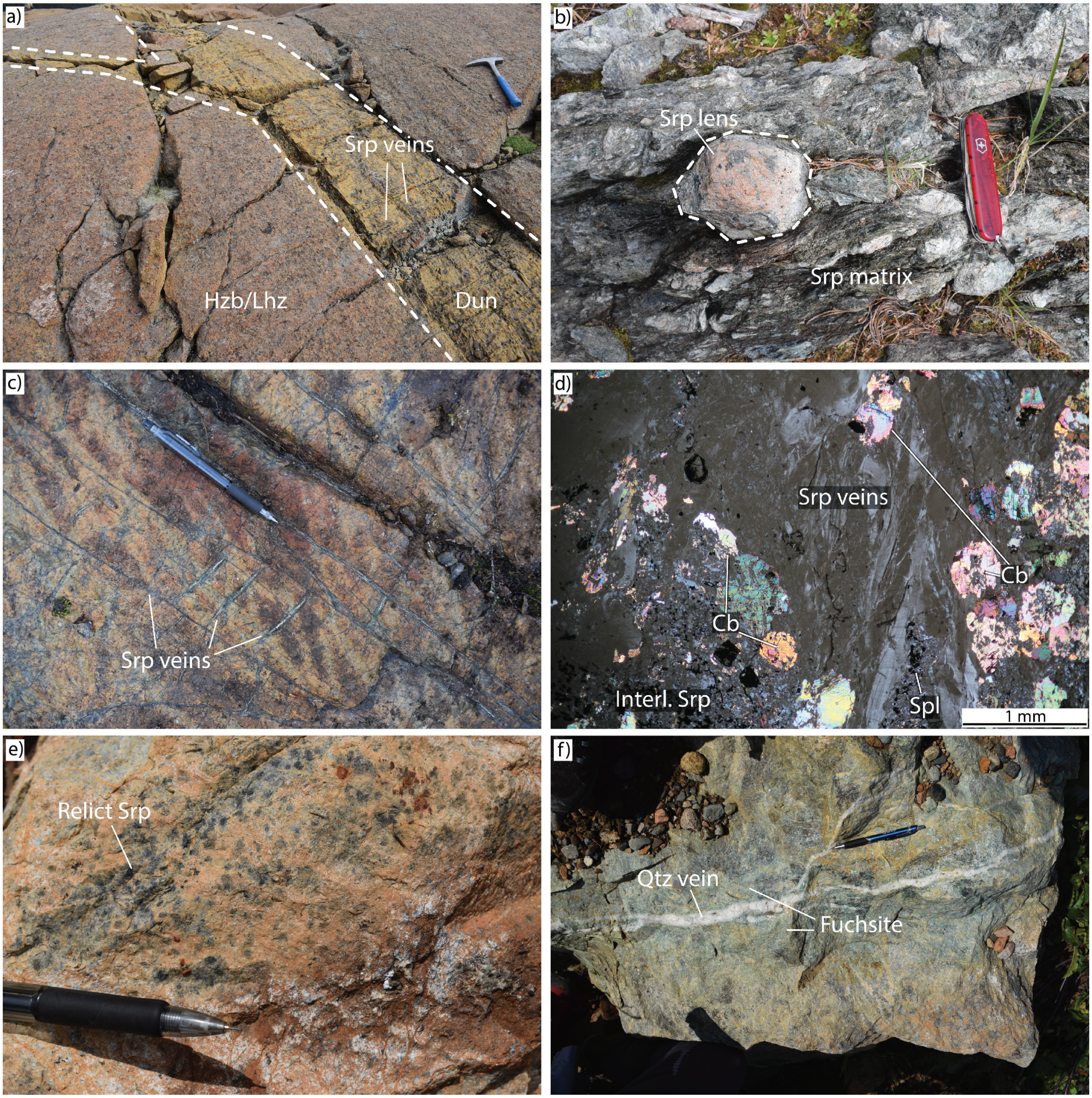

Fig. 4. Partial and pervasive serpentinites, slightly carbonated serpentinites, and listwanite. **a)** Dunite dike in harzburgite (±lherzolite) with serpentine (Srp) veins. **b)** Pervasive serpentinite (Srp) lens in a scaly serpentinite (Srp) matrix. **c)** Pervasive serpentinite with polygonal pattern of serpentine (Srp) veins. **d)** Slightly carbonated pervasive serpentinite with serpentine (Srp) veins, interlocking serpentine texture (Interl. Srp.), carbonate grains (Cb), and secondary spinel (Spl) (crossed-polarized light). **e)** Nearly fully carbonated serpentinite showing relict serpentinite (Srp) texture. **f)** Listwanite with a quartz (Qtz) vein bounded by fuchsite.

5. Serpentinized Trembleur ultramafite

All the rocks we observed in the field and collected for this study are serpentinized and/or carbonated to some extent. For ease of discussion, we subdivide the altered rocks into partial serpentinite, pervasive serpentinite, ophicarbonates and soapstone-listwanite. Partial serpentinite is typically grey, preserves obvious primary textures, and contains ca. 30-70 vol% relict minerals (olivine and pyroxenes). In contrast, pervasive serpentinite is light to dark green, contains ca. 0-30 vol% relict minerals, and commonly displays a foliation. The serpentinization process results in volume increases (up to 40%: Komor et al., 1985) and produces alteration minerals (e.g., olivine + H_2O goes to serpentine group minerals + magnetite + awaruite + brucite; Johannes, 1968; Britten, 2017). Carbonatization results in breakdown of the serpentinization minerals (e.g., brucite + CO_2 goes to magnesite + H_2O; Hansen et al., 2005). Increasing the intensity of CO_2alteration results in a progressive decrease in the volume of the relict serpentinite enclaves from ophicarbonates to soapstone to complete conversion to listwanite. Chemical reactions that change volume (density) and abundance of magnetite can be used as first-order proxies for the degree and type of alteration (Komor et al., 1985; Toft et al., 1990; Hansen et al., 2005; Cutts et al., in press).

5.1. Serpentinization and protolith variability

In partially serpentinized rocks, the serpentinization textures, alteration minerals, and extent of alteration appear to vary between protoliths. In dunite-rich outcrops, serpentine veins are generally subparallel to dunite dikes or layers, rather than penetrating into the surrounding harzburgite or lherzolite (Fig. 4a). In dunite, serpentine veins crosscut primary olivine grains and these veins are progressively thicker and more abundant with increasing degrees of serpentinization (compare Figs. 3a and 3b). In dunite, the pyroxene, if present, is typically strongly altered to bastite.

In contrast, although harzburgite and lherzolite contain serpentine veins (Fig. 3c), with further alteration serpentine principally occurs in the groundmass after olivine and as bastite alteration of pyroxene (Figs. 3d, e). With increasing degree of alteration, bastite colour ranges from beige to dark brown to grey or light yellow, and grain shapes range from subhedral to anhedral (Figs. 3c-e). Altered bastite grains commonly contain secondary magnetite and crosscutting serpentine veins. In partial and pervasive serpentinites, olivine is the least preserved, followed by orthopyroxene and then clinopyroxene (Fig. 3d). Orthopyroxene grains or their bastite equivalents are consistently more altered than clinopyroxene, which typically retains a subhedral shape and high birefringence (Fig. 3e). Olivine-poor pyroxenite-rich dikes are relatively unaltered and the few observed olivine grains, which are interlocked with pyroxene, appear to be the most altered minerals in the assemblage.

5.2. Serpentinite and serpentine texture

Typically, the fresh surface of serpentinite is light to dark grey-green, rarely vibrant green and weathers grey-brown-green to off-white. Pervasive serpentinites locally contain lenses of relatively competent serpentinite in an anastomosing scaly serpentinite matrix and contain serpentine veins parallel to one another (Fig. 4b). Locally, pervasive serpentinites are brecciated, whereas others display polygonal patterns of uniformly spaced serpentine veins (Fig. 4c).

The degree of serpentinization is most effectively determined in thin-section by comparing modal abundances of relict primary versus alteration minerals (Fig. 3), identifying alteration minerals, and distinguishing between serpentine textures. In thin section, Decar serpentinites displays mesh (Figs. 3b, e), hourglass, and ribbon textures, which are typical of the lizardite polymorph. Interlocking (Figs. 3d, e; Fig. 4d) and interpenetrating (Fig. 3e) serpentine textures are also present and likely reflect the antigorite polymorph (Wicks and Whittaker, 1977). Many samples contain a mixture of overprinting textures, indicating multi-stage serpentinization. Figure 3f illustrates an example where an interpenetrating texture overprints interlocking texture and serpentine veins. Serpentine veins occur in samples of all protoliths and extents of serpentinization, but they vary in abundance and can be oriented either parallel or oblique to one another. The veins are white-grey-green and weather to grey-white (Fig. 4c), vary in width from <20 μm to >4 cm, and commonly have a massive, wavy, or interlocking texture and rarely, serpentine selvages (Figs. 3; Figs. 4a-d). Serpentine veins wider than 1 cm are commonly fibrous, and likely composed of chrysotile.

In addition to serpentine and relict primary minerals, serpentinites commonly contain the secondary minerals magnetite (Fig. 3f), brucite (Fig. 3b), awaruite, chlorite, talc, and tremolite, and locally, metamorphic olivine and diopside (Britten, 2017; Milidragovic and Grundy, 2019). Brucite is in both partially and pervasively serpentinized rocks, derived from dunite, harzburgite, and lherzolite protoliths. Brucite most commonly occurs in mesh serpentine or adjacent to relict olivine as discrete grains (<150 μm), aggregates, or as thin veins typically spatially associated with serpentine and/ or magnetite (Fig. 3b). In partially serpentinized samples from all protoliths, fine- to coarse- grained magnetite, sulphides, and awaruite are commonly in or close to serpentine veins, whereas in highly serpentinized samples, these minerals are typically in the serpentine groundmass and/or metamorphic olivine. Awaruite grains vary in size (<10 to 800 μm across), shape, and association; they occur as monomineralic grains, locally rimmed by secondary magnetite, or as polymineralic grains intergrown with magnetite and sulphides (e.g., pentlandite, heazlewoodite; Britten, 2017; Milidragovic and Grundy, 2019). Chlorite and talc are common in pyroxene-rich rocks.

6. Carbonate alteration and listwanite

The degree of carbonate alteration and dehydration of ultramafic rocks is highly variable. The CO_2-bearing assemblages form a spectrum consisting of serpentine-magnesite (ophicarbonate), talc-magnesite (soapstone), and quartz-magnesite±fuchsite (listwanite), in order of increasing carbonation. The colour of the rocks, their magnetic susceptibility, and specific gravity vary by the extent to which they have been carbonated (Figs. 4d-f; Cutts et al., in press).

Ophicarbonates are common throughout the Decar area and are nearly indistinguishable from serpentinites in the field but can be identified in thin section and by bulk chemistry. Carbonate minerals occur in partially to highly serpentinized samples or even in samples containing metamorphic olivine. Carbonate veins overprint serpentine veins (±magnetite) and serpentine in groundmass (Fig. 4d), indicating that carbonate alteration post-dated serpentinization. In moderately carbonate-altered samples (Fig. 4e), relict serpentine typically exhibits an interlocking or interpenetrating texture, likely antigorite. Brucite grains occur in weakly carbonated samples but are absent in more carbonated samples. Awaruite, sulphides, and spinel persist except in the most strongly carbonated rocks. In fully carbonated rocks, relict serpentinite is rare, although locally it may occur in small patches, both with or without spinel. Fuchsite is most abundant adjacent to <10 cm thick quartz veins and diminishes in abundance away from the veins (Fig. 4f).

7. Timing of serpentinization and carbonate alteration with respect to dikes in the Trembleur ultramafite

Several generations of non-ultramafic dikes occur in the Decar area. In the Baptiste area, at least some serpentinization and carbonation was after emplacement of a dike that is altered to a rodingite (a non-ultramafic rock that is altered by reduced and alkaline fluids during serpentinization; Barnes et al., 1972; Bach and Klein, 2009; Britten, 2017) and an altered dike of probable Rubyrock igneous complex affinity. A third, relatively fresh fine-grained intermediate dike apparently post-dates serpentinization and is likely Eocene.

8. Discussion and implications

8.1. Origin of dunite

The origin of peridotites in the Trembleur ultramafite has been discussed by Britten (2017), Milidragovic and Grundy (2019) and Grundy (2018). The predominantly harzburgitic mineralogy, with subordinate depleted lherzolite, is consistent with a refractory origin for the Decar peridotites resulting from high degrees of partial melting of a fertile precursor (Britten, 2017; Milidragovic and Grundy, 2019). The harzburgite (±lherzolite) is more depleted (≤2 wt.% Al_2O_3), than the moderately depleted lherzolitic upper mantle (DMM1; 2.38 wt.% Al_2O_3 and ca. 8% clinopyroxene at 1 GPa: Workman and Hart, 2005). Below we consider the origin of the dunite.

Based on fieldwork, the dunite comprises ~15% of the total ultramafic rocks. In contrast, using drill core from the Baptiste deposit, Britten (2017) estimated that dunite makes up only ca. 5% (407 out of 7739 splits) of the peridotite volume at Decar. Britten (2017) may have underestimated the true abundance of dunite because the drill core from Baptiste is highly serpentinized and data were at times collected from splits greater than 5 m. Dunite observed in the field is typically restricted to <0.5 m thick dikes or layers. Consequently, these small dunite bodies could be diluted and misidentified as olivine-rich harzburgite in examination of drill core bulk chemical data (Britten, 2017).

Three origins of dunite have been proposed: 1) as residue from extensive partial melting of fertile peridotite in the mantle (melt fraction >35%; e.g., Takahashi et al., 1993); 2) as a cumulate due to fractionation of olivine from mafic melt or liquids; 3) as a replacement of pyroxene-rich harzburgite or lherzolite by a magnesian±Cr rich magma, commonly at mantle-crust transition zones in ophiolites (Quick, 1981; Nicolas and Prinzhofer, 1983; Kelemen, 1990). At some localities, multiple origins of dunite have been suggested (e.g., the Trinity peridotite; Quick, 1981), but more commonly, one process is predominant. The relationship of the dunite shape, size, and contacts with the host rock (sharp or diffuse) is important in understanding the origin of dunite (Kelemen, 1990; Kubo, 2002; Morgan and Liang, 2003). However, if highly strained the shape of a dunite body (e.g., lenticular lenses) may no longer reflect the original magmatic process (Nicolas and Prinzhofer, 1983). Residue dunite is best distinguished from other origins by bulk-rock and olivine compositions (Kelemen, 1990; Su et al., 2016). Cumulate dunite typically shows systematic layering, with dunite and chromitite at the base, and troctolitic and/or wehrlite, pyroxenite, and gabbro at the top (Nicolas and Prinzhofer, 1983). Replacement dunite is typically irregularly shaped and displays evidence of volume increase, it may contain traces of clinopyroxene (Kelemen, 1990), and spinel should show a more equant habit relative to that in host rocks (Nicolas and Prinzhofer, 1983; Arai, 1994; Dandar et al., 2019).

The discordant and irregular shaped dunite layers and pods described above resemble replacement dunites described by Kelemen and Ghiorso (1986) and Kelemen (1990). Field and thin section observations suggest that spinel is equant and more abundant in dunite compared to the mostly irregular, vermicular, and commonly fine-grained primary spinel in the surrounding harzburgite. A replacement dunite mechanism would also be consistent with the fine-grained clinopyroxene found in dunite resulting from the consumption of orthopyroxene (Kelemen, 1990). These observations suggest that the dunite at Decar, or at least at Mt. Sidney Williams and the unnamed ridge, may have formed by replacement. Further geochemical characterization is underway to determine the origin of dunite at this locality.

8.2. Serpentinization processes

Field and petrographic observations can place constraints on the timing of serpentinization and the source of hydrothermal fluids. Thin-section and outcrop-scale observations indicate that fluid infiltration during serpentinization of dunite differs from that of harzburgite and lherzolite. Movement of H_2O-rich fluids through dunite was apparently along fractures related to veins compared to less focussed flow in harzburgite and lherzolite (Figs. 3a-d). The grain size and modal abundance of primary minerals (i.e., olivine, pyroxenes, spinel) along with the chemistry and pH of fluids can play an important role in the serpentinization rate and variability (Barnes et al., 1972; Lafay et al., 2012). The overall rate of serpentinization is typically fastest for olivine and slowest for clinopyroxene (Coleman and Keith, 1970; Moody, 1976; Wicks and Whittaker, 1977; Komor et al., 1985); however, this general rule can vary as a function of the composition of the serpentinizing fluid. Olivine may be more resistant to serpentinization than orthopyroxene during interactions with high Mg^{2+}-rich fluids such as during seawater-peridotite interaction. In contrast, orthopyroxene tends to be more resistant than olivine during interactions with fluids that are $Si(OH)_4$-rich; such fluids are generated when seawater reacts with crustal rocks before reaching peridotite (Peacock, 1987; O'Hanley, 1996). Observations of partially serpentinized harzburgite and lherzolite show that olivine grains are the most altered, followed by orthopyroxene; clinopyroxene is relatively unaltered (Fig. 3e). The extent of alteration of these primary minerals could indicate that most of the serpentinization did not occur at the seafloor, which is consistent with isotope data indicating a meteoric fluid source (Britten, 2017).

Protolith composition can exert a primary control on alteration mineral assemblages, along with fluid composition, temperature, and pressure. For example, temperature, oxidation of Fe or high SiO_2 can favour formation of serpentine or talc instead of brucite (O'Hanley, 1996; Evans et al., 2013; Sciortino et al., 2015). Harzburgite seems to have a more extensive formation of secondary magnetite relative to dunite which can also be seen in a general higher magnetic susceptibility (Toft et al., 1990; Cutts et al., in press). Possible olivine compositional differences in dunite versus harzburgite could be the cause of variability in awaruite grain size or/and abundance. Future work will explore the formation and stability controls of brucite and awaruite in more detail.

9. Summary

The protoliths of altered rocks in the Trembleur ultramafite are heterogeneous and dunite appears to be more abundant than previously thought. Most of the Trembleur ultramafite is partially to pervasively serpentinized and the primary olivine-pyroxene ratio of the protoliths seems to have exerted a primary control on the types and abundances of alteration minerals, such as brucite and awaruite, and the style of infiltration of serpentinizing fluids. Carbonate alteration post-dated serpentinization, and consumed brucite and awaruite. The heterogeneity in the Trembleur ultramafite protolith and the distribution and extent of alteration thus has implications for the abundance and distribution of brucite and awaruite and therefore on the carbon sequestration and nickel potential of the area.

Acknowledgments

We are grateful for both the Tl'azt'en Nation and Binche Whut'en First Nation for their help and knowledge of the Decar area. Special thanks to Edgar John and Marian Duncan, First Nation representatives, for their help in the field. FPX Nickel Corp. and geologists Peter Bradshaw and Trevor Rabb are thanked for their support, discussions, and knowledge of the Decar area. We also thank Alex Zagorevski for a critical review. This research is funded by Natural Resources Canada Clean Growth Program and FPX Nickel Corp.

References cited

Arai, S., 1994. Characterization of spinel peridotites by olivine-spinel compositional relationships: Review and interpretation. Chemical Geology, 113, 191-204.

Bach, W., and Klein, F., 2009. The petrology of seafloor rodingites: Insights from geochemical reaction path modeling. Lithos, 112, 103-117.

Barnes, I., Rapp, J.B., O'Neil, J.R., Sheppard, R.A., and Gude, A.J., 1972. Metamorphic assemblages and the direction of flow of metamorphic fluids in four instances of serpentinization. Contributions to Mineralogy and Petrology, 35, 263-276.

Britten, R., 2017. Regional metallogeny and genesis of a new deposit type - disseminated awaruite (Ni_3Fe) mineralization hosted in the Cache Creek terrane. Economic Geology, 112, 517-550.

Coleman, R.G., and Keith, T.E., 1970. A chemical study of serpentinization - Burro Mountain, California. Journal of Petrology, 12, 311-28.

Cordey, F., Gordey, S.P., and Orchard, M.J., 1991. New biostratigraphic data from the northern Cache Creek terrane, Teslin map area, southern Yukon. In: Current Research part E. Geological Survey of Canada, Paper 1991-E, pp. 67-76.

Cutts, J.A., Dipple, G.M., Hart, C., and Milidragovic, D., in press. Assessment of the carbon mineralization potential of British Columbia by quantifying the response of physical properties to the alteration of ultramafic rocks. In: Geoscience BC Summary of Activities 2019: Minerals and Mining, Geoscience BC Report 2020-1.

Dandar, O., Okamoto, A., Uno, M., Oyanagi, R., Nagaya, T., Burenjargai, U., Miyamoto, T., and Tsuchiya, N., 2019. Formation of secondary olivine after orthopyroxene during hydration of mantle wedge: evidence from the Khantaishir Ophiolite, western Mongolia. Contributions to Mineralogy and Petrology, 174, 86.

Eckstrand, O.R., 1975. The Dumont serpentinite: A model for control of nickeliferous opaque mineral assemblages by alteration reactions in ultramafic rocks. Economic Geology, 70, 183-201.

Evans, K.A., Powell, R., and Frost, B.R., 2013. Using equilibrium thermodynamics in the study of metasomatic alteration, illustrated by an application to serpentinites. Lithos, 168/169, 67-84.

Golding, M.L., Orchard, M.J., and Zagorevski, A., 2016. Microfossils from the Cache Creek complex in northern British Columbia and southern Yukon. Geological Survey of Canada, Open File 8033, 25 p.

Grundy, R., 2018. Melting and cooling histories of two upper mantle massifs in the Cache Creek terrane, Central British Columbia. Unpublished B.Sc. Thesis, University of Victoria, Victoria, Canada, 60 p.

Hall, C., and Zhao, R., 1995. Listvenite and related rock-perspectives on terminology and mineralogy with reference to an occurrence at Cregganbaun. Mineralium Deposita, 30, 303-313.

Hansen, L.D., Dipple, G.M., Gordon, T.M., and Kellett, D.A., 2005. Carbonated serpentinite (listwanite) at Atlin, British Columbia: A geological analogue to carbon dioxide sequestration. The Canadian Mineralogist, 43, 225-239.

Johannes, W., 1968. Experimental investigation of the reaction forsterite + H_20 ~ = serpentine + brucite. Contributions to Mineralogy and Petrology, 19, 309-315.

Kelemen, P.B., 1990. Reaction between ultramafic rock and fractionating basaltic magma I. Phase relations, the origin of calc-alkaline magma series, and the formation of discordant dunite. Journal of Petrology, 31, 51-98.

Kelemen, P.B., and Ghiorso, M.S., 1986. Assimilation of peridotite in zoned calc-alkaline plutonic complexes: evidence from the Big Jim complex, Washington Cascades. Contributions to Mineralogy and Petrology, 94, 12-28.

Komor, S.C., Elthon, D., and Casey, J.F., 1985. Serpentinization of cumulate ultramafic rocks from the North Arm Mountain massif of the Bay of Islands ophiolite. Geochimica et Cosmochimica Acta, 49, 2331-2338.

Kubo, K., 2002. Dunite formation processes in highly depleted peridotite: Case study of the Iwanaidake Peridotite, Hokkaido, Japan. Journal of Petrology, 43, 423-448.

Lafay, R., Montes-Hernandez, G., Janots, E., Chiriac, R., Findling, N., and Toche, F., 2012. Mineral replacement rate of olivine by chrysotile and brucite under high alkaline conditions. Journal of Crystal Growth, 347, 62-72.

Mihalynuk, M.G., Nelson, J., and Diakow, L J., 1994. Cache Creek terrane entrapment: Oroclinal paradox within Cordillera. Tectonics, 13, 575-595.

Mihalynuk, M.G., Erdmer, P., Cordey, F., Archibald, D.A., Friedman, R.M., and Johannson, G.G., 2004. Coherent French Range blueschist: Subduction to exhumation in less than 2.5 m.y.? Geological Society of America Bulletin, 116, 910-922.

Milidragovic, D., 2019. Geology of the Cache Creek terrane north of Trembleur Lake. British Columbia Ministry of Energy, Mines, and Petroleum Resources, British Columbia Geological Survey Open File 2019-06, 1:50,000 scale.

Milidragovic, D., and Grundy, R., 2019. Geochemistry and petrology of rocks in the Decar area, central British Columbia: Petrologically constrained subdivision of the Cache Creek complex. In: Geological Fieldwork 2018, British Columbia Ministry of Energy, Mines and Petroleum Resources, British Columbia Geological Survey Paper 2019-1, pp. 55-77.

Milidragovic, D., Grundy, R., and Schiarizza, P., 2018. Geology of the Decar area north of Trembleur Lake, NTS 93K/14. In: Geological Fieldwork 2017, British Columbia Ministry of Energy, Mines and Petroleum Resources, British Columbia Geological Survey Paper 2018-1, pp. 129-142.

Monger, J.W.H., and Gibson, H.D., 2019. Mesozoic-Cenozoic deformation in the Canadian Cordillera: The record of a “Continental Bulldozer ” ? Tectonophysics, 757, 153-169.

Moody, J.B., 1976. Serpentinization: a review. Lithos, 9, 125-138..

Morgan, Z., and Liang, Y., 2003. An experimental and numerical study of the kinetics of harzburgite reactive dissolution with applications to dunite dike formation. Earth and Planetary Science Letters, 214, 59-74.

Nicolas, A., and Prinzhofer, A., 1983. Cumulative or residual origin for the transition zone in ophiolites: Structural evidence. Journal of Petrology, 24, 2, 188-206.

O’Hanley, D.S., 1996. Serpentinites record of tectonic and petrological history. Oxford University Press, New York, 247 p.

Peacock, S.M., 1987. Serpentinization and infiltration metasomatism in the Trinity peridotite, Klamath province, northern California: Implications for subduction zones. Contributions to Mineralogy and Petrology, 95, 55-70.

Power, I.M., Wilson, S.A., and Dipple, G.M., 2013. Serpentinite carbonation for CO_2 sequestration. Elements, 9, 115-122.

Quick, J.E., 1981. The origin and significance of large, tabular dunite bodies in the Trinity Peridotite, northern California. Contributions to Mineralogy and Petrology, 78, 413-422.

Su, B., Chen, Y., Guo, S., and Liu, J., 2016. Origins of orogenic dunites: Petrology, geochemistry, and implications. Gondwana Research, 29, 41-59.

Schiarizza, P., and MacIntyre, D.G., 1999. Geology of the Babine Lake-Takla Lake area, central British Columbia (93K/11, 12, 13, 14;93N/3, 4, 5, 6). In: Geological Fieldwork 1998, British Columbia Ministry of Energy, Mines and Petroleum Resources, British Columbia Geological Survey Paper 1999-1, pp. 33-68.

Schiarizza, P., and Massey, N.W.D., 2010. Geochemistry of volcanic and plutonic rocks of the Sitlika assemblage, Takla Lake area, central British Columbia (NTS 093N/04, 05, 12, 13). In: Geological Fieldwork 2009, British Columbia Ministry of Energy, Mines and Petroleum Resources, British Columbia Geological Survey Paper 2010-1, pp. 55-67.

Sciortino, M., Mungall, J.E., and Muinonen, J., 2015. Generation of high-Ni sulfide and alloy phases during serpentinization of dunite in the Dumont sill, Quebec. Economic Geology, 110, 733-761.

Struik, L.C., Schiarizza, P., Orchard, M.J., Cordey, F., Sano, H., MacIntyre, D.G., Lapierre, H., and Tardy, M., 2001. Imbricate architecture of the upper Paleozoic to Jurassic oceanic Cache Creek Terrane, central British Columbia. Canadian Journal of Earth Sciences, 38, 495.

Takahashi, E., Shimazaki, T., Tsuzaki, Y., and Yoshida, H., 1993. Melting study of a peridotite KLB-1 to 6.5 GPa, and the origin of basaltic magmas: Philosophical Transactions, Physical Sciences and Engineering, 342, 105-120.

Toft, P.B., Arkani-Hamed, J., and Haggerty, S.E., 1990. The effects of serpentinization on density and magnetic susceptibility: a petrophysical model. Physics of the Earth and Planetary Interiors, 65, 137-157.

Vanderzee, S.S.S., Dipple, G.M., and Bradshaw, P.M.D., 2019. Targeting highly reactive labile magnesium in ultramafic tailings for greenhouse-gas offsets and potential tailings stabilization at the Baptiste deposit, central British Columbia (NTS 093K/13, 14). In: Geoscience BC Summary of Activities 2018: Minerals and Mining, Geoscience BC Report 2019-1, pp. 109-118.

Wicks, F.J., and Whittaker, E.J.W., 1977. Serpentine textures and serpentinization: The Canadian Mineralogist, 15, 459-488.

Workman, R.K., and Hart, S.R., 2005. Major and trace element composition of the depleted MORB mantle (DMM). Earth and Planetary Science Letters, 231, 53-72.

New geological investigations of the Early Jurassic Polaris ultramafic-mafic Alaskan-type intrusion, north-central British Columbia

James Nott[1, a], Dejan Milidragovic[2], Graham T. Nixon[2], and James S. Scoates[1]

[1] Pacific Centre for Isotopic and Geochemical Research, Department of Earth, Ocean and Atmospheric Sciences, University of British Columbia, Vancouver, BC, V6T 1Z4
[2] British Columbia Geological Survey, Ministry of Energy, Mines and Petroleum Resources, Victoria, BC, V8W 9N3
[a] corresponding author: jnott@eoas.ubc.ca

Recommended citation: Nott, J., Milidragovic, D., Nixon, G.T., and Scoates, J.S., 2020. New geological investigations of the Early Jurassic Polaris ultramafic-mafic Alaskan-type intrusion, north-central British Columbia. In: Geological Fieldwork 2019, British Columbia Ministry of Energy, Mines and Petroleum Resources, British Columbia Geological Survey Paper 2020-01, pp. 59-76.

Abstract

The Polaris Alaskan-type ultramafic-mafic intrusion in north-central British Columbia is an exceptionally well-exposed, north-northwesterly trending sill-like body 14 km long by 3 km across. Rock types are distributed asymmetrically, with dunite prevalent in the east, wehrlite, clinopyroxenite, and zones of chaotically intermingled ultramafic cumulates in central areas, and gabbro-diorite to hornblende clinopyroxenite in the west. Key observations are the variable nature of lithological contacts, complex dike and sill emplacement relationships, evidence for magmatic disruption of ultramafic cumulates, and eastward-directed thrusting of the entire intrusion atop contact aureole rocks in the east. Sharp to diffuse contacts suggest mingling and melt infiltration of previously formed cumulates of olivine clinopyroxenite, wehrlite, and dunite, and localized chaotically intermingled zones incorporating all these rock types. Disrupted chromitite layers hosted primarily by dunite occur as schlieren, folded chromitite layers and isolated blocks containing thin chromitite horizons, features interpreted as remobilized cumulates. Ni-Cu-platinum group element sulphides hosted by clinopyroxenite are mainly found in the western part of the intrusion. Ongoing research aims to establish the temporal and magmatic evolution of the intrusion with implications for the nature and timing of sulphide mineralization.

Keywords: Alaskan-type, ultramafic-mafic intrusion, Polaris intrusion, Lay Range, Quesnellia, Ni-Cu sulphides, platinum-group elements

1. Introduction

Magmatic nickel-copper-platinum group element (Ni-Cu-PGE) deposits at convergent margins are gaining global importance as an economic resource (e.g., Xiarihamu, Song et al., 2016; Aguablanca, Piña, 2019), yet remain poorly understood and underexplored (Nixon et al., 2015; Manor et al., 2016, 2017). The Cordillera of British Columbia and Alaska hosts a number of ultramafic-mafic bodies with Ni-Cu-PGE-mineralization (e.g., Duke Island, Tulameen, Turnagain, Polaris, Giant Mascot; Fig. 1) many of which exhibit broad lithological zonation from a dunite core to a pyroxenite/hornblendite or gabbro-diorite margin. The (Ural-) Alaskan-type or 'concentrically zoned' ultramafic-mafic intrusions described in the literature (e.g., Taylor, 1967; Irvine, 1974a, 1976; Himmelberg and Loney, 1995) form a distinct subclass of convergent margin intrusive bodies distinguished by the predominance of olivine, clinopyroxene, and hornblende±plagioclase, and importantly, by the absence of orthopyroxene (Nixon et al., 2015). In the IUGS classification scheme for ultramafic rocks (Le Maitre, 1989), Alaskan-type rocks are confined to the olivine-clinopyroxene join with variable amounts of hornblende (Fig. 2).

Several Alaskan-type intrusions in British Columbia with known Ni-Cu-PGE sulphide mineralization are being investigated as part of the Geological Survey of Canada's Targeted Geoscience Initiative 5 Program (TGI-5). The principal objective of the research is to establish the nature and timing of Ni-Cu-PGE sulphide mineralization with respect to the temporal and magmatic evolution of the intrusions to develop new models to guide mineral exploration (e.g., Giant Mascot intrusion, Manor et al., 2016, 2017; Turnagain intrusion, Jackson-Brown, 2017; Nixon et al., 2019a). The present study focusses on the Early Jurassic Polaris ultramafic-mafic intrusion, a superbly exposed Alaskan-type body in north-central British Columbia. The intrusion hosts sparsely platiniferous chromitites in dunite, and poorly documented magmatic Ni-Cu-PGE sulphide mineralization (Nixon et al., 1997). Herein, we present the preliminary results of a two week reconnaissance in 2018 and six weeks of detailed mapping in 2019. We describe the main rock types in the intrusion and their contact relationships, the zonation of the intrusion, the distribution of magmatic Ni-Cu-PGE sulphide occurrences, and intrusion-country rock relationships.

2. Previous work

Roots (1954) provided the first detailed descriptions of the Polaris intrusion. This work was followed by petrological studies and internal mapping by Foster (1974) and Irvine

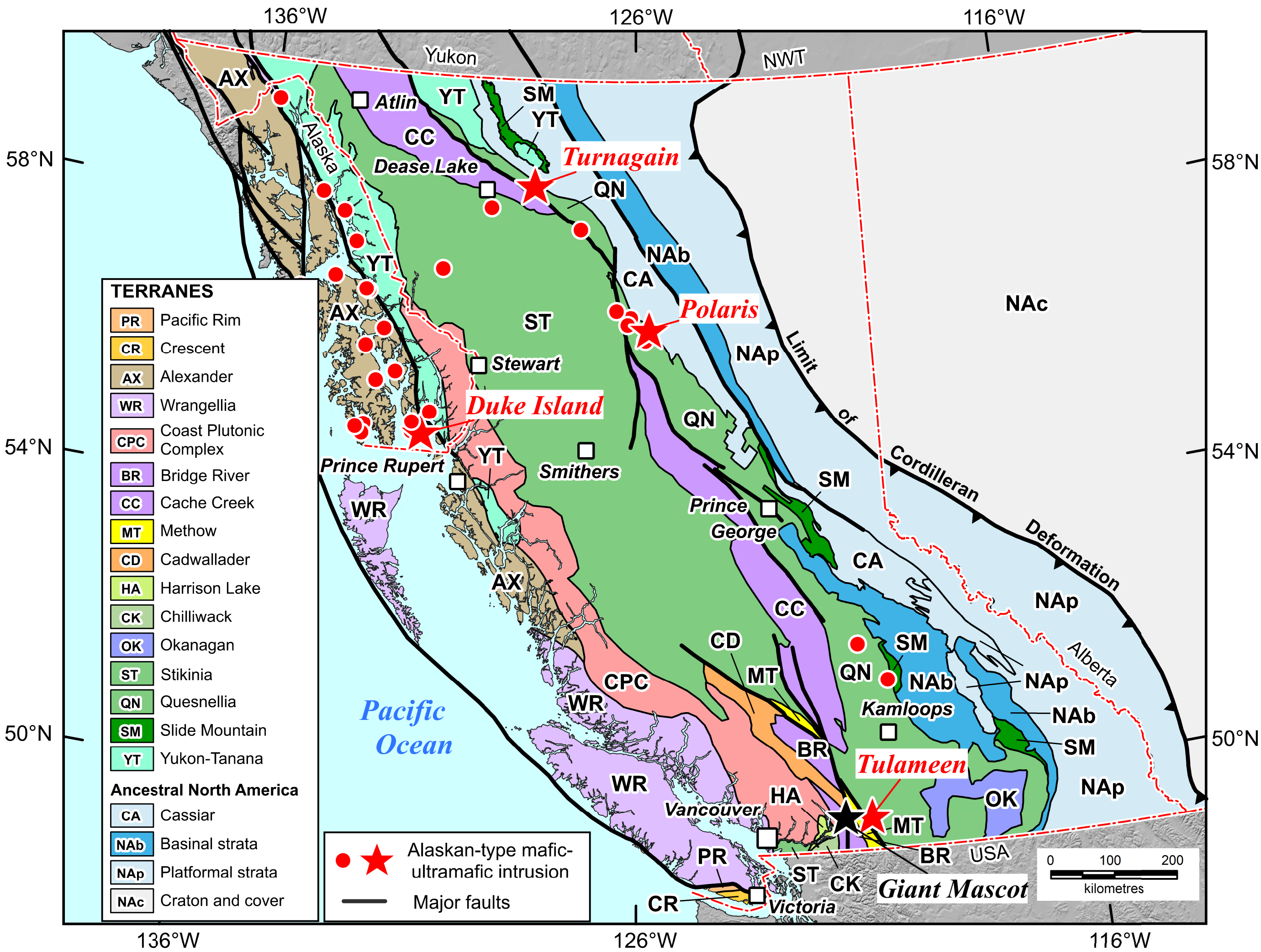

Fig. 1. Location of the Polaris, other Alaskan-type intrusions, and the Giant Mascot orthopyroxene-rich ultramafic-mafic intrusion with respect to terranes of the Canadian Cordillera. Adapted from Nelson et al. (2013) and Nixon et al. (2019).

(1974b, 1976), who recognized the Alaskan-type affinity of the intrusion, and by Nixon et al. (1997) who published detailed geological maps and PGE analyses. The regional context of the intrusion was mapped at a 1:50,000 scale by Ferri et al. (2001). A multi-grain U-Pb zircon date of 186 ±2 Ma (Early Jurassic) was reported by Nixon et al. (1997) from a quartz-hornblende-plagioclase pegmatite in hornblendite near the northwestern margin of the intrusion (Fig. 3). This sample was reprocessed for single-grain CA-TIMS analysis and yielded a more precise date of 186.26 ±0.14 Ma, interpreted as the crystallization age of the pegmatite (Nixon et al., 2019b).

3. Regional geology

The Polaris ultramafic-mafic intrusion (56°30'N, 125°40'W) is in the Lay Range of the Omineca Mountains in north-central British Columbia, approximately 200 km northeast of Smithers (Fig. 1). The intrusion was emplaced into late Paleozoic (Mississippian-Permian) metasedimentary and metavolcanic rocks of the Lay Range assemblage, which forms the substrate for early Mesozoic, arc-derived volcanosedimentary strata of Quesnellia. During the late Paleozoic to early Mesozoic, Quesnellia lay outboard of ancestral North America, separated from the continental margin by the Slide Mountain ocean, which developed as a back-arc basin (e.g., Nelson et al., 2013). At the latitude of Polaris, the Slide Mountain terrane is absent or structurally excised (Ferri, 1997; Ferri et al., 2001), and Quesnellia is in thrust contact with Late Devonian to Permian rocks of the continental margin. Late Devonian to Permian slate, argillite, tuff, and sandstone of the Big Creek group form the uppermost part of the pericratonic Cassiar terrane, a displaced fragment of the Neoproterozoic to Paleozoic ancestral North American margin (Ferri, 1997; Nixon et al., 1997; Ferri et al., 2001; Fig. 3).

Polaris is the largest of several ultramafic-mafic bodies of Alaskan-type affinity that intrude Quesnellia (Irvine, 1976; Nixon et al., 1997). Emplacement of the Polaris intrusion was coeval with the accretion of major arc terranes in the northern Cordillera (ca. 185-186 Ma, Early Jurassic; Nixon et al.,

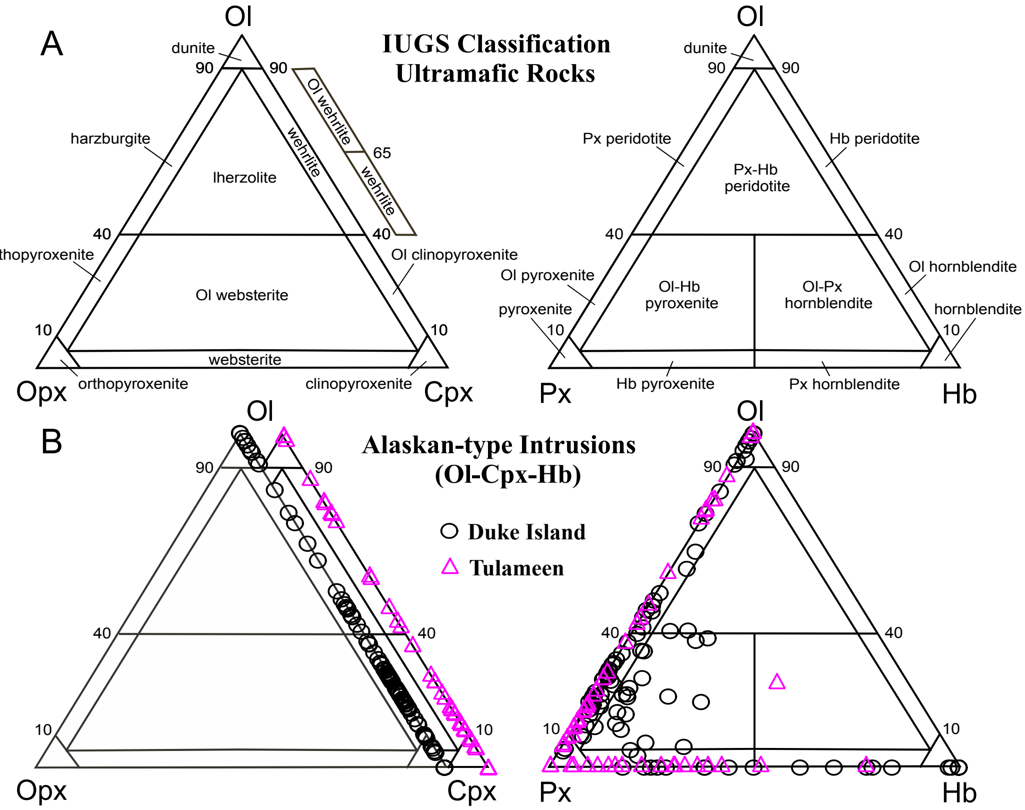

Fig. 2. **a)** IUGS classification of ultramafic rocks (Le Maitre, 1989). **b)** Modal analyses for typical ultramafic rocks in the Duke Island (Irvine, 1959, 1974) and Tulameen (Findlay, 1963) Alaskan-type intrusions showing the characteristic absence of orthopyroxene. Abbreviations: Ol, olivine; Cpx, clinopyroxene; Opx, orthopyroxene; Px, pyroxene (clinopyroxene+orthopyroxene); Hb, hornblende. Adapted from Nixon et al. (2015).

2019a, b), and the thermal aureole was still hot and capable of ductile deformation during thrust emplacement onto the continental margin (Nixon et al., 1997).

4. Geology of the Polaris intrusion

The Polaris intrusion is one of the best exposed Alaskan-type ultramafic-mafic bodies in the Canadian Cordillera, second in size only to the Tulameen intrusion in south-central British Columbia (Nixon et al., 1997; Fig. 1). The Polaris intrusion is a sill-like body (Nixon et al., 1997) that is exposed across an area 14 km long by 3 km across (45 km^2). It is hosted entirely within moderately westward-dipping (40-50°), mafic-intermediate volcanic breccias, flows, and sedimentary strata of the Paleozoic Lay Range assemblage (Roots, 1954). The intrusion consists of asymmetrically distributed ultramafic rocks, which predominate in the eastern part of the intrusion, and hornblende-bearing gabbroic-dioritic and pyroxenitic lithologies in the west (Fig. 3). The principal rock types include: dunite (±chromitite), wehrlite, olivine clinopyroxenite, clinopyroxenite, hornblende-clinopyroxenite, hornblendite, and gabbro-diorite. Accessory minerals such as apatite, titanite, and zircon comprise <2% of the more evolved mafic lithologies. Orthomagmatic sulphides (pyrrhotite, pentlandite, chalcopyrite) are locally encountered in clinopyroxene- and hornblende-rich rocks.

The metamorphic contact aureole in the volcanosedimentary host rocks is upper greenschist to lower amphibolite facies. The aureole locally exhibits an amphibole lineation and foliation. Andalusite has been observed in the southern and eastern contact aureole, constraining the depth of emplacement to less than 12 km (Nixon et al., 1997). Along parts of its eastern margin, the Polaris intrusion is in thrust contact with variably foliated to non-foliated gabbro-diorite, and locally hornfelsed volcanosedimentary rocks of the Big Creek group (Fig. 4). Recent field mapping and integration of aeromagnetic and radiometric survey modelling (CGG Canada Services Ltd., 2018) has enabled refinement of lithological boundaries, especially near the eastern thrust margin (Fig. 3).

4.1. Lithological units

The Polaris intrusion contains all the rock types characteristic of Alaskan-type ultramafic-mafic bodies, including dunite, wehrlite, clinopyroxenite, hornblendite, gabbro-diorite, and felsic pegmatite. In contrast to examples where Alaskan-type intrusions are concentrically zoned (e.g., Tulameen; Nixon, 2018), the distribution of rock types is distinctly asymmetric at Polaris. Lithological contacts are sharp to locally gradational, in cases diffuse (Fig. 5). Variations in grain size and crystal habit occur on cm to m scales.

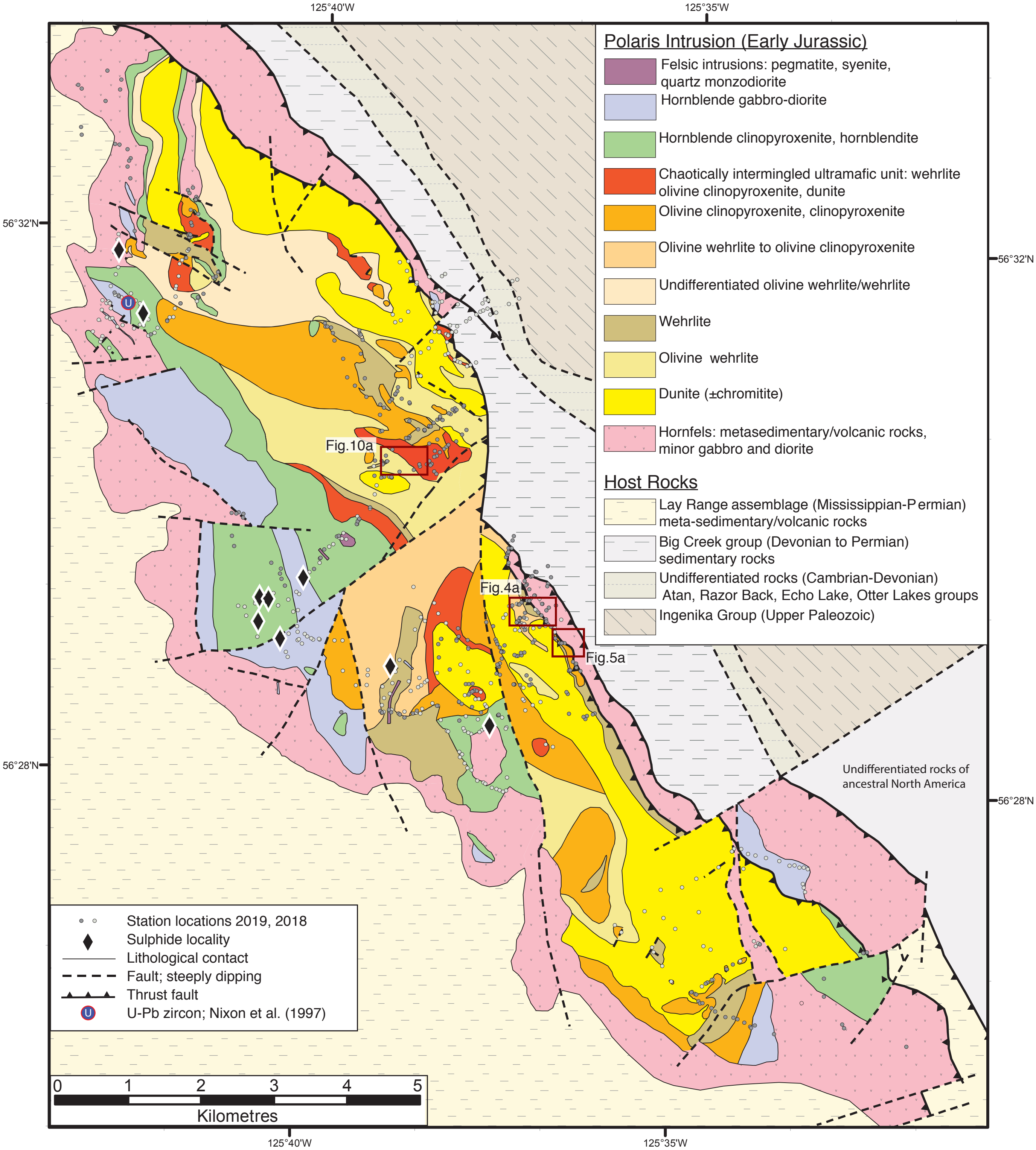

Fig. 3. Generalized geology of the Polaris Alaskan-type ultramafic-mafic intrusion (modified from Nixon et al., 1997) showing regional geology, contact relationships, and intrusive rock types. Locations of photographs in Figures 4a, 5a, 10a are shown.

4.1.1. Dunite

Dunite is generally confined to the eastern part of the intrusion (Fig. 3). Weathered dunite is yellow-brown and displays smooth surfaces with cm-thick weathering rinds; fresh dunite appears dark grey (Fig. 6). Interlocking olivine crystals (<2 mm) exhibit adcumulate textures (i.e., <7 vol.%, of interstitial minerals); dunite with heteradcumulate textures and clinopyroxene oikocrysts occurs locally. All dunite samples contain trace amounts of disseminated, fine-grained, subhedral to euhedral chromite. Dunite is generally weakly serpentinized,

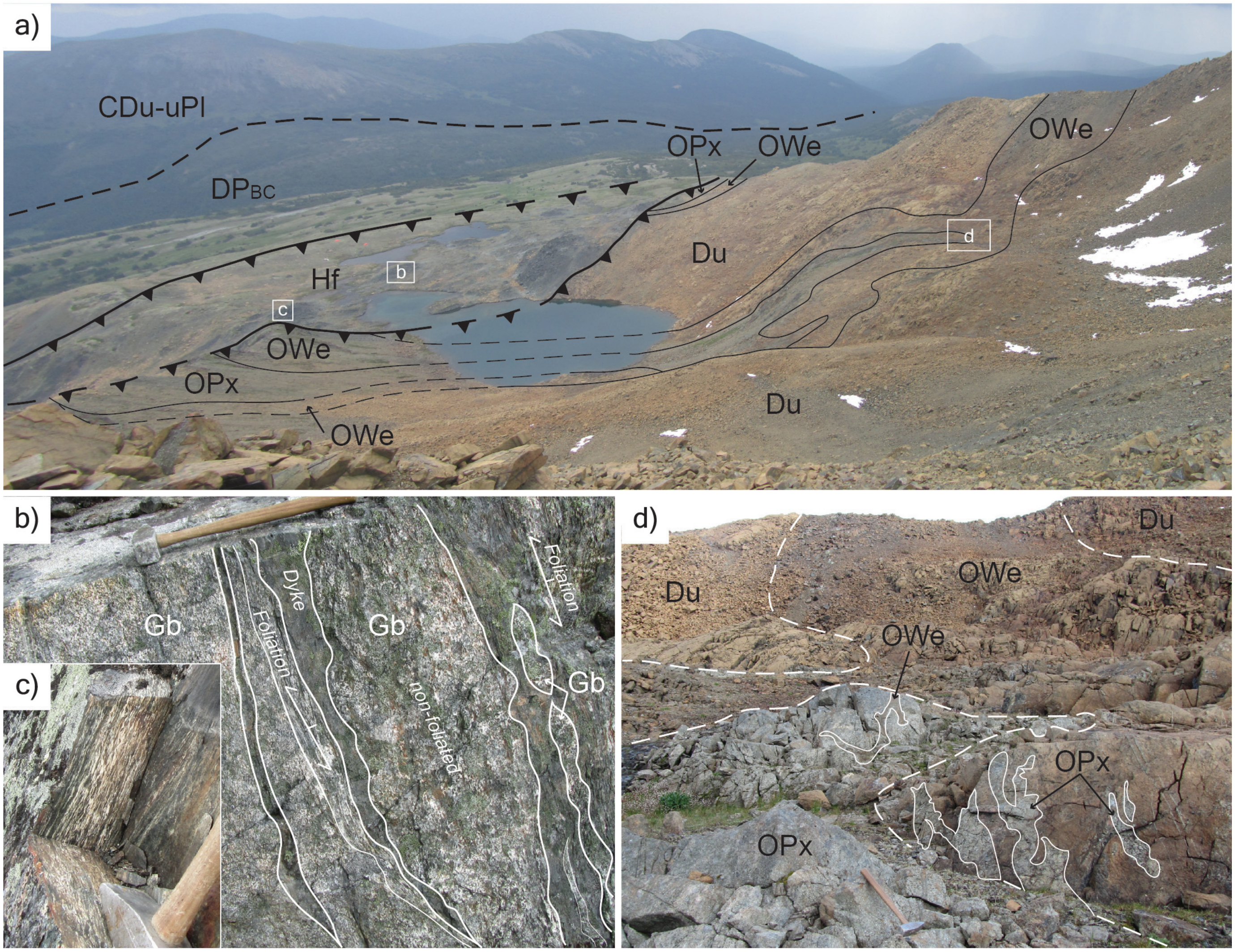

Fig. 4. Contact relationships and internal features at the eastern margin of the Polaris intrusion. **a)** View looking east-southeast showing thrust fault contacts (solid lines with teeth) between ultramafic rocks in the foreground and the metamorphic aureole (Hf), metasedimentary rocks of the Big Creek group (DP_{BC}; Devonian to Permian), and undifferentiated Cambrian-Devonian and upper Paleozoic strata (CDu-uPl) of the ancestral North American continental margin. Polaris ultramafic units include dunite (Du), olivine wehrlite (OWe), and olivine clinopyroxenite (OPx). Locations of photographs in panels b, c, and d are indicated. **b)** Heterogeneously foliated gabbro-diorite (Gb) and mafic dikes forming boudins; Big Creek group. View looking south. **c)** Mylonitic gabbro with fabrics of possible kinematic significance; these fabrics are typically developed at the thrust contact between ultramafic lithologies and host rocks in the eastern contact aureole. View looking north. **d)** Inclusions of olivine wehrlite (OWe) in olivine clinopyroxenite (OPx), and olivine wehrlite in olivine clinopyroxenite, between lobes of dunite (Du). Note the gradational contact between dunite and olivine wehrlite. Contacts: observed, solid line; inferred, dashed line.

except in shear zones where serpentinization is moderate to complete. In several areas, dunite contains a weak foliation, defined by laterally extensive micro-veinlets (<0.5 mm wide) of serpentine group minerals that border local shear zones.

Fine-grained, dunite dikes (up to 30 cm wide), with adcumulate to heteradcumulate textures involving clinopyroxene, intrude the main dunite unit and are only distinguishable where they cut dunite containing mineralogically distinctive features, such as chromitite laminae and/or olivine wehrlite, wehrlite, or olivine clinopyroxenite dikes (e.g., Fig. 7a). Dunite dikes that cross-cut olivine wehrlite/wehrlite and olivine clinopyroxenite commonly exhibit irregular contacts that appear to indicate ductile rheology. Dunite containing rare Mg-Fe mica (phlogopite?) displays pitted surfaces due to recessively weathered mica and occurs near contacts with olivine clinopyroxenite and wehrlite; it is generally concentrated in the eastern parts of the intrusion. Dunite near olivine clinopyroxenite (section 4.1.4.) and chaotically intermingled units (section 4.1.5.) is gradational with olivine wehrlite and wehrlite.

4.1.2. Chromitite

Chromitite occurs in dunite, and less commonly in olivine wehrlite and wehrlite, as m-scale schlieren of massive chromite, and as disrupted blocks of variably deformed chromite interlayered with olivine (Fig. 7). Chromitite occurs as both massive and nearly monomineralic chromite layers, and

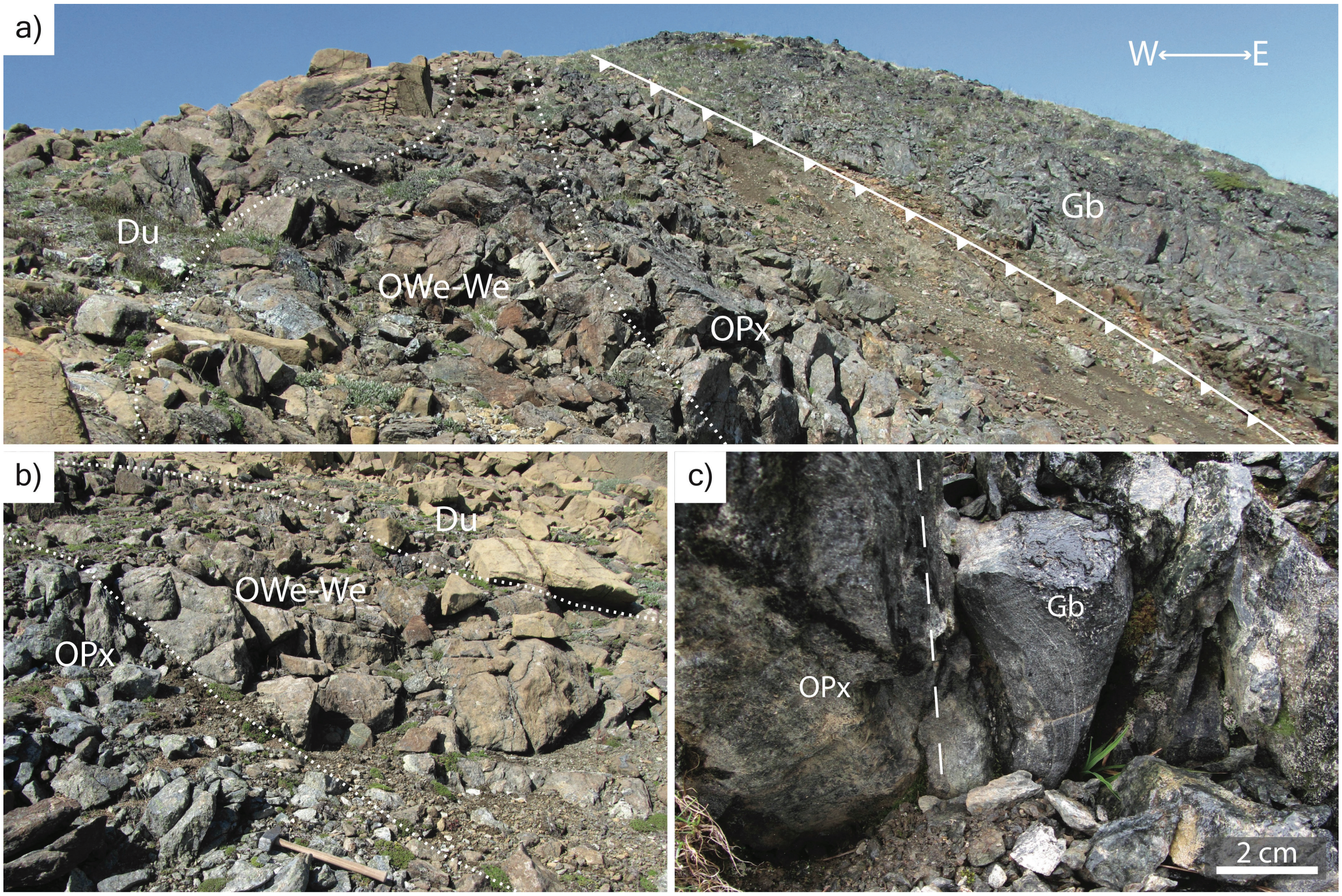

Fig. 5. Contact relationships in the eastern part of the Polaris intrusion. **a)** Footwall gabbro (Gb) in thrust contact with olivine clinopyroxenite (OPx) that grades, from east to west, into olivine wehrlite to wehrlite (OWe-We) and dunite (Du). View looking north. **b)** M-scale gradational contacts of olivine clinopyroxenite, olivine wehrlite to wehrlite, and dunite. **c)** Undeformed coarse-grained (≤5 mm) olivine clinopyroxenite in thrust contact with mylonitic gabbro in the footwall. Contacts: gradational, dotted line; observed/approximate, solid/dashed line.

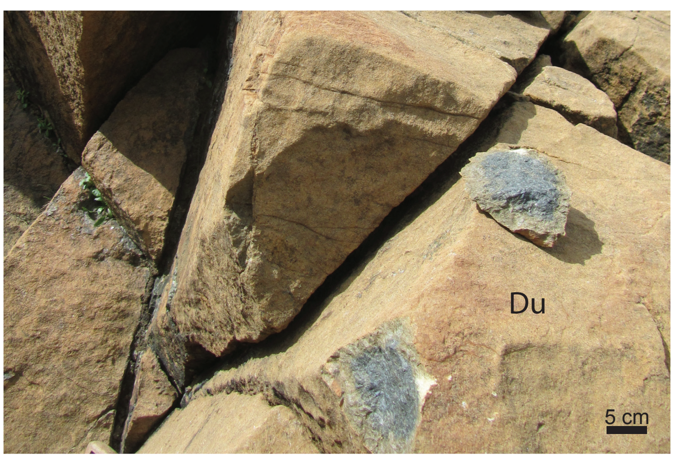

Fig. 6. Typical dunite; fine- to medium-grained (<1-2 mm) adcumulate olivine±minor clinopyroxene. Brown to yellow-brown weathered surface and 1-2 cm thick weathering rind; dark grey fresh surface.

as diffuse layers intergrown with olivine. Typically, chromitite schlieren display features that are consistent with remobilization of previously formed crystal cumulates (Figs. 7a, b, d, e). Chromitite is comparatively rare in wehrlite and is sparsely entrained in wehrlitic dikes.

4.1.3. Olivine wehrlite and wehrlite

Wehrlite forms extensive outcrops in the central and northern parts of the Polaris intrusion. It weathers brown to orange-brown, with rough surfaces from differential weathering of clinopyroxene relative to olivine (Fig. 8b). Wehrlite, like dunite, locally displays pitted surfaces from weathering of phlogopite (Fig. 8c). For mapping purposes, Nixon et al. (1997) distinguished 'olivine wehrlite' (olivine-rich rocks with 10-35% modal clinopyroxene) from wehrlite (35-60% modal clinopyroxene; Fig. 2). Texturally distinct varieties of wehrlite, differentiated by variation in the modal abundance and grain-size (1 mm-10 cm) of clinopyroxene are recognized on scales of 1 to 100s of m. Idiomorphic clinopyroxene (from <1 mm to 10s of cm) occurs in wehrlite (Figs. 8a, b, d). In contrast, olivine wehrlite typically displays a poikilitic texture where clinopyroxene forms irregular (5 mm to 6 cm) oikocrysts enclosing olivine (Fig. 8e). Locally, clustering and grain-size variation of clinopyroxene increases close to contacts with chaotic intermingled units (intermingled olivine clinopyroxenite, wehrlite, and dunite; see section 4.1.5.). Throughout the intrusion, wehrlite occurs as an intermediate lithology with gradational boundaries to olivine clinopyroxenite,

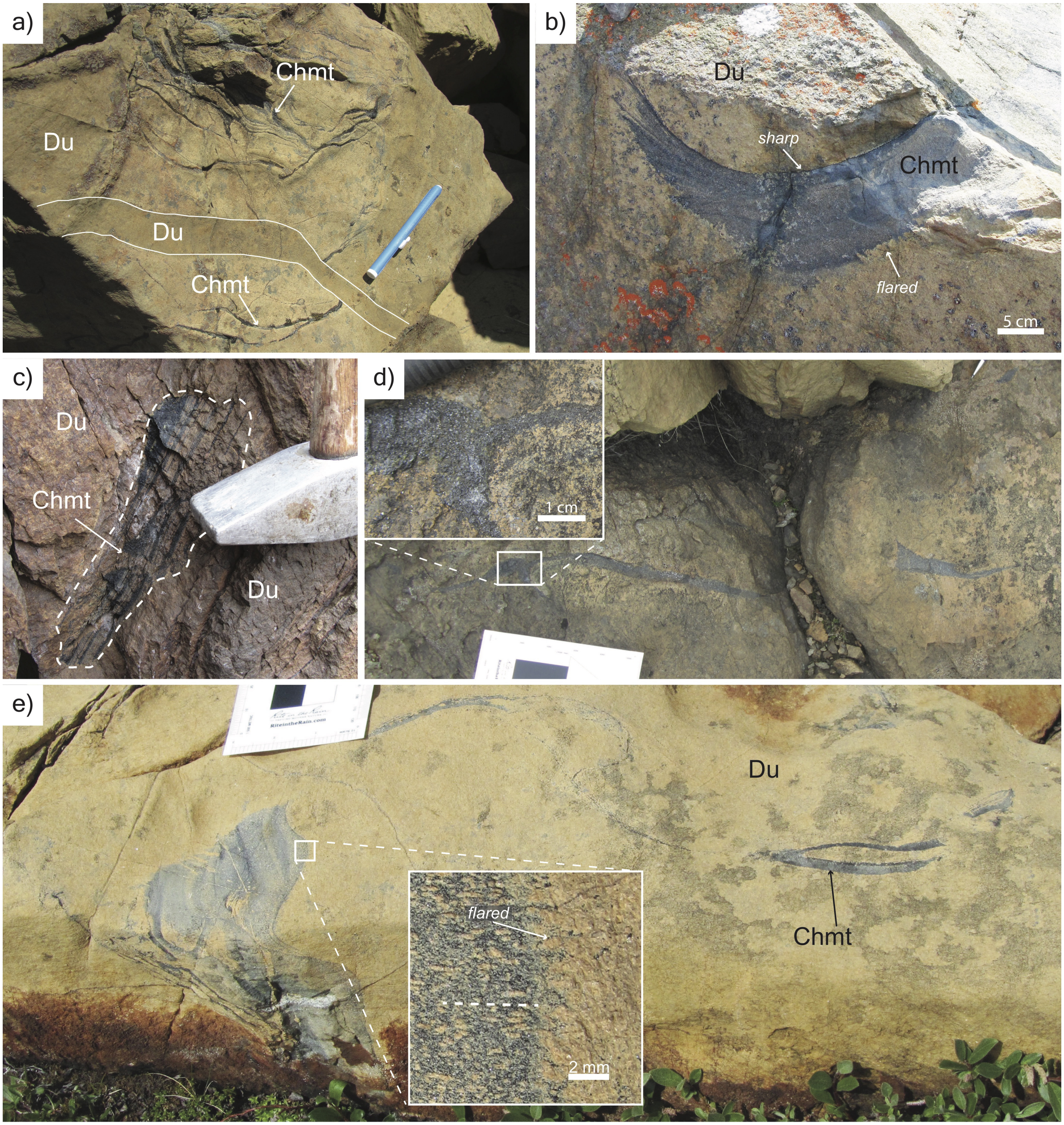

Fig. 7. Chromitite morphologies in the Polaris intrusion. **a)** Block-like mass containing thin (<1 cm thick) chromitite (Chmt) schlieren in dunite (Du). Chromite layers are sub-parallel, slightly crenulated, and locally bifurcate. Dunite dike (solid line) cuts bifurcated chromitite layer. **b)** Bent chromitite schlieren, approximately 15 x 30 x 80 cm in dunite. The upper chromitite-dunite contact is sharp, the lower contact is diffuse and displays cuspate-lobate irregularities. **c)** Chromitite block containing planar chromite layers (2-30 mm thick) in dunite. **d)** Cm-wide discontinuous slightly distorted chromitite layer. Inset shows diffuse boundaries with dunite. **e)** Layered, olivine-rich chromitite schlieren in dunite. Crystal-scale foliation in the chromitite is defined by <0.5 x 1 mm elongated olivine clusters (dashed line on inset).

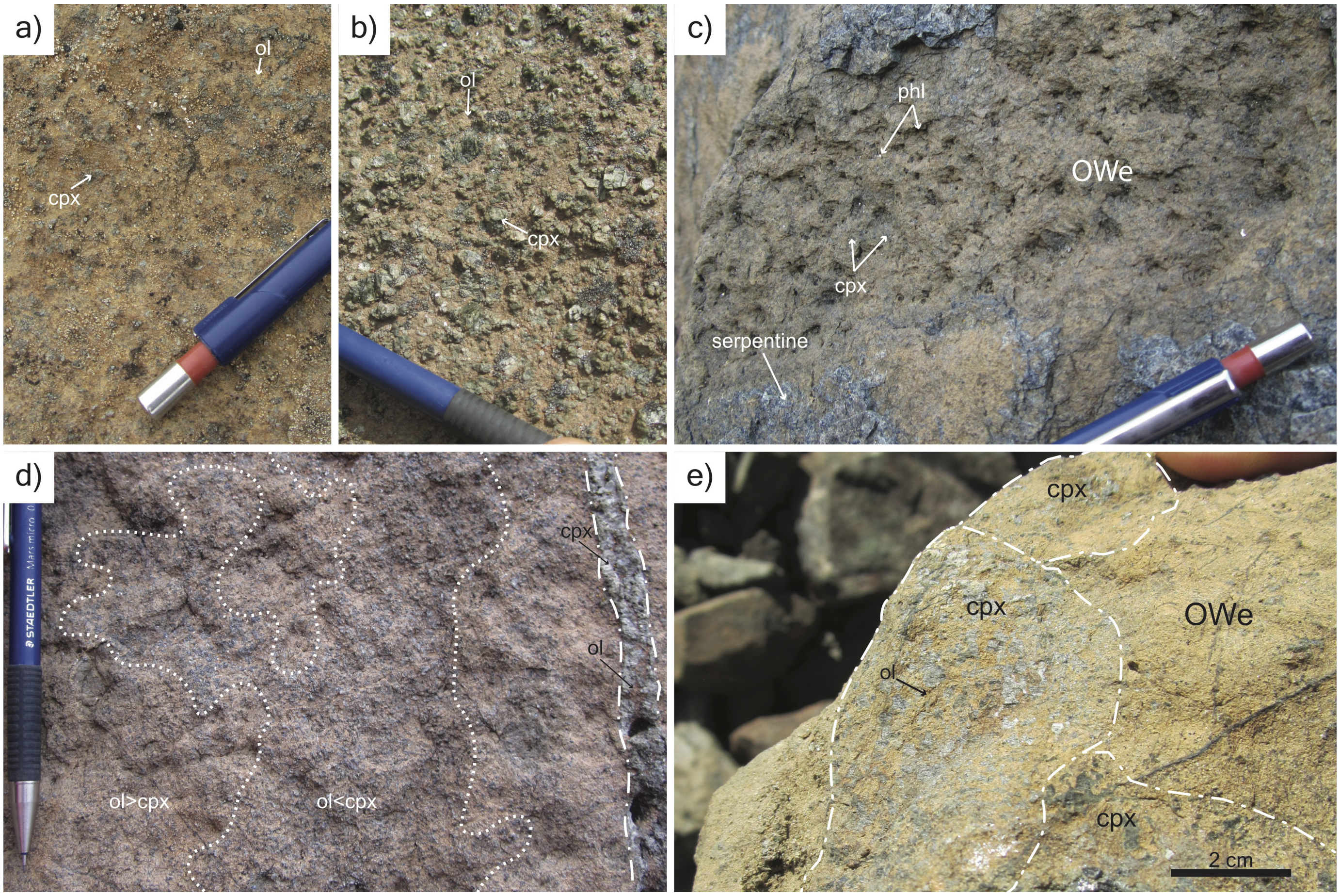

Fig. 8. Textural variations of wehrlite in the Polaris intrusion. **a)** Wehrlite with fine- to medium-grained (<1-2 mm), equant idiomorphic clinopyroxene (cpx) intergrown with olivine crystals. Clinopyroxene forms crystal clusters interstitial to olivine. **b)** Very coarse-grained (~1 cm) clinopyroxene-rich wehrlite in a fine-grained (<1 mm) groundmass of olivine (ol). **c)** Phlogopite(phl)-bearing olivine wehrlite (OWe) displaying characteristic pitting due to recessively weathered phlogopite. A thin serpentinized surface (dark grey-blue) is locally present along joints. **d)** Fine-grained wehrlite with cm-scale modal variations of clinopyroxene and olivine. Dotted line delineates diffusely bounded zones with variable modal clinopyroxene. Along the right side of the image is a centimetre-wide olivine clinopyroxenite veinlet with diffuse boundaries (dash-dot lines). **e)** Poikilitic clinopyroxene (cpx) in olivine wehrlite (OWe). The large oikocryst in the center of the image is ~6 cm x 4 cm and encloses <4 mm diameter patches of fine-grained olivine (ol) crystals.

chaotic intermingled units, and dunite. Coarse to pegmatitic olivine clinopyroxenite/wehrlite dikes, with diffuse contacts, are also observed in wehrlite near chaotic intermingled units.

4.1.4. Olivine clinopyroxenite and clinopyroxenite

Olivine clinopyroxenite and clinopyroxenite are generally distributed along the central axis of the intrusion and at the southern and eastern margins. Olivine clinopyroxenite/clinopyroxenite weathers light to pale green to greenish-grey and has an increasingly mottled rusty-brown appearance with increasing olivine content (Figs. 9a, b). Fresh surfaces are dark greenish-grey. Olivine clinopyroxenite comprises <40% olivine and >60% clinopyroxene, whereas clinopyroxenite has <10% olivine and >90% clinopyroxene (Fig. 2). Mappable units of olivine clinopyroxenite show considerable heterogeneity at the outcrop scale with a tendency for olivine clinopyroxenite to be intermingled with, and contain significant quantities of, dm-scale wehrlite/dunite enclaves with both sharp and gradational boundaries (e.g., Figs. 9a, c). Minor amounts of hornblende and magnetite occur interstitially, and magmatic sulphides (mainly pyrrhotite and chalcopyrite) are locally present. Clinopyroxene crystals are typically 2-10 mm in diameter, fresh, and idiomorphic, with modal abundances varying on scales of 10s of cm.

Pegmatitic dikes of olivine clinopyroxenite and clinopyroxenite have sharp (Fig. 9b) to gradational, in cases diffuse, boundaries (Figs. 10b; 11c, d) throughout the intrusion and they cut all ultramafic rock types. Where close to or in large outcrops of olivine clinopyroxenite or chaotic intermingled units, clinopyroxenite dikes commonly have pegmatitic to diffuse margins, and may incorporate pods of host dunite and/or wehrlite. Late, coarse-grained to pegmatitic olivine clinopyroxenite and clinopyroxenite (±phlogopite) dikes (<2 m wide) have sharp contacts and locally exhibit prismatic clinopyroxene crystals oriented perpendicular to dike contacts.

Bright olive-green, granular and equant (1 mm), anhedral

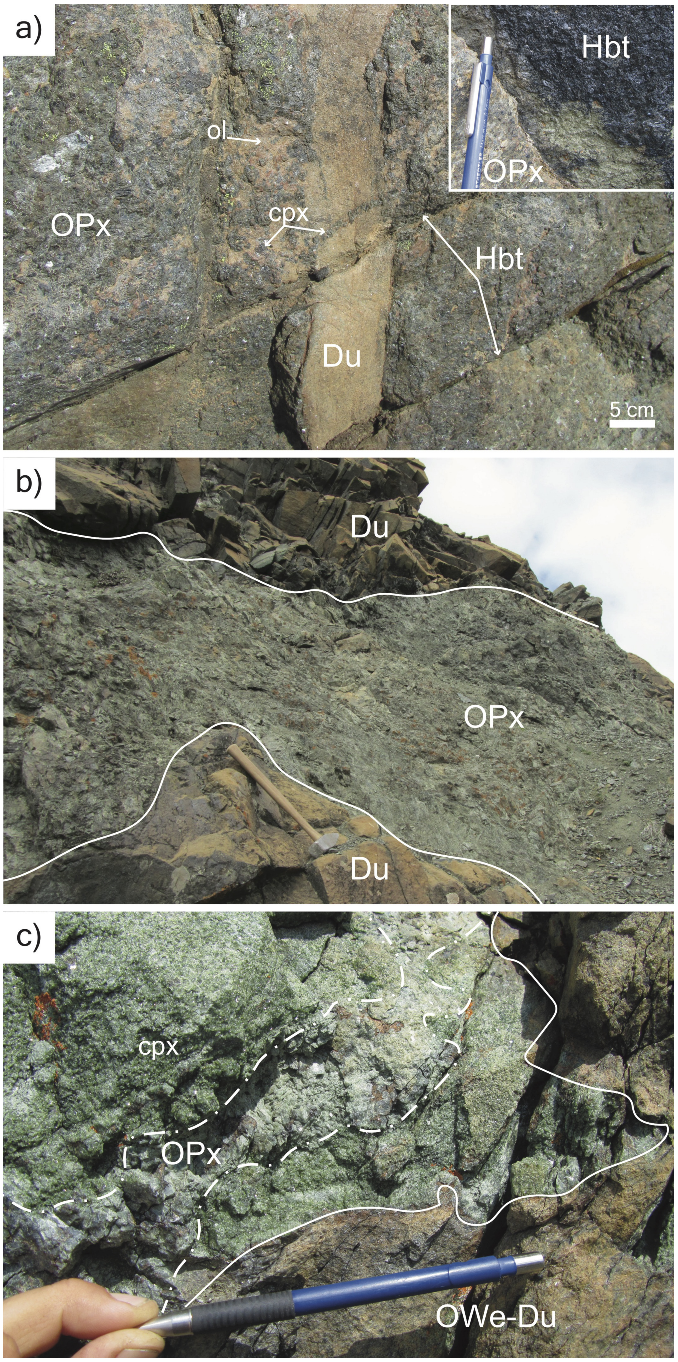

Fig. 9. Textural variations of olivine clinopyroxenite (OPx) in the Polaris intrusion. **a)** Olivine clinopyroxenite cut by fine-grained dunite dike, in turn cut by thin (<10 cm wide) magnetite-bearing hornblendite (Hbt) dikelets. Inset shows joint surface of fine- to medium-grained (<2 mm) magnetite-bearing hornblendite. **b)** M-scale pegmatitic olivine clinopyroxenite dike in sharp contact with dunite. Clinopyroxene crystals are <10 cm in diameter and enclose pods of fine- to medium-grained (<2 mm) olivine crystals. **c)** Granular, equant, anhedral crystals (<1 mm) of bright green clinopyroxene (cpx) intergrown with coarse-grained (2-5 mm) olivine clinopyroxenite (OPx) in dunite-olivine wehrlite (OWe-Du). Contacts: sharp, solid line; diffuse, dot-dash line.

to idiomorphic adcumulate clinopyroxenite (Fig. 9c) crops out in the northern and northeastern parts of the intrusion. This distinct clinopyroxenite occurs in contact with olivine clinopyroxenite and as xenoliths forming deformed pods in dunite and wehrlite. The clinopyroxenite is also intermingled and/or entrained as boudins (up to 8 m long) in a ductile shear zone enclosing olivine clinopyroxenite and phlogopite-bearing wehrlite/dunite.

4.1.5. Chaotically intermingled ultramafic unit

The chaotically intermingled unit is defined by intermingled olivine clinopyroxenite, wehrlite, and dunite on the dm to m scale. This unit is most common near the margins of clinopyroxenite and wehrlite, and less commonly dunite (Fig. 10a). The best examples of chaotically intermingled units are in the central part of the intrusion (Fig. 3), where they include irregular masses and dikes of coarse to pegmatitic (olivine) clinopyroxenite in dunite and wehrlite (Figs. 10b; 11c). Clinopyroxenite is locally cut by dunite or olivine wehrlite/wehrlite dikes (Fig. 10e). Lithological contacts in the intermingled units vary from sharp to gradational and may be diffuse (Figs. 10b-e; 11a-d). Clinopyroxenite and wehrlite incorporate interstitial (1-10 cm) irregular and embayed pods of dunite-wehrlite (Figs. 10b, c, e; 11c, d). Conversely, enclaves of olivine clinopyroxenite occur within, or are cut by, fine- to medium-grained, highly irregular adcumulate dunite dikes (Figs. 10d, e; 11a, b, d). Magmatic breccias (Figs. 12a-c) comprise subangular to subrounded dm-scale tabular blocks of dunite and wehrlite with diffuse to sharp boundaries set in a coarse-grained matrix of olivine clinopyroxenite to wehrlite (±phlogopite±hornblende).

4.1.6. Hornblendite and hornblende clinopyroxenite

Hornblende-bearing clinopyroxenite is predominantly in the northwestern and western parts of the intrusion and less commonly in the central and southern parts (Fig. 3). Hornblende clinopyroxenite and hornblendite weather dark greenish-black; the presence of saussuritized interstitial feldspar is indicated by irregular white to cream-coloured blebs. Hornblendite and hornblende clinopyroxenite are commonly gradational on a hand sample scale; consequently, the two rock types are not distinguishable at the map scale. Locally, hornblende clinopyroxenite has a well-developed mineral lineation defined by the orientation of elongate hornblende crystals. Magmatic layering within m-scale masses of hornblendite occurs in the northwestern parts of the intrusion and is defined by crystal size gradation and alignment, and by an interstitial feldspathic fabric. Clinopyroxene (<1 cm) is typically euhedral; hornblende forms euhedral prisms up to 10 cm long (Figs. 13a-e). Accessory minerals include sulphides, magnetite, apatite, titanite, phlogopite, and zircon. Significant concentrations of magnetite occur in magnetite-hornblendite layers and dikes (Fig. 13d).

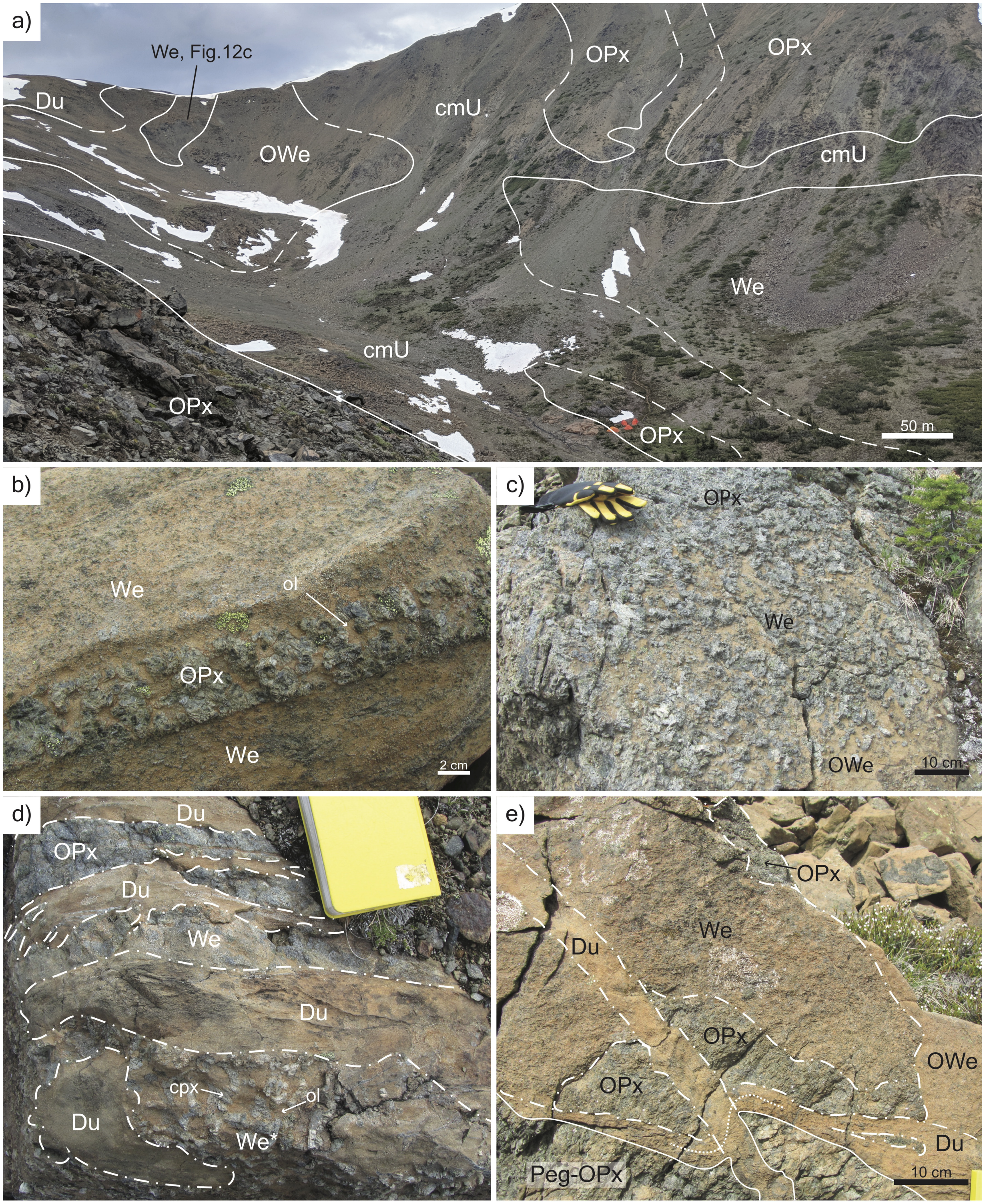

Fig. 10. Textural and lithological relationships in the chaotic intermingled units of the Polaris intrusion. **a)** View looking west (see Fig. 3 for location) illustrating the typical irregular contacts between a chaotic intermingled unit (cmU) and olivine clinopyroxenite (OPx), olivine wehrlite (OWe), wehrlite (We), and dunite (Du). Location of photograph in Fig. 12c is shown. Note orange tents for scale along floor of valley. Contacts: observed, solid line; approximate, dashed line. **b)** Olivine clinopyroxenite (OPx) dike with pegmatitic (1-2 cm) clinopyroxene and fine-grained olivine-rich pods (ol) cutting wehrlite; note diffuse contacts. Wehrlite has 2-5 mm clusters of clinopyroxene crystals (<2 mm) that define modal variation at the centimetre scale. **c)** Subtle modal gradation of pegmatitic (1-4 cm) clinopyroxene and medium-grained (~2 mm) olivine in olivine clinopyroxenite (OPx), wehrlite (We), and olivine wehrlite (OWe). **d)** Interlayered fine-grained dunite, olivine clinopyroxenite, wehrlite, and a distinctive rock with a 'honeycomb' texture of fine-grained olivine pods with coarse (~2 cm) interstitial clinopyroxene (We*). **e)** Complex relationships among dunite (Du), olivine wehrlite (OWe), wehrlite (We), and locally pegmatitic (Peg-OPx) olivine clinopyroxenite (OPx). Offset dunite dike delineated by fine-dashed line. Diffuse contacts, dot-dash line; sharp contacts, solid line.

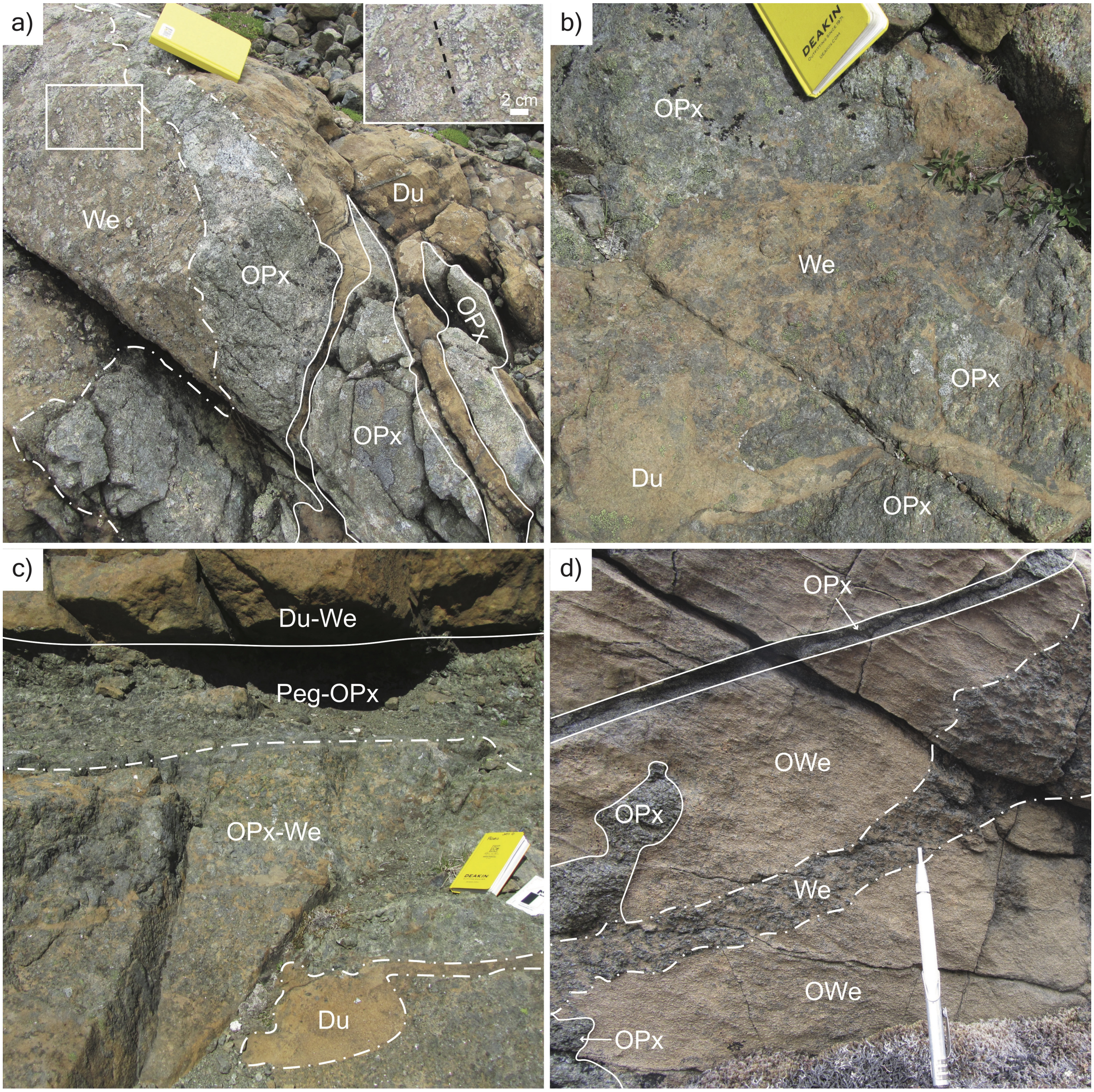

Fig. 11. Representative textures and lithological relationships in chaotic intermingled units (cmU) of the Polaris intrusion. **a)** Coarse-grained olivine clinopyroxenite (OPx) blocks in wehrlite (We), cut by fine-grained dunite dikes (Du). Inset illustrates alignment (dashed line) of subhedral to euhedral clinopyroxene crystals (3-4 cm) in wehrlite. **b)** Heterogeneous zone consisting of dunite (Du) showing gradational boundaries with wehrlite (We) and diffuse to sharp boundary with blocks of olivine clinopyroxenite (OPx). **c)** Pegmatitic (3-10 cm) phlogopite-bearing olivine clinopyroxenite dike (Peg-OPx), with clinopyroxene crystals enclosing centimetre-scale olivine-rich pods. Note the sharp contact between the pegmatite dike and the dunite to wehrlite (Du-We), and the diffuse contact between the dike and coarse-grained olivine clinopyroxenite-wehrlite (OPx-We). The olivine clinopyroxenite-wehrlite contains pods of fine-grained (<1 mm) dunite. **d)** Olivine wehrlite (OWe) with coarse-grained olivine clinopyroxenite (OPx) cut by coarse-grained (<5 mm) clinopyroxene wehrlite (We) with diffuse contacts. Clinopyroxene clusters in wehrlite are ~15 mm and olivine-rich pods have similar textures (equigranular) and grain size as host. Contacts: sharp, solid line; diffuse, dot-dash line.

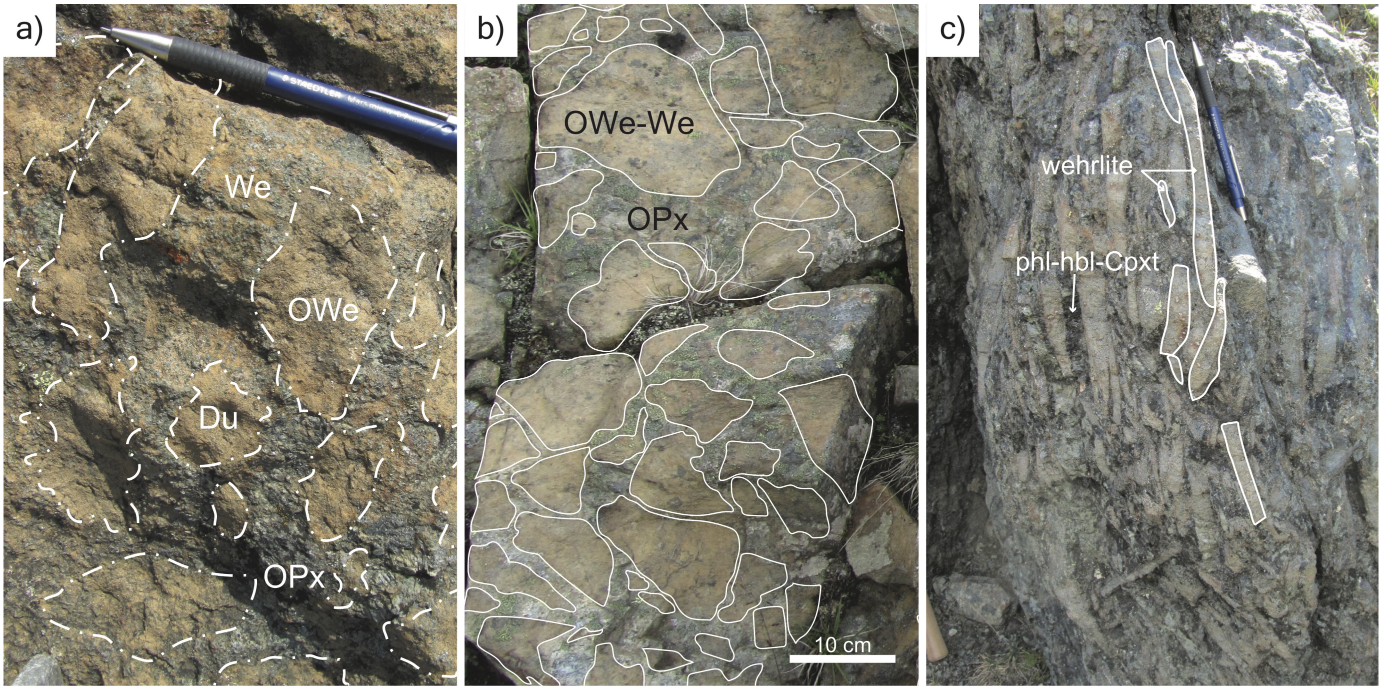

Fig. 12. Magmatic breccias in the Polaris intrusion. **a)** Subrounded fragments (<30 cm) of fine- to medium-grained (<1-3 mm) dunite (Du) and olivine wehrlite (OWe) with diffuse boundaries (dot-dash line) set in medium-grained (<3 mm) wehrlite (We) to olivine-clinopyroxenite (OPx) groundmass. **b)** Angular to rounded blocks of olivine wehrlite- wehrlite (OWe-We) with sharp to weakly gradational boundaries (solid line) set in a groundmass of medium-grained olivine clinopyroxenite (OPx). **c)** Angular to subangular tabular xenoliths of wehrlite in a coarse-grained phlogopite-hornblende-bearing clinopyroxenite groundmass (phl-hbl-Cpxt). See Fig. 10 for location.

4.1.7. Hornblende gabbro-diorite

Hornblende-bearing gabbro-diorite occurs predominately along the margins of the Polaris intrusion with the largest bodies in its western part. Hornblende gabbro-diorite sills also intrude metasedimentary rocks of the Lay Range assemblage in the metamorphic aureole of the intrusion (Nixon et al., 1997). Hornblende gabbro-diorite weathers dark grey and is typically lichen covered. Fresh surfaces are light grey to greenish-grey. Hornblende diorite is heterogeneous with variable grain size (<1-5 mm) and proportions of plagioclase and hornblende±clinopyroxene. Local foliated zones display shear fabrics (Fig. 13f) and hornblende mineral alignment (Fig. 14a). Hornblende-gabbro-diorite pegmatites typically contain 2-5 cm long hornblende crystals; some crystals are more than 15 cm long.

4.1.8. Felsic intrusions

Dm- to m-wide, fine- to medium-grained feldspathic dikes and plugs ranging from syenite to leuco-monzonite, crosscut hornblende clinopyroxenite, olivine clinopyroxenite, wehrlite, and dunite (Figs. 14a, b). Weathered surfaces of these intrusions are light blue-grey (Figs. 14b, c), whereas fresh surfaces are light greyish-white. Finely crystalline biotite is the principal mafic mineral and is only locally present. Feldspathic dikes are predominantly in the central part and, to a lesser extent, in the eastern parts of the intrusion (Fig. 3). Swarms of dikes trend northwest-southeast, roughly parallel to the regional tectonic grain. Less commonly, feldspathic dikes trend north-south. The contact zones of felsic intrusions locally enclose subangular to angular xenoliths of hornblendite, hornblende clinopyroxenite, and clinopyroxenite (Fig. 14c).

4.1.9. Magmatic Ni-Cu-PGE sulphides

Alaskan-type intrusions are generally known for their chromitite-Pt-Fe alloy mineralization hosted by dunite and derivative platiniferous placer deposits (e.g., Tulameen, Nixon et al., 1990). However, occurrences of magmatic Ni-Cu-PGE-sulphide mineralization in these intrusions are becoming increasingly documented (e.g., Turnagain, Scheel et al., 2005; Scheel, 2007; Jackson-Brown et al., 2015; Nixon et al., 2019a; Duke Island, Thakurta et al., 2014; Tulameen, Nixon et al., 2018; Nixon et al., 2019b). Polaris contains sparse Ni-Cu-PGE sulphide mineralization, mainly restricted to the northwestern and central parts of the intrusion. Sulphides are commonly hosted by reddish-brown weathering, malachite-stained, olivine-bearing clinopyroxenite, hornblende clinopyroxenite, and gabbro-diorite; a few sulphide occurrences are found in wehrlitic rocks (Fig. 3). The sulphides typically form fine disseminations in low modal abundances (<5 vol.%). Preliminary examination of mineralized rocks in thin section indicates that the most common sulphides are pyrrhotite, pentlandite, and chalcopyrite, locally accompanied by magnetite, with minor pyrite and bornite (Figs. 15a, b). The sulphides commonly form interstitial accumulations in the silicate framework and ovoid inclusions of crystallized sulphide melt in clinopyroxene or hornblende primocrysts (Figs. 15c, d). Whole rock analyses

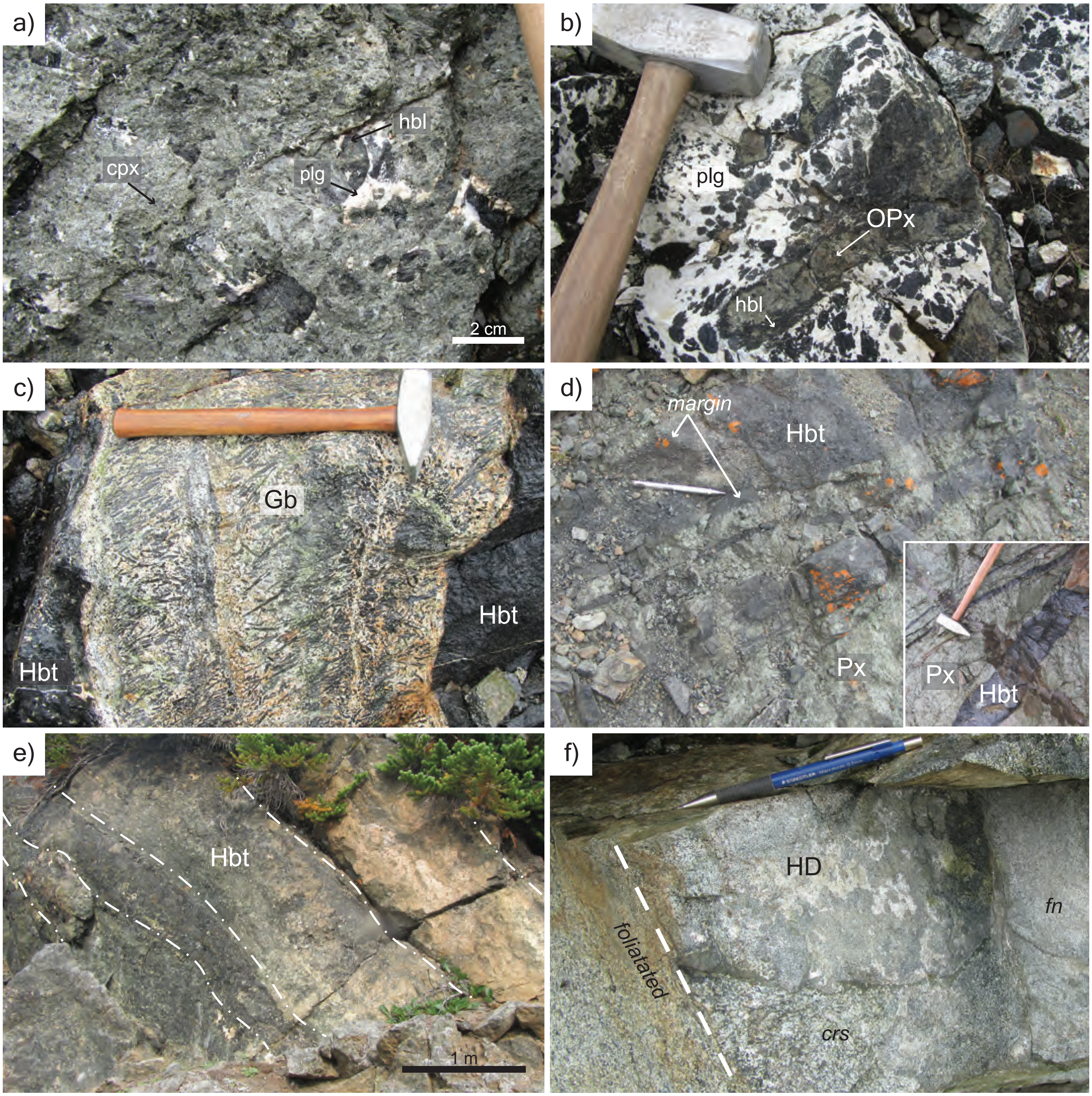

Fig. 13. Hornblende-bearing rocks in the Polaris intrusion. **a)** Feldspathic hornblende clinopyroxenite. Hornblende (hbl) forms euhedral-subhedral prismatic crystals (<2-4 cm long) intergrown with clinopyroxene and in plagioclase-rich segregations. **b)** Pegmatitic hornblende-bearing leucogabbro with highly saussuritized feldspar (plg) and enclaves of olivine clinopyroxenite (OPx) with hornblende-rich (hbl) rims. **c)** Hornblende gabbro dike (Gb) with internal dike-parallel layering. Prismatic hornblende crystals (up to 10 cm long) with long axes at high angles to the sharp external contact with massive pegmatitic hornblendite (Hbt) containing interstitial feldspar. **d)** Fine-grained magnetite-bearing hornblendite (Hbt) dikes with fine-grained margins intruding olivine-bearing clinopyroxenite (Px). Inset shows hornblendite dike and veins in sharp contact with olivine-bearing clinopyroxenite (Px). **e)** Magmatic layering in coarse-grained to pegmatitic (up to15 cm) hornblendite to gabbro (Hbt). **f)** Heterogeneous fine (fn)- to coarse (crs)-grained hornblende diorite (HD); locally foliated and with fabrics of possible kinematic significance.

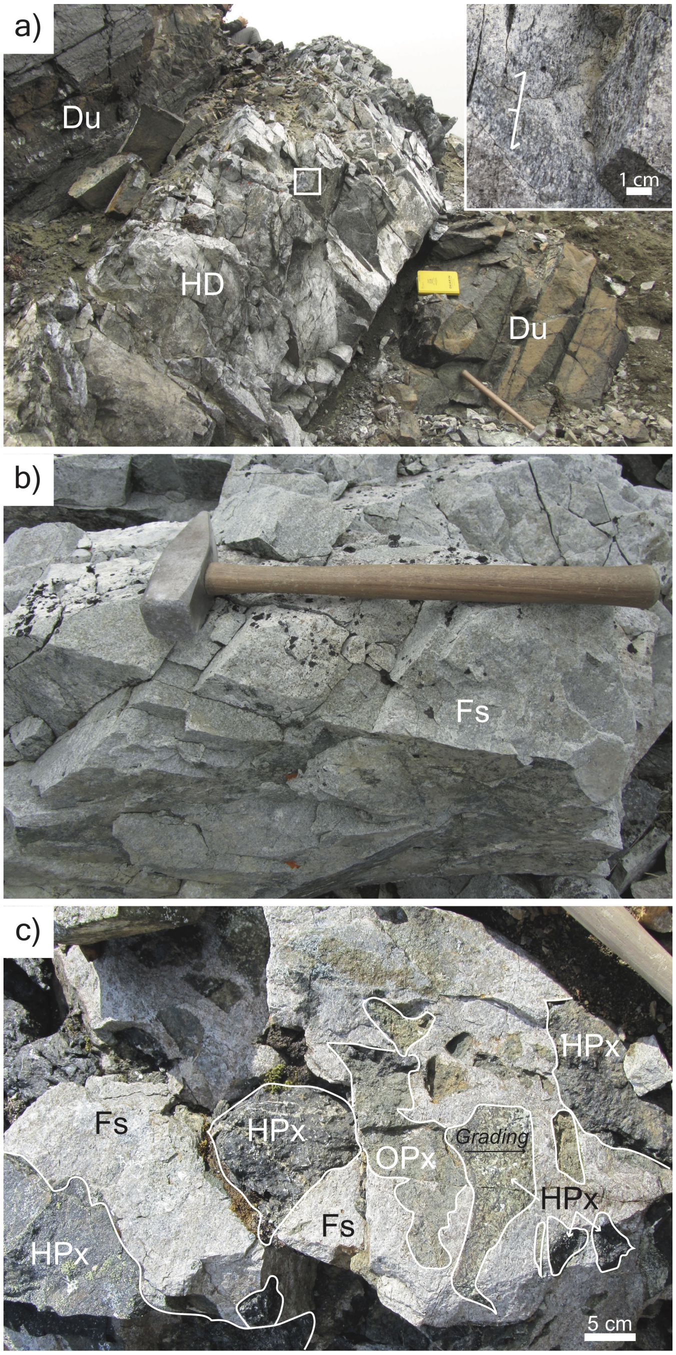

Fig. 14. Intrusive features of felsic to intermediate rocks in the central part of the Polaris intrusion. **a)** Fine- to medium-grained (<3 mm) hornblende-bearing diorite (HD) intruding dunite (Du). Inset shows dike with aligned elongate hornblende crystals. **b)** Medium-grained (<3 mm) hornblende-bearing syenite dike (Fs). **c)** Xenoliths of hornblende clinopyroxenite (HPx) and olivine clinopyroxenite (OPx) in syenite (Fs).

of mineralized hand samples have values up to 0.77 wt.% Cu, 1.3 g/t Pt and 1.8 g/t Pd (Mowat, 2015).

5. Contact aureole and country rocks

The metamorphic aureole of the Polaris intrusion is superimposed on metasedimentary and metavolcanic rocks of the Lay Range assemblage in the west and similar rocks of the Big Creek group in the east preserved beneath eastward-vergent thrust faults (Fig. 3). Hornfelsed rocks in the aureole typically have granoblastic textures, are variably foliated, and locally preserve compositional layering (Fig. 16a). The size of recrystallized grains (0.5 mm to 2 mm) generally increases within a few m of ultramafic-mafic rocks along the western intrusive contact and is accompanied by localized growth of granular (?)cordierite (<2 mm). Porphyroblastic, acicular to tabular amphibole (<5 mm) in the contact aureole has a weak to strong mineral alignment. Mapping beyond the northern termination of the Polaris intrusion identified strongly aligned amphibolite schist with a mineral lineation plunging 40-50° towards the west-southwest and cm-scale relict bedding oriented along the regional structural trend.

In the eastern metamorphic aureole, variably deformed, mylonitic gabbro-diorite intrudes Big Creek group strata in a structural sliver along the central-eastern thrust contact with ultramafic rocks (Figs. 4b, c). A mylonitic zone, typically less than 1 m wide, separates undeformed Polaris ultramafic rocks from the variably foliated gabbroic rocks. The gabbro-bearing thrust slice structurally overlies fissile black-grey phyllitic slates of the Big Creek group to the east (Fig. 3). Gabbroic textures range from fine- to coarse-grained and are cut locally by foliated and sheared basaltic dikes (Fig. 4b). The gabbros are in contact with west-dipping, foliated metasedimentary-metavolcanic strata containing small (≤1 mm) garnet porphyroblasts. Locally, these metasedimentary rocks display mesoscopic east-vergent folds (Fig. 16b).

The gabbroic intrusions in the eastern contact aureole were previously considered coeval with Polaris (Nixon et al., 1997). However, U-Pb age determinations in progress indicate that at least some of these gabbroic bodies may be significantly older (ca. 250 Ma) and genetically unrelated to the Polaris intrusive suite.

6. Discussion

6.1. Intrusion geometry

The Polaris intrusion is an elongate northwest- to southeast-trending intrusive body that locally exhibits weak magmatic layering and foliation in ultramafic, mafic, and hornblende-bearing units. This layering and foliation generally dips 30-50° to the west, broadly concordant with the host rocks. These observations are consistent with the interpretation that the Polaris intrusion is a sill-like body that intruded the Lay Range assemblage (Nixon et al., 1997). The internal distribution of rock types is asymmetric. Dunite, wehrlite, and clinopyroxenite predominate in the eastern and central parts of the intrusion, whereas mafic to feldspathic rocks, hornblende clinopyroxenites, gabbro-diorite, and syenite, occur mostly in the west.

6.2. Internal 'stratigraphy'

Along the eastern thrust margin of the Polaris intrusion, a narrow belt of ultramafic cumulates is locally preserved that

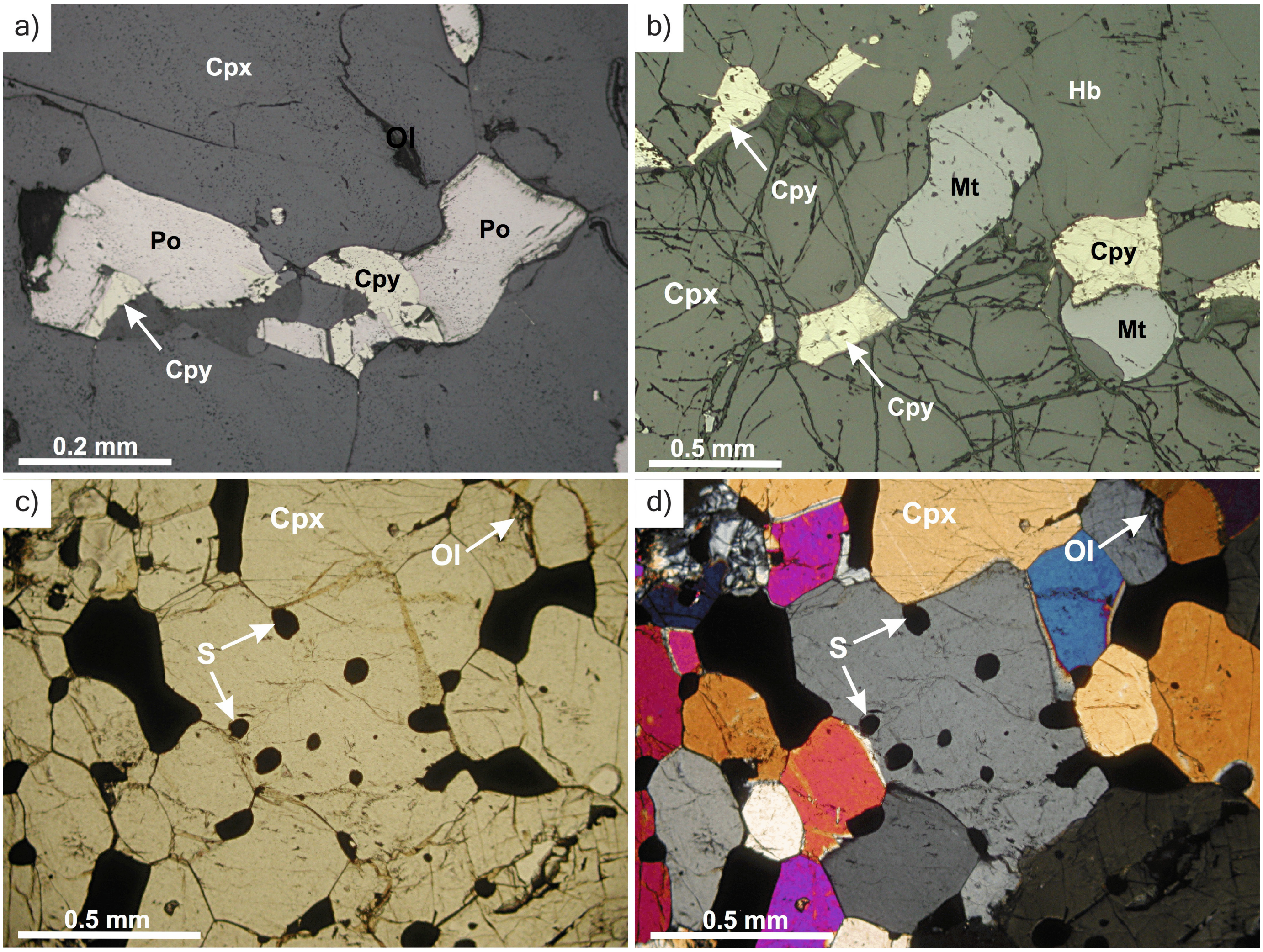

Fig. 15. Photomicrographs of sulphides in the Polaris intrusion. **a)** Finely disseminated chalcopyrite (Cpy) and pyrrhotite (Po) in olivine-bearing clinopyroxenite showing concentrations of sulphides at clinopyroxene (Cpx) grain boundaries. Sample 01GNX1-1-1A, reflected plane-polarized light. **b)** Disseminated chalcopyrite (Cpy) and magnetite (Mt) in hornblende (Hb)-bearing olivine clinopyroxenite. Sample 01GNX1-2-1A, reflected plane-polarized light. **c)** Disseminated magmatic sulphides in olivine (Ol)-bearing clinopyroxenite showing sulphide (S) melt inclusions in clinopyroxene (Cpx) and trapped melt at grain boundaries. Sample 01GNX1-1-1A, plane-polarized light. **d)** Same view as c), cross-polarized light.

passes gradationally (west to east) from dunite through olivine wehrlite and wehrlite to olivine clinopyroxenite at the eastern thrusted margin of the intrusion (Fig. 3). This zonation may have developed at the intrusive contact, which has been removed by faulting. However, the internal distribution of lithologies in the Polaris intrusion overall shows the reverse sense of zonation, from olivine-rich cumulates in the east to hornblende-bearing pyroxenite and gabbro-diorite in the west. This distribution of ultramafic-mafic rock types may represent internal stratigraphy that has been disrupted locally in zones of chaotic intermingling of cumulates.

The disruption of chromitite layers and schlieren in dunite and olivine wehrlite, the irregular and chaotic mixing of ultramafic rock types, localized mineral lineation of intrusive and country rocks, and evidence of repeated dike and sill emplacement indicate a combination of multiple intrusive events, remobilization of partially to fully crystallized cumulates of different competence, and reactive melt infiltration. Remobilization of the cumulate pile is evident from the disrupted and deformed chromitite. Magmatic disruption may have been produced through a variety of processes, including a combination of magmatic recharge, slumping, mechanical mixing of crystal-rich magma slurries, and possible syn-crystallization far-field tectonic stresses.

The chaotically intermingled units are interpreted to represent zones of episodic mingling between variably crystallized and/or consolidated cumulates of differing rheology (e.g., Fig. 10e). Relationships indicating ductile behavior, such as shearing and disaggregation of dunite and wehrlite by intrusion of olivine clinopyroxenite in chaotically intermingled unit rocks, conflict with observations for dunite intrusion into clinopyroxene-rich rocks. These relationships suggest multiple events of mixing

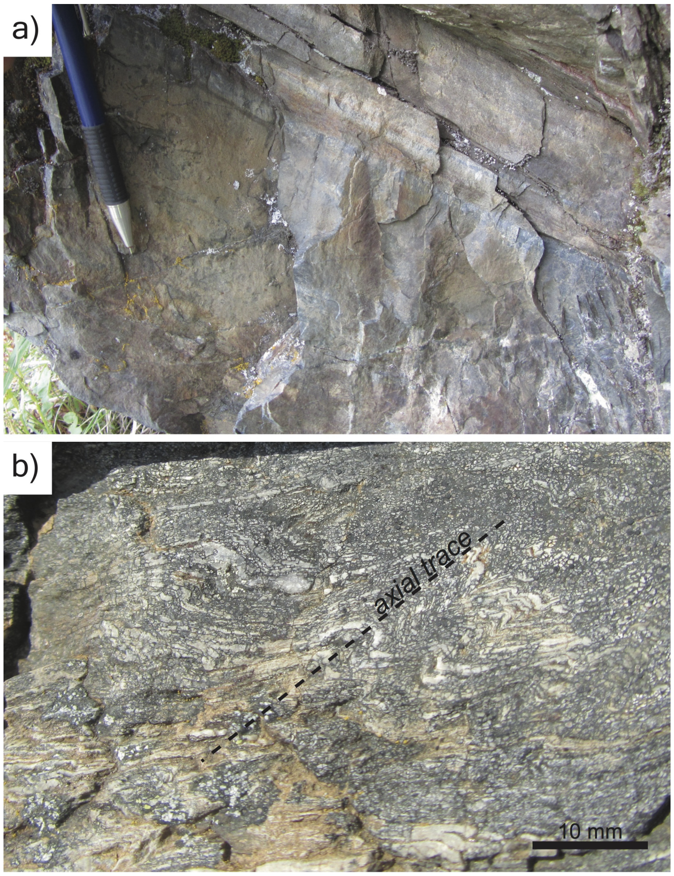

Fig. 16. Hornfelsed metasedimentary rocks in the metamorphic aureole of the Polaris intrusion. **a)** Cm-scale bedding in fine-grained metasedimentary rocks of the Lay Range assemblage, northwestern part of contact aureole. **b)** Foliated, fine-grained siliciclastic rocks of the Big Creek group showing small, open, eastward-vergent folds; hinge line trend and plunge: 308°-14°.

and mingling, involving cumulates at different points in their thermal histories and rheological states. Local dense swarms of (olivine) clinopyroxenite dikes, with cm-scale offshoots, that crosscut dunite and olivine wehrlite suggest that injection of evolved clinopyroxene-saturated magma was locally important. Possible reactive replacement of dunitic/olivine wehrlitic cumulates by these evolved magmas is indicated by the common cm- to m-scale irregular, patchy, clinopyroxene-rich pods and dikes that have gradational contacts, which may be diffuse, with the surrounding olivine-rich rocks (Figs. 10b, c). Olivine clinopyroxenite and clinopyroxenite comprise the matrix in magmatic breccias, and net-veined, ‘honeycomb’-textured rocks, which contain angular to sub-rounded blocks and plates of dunite, olivine wehrlite, and wehrlite (Fig. 12), are consistent with brittle fragmentation of a coherent host. Crosscutting olivine clinopyroxenite dikes with sharp boundaries also indicate late-stage intrusive episodes. Finally, brittle faulting is prevalent throughout the intrusion and accentuated in olivine-rich lithologies as noted by intense and complete serpentinization of the shear planes.

6.3. Inferences from the country rocks

Incorporation and possible assimilation of country rocks by magma(s) parental to the Polaris intrusion is evident from the map-scale xenolithic bodies of hornfelsed country rock within intrusion boundaries. Assimilated country rock is a potential source of sulphur (e.g., Lesher, 2017) and may be a potent reductant (Tomkins et al., 2012), which may have contributed to sulphide saturation in the magma, leading to segregation and crystallization of immiscible sulphide melt. Structures in country rocks along the eastern flank of the intrusion are consistent with previous interpretations (Monger, 1973; Ferri et al., 1993; Nixon et al., 1997) that the Polaris complex was thrust eastward atop the North American continental margin.

7. Conclusion

Detailed mapping has helped to refine lithological units in the Polaris intrusion as defined by Nixon et al. (1997) as well as their contact relationships. The geometry, zonation, and local magmatic layering of the intrusion indicate that it is likely a sill. Variable textures in chromitites and the presence of chaotically intermingled units with evidence for mingling of different melts and cumulates, and characteristics indicative of melt infiltration, suggest a disrupted magma chamber, characterized by periods of episodic magma input and reservoir recharge.

Although the Ni-Cu-PGE potential of Alaskan-type ultramafic-mafic intrusions in British Columbia and Alaska is increasingly recognized (Scheel et al., 2005; Scheel, 2007; Scheel et al., 2009; Thakurta et al., 2014; Jackson-Brown et al., 2015; Jackson-Brown, 2017; Nixon et al., 2018), the fundamentals of how Alaskan-type intrusions form is poorly understood (e.g., Thakurta, 2017). To help better understand these bodies, U-Pb geochronologic, petrographic, and trace element studies of the Polaris intrusion are ongoing.

Acknowledgments

Thank you to the Abraham family of the Takla First Nation for their support and assistance in field accommodation. The senior author thanks the Hogem batholith project team for their support in the field. Thanks to SilverKing helicopters for exemplary service and to Abigail Fraser for expediting field preparations and support throughout the field season. Salary support to the senior author is gratefully acknowledged through an NSERC CGS-M scholarship. Funding for this project is provided by the Geological Survey of Canada’s Targeted Geoscience Initiative 5 Program, the British Columbia Geological Survey, and a NSERC Discovery Grant to James Scoates. Constructive criticisms of the manuscript by Alex Zagorevski, and Fil Ferri are greatly appreciated.

References cited

CGG Canada Services Ltd., 2018. Geophysical survey report MIDAS high resolution magnetic and radiometric survey Search Project Phase III. Geoscience BC Report 2018-2.

Ferri, F., Dudka, S., Reese, C., and Meldrum, D., 1993. Geology of the Aiken Lake and Osilinka River Areas, northern Quesnel trough (94C/2, 3, 5, 6, 12). In: Geological Fieldwork 1992, British

Columbia Ministry of Energy, Mines and Petroleum Resources, British Columbia Geological Survey Paper 1993-1, pp. 109-134.

Ferri, F., 1997. Nina Creek Group and Lay Range Assemblage, north-central British Columbia: Remnants of late Paleozoic oceanic and arc terranes. Canadian Journal of Earth Sciences, 34, 854-874.

Ferri, F., Dudka, S., Rees, C., and Meldrum, D., 2001. Geology of the Aiken Lake area, north-central British Columbia. British Columbia Ministry of Energy, Mines and Petroleum Resources, British Columbia Geological Survey Geoscience Map 2001-10, 1:50,000 scale.

Findlay, D.C., 1963. Petrology of the Tulameen ultramafic complex, Yale District, British Columbia. Unpublished Ph.D. Thesis, Queen's University, Ontario, Canada, 415 p.

Foster, F., 1974. History and origin of the Polaris ultramafic complex in the Aiken Lake area of north-central British Columbia. Unpublished B.Sc. thesis, University of British Columbia, British Columbia, Canada, 66 p.

Himmelberg, G.R., and Loney, R.A., 1995. Characteristics and petrogenesis of Alaskan-type ultramafic-mafic intrusions, southeastern Alaska. US Geological Survey Professional Paper, 1564, 47 p.

Irvine, T.N., 1959. The ultramafic complex and related rocks of Duke Island, southeastern Alaska: unpublished PhD thesis, California Institute of Technology, Pasadena, California, USA, 320p.

Irvine, T.N., 1974a. Petrology of the Duke Island ultramafic complex, southeastern Alaska. Geological Society of America Memoir 138, 240 p.

Irvine, T.N., 1974b. Ultramafic and gabbroic rocks in the Aiken Lake and McConnell Creek map-areas, British Columbia. In: Current Research Part A, Geological Survey of Canada Paper 74-1A, pp. 149-152.

Irvine, T.N., 1976. Studies of Cordilleran gabbroic and ultramafic intrusions, British Columbia; Part 1, Axelgold gabbro intrusion, McConnell Creek map-area; Part 2, Alaskan-type ultramafic-gabbroic bodies in the Aiken Lake, McConnell Creek, and Toodoggone map. In: Current Research Part A, Geological Survey of Canada Paper 76-1A, pp. 75-81.

Jackson-Brown, S., 2017. Origin of Cu-PGE-rich sulphide mineralization in the DJ/DB zone of the Turnagain Alaskan-type intrusion, British Columbia. Unpublished M.Sc. thesis, University of British Columbia, Vancouver, British Columbia, Canada, 272 p.

Jackson-Brown, S., Scoates, J.S., Nixon, G.T., and Ames, D.E., 2015. Preliminary observations of the geology, mineralogy and geochemistry of the DJ/DB zone of the Turnagain intrusion, north-central British Columbia. Geological Survey of Canada Open File 7871, 62 p.

Le Maitre, R.W., 1989. A classification of igneous rocks and glossary of terms. Oxford, Blackwell Scientific Publications, 193 p.

Lesher, C.M., 2017. Roles of xenomelts, xenoliths, xenocrysts, xenovolatiles, residues, and skarns in the genesis, transport, and localization of magmatic Fe-Ni-Cu-PGE sulfides and chromite. Ore Geology Reviews, 90, 465-484.

Manor, M.J., Scoates, J.S., Nixon, G.T., and Ames, D.E., 2016. The Giant Mascot Ni-Cu-PGE deposit, British Columbia: Mineralized conduits in a convergent margin tectonic setting. Economic Geology, 111, 57-87.

Manor, M.J., Scoates, J.S., Wall, C.J., Nixon, G.T., Friedman, R.M., Amini, M., and Ames, D.E., 2017. Age of the late Cretaceous ultramafic-hosted giant mascot Ni-Cu-PGE deposit, southern Canadian Cordillera: Integrating CA-ID-TIMS and LA-ICP-MS U-Pb geochronology and trace element geochemistry of zircon. Economic Geology, 112, 1395-1418.

Monger, J.W.H., 1973. Upper Paleozoic rocks in McConell Creek map area (94D), British Columbia. In: Current Research Part A, Geological Survey of Canada, Paper 76-1A, pp. 51-55.

Mowat, U., 2015. Sampling on the Star 1, 3, 8, 10, 11 and 12 claims. British Columbia Ministry of Energy, Mines and Petroleum Resources, British Columbia Geological Survey Assessment Report 35680, 88 p.

Nelson, J., Colpron, M., and Israel, S., 2013. The Cordillera of British Columbia, Yukon and Alaska: tectonics and metallogeny. In: Colpron, M., Bissig, T., Rusk, B., and Thompson, J.F.H., (Eds.), Tectonics, Metallogeny, and Discovery-the North American Cordillera and Similar Accretionary Settings. Society of Economic Geologists Special Publication 17, pp. 53-109.

Nixon, G.T., 2018. Geology of the Tulameen Alaskan-type ultramafic-mafic intrusion, British Columbia. British Columbia Ministry of Energy, Mines and Petroleum Resources, British Columbia Geological Survey Open File 2018-02, 1:20,000 scale.

Nixon, G.T., Cabri, L.J., and Laflamme, J.H.G., 1990. Platinum-group-element mineralization in lode and placer deposits associated with the Tulameen Alaskan-type complex, British-Columbia. Canadian Mineralogist, 28, 503-535.

Nixon, G.T., Hammack, J.L., Ash, C.H., Cabri, L.J., Case, G., Connelly, J.N., Heaman, L., Laflamme, J.H.G., Nuttall, C., Paterson, W.P.E., and Wong, R.H., 1997. Geology and platinum-group-element mineralization of Alaskan-type ultramafic-mafic complexes in British Columbia. British Columbia Ministry of Employment and Investment, British Columbia Geological Survey Bulletin 93, 142 p.

Nixon, G.T., Manor, M.J., Jackson-Brown, S., Scoates, J.S., and Ames, D.E., 2015. Magmatic Ni-Cu-PGE sulphide deposits at convergent margins. In: Targeted Geoscience Initiative 4 : Canadian Nickel-Copper- Platinum Group Elements-Chromium Ore Systems-Fertility, Pathfinders. Geological Survey of Canada Open File 7856, pp. 17-34.

Nixon, G.T., Manor, M.J., and Scoates, J.S., 2018. Cu-PGE sulphide mineralization in the Tulameen Alaskan-type intrusion: analogue for Cu-PGE reefs in layered intrusions? British Columbia Ministry of Energy, Mines and Petroleum Resources, British Columbia Geological Survey GeoFile 2018-2 (poster).

Nixon, G.T., Scheel, J.E., Scoates, J.S., Friedman, R.M., Wall, C.J., Gabites, J., and Jackson-Brown, S., 2019a. Syn-accretionary multi-stage assembly of an Early Jurassic Alaskan-type intrusion in the Canadian Cordillera: U-Pb and $^{40}Ar/^{39}Ar$ geochronology of the Turnagain ultramafic-mafic intrusive complex, Yukon-Tanana terrane: Canadian Journal of Earth Sciences (in press).

Nixon, G.T., Milidragovic, D., and Scoates, J.S., 2019b. Convergent margin Ni-Cu-PGE-Cr ore systems: temporal and magmatic evolution. In: Targeted Geoscience Initiative 5, Grant Program Interim Reports 2018-2019. Geological Survey of Canada Open File 8620, pp. 49-61.

Piña, R., 2019. The Ni-Cu-(PGE) Aguablanca Ore Deposit (SW Spain). SpringerBriefs in World Mineral Deposits, Springer International Publishing, 78 p.

Roots, E.F., 1954. Geology and mineral deposits of Aiken Lake map-area, British Columbia. Geological Survey of Canada Memoir 274, 246 p.

Scheel, J.E., 2007. Age and origin of the Turnagain Alaskan-type intrusion and associated Ni-sulfide mineralization, north-central British Columbia, Canada. Unpublished M.Sc. thesis, University of British Columbia, Vancouver, Canada, 210 p.

Scheel, J.E., Nixon, G.T., and Scoates, J.S., 2005. New observations on the geology of the Turnagain Alaskan-type ultramafic intrusive suite and associated Ni-Cu-PGE mineralization, British Columbia. In: Geological Fieldwork 2004, British Columbia Ministry of Energy, Mines and Petroleum Resources, British Columbia Geological Survey, Paper 2005-1, pp. 167-176.

Song, X.-Y., Yi, J.-N., Chen, L.-M., She, Y.-W., Liu, C.-Z., Dang, X.-Y., Yang, Q.-A., and Wu, S.-K., 2016. The giant Xiarihamu Ni-Co sulfide deposit in the East Kunlun Orogenic Belt, northern Tibet Plateau, China: Economic Geology, 111, 29-55.

Taylor, H.P., Jr., 1967. The zoned ultramafic complexes of southeastern Alaska. In: Wyllie, P.J., (Ed.), Ultramafic and Related Rocks, Wiley and Sons, New York, pp. 97-121.
Thakurta, J., 2017. Alaskan-type complexes and their associations with economic mineral deposits. In: Mondal, S., Griffen, W., (Eds.), Processes and Ore Deposits of Ultramafic-Mafic Magmas through Space and Time, Elsevier Publishing Company, pp. 269-302.
Thakurta, J., Ripley, E.M., and Li, C., 2014. Platinum group element geochemistry of sulfide-rich horizons in the Ural-Alaskan-type ultramafic complex of Duke Island, southeastern Alaska. Economic Geology, 109, 643-659.
Tomkins, A.G., Rebryna, K.C., Weinberg, R.F., and Schaefer, B.F., 2012. Magmatic sulfide formation by reduction of oxidized arc basalt. Journal of Petrology, 53, 1537-1567.

Geology of the Kinskuch Lake area and Big Bulk porphyry prospect: Syndepositional faulting and local basin formation during the Rhaetian (latest Triassic) transition from the Stuhini to the Hazelton Group

E.A. Miller[1, a], L.A. Kennedy[1], and B.I. van Straaten[2]

[1] Department of Earth, Ocean and Atmospheric Sciences, The University of British Columbia, Vancouver, BC, V6T 1Z4
[2] British Columbia Geological Survey, Ministry of Energy, Mines and Petroleum Resources, Victoria, BC, V8W 9N3
[a] corresponding author: emiller@eoas.ubc.ca

Recommended citation: Miller, E.A., Kennedy, L.A., and van Straaten, B.I., 2020. Geology of the Kinskuch Lake area and Big Bulk porphyry prospect, northwestern British Columbia: Syndepositional faulting and basin formation during the Rhaetian (latest Triassic) transition from the Stuhini to the Hazelton Group. In: Geological Fieldwork 2019, British Columbia Ministry of Energy, Mines and Petroleum Resources, British Columbia Geological Survey Paper 2020-01, pp. 77-99.

Abstract

The Stewart-Iskut district, in the Stikine terrane of northwestern British Columbia, contains numerous Late Triassic to Early Jurassic porphyry Cu-Au and epithermal deposits. These deposits are broadly coeval with the transition from volcano-sedimentary deposits of the Stuhini Group (Late Triassic) to those of the Hazelton Group (latest Triassic to Jurassic), which is marked by strata bearing evidence of significant uplift and erosion. Recent studies in the district have proposed that small pull-apart basins served to localize emplacement of the KSM Cu-Au porphyry system. Detailed (1:10,000 scale) mapping in the Kinskuch Lake area near the Big Bulk Cu-Au porphyry prospect, 50 km southeast of Stewart, indicates that syndepositional faulting in the Rhaetian (latest Triassic) strongly influenced the transition from Stuhini Group to Hazelton Group deposition. Conglomerates, informally referred to herein as the Kinskuch conglomerates, containing Stuhini Group-derived megaclasts (up to 120 m) at the base of the Hazelton Group signify a high-relief, fault-generated paleotopography and mark a fundamental break in the tectonic history of the region. Progressive stripping into deeper parts of the subjacent Stuhini Group section, as recorded by bottom-to-top clast compositions that yield an inverse stratigraphy, signify at least 400 m of Stuhini Group unroofing. These conglomerates are limited to the east side of a prominent northeast-trending dextral fault (Tabletop fault). We propose that the Tabletop fault and likely other northeast-trending faults in the area had an earlier (latest Triassic) history with strike-slip or oblique movement, and that releasing step-overs, splays, or double bends in this fault network created local zones of north-south extension, easterly trending normal faults, and local pull-apart basins. The Big Bulk porphyry diorite stock (204.61 ±0.18 Ma, CA-TIMS, U-Pb zircon, this study), which cuts the lower part of the Hazelton Group, has four intrusive phases all of which are approximately tabular with an east-west trend. Main stage Cu-Au mineralization is in sheeted quartz-chalcopyrite veins, with easterly orientations, consistent with local northerly extension during porphyry emplacement. Hence, like other areas in northwestern Stikinia, sedimentation, magmatism, and porphyry mineralization appear to have had a strong structural control. Along with the prominent northeast-trending strike-slip faults, mid-Cretaceous shortening related to the Skeena fold and thrust belt is expressed as southeast- and east-vergent thrusts and folds. It is likely that many of the mid-Cretaceous structures in the area reactivated pre-existing structures.

Keywords: Kinskuch conglomerates, Big Bulk, Stewart-Iskut district, Hazelton Group, Stuhini Group, Rhaetian, Late Triassic, Early Jurassic, syndepositional faulting, Triassic-Jurassic porphyry, Cu-Au porphyry

1. Introduction

The Kinskuch Lake area is in the Stikine terrane (Stikinia) of the Canadian Cordillera (Fig. 1), near the southern end of the Stewart-Iskut district, a >200 km-long belt of porphyry Cu-Au and epithermal Au mineralization that is hosted by Upper Triassic rocks of the Stuhini Group and overlying uppermost Triassic to Lower Jurassic rocks of the Hazelton Group (Fig. 2a). The Stewart-Iskut district extends from Kitsault northward to Stewart and the Stikine River, in the southern part of a region popularly referred to as the 'Golden Triangle'.

Many mineral deposits in the Stewart-Iskut district are on or near north-south and east-west trending faults and lineaments. Many faults were likely long lived, and such pre-existing structures were probably important in localizing mineralization (Nelson and Kyba, 2014; Kyba and Nelson, 2015; Febbo et al., 2019). These fault systems may have originated in the Paleozoic basement of Stikinia. Some were reactivated in the Cretaceous (Nelson and Kyba, 2014; Febbo et al., 2019), some in the Eocene (Tombe et al., 2018), and others had a controlling influence on rocks as young as those at the Mount Edziza volcanic complex (Miocene-Holocene; Edwards and Russell, 2000; Febbo et al., 2019).

Although porphyry Cu-Au-Mo systems, especially those formed along active continental margins, form in overall

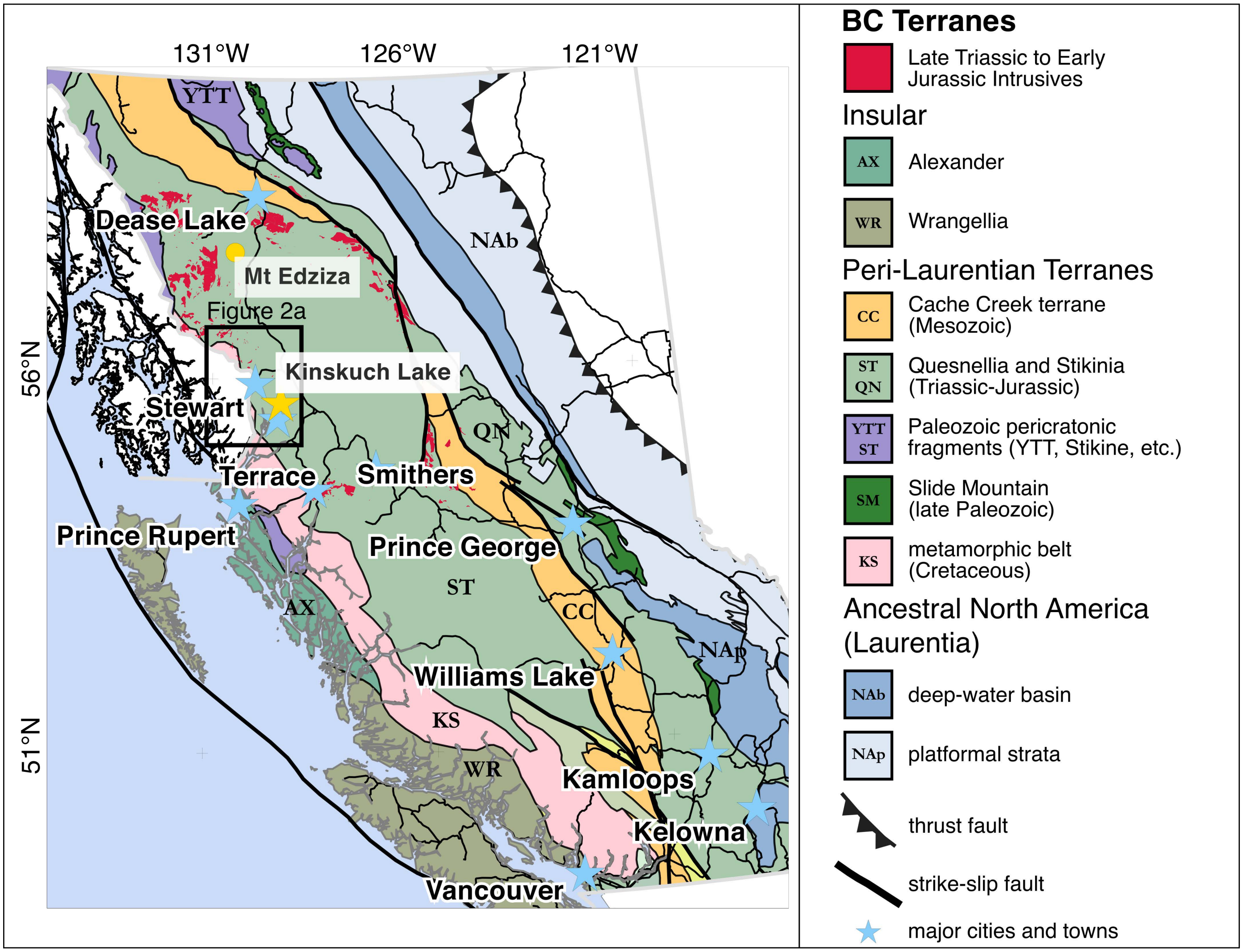

Fig. 1. Location of the Kinskuch Lake area with respect to terranes of British Columbia (after Colpron and Nelson, 2011).

contractional tectonic environments (Tosdal et al., 2009; Sillitoe, 2010), some form in local zones of extension or in zones of pre-existing extensional crustal architectures (e.g., Richards et al., 2001; Richards, 2003; Gow and Walshe, 2005; Cloos and Sapiie, 2013; Piquer et al., 2015). Studies by Nelson and Kyba (2014) and Febbo et al. (2019) at the Kerr-Sulphurets-Mitchell (KSM) deposit demonstrate that syndepositional faulting and coarse siliciclastic deposition accompanied Early Jurassic porphyry emplacement. They proposed that small pull-apart basins along reactivated basement structures served to localize emplacement of individual intrusions of the KSM porphyry system.

To test this model regionally and to better understand the uppermost Triassic to Lower Jurassic structural and tectonic setting of the Stewart-Iskut belt, we undertook detailed (1:10,000 scale) mapping in the Kinskuch Lake area near the Big Bulk porphyry prospect (Fig. 2b), which has characteristics and stratigraphy similar to the KSM deposits. Herein, we present lithological descriptions, stratigraphic analysis, structural data, and geochronology to infer the depositional and structural setting at Kinskuch Lake before and during emplacement of the Big Bulk porphyry system. Our observations at Kinskuch Lake show that syndepositional faulting strongly influenced the transition from the Stuhini Group to the Hazelton Group during the latest Triassic.

2. Regional geology and tectonic setting

The Stikine volcanic island arc terrane encompasses three unconformity-bounded arc-related volcano-sedimentary successions: the Stikine assemblage (Paleozoic); the Stuhini Group (Upper Triassic); and the Hazelton Group (uppermost Triassic to Middle Jurassic; Logan et al., 2000; Nelson et al., 2018). More than 90% of the known copper resources in British Columbia accumulated between ca. 211 and 199 Ma, spanning the transition from Stuhini Group arc development to Hazelton Group volcanism and sedimentation (Logan and Mihalynuk, 2014). Our study focusses on this transition.

Regionally, the Stuhini Group (Late Triassic) comprises

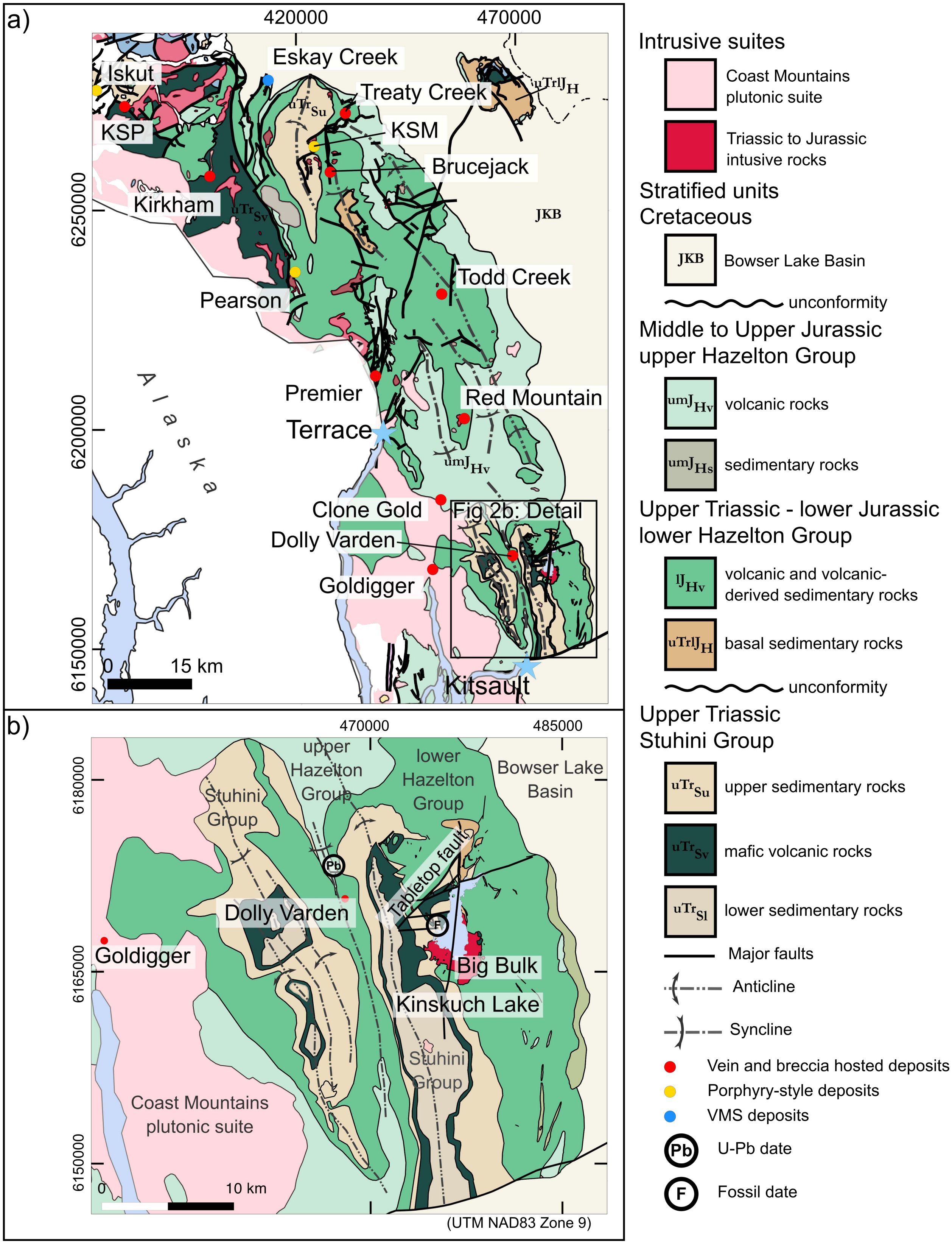

Fig. 2. a) Regional geological and structural setting (after Alldrick et al., 1986; Greig, 1992; and Colpron and Nelson, 2011), with selected Cu(±Au±Mo) porphyry (yellow) and vein and breccia-hosted (including epithermal) deposits (red). **b)** Local geological and structural setting (after Alldrick et al., 1986) with locations of geochronological samples: (Pb) 178.1 ±2.2 Ma felsic tuff in the upper part of the Hazelton Group (U-Pb zircon, Hunter and van Straaten, 2020) and (F)-Rhaetian (latest Triassic) conodont sample (Cordey et al., 1992; Greig et al., 1995; and Golding et al., 2017).

augite-phyric mafic volcanic rocks, volcanic-derived sedimentary rocks, and marine sedimentary rocks including argillite, sandstone, minor limestone, and rare chert. The Stuhini Group is unconformably overlain by intermediate volcanic and volcanic-derived sedimentary rocks of the Hazelton Group (Nelson et al., 2013; 2018). Basal lower Hazelton Group rocks range from as old as latest Triassic (Rhaetian) to Early Jurassic (Hettangian-Sinemurian; e.g., Thorkelson et al., 1995; Barresi et al., 2015; Nelson et al., 2018; Hunter and van Straaten, 2020).

The lower part of the Hazelton Group (uppermost Triassic-Lower Jurassic) consists primarily of feldspar- hornblende -phyric volcanic rocks and volcanic-derived sedimentary rocks. Quartz-bearing sandstones and granitoid clast-bearing conglomerates of the Jack Formation at the base of the Hazelton Group near the KSM deposits and the lower Iskut River display evidence of syndepositional faulting (Nelson and Kyba, 2014). The upper part of the Hazelton Group (Early to Middle Jurassic) is predominantly a post-arc sedimentary package with local bimodal rift-related volcanic rocks (Iskut River Formation; Gagnon et al., 2012; Nelson et al., 2018). Although sections containing bimodal volcanic rocks have not been recognized in the Kinskuch Lake area, Hunter and van Straaten (2020) reported a U-Pb zircon age of 178.1 ±2.2 Ma from a felsic tuff in the nearby Kitsault River valley (Fig. 2b), similar to ages from the Iskut River Formation (see Nelson et al., 2018).

Stratified rocks of northwestern Stikine terrane are cut by several intrusions including: 1) the Stikine and Galore plutonic suites (Late Triassic), which are coeval and comagmatic with the Stuhini Group (Nelson et al., 2018); 2) the Tatogga (latest Triassic) and Texas Creek plutonic suites (Early Jurassic), which are coeval and comagmatic with the lower part of the Hazelton Group (Nelson et al., 2018); and 3) the Hyder plutonic suite (Eocene), the youngest intrusions in and east of the Coast Plutonic complex (Alldrick, 1993).

Rocks in the region were deformed in the mid-Cretaceous during development of the Skeena fold-and-thrust belt, which formed in response to sinistral transpression (Evenchick, 2000; Evenchick et al., 2007). The fold-and-thrust belt affects most of the central Intermontane belt and accommodates a minimum of 44% northeasterly directed shortening (Evenchick et al., 2007). By the middle to Late Cretaceous, large-scale dextral faults initiated, signalling a change in relative plate motions from earlier, predominantly sinistral kinematics (Nelson et al., 2013). The Paleocene to Eocene saw dextral-transtensional tectonics, during which many pre-existing orogen-parallel structures accumulated significant offset (Nelson et al., 2013).

3. Methods

The map area is in a north-south elongate, ridge-bounded depression centred on Kinskuch Lake (Fig. 3). Outcrop is excellent, and mapping was at a scale of 1:10,000, with key sections selected for more detailed work, such as at the Big Bulk porphyry prospect where we mapped at a scale of 1:5,000. Because of their importance (see below), conglomerate and megaclast-bearing beds at the transition between the Stuhini and Hazelton groups were given special attention. At 40 sites we did clast composition counts and determined the dimensions of the 10 largest clasts. These counts were completed by identifying 50 clasts along 20 cm-wide strips in lines perpendicular to bedding.

4. Lithostratigraphy

The oldest rocks in the area are Stuhini Group (Upper Triassic) augite-phyric basalts and marine sedimentary strata, which are primarily exposed on the western side of Kinskuch Lake (Fig. 3). Hazelton Group rocks are mostly exposed on the eastern side of the lake. To ease the following discussion, we illustrate stratigraphic relationships within and between the Stuhini and Hazelton groups in a north-south transect (Fig. 4). The 'Big Bulk' porphyry is on the southeast and south sides of the lake. The area is cut by numerous small, likely Eocene, dikes.

4.1. Stuhini Group (Upper Triassic)

The Stuhini Group consists of augite-phyric volcanic rocks, and sedimentary rocks including conglomerates with augite-bearing clasts, sandstones, argillite, sandstone, minor limestone, and rare chert. The volcanic rocks are exposed near the western shore of the central part of the lake and to the west (Figs. 2b, 3). The overlying sedimentary rocks are in low-lying exposures on the west side of the lake and only locally at low elevations in drainages and along the shoreline east of the lake.

4.1.1. Volcanic and volcanic-derived sedimentary rock unit

The lower part of the Stuhini Group is typified by augite-phyric volcanic rocks and well-stratified, monomictic mafic volcanic clast-bearing conglomerate to volcanic-derived sandstone interstratified with lesser mafic volcanic breccia (Fig. 5a). The unit typically forms 10-50 m thick beds in which conglomerates and sandstones overlie coherent augite-phyric volcanic flows and associated volcanic breccia (Fig. 5b). Conglomerates directly overlying the flows contain angular to subrounded clasts. The flows generally have sharp basal contacts and locally contain subrounded augite-phyric clasts incorporated from underlying sedimentary beds alongside more angular, likely juvenile clasts of similar composition. Near the top of the unit volcanic breccias and augite-phyric coherent rocks gradually become more prominent, although interbedded with increasingly fine-grained sedimentary units. We define the top of the unit as the uppermost level containing coherent mafic flows.

4.1.2. Sedimentary rock unit

This unit consists of interstratified argillite, feldspathic sandstone, conglomerate, and siltstone. Quartz is absent in all rock types. We have divided the unit into two facies mappable at the 1:10,000 scale.

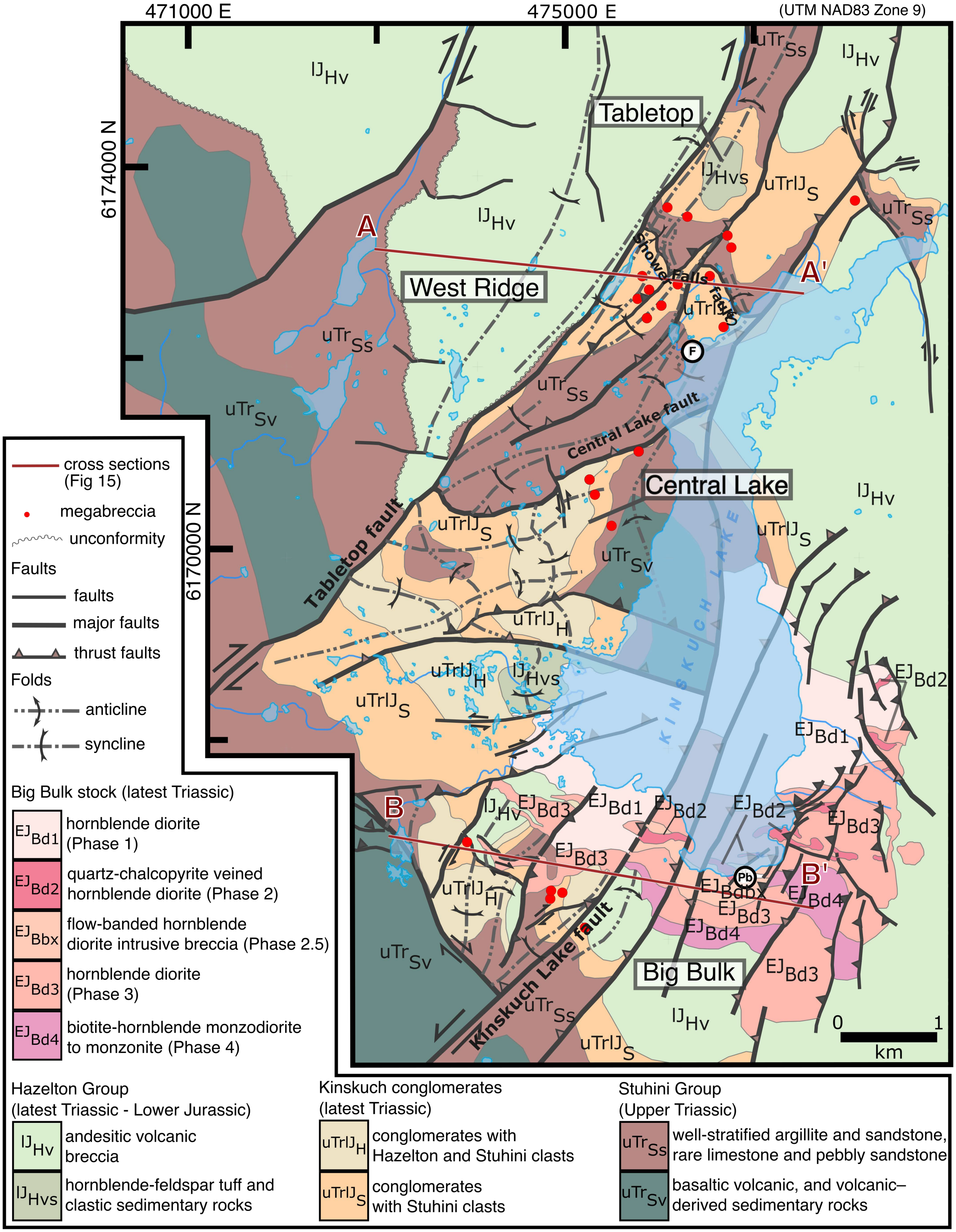

Fig. 3. Geological map of the Kinskuch Lake area. Locations of megaclast-bearing conglomerates shown as red dots. (F)-Rhaetian (latest Triassic) conodont sample (Cordey et al., 1992; Greig et al., 1992; and Golding et al., 2017). (Pb)-U-Pb zircon sample from phase 2 of the Big Bulk stock, with a preliminary CA-TIMS age of 204.61 ±0.18 Ma (this study).

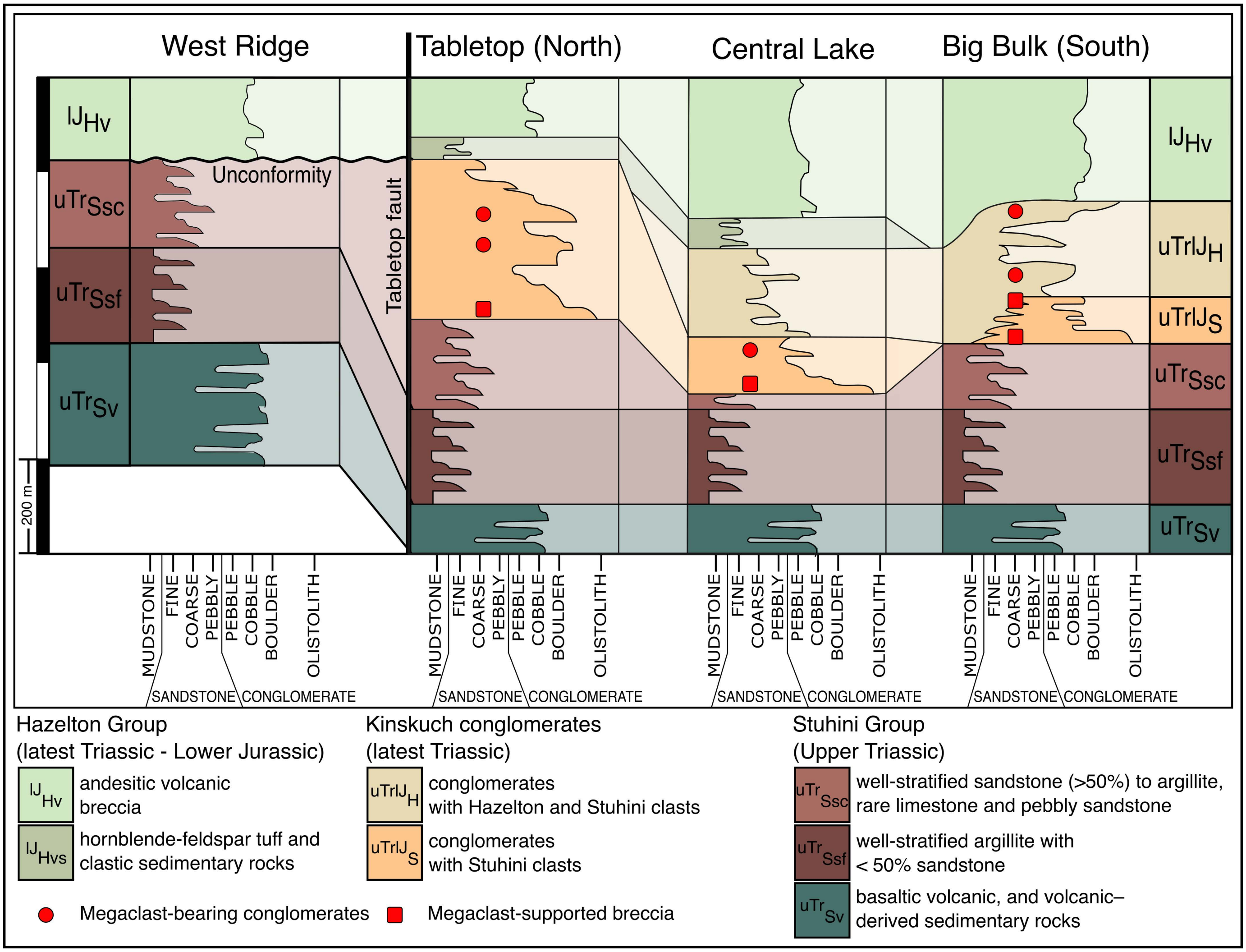

Fig. 4. Schematic north-south stratigraphic cross section illustrating lithologic variations in the Stuhini and Hazelton groups.

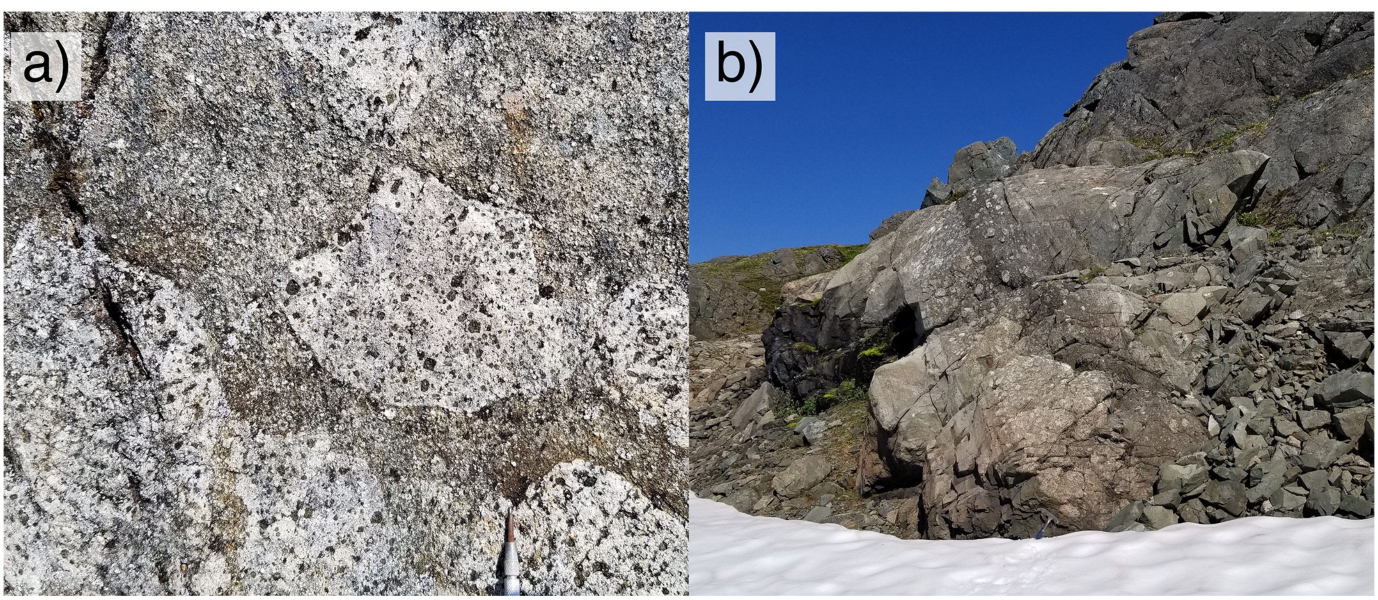

Fig. 5. Stuhini Group volcanic and volcanic-derived sedimentary rocks. **a)** Matrix-supported volcanic breccia with angular augite-phyric clasts and augite phyric groundmass (uTrSv; 473840E, 6168792N). **b)** Volcanic breccia (base of outcrop at left of photo) and interstratified volcanic-derived conglomerates and sandstones younging upward to the north (uTrSv; 472194E, 6172116N UTM NAD83 Zone 9; looking west).

4.1.2.1. Fine-grained sedimentary facies

This facies consists of more than 50% well-bedded argillite and mudstone (locally graphitic), with 1 to 20 cm-thick interbeds of siltstone and very fine- to fine-grained sandstone and lesser, medium-grained sandstone. It also includes rare (<5%) coarse-grained sandstone and pebbly sandstone. Upsection, the number and thicknesses of sandstone beds increases and the proportion of mudrocks decreases as the facies passes gradationally to the compositionally similar coarse-grained sedimentary facies.

4.1.2.2. Coarse-grained sedimentary facies

This facies consists of more than 50% well-bedded siltstone, lithic sandstone, feldspathic sandstone, and pebbly sandstone, with lesser argillite and mudstone (Fig. 6a), rare calcareous sandstone (Fig. 6b), and fossiliferous limestone (Fig. 6c) of limited lateral extent. It represents an upward coarsening from the underlying fine-grained sedimentary facies.

4.2. Hazelton Group

4.2.1. Kinskuch conglomerates (latest Triassic; new name)

This new informal unit consists of massive to poorly stratified pebble to boulder conglomerate with rounded to angular clasts and local megaclasts (up to 120 m). The conglomerates are locally interstratified with lesser coarse-grained sandstone (ranging from lithic arkose to feldspathic litharenite) and pebbly sandstones, none of which contain quartz. Locally coarse-grained sandstone-filled channels cut conglomerates, commonly showing inverse graded bedding. Clast types include sandstone, mudstone, limestone, chert, and augite-phyric basalt similar to rocks in the Stuhini Group (Fig. 7) and hornblende-feldspar-phyric volcanic rocks similar to those in the Hazelton Group (Fig. 8). The conglomerates are generally clast supported with clasts set in a predominantly feldspathic matrix, with local carbonate sand grains and/or calcareous cement, to lesser muddy matrix. Neither the matrix nor the clasts appear to contain detrital quartz. The conglomerates contain rare muscovite and biotite-bearing clasts, including coarse biotite-bearing sandstone and muscovite schists in which internal fabrics are truncated at clast boundaries; the source of these clasts is unknown. The conglomerates are interstratified with basal Hazelton tuffs.

The Kinskuch conglomerates consistently overlie Stuhini Group sedimentary rocks southeast of the Tabletop fault and are absent northwest of the fault (Figs. 3, 4). On the eastern side of the lake they are observed at low elevations in some incised drainages below the steep, west-facing ridge of resistant Hazelton Group volcanic breccias. In northern and southern exposures, the conglomerates contain mainly cobble and larger fragments with minor pebbly interbeds. In contrast, most of the conglomerates in the 'central lake' exposures consist mainly of pebble conglomerates to pebbly sandstones with less abundant coarser beds (Fig. 9). Bedding in the conglomerates appears to be concordant with bedding in subjacent Stuhini Group. The transition from Stuhini Group rocks to Kinskuch conglomerates is typically marked by an abrupt change to boulder and

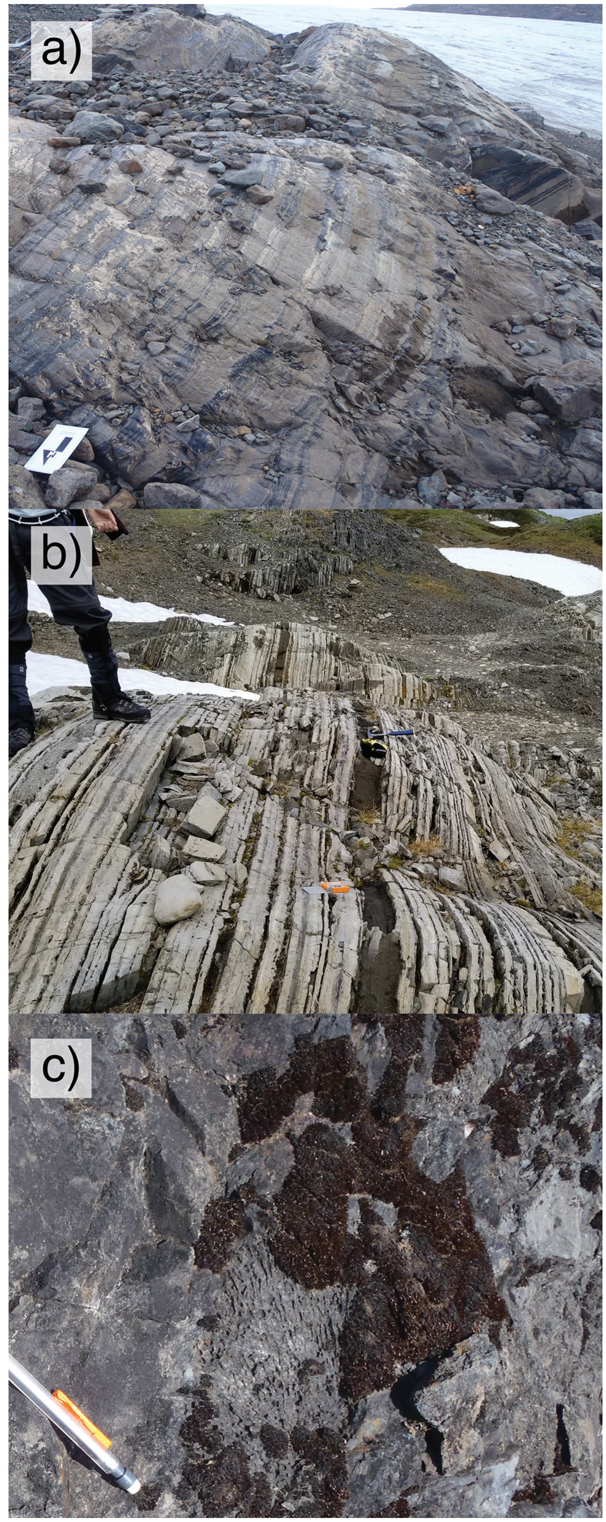

Fig. 6. Stuhini Group sedimentary rocks. **a)** Well-stratified, pale buff weathering feldspathic sandstone and dark-toned mudstone younging upright to the east from sharp-based fining-upward sequences and sandstone load cast and flame structures (uTrSsc) looking S. **b)** Rhythmically interlayerd buff weathered feldspathic sandstone and black argillite with lesser recessive calcareous sandstone beds (uTrSsc) looking north, tops to west. **c)** Grey to buff-weathered fossiliferous limestone (uTrSsc). These limestones are found as clasts in the Kinskuch conglomerates (see below).

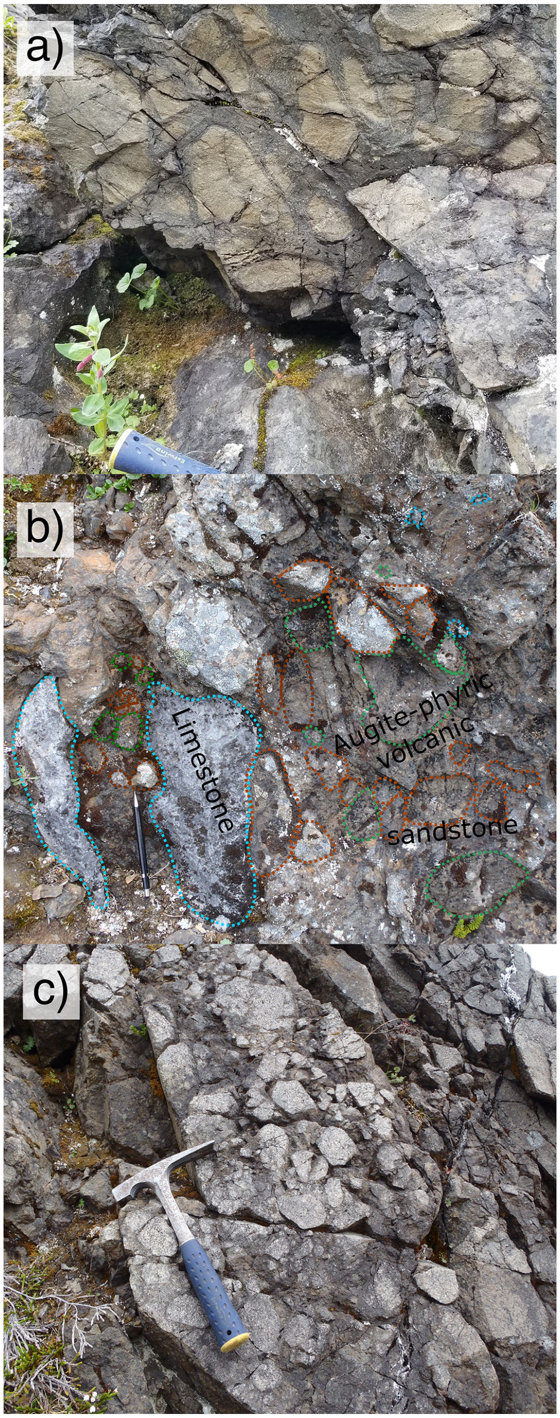

Fig. 7. Stuhini-derived Kinskuch conglomerates (uTrlJs). **a)** Framework-intact monomictic cobble-boulder conglomerate with Stuhini-derived angular to subrounded coarse-grained feldspathic sandstone clasts from near the base of the Kinskuch conglomerates, looking northeast, tops upright to the northeast. Some clasts show fractures that do not exist in matrix. **b)** Framework-intact pebble-cobble conglomerate with Stuhini Group-derived clasts of limestone (with cuspate-lobate margins, outlined in blue), augite-phyric volcanic rock (outlined in green), and sandstone (outlined in red) in a matrix of coarse grained feldspathic litharenite. **c)** Framework-intact monomictic cobble conglomerate with angular to sub-rounded Stuhini Group-derived augite-phyric volcanic clasts in a matrix of coarse-grained augite-bearing feldspathic sandstone (uTrlJsv).

megaclast breccias; due to the size and concentration of the megaclasts they can be mistaken for in situ bedded layers, unless examined along strike.

The clast composition of the conglomerates varies significantly both vertically and laterally. We divide the Kinskuch conglomerates into two mappable subunits based on clast composition: 1) those containing only sedimentary and augite-phyric volcanic rock clasts (Fig. 7; uTrlJs) and, 2) those containing hornblende-feldspar phyric volcanic clasts, sedimentary rocks, and augite-phyric volcanic rock clasts (Fig. 8 uTrlJh). Clast sorting and size varies vertically and laterally from well-sorted to extremely poorly sorted. Clast shape and angularity vary significantly, with some exposures containing predominantly rounded spherical clasts, and some composed mostly of angular and tabular clasts. Chert clasts range from angular to subangular and are mostly spherical. Limestone clasts are mostly rounded to well-rounded but can have irregular cuspate-lobate margins. The volcanic, sandstone, and other sedimentary rocks clasts display a wide range of rounding and sphericity. These features vary gradationally laterally and vertically and are not mappable at a 1:10,000 scale.

Upsection changes in clast compositions, particularly at the Tabletop section (Fig. 4), are interpreted to record progressive erosional stripping into deeper levels of the Stuhini Group. At the base of the section, clasts consist mainly of limestones, sandstones, and lesser argillites, mudstones and cherts, similar to those observed in the uppermost Stuhini Group sedimentary rock unit (uTrSs, Figs. 3, 7a), whereas higher in the section clasts consist mainly of augite-phyric volcanic clasts similar to those in the Stuhini Group volcanic rock unit (uTrSv, Figs. 3, 7c). Augite-phyric clasts also show lateral variation and are both more abundant and observed lower in the stratigraphic section, in the west, closer to the Tabletop fault, than in the east, closer to Kinskuch Lake. In sharp contrast to the evidence of top-to-bottom erosion of the subjacent Stuhini Group section, hornblende-feldspar phyric volcanic clasts, presumably derived from the Hazelton Group, appear above Stuhini-derived conglomerates at the 'central lake' and southern 'Big Bulk' sections, although they also appear to directly overlie the Stuhini Group in the most southern exposures (Fig. 4). Laterally, the most significant map-scale variation in clast composition is that these hornblende-feldspar phyric volcanic clasts are lacking in the northern exposures (Fig. 4).

4.2.1.1. Megaclast deposits

Some of the conglomerates contain megaclasts up to 120 m long. The megaclasts consist mostly of limestone (Fig. 10a) and laminated chert (Fig. 10b) with laminations parallel to original bedding planes. Megaclasts of thinly bedded sedimentary rocks (up to 75 m long, Figs. 10c, d) and augite-phyric volcanic rocks (up to 5 m long) are less common. The chert megaclasts commonly display an internal fracture network with jig-saw fit, suggesting fragmentation with minimal relative movement during transport; locally, megaclasts of chert contain internal

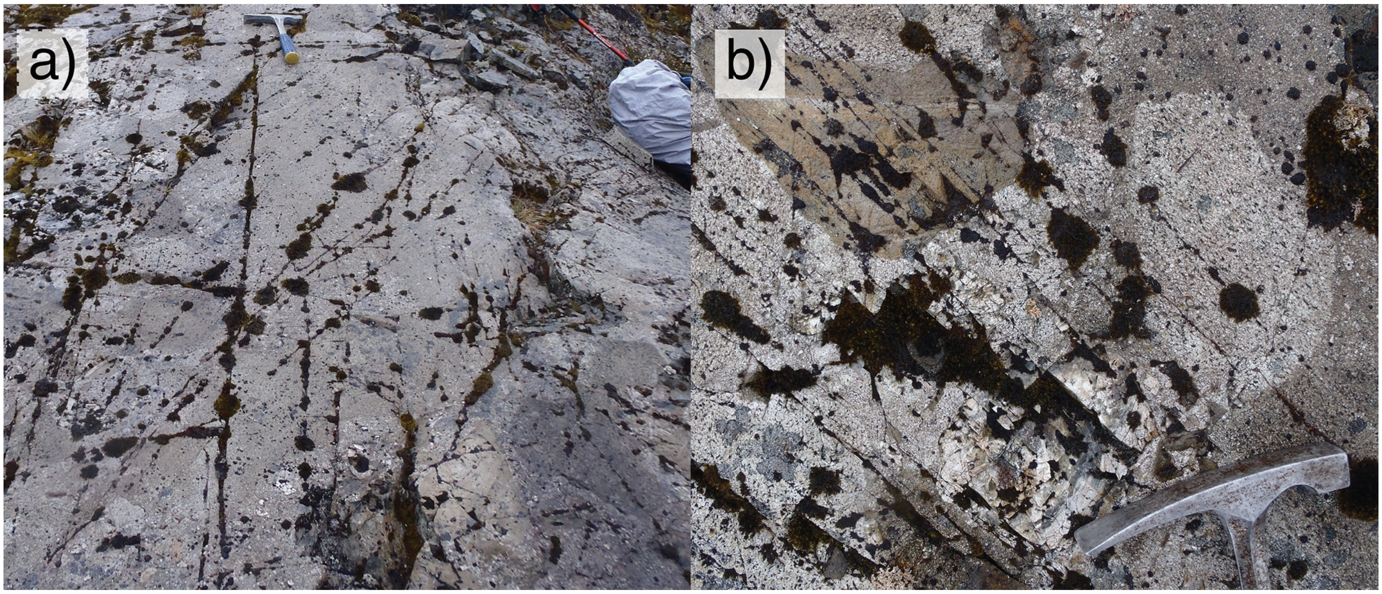

Fig. 8. Stuhini- and Hazelton-derived Kinskuch conglomerates (uTrlJh). **a)** Matrix-supported pebble to boulder conglomerate with angular pebble to cobble chert clasts, rounded pebble to boulder Stuhini-derived sandstone clasts and well-rounded cobble to boulder hornblende-phyric Hazelton Group-sourced clasts in a coarse-grained feldspathic litharenite matrix (uTrlJhs). Looking northwest, tops to northwest. **b)** Detail of above, showing hornblende-phyric Hazelton Group-sourced and Stuhini Group-sourced sandstone and chert clasts.

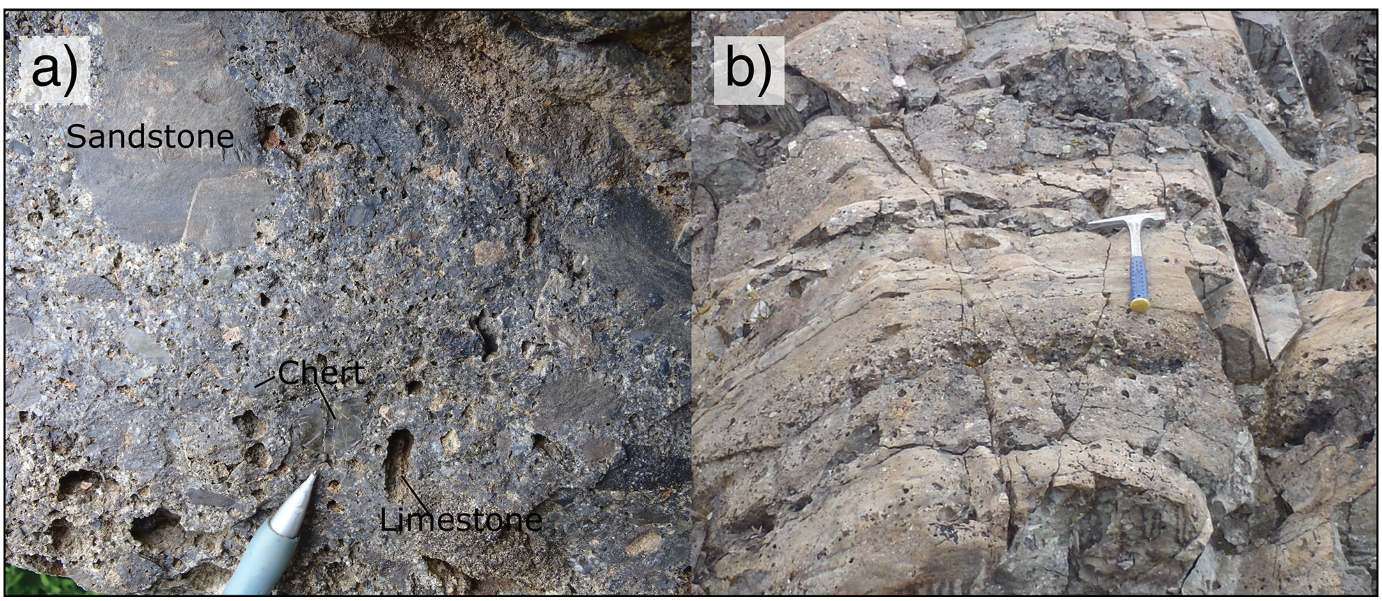

Fig. 9. Mainly pebble Kinskuch conglomerates from the central lake area. **a)** Clast-supported pebble to rare cobble conglomerate with rounded to angular chert clasts, recessively weathering lobate limestone clasts, rounded to subangular sandstone clasts, and rare feldspar-phyric volcanic clasts. **b)** Fining-upward sequences of pebble conglomerate to pebbly litharenite to feldspathic arenite to siltstone; looking northeast, tops northeast.

folds that are truncated at clast boundaries (Fig. 10b). The matrix of the megaclast-bearing conglomerates is composed of coarse-grained lithic arkose to litharenite with no quartz. Along the margins of some megaclasts, monomictic cobble to pebble breccia commonly grades into a more polymictic conglomerate, indicating derivation from less local sources. The matrix surrounding the megaclasts is generally massive.

Locally, megaclast fragments are separated by little intervening matrix and may be confused with in situ protolith. Non-systematic changes in bedding and younging direction in these bodies indicate that they are clasts. In one exposure, near the Big Bulk prospect, thinly bedded sedimentary megaclasts in a megaclast-supported breccia that is interbedded with coarse-grained sandstones have abundant soft-sediment deformation structures including sandstone and mudstone dikes (Figs. 10c, d).

The megabreccias are most prominent at the base of the Kinskuch conglomerate unit (Fig. 4), but they also occur higher

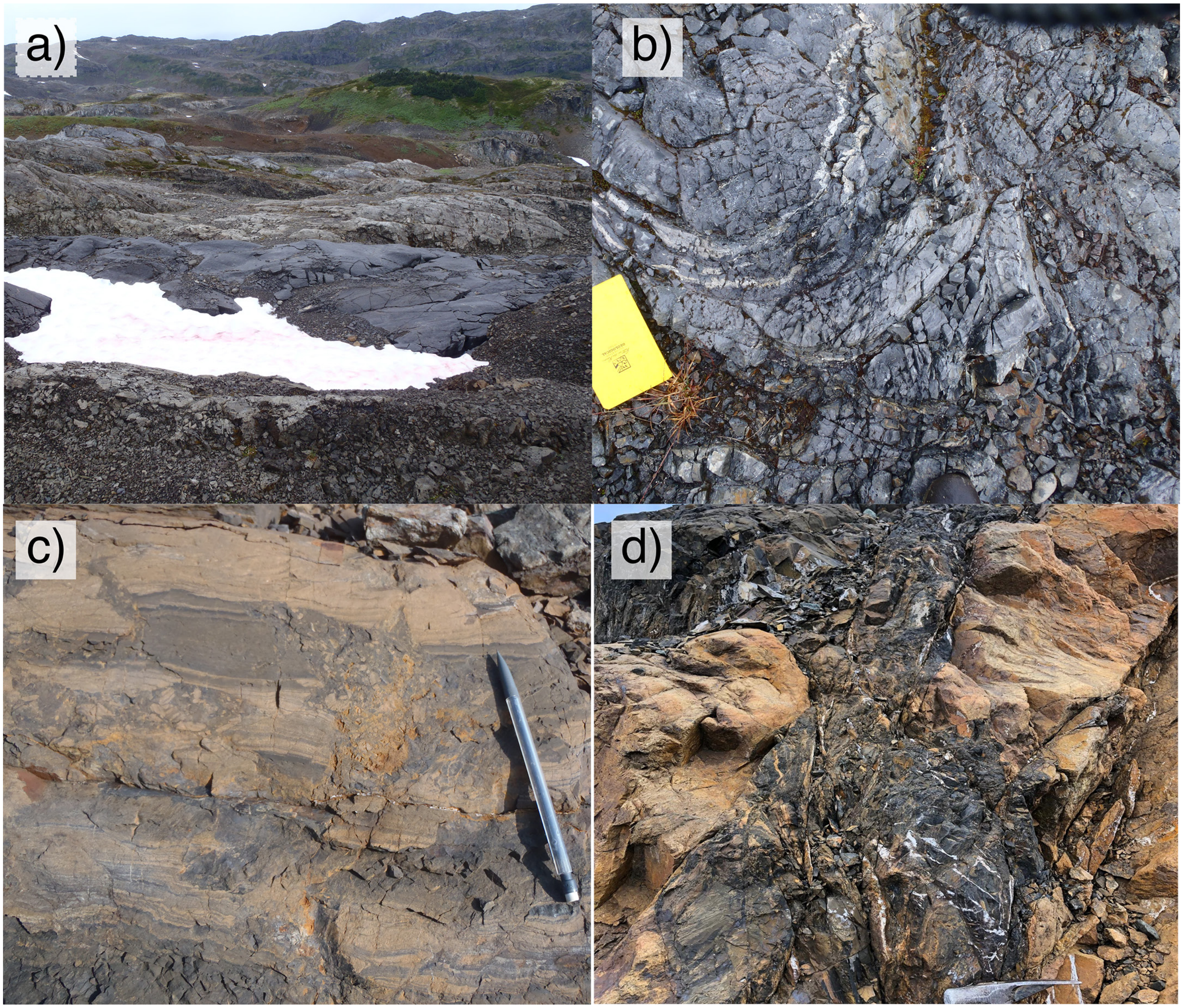

Fig. 10. Megaclast-bearing Kinskuch conglomerates **a)** Dark grey-weathered limestone megaclast in framework-intact clast-supported cobble to boulder conglomerates with fractured subangular to subrounded sandstone, chert and limestone clasts. View to the northwest, tops northwest. **b)** Chert megaclast with internal fold that predates jig-saw fit fracturing and incorporation into the conglomerates. **c)** Megaclast of thinly bedded orange-weathering feldspathic arenite and dark mudrock with soft-sediment deformation structures, including sandstone and mudstone dikes. **d)** Megaclast-supported conglomerate with coarse-grained sandstone megaclasts and disrupted megaclasts of finely bedded dark grey argillites and minor orange-weathering sandstone interbeds.

in the section, including directly beneath Hazelton Group volcanic rocks in the southern part of the map area, near the Big Bulk stock. They are most abundant, particularly at higher stratigraphic levels in the northern and southern parts of the map area (Figs. 3, 4).

Cordey et al. (1992) and Greig et al. (1992) collected conodonts from a limestone exposure that we consider a ≥100 m megaclast near the base of the Kinskuch conglomerate unit. These conodonts, originally interpreted as Late Norian, are now assigned to the Rhaetian (Golding et al., 2017; M. Golding, pers. comm., 2019), providing a maximum age for the Kinskuch conglomerates. Hunter and van Straaten (2020) report a maximum depositional age from detrital zircons (U-Pb, LA-ICPMS) of 206.7 ±1.9 Ma (Rhaetian) for the onset of Hazelton Group volcanism and below we provide an U-Pb zircon CA-TIMS age of 204.61 ±0.18 Ma for phase 2 of the Big Bulk stock, which cuts basal Hazelton Group rocks. Hence, unroofing of the Stuhini Group, and the tectonics it implies, started in the Rhaetian.

4.2.2. Hazelton Group (Upper Triassic-Jurassic) volcanic-sedimentary sequences (lJHvs, lJHv)

Hornblende-feldspar phyric volcanic breccias of the lower Hazelton Group (lJHv) are exposed on the east and south sides of Kinskuch Lake and on the ridge west of the Tabletop fault. Locally, in the central part of Kinskuch Lake and east of the Tabletop fault, the base of the sequence is marked by hornblende-feldspar-rich crystal tuffs interstratified with siliciclastic sedimentary rocks (lJHvs). Southeast of the Tabletop fault, near Kinskuch Lake, these strata overlie the Kinskuch conglomerates, whereas northwest of the Tabletop fault, hornblende-feldspar volcanic breccias are in direct contact with Stuhini Group sedimentary rocks along a very low angle unconformity and intervening Kinskuch conglomerates are absent (Figs. 3, 4).

4.2.2.1. Siliciclastic sedimentary rocks with hornblende-feldspar crystal tuff

On the west side of Kinskuch Lake, unit lJHvs consists of pale-weathering, well-stratified to locally massive, coarse-grained feldspathic sandstone to siltstone with lesser pebble conglomerate, angular hornblende-feldspar-rich medium-to -coarse-grained sandstones and mudstone interstratified with hornblende-feldspar crystal tuff. The pebble conglomerates are polymictic, containing variably rounded to angular clasts of chert, argillite, sandstone, augite-phyric volcanic rocks and lesser hornblende-phyric volcanic rocks, with a wide range of sphericity, similar to the underlying Kinskuch conglomerates. Quartz is not present in any rocks. The sandstones locally show cross bedding and grading. Where this unit is exposed on Tabletop mountain, tuff interlayers are thin (0.5-10 cm) and comprise a maximum of 10% of the rock volume (Fig. 11a).

In the west-central part of the map area tuff beds are 10-40 cm thick and consist mainly of grain-supported, very coarse hornblende and feldspar (Fig. 11b). Several polymictic pebble conglomerates and pebbly sandstones (both containing clasts of limestone, thinly bedded feldspathic sedimentary rocks, and minor chert like those in the underlying Kinskuch conglomerates) are interstratified with these tuffs, suggesting a gradational, conformable contact. The base of the volcanic-sedimentary unit is defined as the first appearance of the tuff.

4.2.2.2. Andesitic volcaniclastic breccia (lJHv)

This unit consists of monomictic to locally polymictic agglomerate containing large (5-30 cm, rarely >50 cm), angular to subrounded hornblende-feldspar-phyric juvenile blocks and bombs. The breccia is matrix- to clast-supported (30-50% clasts); in some cases clasts are more strongly epidote-chlorite altered than surrounding groundmass or show rims suggesting partial resorption. The unit also includes tuff breccia and minor lapillistone with a distinctive hornblende and feldspar crystal-rich matrix (Fig. 11c). Rare feldspar±hornblende crystal tuffs and crystal-rich, volcanic-derived sandstones, with limited strike extent, are locally exposed. The volcanic rocks are cut by rare channels filled with coarse sandstones. Minor sandstone, limestone, argillite and rare augite-phyric volcanic accessory clasts are generally only observed within fifty metres of the contact with underlying Stuhini Group rocks, where they may comprise up to 30% of the clast population. They are commonly moderately to strongly chlorite-epidote altered and range from well rounded to subangular (Fig. 11d).

4.3. Intrusive rocks

4.3.1. ‘Big Bulk stock’ (latest Triassic)

The Big Bulk stock is a multiphase hornblende diorite porphyry that cuts most of the stratified rocks in the map area. Based on crosscutting relationships, we have subdivided it into four phases. Contacts between the phases generally trend east-west. Phases 2 and 3 are locally separated by an intrusive breccia unit consisting of flow-banded hornblende diorite porphyry.

4.3.1.1. Phase 1: Hornblende diorite with accessory magnetite

Phase 1 diorite is the most voluminous by mapped surface exposure and predominates on the north side of the stock. It is a crowded diorite containing approximately 15-20% plagioclase phenocrysts (1-2 mm) and 10-15% hornblende phenocrysts (2-3 mm) in a predominantly fine-grained (<1 mm) groundmass consisting primarily of plagioclase, hornblende, and accessory magnetite. Unlike subsequent phases, it does not contain diorite or vein xenoliths, but commonly contains country rock xenoliths close to external contacts. Phase 1 diorite is locally cut by minor (up to 5%) pyrite and quartz veins including quartz-magnetite±chalcopyrite veins. Veins are most abundant at the southern extent of the phase 1 exposure and are largely absent in the north. Exposures in the northwest have weak chlorite-sericite replacement of hornblende and exposures in the east locally display nearly complete quartz-sericite-pyrite replacement.

4.3.1.2. Phase 2: Quartz-chalcopyrite veined hornblende diorite porphyry

Phase 2 diorite is the least voluminous phase, based on surface exposure, and is surrounded by later phases. It is exposed primarily as two east-west trending bodies with a maximum width of 100 m. Small (10-50 m), isolated bodies of phase 2 are also exposed in the east, in phase 3 rocks. Phase 2 diorite is texturally and mineralogically similar to phase 1. It is moderately biotite-chlorite-magnetite altered (primarily replacing hornblende) with a weak to intense quartz-sericite-pyrite overprint. Quartz-sericite-pyrite alteration is commonly strongest near phase 3 contacts or close to faults.

Phase 2 is the most strongly mineralized phase and characteristically contains significant sheeted quartz-chalcopyrite±bornite±pyrite veins (Fig. 12) commonly forming an orthogonal set (Fig. 13a). The mineralized quartz veins make up 20 to 45% of the rock mass. Pyrite veins and veinlets (<1 cm wide) are locally abundant, spatially correlated with increasing quartz-sericite-pyrite alteration, and cut the quartz-chalcopyrite veins. Phase 2 contains 5% small (0.5-2 cm) xenoliths of hornblende diorite that resemble both phase 1 and phase 2 in mineralogy and texture. The xenoliths have the same alteration assemblage and intensity as the phase 2 diorite and were altered

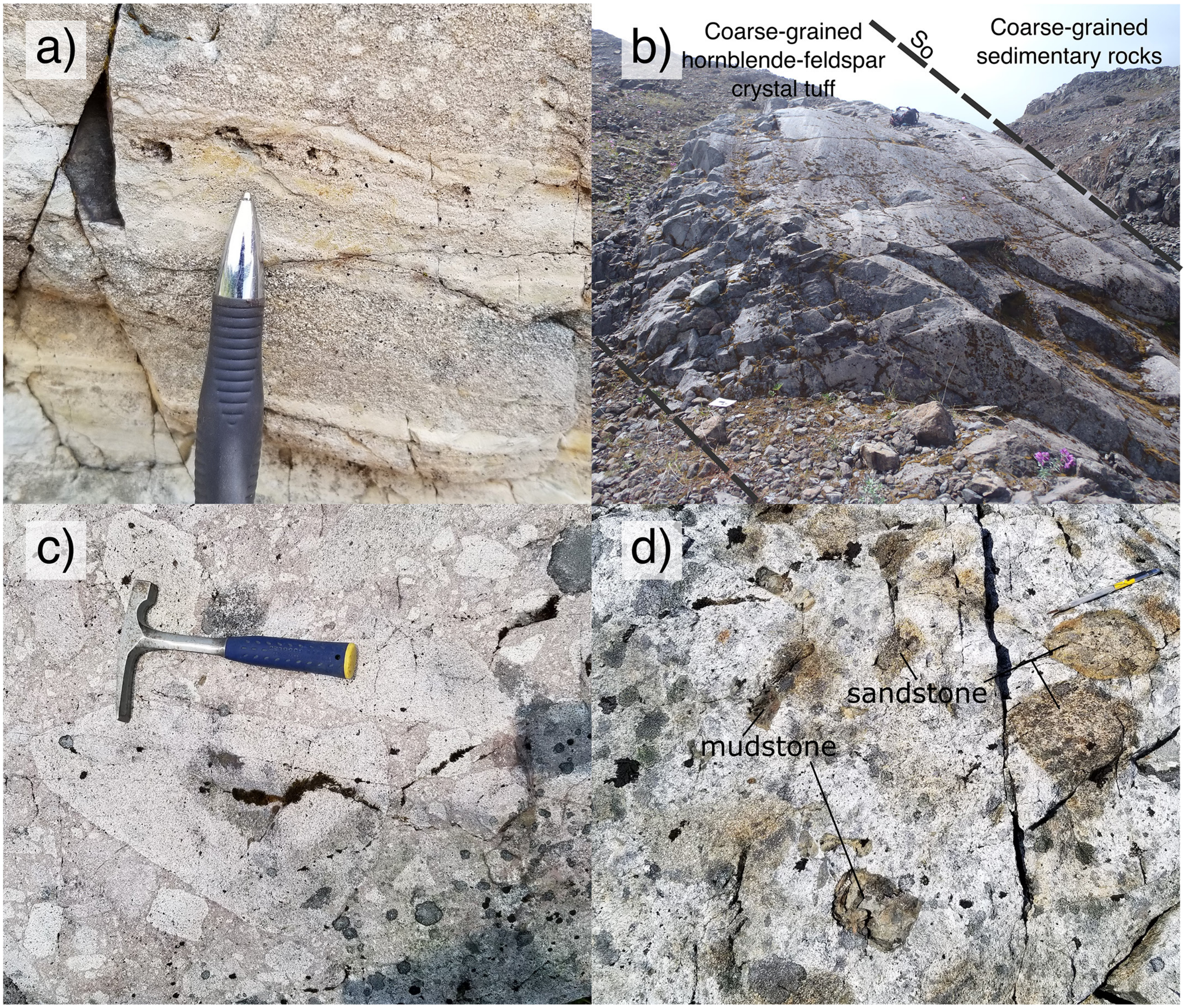

Fig. 11. Hazelton Group volcanic and sedimentary rocks. **a)** Interbedded sandstone, siltstone, and feldspar-crystal tuff younging upright, looking NE. **b)** Coarse-grained hornblende-feldspar crystal tuff interstratified with coarse-grained feldspathic sandstones and polymictic pebble conglomerates, looking northwest tops to the north. **c)** Monomictic volcanic breccia with angular poorly sorted juvenile lapilli to bombs of hornblende- feldspar- phyric intermediate volcanic rock in a similarly composed groundmass. **d)** Volcanic breccia containing juvenile hornblende-feldspar phyric volcanic blocks and lesser Stuhini Group-derived accessory clasts.

after being incorporated. A sample of phase 2 diorite returned a preliminary U-Pb zircon CA-TIMS age of 204.61 ±0.18 Ma (see below).

4.3.1.3. Flow-banded hornblende diorite porphyritic intrusive breccia

An intrusive breccia cuts phase 1 and phase 2 diorites in exposures directly south of Kinskuch Lake. Although it is compositionally similar to other phases it is texturally distinct, with a wider range of phenocrysts, including 2% to locally 15% feldspar and 1% to locally 10% hornblende in a very fine-grained, dark green, strongly chlorite to sericite-pyrite-altered flow-banded groundmass (Fig. 14a). The breccia zone contains between 10-30% xenoliths of hornblende diorite (1-30 cm), and lesser quartz±chalcopyrite vein fragments (1-2 cm). Some diorite xenoliths are much more intensely and variably altered than the groundmass, ranging from weakly to intensely quartz-sericite-pyrite altered, moderately chlorite-pyrite±sericite altered, to nearly unaltered, and some are cut by quartz-chalcopyrite veins that terminate at xenolith boundaries. Thus we infer that these xenoliths have undergone some alteration and porphyry-style veining before, or during incorporation into the intrusive breccia.

Locally, several small (1-3 m wide) clast-rich intrusive breccia and lesser quartz-cemented breccia pipes with steep east-west trending contacts cut the main, flow-banded intrusive

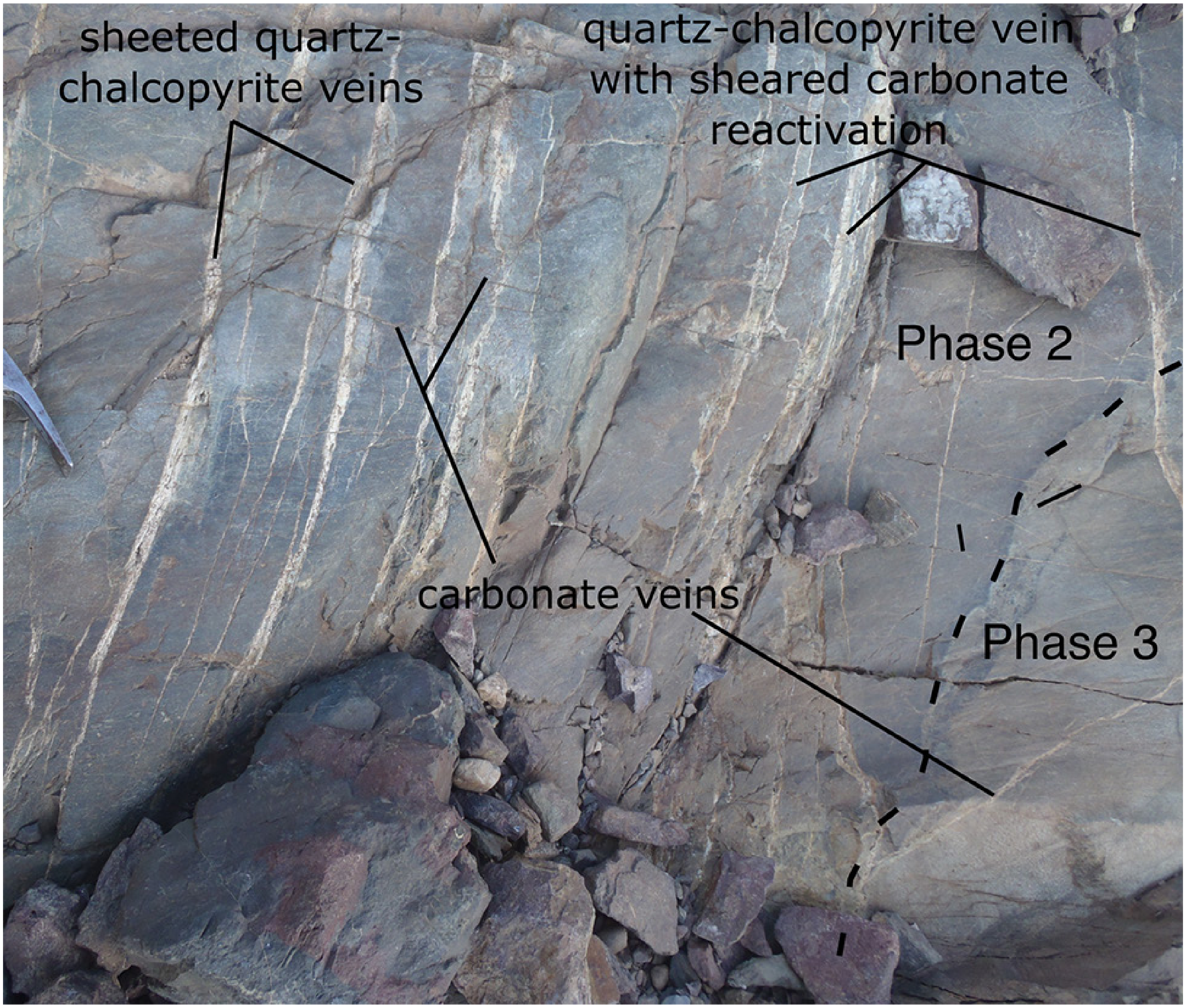

Fig. 12. Phase 2 Big Bulk hornblende diorite cut by phase 3 diorite. East-west oriented sheeted quartz-chalcopyrite veins of stage 2 mineralization in phase 2 diorite cut by thin (1-2 mm) carbonate veins. Some Stage 2 veins have carbonate cores or borders that indicate reactivation by post-mineral fluids. Top of photo is to the east.

breccias (Fig. 14b). They are not observed cutting any other phases. These small breccia pipes contain up to 50% variably altered and mineralized diorite clasts and quartz veins similar to the intrusive breccia that they cut. Very rarely, the matrix of the breccias consists of chalcopyrite-bearing quartz.

4.3.1.4. Phase 3: Hornblende diorite porphyry

Phase 3 diorite is the second most voluminous phase, based on surface exposure. It cuts phase 1, phase 2 and the intrusive breccia and has sharp east-west trending contacts commonly displaying chill margins and ripped up xenoliths of the earlier phases (Fig. 12). Most quartz-chalcopyrite veins in phase 2 diorites are abruptly cut at contacts observed with phase 3. Xenoliths of Stuhini Group and Hazelton Group country rock up to 4 m long are common within about 50 m of a contact. In its southwestern-most exposure, several dikes and sills (1-6 m wide) of phase 3 diorite intrude the surrounding bedded sedimentary rocks. The country rock in contact with phase 3 diorites is often moderately to strongly sericite-pyrite altered.

Although mineralogically and texturally similar, phase 3 is distinguished from phases 1 and 2 primarily by the scarcity of intact quartz-chalcopyrite veins (less than 2%), and the occurrence of fragmented quartz-chalcopyrite veins, and quartz-chalcopyrite veined diorite xenoliths (1-5%). The xenoliths are variably altered (predominantly weakly to strongly quartz-sericite-pyrite±chlorite with lesser moderately chlorite altered) and in most cases are more strongly altered than the diorite into which they are incorporated. Phase 3 is cut by abundant (up to 20%) stockworked pyrite veins and veinlets, most of which are less than 0.5 cm wide, although some can be as wide as 10 cm

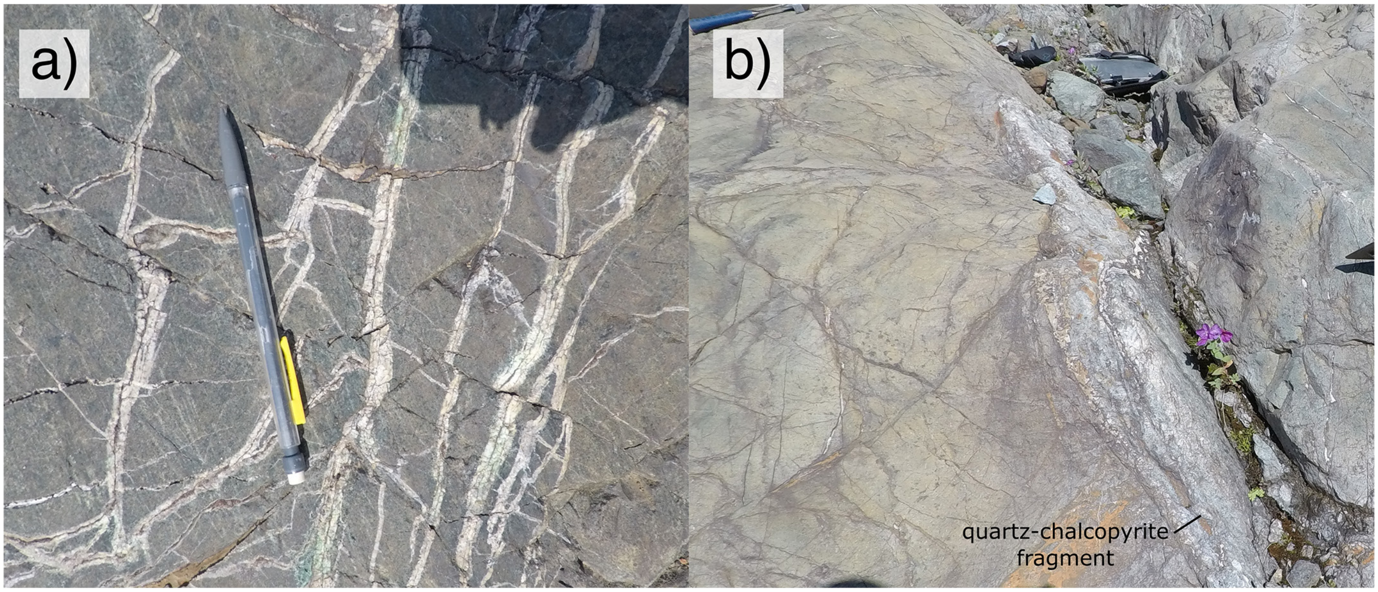

Fig. 13. Big Bulk stock stage 2 (main mineralization) and stage 3 (late mineralization) veins. **a)** Phase 2 hornblende diorite porphyry, with characteristic stage 2 sheeted to orthogonal quartz-chalcopyrite veins with sulphide-rich centres. Recessively weathering carbonate veins cut and offset porphyry related veins. **b)** Phase 3 hornblende diorite porphyry with moderate quartz-sericite-pyrite (phyllic) alteration and abundant stockworked stage 3 pyrite veins, cut by a large laminated iron-carbonate vein with sheared and brecciated quartz-chalcopyrite and massive sulphide vein fragments.

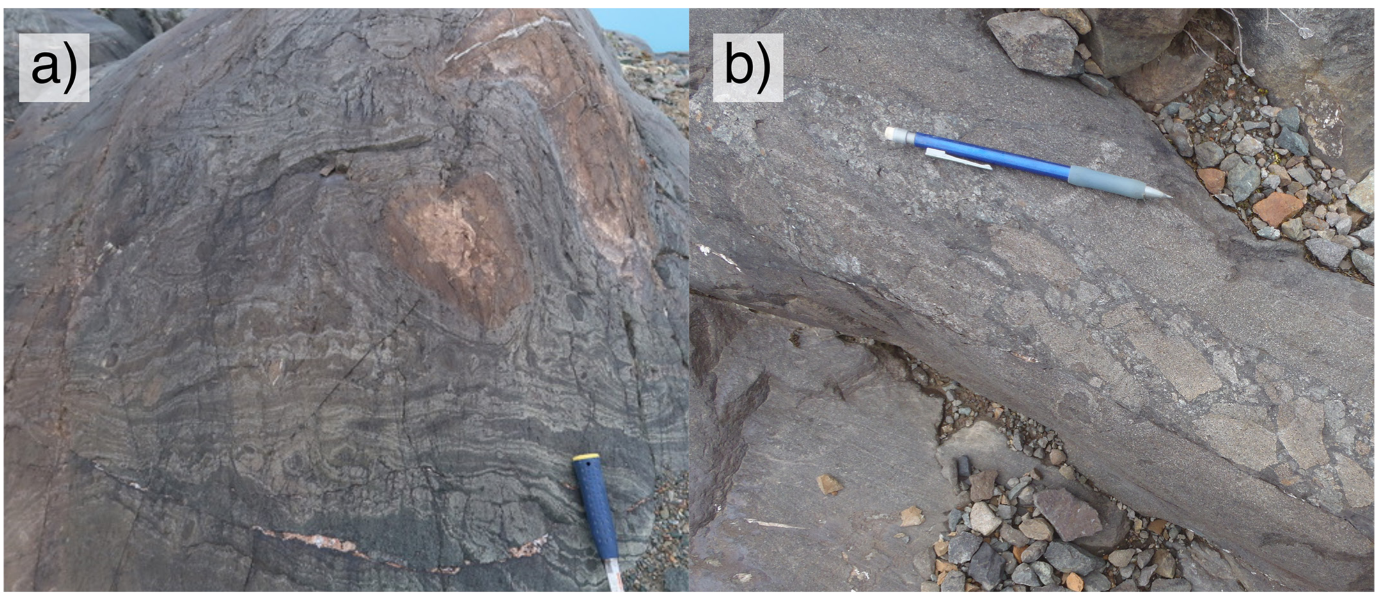

Fig. 14. Big Bulk stock intrusive breccia. **a)** Fine-grained chlorite-sericite altered flow-banded intrusion breccia with xenoliths of variably altered diorites and veins. **b)** Clast-supported intrusive breccia pipe cutting main intrusive breccia.

(Fig. 13b). These pyrite veinlets cut xenoliths and contacts between phase 3 and Phase 2 diorites.

4.3.1.5. Phase 4: Biotite-hornblende monzodiorite to monzonite

Phase 4 is the most mineralogically and texturally distinct of the Big Bulk phases. It is an equigranular to weakly hornblende porphyritic fine- to medium-grained hornblende±biotite monzodiorite to monzonite. It cuts phase 3 at the southern margins of the Big Bulk stock with sharp intrusive contacts. The contacts are commonly visible from a distance, marked by an abrupt decrease in alteration from the rusty weathering of pyrite-rich phase 3 to grey to green weathering of phase 4. Phase 4 monzodiorites are mostly unaltered with local weak to moderate chlorite±epidote alteration of hornblende. Weak quartz-sericite-pyrite alteration, with at most 2% disseminated pyrite, is locally observed close to crosscutting faults. It contains rare (<2%) xenoliths of quartz-chalcopyrite vein-bearing and strongly quartz-sericite-pyrite altered diorites but is otherwise unmineralized.

4.4. Late dikes (Eocene?)

Two distinct suites of nearly unaltered dikes, thought to belong to the Eocene Hyder suite, cut all Triassic-Jurassic rocks and reverse faults in the map area. They are locally offset by steep, dextral brittle faults with m-scale displacement. The two suites display similar orientations: steep to subvertical trending roughly north-south or east-west, and are traceable for up to 1 km along strike. Intermediate biotite-hornblende-feldspar porphyry dikes and stocks are the most prominent and are up to 10 m wide. They contain fine- to medium-grained lathes and needles of hornblende and feldspar in a very fine-grained groundmass. The second suite are dark green to brown weathering mafic dikes up to 5 m wide. They are aphanitic with rare very fine-grained hornblende±feldspar needles as phenocrysts, or calcite-filled amygdules.

5. Structure

The most prominent structures in the Kinskuch Lake area are northerly trending faults and folds (Figs. 3, 15). The map-scale faults are typically expressed as pronounced lineaments (Figs. 16a, b). The east side of Kinskuch Lake has abundant moderately to shallowly, generally west- to northwest-dipping imbricated thrust faults (Figs. 3, 16c) that cut all Triassic to Jurassic units, porphyry related-veins and alteration in the map area. The thrust faults are commonly lined with sheared iron-carbonate±calcite±barite veins and clasts (Fig. 16d), similar to other faults in the region considered to be Cretaceous (see Febbo et al., 2019). Folds related to thrust faults have northeast-trending hinge lines, moderately west-dipping axial surfaces and verge to the east, commonly with overturned eastern limbs (Fig. 15).

In the western part of the map area, the faults are primarily steeply dipping, mainly northeast-trending dextral strike-slip structures such as the Tabletop fault, and east-trending, steeply dipping, south-side-up and north-side-up oblique-slip faults, such as the ‘central lake fault’ (Fig. 3). Folds with m-scale wavelengths and east-west striking, moderately dipping axial surfaces are spatially associated with east-trending faults.

Most of the map-scale folds are asymmetric, tight to open, inclined steeply to moderately to the west, and doubly plunging. Many of the map-scale folds are associated with faults, with axial traces oriented northeast-southwest near Tabletop fault to nearly north-south to northeast-southwest in the central lake area (Fig. 3). Minor, m- to dm-scale tight folds are restricted to fine-grained sedimentary units, commonly paired with minor faults with similar orientation to larger scale folds. These folds are rounded and typically have strongly fractured hinges and axial planar faults. In calcareous rocks, calcite veins are common in the hinge zones. Broad open northeast-trending folds west of the Tabletop fault (Figs. 3, 15a) have axial traces that are oblique to the fault, consistent with dextral strike slip.

Axial planar cleavage is only locally developed as a spaced fracture cleavage in fine-grained sedimentary rocks and absent in most other rock types. However, cleavage is well-developed in strongly phyllic-altered rocks in the Big Bulk deposit. Shear zones, especially in strongly quartz-sericite-pyrite altered rocks in the Big Bulk deposit (Fig. 16c) also have well-developed foliation.

6. Geochronology: Big Bulk stock, phase 2

We collected a sample of the Big Bulk stock phase 2 diorite for U-Pb single-zircon chemical abrasion thermal ionization mass spectrometry (CA-TIMS) geochronology. The analytical work was carried out by Richard Friedman at the Pacific Centre for Isotopic and Geochemical Research (University of British Columbia); detailed methods and results will be presented elsewhere. Preliminary results indicate a young concordant group of zircons that are tentatively interpreted as primary magmatic grains recording a crystallization age of 204.61 ±0.18 Ma (Fig. 17; Table 1). Intriguingly, three of the eight grains analyzed yielded concordant Paleozoic $^{207}Pb/^{206}Pb$ ages (ca. 456-400 Ma) ages. Likely xenocrysts, these older grains provide a window into the nature of basement to Stikinia.

7. Mineralization, and veins at the Big Bulk prospect

7.1. Stage 1: Early mineralization

The earliest porphyry-related veins recognized are mutually crosscutting quartz-magnetite±chalcopyrite±pyrite veins (0.5-1 cm wide) and lesser braided magnetite veinlets (<1 mm) with 1-2 mm wide magnetite-quartz alteration selvages. Both vein types are rare, making up at most 2% of the rock volume. The quartz veins have fine-grained magnetite and sulphide-rich centres. These veins are in phase 1 and 2 diorites and rarely in Hazleton Group volcanic rocks in contact with phase 1 diorites. They are cut by all other vein types.

7.2. Stage 2: Main-phase mineralization

Stage 2 is marked by moderate to strong quartz-sericite-chlorite-biotite alteration and rare potassic feldspar. Remnant secondary biotite is generally only recognizable where later stages of alteration are very weak. Stage 2 veins contain quartz-chalcopyrite±pyrite±bornite and have sulphide-rich centres. Stage 2 veins occur as steeply dipping, sheeted veins (Fig. 12) or form orthogonal sets with northwest and east-northeast trends (Figs. 13a, 18a). Stage 2 veins typically have sharp, planar contacts, but are locally discontinuous and tightly anastomosing, with diffuse boundaries. Stage 2 veins cut phase 1 and 2 diorites. In phase 3 diorite, quartz-chalcopyrite veins occur mostly as xenoliths with few quartz-chalcopyrite veins, suggesting that only minor main-mineralizing phase fluid circulation persisted after intrusion of phase 3 diorites. Quartz-chalcopyrite veins occur as, or within, rare xenoliths within phase 4 monzodiorites.

7.3. Stage 3: Late stage-mineralization

Pyritic veinlets (<1 mm) and veins (1-10 cm) cut stage 1 and stage 2 veins and are associated with strong to intense quartz-sericite-pyrite (QSP) alteration that is commonly pervasive and mineralogically and texturally destructive. They cut all Big Bulk phases, except the phase 4 monzodiorites, and are

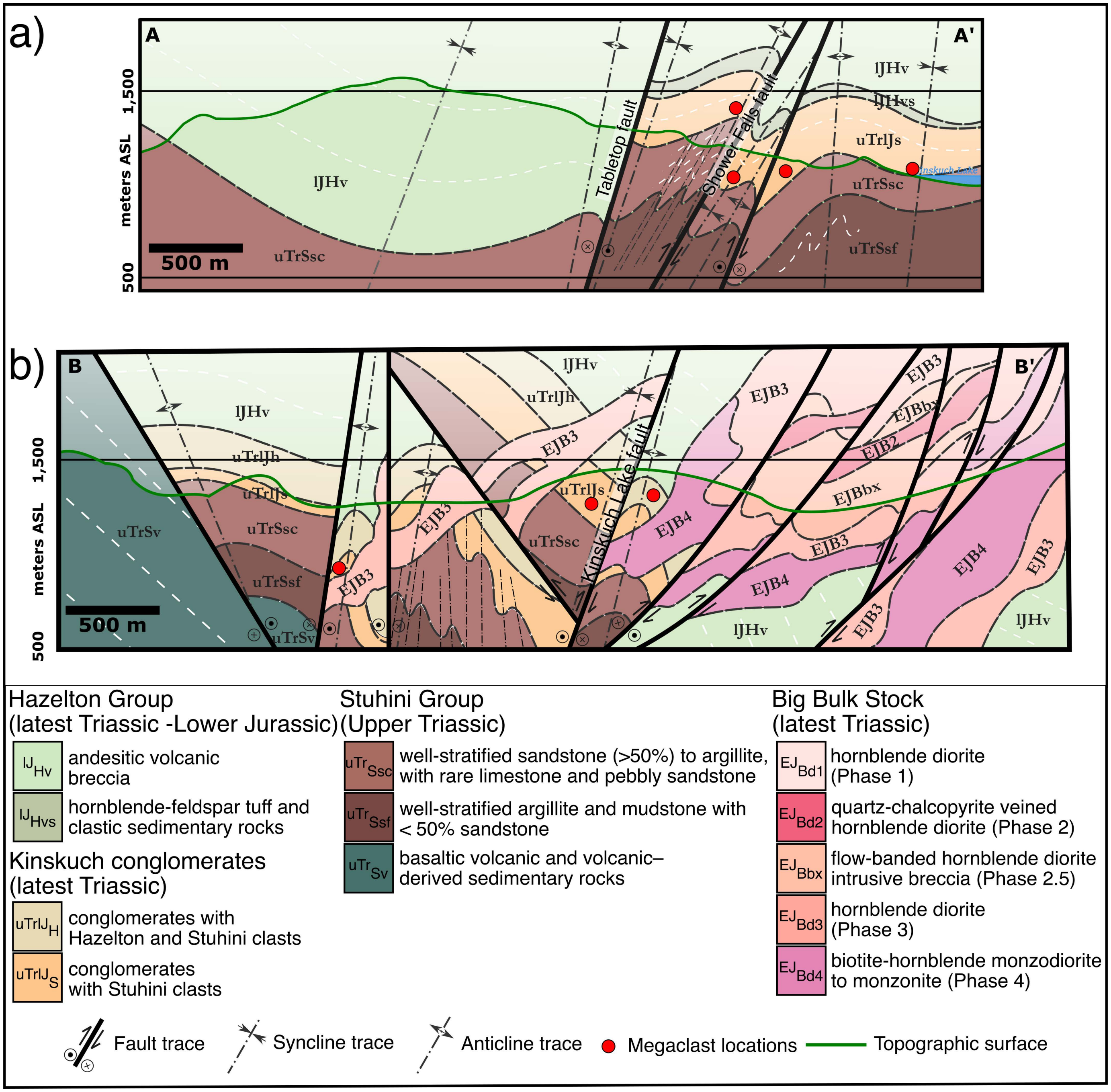

Fig. 15. Structural cross sections (see Fig. 2 for locations). **a)** Section A-A' shows paired faults and folds typical on the western side of the lake. The transitional conglomerates are only developed east of the Tabletop fault; to the west hornblende-feldspar Hazelton Group volcanic breccias are in direct contact with Stuhini Group sedimentary rocks along a very low angle unconformity and intervening transitional conglomerates are absent. **b)** Section B-B' shows the transition from paired folds and faults in stratified units in the west to the imbricate thrust-faulted and tilted Big-Bulk stock to the east.

particularly abundant in and surrounding phase 3 diorites (up to 20%). The veins range from planar to anastomosing and generally form stockworks (Fig. 13b).

7.4. Post-mineral veins

Iron-carbonate±barite and calcite veins (0.2-30 cm wide) are common in the map area and cut all Triassic and Jurassic units as well as all stage 1 through 3 veins (Fig. 13).

8. Discussion

8.1. Latest Triassic to Early Jurassic tectonics and sedimentation

The Kinskuch conglomerates mark a fundamental break in the tectonic history of the region. Thick conglomeratic sections demand topographic relief to expose source rocks to erosional levels and create accommodation space for preservation. This relief is best generated by syndepositional faults. The megaclast-

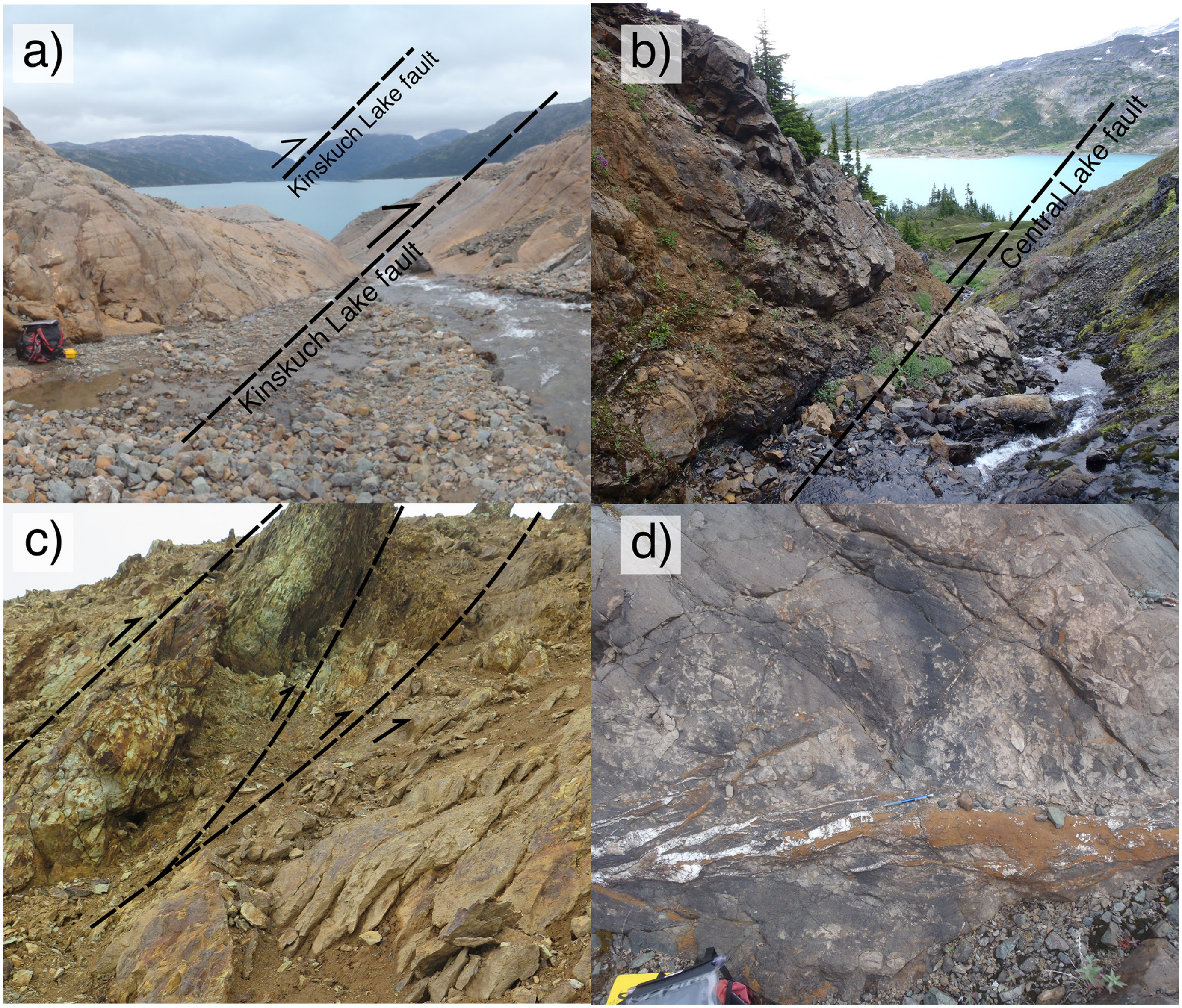

Fig. 16. Typical faults in the map area. **a)** View to the north of the northeast-trending, moderately west-dipping Kinskuch Lake thrust fault cutting Big Bulk diorite. **b)** View to the east of the east-trending central lake fault, which juxtaposes coarse-grained well-stratified sandstone southward above megaclast-bearing Kinskuch conglomerate containing mainly Stuhini Group-derived clasts. **c)** Thrust imbricates in intensely quartz-sericite-pyrite altered hornblende diorite (Big Bulk stock phase 3) with well-developed cleavage. **d)** Iron-carbonate fill spatially related to east-vergent reverse faults on the eastern side of the map area.

bearing conglomerates are particularly significant and were likely deposited immediately adjacent to syndepositional fault scarps. Progressive stripping to deeper parts of the subjacent Stuhini Group section, as recorded by bottom-to-top clast compositions that yield an inverse stratigraphy, signifies approximately 400 m or more, of Stuhini Group unroofing (Figs. 19, 20). Conodonts recovered from a limestone megaclast derived from the Stuhini Group are Rhaetian, providing a limit to the onset of faulting. Faulting continued during deposition of the Hazelton Group, as indicated by intraformational clasts and by interbedding of the conglomerates and basal Hazelton tuffs. The onset of Hazelton Group volcanism in the area is constrained by a U-Pb detrital zircon maximum depositional age of 206.7 ±1.9 Ma (Hunter and van Straaten, 2020) from rocks a few km north of Kinskuch Lake. Phase 2 of the Big Bulk stock, which cuts the basal Hazelton Group, has a U-Pb zircon crystallization age of 204.61 ±0.18 Ma (this paper). Thus, like elsewhere in northwestern Stikinia (see below), the Rhaetian (ca. 208-201 Ma; Cohen et al., 2013) witnessed the demise of the Stuhini arc and a major tectonic and magmatic reorganization.

The conglomerates are notably absent west of the Tabletop fault, leading us to suggest that it is a long-lived structure with an early southeast-side down history that led to unroofing of the Stuhini Group. Furthermore, the large megaclasts of limestone and chert are found close to the present position of east-west

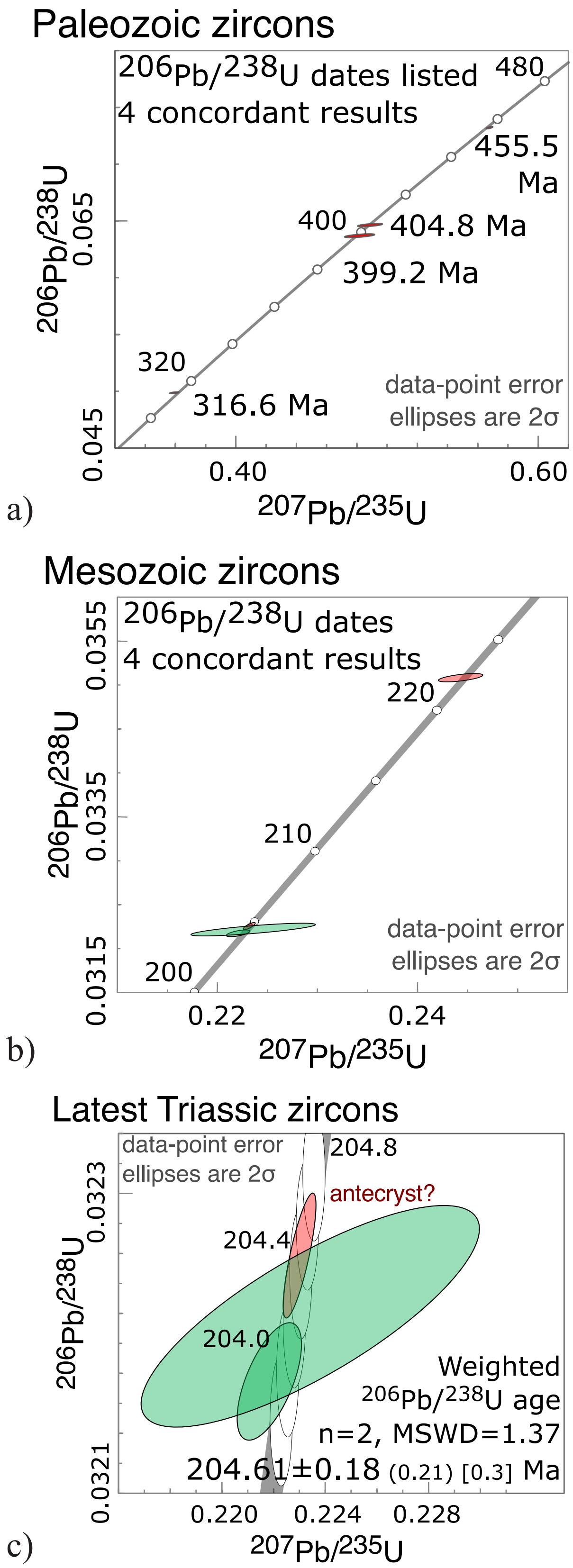

Fig. 17. Concordia plots for CA-TIMS U-Pb analysis of zircons from phase 2 diorite of the Big Bulk stock. **a)** Paleozoic xenocrystic grains. **b)** Mesozoic xenocrystic grains. **c)** Latest Triassic grains yielding a preliminary crystallization age of 204.61 ±0.18 Ma.

trending faults (e.g., 'shower falls' and 'central lake'; Figs. 3, 19), and we speculate they too may have been active during sedimentation to generate significant topographic relief. If so, younger Cretaceous fold and thrust belt deformation has reactivated, inverted, and likely reoriented many of the faults that would have been active during this time, obscuring original kinematics and displacement. We propose that the Tabletop fault and likely other northeast-trending faults in the area had an early (latest Triassic) history with strike-slip or oblique movement, and that releasing step-overs, splays, or double bends in this fault network created local zones of north-south extension, easterly trending normal faults, and local pull-apart basins into which the Kinskuch conglomerates were deposited. Consistent with the notion of local north-south extension and east-west trending normal faults, the Big Bulk phases of intrusion are more or less tabular, with an overall east-west orientation, and the sheeted veins of the main stage porphyry also have an east-west orientation.

8.2. Regional tectonic and metallogenic implications

Similar evidence for latest Triassic to Early Jurassic syndepositional faulting and deposition of conglomeratic rocks has been reported in the KSM and Bronson areas (Nelson and Kyba, 2014; Kyba and Nelson, 2015; Febbo et al., 2019), suggesting widespread, latest Triassic tectonic instability throughout much of the Stewart-Iskut district during the transition from the Stuhini Group to the Hazelton Group. This transition appears to be broadly coeval with latest Triassic to Early Jurassic deformation in the Stewart-Iskut district (e.g., Logan and Koyanagi, 1994; Brown et al., 1996) and is also broadly coeval with uplift and erosion of Stikine plutonic suite batholiths (Late Triassic; Brown et al., 1996; van Straaten and Nelson, 2016). U-Pb detrital zircon studies show that erosion of these batholiths shed detrital material into successions as old as latest Triassic basal Hazelton Group (Nelson et al., 2018; Hunter and van Straaten, 2020).

More regionally, the demise of the Quesnellia-Stikinia (Nicola-Stuhini) magmatic arcs in the Late Triassic is marked by arc uplift and local picritic magmatism, and followed by a period of prolific porphyry Cu emplacement in the latest Triassic to earliest Jurassic (Logan and Mihalynuk, 2014). Work in districts with young porphyry systems, where sea-floor bathymetry can be used to infer the architecture of subducting slabs, suggests that porphyry formation is commonly temporally associated with the subduction of aseismic ridges, seamount chains, and oceanic plateaus (Cooke et al., 2005). Furthermore, it has been suggested that subduction of such features may cause conditions favourable for porphyry emplacement through two primary mechanisms:1) high-volume hydrous melt production within the mantle wedge followed by; 2) the development of local zones of extension that allow magmas to ascend (Richards et al., 2001; Richards, 2003; Cooke et al., 2005; Bertrand et al., 2014)

Logan and Mihalynuk (2014) proposed that subduction of an interarc complex, the Sitlika-Kutcho-Venables arc, resulted

Table 1. TIMS U-Pb zircon results and methods.

	Compositional Parameters									Radiogenic Isotope Ratios								Isotopic Ages					
Sample	Wt. mg	U ppm	Pb ppm	Th/U	$^{206}Pb^*$ x10^{-13} mol	mol % $^{206}Pb^*$	Pb^*/Pb_c	Pb_c (pg)	$^{206}Pb/^{204}Pb$	$^{208}Pb/^{206}Pb$	$^{207}Pb/^{206}Pb$	% err	$^{207}Pb/^{235}U$	% err	$^{206}Pb/^{238}U$	% err	corr. coef.	$^{207}Pb/^{206}Pb$	±	$^{207}Pb/^{235}U$	±	$^{206}Pb/^{238}U$	±
(a)	(b)	(c)	(c)	(d)	(e)	(e)	(e)	(e)	(f)	(g)	(g)	(h)	(g)	(h)	(g)	(h)		(i)	(h)	(i)	(h)	(i)	(h)
2-1	0.0050	22	1.4	0.323	0.2878	98.65%	21	0.32	1371	0.102	0.05489	1.499	0.4835	1.617	0.06389	0.199	0.634	408	34	400.5	5.4	399.23	0.77
2-2	0.0023	108	9.3	0.918	0.7593	99.54%	73	0.29	4043	0.288	0.05611	0.232	0.5664	0.295	0.07321	0.105	0.708	456.7	5.2	455.7	1.1	455.47	0.46
2-7	0.0022	26	1.8	0.515	0.1552	98.02%	15	0.26	936	0.162	0.05485	1.216	0.4901	1.316	0.06481	0.169	0.630	406	27	405.0	4.4	404.81	0.66
2-8	0.0022	57	3.1	0.406	0.2657	98.65%	22	0.30	1375	0.128	0.05262	0.600	0.3652	0.662	0.05034	0.114	0.610	312	14	316.1	1.8	316.63	0.35
2-9	0.0017	258	9.9	0.955	0.5713	99.29%	48	0.34	2612	0.304	0.05006	0.381	0.2221	0.435	0.03218	0.097	0.629	197.6	8.9	203.64	0.80	204.16	0.20
T-3	0.0069	373	12.8	0.571	3.4628	99.89%	291	0.30	17434	0.181	0.05018	0.150	0.2232	0.221	0.03226	0.103	0.806	203.3	3.5	204.56	0.41	204.67	0.21
3-2	0.0006	360	13.3	0.358	0.3164	98.49%	19	0.40	1228	0.114	0.05050	0.678	0.2443	0.741	0.03509	0.111	0.619	218	16	221.9	1.5	222.31	0.24
3-7	0.0007	165	7.5	1.591	0.1547	97.86%	18	0.28	864	0.506	0.05033	2.130	0.2236	2.271	0.03222	0.184	0.789	210	49	204.9	4.2	204.43	0.37

(a) 1, 2 etc. are labels for fractions composed of single zircon grains or fragments; all fractions annealed and chemically abraded after Mattinson (2005) and Scoates and Friedman (2008).
(b) Nominal fraction weights estimated from photomicrographic grain dimensions, adjusted for partial dissolution during chemical abrasion.
(c) Nominal U and total Pb concentrations subject to uncertainty in photomicrographic estimation of weight and partial dissolution during chemical abrasion.
(d) Model Th/U ratio calculated from radiogenic $^{208}Pb/^{206}Pb$ ratio and $^{207}Pb/^{235}U$ age.
(e) Pb* and Pbc represent radiogenic and common Pb, respectively; mol % $^{206}Pb^*$ with respect to radiogenic, blank and initial common Pb.
(f) Measured ratio corrected for spike and fractionation only. Mass discrimination of 0.25 ± 0.04%/amu based on analysis of NBS-982; all Daly analyses.
(g) Corrected for fractionation, spike, and common Pb; all common Pb was assumed to be procedural blank: $^{206}Pb/^{204}Pb$ = 18.50±1.0%; $^{207}Pb/^{204}Pb$ = 15.50±1.0%; 208Pb/204Pb = 38.40±1.0% (±1σ).
(h) Errors are 2σ, propagated using the algorithms of Schmitz and Schoene (2007) and Crowley et al. (2007).
(i) Calculations are based on the decay constants of Jaffey et al. (1971). $^{206}Pb/^{238}U$ and $^{207}Pb/^{206}Pb$ ages corrected for initial disequilibrium in $^{230}Th/^{238}U$ using Th/U [magma] = 3.

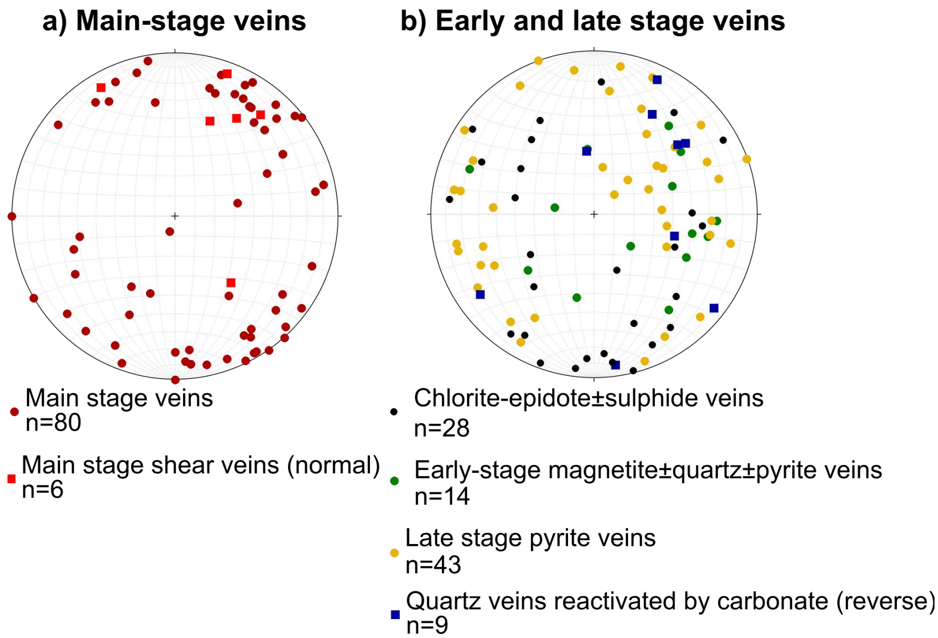

Fig. 18. Equal area stereonets showing poles to porphyry-related veins with interpreted relative timing. Note the contrast between the sheeted/orthogonal main-stage veins and the stockworked early and late-stage veins. **a)** Main-stage extensional quartz-chalcopyrite+/-pyrite veins show two main orientations: NW-SE and E-S to NE-SW. Shear veins of identical mineralogy display down-dip motion. **b)** Early veins (magnetite-bearing), late-stage veins (massive sulphide) and veins with propylitic (epidote-chlorite-pyrite) assemblages of indeterminate timing have no discernable preferred orientation.

in buoyancy-driven stalling of subduction and arc-parallel tearing of the slab. The slab-tear associated with subduction of the Kutcho-Venables-Sitlika primitive arc resulted in the ingress of hot subslab mantle into the hydrated mantle wedge. Accordingly, this promoted extensive partial melting followed by lower degree partial melts that are associated with porphyry formation as the thermal perturbation decayed. Logan and Mihalynuk (2014) emphasised the role that orogen-parallel and transverse structures played in localizing porphyry deposits in Stikinia and Quesnellia.

Consistent with the perturbed subduction model proposed by Logan and Mihalynuk (2014), we suggest that oblique plate convergence during stalled subduction led to enhanced strain partitioning and inboard strike slip (e.g., Teyssier et al., 1995). Accordingly, local zones of extension related to this strike slip led to the formation of small pull-apart basins and permitted the ascent of magmas that formed Late Triassic porphyry deposits like the Big Bulk prospect.

9. Conclusions

Coarse conglomerates at the base of the Hazelton Group at Kinskuch Lake preserve evidence of syndepositional faulting and unroofing of the Stuhini Group in the latest Triassic. The prominent northeast-trending Tabletop fault bounds these conglomerates and defines the western edge of a high-relief depocenter in which conglomerates, including 120 m-scale megaclasts, accumulated. Systematic changes in clast size and composition within the conglomerates are related to syndepositional faults. We propose that in the latest Triassic, the Tabletop fault was a northeast-trending strike-slip or oblique-slip fault and that subordinate east-west faults were generated in releasing step-overs or splays between it and other faults in the area. Syndepositional faulting is constrained to the Rhaetian (latest Triassic) from conodonts reported from a limestone megaclast in the conglomerates, a U-Pb zircon detrital maximum depositional age of 206.7 ±1.9 Ma from basal Hazelton (Hunter and van Straaten, 2020) and the cross-cutting relationships between the Big Bulk stock (204.61 ±0.18 Ma, this paper) and the conglomerates. The east-west trend of the multiphase Big Bulk diorite stock, which hosts porphyry Cu-Au mineralization in sheeted quartz-chalcopyrite veins, is consistent with north-south extension during porphyry emplacement.

We suggest that latest Triassic to earliest Jurassic local basin formation in proximity (temporally and spatially) to porphyry systems is consistent with the stalled subduction model proposed by Logan and Mihalynuk (2014). Local extensional regimes and fault systems may have promoted and focussed the ascent of magmas associated with latest Triassic to early Jurassic porphyry Cu mineralization in northwestern British Columbia.

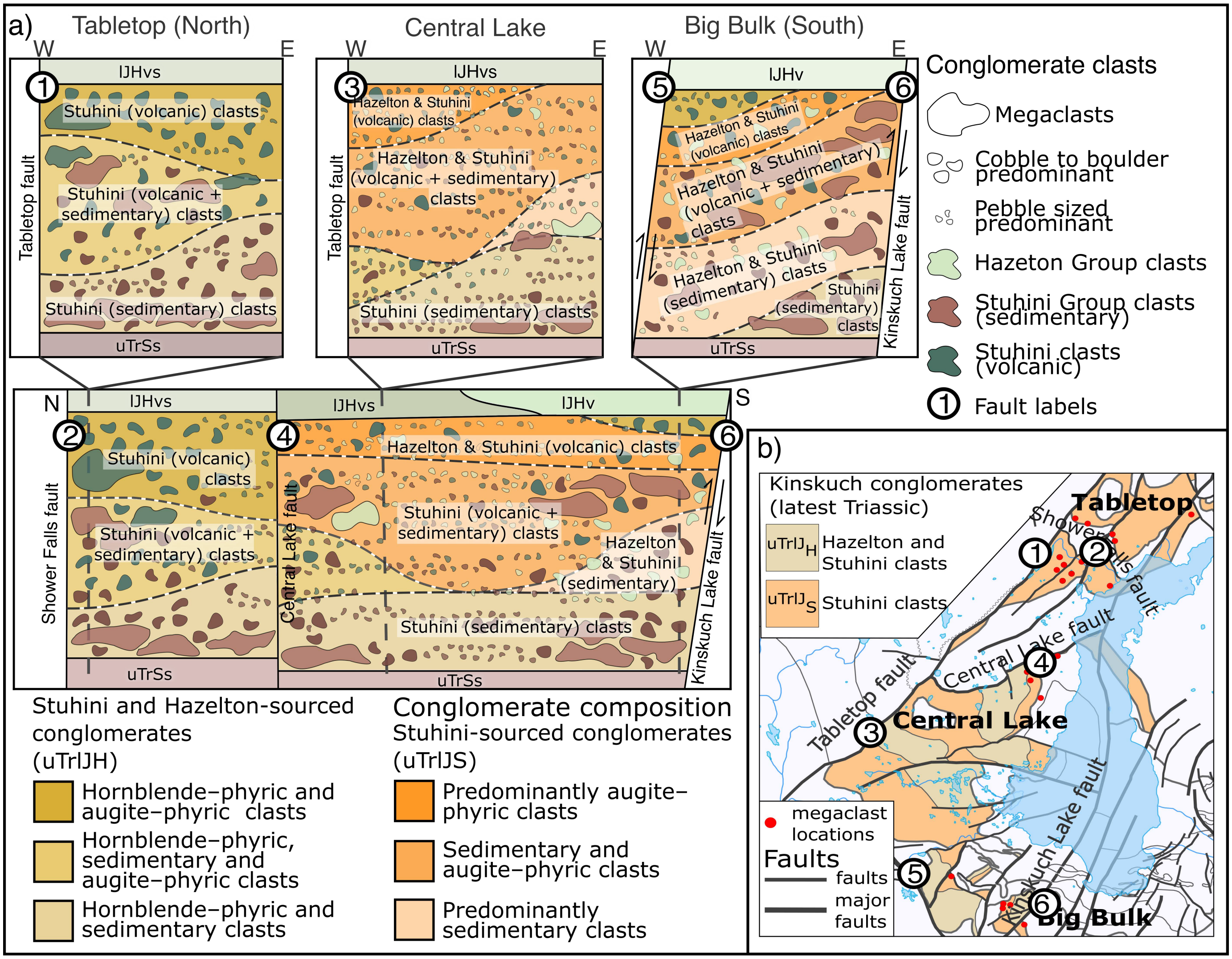

Fig. 19. Stratigraphic variation of clast compositions in the Kinskuch conglomerates. Contacts between conglomerates of different clast composition are presented as 6 main units to highlight the systematic vertical and lateral variation in clast content. **a)** At top, schematic stratigraphic section illustrating variations from east to west (relative to north-south trending faults); at bottom, schematic stratigraphic section illustrating variations from north to south (relative to east-west trending faults). **b)** Transitional conglomerate distribution in map view with locations and fault references for the stratigraphic sections presented in a).

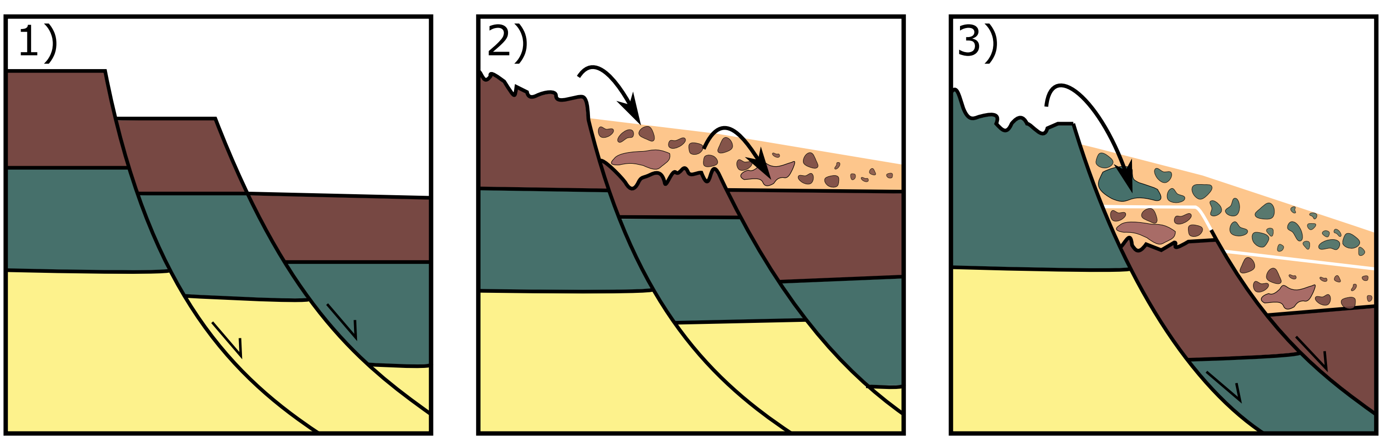

Fig. 20. Schematic diagram for generating the inverse stratigraphy recorded by clast compositions in the Kinskuch conglomerate by incision of the Stuhini Group to progressively deeper levels.

Acknowledgments

Funding for this research was provided by a Natural Resources Canada-Targeted Geoscience Initiative Grant to Lori Kennedy and Bram van Straaten, a 2018 Geoscience BC scholarship to Emily Miller, and a Mitacs grant in conjunction with Dolly Varden and Norra Minerals. This project would not have been possible without the generous in-kind support provided by Dolly Varden Silver Corp., Norra Minerals, and Hecla Mining Company. Hayley McIntyre and Gayle Febbo generously provided their field descriptions, maps, and GIS data from work completed at Big Bulk during the 2017 field season. The authors deeply appreciate the very helpful reviews by Lawrence Aspler and JoAnne Nelson, which undoubtably led to a significantly better manuscript.

References cited

Alldrick, D.J., 1993. Geology and metallogeny of the Stewart mining camp, British Columbia. British Columbia Ministry of Energy, Mines and Petroleum Resources Bulletin No. 85, 105 p.

Alldrick, D.J., Dawson, G.L., Bosher, J.A., and Webster, I.C.L., 1986. Geology of the Kitsault river area (NTS 103P), British Columbia Ministry of Energy, Mines and Petroleum Resources, British Columbia Geological Survey, Open File 1986-02, 1:50,000 scale.

Barresi, T., Nelson, J.L., Dostal, J., and Friedman, R., 2015. Evolution of the Hazelton arc near Terrace, British Columbia: stratigraphic, geochronological, and geochemical constraints on a Late Triassic - Early Jurassic arc and Cu-Au porphyry belt. Canadian Journal of Earth Sciences, 52, 466-494.

Bertrand G., Guillou-Frottier, L., and Loiselet, C., 2014. Distribution of porphyry copper deposits along the western Tethyan and Andean subduction zones: Insights from a paleotectonic approach. Ore Geology Reviews, 60, 174-190.

Brown, D.A., Gunning, M.H., and Greig, C.J., 1996. The Stikine project: Geology of western Telegraph Creek map area, northwestern British Columbia. British Columbia Ministry of Employment and Investment, British Columbia Geological Survey Bulletin 95, 175 p.

Cloos, M., and Sapiie, B., 2013. Porphyry copper deposits: strike-slip faulting and throttling cupolas. International Geology Review, 55, 43-65.

Cohen, K.M., Finney, S.C., Gibbard, P.L., and Fan, J.-X., 2013. The ICS international chronostratigraphic chart (updated, v. 2019/05), 36, 199-204.

Colpron, M., and Nelson, J., 2011. A digital atlas of terranes for the northern Cordillera, BC. Ministry of Energy, Mines and Petroleum Resources, British Columbia Geological Survey, GeoFile 2011-11.

Cooke D.R., Hollings, P., and Walshe, J.L., 2005. Giant porphyry deposits: Characteristics, distribution, and tectonic controls. Economic Geology, 100, 801-818.

Cordey, F., Greig, C.J., and Orchard, M.J., 1992. Permian, Triassic, and Middle Jurassic microfaunal associations, Stikine terrane, Owegee and Kinskuch areas, northwestern British Columbia. In: Current Research Part E, Geological Survey of Canada Paper 92-1E, pp. 107-116.

Edwards, B.R., and Russel, J.K., 2000, Distribution, nature, and origin of Neogene-Quaternary magmatism in the northern Cordilleran volcanic province, Canada. Geological Survey of America Bulletin, 112, 1280-1295.

Evenchick, C.A., 2000. Northeast-trending folds in the western Skeena Fold Belt, northern Canadian Cordillera: a record of Early Cretaceous sinistral plate convergence. Journal of Structural Geology, 23, 1123-1140.

Evenchick, C.A., McMechan, M.E., McNicoll, V.J., and Carr, S.D., 2007. A synthesis of the Jurassic-Cretaceous tectonic evolution of the central and southeastern Canadian Cordillera: exploring links across the orogen, In: Sears, J.W., Harms, T.A., Evenchick, C.A., (Eds.), Whence the mountains? Inquiries into the evolution of orogenic systems: A volume in Honor of Raymond A. Price. Geological Society of America Special Paper 433, pp. 117-145.

Febbo, G.E., Kennedy, L.A., Nelson, J.L., Savell, M.J., Campbell, M.E., Creaser, R.A., Friedman, R.M., van Straaten, B.I., and Stein, H.J., 2019. The evolution and structural modification of the supergiant Mitchell Au-Cu porphyry, northwestern British Columbia. Economic Geology, 114, 303-324.

Gagnon, J.-F., Barresi, T., Waldron, J.W.F., Nelson, J.L., Poulton, T.P., Cordey, F., and Colpron, M., 2012. Stratigraphy of the upper Hazelton Group and the Jurassic evolution of the Stikine terrane, British Columbia. Canadian Journal of Earth Sciences, 49, 1027-1052.

Golding, M.L., Orchard, M.J., and Zagorevski, A., 2017. Conodonts from the Stikine Terrane in northern British Columbia and southern Yukon. Geological Survey of Canada Open File 8278, 23 p.

Gow, P.A., and Walshe, J.L., 2005. The role of pre-existing geologic architecture in the formation of giant porphyry-related Cu-Au deposits: Examples from New Guinea and Chile. Economic Geology, 100, 819-833.

Greig, C.J., 1992. Fieldwork in the Oweegee and Snowslide ranges and Kinskuch Lake area, northwestern British Columbia. In: Current Research, Part A, Geological Survey of Canada Paper 1992-1A, pp. 145-156.

Greig, C.J., Cordey, F., and Orchard, M.J., 1995. Tectonic Significance of Early Permian to Late Triassic radiolarian cherts, Kinskuch Lake-Cambria Icefield area, SE of Stewart, NW BC; GAC/MAC annual meeting, Victoria '95, Program and abstracts, A38.

Hunter, R.C., and van Straaten, B.I., 2020. Preliminary stratigraphy and geochronology of the Hazelton Group, Kitsault River area, Stikine terrane, northwest British Columbia. In: Geological Fieldwork 2019, British Columbia Ministry of Energy, Mines, and Petroleum Resources, British Columbia Geological Survey Paper 2020-1, pp. 101-118.

Kyba, J., and Nelson, J., 2015. Stratigraphic and tectonic framework of the Khyber-Sericite-Pins mineralized trend, lower Iskut River, northwest British Columbia. In: Geological Fieldwork 2014, British Columbia Ministry of Energy, Mines and Petroleum Resources, British Columbia Geological Survey Paper 2015-1, pp. 41-58.

Logan, J.M., and Koyanagi, V.M., 1994. Geology and mineral deposits of the Galore Creek area, northwestern British Columbia (104G/3 and 4). British Columbia Ministry of Energy, Mines and Petroleum Resources, British Columbia Geological Survey Bulletin 92, 96 p.

Logan, J.M., and Mihalynuk, M.G., 2014. Tectonic controls on early Mesozoic paired alkaline porphyry deposit belts (Cu-Au±Ag-Pt-Pd-Mo) within the Canadian Cordillera. Economic Geology, 109, 827-858.

Logan, J.M., Drobe, J.R., and McClelland, W.C., 2000. Geology of the Forest Kerr-Mess Creek area, northwestern British Columbia. British Columbia Ministry of Energy, Mines and Petroleum Resources, British Columbia Geological Survey Bulletin 104, 164 p.

Nelson, J., and Kyba, J., 2014. Structural and stratigraphic control of porphyry and related mineralization in the Treaty Glacier-KSM-Brucejack-Stewart trend of western Stikinia, In: Geological Fieldwork 2013, BC Ministry of Energy, Mines and Petroleum Resources, BC Geological Survey Paper 2014-1, pp. 111-140.

Nelson, J.L., Colpron, M., and Israel, S., 2013, The Cordillera of British Columbia, Yukon, and Alaska: Tectonics and Metallogeny.

In: Colpron, M., Bissig, T., Rusk, B.G., Thompson, J.F.H., (Eds.), Tectonics, Metallogeny, and Discovery: The North American Cordillera and Similar Accretionary Settings. Society of Economic Geologists Special Publication 17, pp. 53-109.

Nelson, J., Waldron, J., van Straaten, B., Zagorevski, A., and Rees, C., 2018. Revised stratigraphy of the Hazelton Group in the Iskut River region, northwestern British Columbia. In: Geological Fieldwork 2017, British Columbia Ministry of Energy, Mines and Petroleum Resources, British Columbia Geological Survey Paper 2018-01, pp. 15-38.

Piquer, J., Skarmeta, J., and Cooke, D.R., 2015. Structural Evolution of the Rio Blanco-Los Bronces district, Andes of central Chili, controls on stratigraphy, magmatism and mineralization. Economic Geology, 110, 1195-2023.

Richards, J.P., 2003. Tectono-magmatic precursors for porphyry Cu-(Mo-Au) deposit formation. Economic Geology, 98, 1515-1533.

Richards, J.P., Boyce, A.J., and Pringle, M.S., 2001. Geological evolution of the Escondida area, Northern Chile: A model for spatial and temporal localization of porphyry Cu mineralization. Economic Geology, 96, 271-305.

Sillitoe, R.H., 2010. Porphyry copper systems. Economic Geology, 105, 3-41.

Teyssier, C., Tikoff, B., and Markley, M., 1995. Oblique plate motion and continental tectonics. Geology, 23, 447-450.

Thorkelson, D.J., Mortensen, J.K., Marsden, H., and Taylor, D.C. 1995. Age and tectonic setting of Early Jurassic episodic volcanism along the northeastern margin of the Hazelton Trough, northern British Columbia. In: Miller, D.M., Busby, C.J., (Eds.), Jurassic magmatism and tectonics of the North American Cordillera. Geological Society of America Special Paper 299, pp. 83-94.

Tombe, S.P., Richards, J.P., Greig, C.J., Board, W.S., Creaser, R.A., Muehlenbachs, K.A., Larson, P.B., DuFrane, S.A., and Spell, T., 2018. Origin of the high-grade Early Jurassic Brucejack epithermal Au-Ag deposits, Sulphurets mining camp, northwestern British Columbia. Ore Geology Reviews, 95, 480-517.

Tosdal, R.M, Dilles, J.H., and Cooke, D.R., 2009. From source to sinks in auriferous magmatic-hydrothermal porphyry and epithermal deposits. Elements, 5, 289-295.

van Straaten, B.I., and Nelson, J.L., 2016. Syncollisional late Early to early Late Jurassic volcanism, plutonism, and porphyry-style alteration on the northeastern margin of Stikinia. In: Geological Fieldwork 2015, British Columbia Ministry of Energy, Mines and Petroleum Resources, British Columbia Geological Survey Paper 2016-1, pp. 113-143.

Preliminary stratigraphy and geochronology of the Hazelton Group, Kitsault River area, Stikine terrane, northwest British Columbia

Rebecca C. Hunter[1, a], and Bram I. van Straaten[1]

[1] British Columbia Geological Survey, Ministry of Energy, Mines and Petroleum Resources, Victoria, BC, V8W 9N3
[a] corresponding author: Rebecca.Hunter@gov.bc.ca

Recommended citation: Hunter, R.C., and van Straaten, B.I., 2020. Preliminary stratigraphy and geochronology of the Hazelton Group, Kitsault River area, Stikine terrane, northwest British Columbia. In: Geological Fieldwork 2019, British Columbia Ministry of Energy, Mines and Petroleum Resources, British Columbia Geological Survey Paper 2020-01, pp. 101-118.

Abstract

The Kitsault River area, at the southern end of the Iskut-Stewart mineral belt of northwestern Stikinia, hosts porphyry Cu-Au, porphyry-related gold, and precious metal-rich VMS deposits in Hazelton Group volcano-sedimentary rocks. Based on new mapping northwest and east of Kinskuch Lake, we further resolve stratigraphic relationships in the lower part of the Hazelton Group and recognize three new facies and two new sub-facies. Facies 1 and 3 consist of lapilli tuff to tuff breccia with hornblende-plagioclase-phyric clasts and minor interbedded epiclastic rocks. Facies 2 consists of predominantly epiclastic rocks. Facies 3 is further subdivided into sub-facies 3a, a distinctive unit of K-feldspar- and plagioclase-phyric flows and lapilli tuffs to tuff breccia and sub-facies 3b, a mixed volcano-sedimentary unit with local features indicating subaerial deposition. New U-Pb zircon data provide age constraints to the Hazelton Group in the area, including a maximum depositional age from detrital zircons (U-Pb, LA-ICPMS) of ca. 206 Ma (Rhaetian) for the onset of Hazelton Group volcanism. A monzonite dike from near the Homestake Ridge deposit gave an age of ca. 191 Ma (U-Pb CA-TIMS), indicating that Cu-Au mineralizing systems in the Kitsault River area are Early Jurassic. A felsic lapilli tuff from directly beneath the Wolf deposit yielded a crystallization age of ca. 178 Ma (U-Pb, LA-ICPMS), suggesting that upper parts of the Hazelton Group are developed in the Kitsault River valley area and host some VMS related mineralization. Consistent with this conclusion, a volcanic-derived sandstone sample from the southern shore of Kitsault Lake returned a detrital zircon maximum depositional age of ca. 169 Ma (U-Pb, LA-ICPMS). These upper Hazelton Group units differ from those in the Eskay rift and at the Anyox deposit, which contain abundant bimodal felsic and mafic volcanic rocks. Nonetheless, these coeval syngenetic mineralizing systems are likely related and we interpret that VMS mineralization in the Kitsault River area reflects hydro-magmatic fluids flowing along syndepositional faults to near-surface levels. Extensional processes that operated at Eskay may have extended into in the Kitsault River area but without producing a large rift basin.

Keywords: Kitsault River, Hazelton Group, Stikine terrane, Jurassic, VMS, Eskay rift, silver, copper, gold

1. Introduction

Northwest British Columbia is endowed with significant porphyry Cu-Au, epithermal Au, and volcanogenic massive sulphide (VMS) precious and base metal deposits in Triassic and Jurassic rocks of the Stikine terrane (also known as Stikinia), particularly volcano-sedimentary successions of the Hazelton Group and allied plutons (Fig. 1; Höy, 1991; Childe, 1997; Nelson et al., 2013; Logan and Mihalynuk, 2014; Barresi et al., 2015; Nelson et al., 2018). Richly endowed porphyry systems extend along the length of the Canadian Cordillera generated by Late Triassic to Early Jurassic arc magmatism (Nelson et al., 2013; Logan and Mihalynuk, 2014). Examples of deposits in the Stikine terrane include Big Missouri, Schaft Creek, Galore Creek/Copper Canyon, Red Chris, the KSM porphyry trend, and Red Mountain (Fig. 2). Similarly, epithermal precious metal hydrothermal systems formed in response to Early Jurassic volcanism and related plutonic activity (Diakow et al., 1991; Nelson et al., 2013; Logan and Mihalynuk, 2014) led to mineralization at the Toodoggone, Premier, Snip, and Bronson deposits (Fig. 2). During the Middle Jurassic, mineralizing systems evolved into VMS-type settings that were active during deposition of the upper part of the Hazelton Group (Gagnon et al., 2012). Primary examples include the Eskay Creek deposit (Au-rich; Barrett and Sherlock, 1996; Childe, 1996; MacDonald et al., 1996a; Roth et al., 1999; Sherlock et al., 1999; Barresi and Dostal, 2005) and the Anyox deposit (Fig. 2; Cu-rich; Smith, 1993; MacDonald et al., 1996b; Evenchick and McNicoll, 2002). All of these are hosted by the Iskut River Formation, a bimodal felsic-mafic volcanic and sedimentary rock succession that constitutes the fill of the Eskay rift (Gagnon et al., 2012; Nelson et al., 2013, 2018).

Detailed mapping of the Hazelton Group and better age constraints are vital for understanding the depositional and volcanic environments that were responsible for VMS and epithermal-type mineralizing systems throughout western Stikinia. Herein we report the preliminary results of detailed mapping and geochronology in the Kitsault River area (Figs. 2, 3). We: 1) present composite stratigraphic sections based on

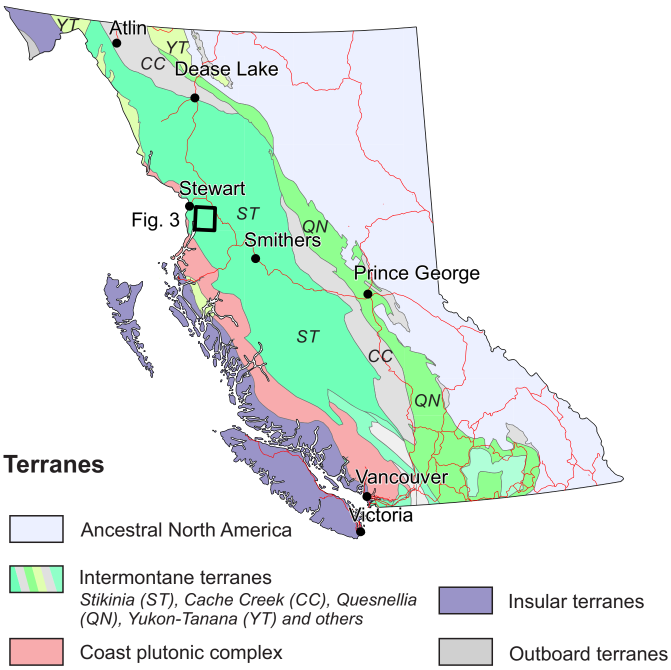

Fig. 1. Location of study area (after Nelson et al., 2013).

map data from north and east of Kinskuch Lake; 2) define volcano-sedimentary facies of the Hazelton Group in these sections and offer general environmental interpretations; 3) provide four preliminary U-Pb zircon and two $^{40}Ar/^{39}Ar$ ages; 4) compare Hazelton Group rocks in the Kitsault River area to those farther north in the Stewart-Iskut region such as described by Nelson et al. (2018); and 5) consider the implications for mineralizing systems in the area.

2. Geological setting

The Kitsault River study area is along the west-central margin of Stikinia, in the Intermontane belt of the Canadian Cordillera (Fig. 1). It lies in a belt of Triassic and Jurassic rocks that is bounded to the west by Eocene quartz monzonite to granodiorite of the Coast Plutonic Complex (Figs. 2, 3) and to the east by the Bowser basin (Middle Jurassic to Cretaceous; Fig. 3; Dawson and Alldrick, 1986). Terranes of the Intermontane belt (Slide Mountain, Yukon-Tanana, Quesnel, Stikine, Cache Creek, and Bridge River) were largely accreted to the western margin of Laurentia during the Jurassic and Triassic (Coney et al., 1980; Monger et al., 1982; Monger et al., 1991; Wheeler et al., 1991, Colpron et al., 2007; Nelson et al., 2013). Stikinia is a polyphase island arc terrane made up of the Stikine assemblage (Devonian to Mississippian; Anderson, 1989; Greig, 1992; Logan et al., 2000), the Stuhini and Takla groups (Middle to Late Triassic; Monger, 1977; Brown et al., 1996), and the Hazelton Group (latest Triassic to Middle Jurassic; Marsden and Thorkelson, 1992; Gagnon et al., 2012; Nelson et al., 2018).

The Stuhini Group preserves arc-related strata consisting of augite-rich basalt to basaltic andesite, crystal-lithic lapilli tuff, and epiclastic strata including greywacke, siltstone, tuff, and limestone units (Brown et al., 1996). The Hazelton Group overlies the Stuhini Group and older rocks largely along a regional unconformity (Greig, 2014; Nelson and Kyba, 2014). The Hazelton Group is an extensive package of volcanic and sedimentary rocks that span the entire width of the Stikine terrane (Marsden and Thorkelson, 1992; Gagnon et al., 2012; Nelson et al., 2018). It is subdivided into a lower part consisting mainly of siliciclastic rocks of the Jack Formation (which includes the Snippaker unit), and andesitic and lesser felsic volcaniclastic rocks of the Klastline and Betty Creek formations (Nelson et al., 2018 and references therein). The upper part of the Hazelton Group comprises mainly sedimentary rocks of the Spatsizi and Quock formations, subaerial dacite and rhyolite flows of the Mount Dilworth Formation, and bimodal volcanic and sedimentary rocks of the Iskut River Formation (Nelson et al., 2018). VMS-type mineralization is hosted in carbonaceous mudstone and rhyolites of the Iskut River Formation at the Au-Ag-rich Eskay Creek deposit (Barrett and Sherlock, 1996; Childe, 1996; MacDonald et al., 1996a; Roth et al., 1999; Barresi et al., 2015) and in inferred Iskut River Formation equivalent mafic volcanic and sedimentary rocks at the Cu-rich Anyox deposits (Smith, 1993; MacDonald et al., 1996b; Evenchick and McNicoll, 2002).

Overlying the Hazelton Group are widespread upper Middle Jurassic to mid-Cretaceous, marine and nonmarine sandstones, siltstones, and conglomerates of the Bowser Lake Group (Tipper and Richards, 1976; Eisbacher, 1981; Evenchick and Thorkelson, 2005; Evenchick et al., 2007). Post-Jurassic intrusive rocks in the Kitsault River area include the Ajax quartz monzonite (ca. 55.1 ±3 Ma, K-Ar; Carter, 1981; Dawson and Alldrick, 1986), quartz monzonite to granodiorite of the Coast Mountains Batholith (ca. 43 to 51 Ma; Carter, 1981) and inferred Eocene and younger microdiorite, diorite and lamprophyre dikes (Dawson and Alldrick et al., 1986; Devlin, 1987).

3. Notable mineral deposits in the Kitsault area

The study area is in the southern part of 'Golden Triangle', the popular name for a loosely defined region that includes most of the major gold, silver, and copper deposits in west-central Stikinia (Fig. 2). Notable deposits in the immediate study area include Homestake Ridge and Dolly Varden (Figs. 2, 3).

3.1. Homestake Ridge (MINFILE 103P 216)

The Homestake Ridge deposit (Figs. 2, 3) consists of the Homestake main, Homestake silver and South reef zones, with total Indicated resources of 0.624 Mt at 6.25 g/t Au, 47.9 g/t Ag and 0.18% Cu and Inferred resources of 7.245 Mt at 4.0 g/t Au, 90.0 g/t Ag and 0.11% Cu (Ross and Chamois, 2017). Volcanic rocks of the Hazelton Group host pyrite-chalcopyrite-galena-sphalerite mineralization in tabular zones of silica±carbonate±sericite±chlorite alteration, quartz veins, and quartz-carbonate hydrothermal breccias (Swanton et al., 2013; Ross and Chamois, 2017). West of the deposit area, across a thrust fault, sedimentary rocks (Stuhini Group) and andesitic volcanic

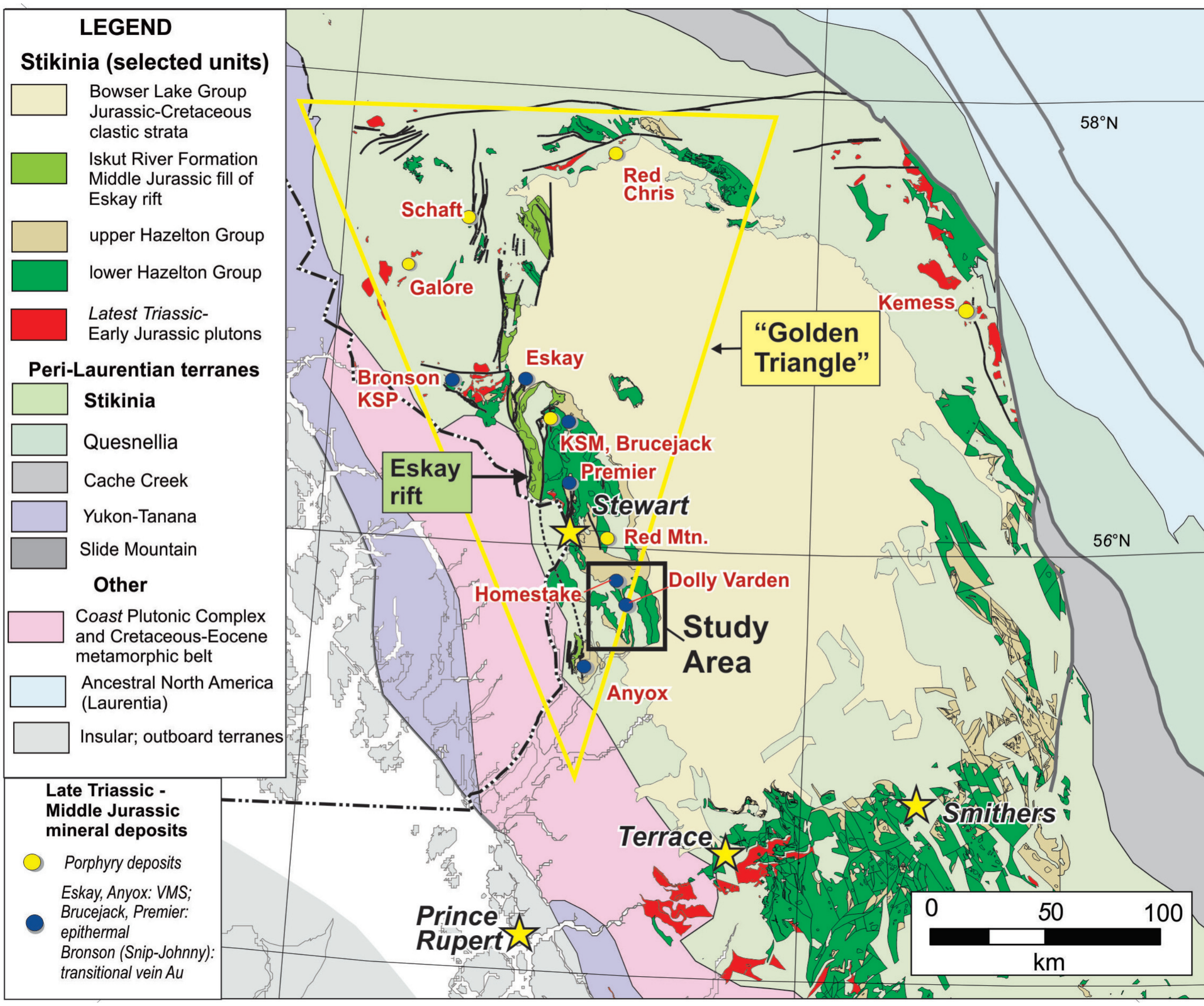

Fig. 2. Kitsault River study area with respect to major Late Triassic to Middle Jurassic mineral deposits in northwestern Stikinia (after Nelson et al., 2018).

rocks (Hazelton Group) are cut by numerous equigranular hornblende monzonite to hornblende-feldspar porphyritic dikes, and widespread quartz-pyrite±sericite±chlorite alteration locally obscures original protolith textures (Swanton et al., 2013). In contrast, the deposit area lacks monzonite dikes, aerially extensive alteration, and is underlain by Hazelton Group rocks, observations used by Swanton et al. (2013) to suggest that the western area may represent the deeper part of a hydrothermal system. Swanton et al. (2013) considered that the dikes west of the deposit area span the timing of alteration and suggested that they may be coeval with mineralization at Homestake Ridge. Below we report a new U-Pb zircon (CA-TIMS) age of ca. 191 Ma from a monzonite dike sampled near the Homestake Ridge deposit.

3.2. Dolly Varden, Torbrit, North Star, and Wolf (MINFILE 103P 188, 189, 191, 198)

The Dolly Varden Silver Corp. property contains the historical Dolly Varden, North Star, Torbrit, and Wolf deposits (Fig. 2), with total Indicated resources of 3.417 Mt at 299.8 g/t Ag and Inferred resources of 1.285 Mt at 277.0 g/t Ag (Turner and Nicholls, 2019). Between 1919 and 1959 the property produced approximately 20 Moz of silver (Dawson and Alldrick, 1986). Lithogeochemical studies throughout the Dolly Varden property suggest the volcanic country rocks are calc-alkaline (Sebert and Ramsay, 2012).

The Dolly Varden (MINFILE 103P 188), Torbrit (MINFILE 103P 191), and North Star (MINFILE 103P 189) deposits are described as exhalative and stratiform to locally vein-hosted silver-zinc-lead-barite orebodies underlain by andesitic crystal tuff and overlain by andesitic tuff of the Hazelton Group

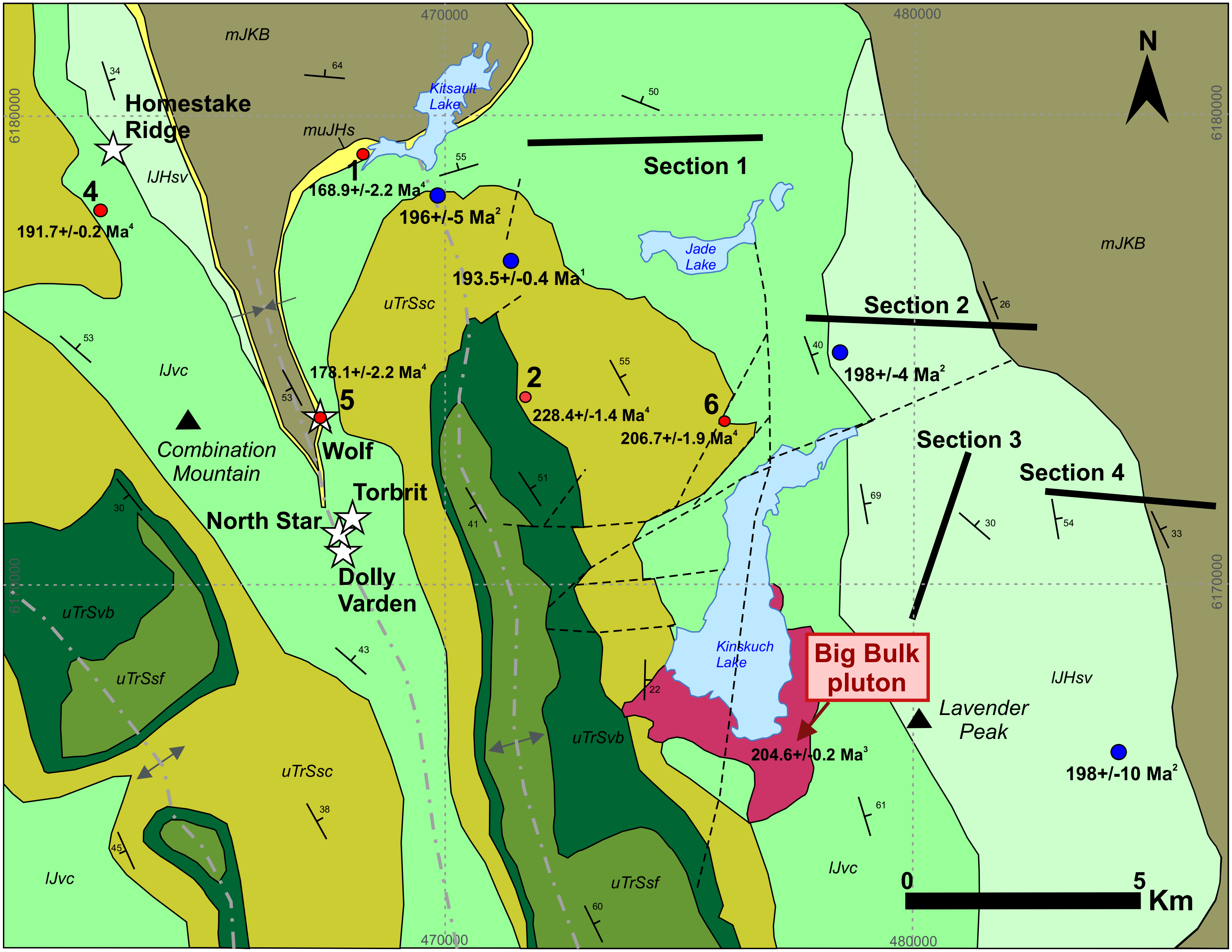

Fig. 3. Simplified geology of the Kitsault River area (after Alldrick et al., 1986; MacIntyre et al., 1994; Miller et al., 2020). Sources of geochronology: [1]Mortensen and Kirkham (1992); [2]Greig and Gehrels (1995); [3]Miller et al. (2020); [4]this study.

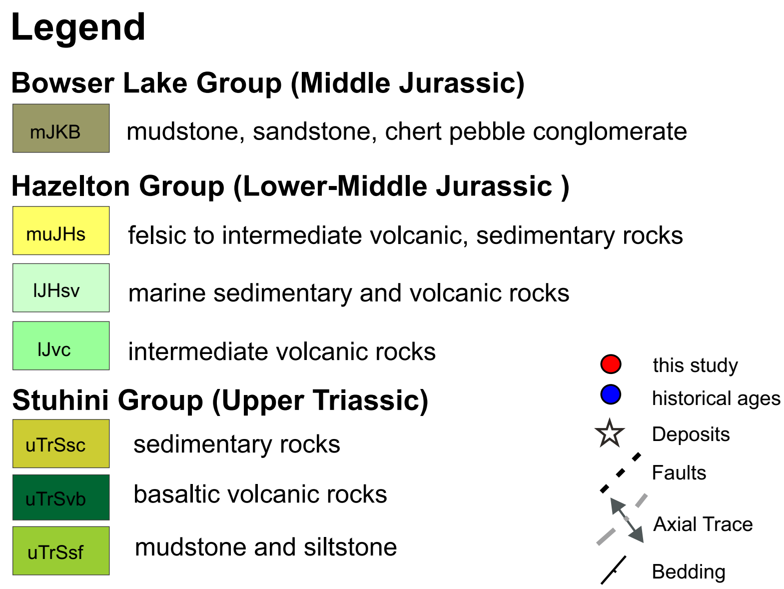

Fig. 3. Continued.

(Black, 1951; Campbell, 1959; Devlin, 1987, Higgs, 2015, McCuaig and Sebert, 2017). The Dolly Varden deposit is from 1 to 9 m thick and is divided into an east- to northeast-striking East Segment, and a west- to northwest-striking West Segment. Sulphide minerals at Dolly Varden East consist of pyrite, minor chalcopyrite, and trace argentite, pyrargyrite, and native silver disseminations and massive accumulations in white quartz veins (MINFILE 103P 188 and references therein). The Dolly Varden West mineralization is made up of sphalerite and galena, and minor pyrite, chalcopyrite, and tetrahedrite, with trace native silver as bands, disseminations, and stringers in calcite, quartz, siderite and barite gangue (MINFILE 103P 188 and references therein; Devlin, 1987).

The Torbrit deposit is hosted in rocks that have undergone propylitic, silica, and carbonate alteration, which extends approximately 30 m away from the ore zone (MINFILE 103P 191 and references therein). The mineralization consists of pyrite, sphalerite, and galena, with lesser chalcopyrite and trace pyrargyrite, argentite, and tetrahedrite interlaminated with brecciated quartz, calcite, barite, hematite, jasper, siderite, magnetite, and chlorite (MINFILE 103P 191 and references therein; Devlin, 1987). Locally, the Torbrit mineralization is formed together with colloform to crustiform banding and bladed open-space vein-filling textures (Higgs, 2015).

The North Star deposit shares many similarities with the Dolly Varden and Torbrit deposits and consists of bands, disseminations, and stringers of sphalerite and galena, minor pyrite, chalcopyrite, and tetrahedrite, and trace native silver and pyrargyrite hosted in calcite, quartz, siderite and barite exhalite (MINFILE 103P 189 and references therein). The deposit extends for about 100 m, is 1 to 24 m wide, and is cut by steeply dipping northwest-striking faults (MINFILE 103P 189 and references therein).

The Wolf deposit (MINFILE 103P 198) consists of several tabular mineralized zones. The No. 2 and No. 3 zones are the largest and are interpreted to be fault offset portions of the same body (Sebert and Ramsay, 2012). Sulphide minerals include pyrite, sphalerite, ruby silver, galena, tetrahedrite and possibly argentite in a gangue of banded and brecciated quartz±carbonate with open-space filling textures, including colloform banded quartz and pyrite, crustiform quartz, hematite, and bladed carbonate (Sebert and Ramsay, 2012). Pervasive chlorite-sericite alteration is common near the Wolf deposit, and silica, K-feldspar and Fe-carbonate alteration is close to the mineralized zones (Sebert and Ramsay, 2012). The No. 2 and No. 3 zones appear to be discordant to bedding and are interpreted to have been emplaced along an originally shallowly dipping fault; other mineralized zones may be concordant to bedding (Sebert and Ramsay, 2012). Although epigenetic textures predominate, possible local clastic sulphides and the presence of altered and mineralized clasts may suggest a syngenetic component (Sebert and Ramsay, 2012). Most of the tabular mineralized zones are close to the contact between intermediate tuff breccia and lapilli tuff and overlying intermediate lithic and/or crystal-rich volcaniclastic rocks. Limited fluid inclusion studies of the Wolf veins suggest formation at ~5 bar, implying moderate water depths (<50 m) or shallow burial by sedimentary-volcanic cover (<20 m) and formation in a near-surface setting (Dunne and Pinsent, 2002). Previous Pb isotope data from the Wolf deposit and other Dolly Varden deposits suggested a Jurassic depositional age (Godwin et al., 1991) but did not distinguish between the earliest part of the Early Jurassic (coeval with the lower Hazelton Group) or youngest part (Toarcian, coeval with the upper Hazelton Group). Below we present a new U-Pb zircon crystallization age (LA-ICPMS) of ca. 178 Ma from a felsic lapilli tuff sampled directly beneath the Wolf deposit indicating that these rocks are in the upper part of the Hazelton Group.

4. Geology of the Kitsault River area

Previous mapping in the region was by McConnell (1913), Turnbull (1916), Hanson (1922, 1923, 1928), Black (1951), Carter (1981), Alldrick et al. (1986), Dawson and Alldrick (1986); Grove (1986), Greig (1991); Greig et al. (1994); and Evenchick et al. (2008). Six informal stratigraphic units were recognized by Alldrick et al. (1986); Dawson and Alldrick (1986) and Greig (1991), including: 1) a 'lower sedimentary unit' of interbedded black siltstone, argillite, feldspathic wacke, and rare augite porphyritic basalt and hornblende porphyritic andesite; 2) a 'mafic volcanic unit' of augite, feldspar, and olivine basalt flows, pyroclastic rocks, conglomerates, and local limestones; 3) a 'middle sedimentary unit' of siltstone, sandstone, greywacke, conglomerate, and volcanic breccia containing limestone clasts; 4) an 'intermediate volcanic unit' of andesitic pyroclastic rocks (lapilli tuff to tuff breccia), and lesser lenses of argillite, limestone, chert and barite; 5) an 'epiclastic and felsic volcanic unit' of volcanic breccia, conglomerate, lesser dacite flows, pyroclastic rocks, minor siltstone and limestone, and local hornblende-feldspar porphyry flows; and 6) an 'upper sedimentary unit' of fossiliferous greywacke with belemnites and bivalves, black siltstone, sandstone, limestone, and arkose.

Previous Hazelton Group geochronology in the area includes U-Pb zircon ages of 193.5 ±0.4 Ma (Mortensen and Kirkham, 1992) and 196 ±5 Ma (Greig and Gehrels, 1995) from feldspar-phyric lapilli tuffs near Kitsault Lake (Fig. 3), and 198 ±4 Ma from K-feldspar- and plagioclase-phyric dacite-andesite flows north of Kinskuch Lake and 198 ±10 Ma from feldspar-phyric lapilli tuff to tuff breccia east of Lavender Peak (Fig. 3; Greig and Gehrels, 1995).

5. Stratigraphy and facies analysis

We present four composite stratigraphic sections based on 2019 mapping north of Kitsault Lake (Figs. 3, 4). These sections include the previously recognized (see above) unit 4 ('intermediate volcanic unit'; Lower to Middle Jurassic), unit 5 (epiclastic and felsic volcanic unit'), and unit 6 ('upper sedimentary unit'; Middle to Upper Jurassic). Given that volcano-sedimentary depositional systems generate environments that are repeated in time and space (e.g., Orton, 1995), below we adopt a facies approach to describe these rocks. Classification diagrams of Fisher (1966), Dott (1964), and Schmid (1981) were used to describe the pyroclastic and epiclastic rocks.

5.1. Lower part of the Hazelton Group

5.1.1. Facies 1; hornblende-plagioclase-phyric pyroclastic and epiclastic facies

Facies 1 was observed at section 1, where it is repeated, and at section 2 (Fig. 3). It is 1000 to 2500 m thick, but lower and upper contacts were not observed. Facies 1 consists mainly of poorly-sorted lapilli tuff to tuff breccia with subrounded to subangular hornblende-plagioclase-phyric clasts in a hornblende-plagioclase-crystal-bearing matrix (Fig. 5a). Limestone clasts, and partially to entirely weathered-out pits inferred to have been limestone clasts, are present locally. Some outcrops have m-scale hornblende- plagioclase-phyric blocks and accessory clasts of limestone and chert in a feldspar crystal-bearing matrix. Intercalated with the previously described units are minor m-scale coarse-grained tuff , limestone, feldspathic wacke, limestone clast-bearing lapillistone (Fig. 5b), and rare chert. A 10 m thick, green-weathering lapilli tuff to tuff breccia is in the central part of the facies. It consists of matrix-supported, poorly sorted, 0.1-1.0 cm subangular white aphyric possible felsic clasts, pink pumice lapilli, and 1-3% hornblende crystals (0.5-2 mm) in a tuff matrix (Fig. 5c). Near the top of the facies are 50-100 m thick beds of biotite-bearing, matrix- to clast-supported lapilli tuff to tuff breccia with subrounded to subangular 3 mm to 10 cm biotite- plagioclase-phyric clasts in a biotite and plagioclase crystal-bearing matrix (Fig. 6). It is interbedded with more recessive intervals consisting of feldspathic wacke. Near the base of facies 1 (Fig. 4), a 5 m thick, coherent, augite-plagioclase-phyric unit is present within lapilli tuff to tuff breccia and is inferred to be a sill.

5.1.2. Facies 2; epiclastic facies

The epiclastic facies was observed at section 1 and has an approximate thickness of 1500 m (Fig. 4). Contacts with facies 1 are gradational and are characterized by an increased proportion of epiclastic units adjacent to the facies 2 contact. Facies 2 consists of 50-100 m thick recessive beds of siltstone and fine-grained feldspathic sandstone in repeating fining upward sequences with 10-50 m-thick muddy limestone, feldspathic sandstone, conglomerate and rare chert all interbedded with competent 50-200 m-thick lapilli tuff to tuff breccia with local limestone clasts, and local plagioclase crystal-rich tuff. Interbeds of plagioclase crystal-rich tuff to lapilli tuff are moderately well-bedded, display weak grading and local 10-30 cm thick cross stratification (Fig. 7a). Interbedded 1-3 m thick conglomerates contain abundant maroon, gray, and white chert clasts, in addition to tuffaceous and hornblende-plagioclase-phyric clasts (Fig. 7b). Facies 2 includes minor 5-10 m-scale interbeds of lapilli tuff to tuff breccia with subrounded hornblende-plagioclase-phyric clasts in a hornblende and plagioclase crystal-bearing matrix.

5.1.3. Facies 3; hornblende-plagioclase-phyric volcanic facies

Facies 3 was observed at sections 2, 3, and 4 and is 250 to 1500 m thick (Fig. 4). Contact relationship with facies 1 were not observed; at the tops of sections 2 and 4, it appears to be in fault contact with rocks we consider part of the Bowser Lake Group. Facies 3 is subdivided into two distinct sub-facies (3a and 3b), which appear to be localized to the areas northeast and east of Kinskuch Lake. Facies 3 is a thick to very thick bedded, hornblende-plagioclase lapilli tuff, lapillistone, tuff breccia and pyroclastic breccia. It contains large (0.4 to 60 cm), subangular to subrounded, moderately to poorly sorted clasts in a fine- to coarse-ash matrix containing 2-5% hornblende

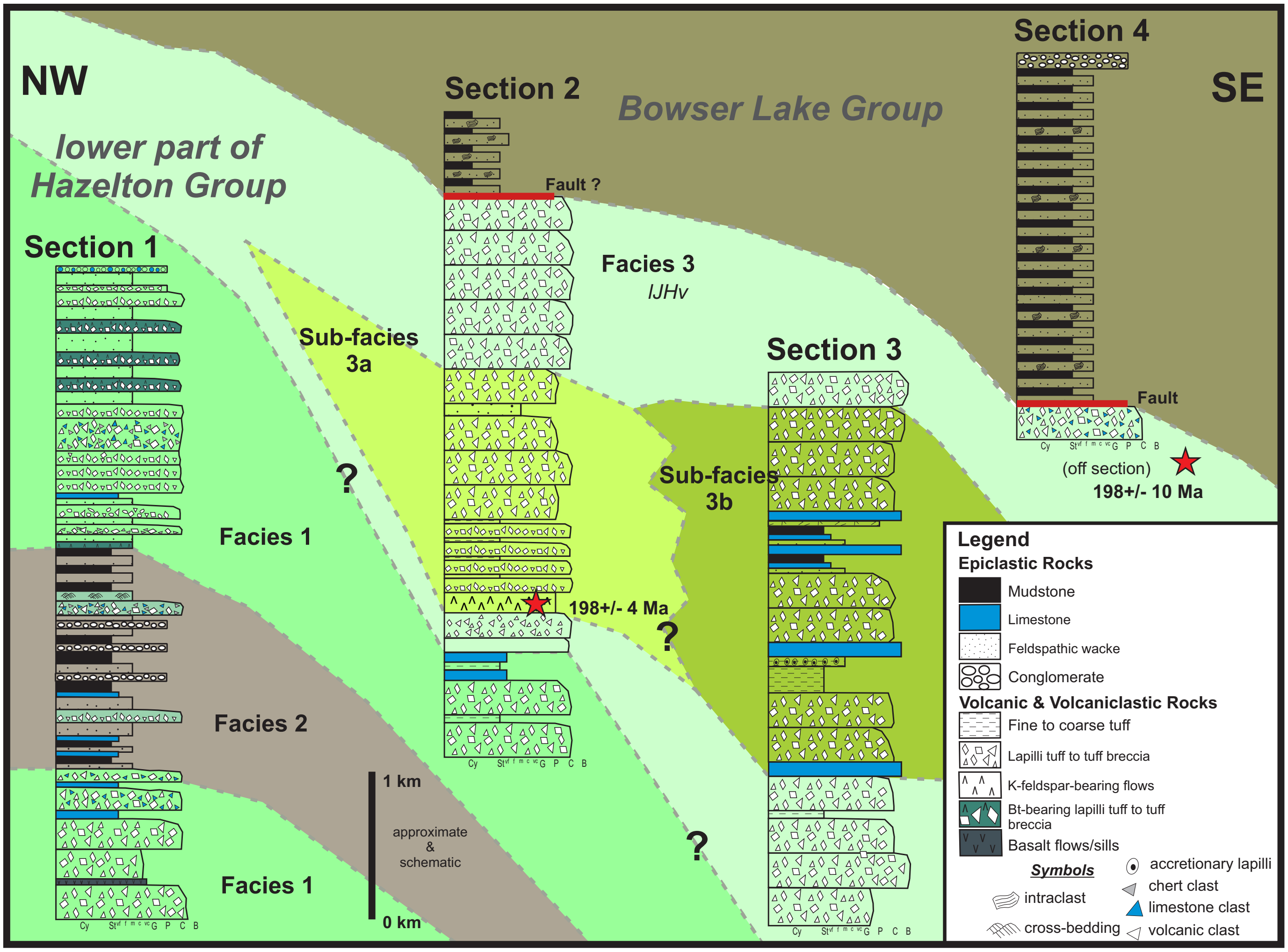

Fig. 4. Simplified composite stratigraphic sections based on map data in the Kitsault River area outlining three volcano-sedimentary facies and two sub-facies in the lower part of the Hazelton Group and their interpreted correlations. U-Pb zircon ages are from Greig and Gehrels (1995). See Figure 3 for section locations.

and abundant plagioclase crystals (Fig. 8a). Clasts are predominantly volcanic-derived hornblende- and plagioclase-phyric (1-5 mm) with varying phenocryst percentages (3-20%); the unit includes lesser aphyric clasts and rare limestone clasts. The unit varies from matrix- to clast-supported and is ungraded to weakly graded. Clasts have a range of colours including cream, gray, pink, brown, white and maroon and locally have cuspate to serrated edges. Up to 1 m thick, irregular and laterally-discontinuous beds of graded coarse- to fine-tuff locally separate layers of lapilli tuff to tuff breccia. Interbeds of maroon, thick-bedded, largely monomictic, matrix-supported lapilli tuff to tuff breccia are locally developed (Fig. 8b). These beds are poorly sorted, with uniform feldspar-phyric clasts that display irregular to wispy cuspate-lobate clast boundaries (suggesting they were still hot and ductile when deposited) in a fine-grained feldspar crystal and tuff matrix. Local rounded to subrounded hornblende-plagioclase-phyric bombs are in the largely monomictic beds. The U-Pb zircon age of 198 ±10 Ma reported by Greig and Gehrels (1995) for a feldspar-phyric lapilli tuff to tuff breccia seems to have been from a sample collected from facies 3 south of section 4.

5.1.3.1. Sub-facies 3a; K-feldspar and plagioclase porphyry

Sub-facies 3a is a distinct K-feldspar, hornblende, and plagioclase porphyry to crystal tuff observed northeast of Kinskuch Lake and in a small (~5 m) localized area north of Lavender Peak. It has a total thickness of approximately 1000 m and is interbedded with 100 m-thick units of hornblende-plagioclase-phyric lapilli tuff to tuff breccia (Fig. 4). Its contact appears conformable with underlying and overlying non-K feldspar-bearing facies 3. It varies in texture from massive, to flow-banded coherent rock, to plagioclase- and K-feldspar-bearing crystal tuff with K-feldspar crystals aligned along bedding (Fig. 9). These units are porphyritic with 2-5 mm plagioclase (2-5%) phenocrysts and locally 1-3 cm phenocrysts of K-feldspar (1-3%). The unit contains quartz (1-3%), hornblende (5-10%), plagioclase (10-20%), and K-feldspar (70-85%). The feldspar porphyry to crystal tuff is interbedded

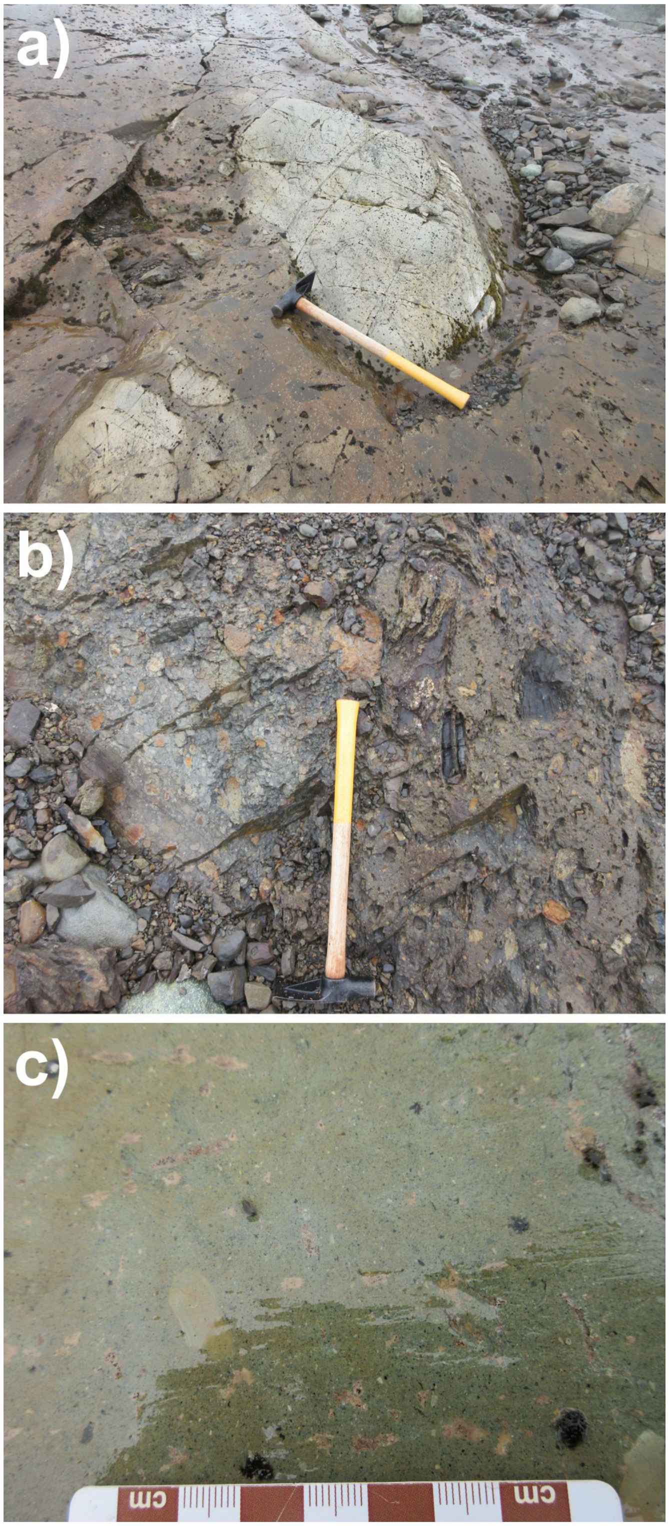

Fig. 5. Lapilli tuff to tuff breccia unit of facies 1. **a)** Angular m-scale hornblende-plagioclase volcanic clasts in a thick-bedded tuff breccia unit (UTM 474981E; 6179756N). **b)** Clast-supported lapillistone with plagioclase-phyric volcanic and limestone clasts (UTM 476634E; 6179605N). **c)** Distinct green-weathering polymictic lapilli tuff with cream to black aphanitic angular clasts and ameboid vesicular pumice clasts floating in a fine-grained plagioclase-rich matrix (UTM 474541E; 6179496N).

Fig. 6. Lower Hazelton Group facies 1, matrix-supported lapilli tuff with poorly sorted subangular biotite-hornblende-plagioclase-phyric clasts in a biotite-plagioclase matrix (UTM 475438E; 6179368N).

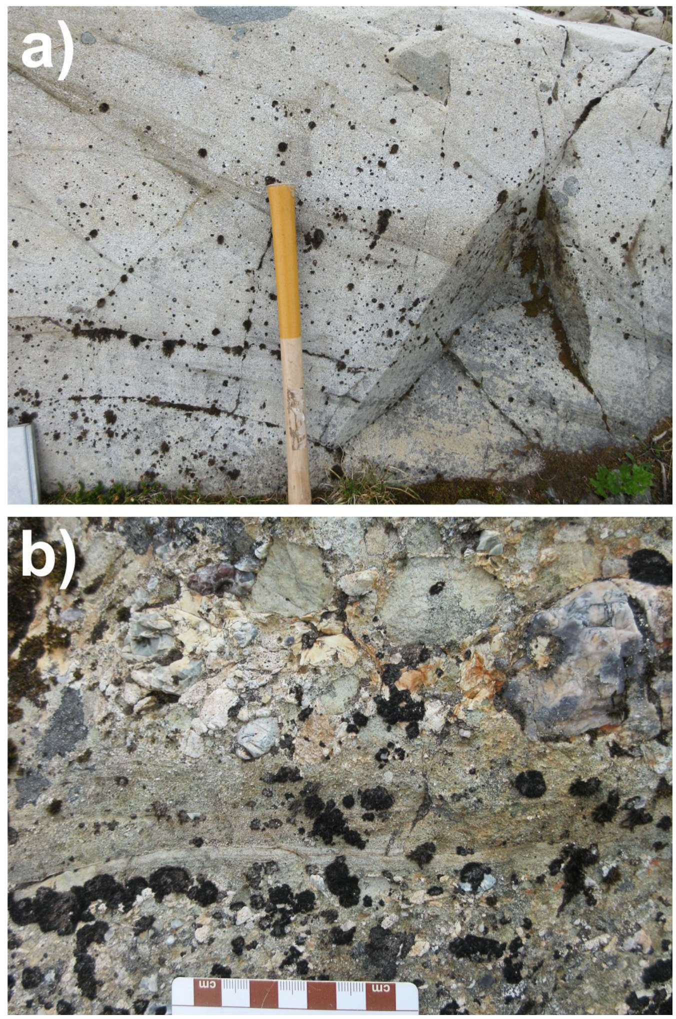

Fig. 7. Lower Hazelton Group facies 2, epiclastic units. **a)** Cross-stratified and parallel-stratified plagioclase crystal-rich tuff (UTM 473730E; 6179381N). **b)** Beds of clast- to matrix-supported polymictic conglomerate with rounded to subrounded clasts of chert, fine-grained tuff, and various plagioclase porphyritic fragments separated by a volcanic-derived sandstone layer (UTM 474247E; 6179466N).

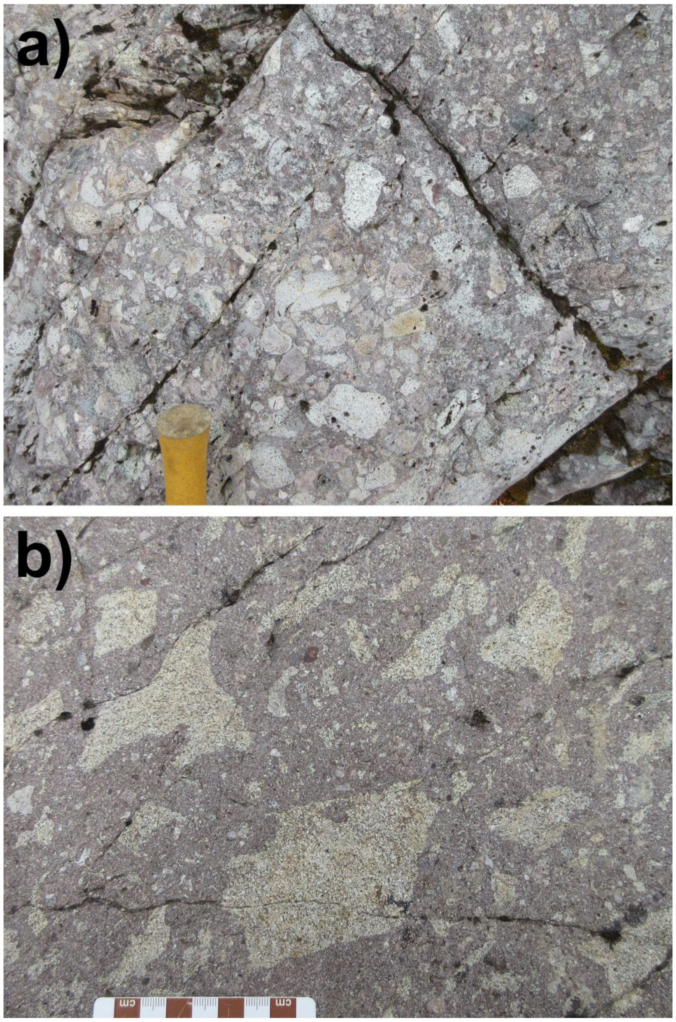

Fig. 8. Lower Hazelton Group facies 3, volcaniclastic rocks. **a)** Clast-supported lapillistone to lapilli tuff with subrounded to subangular hornblende-feldspar-phyric clasts with variable hornblende/plagioclase percentages (UTM 479119E; 6172627N). **b)** Largely monomictic lapilli tuff with crowded, coarse-grained plagioclase-phyric clasts with lobate-cuspate margins in a feldspar-phyric maroon tuff matrix containing local subrounded dark maroon fine-grained clasts (UTM 479084E; 6172610N).

with gray to maroon lapilli tuff to tuff breccia with 1-20 cm subrounded hornblende-plagioclase-phyric clasts (phenocryst percentages vary from 3-25%) in a hornblende and plagioclase crystal matrix. Weakly graded, thin- to medium-bedded, coarse- to fine-tuff interbeds are present locally. Lenticular and discontinuous beds of brown weathering, coarse- to very coarse-grained sandstone, 3-5 m thick are interlayered with the feldspar porphyry and lapilli tuff to tuff breccia units. Greig and Gehrels (1995) reported a 198 ±4 Ma zircon U-Pb age for a K-feldspar/plagioclase-phyric dacite/andesite sample collected in sub-facies 3a along section 2 (Fig. 4).

5.1.3.2. Sub-facies 3b; hornblende-plagioclase-phyric volcanic rocks, tuff and limestone

At section 3, sub-facies 3b conformably overlies facies 3 rocks

Fig. 9. Lower Hazelton Group facies 3a, hornblende-plagioclase-K-feldspar porphyry with zoned K-feldspar crystals up to 3 cm long aligned along bedding (UTM 479658E; 6175426N).

and is about 2000 m thick (Fig. 3). The unit consists of lapilli tuff, lapillistone, and tuff breccia, and rocks such as limestone, limestone clast-rich conglomerate, fine-grained sandstone, and mudstone. The tuff unit consists of interbedded (1-20 cm scale) rhythmically laminated fine and coarse tuff and lapilli tuff with 1-3 mm aphyric, white to cream lapilli (Fig. 10a). M-thick beds of lapillistone containing 2-5 mm concentrically zoned aphyric accretionary lapilli in a coarse tuff matrix are locally developed (Fig. 10b). A local variety of lapilli tuff to tuff breccia contains characteristic sparse subrounded black, glassy lapilli fragments with 1-5% plagioclase phenocrysts floating in a feldspar-rich crystal matrix (Fig. 10c). These glassy lapilli and their feldspar-rich matrix form distinct 10-30 cm subrounded clasts in the same unit (Fig. 10d).

Calcareous mudstone and limestone form abundant 1-2 m thick beds in facies 3b. The limestone forms cm-scale lenses, discontinuous layers, and ovoid bodies in the calcareous mudstone (Fig. 11a). Parts of the sequence with abundant limestone also contains fine-grained sandstone and mudstone with well-developed grading and abundant load casts and flame structures and other soft-sediment deformation features (Fig. 11b) and minor beds of medium- to coarse-grained feldspathic sandstone.

5.2. Bowser Lake Group

5.2.1. Interbedded feldspathic wacke, mudstone, and chert clast-bearing pebble conglomerate

Interbedded gray to brown, laminated- to medium-bedded, fine- to medium-grained feldspathic wacke and mudstone (Fig. 12a) is present along the eastern margin of Kitsault River map area. Load and flame structures are well developed, and 1-5 cm subrounded mudstone intraclasts are observed throughout the unit. The chert-pebble conglomerate forms m-scale beds containing granules and pebbles in a coarse sandstone matrix (Fig. 12b). Clasts are subrounded and consist

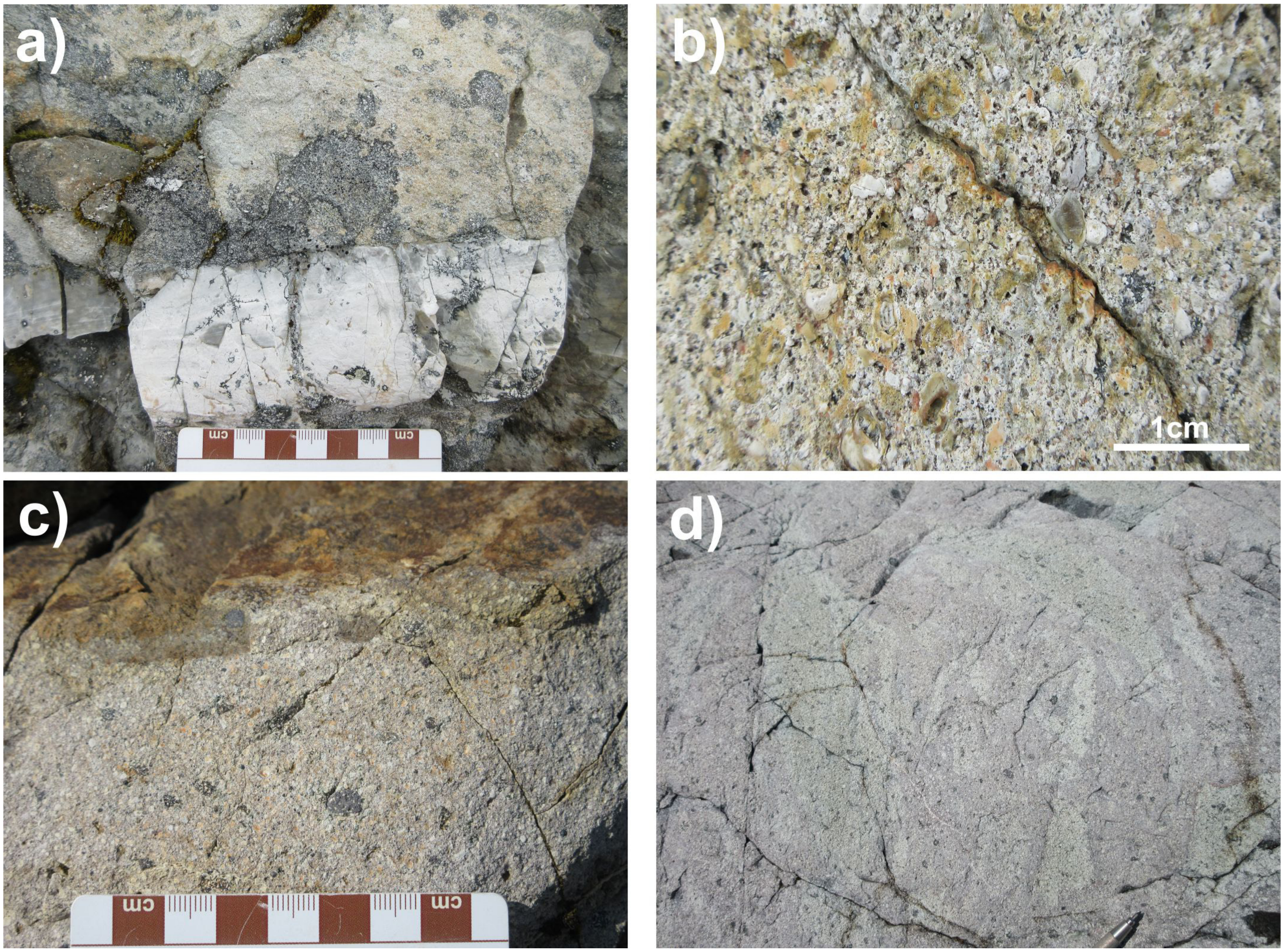

Fig. 10. Lower Hazelton Group facies 3b pyroclastic units. **a)** Dm-scale interlayers of light-toned rhythmically laminated fine tuff and dark-toned beds of coarse tuff, with internal thin layering (UTM 480620E; 6170990N). **b)** Clast-supported lapillistone with abundant accretionary lapilli (UTM 480620E; 6170990N). **c)** Sparse black, cm-scale rounded glassy lapilli fragments in plagioclase crystal matrix (UTM 480074E; 6169483N). **d)** Tuff breccia with tabular, aligned breccia- to lapilli-sized clasts, up to 10 cm, of similar composition to c) (UTM 480048E; 6169615N).

of white, tan, gray, and black chert. The conglomerate is interbedded with cm-scale gray siltstones.

6. Geochronology

Below we report the preliminary results from four Laser Ablation Inductively Coupled Plasma Mass Spectrometry (LA-ICPMS) U-Pb zircon samples, one Chemical Abrasion Thermal Ionization Mass Spectrometry (CA-TIMS) U-Pb zircon sample, and two $^{40}Ar/^{39}Ar$ K-feldspar samples collected during 2015 mapping (Fig. 3; Table 1). Our sample of hornblende diorite from a plutonic body on the southeast shore of Kinskuch Lake that hosts the Big Bulk porphyry Cu-Au prospect (see Miller et al., 2020) failed to yield adequate zircons for analysis. However, Miller et al. (2020) report a preliminary U-Pb zircon CA-TIMS age of from an early diorite phase at the property of 204.61 ±0.18 Ma.

Detailed methods and final results will be reported elsewhere. U-Pb zircon and $^{40}Ar/^{39}Ar$ K-feldspar analyses were carried out at the Pacific Centre for Isotopic and Geochemical Research

Table 1. Location and analysis information for reported 2015 geochronological samples. Coordinates are in UTM Zone 9N, NAD83.

Sample	Easting	Northing	Analysis
1	468325	6179294	U-Pb zrn detrital
2	471841	6174086	U-Pb zrn detrital
4	462704	6178223	U-Pb zrn TIMS igneous
5	467432	6173676	U-Pb zrn LA-ICP-MS igneous
6	476098	6173707	U-Pb zrn detrital
7	467257	6173616	Ar-Ar adularia
8	467312	6173724	Ar-Ar adularia

(University of British Columbia). For all LA-ICPMS analyses, we exclude individual grain ages with <0.05 probability of concordance (calculated using the Isoplot routine of Ludwig, 2012). We calculated preliminary maximum depositional ages for detrital zircon samples using: 1) the youngest graphical probability peak (YPP) in a probability density plot (PDP)

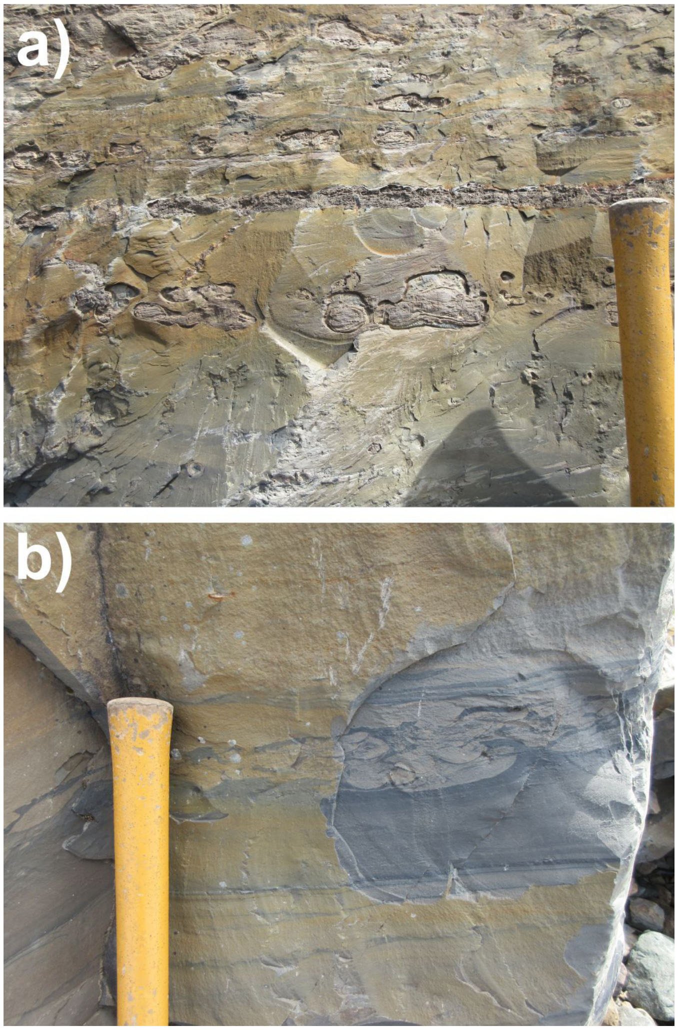

Fig. 11. Facies 3b epiclastic units. **a)** Laminated calcareous mudstone with cm-scale layers, lenses, and ovoid limestone bodies. **b)** Sharp-based fining upward sequences with graded fine-grained sandstone to mudstone; load casts and flame structures at top of hammer handle. Both units located at (UTM 480251E; 6171402N).

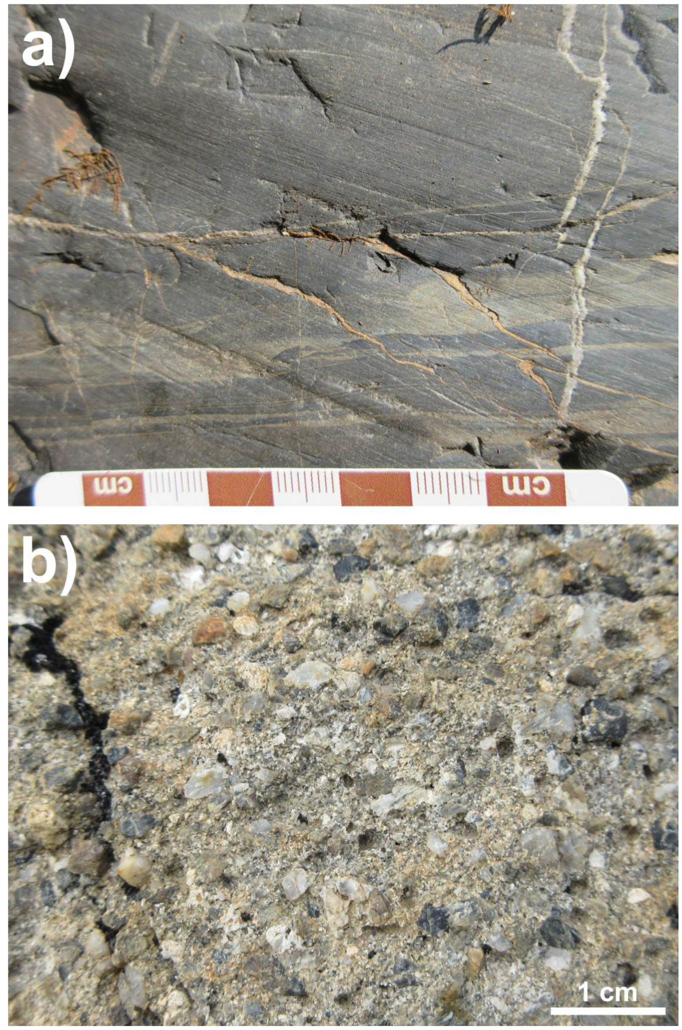

Fig. 12. Bowser Lake Group. **a)** Interlayered mudstone and siltstone (dark toned) and fine-grained sandstone (light toned) (UTM 482152E; 6175728N). **b)** Chert-granule pebble conglomerate in a very coarse-grained sandstone matrix (UTM 485798E; 6171726N).

constructed in Isoplot (Ludwig, 2012); 2) the youngest statistical population (YSP, Coutts et al., 2019); 3) the TuffZirc routine in Isoplot (Ludwig, 2012); and 4) the youngest cluster of two or more grains that overlap in age at 1 sigma (YC1σ(2+), Dickinson and Gehrels, 2009). Following Herriott et al. (2019) we choose YPP as the preferred preliminary maximum depositional age.

6.1. Lower part of the Hazelton Group

6.1.1. Sample 15BvS-37-08, detrital zircon from volcanic-derived sandstone (LA-ICPMS) This sample was collected from the base of the Hazelton Group northwest of Kinskuch Lake (Sample 2, on Fig. 3). It is from a well-stratified hornblende crystal-bearing and plagioclase crystal-rich volcanic-derived sandstone that is interbedded with argillite. The sandstone appears to unconformably overlie Stuhini Group argillite and chert containing limestone, augite-phyric volcanic, and chert megaclasts (see Miller et al., 2020). The sample returned a unimodal Late Triassic detrital zircon population, and the youngest statistical population yielded a 228.4 ±1.4 Ma preliminary maximum depositional age (Fig. 13d).

6.1.2. Sample 15BvS-36-13, detrital zircon from polymictic pebble conglomerate (LA-ICPMS)

This sample is from a polymictic pebble conglomerate containing clasts of hornblende-plagioclase-phyric volcanic rock, grey limestone, black chert, sandstone, conglomerate, and rare maroon plagioclase-phyric volcanic rock at the base of the Hazelton Group about 1 km northwest of Kinskuch Lake (Sample 6 on Fig. 3). This conglomerate is overlain by volcanic breccia with hornblende-plagioclase-phyric clasts interbedded with crystal tuff, typical of the lower part of the Hazelton Group throughout the Stewart-Iskut area. At this location, the polymictic pebble conglomerate appears to overlie Stuhini

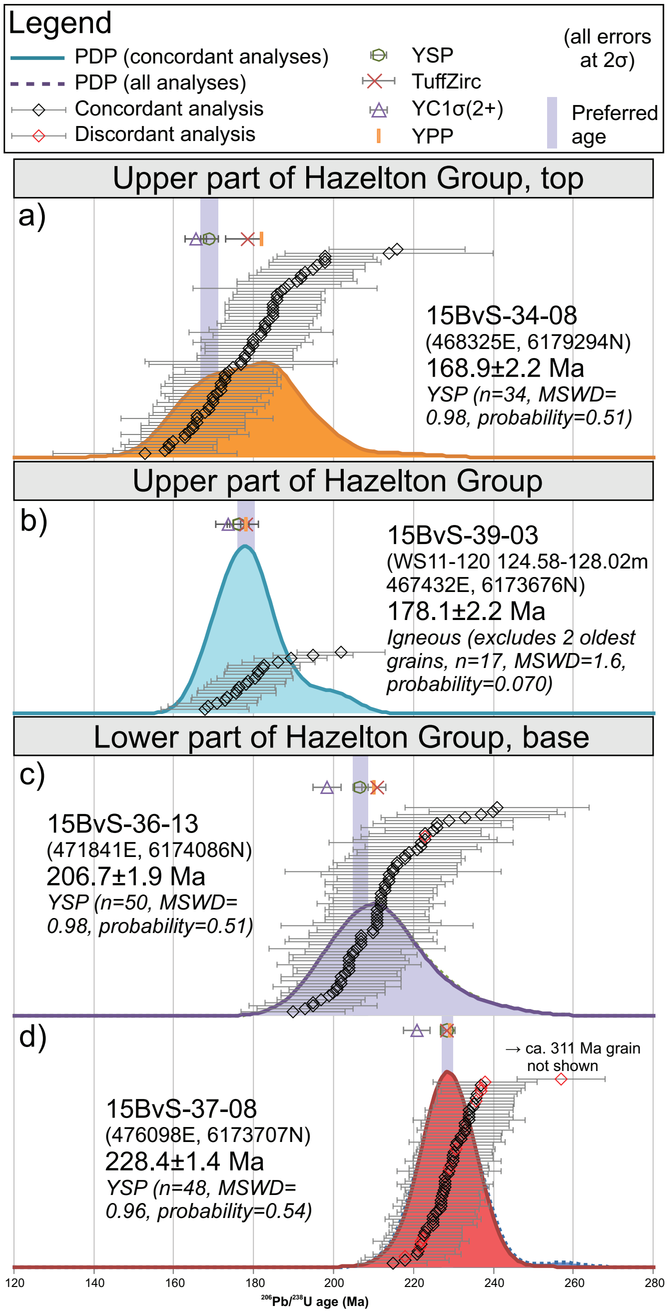

Fig. 13. LA-ICP-MS zircon $^{206}Pb/^{238}U$ probability density plot (PDP), individual grain ages, and preliminary maximum depositional or igneous age. **a)** Volcanic-derived sandstone bed in upper part of the Hazelton Group, immediately below the Quock Formation. **b)** Felsic lapilli tuff in the footwall of the Wolf deposit, upper part of the Hazelton Group. **c)** Polymictic pebble conglomerate at the base of the Hazelton Group. **d)** Volcanic-derived sandstone interbedded with argillite at the base of the Hazelton Group. Preliminary maximum depositional ages are constrained using the youngest graphical probability peak (YPP), youngest statistical population (YSP), TuffZirc, and youngest cluster of two or more grains that overlap in age at 1 sigma (YC1σ(2+)).

Group interstratified argillite, sandstone, and conglomerate without a marked discordance. The Stuhini Group conglomerate beds include augite-phyric volcanic clasts, plagioclase-phyric volcanic clasts, purple volcanic clasts, and argillite intraclasts, but lack hornblende-plagioclase-phyric volcanic and limestone clasts typical of conglomerates in the overlying lower Hazelton Group. The youngest statistical population returned a 206.7 ±1.9 Ma preliminary maximum depositional age (Fig. 13c).

6.2. Sample 15BvS-38-01, monzonite dike at the Homestake Ridge deposit area (CA-TIMS)

We sampled a variably-altered monzonite dike with locally well-preserved 3-7 mm blocky to tabular hornblende west of the Homestake Ridge deposit area (Sample 4 on Fig. 3). The dike cuts recessive interbedded argillite and fine-grained sandstone (likely part of the Stuhini Group). The sample returned a preliminary U-Pb zircon crystallization age of 191.71 ±0.20 Ma (Fig. 14).

6.3. Upper part of the Hazelton Group

6.3.1. Sample 15BvS-39-03, felsic lapilli tuff (LA-ICPMS)

This drill core (DDH WS11-120, 124.6-128.0 m downhole) sample is from the footwall of the Wolf No. 2 zone (Sample 5 on Fig. 3; Fig. 15; Sebert and Ramsay, 2012). It is from a lower sequence of tuffaceous sandstone and argillaceous tuff that is overlain by a section of intermediate lithic and/or crystal-rich volcaniclastic rocks (Sebert and Ramsay, 2012). The upper volcanic rock package is in turn overlain by argillite and calcareous sandstone that occupy the core of a syncline in the Kitsault River valley (Alldrick et al., 1986; Sebert and Ramsay, 2012). These argillites and calcareous sandstones were previously assigned to an undivided upper sedimentary unit (Alldrick et al., 1986) or the Salmon River Formation (Sebert and Ramsay, 2012). Following mapping to the north by Greig et al. (1994) and an updated regional stratigraphic framework by Nelson et al. (2018), we suggest that these rocks are best assigned to the Quock Formation (upper part

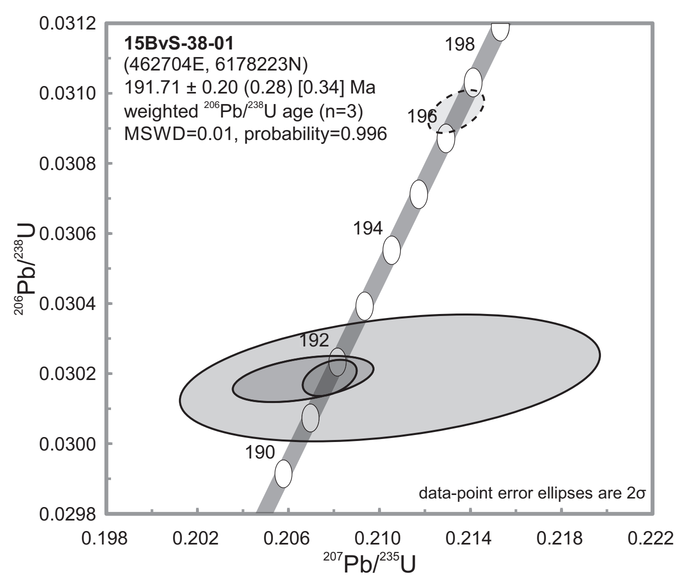

Fig. 14. U-Pb zircon concordia diagram showing CA-TIMS results from a hornblende monzonite dike west of the Homestake Ridge deposit.

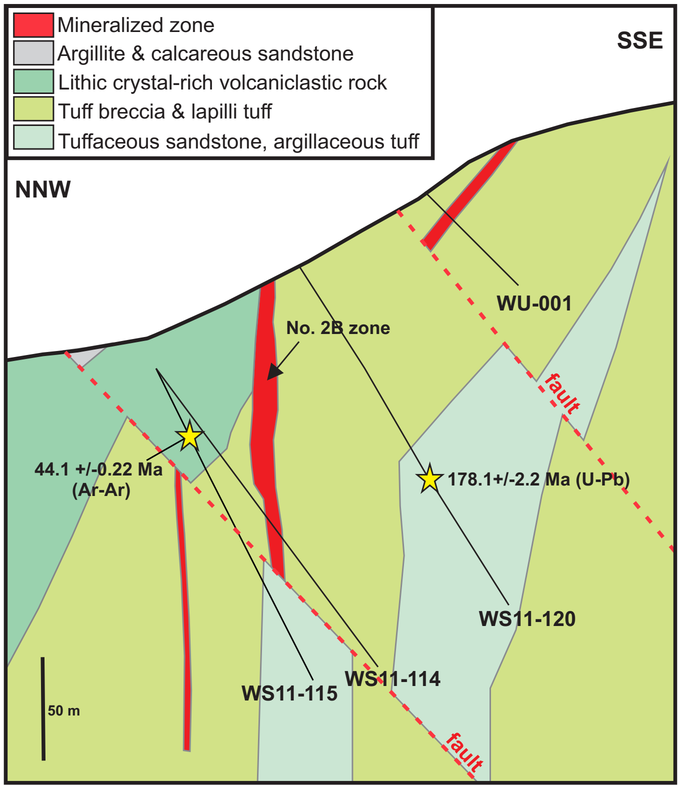

Fig. 15. Simplified schematic cross section through the Wolf deposit modified from sections 1250 N, 1300 N and 1350N in Sebert and Ramsay (2012). Ages are from this study.

of the Hazelton Group) and Bowser Lake Group. The sample returned a preliminary U-Pb zircon LA-ICPMS crystallization age of 178.1 ±2.2 Ma (Fig. 13b). Based on this age and stratigraphic position directly beneath sedimentary rocks of the Quock Formation or Bowser Lake Group, these rocks are best assigned to the upper part of the Hazelton Group.

6.3.2. Sample 15BvS-34-08, volcanic-derived sandstone (LA-ICPMS)

This sample was taken from near the southwest arm of Kitsault Lake (Sample 1 on Fig. 3). It is from a sandstone interval, about 8 m thick and containing common belemnite casts, that gradationally overlies volcanic rocks with cm-scale, light-coloured aphanitic to plagioclase-phyric felsic volcanic clasts. Both units are interpreted here as part of the upper Hazelton Group. The sandstones are overlain by a 65 m-thick succession of interstratified dark grey siltstone, pale grey siliceous siltstone, and fine felsic tuff of the Quock Formation (upper Hazelton Group), which is in turn is overlain by laminated to medium-bedded argillite, siltstone, and fine-grained feldspathic arenite of the Bowser Lake Group. The sample returned a unimodal, largely Early to Middle Jurassic detrital zircon population. The youngest statistical population yields a 168.9 ±2.2 Ma preliminary maximum depositional age, which accords well with a ca. 170 Ma shoulder on the probability density plot (Fig. 13a).

6.4. Hydrothermal alteration

6.4.1. Sample 15BvS-39-01, altered volcaniclastic rock, $^{40}Ar/^{39}Ar$ K-feldspar

This is a drill core sample from the Wolf deposit (sample 7, Fig. 3) taken from DDH WS11-108, 122.4-123.5 m downhole. The sample was taken approximately 63 m above (measured along the drill hole) mineralization at the No. 2 zone (Sebert and Ramsay, 2012). We analyzed a pale K-feldspar altered, generally massive, poorly-sorted volcaniclastic rock with minor matrix-supported, subrounded to subangular andesitic volcanic clasts in a crystal-rich matrix. The sample did not return a robust Ar-Ar K-feldspar plateau age (using criteria defined by Ludwig, 2012). However, combination of heating steps 7-9 yields a preliminary age of 44.23 ±0.43 Ma that includes 35.6% of ^{39}Ar (Fig. 16).

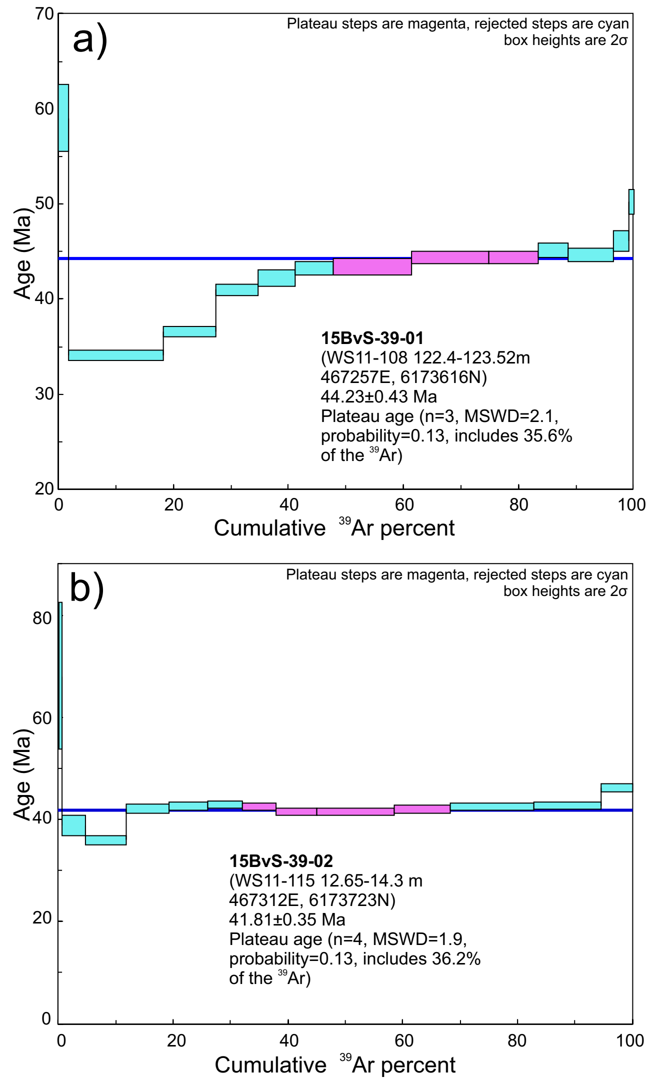

Fig. 16. Ar-Ar K-feldspar step-heating spectra from altered rocks at the Wolf deposit.

6.4.2. Sample 15BvS-39-02, altered volcaniclastic rock, $^{40}Ar/^{39}Ar$ K-feldspar

This is a drill core sample from the Wolf deposit (sample 8,

Fig. 3, Fig. 15), taken from DDH WS11-115, 12.7-12.9 m and 13.5-14.3 m downhole. The sample is about 21 m above (measured along the drill hole) mineralization at the No. 2B zone, which is at the contact between a unit of intermediate tuff breccia and lapilli tuff and an overlying unit of intermediate lithic and/or crystal-rich volcaniclastic rocks (Fig. 15; Sebert and Ramsay, 2012). We analyzed a K-feldspar-, sericite-, and locally Fe carbonate-altered, largely massive and poorly sorted volcaniclastic rock with matrix- to locally clast-supported subrounded to angular andesitic clasts in a crystal-bearing matrix. The sample did not return a robust Ar-Ar K-feldspar plateau age (using criteria defined by Ludwig, 2012). However, combination of heating steps 7-10 yields a preliminary age of 42.11 ±0.22 Ma that includes 36.2% of ^{39}Ar (Fig. 16).

7. Discussion

7.1. Preliminary environmental interpretations

Most of the lower Hazelton Group consists of lapilli tuff to tuff breccia with hornblende-plagioclase-phyric volcanic-derived clasts. Facies 1 consists mainly of coarse-grained pyroclastic rocks, indicating proximal-type explosive volcanism; m-scale intercalations of limestone and chert may indicate a subaqueous setting but abundant accessory limestone and chert clasts in pyroclastic rocks indicate coeval erosional stripping. Epiclastic rocks of facies 2 may mark a relative hiatus in volcanism. Abundant mudrocks with lesser muddy limestones and rare chert beds likely signify subaqueous sedimentation but polymictic conglomerates with well-rounded volcanic and chert clasts indicate intraformational erosion and subaerial and/or shallow-water reworking. Facies 3 also consists mainly of coarse pyroclastic rocks indicating proximal explosive volcanism; that some clasts with cuspate-lobate boundaries (suggesting ductility during emplacement) lack welding may signify subaqueous deposition. Sub-facies 3a is similar to facies 3 except that it contains abundant coarse-grained to megacrystic K-feldspar crystals and distinctly coherent and flow-banded textures. In facies 3b, the preservation of rhythmically laminated fine-grained sandstone to mudstone in sharp-based fining upward-sequences likely indicates mass flow sedimentation below fair-weather wave base. Sub-facies 3b also contains abundant limestone beds; local accretionary lapilli and glassy lapilli were likely derived from laterally adjacent subaerial eruptions (see e.g., McPhie et al., 1993).

7.2. Ages and regional correlations

Geochronology data presented above from the lower Hazelton Group yielded maximum depositional ages of 228.4 ±1.4 Ma (hornblende-plagioclase crystal-rich sandstone) and 206.7 ±1.9 Ma (polymictic pebble conglomerate). The detrital zircon population of the sandstone suggests derivation from erosion of Stikine plutonic suite sources (Late Triassic, ca. 229-216 Ma), similar to other detrital zircon samples from basal lower Hazelton Group throughout the Stewart-Iskut area (e.g., Nelson et al., 2018). The polymictic pebble conglomerate sample returned a unimodal Late Triassic to earliest Jurassic detrital zircon population, likely resulting from overlapping penecontemporaneous lower Hazelton Group volcanic sources (latest Triassic to earliest Jurassic). Deposition of the lower part of the Hazelton Group in the Kitsault River area was likely between ca. 206 Ma (Rhaetian) to ca. 196 Ma (Greig and Gehrels, 1995; Sinemurian).

The ca. 206 Ma volcanic-derived sandstone is potentially correlative to the Jack Formation (Nelson et al., 2018) of the southern Iskut Region and may similarly signify a break between the Hazelton Group rocks from the underlying Stuhini Group (Nelson et al., 2018). The ca. 196 Ma lapilli tuff to tuff breccias of facies 1 and 3, may be temporal equivalents to the Unuk River andesite unit described by Nelson et al. (2018). Predominantly epiclastic rocks of facies 2 are likely a local stratigraphic variation within the predominantly andesite unit. Sub-facies 3a (K-feldspar porphyritic unit) could be correlative to ca. 196 Ma porphyritic diorite (J. Nelson unpublished data, 2017) observed northwest of Brucejack Lake (Nelson et al., 2018). Alternatively, it may be related to the Brucejack Lake felsic unit, which is described as a felsic deposit, including K-feldspar-, plagioclase- and hornblende-phyric flows, breccias and bedded welded to non-welded tuffs (MacDonald, 1993). In the Brucejack area, this porphyritic unit has yielded a U-Pb age of ca. 183-188 Ma, which is younger than the ca. 196 Ma age from Grieg and Gehrels (1995).

The altered ca. 191 Ma monzonite dyke sampled west of the Homestake Ridge deposit is close to the ca. 196 Ma age (Greig and Gehrels, 1995) andesitic lapilli tuff to tuff breccia and K-feldspar porphyries. It is therefore possible that the Homestake Ridge mineralization is Early Jurassic. Felsic lapilli tuff in the footwall of the Wolf deposit in the Kitsault River valley west of our 2019 study area (Fig. 2) gave a crystallization age of 178.1 ±2.2 Ma (Toarcian), indicating that the area is underlain by the upper part of the Hazelton Group (Toarcian and younger). However, the bimodal mafic-felsic volcanic package characteristic of the similarly aged Iskut River Formation (Nelson et al., 2018) has not been observed in the Kitsault River valley.

Volcanic-derived sandstone with belemnite casts sampled near Kitsault Lake returned a preliminary maximum depositional age of 168.9 ±2.2 Ma, which suggests rocks temporally equivalent to the Quock Formation are present along the northern margin of the Kitsault River area and likely continue into the Kitsault River valley where the Dolly Varden deposits are located.

K-feldspar ^{40}Ar/^{39}Ar ages of ca. 42 and 44 Ma were interpreted from altered lapilli tuff units sampled above the Ag-rich mineralization at the Wolf deposit. K-feldspar, including both coarse- and fine-grained low-temperature polymorph adularia, has been successfully used to date epithermal deposits (e.g., Henry et al., 1997). The closure temperature of K-feldspar in the argon system ranges from 150-300°C and likely records late cooling histories, intermediate between ^{40}Ar/^{39}Ar biotite and apatite fission track data (Kelley, 2002; Streepey et al., 2002). We tentatively interpret the ca. 42-44 Ma ages record thermal perturbations and/or fluid flow associated with the formation of the Coast Plutonic Complex and related Eocene intrusions.

7.3. Implications for VMS-type mineralization systems of the Kitsault River area

VMS deposits form at or immediately beneath the seafloor in response to hydrothermal systems active during volcanism, and consist of syngenetic, stratabound, and locally stratiform lenses of massive sulphide and discordant vein- and/or stockwork-hosted sulphide (Large et al., 2001; Franklin et al., 2005; Galley et al., 2007). In the Kitsault River area, the lower part of the Hazelton Group hosts several high-grade Ag-Pb-Zn stratabound, vein- and breccia-hosted deposits, including the Dolly Varden, Torbrit and North Star mines that were active between 1915 and 1959 (Hanson, 1922; Black, 1951; Campbell, 1959; Dawson and Alldrick, 1986; Devlin and Godwin, 1986; Pinsent, 2001; Dunne and Pinsent, 2002). These deposits lie well to the east of the main Eskay rift trend (Fig. 2). The Ag-Pb-Zn mineralization in the Kitsault River area has been variably interpreted as epithermal vein-related (Grove, 1986), stratiform VMS (Devlin and Godwin, 1985; Devlin, 1987) or related to shallow subaqueous hot springs (Dunne and Pinsent, 2002). Our new age of ca. 178 Ma shows this mineralization is cogenetic with precious and base metal-rich VMS deposits hosted in the upper part of the Hazelton Group elsewhere, such as at Eskay Creek and Anyox (Alldrick, 1993; Smith, 1993; Barrett and Sherlock, 1996; Evenchick and McNicoll, 2002; MacDonald et al., 1996a; Macdonald et al., 1996b; Roth et al., 1999; Sherlock et al., 1999; Barresi and Dostal, 2005). Although upper Hazelton rocks appear to be developed along the Kitsault River valley hosting the Ag-rich Wolf deposit, preliminary mapping northwest and east of Kinskuch Lake suggests that only the lower part of the Hazelton Group is present, and rocks at the Dolly Varden deposit area appear to be similar to lower Hazelton Group rocks described in this study (intermediate tuff, lapilli tuff, porphyritic andesite; Devlin, 1987). The Kitsault River area also hosts porphyry Cu-Au systems (e.g., Big Bulk; Miller et al., 2020) and vein-hosted Au-Ag-Cu occurrences, which based on new geochronology data presented herein are likely related to magmatic activity during lower Hazelton Group volcanism.

The Dolly Varden and Wolf deposits contrast to the Eskay and Anyox deposits, both in mineralization type (e.g., Ag-rich versus Au- and Cu-rich), and host rock types (calc-alkaline intermediate-felsic volcanic rocks versus bimodal tholeiitic mafic to felsic volcanic rocks, some mudstone and mafic volcanic rocks). Similarities include complex stratiform and discordant vein-type mineralization styles with varying textures and mineralogy. The Eskay Creek deposit encompasses several stratiform to discordant Au-Ag-Pb-Zn-Cu zones with disseminated, massive to semi-massive sulphides and sulphosalts with varying amounts of barite content (Sherlock et al., 1999). The Anyox deposits consist of stratiform to stockwork Cu-Zn-Pb massive sulphide accumulations (MacDonald et al., 1996b) and the mineralization along the Dolly Varden trend are stratiform to slightly discordant Ag-Pb-Zn-barite deposits (Devlin and Godwin, 1986; Devlin, 1987). It seems that mineralization in the Kitsault River area was dispersed rather than focused in a discrete rift. Miller et al. (2020) present strong evidence for syndepositional faulting in the Kinskuch Lake area in the form of megaclast-bearing conglomerates similar to those described by Nelson and Kyba (2014) from the Jack Formation near the base of the Hazelton Group at Brucejack. We speculate that such syndepositional faults record extensional processes analogous to those that formed the Eskay rift and served as conduits for the passage of mineralizing hydro-magmatic fluids. Other Au-Ag-rich VMS-type mineralization in late Early to Middle Jurassic Hazelton Group rocks includes new discoveries southeast of the Brucejack Mine (Pretium Resources Inc., 2019), north of the Premier deposit at Silver Hill (Ascot Resources Ltd., 2019), and 30 km northeast of Stewart at Todd Creek (ArcWest Exploration Inc., 2019). These examples demonstrate the vast VMS-type mineralization potential of the Hazelton Group outside of the traditional Eskay rift.

8. Summary

Results from the first year of our multi-year study provide new resolution to the lower Hazelton Group stratigraphy and new U-Pb ages for the Hazelton Group and VMS-style mineralization in the Kitsault River area. The Hazelton Group rocks from Kitsault to Kinskuch Lake area are divided into three facies and two sub-facies. Facies 1 consists of lapilli tuff to tuff breccia with hornblende-plagioclase-phyric clasts and minor interbedded epiclastic rocks. Facies 2 consists mainly of epiclastic rocks. Facies 3 is predominantly lapilli tuff to tuff breccia with hornblende-plagioclase-phyric clasts and rare epiclastic rocks. Sub-facies 3a consists of K-feldspar-plagioclase porphyritic flows and lapilli tuff to tuff breccia with a plagioclase crystal-rich matrix and sub-facies 3b is a mixed unit with abundant volcanically derived tuff, lapilli tuff, and tuff breccia with thick limestone and mudstone-sandstone beds and local features indicating subaerial exposure. A sample of polymictic conglomerate from the base of the Hazelton Group yielded a maximum detrital zircon age (U-Pb, LA-ICPMS) of ca. 206 Ma, indicating that the onset of Hazelton Group volcanism was post-Rhaetian. A monzonite dike from the Homestake River deposit area returned a U-Pb CA-TIMS age of ca. 191 Ma suggesting the mineralization could be Early Jurassic. A lapilli tuff unit in the footwall of Ag-rich VMS mineralization at the Wolf deposit yielded a ca. 178 Ma age (U-Pb, LA-ICPMS), and a detrital zircon sample from a volcanic-derived sandstone yielded a maximum depositional age of ca. 169 Ma (U-Pb, LA-ICPMS), indicating that upper Hazelton Group units could be present in the Kitsault River valley close to the Dolly Varden mineralization trend.

Preliminary stratigraphic and geochronological results suggest that VMS-type mineralization in the Kitsault River area is related to shallow-level hydro-magmatic processes in an area of syndepositional faulting, parallel to the fully developed

Eskay rift. Coeval syngenetic mineralization systems in the two areas are likely related. Future work in the Kitsault River area will include geological mapping to better resolve the stratigraphy, timing, and geochemistry of the Hazelton Group.

Acknowledgments

We thank Dolly Varden Silver Corporation for logistical and helicopter support and a warm welcome in their Alice Arm exploration camp in 2015 and 2019. Cheerful and dedicated field assistance was provided by Meghan Holowath. Thanks to JoAnne Nelson for initiating reconnaissance studies in the Kitsault River area, co-collecting geochronology samples in 2015, and inspirational mentorship. A field visit in 2019 by Filippo Ferri was beneficial to our understanding of the field area. Chris Sebert is thanked for providing diamond drill hole geochronology samples, enlightening discussions, and showing us key outcrops and drill core in 2019. We also thank Richard Friedman (University of British Columbia, Vancouver) for providing preliminary U-Pb zircon geochronology results and Janet Gabites (University of British Columbia, Vancouver) for providing preliminary Ar-Ar K-feldspar geochronology results. A review by JoAnne Nelson significantly improved this manuscript.

References cited

Alldrick, D.J., 1993. Geology and metallogeny of the Stewart mining camp, northwestern British Columbia. British Columbia Ministry of Energy, Mines and Petroleum Resources, British Columbia Geological Survey Bulletin 85, 105 p.

Alldrick, D.J., Dawson, G.L., Bosher, J.A., and Webster, I.C.L., 1986. Geology of the Kitsault River area (NTS 103P). British Columbia Ministry of Energy, Mines and Petroleum Resources, British Columbia Geological Survey Open File 1986-02, 1:50,000 scale.

Anderson, R.G., 1989. A stratigraphic, plutonic and structural framework for the Iskut map area, northwestern British Columbia. In: Current Research, Part E, Geological Survey of Canada, Paper 89-1, pp. 145-154.

ArcWest Exploration Inc. 2019. ArcWest Exploration Inc. expands Yellow Bowl porphyry copper-gold target, Todd Creek project. https://arcwestexploration.com/2019/11/27/arcwest-exploration-inc-expands-yellow-bowl-porphyry-copper-gold-target-todd-creek-project/, last accessed December 2019.

Ascot Resources Ltd., 2019. Ascot intersects 880 g/t silver over 1.00 metre at new Silver Hill target. https://ascotgold.com/news-releases/2019/ascot-intersects-880g-t-silver-over-1.00-metre-at-new-silver-hill-target/, last accessed December 2019.

Barresi, T., and Dostal, J., 2005. Geochemistry and petrography of upper Hazelton Group volcanics: VHMS-favourable stratigraphy in the Iskut River and Telegraph Creek map areas, northwestern British Columbia. In: Geological Fieldwork 2004, British Columbia Ministry of Energy and Mines, British Columbia Geological Survey Paper 2005-1, pp. 39-47.

Barresi, T., Nelson, J.L., and Dostal, J., 2015. Geochemical constraints on magmatic and metallogenic processes: Iskut River Formation, volcanogenic massive sulfide-hosting basalts, NW British Columbia, Canada. Canadian Journal of Earth Sciences, 52, 1-20.

Barrett, T.J., and Sherlock, R.L., 1996. Geology, lithogeochemistry and volcanic setting of the Eskay Creek Au-Ag-Cu-Zn deposit, northwestern British Columbia. Exploration and Mining Geology, 5, 339-368.

Black, J.M., 1951. Geology and mineral occurrences of the Upper Kitsault Valley. In: British Columbia Ministry of Energy, Mines and Petroleum Resources, British Columbia Geological Survey Annual Report, pp. A76-A83.

Brown, D.A., Gunning, M.H., and Greig, C.J., 1996. The Stikine project: Geology of western Telegraph Creek map area, northwestern British Columbia. British Columbia Ministry of Employment and Investment, British Columbia Geological Survey Bulletin 95, 130 p.

Campbell, F.A., 1959. The geology of Torbrit Silver Mine, British Columbia. Economic Geology, 54, 1461-1495. doi: 10.2113/gsecongeo.54.8.1461.

Carter, N.C., 1981. Porphyry copper and molybdenum deposits, west-central British Columbia. In: British Columbia Ministry of Energy Mines and Petroleum Resources, British Columbia Geological Survey Bulletin 64, 81 p.

Childe, F., 1996. U-Pb geochronology and Nd and Pb isotope characteristics of the Au-Ag-rich Eskay Creek volcanogenic massive sulfide deposit, British Columbia. Economic Geology, 91, 1209-1224. doi: 10.2113/gsecongeo.91.7.1209.

Childe, F.C., 1997. Timing and tectonic setting of volcanogenic massive sulphide deposits in British Columbia: constraints from U-Pb geochronology, radiogenic isotopes, and geochemistry. Unpublished Ph.D. thesis, The University of British Columbia, Vancouver, B.C., Canada. Available from https://circle.ubc.ca/handle/2429/7311 accessed April, 2012.

Colpron, M., Nelson, J.L., and Murphy, D.C., 2007. Northern Cordilleran terranes and their interactions through time. GSA Today, 17, 4-10.

Coney, P.J., Jones, D.L., and Monger, J.W.H., 1980. Cordilleran suspect terranes. Nature, 288, 329-333. doi: 10.1038/288329a0.

Coutts, D.S., Matthews, W.A., and Hubbard, S.M., 2019. Assessment of widely used methods to derive depositional ages from detrital zircon populations. Geoscience Frontiers, 10, 1421-1435. doi: 10.1016/j.gsf.2018.11.002.

Dawson, G.L., and Alldrick, D.J., 1986. Geology and mineral deposits of the Kitsault Valley. In: Geological Fieldwork 1985, British Columbia Ministry of Energy, Mines and Petroleum Resources, British Columbia Geological Survey Paper 1986-1, pp. 219-224.

Devlin, B.D., 1987. Geology and genesis of the Dolly Varden silver camp, Alice Arm area, northwestern British Columbia. Unpublished M.Sc. thesis, The University of British Columbia, Vancouver, B.C., Canada. Available from https://open.library.ubc.ca/cIRcle/collections/ubctheses/831/items/1.0052815 accessed November 5, 2015.

Devlin, B.D., and Godwin, C.I., 1986. Geology of the Dolly Varden camp, Alice Arm area. In: Geological Fieldwork 1985, British Columbia Ministry of Energy, Mines and Petroleum Resources, British Columbia Geological Survey Paper 1986-1, pp. 327-330.

Diakow, L.J., Panteleyev, A., and Schroeter, T.G., 1991. Jurassic epithermal deposits in the Toodoggone River area, northern British Columbia; examples of well-preserved, volcanic-hosted, precious metal mineralization. Economic Geology, 86, 529-554. doi: 10.2113/gsecongeo.86.3.529.

Dickinson, W.R., and Gehrels, G.E., 2009. Use of U-Pb ages of detrital zircons to infer maximum depositional ages of strata: A test against a Colorado Plateau Mesozoic database. Earth and Planetary Science Letters, 288, 115-125. doi: 10.1016/j.epsl.2009.09.013.

Dott, R.H., 1964. Wacke, graywacke and matrix; what approach to immature sandstone classification? Journal of Sedimentary Research, 34, 625-632. doi: 10.1306/74D71109-2B21-11D7-8648000102C1865D.

Dunne, K.P.E., and Pinsent, R.H., 2002. Depositional setting of silver-rich quartz-sulphate-carbonate deposits of the upper Kitsault River area, northwest British Columbia. In: Geological Fieldwork 2001, British Columbia Ministry of Energy, Mines and Petroleum

Resources, British Columbia Geological Survey Paper 2002-01, pp. 177-196.
Eisbacher, G.H., 1981. Late Mesozoic-Paleogene Bowser Basin molasse and Cordilleran tectonics, western Canada. In: Miall, A.D., (Ed.), Sedimentation and Tectonics in Alluvial Basins, Geological Association of Canada Special Paper 23, pp. 125-151.
Evenchick, C.A., and McNicoll, V.J., 2002. Stratigraphy, structure, and geochronology of the Anyox Pendant, northwest British Columbia, and implications for mineral exploration. Canadian Journal of Earth Sciences, 39, 1313-1332. doi: 10.1139/e02-036.
Evenchick, C.A., and Thorkelson, D.J., 2005. Geology of the Spatsizi River map area, north-central British Columbia. Geological Survey of Canada Bulletin 577, 276 p.
Evenchick, C.A., McMechan, M.E., McNicoll, V.J., and Carr, S.D., 2007. A synthesis of the Jurassic-Cretaceous tectonic evolution of the central and southeastern Canadian Cordillera: Exploring links across the orogen. In: Sears, J.W., Harms, T.A. and Evenchick, C.A., (Eds.), Whence the mountains? Inquiries in the evolution of orogenic systems: A volume in honor or Raymond A. Price, Geological Society of America Special Paper 433, pp. 117-145.
Evenchick, C.A., Mustard, P.S., Greig, C.J., McMechan, M.E., Ritcey, D.H., Smith, G.T., and Ferri, F., 2008. Geology, Nass River, British Columbia. Open File, Geological Survey of Canada. Available from http://geoscan.ess.nrcan.gc.ca/cgi-bin/starfinder/0?path=geoscan.fl&id=fastlink&pass=&search=R%3D225792&format=FLFULL accessed June 9, 2015.
Fisher, R.V., 1966. Rocks composed of volcanic fragments. Earth-Science Reviews, 1, 287-298.
Franklin, J.M., Gibson, H.L., Jonasson, I.R., and Galley, A.G., 2005. Volcanogenic massive sulfide deposits. In: Hedenquist, J.W., Thompson, J.F.H., Goldfarb, R.J., and Richards, J.P., (Eds.), Economic Geology 100th Anniversary Volume, The Economic Geology Publishing Company, pp. 523-560.
Gagnon, J.-F., Barresi, T., Waldron, J.W.F., Nelson, J.L., Poulton, T.P., and Cordey, F., 2012. Stratigraphy of the upper Hazelton Group and the Jurassic evolution of the Stikine terrane, British Columbia. Canadian Journal of Earth Sciences, 49, 1027-1052. doi: 10.1139/e2012-042.
Galley, A.G., Hannington, M.D., and Jonasson, M., 2007. Volcanogenic massive sulphide deposits. In: Goodfellow, W.D., (Ed.), Mineral deposits of Canada: A synthesis of major deposit types, district metallogeny, the evolution of geological provinces, and exploration methods, Geological Association of Canada, Mineral Deposits Division, Special Publication 5, pp. 141-161.
Godwin, C.I., Pickering, D.R., Gabites, J.E., and Alldrick, D.J., 1991. Interpretation of galena lead isotopes from the Stewart-Iskut area (103O, P; 104A, B G). In: Geological Fieldwork 1990, British Columbia Ministry of Energy and Mines, British Columbia Geological Survey Paper 1991-01, pp. 235-243.
Greig, C.J., 1991. Stratigraphic and structural relations along the west-central margin of the Bowser Basin, Oweegee and Kinskuch areas, northwestern British Columbia. In: Current Research, Part A, Geological Survey of Canada Paper 91-1A, pp. 197-205.
Greig, C.J., 1992. Jurassic and Cretaceous plutonic and structural styles of the Eagle Plutonic Complex, southwestern British Columbia, and their regional significance. Canadian Journal of Earth Sciences, 29, 793-811. doi: 10.1139/e92-067.
Greig, C., 2014. Latest Triassic-Earliest Jurassic contractional deformation, uplift and erosion in Stikinia, northwest British Columbia. 2014 GSA Annual Meeting in Vancouver, British Columbia (19-22 October 2014), GSA. Available from https://gsa.confex.com/gsa/2014AM/webprogram/Paper248914.html accessed November 8, 2019.
Greig, C.J., and Gehrels, G.E., 1995. U-Pb zircon geochronology of Lower Jurassic and Paleozoic Stikinian strata and Tertiary intrusions, northwestern British Columbia. Canadian Journal of Earth Sciences, 32, 1155-1171. doi: 10.1139/e95-095.
Greig, C.J., Anderson, R.G., Daubeny, P.H., and Bull, K.F., 1994. Geology of the Cambria Icefield: Stewart (103P/13), Bear River (104A/4), and parts of Meziadin Lake (104A/3) and Paw Lake (103P/12) map areas, northwestern British Columbia, 1:50,000 scale.
Grove, E.W., 1986. Geology and mineral deposits of the Stewart area, British Columbia. British Columbia Ministry of Energy, Mines and Petroleum Resources, British Columbia Geological Survey Bulletin 58, 219 p.
Hanson, G., 1922. Upper Kitsault Valley, British Columbia. In: Geological Survey of Canada, Summary Report Part A, pp. 7-21.
Hanson, G., 1923. Reconnaissance between the Skeena River and Stewart, British Columbia. In: Geological Survey of Canada, Summary Report Part A, pp. 29-45.
Hanson, G., 1928. Mineral deposits of the Alice Arm district. In: Geological Survey of Canada, Summary Report Part A, p. 27.
Henry, C.D., Elson, H.B., McIntosh, W.C., Heizler, M.T., and Castor, S.B., 1997. Brief duration of hydrothermal activity at Round Mountain, Nevada, determined from $^{40}Ar/^{39}Ar$ geochronology. Economic Geology, 92, 807-826. doi: 10.2113/gsecongeo.92.7-8.807.
Herriott, T.M., Crowley, J.L., Schmitz, M.D., Wartes, M.A., and Gillis, R.J., 2019. Exploring the law of detrital zircon: LA-ICP-MS and CA-TIMS geochronology of Jurassic forearc strata, Cook Inlet, Alaska, USA. Geology, 47, 1044-1048. doi: 10.1130/G46312.1.
Higgs, A.A., 2015. 2015 Technical Report for the Dolly Varden Property, Skeena Mining Division (NTS 103P/11, 12, 13, and 14), 133p, https://www.dollyvardensilver.com/site/assets/files/1326/dv-2015-04-16-43-101-technical-report.pdf, last accessed December 2019.
Hoy, T., 1991. Volcanogenic massive sulphide deposits in British Columbia. In: McMillan, W.J., (Ed.), Ore Deposits, Tectonics and Metallogeny in the Canadian Cordillera, British Columbia Ministry of Energy, Mines and Petroleum Resources, British Columbia Geological Survey Paper 1991-4, pp. 89-124.
Kelley, S., 2002. K-Ar and Ar-Ar dating. Reviews in Mineralogy and Geochemistry, 47, 785-818. doi: 10.2138/rmg.2002.47.17.
Large, R.R., McPhie, J., Gemmell, J.B., Herrmann, W., and Davidson, G.J., 2001. The spectrum of ore deposit types, volcanic environments, alteration halos, and related exploration vectors in submarine volcanic successions: Some examples from Australia. Economic Geology, 96, 913-938. doi: 10.2113/gsecongeo.96.5.913.
Logan, J.M., Drobe, J.R., and McClelland, W.C., 2000. Geology of the Forrest Kerr-Mess Creek area, northwestern British Columbia. British Columbia Geological Survey Bulletin 104, 132 p.
Logan, J.M., and Mihalynuk, M.G., 2014. Tectonic controls on Early Mesozoic paired alkaline porphyry deposit belts (Cu-Au ±Ag-Pt-Pd-Mo) within the Canadian Cordillera. Economic Geology, 109, 827-858. doi: 10.2113/econgeo.109.4.827.
Ludwig, K.R., 2012. Isoplot 3.75. A geochronological toolkit for Microsoft Excel. Special Publication, Berkley Geochronology Center, 75 p.
MacDonald, A.J., 1993. Lithostratigraphy and geochronometry, Brucejack Lake, northwestern British Columbia (104B/08E). In: Geological Fieldwork 1992, British Columbia Ministry of Energy and Mines, British Columbia Geological Survey Paper 1993-1, pp. 315-323.
Macdonald, A.J., Lewis, P.D., Thompson, J.F.H., Nadaraju, G., Bartsch, R., Bridge, D.J., Rhys, D.A., Roth, T., Kaip, A., Godwin, C.I., and Sinclair, A.J., 1996a. Metallogeny of an Early to Middle Jurassic arc, Iskut River area, northwestern British Columbia. Economic Geology, 91, 1098-1114. doi: 10.2113/gsecongeo.91.6.1098.
MacDonald, R.W.J., Barrett, T.J., and Sherlock, R.L., 1996b. Geology and lithogeochemistry at the Hidden Creek massive

sulfide deposit, Anyox, west-central British Columbia. Exploration and Mining Geology, 5, 369-398.
MacIntyre, D., Ash, C., and Britton, J., 1994. Geological compilation Skeena-Nass area, west central British Columbia. In: British Columbia Ministry of Energy, Mines and Petroleum Resources, British Columbia Geological Survey Open File 1994-14, 1:250,000 scale.
Marsden, H., and Thorkelson, D.J., 1992. Geology of the Hazelton volcanic belt in British Columbia: Implications for the Early to Middle Jurassic evolution of Stikinia. Tectonics, 11, pp. 1266-1287. doi: 199210.1029/92TC00276.
McConnell, R.G., 1913. Portions of Portland Canal and Skeena Mining Divisions, Skeena District, British Columbia. Geological Survey of Canada, Memoir 32, 101 p.
McCuaig, M., and Sebert, C., 2017. 2016 Technical Report for the Dolly Varden Property, Skeena Mining Division. British Columbia Ministry of Energy, Mines and Petroleum Resources Assessment Report 36934.
McPhie, J., Doyle, M., and Allen, R., 1993. Volcanic textures. A guide to the interpretation of textures in volcanic rocks. Centre for Ore Deposits and Exploration Studies, University of Tasmania, Hobart, Australia, 198 p.
Miller, E.A., Kennedy, L.A., and van Straaten, B.I., 2020. Geology of the Kinskuch Lake area and Big Bulk porphyry prospect: Syndepositional faulting and local basin formation during the Rhaetian (latest Triassic) transition from the Stuhini to the Hazelton Group In: Geological Fieldwork 2019, British Columbia Ministry of Energy, Mines and Petroleum Resources, British Columbia Geological Survey Paper 2020-01, pp. 77-99.
Monger, J.W.H., 1977. The Triassic Takla Group in McConnell Creek map-area, north central British Columbia. Geological Survey of Canada Paper 76-29, 45 p.
Monger, J.W.H., Price, R.A., and Tempelman-Kluit, D.J., 1982. Tectonic accretion and the origin of the two major metamorphic and plutonic welts in the Canadian Cordillera. Geology, 10, 70-75. doi: 10.1130/0091-7613(1982)10<70:TAATOO>2.0.CO;2.
Monger, J.W.H., Wheeler, J.O., Tipper, H.W., Gabrielse, H., Harms, T., Struik, L.C., Campbell, R.B., Dodds, C.J., Gehrels, G.E., and O'Brien, J., 1991. Part B. Cordilleran Terranes. In: Gabrielse, H., and Yorath, C.J., (Eds.), Upper Devonian to Middle Jurassic assemblages, Chapter 8, Geology of the Cordilleran Orogen in Canada 4, pp. 281-327.
Mortensen, J.K., and Kirkham, R.V., 1992. A U-Pb zircon age for host rocks of a syngenetic strontium(-zinc) occurrence in the Kitsault Lake area, west-central British Columbia. In: Radiogenic Age and Isotopic Studies, Report 5, Geological Survey of Canada, Paper 91.2, pp. 181-185.
Nelson, J.L., Colpron, M., and Israel, S., 2013. The Cordillera of British Columbia, Yukon and Alaska: Tectonics and metallogeny. In: Colpron, M., Bissig, T., Rusk, B. G., and Thompson, J., (Eds.), Tectonics, Metallogeny and Discovery: The North American Cordillera and Similar Accretionary Settings, Society of Economic Geologists Special Publication 17, pp. 53-110.
Nelson, J.L., and Kyba, J., 2014. Structural and stratigraphic control of porphyry and related mineralization in the Treaty Glacier-KSM-Brucejack-Stewart trend of western Stikinia. In: Geological Fieldwork 2013, British Columbia Ministry of Energy, Mines and Petroleum Resources, British Columbia Geological Survey Paper 2014-1, pp. 111-140.
Nelson, J.L., Waldron, J., van Straaten, B.I., Zagorevski, A., and Rees, C., 2018. Revised stratigraphy of the Hazelton Group in the Iskut River region, northwestern British Columbia. In: Geological Fieldwork 2017, British Columbia Ministry of Energy, Mines and Petroleum Resources, British Columbia Geological Survey Paper 2018-1, pp. 15-38.
Orton, G.J., 1995. Facies models in volcanic terrains: Time's arrow versus time's cycle. In: Plint, A.G., (Ed.), Sedimentary Facies Analysis, International Association of Sedimentologists Special Publication 22, pp. 157-193.
Pinsent, R.H., 2001. Mineral deposits of the upper Kitsault River area, British Columbia. In: Geological Fieldwork 2000, British Columbia Ministry of Energy and Mines, British Columbia Geological Survey Paper 2001-1, pp. 313-326.
Pretium Resources Inc., 2019. Pretium exploration and Brucejack update. https://www.pretivm.com/news/news-release-details/2019/Pretivm-Exploration-And-Brucejack-Update/default.aspx, last accessed December 2019.
Ross, D., and Chamois, P., 2017. Technical report on the Homestake Ridge project, Skeena mining division, northwestern British Columbia. Report prepared for Auryn Resources Inc., https://www.aurynresources.com/site/assets/files/2343/auryn_resources_homestake_ridge_ni_43-101_23oct2017.pdf, last accessed December 2019.
Roth, T., Thompson, J.F.H., and Barrett, T.J., 1999. The precious metal-rich Eskay Creek deposit, northwestern British Columbia. In: Barrie, C. T., and Hannington, M.D., (Eds.), Volcanic-associated massive sulfide deposits: processes and examples in modern and ancient setting, Reviews in Economic Geology 8, pp. 357-374.
Schmid, R., 1981. Descriptive nomenclature and classification of pyroclastic deposits and fragments: Recommendations of the IUGS Subcommission on the Systematics of Igneous Rocks. Geology, 9, 41-43. doi: 10.1130/0091-7613(1981)9<41:DNACOP >2.0.CO;2.
Sebert, C., and Ramsay, A., 2012. Technical report on the Wolf deposit 2011 exploration program: Geology and diamond drilling. Ministry of Energy and Mines, British Columbia Geological Survey Assessment Report 33326, 55 p.
Sherlock, R.L., Roth, T., Spooner, E.T.C., and Bray, C.J., 1999. Origin of the Eskay Creek precious metal-rich volcanogenic massive sulfide deposit; fluid inclusion and stable isotope evidence. Economic Geology, 94, 803-824. doi: 10.2113/gsecongeo.94.6.803.
Smith, A.D., 1993. Geochemistry and tectonic setting of volcanics from the Anyox mining camp, British Columbia. Canadian Journal of Earth Sciences, 30, 48-59. doi: 10.1139/e93-005.
Streepey, M.M., Hall, C.M., and van der Pluijm, B.A., 2002. The ^{40}Ar-^{39}Ar laser analysis of K-feldspar: Constraints on the uplift history of the Grenville Province in Ontario and New York. Journal of Geophysical Research: Solid Earth, 107, 1-11. doi: 10.1029/2001JB001094.
Swanton, D., Baker, D., Hughes, C., Marsden, H., and Lajoie, J., 2013. 2013 diamond drilling, geological, geochemical and geophysical report Homestake Ridge project. Ministry of Energy and Mines, British Columbia Geological Survey Assessment Report 34433, 94 p.
Tipper, H.W., and Richards, T.A., 1976. Jurassic stratigraphy and history of north-central British Columbia. Geological Survey of Canada Bulletin 270, 82 p.
Turnbull, J.M., 1916. Alice Arm district. In: British Columbia Ministry of Energy Mines and Petroleum Resources, British Columbia Geological Survey Annual Report 1916, pp. 53-84.
Turner, A.J., and Nicholls, S.J., 2019. Technical report and mineral resource update for the Dolly Varden property, British Columbia, Canada. NI 43-101 Report prepared for Dolly Varden Silver Corporation, 175p, https://www.dollyvardensilver.com/site/assets/files/1652/dolly-varden-ni43-101-21june2019-apex.pdf, last accessed December 2019.
Wheeler, J.O., Brookfield, A.J., Gabrielse, H., Monger, J.W.H., Tipper, H.W., and Woodsworth, G.J., 1991. Terrane map of the Canadian Cordillera. Geological Survey of Canada Map 1713A, 1:2,000,000 scale.

Late Neogene porphyry Cu-Mo(±Au-Ag) mineralization in British Columbia: the Klaskish Plutonic Suite, northern Vancouver Island

Graham T. Nixon[1, a], Richard M. Friedman[2], and Robert A. Creaser[3]

[1] British Columbia Geological Survey, Ministry of Energy, Mines and Petroleum Resources, Victoria, BC, V8W 9N3
[2] Pacific Centre for Geochemical and Isotopic Research, Department of Earth, Ocean and Atmospheric Sciences, University of British Columbia, Vancouver, BC, V6T 1Z4
[3] Department of Earth and Atmospheric Sciences, University of Alberta, Edmonton, AB, T6G 2E3
[a] corresponding author: Graham.Nixon@gov.bc.ca

Recommended citation: Nixon, G.T., Friedman, R.M., and Creaser, R.A., 2020. Late Neogene porphyry Cu-Mo(±Au-Ag) mineralization in British Columbia: the Klaskish Plutonic Suite, northern Vancouver Island. In: Geological Fieldwork 2019, British Columbia Ministry of Energy, Mines and Petroleum Resources, British Columbia Geological Survey Paper 2020-01, pp. 119-132.

Abstract

Late Neogene porphyry Cu-Mo mineralization hosted by the Klaskish Plutonic Suite (new formal name) in northern Vancouver Island occupies a unique position in the forearc of the Cascadia subduction zone. The Klaskish granitoid plutons and Alert Bay volcanic rocks comprise the Brooks magmatic suite, which forms a northeast-oriented zone, the Brooks-Haddington tract, extending for 65 km across the island from the Pacific coast to Queen Charlotte Strait in the east. The southern part of the Brooks-Haddington tract is marked by a narrow (10 km) structural corridor, the Brooks Peninsula fault zone, which hosts the mineralized Klaskish intrusions. The northern part of the tract is occupied by eroded edifices of the Alert Bay volcanic suite. High-precision U-Pb zircon and Re-Os molybdenite dates for mineralized stocks of the Klaskish Plutonic Suite (ca. 7-4.6 Ma) confirm that their emplacement was coeval with older phases of Alert Bay volcanism (8-2.5 Ma), and that porphyry Cu-Mo magmatic-hydrothermal systems are genetically linked to pluton emplacement and crystallization. Neogene plutons associated with porphyry Mo/Cu-Mo mineralization elsewhere in British Columbia are restricted to the Pemberton arc in the southeastern Coast Mountains, where pluton ages diminish progressively northwards. The late Neogene porphyry Cu-Mo mineralizing systems in the Pemberton arc and forearc environment of northern Vancouver Island are linked to the plate tectonic evolution of the northern Cascadia subduction zone, notably plate-edge effects generated by subduction of the Juan de Fuca plate and newly redefined Nootka fault zone in the oceanic crust. The young Cu-Mo porphyry mineralization in northern Vancouver Island forms a well-defined metallotect that is underexplored and rich in opportunities for discovering economic porphyry deposits.

Keywords: Porphyry Cu-Mo, Klaskish Plutonic Suite, northern Vancouver Island, geochronology, regional geology, Alert Bay volcanic rocks, Brooks magmatic suite, Brooks-Haddington tract, Wrangellia, Pemberton arc, Neogene magmatism, Juan de Fuca plate, Explorer plate, Nootka fault zone, Cascadia subduction zone

1. Introduction

British Columbia is the leading producer of copper and only producer of molybdenum in Canada thanks to its rich endowment of porphyry copper deposits in the accreted magmatic arc terranes of the Cordillera. Of eleven operating metal mines in the province in 2018, copper production at seven bulk tonnage operations amounted to \$2.46 billion (Natural Resources Canada, 2019) and accounted for 70% of the value of all metal mine production excluding the principal by-product commodities of Au, Ag, and Mo (Clarke et al., 2019). The most prodigious epoch for the formation of porphyry copper deposits in British Columbia is a 15 million-year time interval (ca. 210-195 Ma) straddling the Triassic-Jurassic boundary. Porphyry production was particularly prolific within a 6 million-year window centred on ca. 205 Ma (latest Triassic) when more than 90% of the known copper endowment was acquired in the accreted magmatic arc terranes of Quesnellia and Stikinia (Logan and Mihalynuk, 2014).

The largest bulk tonnage operation on Vancouver Island was the former Island Copper mine (1971-1995), which produced 1.2 billion kg Cu, 32 million kg Mo, 294,106 kg Ag, 35,268 kg Au, and 236 kg Re from 367 Mt of ore (MINFILE 092L 158). The flooded open pit lies on Rupert Inlet adjacent to the Holberg fault near the eastern extremity of a belt of Middle Jurassic volcanic rocks of the Bonanza Group and well-mineralized, coeval intrusions of the Island Plutonic Suite that include the porphyry Cu-Mo-Au deposits of Hushamu (MINFILE 092L 240) and Red Dog (MINFILE 092L 200; Nixon et al., 2011a; Fig. 1). Estimates for drill-indicated and inferred resources at Hushamu total 532.5 Mt at a grade of 0.22% Cu, 0.0076% Mo, 0.265 g/t Au and 0.47 ppm Re; and for Red Dog are 38.3 Mt at 0.267% Cu, 0.0048% Mo and 0.376 g/t Au (Northisle Copper and Gold Inc., 2019).

The late Neogene Klaskish Plutonic Suite in northern Vancouver Island comprises some of the youngest granitoid intrusions in the Cordillera. As shown below, these intrusions

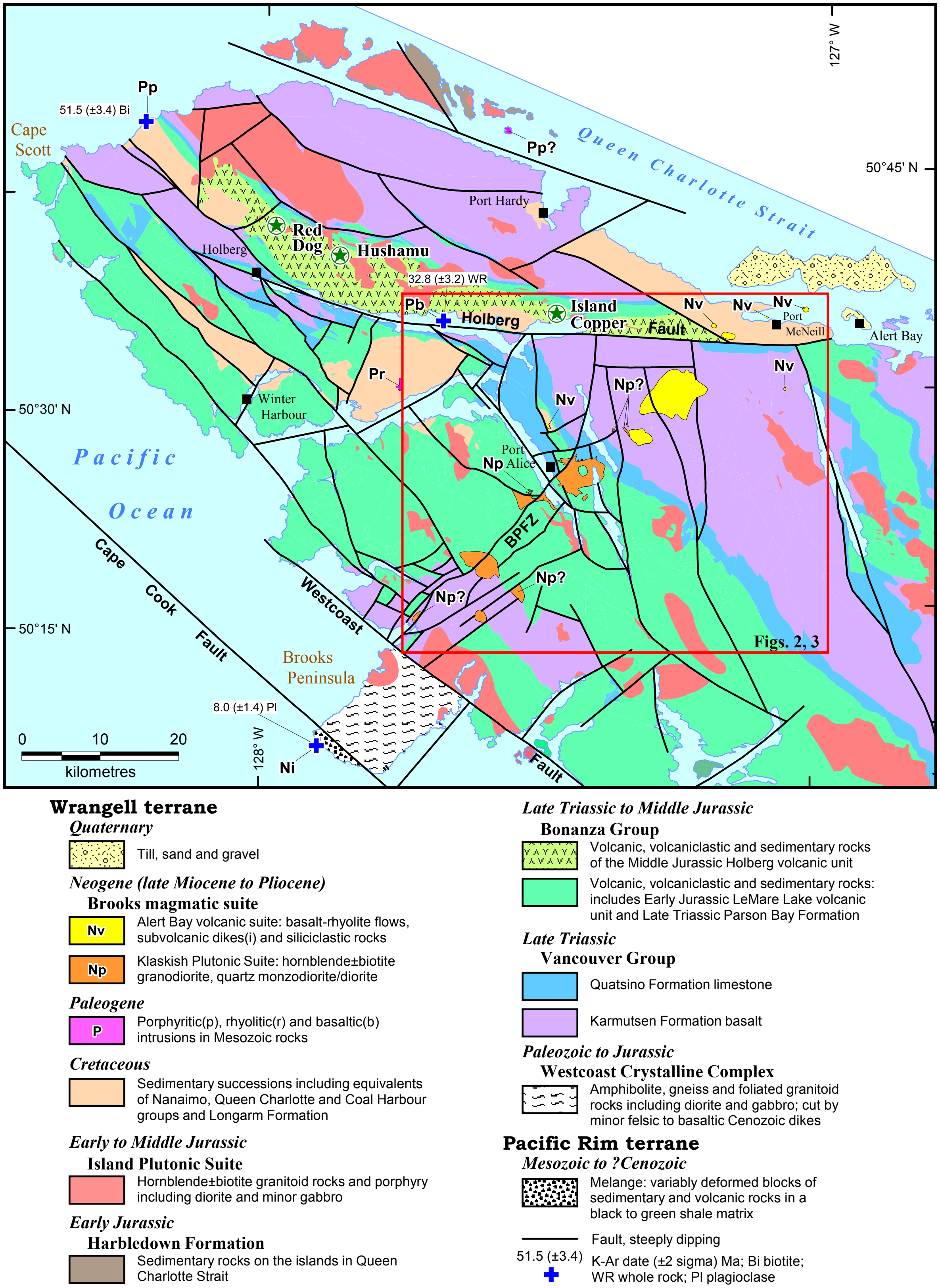

Fig. 1. Generalized geology of northern Vancouver Island showing the principal Mesozoic-Cenozoic stratigraphic and intrusive units (after Muller et al., 1974 and Nixon et al., 2011a-e with minor modifications). K-Ar dates are given for Paleogene and late Neogene localities situated outside Figs. 2 and 3 (red inset box). Geochronological data are from Muller et al. (1974) and Armstrong et al. (1985) corrected for modern decay constants where necessary (Steiger and Jäger, 1977; Breitsprecher and Mortensen, 2004). Middle Jurassic Cu-Mo-Au porphyry deposits (green stars) at the former Island Copper mine (1971-1995), Red Dog and Hushamu are shown for reference. BPFZ, Brooks Peninsula fault zone.

are spatially associated with various mineral occurrences, including genetically related and potentially economic porphyry Cu-Mo(±Au±Ag) mineralization. The Klaskish intrusions mineralogically resemble members of the Early to Middle Jurassic Island Plutonic Suite and have been mapped as such in the past. Confident discrimination between the two intrusive suites is best achieved using U-Pb dating techniques. The diverse mineral occurrences previously documented in this intrusive belt are re-evaluated herein for their porphyry copper potential. The results are encouraging and extend the prospective ground for targeting exploration throughout this young metallogenic tract.

The principal objectives of this contribution are to 1) document the spatiotemporal distribution of late Neogene plutonic and volcanic suites on northern Vancouver Island using previously published and unpublished isotopic age determinations; 2) demonstrate the intimate timing and de facto genetic relationship between pluton crystallization and porphyry mineralization using high-precision U-Pb and Re-Os geochronology; and 3) underscore the fundamental influence that plate tectonic events at the northern margin of the Cascadia subduction zone have played in the late Neogene magmatism and mineralization.

2. Previous work

The first comprehensive regional map (1:250,000 scale) and descriptions of the geology of northern Vancouver Island (NTS 102I/92L) were published by Muller and coworkers, who also summarized earlier work in the area (Muller et al., 1974; Muller and Roddick, 1983). Subsequent regional mapping (1:50,000 scale) by Nixon et al. (2011a-e) resulted in revisions to the Mesozoic stratigraphy (Nixon and Orr, 2007) and revealed the presence of late Neogene granitoid intrusions, the Klaskish Plutonic Suite, which are coeval with previously documented Alert Bay volcanic rocks (Muller et al., 1974; Armstrong et al., 1985). The Mesozoic-early Cenozoic bedrock units of northern Vancouver Island are described briefly below before focusing on the late Neogene magmatic suite and associated mineralization.

3. Geological setting

Northern Vancouver Island is predominantly underlain by a faulted, westerly to southerly dipping, homoclinal stratigraphic succession of early Mesozoic strata intruded by granitoid plutons and unconformably overlain by the eroded remnants of Cretaceous stratigraphy (Fig. 1). The oldest exposed rocks on northern Vancouver Island are the Late Triassic Karmutsen Formation and overlying Quatsino limestone of the Vancouver Group, which form part of an accreted oceanic plateau unique to the Wrangell terrane (Greene et al., 2010; Fig. 1). Older rocks underlying the Karmutsen basalts, the Middle to Upper Triassic 'sediment-sill' unit and Paleozoic Sicker Group are exposed 35 km east of the map area near Schoen Lake (Muller et al., 1974), and are considered to form the substrate of northern Vancouver Island. The Vancouver Group is overlain by arc-related volcanic and sedimentary strata of the Bonanza Group including, from base to top, the Late Triassic Parson Bay Formation and overlying Early to Middle Jurassic LeMare Lake and Holberg volcanic units together with coeval intrusions of the Island Plutonic Suite (Fig. 1; Nixon and Orr, 2007). Exposures of marine tuffaceous argillites of the Early Jurassic Harbledown Formation, correlative in part with the Bonanza Group, are restricted to islands in Queen Charlotte Strait. Cretaceous sedimentary sequences deposited in fault-disrupted marine basins rest unconformably on these deformed, uplifted and eroded older rocks. Isolated occurrences of Paleogene rhyolitic to basaltic dikes (ca. 51-33 Ma; Eocene-Oligocene) cut Cretaceous and older units (Fig. 1).

The Triassic-Jurassic stratigraphy of northern Vancouver Island is separated from the uplifted block of Brooks Peninsula by the Westcoast fault (Fig. 1). The Westcoast Crystalline complex underlies most of the peninsula and comprises meta-igneous and metasedimentary rocks including amphibolite, gneiss, migmatite, agmatite and gabbroic to granodioritic plutons distinguished from the Island Plutonic Suite by the presence of a penetrative fabric. These deformed and metamorphosed rocks are considered to represent the lower crustal equivalents of Triassic-Jurassic stratigraphic units and plutons exposed to the east (Muller et al., 1974; DeBari et al., 1999). At the tip of the Brooks Peninsula, the Westcoast complex lies in fault contact with a fault sliver of the Pacific Rim terrane, an olistostromal mélange containing blocks of chert, conglomerate, greywacke and basalt set in a black shale matrix (Smyth, 1985). The Brooks Peninsula is likely bounded by northeasterly-trending, steeply dipping faults as reflected by the orientation of undeformed Cenozoic dikes mapped by Smyth (1985) along the north and south shores of the peninsula. One such basaltic dike cutting the mélange at the southwestern tip of the peninsula has yielded a late Neogene K-Ar age (ca. 8 Ma; Armstrong et al., 1985) and belongs to the Alert Bay volcanic suite (Fig. 1). The significance of the Brooks Peninsula fault zone (Fig. 1; Muller et al., 1974) with respect to late Neogene magmatism is explored below.

4. Late Neogene Brooks magmatic suite

Late Neogene volcanic rocks of the Alert Bay suite (Muller et al., 1974; Armstrong et al., 1985) and more recently identified, partly coeval granitoid intrusions of the Klaskish Plutonic Suite (Nixon et al., 2011c-d) are collectively termed the Brooks magmatic suite in this study. The volcanic and intrusive rocks are exposed discontinuously along a northeast-oriented tract, herein named the Brooks-Haddington tract, that extends 65 km across northern Vancouver Island from the Pacific coast near the Brooks Peninsula to Haddington Island east of Port McNeill (Fig. 1). The southern part of this tract hosts the Klaskish Plutonic Suite and is marked by closely spaced, steeply dipping faults, collectively known as the Brooks Peninsula fault zone (Fig. 1; Muller et al., 1974). Minor subvolcanic dikes of Alert Bay affinity continue this intrusive-structural trend for another 20 km southwest, to the tip of the Brooks Peninsula. Erosional remnants of dikes, sills, lavas and volcaniclastic rocks of the Alert Bay volcanic suite predominate in the northern part of the Brooks-Haddington tract. An island of volcanic rocks 10 km north of Port Hardy in Queen Charlotte Strait was assigned to the Alert Bay map unit by Muller et al. (1974) but they provided no description of the rocks. We have tentatively reassigned this undated unit to the Paleogene (Fig. 1). Geochronological results for the Brooks magmatic suite are summarized in Figure 2 and discussed below.

4.1. Alert Bay volcanic rocks

Isolated outcrops of Alert Bay volcanic rocks define the northeastern part of the Brooks-Haddington tract which extends for 27 km beyond the termination of the Brooks Peninsula fault zone and attains a width approaching 15 km. K-Ar whole rock ages for Alert Bay volcanic rocks in this part of the Brooks-Haddington tract include rhyolite on Haddington Island (ca. 3.7 Ma) and Cluxewe Mountain (ca. 2.5 Ma); dacite due north of Port Alice (ca. 3 Ma); and basalt, andesite and rhyodacite lavas at the voluminous Twin Peaks volcanic edifice (ca. 3-4.7 Ma; Armstrong et al., 1985; Fig. 2). According to the time-scale of Cohen et al. (2013), these ages are Pliocene except for the youngest K-Ar determination at Cluxewe Mountain that statistically falls on the Pliocene-Pleistocene boundary. Clasts of plagioclase-phyric basalt in conglomerate northwest of Cluxewe Mountain yield a highly imprecise K-Ar age due to very high atmospheric argon inherent to this sample (Armstrong et al., 1985; Fig. 2).

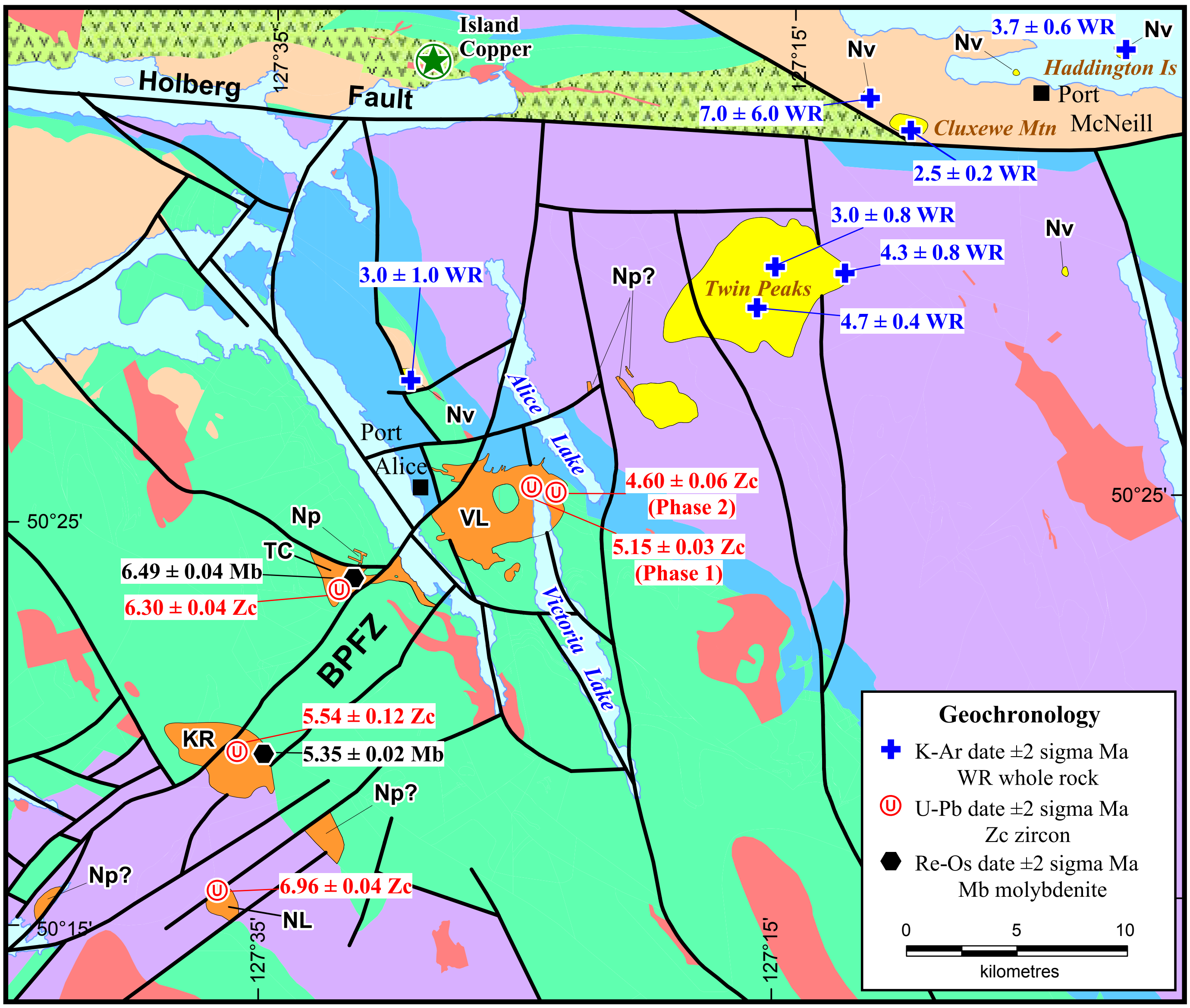

Fig. 2. Summary of currently available geochronological results for the late Neogene (latest Miocene-Pliocene) Brooks magmatic suite. K-Ar dates are from Armstrong et al. (1985); U-Pb and Re-Os dates from Nixon et al. (2011c-d and G.T. Nixon, unpublished data). Labels for Klaskish Plutonic Suite: NL, Nasparti Lake pluton; KR, Klaskish River pluton; TC, Teeta Creek pluton; VL, Victoria Lake pluton. Geological units and other symbols as in Fig. 1.

4.2. Klaskish Plutonic Suite (new formal name)

The late Neogene Klaskish Plutonic Suite was first introduced by Nixon et al. (2011c-d) as an informal map unit and is formally designated herein as a distinct lithodemic unit in accordance with the North American Stratigraphic Code (2005). The suite is named after the Klaskish River pluton approximately 20 km southwest of Port Alice (Nixon et al., 2011c), and comprises three other named lithodemes, the Nasparti Lake, Teeta Creek and Victoria Lake plutons, and some unnamed affiliated(?) intrusions (Fig. 2). The suite is constrained geographically within the Brooks Peninsula fault zone in the southern part of the Brooks-Haddington tract. The Klaskish River pluton is composed mainly of equigranular hornblende±biotite granodiorite and is genetically associated with Cu-Mo porphyry and Cu-Fe skarn mineralization. Other members of the Klaskish Plutonic Suite are also mineralized, and range in composition from biotite-hornblende granodiorite through monzodiorite to quartz diorite/diorite with ancillary feldspar±quartz porphyry and granitic phases (Nixon et al., 2011c-d).

The Klaskish Plutonic Suite occupies a narrow (10 km wide), northeast-trending structural corridor defined by the Brooks Peninsula fault zone (Fig. 1; Muller et al., 1974). The plutonic rocks follow this structural zone from the Pacific coast for at least 38 km to terminate east of Alice Lake at a group of minor intrusions near the first extensive exposures of Alert Bay lavas. Here, northeast-oriented faults give way to north-trending structures that appear to terminate near the Holberg fault.

4.2.1. U-Pb geochronology

U-Pb age determinations for intrusions of the Klaskish Plutonic Suite are taken from Nixon et al. (2011c-d and G.T. Nixon, unpublished data) and were done at the Pacific Centre for Isotopic and Geochemical Research, Department of Earth, Ocean and Atmospheric Sciences, University of British Columbia. The results represent concordant weighted-average $^{206}Pb/^{238}U$ dates on air-abraded (Krogh, 1982) or chemically abraded zircon (Mattinson, 2005; as modified by Scoates and Friedman, 2008).

High-precision $^{206}Pb/^{238}U$ dates on zircon, interpreted as crystallization ages, have been determined for four intrusions of the Klaskish Plutonic Suite: the Klaskish River, Nasparti Lake, Teeta Creek and Victoria Lake plutons (Fig. 2). The Nasparti Lake granodiorite in the south yielded the oldest crystallization age (ca. 7.0 Ma), followed by the Teeta Creek quartz diorite (ca. 6.3 Ma) and Klaskish River granodiorite (ca. 5.5 Ma) plutons. Two intrusive phases separated by about half a million years are recognized in the Victoria Lake pluton: an early Phase 1 granodiorite (ca. 5.15 Ma) and later Phase 2 quartz monzodiorite (ca. 4.60 Ma). The pluton crystallization ages span latest Miocene to early Pliocene (Cohen et al., 2013). The youngest intrusive phase of the Victoria Lake pluton (Phase 2, ~4.6 Ma), near the northern end of the Klaskish plutonic zone, is statistically coeval with the oldest K-Ar dated lava at Twin Peaks (~4.7 Ma; Fig. 2). Armstrong et al. (1985) noted that the youngest eruptive products of the Alert Bay volcanic suite occur at the northern end of the Brooks-Haddington tract relative to a K-Ar date (ca. 8 Ma) on a basaltic dike at the tip of the Brooks Peninsula (Fig. 1). Our U-Pb dates for the Klaskish Plutonic Suite show a similar younging trend from south to north along the southern part of this tract (Brooks Peninsula fault zone), although this trend is not smoothly progressive (cf., Teeta Creek; Fig. 2). The combined K-Ar and U-Pb dating results, therefore, appear to indicate a general age progression in which the rocks get younger from southwest to northeast within the Brooks magmatic suite.

5. Mineralization in the Brooks-Haddington tract

Mineral occurrences compiled from the MINFILE database that are spatially associated with the late Neogene Brooks-Haddington tract are listed in Table 1 and shown in Figure 3. The deposit types include porphyry Cu±Mo±Au±Ag (7), base- and precious-metal stockwork/vein systems (11), skarns/igneous contact mineralization (10), volcanic redbed Cu (2), industrial minerals (2) and some unspecified (6) deposit types. We have inferred an alternative deposit type based on the MINFILE descriptions for a number of these mineral occurrences (Table 1). Descriptions of the various deposit types given below focus on the spatial relationship between the plutons and mineralization; assay results from grab samples, trenching and drill intersections are provided in the specific MINFILE summaries (Table 1) and ARIS reports listed therein. As discussed below, the age of the mineralization has been established by Re-Os dating of molybdenite for only two porphyry occurrences. However, practically all these mineral occurrences are spatially related to structures in the Brooks-Haddington tract and/or intrusions of the Klaskish Plutonic Suite, and therefore mineralization may be late Neogene rather than Jurassic as has been traditionally assumed.

5.1. Porphyry Cu-Mo mineralization

Porphyry Cu-Mo(±Au±Ag) mineralization is hosted by the Nasparti Lake, Klaskish River and Teeta Creek plutons and is particularly widespread in the southern part of the Brooks Peninsula fault zone (Fig. 3). The principal sulphide minerals are typically chalcopyrite and pyrite±molybdenite, accompanied locally by bornite, sphalerite, arsenopyrite, trace galena and rare native gold. Chalcopyrite and pyrite are generally disseminated or contained in fractures and quartz vein stockworks along with molybdenite where present. The mineralogy of the silver minerals is currently unknown.

The mineralized Nasparti Lake (or 'Lois') granodiorite-quartz diorite is cut by rhyolitic breccias in the core and near the periphery of the stock (Stevenson, 1992; 4-5, Fig. 3; Table 1). Chalcopyrite and molybdenite are associated with pervasive potassic (biotite) alteration in the diorite; arsenopyrite and minor sphalerite are found in the rhyolitic breccias. The stock is cut by fine-grained rhyolitic dikes that are weakly mineralized and a post-mineral, partly devitrified obsidian dike, a subvolcanic member of the Alert Bay suite. Porphyry Cu-Mo

Table 1. Late Neogene mineral occurrences in the Brooks-Haddington tract and Coast Belt and selected Middle Jurassic porphyry deposits.

ID[1]	MINFILE	Name	Commodities[2]	MINFILE Deposit Type	Alternate Deposit Type[3]	Status	UTM X[4]	UTM Y[4]
	Late Neogene (late Miocene-Pliocene) - Brooks Peninsula Fault Zone (Fig. 3)							
1	092L 251	BROOKS	Cu, Pb, Zn	Cu skarn		Showing	591084	5566868
2	092L 334	NASPARTI LAKE	Cu	Cu±Ag quartz veins/ volcanic redbed Cu	Cu-Ag veins	Showing	599632	5567393
3	092L 258	PABLO 24-2	Cu, Ag	Porphyry Cu±Mo±Au	Porphyry Cu-Ag	Showing	589772	5568298
4	092L 330	LOIS	Cu, Mo, Zn, Pb, Au, Ag, Co	Porphyry Cu±Mo±Au		Prospect	598624	5568331
5	092L 447	NIC MSV	Ag, Cu, Zn	Vein/stockwork Cu-Ag-Au	Porphyry Cu-related	Showing	598297	5568912
6	092L 331	LONDON 1	ma, Fe, Cu, Zn	Unknown	Cu-Zn veins	Showing	602128	5569479
7	092L 228	IRON COP	Cu, Co, Ag, Au, Fe	Porphyry Cu±Mo±Au	Porphyry Cu-Ag-Au	Prospect	599848	5569590
8	092L 446	BERKINSHIRE	Au, Ag, Cu	Vein/stockwork Cu-Ag-Au	Porphyry Cu-Ag-Au	Prospect	599091	5569823
9	092L 001	HEART	Cu, Fe	Porphyry Cu±Mo±Au		Showing	604988	5570060
10	092L 449	KLASKINO 2	Cu, Ag	Vein/stockwork Cu-Ag)	Porphyry Cu-Ag	Showing	591555	5571665
11	092L 182	RH 1-24	Cu, Mo	Porphyry Cu±Mo±Au		Showing	605050	5571915
12	092L 265	FANG	Cu	Unknown	Porphyry Cu-related?	Prospect	600945	5572299
13	092L 237	RUF 41	Cu, Mo, Ag	Skarn	Porphyry Cu-Mo-Ag±Au	Showing	590582	5573039
14	092L 448	NIC EAST	Ag, Cu	Vein/stockwork Cu-Ag-Au	Porphyry Cu-related	Showing	601386	5573049
15	092L 191	JARR	Cu	Skarn	Cu skarn	Showing	592841	5574004
16	092L 144	SINKER	Cu, Ni, Co, Mo	Unknown	Cu skarn/porphyry Cu-related?	Showing	588777	5574491
17	092L 445	NIC NORTH SKARN	Cu, Au, Ag, Fe	Cu skarn		Showing	600538	5575010
18	092L 266	TENT	Cu, Mo, Au, Ag	Porphyry Cu±Mo±Au		Showing	599745	5575057
19	092L 176	BRAD	Cu	skarn	Cu skarn	Showing	594991	5575433
20	092L 259	MAHATTA	Au, Ag, Cu	Ag-Pb-Zn±Au veins		Showing	592744	5576134
21	092L 054	QUATSINO KING (L.676)	Cu, Au, Ag, Zn	Cu±Ag quartz veins	Cu-Ag-Au veins	Showing	606221	5582598
22	092L 235	STAR 24	Cu, Mo	Porphyry Cu±Mo±Au	Porphyry Cu-Mo-Ag±Au	Showing	605288	5582826
23	092L 453	STAR 22	Au, Ag	Vein/stockwork Cu-Ag-Au	Porphyry Cu-Ag-Au	Showing	605773	5583269
24	092L 454	JRB NO.1	Au	Unknown	Porphyry Cu-Mo-Au	Showing	604722	5583464
25	092L 455	JR 2	Au, Zn	Vein/stockwork Zn-Au	Porphyry Cu-related?	Showing	606636	5583564
26	092L 053	PAYSTREAK	Cu, Zn, Au, Ag	Cu±Ag quartz veins	Cu-Ag-Au veins	Showing	606294	5583897
27	092L 466	PANDORA	Ag, Pb, Zn	Pb-Zn-Ag veins		Showing	611618	5587066
28	092L 057	PILGRIM (L.2035)	Zn, Ag, Au, Pb, Cd	Pb-Zn skarn	Zn-Pb-Ag-Au skarn	Developed Prospect	613914	5587702
29	092L 056	JUNE (L.180)	Fe, Cu, Au, Ag, S, Zn, Pb, ma	Skarn/porphyry	Fe-Cu-Ag skarn	Prospect	612817	5588234
30	092L 314	BIG ZINC	Zn	Pb-Zn Skarn		Showing	611172	5588570
31	092L 112	MINERVA FR. (L.171,183)	Zn, Cu, Fe, ma	Skarn	Zn-Cu skarn	Prospect	612316	5588595
32	092L 055	ALICE LAKE	Au, Ag, Pb, Zn	Manto Ag-Pb-Zn	Ag-Pb-Zn-Au manto	Prospect	611912	5589049
33	092L 234	ECILA	Cu, ma, Fe	Industrial mineral	Porphyry Cu-related?	Showing	616366	5592854
34	092L 232	BLUE	Cu	Unknown	Porphyry Cu-related?	Showing	617222	5594263
35	092L 233	BLUE 44	Cu	Unknown	Porphyry Cu-related?	Showing	615366	5595304
36	092L 321	KEOGH	Cu, Mo, Ni	Igneous contact	Porphyry Cu-Mo-related?	Showing	629076	5597260
37	092L 141	WALT	Cu	Volcanic redbed Cu	Porphyry Cu-related?	Showing	626252	5599973
38	092L 146	HADDINGTON ISLAND	Building stone	Building stone		Past Producer	640181	5607187
	Middle Jurassic - northern Vancouver Island (Fig. 1)							
	092L 158	ISLAND COPPER	Cu Mo, Ag, Au, Zn, Pb, Re	Porphyry Cu±Mo±Au		Past Producer	607924	5606424
	092L 240	HUSHAMU	Cu, Au, Mo	Porphyry Cu±Mo±Au		Developed Prospect	580687	5614338
	092L 200	RED DOG	Cu, Au, Mo, Ag	Porphyry Cu±Mo±Au		Developed Prospect	572566	5618142
	Late Neogene (Miocene) - Coast Crystalline Complex (Fig. 4)						**UTM X[5]**	**UTM Y[5]**
39	092N 029	HOODOO NORTH	Mo, Ag, Zn, Pb, wo	Porphyry Mo		Prospect	319015	5692727
40	092N 028	HANNAH 8,10,11	Au, Ag, Cu, Mo	Porphyry Cu±Mo±Au		Prospect	332349	5684913
41	092JW 005	SALAL CREEK	Mo, Cu, Zn, Pb	Porphyry Mo		Prospect	471141	5622907
42	092JW 015	FALL	Mo	Porphyry Mo		Showing	465288	5612194
43	092JSE034	ROGERS CREEK	Cu, Ag, Mo, Au	Unknown	Porphyry Cu-Mo±Au±Ag	Showing	539513	5544583
44	092HSW037	MARY JANE	Mo, Au, Ag, Cu	Porphyry Mo		Showing	595706	5455678
45	092HSW065	MOUNT CHEAM 2	Cu, Zn	Skarn	Cu skarn	Showing	594700	5450688
46	092HSW007	LUCKY FOUR (L.989)	Cu, Mo, Ag, Au	Cu skarn		Developed Prospect	603402	5446427

[1] Label shown on Figs. 3 and 4; [2] wo, wollastonite, ma, magnetite; [3] Deposit Type inferred in this study; [4] UTM Zone 9 NAD 1983; [5] UTM Zone 10 NAD 1983

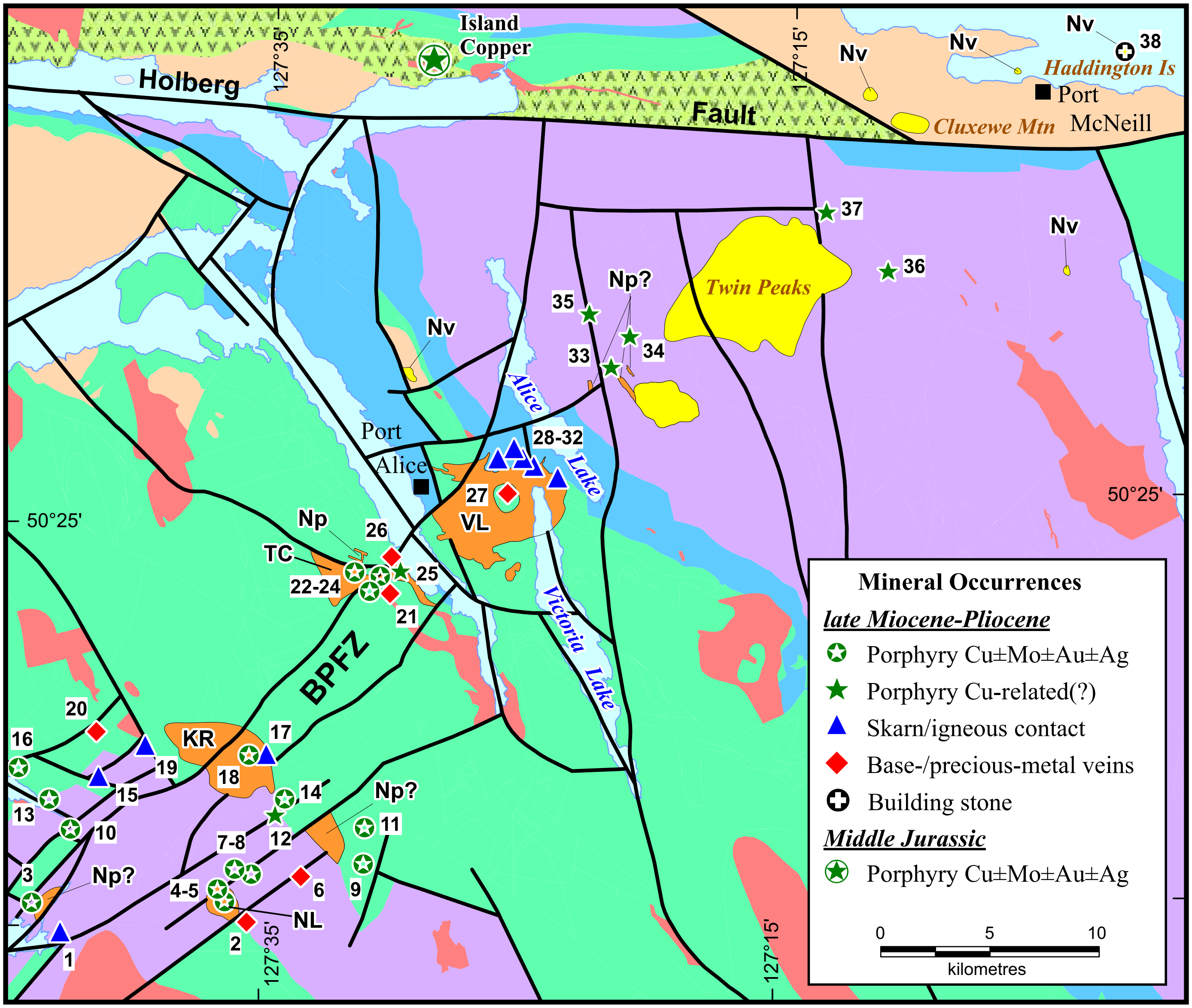

Fig. 3. Porphyry copper, skarn and vein mineral occurrences spatially associated with the Brooks magmatic suite. Mineral occurrences are taken from the MINFILE database and numbered according to Table 1. Age of the mineralization is based on direct dating results (Fig. 2) or the spatial association with inferred late Neogene intrusions. Geological units and other symbols as in Figs. 1 and 2.

mineralization also occurs 2 km to the north along northeast-trending structures and proximal to a small dioritic stock (7-8, Fig. 3; Table 1). Quartz-vein stockworks and shears hosted by Karmutsen Formation basalts carry chalcopyrite and pyrite. A Jurassic(?) pluton farther north along the same structure may also belong to the Klaskish Plutonic Suite and extend to the east in the subsurface where porphyry Cu-Mo mineralization is spatially associated with small bodies of granodiorite-diorite (9, 11, Fig. 3; Table 1).

Mineralization hosted by granodiorite and quartz diorite in the Klaskish River pluton locally contains chalcopyrite, pyrite and molybdenite in disseminations, fractures and locally well-developed quartz vein stockworks that have anomalous abundances of Au and Ag (18, Fig. 3; Table 1). Secondary biotite and kaolinite are reported to be associated with the Cu-sulphide mineralization, and sodic metasomatism of the granodiorite is locally pronounced (Nixon et al., 2011c). Petrographic examination of the latter rocks confirms the presence of secondary 'chequerboard' albite thereby distinguishing these metasomatized rocks from igneous tonalite. The most recent work on Cu-Mo mineralization in the Klaskish River pluton and surrounding area is summarized by Houle (2012).

Cu-Mo±Au±Ag mineralization in the Teeta Creek quartz diorite-granodiorite-porphyry intrusive complex occurs in disseminations, shears and quartz vein stockworks containing chalcopyrite, molybdenite, pyrite and pyrrhotite, and rare narrow massive sulphide veins (22-25, Fig. 3; Table 1). A rhyolite porphyry dike complex cuts Bonanza volcanic stratigraphy at the northern margin of the pluton, and hydrothermal breccia pipes are exposed in road cuts on the northern slopes of Teeta Creek. In addition to the porphyry Cu-Mo mineralization, prospecting on the south side of Teeta Creek identified a zone of anomalous gold values in quartz veins trending subparallel to the Teeta Creek fault in the valley bottom. The gold is accompanied locally by anomalous Cu, Pb and Zn abundances and the mineralization has been interpreted as part of an epithermal system above a Cu-Mo porphyry at depth. Pyritic volcanic host rocks exposed in new logging roads south of Teeta Creek may represent an outer sulphidic halo related to the Cu-Mo-Au mineralization. Previous exploration work in the Teeta Creek area is summarized by Sookochoff (2013) and includes historical drill results from holes collared in the Teeta Creek valley bottom where an intersection of 146 m at 0.256% Cu was reported. Due to the presence of porphyry-style mineralization on both sides of Teeta Creek, we infer that the Teeta Creek pluton extends south and east towards Neroutsos Inlet where it may be genetically linked to a telescoped or peripheral precious-metal epithermal system.

A number of porphyry Cu-Mo occurrences are found in the Brooks Peninsula fault zone southwest of the Klaskish River pluton. One occurrence (3, Fig. 3; Table 1) is related to a small late Neogene(?) dioritic intrusion where chalcopyrite and bornite are hosted by a breccia zone at the margin of the body. Other occurrences (10, 13, 16, Fig. 3; Table 1) contain quartz-molybdenite stockworks or chalcopyrite and pyrrhotite stringers hosted by Late Triassic volcanic and sedimentary rocks and invite further investigation.

In the northern part of the Brooks-Haddington tract southwest of Twin Peaks, several mineral showings occur near north-trending faults and dike-like dioritic to feldspar porphyry intrusions hosted by Karmutsen Formation basalts (33-35, Fig. 3; Table 1). These intrusions were originally mapped as Jurassic except for one composite diorite-rhyolite dike where the rhyolite was assigned to the Alert Bay volcanic suite (Nixon et al., 2011d). We now speculate that these granitoid intrusions belong to the Klaskish Plutonic Suite and may well be genetically related to mineral occurrences in the surrounding area. The mineralization is described as disseminated chalcopyrite and bornite within the basalts, and locally silicified breccia contains chalcopyrite and magnetite accompanied by pyrrhotite and pyrite in fracture fillings. Similar Cu-Fe sulphide mineralization is also found northeast of Twin Peaks where molybdenite is reported in quartz vein stockworks and shears along with chalcopyrite, pyrite and pyrrhotite (36-37, Fig. 3; Table 1). Small dioritic intrusions occur in this area and a larger Jurassic(?) body is shown on maps by Muller et al. (1974) and Muller and Roddick (1983). We suspect that these mineral occurrences are vestiges of late Neogene porphyry Cu-Mo systems.

5.2. Skarns

A cluster of skarn deposits, some with historic reserves, occur near the contact between the Victoria Lake pluton and limestone of the Quatsino Formation (28-32, Table 1; Fig. 3). The Zn-Pb skarns generally form disseminations or massive replacements of limestone that are locally intruded by quartz diorite, aplite and porphyry dikes emanating from the pluton. The ore minerals include sphalerite, pyrrhotite, galena, bornite, pyrite and arsenopyrite; the latter two minerals were reported in assessment work to carry anomalous abundances of Au and Ag. Gangue minerals include epidote, chlorite, garnet and tremolite. One occurrence contains massive sphalerite (30, Table 1) and one developed prospect has historical resources (non-NI 43-101 compliant) of 46,266 tonnes of ore grading 8.7% Zn and 32.6 g/t Ag with anomalous Cd, in addition to a similar tonnage classed as probable reserves (28, Table 1).

The southern part of the Brooks Peninsula fault zone contains numerous isolated skarn occurrences at the margin of the Klaskish River pluton and associated with northeast- and northwest-trending faults in an area of widespread porphyry Cu-Mo mineralization (Fig. 3). Disseminated chalcopyrite, pyrite, magnetite and pyrrhotite are developed in calcareous sedimentary rocks of the Parson Bay Formation and basalts of the Karmutsen Formation. Assessment work has documented chalcopyrite and pyrite in localized quartz vein stockworks; and a thin (~20 cm) massive Fe-Cu skarn carrying chalcopyrite and magnetite near the eastern margin of the Klaskish River pluton (17, Table 1).

5.3. Base- and precious-metal stockworks and veins

Base- and precious-metal veins and stockworks commonly occur peripheral to plutons that host porphyry Cu-Mo mineralization and/or adjacent to faults (Fig. 3). Thin (2-25 cm) quartz±calcite veins are generally steeply dipping and contain chalcopyrite±pyrite (2, 20, Table 1). A magnetite-rich vein occurrence is cut by sulphide stringers carrying pyrite, chalcopyrite and sphalerite (6, Table 1). Quartz veins along easterly trending structures near the Teeta Creek pluton are reported to contain pyrrhotite, sphalerite, pyrite and chalcopyrite (26, Table 1). A vein occurrence within a roof pendant of pyrite-impregnated volcanic-sedimentary rocks enclosed by the Victoria Lake pluton was reported in assessment work to have anomalous Ag, Pb, and Zn values (27, Table 3).

5.4. Age of porphyry Cu-Mo mineralization

High-precision Re-Os age determinations on molybdenite in the Klaskish River and Teeta Creek plutons were done at the University of Alberta following analytical protocols described by Selby and Creaser (2004) and Markey et al. (1998, 2007). The results are shown in Figure 2. Molybdenite in these plutons occurs in quartz stockworks and fractures accompanied by chalcopyrite±pyrite and is associated with a broader signature of porphyry Cu-Mo±Ag±Au mineralization. The Re-Os dates for molybdenite mineralization in the Klaskish River (ca. 5.35 Ma) and Teeta Creek (ca. 6.49 Ma) plutons are within about 200,000 years of the U-Pb zircon crystallization dates (Fig. 2). These results are interpreted to indicate that porphyry Cu-Mo mineralization is genetically linked to the emplacement and crystallization of late Miocene-Pliocene intrusions of the Klaskish Plutonic Suite. These intrusions are related to the structural development of the Brooks Peninsula fault zone as discussed below.

6. Structural evolution of the Brooks-Haddington tract

The structural evolution of the Brooks-Haddington tract is constrained by the geochronological data. Northeast-oriented structural lineaments defining the Brooks Peninsula fault zone cut the Klaskish River and Teeta Creek plutons, indicating that faulting post-dated their emplacement and crystallization (i.e., younger than ca. 5.5 Ma; latest Miocene). These faults were evidently active before 5.5 Ma because the Klaskish River pluton cuts one of these structures (Fig. 2). Similar relationships are apparent farther east where northerly trending faults predate emplacement of the Victoria Lake pluton (ca. 5.15-4.6 Ma), and faulting at Twin Peaks predates and postdates extrusion of Pliocene lavas (ca. 4.7-3.0 Ma). Furthermore, undeformed Cenozoic basaltic to rhyolitic dikes intruding rocks on Brooks Peninsula, including one dated basaltic dike, are oriented parallel to the projected southern extension of the Brooks Peninsula fault zone (Smyth, 1985), and provide evidence for fault motion predating or broadly synchronous with dike emplacement and cooling at ca. 8 Ma (Fig. 1). From the geochronological constraints, therefore, the northeast-oriented structures forming the Brooks Peninsula fault zone and northerly trending faults farther east appear to have developed during an interval of at least 5 million years (ca. 8-3 Ma). Evidence from seismicity in the Brooks Peninsula fault zone and in the crust offshore of the Brooks Peninsula indicates that faulting in this zone of structural weakness continues today (Savard et al., 2019).

7. Late Neogene porphyry Cu-Mo mineralization in the Coast Belt

The major porphyry Cu deposits in British Columbia are Late Triassic to Early Jurassic in age and confined almost exclusively to the accreted magmatic arc terranes of Quesnellia and Stikinia (Logan and Mihalynuk, 2014; Fig. 4). Beyond Vancouver Island, the youngest porphyry Cu-Mo and skarn occurrences in the province are spatially associated with Miocene plutons in the Pemberton magmatic arc in the southeastern Coast Mountains (Fig. 4; Table 1). These small, high-level stocks of the Chilliwack Suite (Woodsworth et al., 1991) extend northwards from near the British Columbia-Washington border to at least 51°25' N, coincident with erosional remnants of coeval and cogenetic Mio-Pliocene volcanic rocks (Souther, 1991).

Porphyry Mo mineralization considered genetically related to the Miocene plutons occurs at the Hoodoo (39), Salal Creek (41), Fall (42) and Mary Jane (44) MINFILE occurrences; porphyry Cu-Mo occurrences are found at Hannah (40) and the Rogers Creek cluster (43, Fig. 4; Table 1). The youngest known Cu skarns in the province are peripheral to the Mount Barr batholith (ca. 18 Ma, U-Pb zircon; Mullen et al., 2018) which hosts the Mary Jane porphyry Mo showing (45-46, Fig. 4; Table 1).

Early K-Ar dating studies detected a northward decrease in the age of the Pemberton plutons (and associated volcanic rocks) from about 35 Ma in the south near the US border (late Paleogene phase of the Chilliwack batholith) to 7 Ma in the north (Franklin Glacier stock, Woodsworth et al., 1991; Breitsprecher and Mortensen, 2004; 40, Fig. 4). Recent U-Pb zircon geochronology by Mullen et al. (2018) corroborates this northward age decrease (Fig. 5a). We show below that the distribution and age of Neogene plutons and related porphyry mineralization in the Pemberton magmatic arc and their counterparts in northern Vancouver Island are manifestations of a common plate tectonic evolution. We first address the plate tectonic history pertinent to northern Cascadia and subsequently attempt to rationalize our observations and geochronological results within this tectonic framework.

8. Plate tectonic setting of northern Cascadia

Vancouver Island lies at the northern termination of the Cascadia subduction zone in a region where late Cenozoic interactions between oceanic and continental lithosphere are complex (Fig. 5). In the plate tectonic model for Cascadia presented by Madsen et al. (2006), at about 10 Ma the Pacific-Juan de Fuca-North America triple junction (Juan de Fuca ridge-trench-Queen Charlotte fault intersection) lay to the north of Vancouver Island in Queen Charlotte Sound. Vancouver Island at this time was underlain by the subducting Juan de Fuca plate whereas a slab-absent region (slab window) existed to the north of the triple junction. After plate readjustments, the triple junction and northern edge of the subducted Juan de Fuca plate migrated southwards to arrive near the Brooks Peninsula at ~8-9 Ma (Madsen et al., 2006; Fig. 5a). This interpretation differs from the plate tectonic model of Mullen et al. (2018) who reconciled the northward decrease in pluton ages in the Pemberton arc with progressive northward migration of the edge of the subducted Juan de Fuca slab during the last 35 million years.

In the simple rigid-plate geometry model proposed by Riddihough (1977) using offshore magnetic anomalies, the Juan de Fuca ridge remained in a stable position near the Brooks Peninsula from about 10 Ma to 5 Ma, and the northwestern edge of the subducted Juan de Fuca plate was inferred to have a northeast trajectory beneath the Brooks Peninsula. The residence time for the triple junction at this position is limited by the inception of the Nootka fault at ~3.5 Ma. This event spalled away a fragment of the formerly contiguous Juan de Fuca plate as ocean floor spreading opposite the Brooks Peninsula ceased and the Juan de Fuca ridge shifted northwest to complete the formation of the Explorer plate (Savard et al., 2019; Fig. 5b).

The boundary separating the Explorer and Juan de Fuca plates, the Nootka fault zone, has been depicted as a left-lateral transform fault extending northeasterly from the Juan de Fuca ridge towards Nootka Island (Hyndman et al., 1979; Fig. 5b). Recent geophysical studies summarized by Savard et al. (2019)

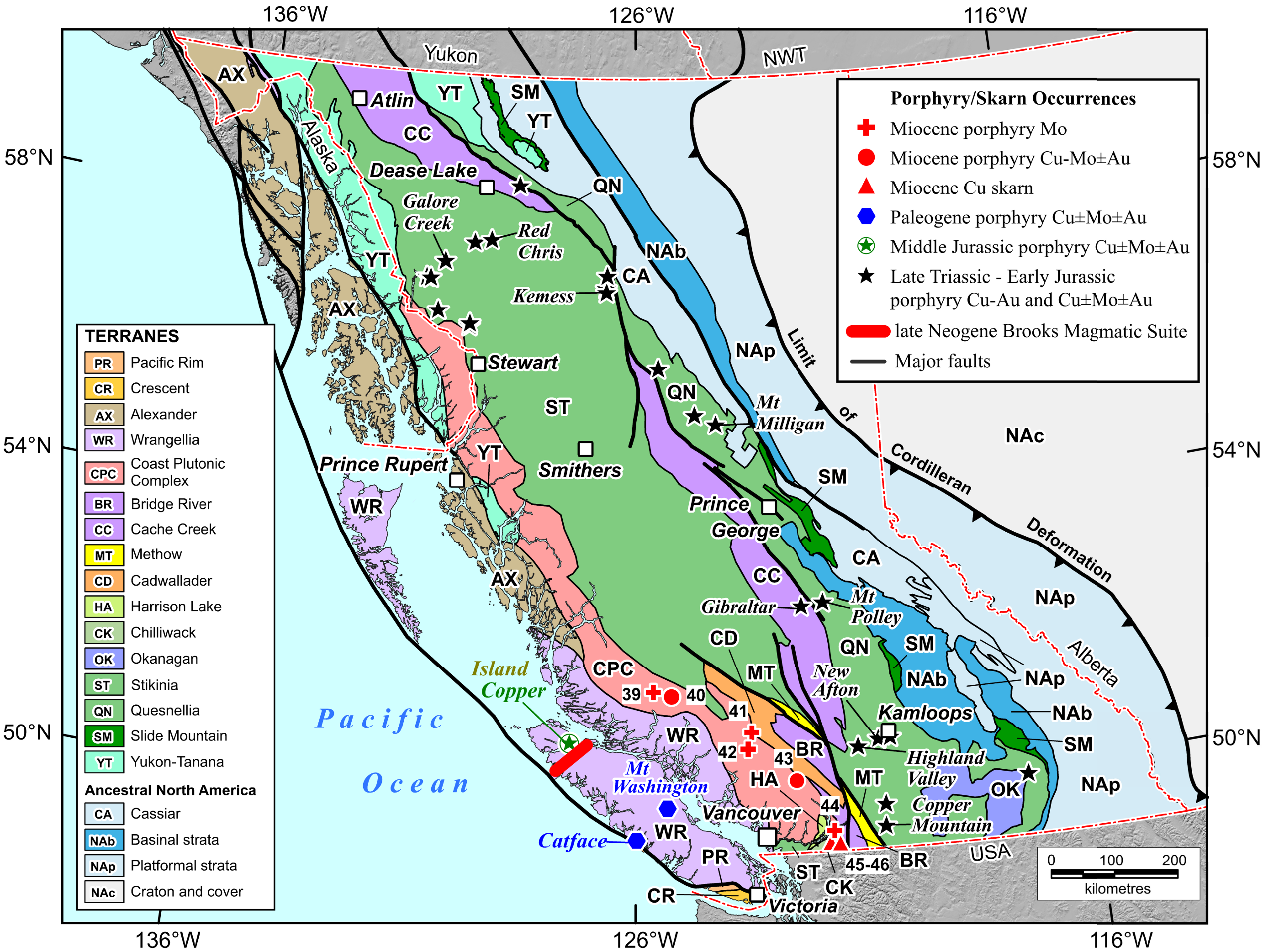

Fig. 4. Distribution of selected Mesozoic-Cenozoic porphyry copper and skarn occurrences in British Columbia and their terrane affiliation. Named Late Triassic-Early Jurassic deposits identify operating mines or deposits at an advanced stage of development in 2018 (Clarke et al., 2019). Numbered Miocene occurrences are listed in Table 1. Mesozoic porphyry copper deposits after Logan and Mihalynuk (2014); Cenozoic mineral occurrences compiled from the MINFILE database; terranes after Colpron and Nelson (2011) and Nelson et al. (2013). Note that late Neogene porphyry/skarn occurrences are confined to the southeastern part of the Coast Plutonic Complex and the forearc region of the Brooks-Haddington tract.

have demonstrated that the Nootka fault, a ~20 km-wide zone of complex faulting in the ocean floor, assumes a more north-northeast orientation than traditionally shown. These authors argue that, since the inception of the Nootka fault at ~3.5 Ma, the zone of deformation offshore has widened and the landward continuation has broadened reflecting a component of extension across the fault zone resulting from the differing subduction rates of the Explorer and Juan de Fuca plates. The eastern boundary of the Nootka fault zone defines the present-day location of the northwestern edge of the Juan de Fuca plate, which can be extrapolated in the subsurface across Vancouver Island. The leading edge of the subducted Juan de Fuca slab has advanced no farther than the northeast coast of Vancouver Island (below Haddington Island) constrained by the relative rates of convergence of the Juan de Fuca/North America plates (Fig. 5b). The western edge of the Nootka fault zone marks the margin of the Explorer plate whose leading edge presently underlies the Brooks Peninsula because it is underthrusting North America at about half the rate of the Juan de Fuca plate (Savard et al., 2019; Fig. 5b).

9. Plates, magmatism and porphyries

Armstrong et al. (1985) noted the spatiotemporal correspondence between the descending Juan de Fuca plate edge as proposed by Riddihough (1977), the Brooks Peninsula fault zone and the 8-2.5 Ma Alert Bay volcanic suite, remarked on an apparent eastward shift in the volcanic activity, and interpreted the forearc location and 'within-plate' geochemical signature of the volcanic rocks as an enigmatic product of descending plate-edge magmatism. We examine these observations below within the context of the newly advanced plate configuration described above and our geochronological

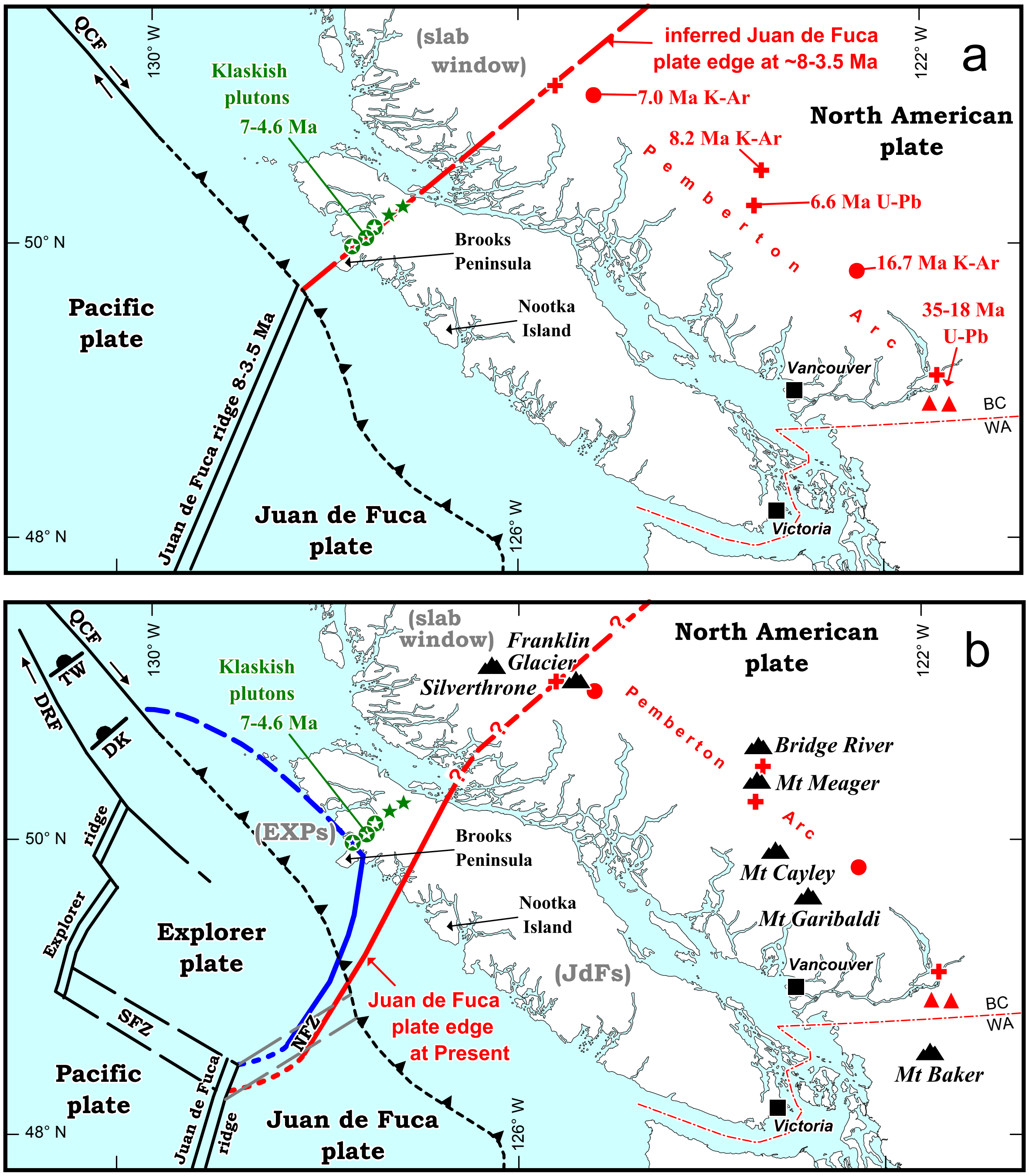

Fig. 5. Late Neogene to present plate configuration at the northern termination of the Cascadia subduction zone (after Savard et al., 2019) showing the distribution of late Neogene porphyry Cu-Mo and Mo systems in the Pemberton arc and forearc region of northern Vancouver Island. **a)** Inferred position of the Juan de Fuca ridge (Pacific-Juan de Fuca-North America triple junction) offshore of the Brooks Peninsula and subducted plate edge at 8-3.5 Ma (Riddihough, 1977; this study). Note that a slab-absent region (slab window) exists north of the subducted Juan de Fuca plate edge at this time. Isotopic age dates for mineralized plutons in the Pemberton arc are from Mullen et al. (2018, U-Pb zircon) and Wanless et al. (1978, K-Ar, corrected for the decay constants of Steiger and Jäger, 1977, by Breitsprecker and Mortensen, 2004). Age determinations for the Klaskish Plutonic Suite in the Brooks-Haddington tract on northern Vancouver Island are from this study and Nixon et al. (2011c-d). **b)** Plate configuration at present showing the redefined location of the Nootka fault zone (NFZ, solid red and blue lines; Rohr et al., 2018) extrapolated to its present position under Vancouver Island according to the relative convergence velocities of these plates with respect to North America (Savard et al., 2019). The Nootka fault zone was initiated at ~3.5 Ma and delineates the boundary between the Explorer and Juan de Fuca plates. Also shown are the inferred extension of the Nootka fault zone to the Juan de Fuca ridge (short-dash red and blue lines); the subducted leading edge of the Explorer plate (long-dash blue line; Savard et al., 2019) and inferred position of the Juan de Fuca plate edge (long-dash red line); the subducted portions of the Explorer (EXPs) and Juan de Fuca (JdFs) plates and slab window to the north; the traditionally depicted orientation of the Nootka fault zone (grey dashed lines); the limit of deformation in the Cascadia subduction zone (dashed barbed line); and modern volcanoes of the northern Cascade arc (Garibaldi belt). Symbols as in Figs. 3 and 4. Other abbreviations: QCF, Queen Charlotte fault; DRF, Dellwood-Revere fault; DK, Dellwood Knolls; TW, Tuzo Wilson seamounts; NFZ, Nootka fault zone; SFZ, Sovanco fracture zone.

data for late Neogene plutons and genetically related porphyry Cu-Mo mineralization on northern Vancouver Island and in the Coast Mountains.

The inferred northeasterly trajectory of the northwestern edge of the Juan de Fuca plate during the late Neogene (≥8 Ma to ~3.5 Ma) underlies the loci of Alert Bay volcanism, Klaskish plutonism and related porphyry Cu-Mo systems of the Brooks magmatic suite that form the Brooks-Haddington tract, and passes beneath the northernmost mineralized pluton in the Pemberton arc (39, Figs. 3, 5a). The northward age progression of granitoid intrusions in the Pemberton arc in the late Cenozoic (ca. 35-7 Ma) appears to fit the northward migrating slab model of Mullen et al. (2018). However, in their model the subducted edge of the Juan de Fuca slab does not arrive beneath the Brooks Peninsula until the present day, contrary to our interpretation (Fig. 5a). One of the youngest mineralized plutons in the Pemberton arc (Franklin Glacier stock dated at 7 Ma by K-Ar; Wanless et al., 1978; Breitsprecker and Mortensen, 2004; Fig. 5a) is similar in age to the Teeta Creek and Nasparti Lake plutons (~6.3-7 Ma, U-Pb zircon). Thus, we consider that forearc plutons and porphyry Cu-Mo systems on northern Vancouver Island and their northernmost counterparts in the Pemberton arc (39-40, Fig. 5a) formed above or close to the projected edge of the subducted Juan de Fuca plate in the late Neogene. The present location of the northwestern edge of the subducted Juan de Fuca slab is uncertain but appears to also limit the distribution of Quaternary volcanoes in the Garibaldi belt (Fig. 5b).

A minimum time of arrival for the Juan de Fuca ridge opposite Brooks Peninsula is concomitant with the early stages of development of the Brook Peninsula fault zone and late Cenozoic dike emplacement and cooling at ca. 8 Ma (Armstrong et al., 1985; Figs. 1 and 5). The Klaskish plutons and porphyry Cu-Mo systems (7-4.6 Ma) are coeval with the older rocks of the Alert Bay volcanic suite (8-4.7 Ma), and structural development of the Brooks Peninsula fault zone continued until at least 4.6 Ma. The stable position of the triple junction and northwestern edge of the subducted Juan de Fuca plate during this period resulted in focused faulting that facilitated magma transit through the crust.

The well-defined narrow structural corridor that hosts the Klaskish plutons and porphyry mineralization in the southwest is interrupted in the northeast by north-trending faults, and the plutons transition to younger Alert Bay volcanic rocks (ca. 4.3-2.5 Ma) coupled with an apparent widening of the Brooks-Haddington tract. We speculate that the eastward younging of Alert Bay volcanism noted by Armstrong et al. (1985) and northerly oriented structures reflect the eastward motion of the subducted Juan de Fuca plate edge relative to North America and evolving Nootka fault zone from ~3.5 Ma to Present.

The geochemical signature of the Alert Bay volcanic suite has been interpreted to have ambivalent within-plate or volcanic arc (Armstrong et al., 1985) or mid-ocean ridge basalt (Lewis et al., 1997) affinity, implying the involvement of sub-slab mantle source(s) in magma genesis. The widening of the Nootka fault zone during eastward migration of the Juan de Fuca slab and its subduction beneath Vancouver Island would allow the ascent of asthenospheric mantle and promote mixing of depleted and subduction-modified mantle sources. Given the global proclivity for the formation of porphyry copper deposits above subduction zones, porphyry Cu-Mo mineralization in the forearc of the Cascadia subduction zone would appear to require a component of subduction-modified mantle in the source regions of the late Neogene Klaskish Plutonic Suite. Future geochemical studies of the Brooks magmatic suite may help to resolve this intriguing issue.

10. Summary and conclusions

The foundation for this study was laid by a diverse array of previous work on northern Vancouver Island and in the offshore region that included regional mapping, paleontological, geochronological, geochemical and geophysical studies, mineral occurrence data gathered by the exploration community and made available through the MINFILE and ARIS databases, and plate tectonic reconstructions. Building on this infrastructure, our study advances the understanding of the mineral potential of northern Vancouver Island in several respects.

Late Neogene magmatism on northern Vancouver Island is restricted to the Brooks magmatic suite, which comprises volcanic (Alert Bay) and plutonic (Klaskish Plutonic Suite) components. Magmatism developed above the subducted edge of the Juan de Fuca plate and landward extension of the Nootka fault zone. The Klaskish Plutonic Suite occupies an anomalous forearc setting in the Cascadia subduction zone and hosts porphyry Cu-Mo mineralization. High-precision U-Pb and Re-Os dating of Klaskish plutons confirms that these intrusions are coeval with the older volcanic rocks of the Alert Bay suite and establishes a genetic relationship between pluton emplacement, crystallization and mineralization. The dating is crucial for distinguishing these Neogene plutons from Early to Middle Jurassic intrusions of the Island Plutonic Suite which are proven ground for major porphyry Cu-Mo-Au-Ag deposits. The underexplored late Neogene Klaskish metallogenic belt occupies a well-defined structural zone, the Brooks Peninsula fault zone, and this young metallotect offers fertile ground for future economic discoveries.

Acknowledgments

Participants of the BC Geological Survey regional mapping projects on northern Vancouver Island in the early 1990s and mid-2000s (Nixon et al., 2011a-e) provided the geological framework for geochronological studies that first identified the presence of mineralized Neogene plutons in the area. We thank Dan Berkshire (Compliance Energy Corporation) for providing logistical and financial support for collecting and processing samples from the Nasparti pluton; and Tyler Ruks (ArcWest Exploration Inc.) for leading a field excursion to examine Cu-Mo mineralization in the Teeta Creek pluton and for contributing a Re-Os date to this study. Genevieve Savard kindly provided GIS data for Figure 5, and discussions with Michael Bostock are greatly appreciated. Bruce Northcote is thanked for helpful comments on the manuscript.

References cited

Armstrong, R.L., Muller, J.E., Harakal, J.E., and Muehlenbachs, K., 1985. The Neogene Alert Bay volcanic belt of northern Vancouver Island, Canada; descending-plate-edge volcanism in the arc-trench gap. Journal of Volcanology and Geothermal Research, 26, 75-98.

Breitsprecher, K., and Mortensen, J.K., 2004. B.C. Age 2004A-1 (release 3, October 2004) - a database of isotopic age determinations for rock units from British Columbia. British Columbia Ministry of Energy, Mines and Petroleum Resources, British Columbia Geological Survey Open File 2004-03 (digital file).

Clarke, G., Northcote, B., Katay, F., and DeGrace, J.R., 2019. Exploration and mining in British Columbia, 2018: a summary. In: British Columbia Ministry of Energy, Mines and Petroleum Resources, British Columbia Geological Survey Information Circular 2019-01, pp. 1-37.

Cohen, K.M., Finney, S.C., Gibbard, P.L., and Fan, J.-X., 2013. The ICS international chronostratigraphic chart (updated, v. 2019/05). Episodes, 36, 199-204. http://www.stratigraphy.org/ICSchart/ChronostratChart2019-05.pdf.

Colpron, M., and Nelson, J.L., 2011. A digital atlas of terranes for the Northern Cordillera. British Columbia Ministry of Energy and Mines, British Columbia Geological Survey GeoFile 2011-11 (digital file).

DeBari, S.M., Anderson, R.G., and Mortensen, J.K., 1999. Correlation among lower to upper crustal components in an island arc: the Jurassic Bonanza arc, Vancouver Island, Canada. Canadian Journal of Earth Sciences, 36, 1371-1413.

Greene, A.R., Scoates, J.S., Weis, D., Katvala, E.C., Israel, S., and Nixon, G.T., 2010. The architecture of oceanic plateaus revealed by the volcanic stratigraphy of the accreted Wrangellia oceanic plateau. Geosphere, 6, 47-73.

Houle, J., 2012. Archaeology, geology, geochemistry, geophysics and diamond drilling on the NIC property. British Columbia Ministry of Energy and Mines, British Columbia Geological Survey Assessment Report 32773, 656 p.

Hyndman, R.D., Riddihough, R.P., and Herzer, R., 1979. The Nootka Fault Zone - a new plate boundary off western Canada. Geophysical Journal International, 58, 667-683.

Krogh, T.E., 1982. Improved accuracy of U-Pb zircon ages by the creation of more concordant systems using an air abrasion technique. Geochimica et Cosmochimica Acta, 46, 637-649.

Lewis, T.J., Lowe, C., and Hamilton, T.S., 1997. Continental signature of a ridge-trench-triple junction: northern Vancouver Island. Journal of Geophysical Research, Solid Earth, 102, 7767-7781.

Logan, J.M., and Mihalynuk, M.G., 2014. Tectonic controls on early Mesozoic paired alkaline porphyry deposit belts (Cu-Au±Ag-Pt-Pd-Mo) within the Canadian Cordillera. Society of Economic Geologists, Economic Geology, 109, 827-858.

Madsen, J.K., Thorkelson, D.J., Friedman, R.M., and Marshall, D.D., 2006. Cenozoic to Recent plate configurations in the Pacific Basin: ridge subduction and slab window magmatism in western North America. Geosphere, 2, 11-34.

Markey, R.J., Stein, H.J., and Morgan, J.W., 1998. Highly precise Re-Os dating for molybdenite using alkaline fusion and NTIMS. Talanta, 45, 935-946.

Markey, R., Stein, H.J., Hannah, J.L., Zimmerman, A., Selby, D., and Creaser, R.A., 2007. Standardizing Re-Os geochronology: a new molybdenite reference material (Henderson, USA) and the stoichiometry of Os salts. Chemical Geology, 244, 74-87.

Mattinson, J.M., 2005. Zircon U-Pb chemical abrasion ("CA-TIMS") method: combined annealing and multi-step partial dissolution analysis for improved precision and accuracy of zircon ages. Chemical Geology, 220, 47-66.

Mullen, E.K., Paquette, J.-L., Tepper, J.H., and McCallum, I.S., 2018. Temporal and spatial evolution of Northern Cascade Arc magmatism revealed by LA-ICP-MS U-Pb zircon dating. Canadian Journal of Earth Sciences, 55, 443-462.

Muller, J.E., and Roddick, J.A., 1983. Alert Bay-Cape Scott: Geological Survey of Canada, Map 1552A,1:250,000 scale.

Muller, J.E., Northcote, K.E., and Carlisle, D., 1974. Geology and mineral deposits of Alert Bay-Cape Scott map-area, Vancouver Island, British Columbia. Geological Survey of Canada, Paper 74-8, 77 p.

Natural Resources Canada, 2019. https://www2.gov.bc.ca/gov/content/industry/mineral-exploration-mining/further-information/statistics/production (5 November 2019).

Nelson, J.L., Colpron, M., and Israel, S., 2013. The Cordillera of British Columbia, Yukon and Alaska: tectonics and metallogeny. In: Colpron, M., Bissig, T., Rusk, B.J., and Thompson, J.F.H., (Eds.), Tectonics, Metallogeny, and Discovery: The North American Cordillera and Similar Accretionary Settings. Society of Economic Geologists, Special Publication 17, pp. 53-109.

Nixon, G.T., and Orr, A.J., 2007. Recent revisions to the Early Mesozoic stratigraphy of northern Vancouver Island (NTS 102I; 092L) and metallogenic implications. In: Geological Fieldwork 2006, British Columbia Ministry of Energy and Mines, British Columbia Geological Survey Paper 2007-1, pp. 163-177.

Nixon, G.T., Hammack, J.L., Koyanagi, V.M., Snyder, L.D., Payie, G.J., Panteleyev, A., Massey, N.W.D., Hamilton, J.V., Orr, A.J., Friedman, R.M., Archibald, D.A., Haggart, J.W., Orchard, M.J., Tozer, E.T., Tipper, H.W., Poulton, T.P., Palfy, J., and Cordey, F., 2011a. Geology, geochronology, lithogeochemistry and metamorphism of the Holberg-Winter Harbour area, northern Vancouver Island (parts of NTS 092L/05, 12, 13; 102I/08, 09 & 16). British Columbia Ministry of Energy and Mines, British Columbia Geological Survey Geoscience Map 2011-1, 1:50,000 scale.

Nixon, G.T., Hammack, J.L., Koyanagi, V.M., Payie, G.J., Orr, A.J., Haggart, J.W., Orchard, M.J., Tozer, E.T., Friedman, R.M., Archibald, D.A., Palfy, J., and Cordey, F., 2011b. Geology, geochronology, lithogeochemistry and metamorphism of the Quatsino-Port McNeill area, northern Vancouver Island (NTS 092L/11, and parts of 092L/05, 12 & 13). British Columbia Ministry of Energy and Mines, British Columbia Geological Survey Geoscience Map 2011-2, 1:50,000 scale.

Nixon, G.T., Hammack, J.L., Hamilton, J.V., Jennings, H., Larocque, J.P., Orr, A.J., Friedman, R.M., Archibald, D.A., Creaser, R.A., Orchard, M.J., Haggart, J.W., Tipper, H.W., Tozer, E.T., Cordey, F., and McRoberts, C.A., 2011c. Geology, geochronology, lithogeochemistry and metamorphism of the Mahatta Creek area, northern Vancouver Island (NTS 092L/05). British Columbia Ministry of Energy and Mines, British Columbia Geological Survey Geoscience Map 2011-3, 1:50,000 scale.

Nixon, G.T., Snyder, L.D., Payie, G.J., Long, S., Finnie, A., Orr, A.J., Friedman, R.M., Archibald, D.A., Orchard, M.J., Tozer, E.T., Poulton, T.P., and Haggart, J.W., 2011d. Geology, geochronology, lithogeochemistry and metamorphism of the Alice Lake area, northern Vancouver Island (NTS 092L/06, and part of 092L/10). British Columbia Ministry of Energy and Mines, British Columbia Geological Survey Geoscience Map 2011-4, 1:50,000 scale.

Nixon, G.T., Kelman, M.C., Larocque, J.P., Stevenson, D.B., Stokes, L.A., Pals, A., Styan, J., Johnston, K.A., Friedman, R.M., Mortensen, J.K., Orchard, M.J., and McRoberts, C.A., 2011e. Geology, geochronology, lithogeochemistry and metamorphism of the Nimpkish-Telegraph Cove area, northern Vancouver Island (NTS 092L/07, and part of 092L/10). British Columbia Ministry of Energy and Mines, British Columbia Geological Survey

Geoscience Map 2011-5, 1:50,000 scale.
North American Commission on Stratigraphic Nomenclature, 2005. North American Stratigraphic Code. American Association of Petroleum Geologists Bulletin, 89, 1547-1591.
Northisle Copper and Gold Inc., 2019. www.northisle.ca (30 April 2019).
Riddihough, R.P., 1977. A model for recent plate interactions off Canada's west coast. Canadian Journal of Earth Sciences, 14, 384-396.
Rohr, K.M.M., Furlong, K.P., and Riedel, M., 2018. Initiation of strike-slip faults, serpentinization, and methane: The Nootka Fault Zone, the Juan de Fuca-Explorer Plate Boundary. Geochemistry, Geophysics, Geosystems, 19, 4290-4312.
Savard, G., Bostock, M.G., Hutchinson, J., Kao, H., Christensen, N.I., and Peacock, S.M., 2019. Plate deformation at Cascadia's northern terminus. Journal of Geophysical Research-Solid Earth (in review).
Scoates, J.S., and Friedman, R.M., 2008. Precise age of the platiniferous Merensky Reef, Bushveld Complex, South Africa, by the U-Pb zircon chemical abrasion ID-TIMS technique. Economic Geology, 103, 465-471.
Selby, D., and Creaser, R.A., 2004. Macroscale NTIMS and microscale LA-MC-ICP-MS Re-Os isotopic analysis of molybdenite: testing spatial restrictions for reliable Re-Os age determinations, and implications for the decoupling of Re and Os within molybdenite. Geochimica et Cosmochimica Acta, 68, 3897-3908.
Smyth, W.R., 1985. Geology of the Brooks Peninsula, Vancouver Island (92L/4). In: Geological Fieldwork 1984, British Columbia Ministry of Energy, Mines and Petroleum Resources, British Columbia Geological Survey Paper 1985-1, pp. 161-169.
Sookochoff, L., 2013. Structural analysis of the Quatsino King property. British Columbia Ministry of Energy and Mines, British Columbia Geological Survey Assessment Report 34193, 46 p.
Souther, J.G., 1991. Volcanic regimes. In: Gabrielse, H., and Yorath, C.J., (Eds.), Geology of the Cordilleran Orogen in Canada, Geological Survey of Canada, Geology of Canada no. 4, pp. 457-490.
Steiger, R.H., and Jäger, E., 1977. Subcommission on geochronology: convention on the use of decay constants in geo- and cosmochronology. Earth and Planetary Science Letters, 36, 359-362.
Stevenson, J.P., 1992. Assessment Report on the Lois Property, Brooks Peninsula Area, northwest Vancouver Island. British Columbia Ministry of Energy and Mines, British Columbia Geological Survey Assessment Report 21755, 145 p.
Wanless, R.K., Stevens, A.O., Lachance, G.R., and Delabio, R.N., 1978. Age determinations and geologic studies, K-Ar isotopic ages, Report 13. Geological Survey of Canada, Paper 77-2, 60 p.
Woodsworth, G.J., Anderson, R.G., and Armstrong, R.L., 1991. Plutonic regimes. In: Gabrielse, H., and Yorath, C.J., (Eds.), Geology of the Cordilleran Orogen in Canada, Geological Survey of Canada, Geology of Canada no. 4, pp. 491-531.

Multi-media geochemical and Pb isotopic evaluation of modern drainages on Vancouver Island

Alexei S. Rukhlov[1, a], Gabe Fortin[1], Gennady N. Kaplenkov[2], Ray E. Lett[3], Vivian W.-M. Lai[4], and Dominique Weis[4]

[1] British Columbia Geological Survey, Ministry of Energy, Mines and Petroleum Resources, Victoria, BC, V8W 9N3
[2] 2874 Eton Street, Vancouver, BC, Canada, V5K 1K5
[3] 3936 Ashford Road, Victoria, BC, Canada, V8P 3S5
[4] Pacific Centre for Isotopic and Geochemical Research, Department of Earth, Ocean and Atmospheric Sciences, University of British Columbia, Vancouver, BC, Canada, V6T 1Z4
[a] corresponding author: Alexei.Rukhlov@gov.bc.ca

Recommended citation: Rukhlov, A.S., Fortin, G., Kaplenkov, G.N., Lett, R.E., Lai, V. W.-M., and Weis, D., 2020. Multi-media geochemical and Pb isotopic evaluation of modern drainages on Vancouver Island. In: Geological Fieldwork 2019, British Columbia Ministry of Energy, Mines and Petroleum Resources, British Columbia Geological Survey Paper 2020-01, pp. 133-167.

Abstract

Prognostic geochemistry attempts to identify prospective areas for economic deposits of a wide range of commodities, including non-traditional deposit-types. Although the geochemistry of panned heavy mineral concentrates (HMC) from stream sediments has been used elsewhere to discover economic metal deposits that were missed by conventional stream-sediment surveys, the method has not been used extensively for regional geochemical surveys (RGS) in British Columbia. Instead, such surveys tend to use elaborate laboratory processing of bulk samples to recover HMC and indicator minerals, which although robust, are at a cost that is prohibitive for most prospectors. With the objective of developing geochemical exploration methods that are both effective and inexpensive, herein we use the <1 mm fraction of HMC samples (200-400 g) recovered by sluicing and panning of 11-16 kg of the <2 mm fraction of bulk alluvium in the field. We analyzed these heavy mineral concentrates, stream waters, and conventional stream and moss-captured sediments (<0.18 mm fraction) from several Vancouver Island drainages for a wide range of elements using different analytical methods. Analysis of the field-processed HMC samples greatly enhanced the geochemical anomaly contrast and confidently identified visually confirmed mineralization even at the mouths of third- to fifth-order streams, many km downstream from known mineralization. In contrast, analysis of the conventional stream and moss-captured sediments commonly failed to detect even proximal mineralization. In addition, for the first time, we measured Pb isotopic compositions of stream waters and 2.5N HCl leachates of the sediments and HMC by economic ICP-MS. These Pb isotopic compositions fingerprint mineralization isotopically distinct from country rocks. Strongly acidic (sulphuric) waters of Hushamu Creek drain blind porphyry Cu-Mo-Au and epithermal Au-Ag-Cu deposits hosted by volcanic rocks of the Bonanza magmatic arc (Late Triassic to Middle Jurassic) on northern Vancouver Island. The geochemistry of HMC and water samples reveals strong lithochemical (mechanical) Au-Ag-Se-Bi-Te-Mo-Pb-Re-Hg-Ba-Sn-Co-Tl-In-Cu and hydrochemical Co-Mn-Al-Sn-Fe-Zn-Cu-Cd-Y-Ni-La-Ba dispersion in the Hushamu watershed. Above-background productivities (tonnes per 1 m depth) of Au (315), Ag (24), Ba (22350), V (4964), Zr (4584), P (4050), Zn (1146), Pb (247), B (228), Se (569), Sn (75), Co (52), Bi (49), Te (34), Cs (27), Li (17), Sb (16), Hg (9), Tl (8), and In (2) reflect epithermal Au-Ag-Cu and the uppermost primary dispersion halo of the blind porphyry Cu-Mo-Au system under the extensive leached cap in the Hushamu basin. Multiplicative ratios of highly mobile to less mobile ore and indicator elements such as (Cu·Pb·Zn)/(Sn·Co·Mo) or (Ag·Hg·Sb)/(W·Sn·Bi) also indicate shallow level of erosion or blind mineralization. Strong LREE-Y-V-Ba-Sr-P-Zr-Hf-Nb-Ta-U-Th dispersion in some drainages on northern Vancouver Island may indicate undiscovered peralkaline granite- or carbonatite-hosted, rare-metal mineralization possibly related to Neogene extension in the Queen Charlotte basin and similar to deposits in Alaska. HMC samples at Loss Creek on southern Vancouver Island yield (tonnes/m): 833 Au, 78 Ag, 2568 W, plus 3066533 Mn, 86132 Y, 41516 ∑HREE (Gd+Tb+Dy+Ho+Er+Tm+Yb+Lu), 38542 Cr, 28724 Zn, 14377 Li, 5553 Sc, 3511 Ba, 2873 ∑LREE (La+Ce+Pr+Nd+Sm+Eu), 2182 Ni, 1640 Ga, 1532 Se, 871 Co, 753 Ge, 661 B, 621 Pb, 613 Cd, 594 Nb, 235 Hf, 207 Th, and 76 Ta. The prognostic geochemical resources not only confirm placer gold and its orogenic Au-type source in the Loss Creek basin, but also indicate a large, unconventional type of a placer garnet-hosted HREE-Y-Sc-Mn deposit and other 'critical' commodities. Water chemistry provides an important control on hydrochemical dispersion and constrains ore mineral assemblages. We propose a three-stage method for drainage geochemical surveys that is rapid, inexpensive, and effective.

Keywords: Drainage geochemical survey, mineral exploration, stream sediment, moss-mat sediment, heavy mineral concentrate (HMC), sluice, pan, dispersion streams, geochemical anomaly, basin productivity, geochemical resources, lithochemistry, hydrochemistry, Pb isotopic data, northern Vancouver Island, Hushamu, porphyry Cu-Mo-Au, epithermal Au-Ag-Cu, unconventional garnet-hosted HREE-Y-Sc deposit, peralkaline intrusion- or carbonatite-hosted LREE and rare-metal mineralization, indicator mineral

1. Introduction

Regional geochemical surveys support the societal resource base by identifying prospective areas for large-tonnage economic deposits in undeveloped and underexplored regions. Such surveys are based on pioneering studies of the migration, dispersion, and concentration of elements by V.I. Vernadsky, V.M. Goldschmidt, and A.E. Fersman, along with studies of ore deposits and dispersion of indicator elements (Safronov, 1971). The first 'metallometric surveys' carried out in several mining regions by N.I. Safronov and A.P. Solovov in 1931-1932 demonstrated the effectiveness of the new 'physico-chemical exploration method' based on the theory of geochemical field and anomaly, analogous to geophysical methods. At the same time, V.A. Sokolov developed geochemical methods for oil and gas exploration (Grigoryan et al., 1983; Solovov, 1985; Solovov et al., 1990; Matveev, 2003). In 1956, V.I. Krasnikov outlined the theory and practice of modern lithochemical, hydrochemical, atmochemical, and biochemical exploration methods. These methods have since been widely applied, leading to the discovery of hundreds of ore deposits, including very large ones such as Escondida Cu, Chile; Salobo Cu, Brazil; Cerro Colorado Cu-Mo, Panama; Carlin Au in Nevada, USA; McArthur River and Woodlawn Pb-Zn-Ag±Cu, Australia; Husky Ag-Pb-Zn and Casino Cu-Au-Mo-Ag in Yukon, Canada (Hawkes, 1976; Rose et al., 1979; Matveev, 2003).

In British Columbia, stream, lake, and moss-mat sediments, and waters have been analyzed in regional drainage geochemical survey (RGS) programs carried out by mining companies since 1950s and later managed by the Geological Survey of Canada, the British Columbia Geological Survey, and Geoscience BC. Interpretation of these data has led to the discovery of many precious and base metal deposits in the province such as Highland Valley Copper, Northair Gold, Galore Creek, Berg, Huckleberry, Equity Silver, and Island Copper on northern Vancouver Island (Lett and Rukhlov, 2017).

Most ore deposits have been found by prospectors. Proven by centuries of prospecting, panning of stream sediment is effective for finding economic deposits of placer gold, diamonds, tin, tungsten, and other commodities. Although the geochemistry of heavy mineral concentrates (HMC) samples from stream sediments was used in eastern Chukotka to discover several large base and precious metal deposits that were missed by conventional, stream-sediment surveys (Kukanov et al., 1983; Petrenko et al., 1986; Kaplenkov, 2003, 2006, 2008), this method has not been widely used in regional geochemical survey programs in British Columbia (see Rukhlov and Gorham, 2007 for an exception). Instead, stream-sediment and till geochemical surveys in the province tend to use elaborate laboratory processing of bulk samples to recover HMC and indicator minerals (see Lett and Rukhlov, 2017 for review). Although indicator minerals are robust tools, the cost of such processing is prohibitive for most prospectors.

In this study we evaluate a new drainage geochemical survey method using the <1 mm fraction of HMC samples (200-400 g) recovered by sluicing and panning of 11-16 kg of the <2 mm fraction of bulk alluvium in the field. We also consider other sample media such as conventional stream and moss-mat sediments (<0.18 mm fraction), stream water geochemistry, and, for the first time, Pb isotopes. We begin by testing different preparation and analytical methods on samples from a placer gold occurrence near the mouth of Loss Creek on southern Vancouver Island. Next, we present the results of an orientation survey on northern Vancouver Island using samples from streams draining prospective rocks of the Bonanza arc (Triassic to Middle Jurassic) with porphyry Cu-Mo-Au, epithermal Au-Ag-Cu, and other styles of mineralization (Northcote and Muller, 1972; Muller et al., 1974; Panteleyev, 1992; Panteleyev and Koyanagi, 1993, 1994; Panteleyev et al., 1995; Perelló et al., 1995; Tahija et al., 2017). We conclude by proposing a revised, three-stage method for regional geochemical surveys to identify prospective areas for large, economic deposits of a wide range of commodities, including non-traditional deposit-types. The new method is rapid, economic, and effective, and thus we recommend it to prospectors. The raw data upon which this study is based are provided in Rukhlov et al. (2019).

2. Previous geochemical studies on Vancouver Island

The first RGS programs that used conventional stream and moss-captured sediment samples (<0.18 mm-fraction) were carried out on northern Vancouver Island by Matysek and Day (1988), Gravel and Matysek (1989), and Matysek et al. (1989). Kerr et al. (1992) and Bobrowsky and Sibbick (1996) carried out regional till geochemical surveys. Koyanagi and Panteleyev (1993, 1994), Sibbick and Laurus (1995a), and Panteleyev et al. (1996b) carried out detailed hydrochemical surveys of several natural acid drainages. Sibbick (1994), Sibbick and Laurus (1995b), and Arne and Brown (2015) performed statistical catchment analysis of the historical RGS data on northern Vancouver Island, and Lett (2008) summarized historical drainage geochemical surveys and discussed the results of multi-media orientation studies. More recently, Jackaman (2011, 2013a, b, 2014) reanalyzed archived RGS stream-sediment and till samples and carried out new infill regional drainage moss-mat sediment and till geochemical work.

3. Geology, mineralization, and physiography

Vancouver Island is mainly underlain by Late Paleozoic to Early Mesozoic rocks of Wrangell terrane, with slivers of Pacific Rim and Crescent terranes along the west coast and southern tip of the Island (Fig. 1; Muller, 1977; Nelson et al., 2013). Amalgamated with Alexander terrane by the Late Carboniferous, Wrangellia, now part of the Insular superterrane, accreted to inboard terranes of the Coast and Intermontane belts between Middle Jurassic and mid-Cretaceous (Neslon et al., 2013; Monger, 2014).

Lithologic units at Loss Creek site (Fig. 2) consist of staurolite-garnet schists and argillites of the Leech River complex (Jurassic to Cretaceous), juxtaposed against basalts and gabbro of the Metchosin Igneous complex (Paleocene to Eocene) along the Leech River fault. Along the coast, these older rocks are overlain by a narrow fringe of siliciclastic rocks of the Carmanah Group (Late Eocene to Oligocene). Intermediate intrusions of the Mount Washington plutonic suite (Eocene to Oligocene) intrude the metamorphic rocks of the Leech River complex (Muller, 1977, 1980, 1982). Orogenic Au veins such as the Ox and Sombrio 2 showings (MINFILE

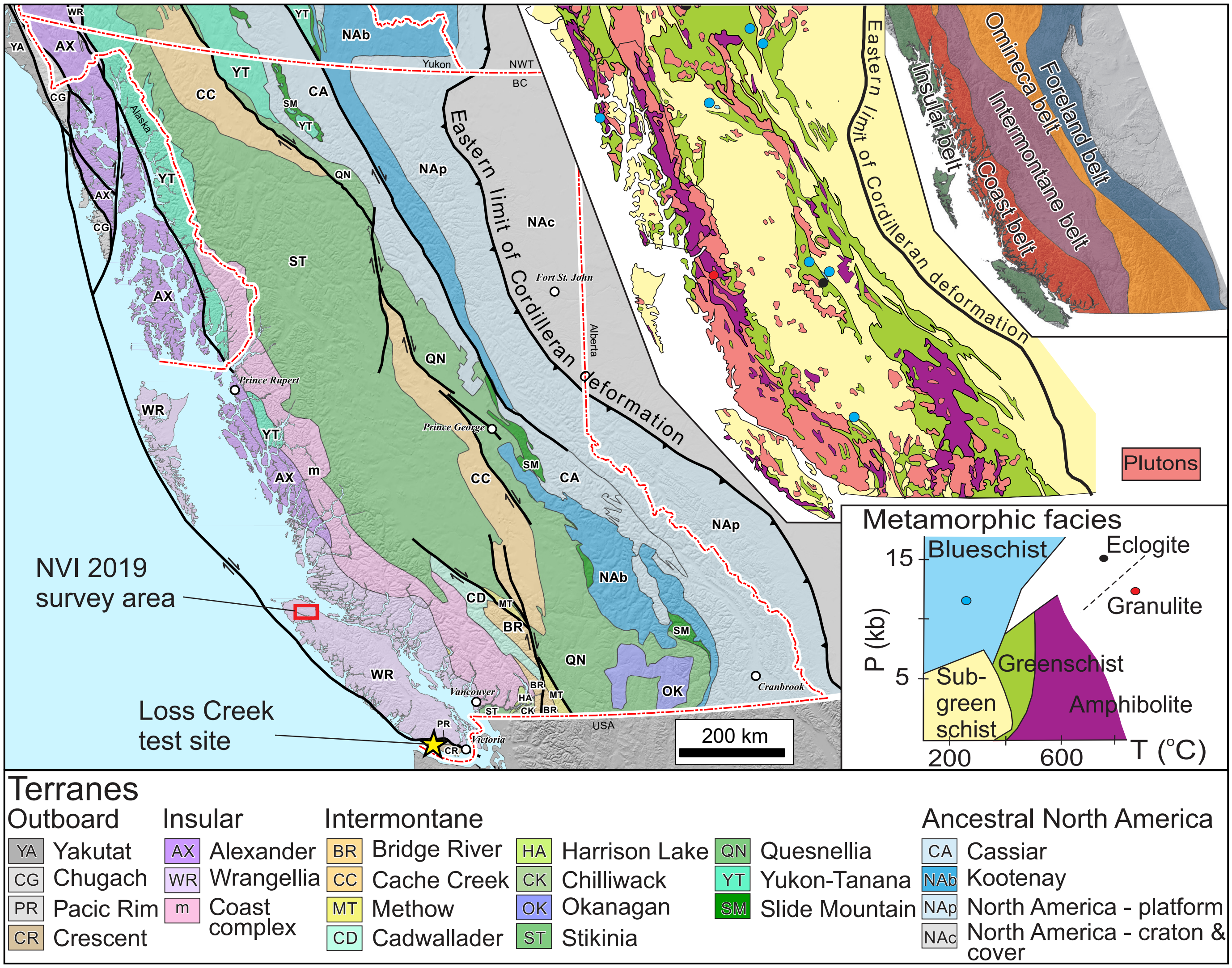

Fig. 1. Location of Loss Creek sampling site and northern Vancouver Island survey area. Terrane geology after Nelson et al. (2013). Metamorphic and plutonic rocks after Monger and Hutchison (1971), Read et al. (1991), and Monger (2014). Cordilleran morphogeological belts after Gabrielse et al. (1991).

092C 059 and 214) are possible sources of placer gold in Loss Creek (MINFILE 092C 236 and 235) and at Sombrio beach (MINFILE 092C 044). Mafic rock-hosted, shear-related and felsic intrusion-related Cu±Ag±Au mineralization also occurs in the area (MINFILE 092C 137, 138, 171, and 218).

Dawson (1887a, b) made the first geological investigation of northern Vancouver Island. Subsequent bedrock mapping and studies of the stratigraphy, magmatism, and mineralization of the area (Fig. 3) were carried out by Jeffrey (1962), Northcote (1969, 1971), Northcote and Muller (1972), Muller et al. (1974), Muller and Roddick (1983), Massey and Melville (1991), Panteleyev (1992), Panteleyev and Koyanagi (1993, 1994), Hammack et al. (1994, 1995), Nixon et al. (1994, 1995, 1997, 2000, 2006a, b, 2011a, b), Archibald and Nixon (1995), Panteleyev et al. (1995, 1996a), Perelló et al. (1995), DeBari et al. (1999), Nixon and Orr (2007), and Nixon et al. (2008). Northern Vancouver Island is mainly underlain by the Vancouver and Bonanza groups (Nixon and Orr, 2007). The Vancouver Group (Late Triassic) consists of flood basalts of the Karmutsen Formation overlain by limestone of the Quatsino Formation. The older rocks are unconformably overlain by the Bonanza Group (Late Triassic to Middle Jurassic), which includes a basal carbonate-siliciclastic-volcanic succession, the Parson Bay Formation (Norian to Rhaetian) that is overlain by volcano-sedimentary strata and the main volcanic phases of the Nahwitti River, Pegattem Creek, LeMare Lake, Hathaway Creek, and Holberg units (Late Triassic to Middle Jurassic). The stratigraphy of the Bonanza magmatic arc reflects basaltic to andesitic volcanism in the Late Triassic (Parson Bay Formation), followed by basaltic to rhyolitic volcanism of the main phase in the earliest Jurassic (LeMare Lake volcanics), and basaltic to rhyolitic arc of the final phase in the early Middle Jurassic (Holberg volcanics). The largely subaerial volcanism of the main and final phases was accompanied by

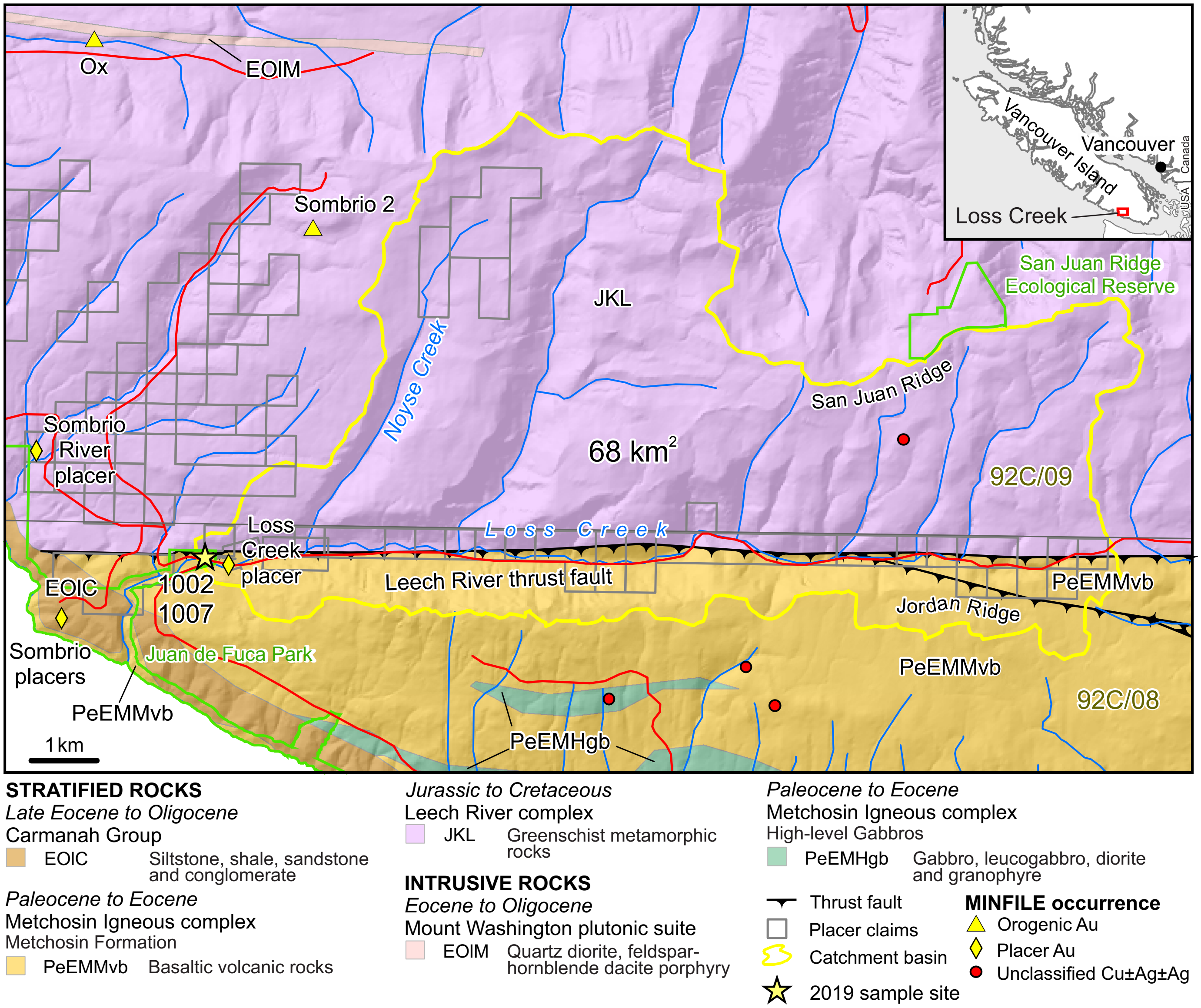

Fig. 2. Loss Creek sampling site and catchment area. Geology after Muller et al. (1977, 1980, 1982).

the emplacement of coeval granitoids of the Island Plutonic suite (Northcote and Muller, 1972; DeBari et al., 1999; Nixon and Orr, 2007). Cyclical marine and continental sedimentary sequences containing coal beds of the Coal Harbour (Early Cretaceous), and Queen Charlotte and Nanaimo (Late Cretaceous) groups mark deposition in fault bounded basins along the northern (Queen Charlotte Group) and eastern (Nanaimo Group) margins of the island (Muller, 1977; Lewis et al., 1997).

The evolution of the Bonanza magmatic arc brought about major porphyry Cu-Mo±Au deposits such as Island Copper (past producer - MINFILE 092L 158), Hushamu (MINFILE 092L 240), Hep (MINFILE 092L 078), Red Dog (MINFILE 092L 200), and related epithermal Au-Ag-Cu (Hushamu), base metal skarn (e.g., Caledonia; MINFILE 092L 061), polymetallic vein (MINFILE 092L 131), and other styles of mineralization (Northcote and Muller, 1972; Muller et al., 1974; Panteleyev, 1992; Panteleyev and Koyanagi, 1993, 1994; Panteleyev et al., 1995; Perelló et al., 1995; Tahija et al., 2017). The Klaskish Plutonic Suite (Late Neogene) also carries porphyry Cu-Mo±Au mineralization immediately to the south of Holberg fault, marking another metallogenic event associated with extension in the Queen Charlotte basin (Lewis et al., 1997; Nixon et al., 2020). In addition, high-Mg basalts of the Karmutsen Formation raise the possibility of magmatic Ni-Cu-PGE deposits (Nixon et al., 2008).

The Insular Mountains, forming the backbone of Vancouver Island, display U-shaped valleys with steep slopes and summits up to 2200 m above sea level (Holland, 1976; Muller, 1977). The Nahwitti lowland of the Coastal trough characterizes the physiography of northern Vancouver Island, with low hills (up to 600 m above sea level) and low-lying coastal plains (Holland,

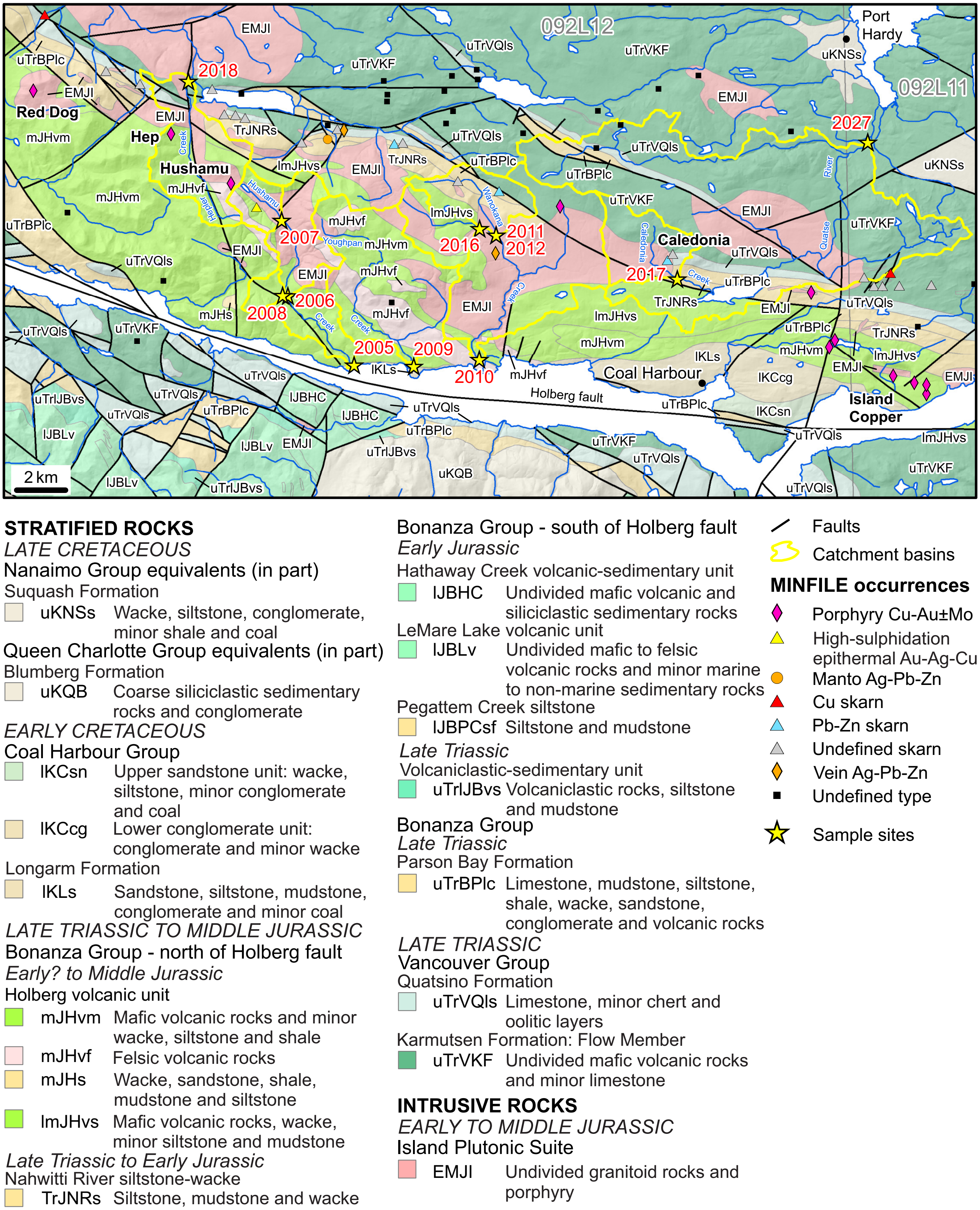

Fig. 3. Sampling sites and catchment basins in the northern Vancouver Island area. Geology based on Jeffrey (1962), Northcote (1969, 1971), Muller et al. (1974), Muller and Roddick (1983), Hammack et al. (1994, 1995), Nixon et al. (1994, 1997, 2000, 2006a, b, 2011a, b), and Nixon and Orr (2007).

1976). Most of the surficial deposits on Vancouver Island formed during or after the Fraser Glaciation (see Lett, 2008 for an overview). Surficial mapping of northern Vancouver Island was carried out by Clague et al. (1982), Kerr (1992), Bobrowsky and Meldrum (1994a, b), Meldrum and Bobrowsky (1994), Bobrowsky et al. (1995), and Bobrowsky (1997).

4. Methods

4.1. Sample collection

To test different sample media and analytical methods, we collected stream and moss-captured sediment, HMC, and water samples from Loss Creek, southern Vancouver Island (Fig. 2) in April and June, 2019. In August, we sampled stream water, sediment, and HMC, and stream boulders representing a local Cu-Zn-Pb mineralization on northern Vancouver Island (Fig. 3). Field duplicates of water, stream sediment, and HMC were collected at random sites. Field observations regarding local terrain, sample site, and sample type, including lithological and shape counting of pebbles, were captured into a MS Access form based on a modified GSC sediment sampling card (Martin McCurdy, personal communication). The field data are listed in Appendix 1 of Rukhlov et al. (2019).

4.1.1. Stream and moss-mat sediment, and heavy mineral concentrate

Stream sediment samples weighing 1.2 to 3.2 kg consisted of mainly the <2 mm sieved fraction or bulk (if wet) alluvium, collected from active stream channels, 10-15 cm above the water level. In addition to stream sediment, moss-mat sediment (0.9 kg) was sampled at Loss Creek.

More representative HMC samples were recovered from the wet-sieved <2 mm fraction of alluvium (11-16 kg) collected from gravel bars immediately downstream of boulders or logs, which serve as natural traps of heavy particles (Fig. 4). We used 12 mm- and 2 mm-size opening stainless-steel sieves stacked on a bucket to process bulk alluvium samples (110-150 L or 4-5 buckets). A portable, gas-powered, 2.5 cm-diameter water pump with a 100-µm nylon foot valve sock and a garden hose permitted most samples being processed far enough from an active stream to prevent silt-laden water entering the stream.

Fig. 4. Typical stream sediment and HMC sampling site on a gravelly stream.

To test HMC recovered by different methods, a 15 kg sample of the <2 mm fraction of bulk stream sediment collected from Loss Creek in April was dried in an oven at 36°C and split by a Jones splitter into two sub-samples. One 7.5 kg sub-sample was panned, and the other 7.5 kg sub-sample was concentrated on a Wilfley shaking table at the British Columbia Geological Survey. We collected two additional duplicate bulk alluvium samples (11 kg each) from the same site in June. One duplicate was concentrated by sluicing on site as described below and the other was archived for testing a spiral Morfee concentrator at the British Columbia Geological Survey.

For recovering HMC from the bulk alluvium in the field, we used a Keene Engineering A-51 mini-sluice box (25.5 x 91.4 x 11.4 cm), lined with a grooved rubber matting and coupled with a shower feeder assembly fitting a garden hose (Fig. 5). Based on the experience (Gene Dodd, personal communication), the sluice was levelled on a frame and operated at a consistent forward slope of 10-11° and water flow of 33-35 L/min, supplied by a 2.5 cm-diameter pump. The rate of sample

Fig. 5. A sluice box (25.5 cm wide) coupled with shower sample feeder set up on a stream bank.

feeding was adjusted to achieve even sediment flow across the sluice box, which avoided clogging of the sluice ladders and metal mesh above the rubber matting. Typical processing time was 20-30 minutes per 11-15 kg sample. Sluice concentrate was then transferred into a clean bucket and further refined by quick panning to wash off coarse mica, feldspar, and other low-density minerals, yielding 200-500 g (wet mass) HMC samples. The samples were transferred into Hubco® bags, which in turn were placed in zip-lock plastic bags, drained, and weighed. Plastic bags were removed and samples were let dry on racks. Cleaned with a nylon brush and visually examined, the sluice box and hopper were transported in plastic bags.

4.1.2. Water

We adopted a modified GSC water sampling procedure, collecting water midstream with a high-density polyethylene (HDPE) bottle attached to a Nasco extendable-pole swing sampler. Pre-cleaned with nitric acid by the manufacturer, a new 250 mL sampling bottle was used for each sample, which was rinsed a few times with stream water. Water temperature, pH, conductivity, and total dissolved solids (TDS) were measured with an Oakton PCTSTestr 50 combination-electrode meter in the field. For the measurements, a new 50 mL polypropylene beaker was rinsed first with deionized (18.2 MΩ·cm) water and then with stream water. We calibrated the meter daily, using pH (4.01, 7.01, and 10.01) and conductivity/TDS (23, 84, 447, and 1413 µS/cm) reference solutions. The same conductivity solutions were used for TDS calibration, applying factor 0.5. The meter electrodes were rinsed with deionized water and stream water before the measurements, and with 95% ethanol and deionized water after the measurements. A piece of wet wipe paper was placed in the cap protecting the electrodes during the day; the electrodes were soaked in tap water overnight.

ALS Canada (Environmental) Ltd., Vancouver, British Columbia (ALS-Environmental) supplied pre-cleaned sample containers with preserving acids in individual vials for laboratory analysis. For Pb isotopic analysis, we used Falcon 50 mL polypropylene tubes, which were cleaned and pre-charged with 0.5 mL of 50% HNO_3 in a clean laboratory at the Pacific Centre for Isotopic and Geochemical Research, University of British Columbia (PCIGR) two weeks before collecting the samples. Earlier tests showed that after storing 0.5 mL 50% HNO_3 in the tubes for up to 26 days, the acid blanks were 0.7-3.6 pg Pb (n = 4), which is a typical acid blank level at PCIGR. All sample containers were placed along with the corresponding acid vials in individual zip-lock plastic bags in a Class 100 clean zone before transporting to the field.

For anion analysis, a 0.5 L HDPE bottle was filled with untreated stream water, whereas water samples for cation and Pb isotopic analysis were filtered and immediately acidified in the field. We used a Sterivex-HV polyvinylidene fluoride (PVDF) 0.45 µm filter units and all-plastic HSW Norm-Ject™ 50 mL syringes; a new syringe was used for each sample. After removing the plunger and attaching the filter unit, the syringe was filled with deionized water while not touching the plunger or tips of the syringe and filter unit. The plunger was rinsed with deionized water and inserted into the syringe, discarding the deionized water through the filter. The syringe and filter were rinsed again with stream water before filtering the water sample into a 20 mL glass bottle for dissolved Hg analysis, a 50 mL HDPE bottle for other cations, and a 50 mL polypropylene tube for Pb isotopic analysis. Filtered water samples were immediately preserved with 0.3 mL 1:1 hydrochloric acid (for Hg) and with about 1 mL 18% nitric acid (for other cations). The sample containers for Pb isotopic analysis were already pre-charged with 0.5 mL 50% nitric acid. Filled water sample containers were placed back into their plastic bags and immediately stored in a cooler with ice packs. All water samples were kept refrigerated at about 4°C until shipped in coolers with ice to ALS-Environmental and PCIGR for analysis.

We monitored three types of water blanks. The acid blank is the unfiltered, deionized water drawn directly from the water purification system and acidified in a Class 100 clean zone at BCGS; acid blanks did not travel to the field. The travel blank is the unfiltered, deionized water drawn directly from the water purification system in a Class 100 clean zone at BCGS and acidified in the field. The filtration blank is the deionized water from a clean HDPE container transported to the field and filtered and acidified in the field the same way as routine samples. To evaluate seasonal variations in water chemistry, we sampled water from Loss Creek during spring runoff in April and at lower discharge in June. We also collected four water samples at the same site from the Quatse River, northern Vancouver Island every third day during the survey in August to monitor short-term variations.

4.2. Sample preparation

Rock samples were crushed in a jaw crusher and screened on a 10-mesh stainless-steel sieve. After manually removing fragments with surface oxidation, a split of the >2 mm material (about 60 g) was pulverized to >90% passing <75 µm particle size in a Cr-steel bowl. All sediment and HMC samples were oven dried at 36°C, sieved through stainless-steel sieves, and then split using a Jones splitter at BCGS. Blind quality controls, including analytical (pulp) duplicates, preparation blanks (Aldrich 99.995% SiO_2), and reference materials were inserted in each sample batch of 12-23 samples. Consistent with the provincial RGS programs, the <0.18 mm, sieved fraction of stream and moss-mat sediment samples was used for analysis. The whole 1-2 mm and 1/8th split of 0.5-1.0 mm-size, sieved fractions of HMC samples were kept for mineralogical examination. Splits of the <1 mm-size, sieved fraction were pulverized for elemental and Pb isotopic analyses. Panned and Wilfley table HMC samples, rocks, and the corresponding preparation silica blanks were milled in a Cr-steel bowl at BCGS. Sluice HMC samples and the corresponding preparation silica blanks were milled in a ceramic bowl at Bureau Veritas Commodities (Minerals) Canada Ltd., Vancouver, B.C. (BVM), or by using an agate pestle and mortar at Activation

Laboratories Ltd., Ancaster, Ontario (Actlabs).

For Pb isotopic analysis, splits of the sluice HMC samples and the corresponding preparation silica blanks were pulverized at BCGS. One HMC sample (number 2005) was milled using a low-Cr steel pestle and mortar. Because the equipment partially magnetized the sample, a duplicate HMC sample number 2005 and the rest of the HMC samples were pulverized using an agate pestle and mortar. All grinding equipment was cleaned by pulverizing silica sand between samples. BVM used an extra cleaning sand cycle to minimize potential carry-over contamination. Both commercial laboratories analyzed random samples of their cleaning sand. Blind preparation silica blanks were sieved, split, and pulverized the same way as routine samples. Stream and moss-mat sediment, HMC, rock samples, and blind quality controls are listed in Appendix 2 in Rukhlov et al. (2019).

4.3. Sample analysis
4.3.1. Lithochemistry

Stream sediment, moss-mat sediment and HMC samples from Loss Creek were analyzed by several standard analytical methods in commercial laboratories. Three different digestions, combined with inductively coupled plasma emission spectrometry (ICP-ES), inductively coupled plasma mass spectrometry (ICP-MS), and X-ray fluorescence (XRF) analysis were performed at BVM.

A split of the <0.18 mm material (30 g) was digested in a H_2O-HCl-HNO_3 (1:1:1 v/v) mixture (modified aqua regia) at 95°C. The supernatant solution was diluted and analyzed by ICP-ES for major elements and by ICP-MS for trace elements, determining a total of 65 analytes with the lowest detection limits. Although the H_2O-HCl-HNO_3 digestion can dissolve gold, carbonates, and sulphides, it does not fully dissolve silicates, oxides and other refractory minerals such as barite. Therefore, concentrations of elements determined by aqua regia digestion should be treated as 'partial' rather than 'total'.

A more aggressive digestion in a HF-$HClO_4$-HNO_3 mixture heated to fuming, followed by dissolution of the dried residue using HCl breaks down most minerals. After digesting a 0.25 g sample in HF-$HClO_4$-HNO_3 and HCl, combined ICP-ES and ICP-MS analysis determines 59 elements. The four-acid digestion is considered 'near-total', because some refractory minerals such as barite, zircon, titanite, and oxides of Al, Fe, Mn, Nb, Sn, REE, Ta, Ti, and W may not be fully dissolved or stable in solution. Furthermore, fuming of HF-$HClO_4$-HNO_3 results in erratic volatilization of some elements, including As, Cr, S, Sb, Se and U. Hence, these elements plus Au and Hg cannot be accurately determined with the four-acid digestion.

Fusion of the sample (0.7 g) with $Li_2B_4O_7$-$LiBO_2$ combined with XRF and laser ablation ICP-MS (LA-ICP-MS) analysis on the fused glass disk results in the determination of 'total' concentrations for 65 elements with the lowest detection limits compared to those of other 'total' methods. In addition, loss on ignition (LOI) at 1000°C is determined gravimetrically. Combining LA-ICP-MS and XRF extends the dynamic range for some analytes such as Sn from sub-ppm to percent level thus eliminating over-limit results. This method requires pulverizing samples to <75 µm to ensure complete fusion of resistate minerals, but strong oxidizing agents are required to fully digest sulphide-rich samples. Some elements such as As, Sb, and Se are partially volatilized by the fusion, and Au is not analyzed by this method.

Splits of the samples were also analyzed at Actlabs by different methods. Thermal instrumental neutron activation analysis (INAA) was performed on 10-51 g samples irradiated for 30 minutes in a neutron flux of $7 \cdot 10^{12}$ neutrons$\cdot$cm$^{-2}\cdot$s^{-1}. After a period of 7 days to allow ^{24}Na to decay, characteristic gamma-ray emissions for 34 elements were measured using a gamma-ray spectrometer with a high-resolution, coaxial Ge detector. Counting time is about 15 minutes per sample. INAA determines 'total' element concentrations and irradiating with thermal neutrons avoids inaccurate (low) Au values due to the self-shielding effect resulting from irradiation with epithermal neutrons. Although INAA is non-destructive, activated material is radioactive and thus not immediately available for analysis by other methods. Another major limitation is poor sensitivity for Ag, Ba, Br, Ca, Cs, Hg, Ir, Mo, Nd, Ni, Rb, Se, Sr, and Zn, resulting in most determinations being below detection limit or having poor precision. Furthermore, INAA cannot measure a number of elements, including key commodity metals such as Pb and Cu. These elements were determined on a separate split of the sample (0.5 g) digested in a hot HCl-H_2O-HNO_3 mixture. The supernatant solution was analyzed for Hg by cold vapour atomic absorption spectrophotometry (CVAAS) and for Ag, Cd, Cu, Mn, Mo, Ni, Pb, S, and Zn by ICP-ES.

A split of the sample (0.8 g), pulverized to <75 µm particle size, was sintered with Na_2O_2 in a zirconium crucible at 560°C in a muffle furnace. The fused sample was dissolved in deionized water and acidified with concentrated HNO_3 and HCl. The resulting solution was diluted and analyzed on a Varian 735 ICP-ES and on an Agilent 7900 ICP-MS for a total of 55 elements. In addition, rhenium was analyzed in some HMC samples, with all results being below the detection limit. Phosphorus and zirconium were also determined on a Panalytical Axios Advanced wavelength dispersive XRF on a fused glass disk prepared from a separate split (0.8 g) fused with $Li_2B_4O_7$-$LiBO_2$ in a Pt crucible. The sodium peroxide fusion is strongly oxidizing and thus is effective for decomposing sulphides and most refractory minerals. The relatively low temperature of the sintering minimizes the loss of volatile elements. Hence, element concentrations determined by this method are considered 'total'. Although Na and some of the key commodity elements such as Ag and Au are not determined, the advantage of the method is that determinations for B and Li, which cannot be analyzed by $Li_2B_4O_7$-$LiBO_2$ fusion are 'total'.

Splits (30 g) of stream sediment, HMC, and rock samples from northern Vancouver Island were analyzed by the H_2O-HCl-HNO_3 digestion - ICP-ES/MS at BVM. In addition, splits of the HMC and rock samples were analyzed by the $Li_2B_4O_7$-$LiBO_2$ fusion - LA-ICP-MS combined with XRF on fused glass disk at the same laboratory, and by Na_2O_2 sintering - ICP-MS/ES on solution at Actlabs. Lithochemical analyses are listed in Appendix 3 of Rukhlov et al. (2019).

4.3.2. Hydrochemistry

Water samples were analyzed for elemental compositions at ALS-Environmental. Concentrations of Br^-, Cl^-, F^-, NO_3^-, NO_2^-, and SO_4^{2-} anions in untreated water were determined by ion chromatography after the United States Environmental Protection Agency (USEPA) method reference 300.1. Filtered (0.45 µm) and preserved with hydrochloric acid, water samples underwent cold-oxidation with bromine monochloride, followed by reduction with stannous chloride. Dissolved Hg was then analyzed by CVAAS or cold vapour atomic fluorescence spectroscopy (CVAFS) after the American Public Health Association (APHA) method reference 3030B and USEPA method reference 1631EB. Filtered (0.45 µm) and preserved with nitric acid water samples were analyzed for a total of 45 dissolved metals by collision-reaction cell ICP-MS (CRC-ICP-MS) after USEPA method reference 6020B. Water field measurements and laboratory analyses are listed in Appendix 4 of Rukhlov et al. (2019).

4.3.3. Lead isotopic analysis

Lead isotopic ratios were measured in water and leachates of stream sediment, moss-mat sediment, HMC, and rock samples using a direct solution analysis on ICP-MS. Lead isotopic analysis of water samples that were filtered (0.45 µm) and acidified with nitric acid was performed at PCIGR. Water samples were concentrated approximately 20 times in two steps and then diluted with 2% HNO_3 to about 0.2 ppb Pb level. All blanks and sample number 2018 (with low-Pb) were brought up to a minimum volume to run the samples. Lead isotopic ratios in water were measured on a Nu AttoM double-focusing, high-resolution magnetic sector ICP-MS (HR-ICP-MS), using sample-standard bracketing correction for instrumental mass bias.

During the test part of this study at Loss Creek, we analyzed Pb isotopic ratios in leachates of stream sediment, moss-mat sediment, and HMC samples using different digestions in two laboratories. A split (0.5 g) was digested in aqua regia, and Pb isotopic ratios were measured in the supernatant solution by ICP-MS at ALS Canada (Geochemistry) Ltd., Vancouver, British Columbia (ALS-Geochemistry). A second split (0.4 g) was leached in 2.5N HCl as described below and Pb isotopic ratios were measured in the supernatant solution on the Nu AttoM HR-ICP-MS at PCIGR. We preferred this method for subsequent Pb isotopic analysis of samples from northern Vancouver Island. Samples were mixed with 8-10 mL of 2.5N HCl and the mixtures were shaken on a bench shaker at room temperature for 2 hours. The samples were then centrifuged at 2500 rpm for 30 minutes, or at 4000 rpm for 15 minutes. The supernatants were transferred to Savillex vials and evaporated to dryness. Concentrated nitric acid (1-2 mL) was added to the dry residues and evaporated to dryness. The final residues were re-dissolved in 2% HNO_3 and the solutions were centrifuged at 14,500 rpm for 6 minutes to preclude any suspended particles from entering the ICP-MS sample introduction system. The solutions were then diluted with 2% HNO_3 to about 0.5 ppb Pb and measured for Pb isotopic ratios on the AttoM HR-ICP-MS, using sample-standard bracketing correction for instrumental mass bias. The Pb isotopic data are listed in Appendix 5 of Rukhlov et al. (2019).

4.3.4. Modal mineralogy

Sieved, 1-2 mm and 0.5-1.0 mm-size fractions of HMC samples were examined under the binocular microscope, with ambiguous mineral grains identified by a portable XRF (Rukhlov et al., 2018) at BCGS. Automated bulk mineralogical analysis (BMA) on the 0.5-1.0 mm fraction of selected HMC samples was performed at Actlabs. Representative splits (2 g) were embedded in the epoxy resin for preparing round polished sections. The modal mineralogy was determined by a FEI QEMSCAN 650F field emission gun-scanning electron microscope (FEG-SEM), equipped with high-resolution back-scattered electron (BSE) and two Bruker 5030D energy dispersive spectrometers (EDS), using an accelerating voltage of 25 kV, a spot size of 5.8 µm, and a working distance of 13 mm. A custom mineral reference library was built for the samples. The BMA results are listed in Appendix 6 of Rukhlov et al. (2019).

4.4. Quality control

To evaluate the variability introduced by the sampling and analytical methods, we analyzed field duplicate samples, along with blind analytical duplicates (i.e., splits of recovered sieved fraction or pulverized material), matrix matching in-house and certified reference materials, and preparation blanks such as splits of pure silica sand processed the same way as routine samples (see Appendix 2 in Rukhlov et al., 2019). An average coefficient of variation, CV_{avr} (%), estimates the relative precision of the analytical results per analyte based on the field and analytical duplicates:

$$CV_{avr}(\%) = 100 \cdot \sqrt{\frac{2}{N}\sum_{i=1}^{N}\left(\frac{(a_i - b_i)^2}{(a_i + b_i)^2}\right)} \qquad \text{(Eq. 1)}$$

where a_i and b_i are duplicate results, and N is the number of duplicate pairs (after Abzalov, 2008). Appendices 3d, 4b, and 5a in Rukhlov et al. (2019) list the calculated CV_{avr}(%) values per analyte in different sample media. Values below an arbitrary 30% threshold indicate generally acceptable reproducibility of the analytical data, although those greater than 30% may also reflect sample media heterogeneity such as size fraction and nugget effect. Analysis of reference materials monitors accuracy or systematic bias of the analytical data. Blanks monitor contamination introduced by preparation and analytical methods.

4.4.1. Stream and moss mat-sediment, heavy mineral concentrate, and rock analysis

Lithochemical analyses using different digestions combined with ICP-MS/ES and XRF instrumentation have acceptable precision for most analytes (Appendix 3d in Rukhlov et al., 2019). Aqua regia digestion–ICP-MS/ES analysis on a 30 g split of <0.18 mm material has marginal to poor precision for Ag, Au, B, Hg, In, Re, and Na. Repeated analysis of reference materials (Appendix 3b in Rukhlov et al., 2019) indicates good precision and accuracy for these analytes, except Na, which is 'partial' by aqua regia digestion. Hence, site-specific sample heterogeneity is clearly contributing the variability of these elements. CV_{avr} (%) values for 'total' concentrations analyzed by lithium borate fusion - combined LA-ICP-MS and XRF on fused glass disk indicate similar marginal to poor precision for Ag, Bi, and Re, but Au, B and Hg are not determined by this method. In the case of sodium peroxide fusion–ICP-MS/ES analysis, poor precision for 'total' concentrations of B, Cd, Hf, Ho, Mo, Pb, Se, Sn, and W can be attributed to higher detection limits (10-100 times) for some of the analytes or erratic, elevated blanks compared to those of other analytical methods (Appendices 3b and c in Rukhlov et al., 2019). Precision of thermal INAA, combined with CVAAS and ICP-ES on a separate split of the sample digested in aqua regia, and of multi-acid digestion–ICP-MS/ES cannot be adequately assessed here, because these analytical methods were used only to test a few splits of HMC samples early in this study. Thermal INAA has poor precision for 'total' concentrations of Eu, Tb, U, and W, based on one duplicate pair. Multi-acid digestion–ICP-ES/MS also has poor precision for 'near total' values of Ag, Bi, and Re, based on two pairs of duplicates.

Repeated analysis of reference materials estimates both precision and accuracy of the analytical data. Appendix 3b of Rukhlov et al. (2019) lists analytical results of blind reference materials, 2σ ranges (±2 times standard deviation) of their expected mean 'total' and 'partial' values, blind preparation blanks, and blanks inserted by the commercial laboratories. Randomly inserted silica blanks (Aldrich 99.995% SiO_2 material) are generally below detection limits for most elements. Silica blanks pulverized in Cr-steel bowl at BCGS indicate 4-200 ppb Ag, 4-19 ppb Au, 36-430 ppm Cr, 0.09-0.36 wt.% Fe, 20-116 ppm Mn, 2-20 ppm Ni, 0.3-2.4 ppm Y, and 1-40 ppm Zn (n = 10), reflecting both carry-over contamination (e.g., gold lamination) and contribution from the grinding equipment. Sieved (<0.18 mm fraction) silica blanks and those pulverized in a ceramic bowl in a batch of HMC samples with an extra cycle of silica sand cleaning at BVM all indicate near-detection level of Au (0.4-1.6 ppb) and negligible or below detection limit values of other elements (Appendix 3b in Rukhlov et al., 2019).

Appendix 3c in Rukhlov et al. (2019) lists minimum detection limits (MDL) and sensitivity of the analytical methods in terms of percentage of results above the detection limit per analyte. Owing to generally low MDLs, acid digestion–ICP-ES/MS and lithium borate fusion–combined LA-ICP-MS and XRF on fused glass have good sensitivity for 95% analytes (total 59 to 66), based on 8 to 45 analyses. Mostly undetected analytes include Pd, Pt, and Ta by aqua regia digestion–ICP-ES/MS; Be, Re, and S by four-acid digestion–ICP-ES/MS; and Se, Te, and Tl by lithium borate fusion–LA-ICP-MS. Generally higher MDLs of sodium peroxide fusion–ICP-ES/MS method result in poor sensitivity (i.e., >50% results per element below MDL) for 17% analytes (total 59), including B, Be, Bi, Cd, Hf, In, Re, Sb, Te, and W, based on 25 analyses. Thermal INAA combined with aqua regia digestion–CVAAS and ICP-ES on a separate split have poor sensitivity for 50% analytes (total 44), based on 7 analyses (Appendix 3c in Rukhlov et al., 2019).

4.4.2. Water analysis

Precision of water data is estimated based on one field duplicate pair and replicate analyses of National Research Council of Canada (NRC) SLRS-6 river water certified reference material. Parameters measured in the field by a combination-electrode meter (T, pH, conductivity, and TDS) have CV_{avr} values of <1% indicating good reproducibility. Concentrations of anions in untreated water and dissolved metals in filtered (0.45 μm), acidified water all have acceptable precision, except Se, which has a CV_{avr} value of 43% (Appendix 4a in Rukhlov et al., 2019). Reported concentrations of NO_3^- and NO_2^- anions determined by ion chromatography should be treated with caution because most samples exceeded the recommended holding time of 3 days before analysis (4-18 days). Nitrite and bromide anions were not detected in water samples analyzed in this study. Only 29% (total 17) showed detectable F^-. Dissolved Hg in filtered (0.45 μm) and acidified with hydrochloric acid water by CVAAS/ CVAFS was detected in one of 18 analyzed samples. CRC-ICP-MS analysis of other dissolved metals in filtered (0.45 μm) and acidified with nitric acid water has good sensitivity (i.e., <50% results per element below MDL) for 67% analytes (total 45). Bismuth, gallium, niobium, phosphorus, silver, tantalum, tellurium, and tungsten cations were not detected in water samples analyzed in this study.

Results of replicate analyses of NRC SLRS-6 river water standard are within uncertainties of the certified values, indicating good accuracy of the data (Appendix 4b in Rukhlov et al., 2019). Concentrations of anions were not analyzed in water blanks. Concentrations of dissolved metals measured in water blanks were generally below the MDLs, except erratic positive values for Ba, Ca, Cu, Fe, Pb, and Zn, thus ruling out significant contamination introduced by the sampling method. Water data are listed in Appendix 4 of Rukhlov et al. (2019).

4.4.3. Lead isotopic analysis

Based on 22 duplicate pairs, Pb isotopic ratios measured in 2.5N HCl leachates of stream and moss-mat sediment, HMC, and rock samples on the AttoM HR-ICP-MS at PCIGR have CV_{avr} values of 0.15% for $^{208}Pb/^{206}Pb$ ratio, 0.28% for $^{206}Pb/^{207}Pb$, 0.42% for $^{208}Pb/^{204}Pb$, 0.43% for $^{206}Pb/^{204}Pb$, and 0.49% for $^{207}Pb/^{204}Pb$. Precision of Pb isotopic ratios measured in water samples on the same instrumentation at PCIGR is about 1.3-2.0 times the above CV_{avr} (%) values, based on 6 duplicate pairs. Lead isotopic ratios measured in aqua regia leachates of stream and moss-mat sediment, and HMC samples by ICP-MS at ALS-Geochemistry have larger CV_{avr} values of 0.55% for $^{208}Pb/^{206}Pb$ ratio, 0.46% for $^{206}Pb/^{207}Pb$, 0.96% for $^{208}Pb/^{204}Pb$, 0.72% for $^{206}Pb/^{204}Pb$, and 0.78% for $^{207}Pb/^{204}Pb$, based on eight duplicate pairs. Hence, precision of the analysis by ICP-MS is enough to resolve natural Pb isotopic variability between the analyzed samples, showing maximum contrast of 1.5-2.7% for $^{208}Pb/^{206}Pb$ ratio, 1.4-2.7% for $^{206}Pb/^{207}Pb$, 2.4-4.8% for $^{208}Pb/^{204}Pb$, 2.3-5.2% for $^{206}Pb/^{204}Pb$, and 2.5-4.2% for $^{207}Pb/^{204}Pb$. Replicate analyses of USGS BCR-2 reference material are consistent within the uncertainties with the published values by multi-collector ICP-MS and thermal ionization mass spectrometry, thus validating accuracy of the data reported here. Lead isotopic data, including reference materials and preparation and laboratory procedural blanks, are listed in Appendix 5 of Rukhlov et al. (2019).

5. Results

5.1. Loss Creek

5.1.1. Lithochemistry

Analytical results for stream and moss mat-sediment (<0.18 mm sieved fraction) and HMC (milled, <1 mm sieved fraction) samples are listed in Appendix 3a of Rukhlov et al. (2019). Ranked element contrast (REC) plots (Fig. 6) are log plots of sorted (maximum to minimum) analytical results normalized to survey minimum values, specific for HMC and stream and moss-mat sediment samples. Normalizing to minimum sets the Y-axis origin to unity and thus simplifies the plot by avoiding fractions; normalizing to the median does not change the REC pattern. REC plots reveal associations of elements showing the maximum contrast to minimum or background (ranked leaders) and the magnitude of the contrast (geochemical anomaly), which reflects dispersion in a stream system. Contrast leaders (maximum/minimum) of the HMC samples at Loss Creek are Au (36752), Ag (121), W (107), Mn (59), heavy rare earth elements (HREE) such as Yb (58), Tm (54), Er (46), Ho (45), Lu (43), Dy (30), and Tb (15), plus Y (41). The magnitude of contrast for Au ($n \cdot 10^4$) and HREE+Y ($n \cdot 10^1$) are impressive. The anomalous element association reflects the occurrence of placer Au and abundant garnet (host of Mn, Y and HREE) at Loss Creek (Fig. 7). Anomalous Au-Ag-W is a signature of orogenic Au veins in the catchment area (Fig. 2). Notably, both the low-volume, bulk stream and moss-mat sediment materials, which are conventionally sampled in RGS surveys, missed the Au-Ag-W-HREE-Y anomaly and yielded only background levels. In contrast, HMC samples greatly enhanced the anomaly contrast and are thus much more effective. Furthermore, panning or sluicing in the field is inexpensive and rapid relative to costly and time-consuming processing of bulk samples in a laboratory and is well-suited for prospectors. As many elements as possible should be analyzed to minimize missing anomalous elements and keeping an open mind for non-traditional types of ore deposits. At a minimum, we recommend aqua regia digestion–ultra-trace ICP-MS/ES analysis of a full suite of elements (currently 65). Ideally, this method should be supplemented with fusion–combined LA-ICP-MS and XRF on the fused glass, which determine 'total' concentrations of 65 elements plus LOI, including constituents of refractory minerals, which aqua regia digestion cannot break down.

5.1.2. Hydrochemistry

Complete analytical results for stream water are listed in Appendix 4a of Rukhlov et al. (2019). Loss Creek water sampled in April was Na-Cl type with 3.6 mg/L HCO_3^- estimated by ion charge imbalance. The stream water became Ca-HCO_3 type with 11.66 mg/L HCO_3^- estimated by ion charge imbalance in June. Both April and June water samples had similar pH (6.8-7.2), conductivity (36 µS/cm), ionic strength (0.20-0.41 mmol/L), and major ion compositions (Fig. 8), but distinct abundances of dissolved trace metals (Fig. 9). A REC plot for Loss Creek water (Fig. 10) highlights the subtle differences in Loss Creek water chemistry between the spring runoff and lower discharges later in the summer. Ranked contrast (result/survey minimum) leaders in water sampled in April are Ti (19), Al (5), V (4), and Rb (4), whereas contrast leaders in water sampled in June are Mn (12), Rb (11), V (9), K (6), and Co (5). Note that Rb^+ and anion-forming V^{3+}, soluble in neutral water, are invariable contrast leaders, reflecting the chemistry of country rocks, including staurolite-garnet schists of Leech River complex and basalts of Metchosin Formation. Although the subtle differences in dissolved metal contents reflect seasonal variability, water chemistry is an objective indicator of hydrochemical dispersion as will be discussed below.

5.1.3. Lead isotopes

Analytical results on water and leachates of stream and moss-mat sediment and HMC samples are listed in Appendix 5a of Rukhlov et al. (2019). Lead isotopic ratios in leachates range from 18.52 to 19.30 for $^{206}Pb/^{204}Pb$, 15.41 to 16.11 for $^{207}Pb/^{204}Pb$, 37.51 to 39.71 for $^{208}Pb/^{204}Pb$, 1.187 to 1.211 for $^{206}Pb/^{207}Pb$, and 2.026 to 2.083 for $^{208}Pb/^{206}Pb$. Data for aqua regia leachates show more scattering in the Pb isotopic ratio plots than are those for 2.5N HCl leachates, which define linear trends in all diagrams (Figs. 10b-g). Although the larger uncertainties of the aqua regia leachates can partly explain the discrepancy, 2.5N HCl leachates of panned HMC samples have more radiogenic Pb isotopic ratios than are aqua regia leachates on splits of the same samples. The isotopic composition of water extends the linear data arrays of leachates in both $^{206}Pb/^{204}Pb$ vs. $^{207}Pb/^{204}Pb$ and $^{206}Pb/^{204}Pb$ vs. $^{208}Pb/^{204}Pb$ diagrams and falls in the middle of the linear trend in $^{206}Pb/^{207}Pb$ vs. $^{208}Pb/^{206}Pb$ diagram (Figs. 10e-g). Linear trends in the Pb isotopic ratio correlation diagrams could reflect mixing of two isotopically distinct end members or a secondary isochron (Gulson, 1986; Bell and Franklin, 1993; Bell and Murton, 1995; Simonetti et

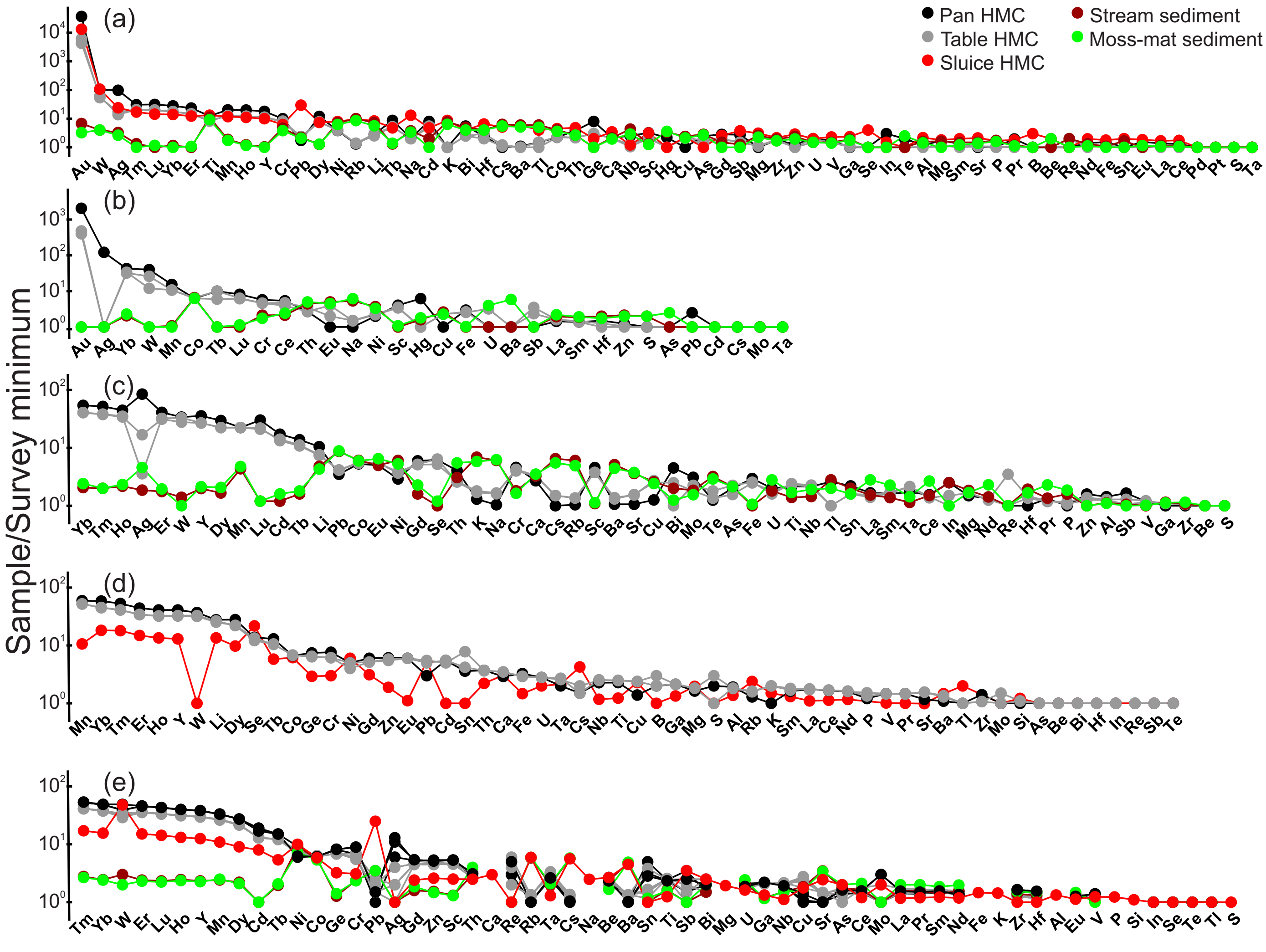

Fig. 6. Loss Creek ranked element contrast plots relative to survey minimum for stream sediment, moss-mat sediment, and heavy mineral concentrates by different analytical methods. **a)** H_2O-HCl-HNO_3 digestion of <0.18 mm fraction or milled material (30 g) combined with inductively coupled plasma emission spectrometry (ICP-ES) and inductively coupled plasma mass spectrometry (ICP-MS) on the solution, determining 'partial' concentrations of 65 elements. **b)** Thermal instrumental neutron activation analysis (INAA) on <0.18 mm fraction or milled material (10-51 g), determining 'total' concentrations of 34 elements, combined with Hg by cold vapour atomic absorption spectrophotometry (CVAAS) and Ag, Cd, Cu, Mn, Mo, Ni, Pb, S, and Zn by ICP-ES on a separate split (0.5 g) digested in aqua regia. **c)** HF-$HClO_4$-HNO_3-HCl digestion of <0.18 fraction or milled material (0.25 g) combined with ICP-ES/MS on the solution, determining 'near-total' concentrations of 59 elements. **d)** Na_2O_2 digestion of <75 µm milled material (0.8 g), followed by ICP-ES/MS on the solution, combined with $Li_2B_4O_7$-$LiBO_2$ fusion of a separate split (0.8 g), followed by P and Zr analysis by X-ray fluorescence (XRF) on the fused glass disk, determining 'total' concentrations of 58 elements. **e)** $Li_2B_4O_7$-$LiBO_2$ fusion of <75 µm milled material (0.7 g) combined with XRF and laser ablation ICP-MS (LA-ICP-MS) analysis on the fused glass disk, determining 'total' concentrations of 65 elements plus loss on ignition (LOI) at 1000°C gravimetrically.

al., 1996; Hussein et al., 2003; Rukhlov and Ferbey, 2015). In case of binary mixing, data points define hyperbolic curves in terms of Pb concentration versus Pb isotopic ratio (Figs. 11a-c). In these diagrams, the 2.5N HCl leachates of stream and moss-mat sediment and HMC samples partly overlap a binary mixing trend defined by MC-ICP-MS data for 2.5N HCl leachates of till matrix (<64 µm-size fraction), massive sulphide ore, and country diorite in southwestern British Columbia (Rukhlov and Ferbey, 2015).

Lead isotopic signature diagrams for Loss Creek leachates of stream and moss mat-sediment, HMC, and water samples, (Figs. 11d-f) are linear plots of Pb isotopic ratios recast as δ values (in %) relative to survey minimum values

(Eq. 2)

$$\delta^{20i}Pb/^{20j}Pb\ (\%) = 10^2 \cdot \frac{(^{20i}Pb/^{20j}Pb_{sample} - {}^{20i}Pb/^{20j}Pb_{minimum})}{^{20i}Pb/^{20j}Pb_{minimum}}$$

where $^{20i}Pb/^{20j}Pb_{sample}$ is measured Pb isotopic ratio in a sample and $^{20i}Pb/^{20j}Pb_{minimum}$ is the survey minimum value of the ratio. δPb (%) values define Pb isotopic signature of a sample, which fingerprints the distinct Pb sources such as Pb-rich ore and host crustal rocks. The δPb (%) signature plots highlight the

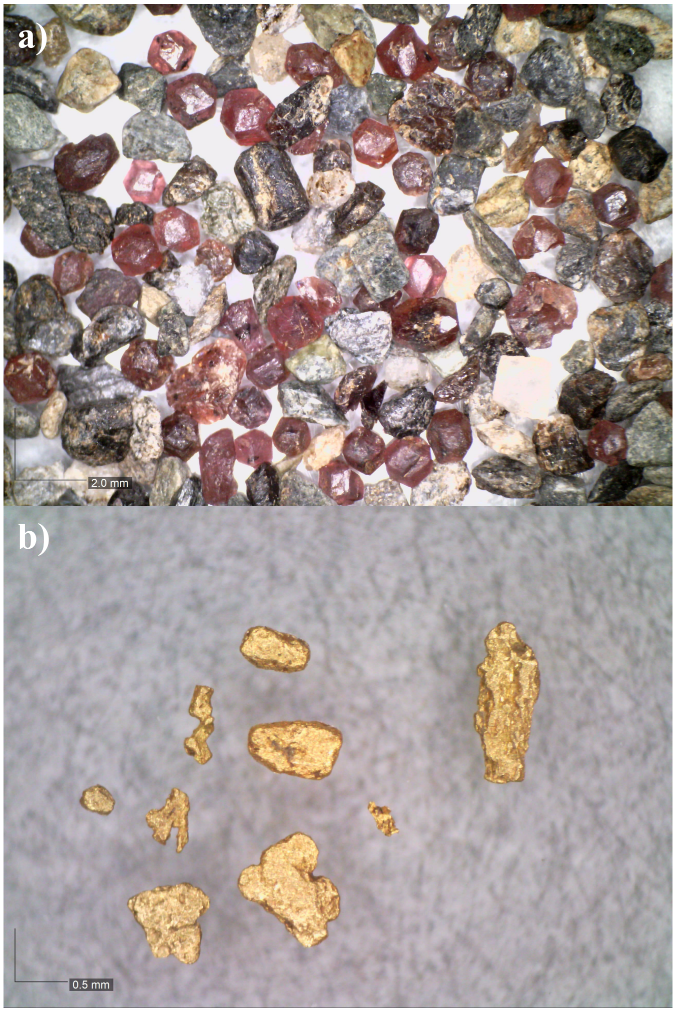

Fig. 7. Photomicrographs of panned sluice heavy mineral concentrate at Loss Creek (sample 1002). **a)** Abundant pink euhedral Mn-rich almandine, $(Fe^{2+}, Mn^{2+})_3(Al, Fe^{3+})_2(SiO_4)_3$ in 1-2 mm fraction. **b)** Gold grains.

Pb isotopic contrast between the aqua regia and 2.5N HCl leachates of the HMC samples discussed above. Water and aqua regia leachate of stream sediment (<0.18 mm fraction) samples have the lowest δPb (%) values, whereas leachates of HMC samples (<1 mm-size) have more radiogenic Pb isotopic compositions with δPb values up to 6% in $^{208}Pb/^{204}Pb$.

5.2. Northern Vancouver Island

Please see Rukhlov et al. (2019) for complete lithochemical analyses of 14 stream-sediment (<0.18 mm fraction), 14 panned sluice HMC (<1 mm fraction), and 2 rock samples collected at 13 sites from 6 major watersheds and their tributaries on northern Vancouver Island (Appendix 3a), water pH, conductivity, TDS, and concentrations of anions and dissolved metals in 15 samples from these streams (Appendix 4a), and Pb isotopic compositions of water (21) and 2.5N HCl leachates of HMC (17) and rock (2) (Appendix 5a). δPb (%) values for the northern Vancouver Island data are relative to the composition of 2.5N HCl leachate of galena-bearing sample 19ARU001 from Caledonia Pb-Zn skarn occurrence (MINFILE 092L 061): $^{206}Pb/^{204}Pb$ = 18.427, $^{207}Pb/^{204}Pb$ = 15.478, $^{208}Pb/^{204}Pb$ = 37.901, $^{206}Pb/^{207}Pb$ = 1.1905, and $^{208}Pb/^{206}Pb$ = 2.0568.

5.2.1. Geochemistry and Pb isotopic composition of water

Analyzed stream waters range from Na-Cl and Ca-HCO_3 types (ionic strength 0.29-0.57 mmol/L) to Ca-SO_4 type (ionic strength 1.11-1.70 mmol/L). Significant ranges of pH (3.81-7.02), conductivity (27.5-138.2 µS/cm), and TDS (12.8-66.5 ppm) values, and major and trace ion compositions (Figs. 8, 9) are consistent with the historical drainage geochemical data (Matysek and Day, 1988; Gravel and Matysek, 1989; Matysek et al., 1989; Koyanagi and Panteleyev, 1993, 1994; Sibbick and Laurus, 1995a; Panteleyev et al., 1996b; Jackaman, 2011, 2013a). Lead isotopic ratios of the waters range from 18.17 to 18.63 for $^{206}Pb/^{204}Pb$, 15.32 to 15.71 for $^{207}Pb/^{204}Pb$, 37.46 to 38.36 for $^{208}Pb/^{204}Pb$, 1.173 to 1.196 for $^{206}Pb/^{207}Pb$, and 2.049 to 2.079 for $^{208}Pb/^{206}Pb$. The acidic (pH 3.81-4.30), Ca-SO_4 waters of Hushamu and Youghpan creeks have high conductivity (108.4-138.2 µS/cm), TDS (52.4-66.5 ppm), F^-, Mg^{2+}, Fe^{3+}, Al^{3+}, Mn^{2+}, Ba^{2+}, Zn^{2+}, Cu^{2+}, Co^{3+}, Ni^{2+}, Sn^{2+}, and Pb^{2+} cations compared with other streams. The Ca-SO_4 water of Hepler Creek has higher pH (6.8), lower conductivity (81.5 µS/cm), TDS (39.5 ppm), F^-, Fe^{3+}, and Al^{3+}, but similar concentrations of Mg^{2+} and most trace dissolved metals. In contrast, Na-Cl and Ca-HCO_3 waters from other streams have higher concentrations of NO_3^-, V^{3+}, and Cr^{3+}, but generally lower abundances of other ions (Figs. 8, 9). Quatse River water was sampled every third day in August to monitor variability of water chemistry. Following a heavy rainfall the previous day, on August 2 the river had a much higher discharge than during the rainless period between August 3 and August 11. Concentrations of Cl^-, $B(OH)_3$, K^+, and Rb^+ increased slightly, whereas NO_3^-, Al^{3+}, Fe^{3+}, Mn^{2+}, Ni^{2+}, and Zn^{2+} decreased slightly between August 2 to August 11. Water pH and concentrations of other ions remained generally consistent (Fig. 12).

Element contrast leaders (result/survey minimum) in stream water samples highlight anomalous element associations, which reflect variable solubility of metals depending on water pH and primary and secondary halos of hydrothermal ore systems drained by the streams (Figs. 13-17). Element contrast leaders in waters of Hushamu, Youghpan, and Hepler creeks are Co (91-243), Mn (52-123), Al (1-54), SO_4 (25-46), Fe (5-46), Zn (13-31), and Cu (5-26), which reflect soluble species in acidic waters draining argillic-altered volcanic rocks of the Bonanza Group, which host sulphide mineralization in the stream catchments (Northcote and Muller, 1972; Panteleyev, 1992; Panteleyev and Koyanagi, 1993, 1994; Panteleyev et al., 1995; Perelló et al., 1995; Tahija et al., 2017). In contrast, REC leaders in waters of a Hushamu Creek tributary, Wanokana and Caledonia creeks, and Quatse River are Ti-V-Zr±NO_3±U±Al±Mo±Mn±Sn, reflecting hydrochemical dispersion of anion-forming and carbonate complexes of these metals soluble in neutral waters draining mainly mafic volcanic rocks. Waters of Hushamu and

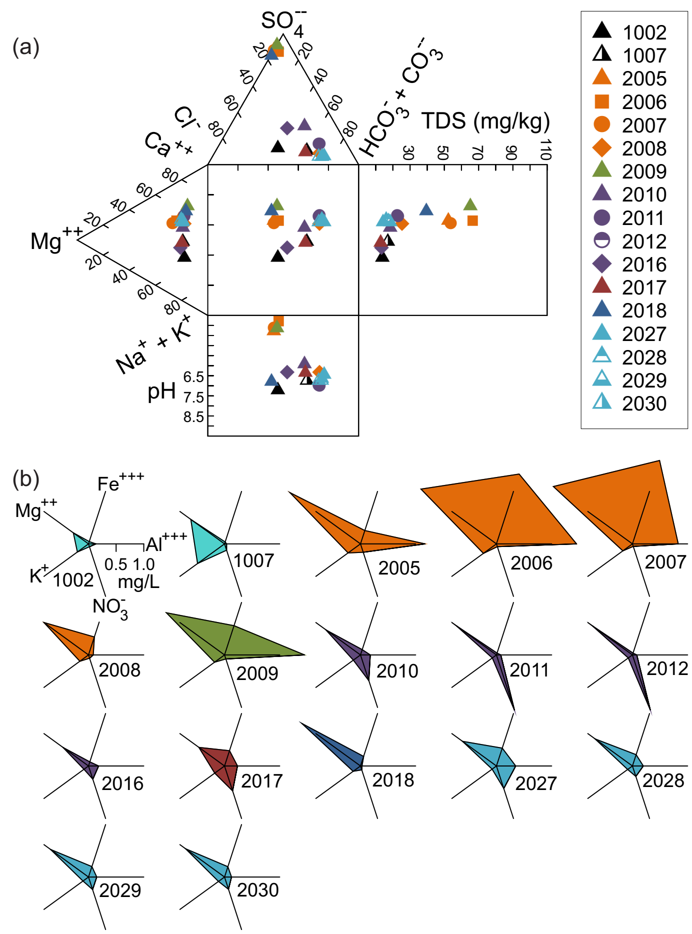

Fig. 8. Composition of Loss Creek and northern Vancouver Island stream water. **a)** Durov diagram, representing major ions (SO_4^{2-}, HCO_3^- + CO_3^{2-}, Ca^{2+}, Mg^{2+}, and $Na^+ + K^+$), total dissolved solids (TDS), and pH; and **b)** Radial plots in terms of K^+ - Mg^{2+} - Fe^{3+} - Al^{3+} - NO_3^- ions (in mg/L). See Appendix 4 in Rukhlov et al. (2019) for details.

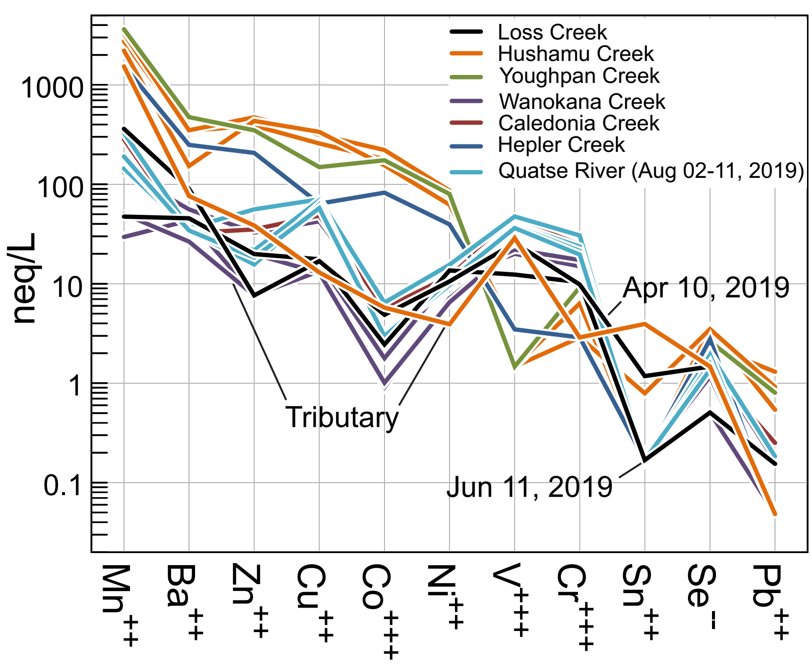

Fig. 9. Schoeller diagram for Vancouver Island streams showing patterns of minor ions in nanoequivalent concentration (neq/L).

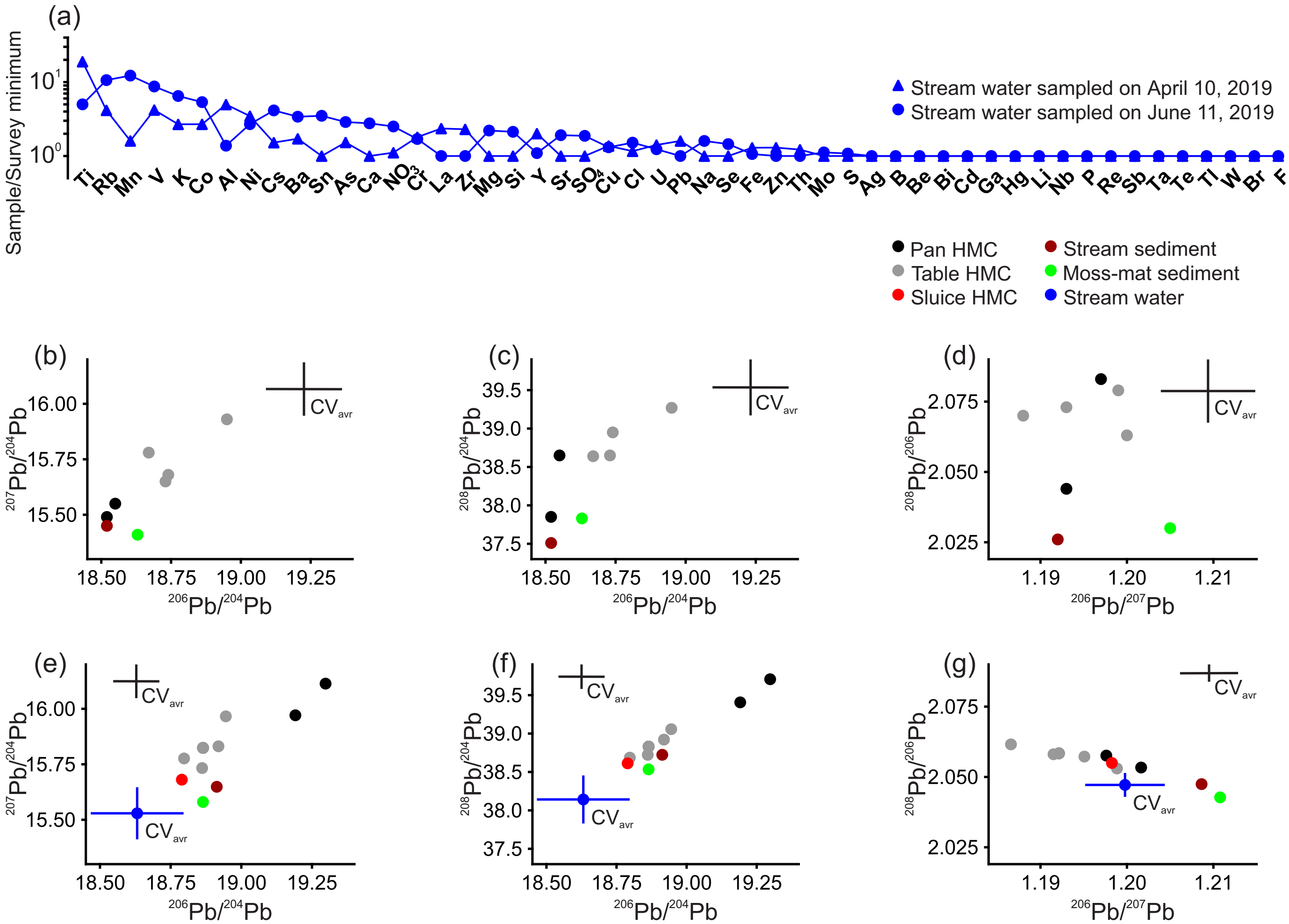

Fig. 10. a) Ranked element contrast plot relative to survey minimum for water samples collected at Loss Creek in April and June, 2019. Concentrations of bromide, chloride, fluoride, nitrate, and sulphate anions in untreated water by ion chromatography; dissolved Hg in filtered (0.45 µm) and acidified with hydrochloric acid water by cold vapour atomic absorption spectrophotometry (CVAAS) or cold vapour atomic fluorescence spectroscopy (CVAFS); dissolved 45 other metals in filtered (0.45 µm) and acidified with nitric acid water by collision-reaction cell inductively coupled plasma mass spectrometry (CRC-ICP-MS). **(b-d)** Lead isotopic ratio plots for aqua regia leachates of stream sediment, moss-mat-sediment, and heavy mineral concentrate samples (0.5 g) from Loss Creek analyzed on ICP-MS at ALS Canada (Geochemistry) Ltd., Vancouver, British Columbia. **(e-g)** Lead isotopic ratio plots for filtered (0.45 µm), acidified with nitric acid, water samples (50 mL) and for 2.5N HCl leachates of stream sediment, moss-mat-sediment, and heavy mineral concentrate samples (0.3-0.5 g) from Loss Creek analyzed on a Nu AttoM double-focusing, high-resolution magnetic sector ICP-MS (HR-ICP-MS) at the Pacific Centre for Isotopic and Geochemical Research, University of British Columbia (PCIGR), Vancouver, British Columbia. **(b, e)** ^{206}Pb/^{204}Pb vs. ^{207}Pb/^{204}Pb. **(c, f)** ^{206}Pb/^{204}Pb vs ^{208}Pb/^{204}Pb. **(d, g)** ^{206}Pb/^{207}Pb vs ^{208}Pb/^{206}Pb. Uncertainties in terms of average coefficient of variation (CV_{avr}) based on at least 6 duplicate pairs (after Abzalov, 2008).

Youghpan creeks also have distinct δPb (%) patterns with low δPb (%) values, which reflect sources having unradiogenic Pb isotopic compositions such as galena-bearing Caledonia Pb-Zn skarn (MINFILE 092L 061; Figs. 13, 15). Different δPb (%) patterns of stream waters indicate isotopically heterogeneous sources.

5.2.2. Geochemistry and Pb isotopic composition of stream sediment and heavy mineral concentrate

Geochemistry of stream sediment (<0.18 mm fraction) and HMC (<1 mm fraction) samples reveals different REC leaders, which are Au, Bi, Se, Te, Mo, Pb, Re, S, Sn, Tl, In, and Cu at the headwaters of Hushamu Creek (Fig. 13). The anomalous element association confirms not only epithermal Au-Ag-Cu (MINFILE 092L 185) and porphyry Cu-Mo±Au (MINFILE 092L 240) mineralization immediately upstream, but also suggests shallow erosion of the mineralization (Panteleyev, 1992; Panteleyev and Koyanagi, 1993, 1994; Panteleyev et al., 1995; Perelló et al., 1995; Tahija et al., 2017). HMC samples collected farther downstream and near the mouth of Hushamu Creek (catchment, 20.5 km^2) also show maximum element contrast for Au (30709 times background), S, Se, Ag, Bi, Te, Mo, Re, and Pb. Subdued contrast and distinct element association (Se-Mo-Bi-Co-Te-S-Li-Cs) in an HMC sample

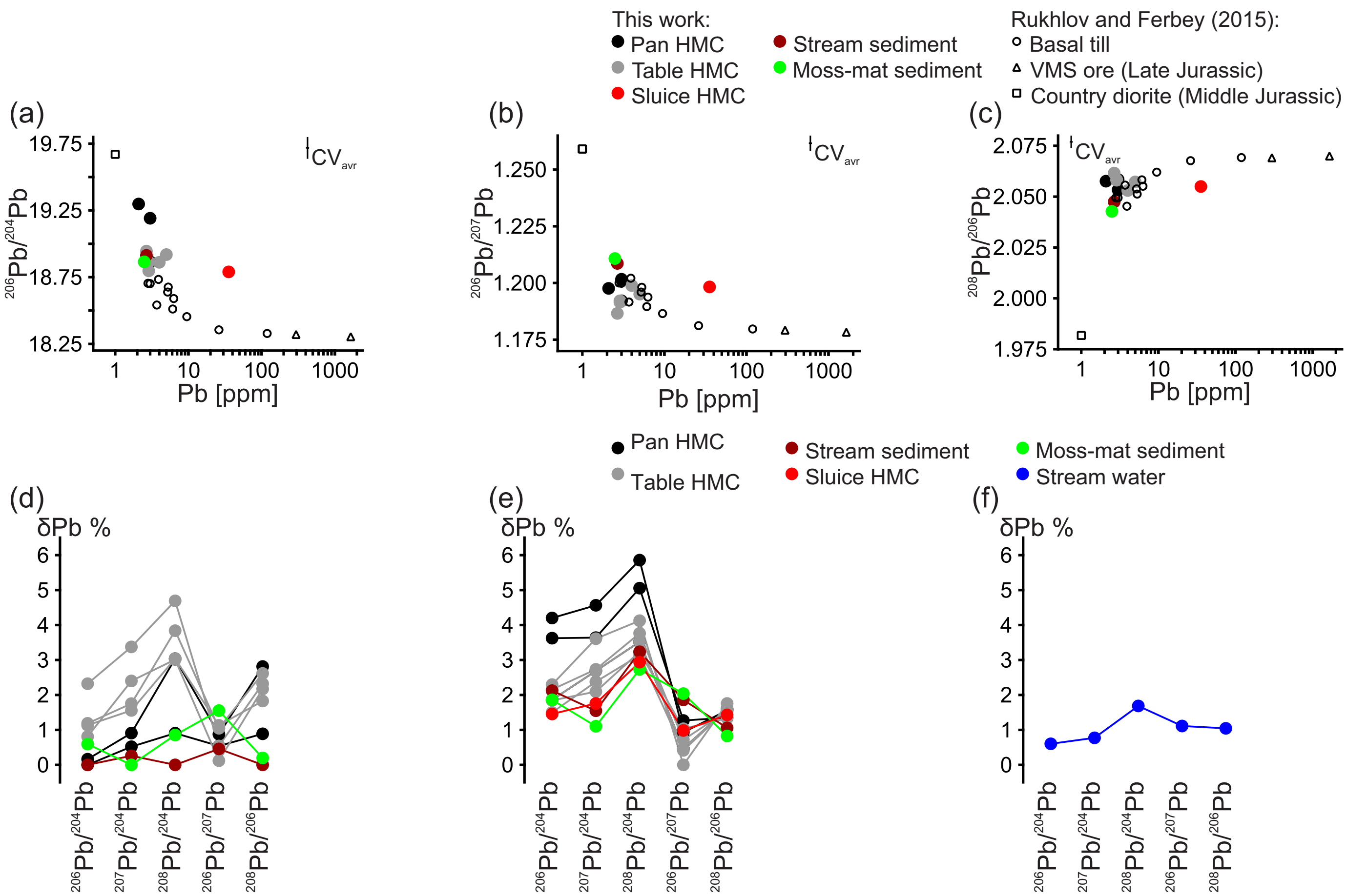

Fig. 11. (a-c) Mixing plots for stream sediment, moss mat-sediment, and heavy mineral concentrate samples from Loss Creek in terms of Pb concentration by aqua regia digestion–inductively coupled plasma mass spectrometry (ICP-MS) vs. Pb isotopic ratio in 2.5N HCl leachates of the samples analyzed on a Nu AttoM double-focusing, high-resolution magnetic sector ICP-MS (HR-ICP-MS). **a)** Pb [ppm] vs $^{206}Pb/^{204}Pb$. **b)** Pb [ppm] vs. $^{206}Pb/^{207}Pb$. **c)** Pb [ppm] vs. $^{208}Pb/^{206}Pb$. Multi-collector ICP-MS (MC-ICP-MS) data for 2.5N HCl leachates of <63 µm-size, sieved fraction of basal till matrix, massive sulphide ore, and country diorite from southern British Columbia after Rukhlov and Ferbey (2015). Uncertainties in terms of average coefficient of variation (CV_{avr}) based on 22 duplicate pairs (after Abzalov, 2008). **(d-f)** Lead isotopic signature plots for stream sediment, moss mat-sediment, heavy mineral concentrate, and water samples from Loss Creek in terms of Pb isotopic ratios recast as δ values (in %) relative to the survey minimum values as follows: $\delta^{20i}Pb/^{20j}Pb\ (\%) = 100\cdot(^{20i}Pb/^{20j}Pb_{sample} - {}^{20i}Pb/^{20j}Pb_{minimum})/{}^{20i}Pb/^{20j}Pb_{minimum}$. **d)** δPb (%) plots for $^{206}Pb/^{204}Pb$, $^{207}Pb/^{204}Pb$, $^{208}Pb/^{204}Pb$, $^{206}Pb/^{207}Pb$, and $^{208}Pb/^{206}Pb$ values in aqua regia leachates of stream sediment, moss mat-sediment, and heavy mineral concentrate samples analyzed on ICP-MS at ALS Canada (Geochemistry) Ltd., Vancouver, British Columbia. **e)** δPb (%) plots for $^{206}Pb/^{204}Pb$, $^{207}Pb/^{204}Pb$, $^{208}Pb/^{204}Pb$, $^{206}Pb/^{207}Pb$, and $^{208}Pb/^{206}Pb$ values in 2.5N HCl leachates of stream sediment, moss mat-sediment, and heavy mineral concentrate samples analyzed on a Nu AttoM double-focusing, high-resolution magnetic sector ICP-MS (HR-ICP-MS) at the Pacific Centre for Isotopic and Geochemical Research, University of British Columbia (PCIGR), Vancouver, British Columbia. **f)** δPb (%) plots for $^{206}Pb/^{204}Pb$, $^{207}Pb/^{204}Pb$, $^{208}Pb/^{204}Pb$, $^{206}Pb/^{207}Pb$, and $^{208}Pb/^{206}Pb$ values in filtered (0.45 µm), acidified with nitric acid, water sample analyzed on the AttoM HR-ICP-MS at PCIGR.

collected near the mouth of a Hushamu Creek tributary rule out significant mineralization in that basin (Fig. 13).

HMC samples collected near mouths of Youghpan (catchment, 25.0 km^2) and Wanokana (catchment, 43.5 km^2) creeks show maximum contrast for Au (1779-22328 times background), S, Ag, Bi, Se, Te, Mo, Co, Ba, Re, Tl, Hg, and Pb, indicating significant epithermal Au-Ag-Cu and blind porphyry Cu-Mo-Au mineralization (Figs. 15, 16). HMC samples collected at the headwaters of Wanokana Creek and near the mouth of Quatse River (catchment, 89.4 km^2) have a distinct geochemical signature with anomalous Hg±Au±Ag and elevated background for Ti, Ni, Co, and Ca, reflecting mafic rock types (Figs. 16, 17). HMC sample from Caledonia Creek (catchment, 9.35 km^2), downstream of a Pb-Zn skarn occurrence (MINFILE 092L 061), shows a weak contrast and elevated background for W, Mo, Co, Ti, Ca, Bi, Na, Ni, Mn, Au, Pb, and Cd, which rule out significant mineralization in that basin (Fig. 17). Lead isotopic compositions also discriminate between the two groups of HMC samples. Smoother δPb (%) patterns with values about zero characterize 2.5N leachates of HMC samples from Hushamu and Youghpan creeks, whereas others have more variable δPb (%) patterns indicating Pb isotopic heterogeneity in the catchment basins (Figs. 13, 15-17).

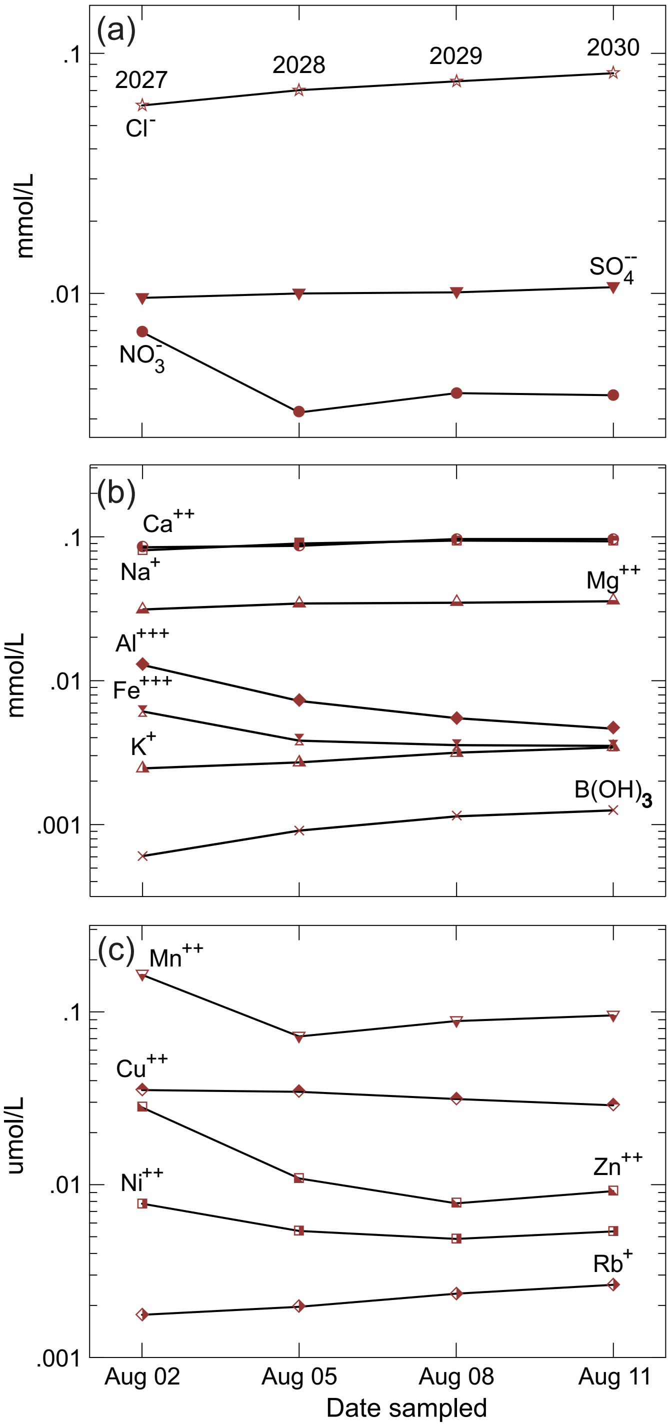

Fig. 12. Sampling date versus composition of Quatse River water at monitor site, northern Vancouver Island. **a)** Cl^-, SO_4^{2-}, and NO_3^- anions (mmol/L). **b)** Na^+, K^+, Ca^{2+}, Mg^{2+}, Al^{3+}, and Fe^{3+} cations, and $B(OH)_3$ component (mmol/L). **c)** Rb^+, Cu^{2+}, Mn^{2+}, Ni^{2+}, and Zn^{2+} cations (µmol/L).

In summary, near-mouth HMC samples (<1 mm fraction) confidently identify epithermal Au-Ag-Cu and blind porphyry Cu-Mo±Au mineralization in the Hushamu, Youghpan, and Wanokana watersheds (20.5-43.5 km^2). In contrast, all stream-sediment samples (<0.18 mm fraction) collected near mouths of these basins have background concentrations of Au and Ag, consistent with previous moss-mat sediment RGS data (Figs. 13, 15, 16; Matysek and Day, 1988; Gravel and Matysek, 1989; Matysek et al., 1989; Jackaman, 2011, 2013a, 2014). Conventional RGS sample media contrast ore metals only immediately downstream of known mineralization such as the Hushamu deposit, whereas HMC samples greatly enhance the geochemical anomaly contrast for a much larger catchment area. For regional geochemical drainage surveys, we recommend collecting one near-mouth HMC sample (200-400 g), recovered from 10-15 kg of bulk alluvium (<2 mm fraction). Geochemistry of the 'grey' HMC (<1 mm fraction), which retains sulphides, garnet, and other indicator minerals (i.e., not 'black sand' with specific gravity >5 g·cm^{-3}), is more representative of element dispersion in a stream system and thus basin metallogeny than are low-volume, bulk stream and moss-mat sediment samples.

5.3. Mineralogy of heavy mineral concentrate

Microscopic examination of 1-2 mm and 0.5-1.0 mm fractions of HMC samples, coupled with pXRF identification on single grains of ambiguous minerals, provides information on ore minerals such as gold and diamonds and indicators of hydrothermal alteration and ore systems. Appendix 6 in Rukhlov et al. (2019) lists BMA results on selected HMC samples (0.5-1.0 mm fraction) by QEMSCAN. Panned sluice HMC recovered from alluvium at Loss Creek has abundant Mn-rich almandine (25%), staurolite, and amphibole derived from staurolite-garnet schists (Fig. 7a). The delicate shape of detrital gold grains (wires and leaves; Fig. 7b) indicates a nearby bedrock source, such as the orogenic Au veins in the area (MINFILE 092C 214, 213, 217, and 059). In contrast, alluvial HMC samples from northern Vancouver Island have 1-2% garnet, including brown-red spessartine and pink almandine (Fig. 18). Glacial dispersion of spessartine garnet in tills has been successfully used in exploring for epithermal Au-Ag-Cu deposits of the Interior Plateau (Lett and Rukhlov, 2017 and references therein). Other porphyry Cu-Mo-Au and epithermal Au-Ag-Cu indicator minerals in alluvial HMC samples from Hushamu Creek include pyrite, magnetite, goethite, rutile, ardealite, alunite, anhydrite, böhmite, titanite, epidote, muscovite, illite, chlorite, Si-Al clays, siderite, and apatite (Appendix 6 in Rukhlov et al., 2019). A near-mouth HMC sample from Wanokana Creek contains abundant plagioclase, K-feldspar, amphibole, and epidote, and elevated counts of hematite, ilmenite, titanite, and apatite relative to other HMC samples (Appendix 6 in Rukhlov et al., 2019).

6. Discussion

6.1. Basic principles

Weathering of an in situ ore body and its primary dispersion halo results in hypergene enrichment of nearby surficial materials in ore and related elements, forming a secondary dispersion halo. This secondary geochemical anomaly generally mimics the shape of the primary bedrock anomaly in plan view but has

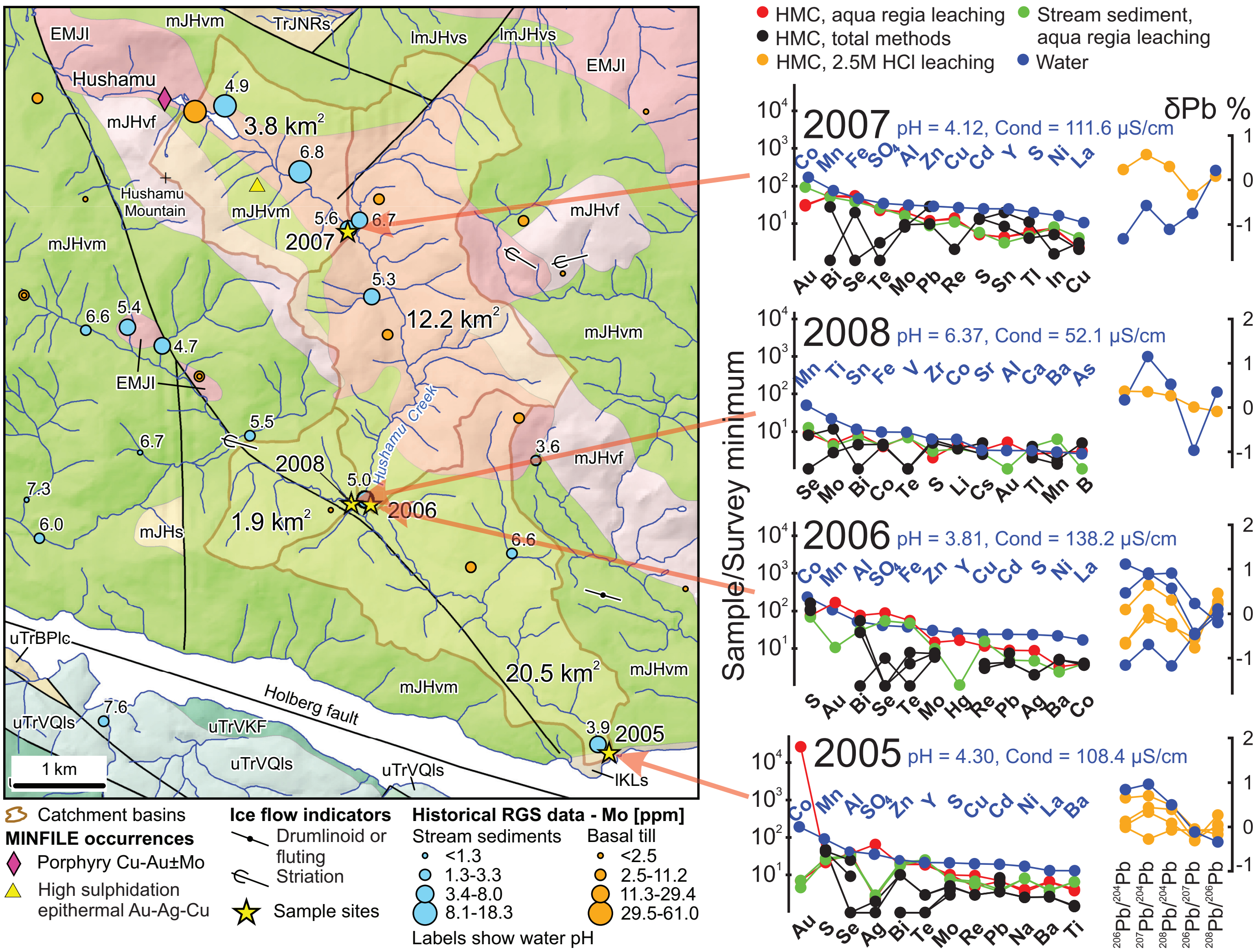

Fig. 13. Hushamu Creek catchment, northern Vancouver Island. Leaders of ranked element contrast relative to survey minimum and $\delta^{206}Pb/^{204}Pb$, $\delta^{207}Pb/^{204}Pb$, $\delta^{208}Pb/^{204}Pb$, $\delta^{206}Pb/^{207}Pb$, and $\delta^{208}Pb/^{206}Pb$ patterns (in %) for stream sediment, heavy mineral concentrate, and water samples. Water pH, conductivity, and analyte labels shown above patterns. δPb (%) values calculated as follows: $\delta^{20i}Pb/^{20j}Pb\ (\%) = 100\cdot(^{20i}Pb/^{20j}Pb_{sample} - {}^{20i}Pb/^{20j}Pb_{galena})/{}^{20i}Pb/^{20j}Pb_{galena}$, where $^{20i}Pb/^{20j}Pb_{galena}$ is the Pb isotopic composition of 2.5N HCl leachate of galena-bearing mineralization (sample 19ARU001; MINFILE 092L 061). Ice-flow indicators from Clague et al. (1982), Kerr (1992), Meldrum and Bobrowsky (1994), Bobrowsky et al. (1995), Bobrowsky (1997), and Bobrowsky and Meldrum (1994a, b). Regional geochemical survey (RGS) data after Matysek and Day (1988), Gravel and Matysek (1989), Matysek et al. (1989), Kerr et al. (1992), Bobrowsky and Sibbick (1996), and Jackaman (2011, 2013a, b, 2014). Bedrock legend as in Figure 3.

a much larger footprint. The mechanical, hydrous, and gaseous dispersion of a primary bedrock anomaly or its secondary dispersion halo in a drainage system further generates a geochemically anomalous dispersion stream. Concentrations of elements in dispersion streams are intermediate between local background and the higher values of secondary and primary geochemical anomalies near-ore sources. Extending for many km from these sources, these dispersion streams eventually become diluted and approach background levels. However, high concentrations of Cu (REC leader) in alluvial HMC samples from the Fraser River delta (Kaplenkov, unpublished data) reflect a prominent dispersion stream from large porphyry copper deposits even 100s of km upstream in a catchment basin of 220,000 km²! Secondary dispersion halos and dispersion streams develop in all geospheres, encompassing bedrock, its weathered products and soils, surficial and underground waters, air, and living organisms. According to Vernadsky's law, lithochemical, hydrochemical, atmochemical, and biochemical secondary dispersion halos and streams are closely related due to the universal dispersion and migration of elements and constant interaction between all geospheres (Safronov, 1971; Hawkes, 1976; Rose et al., 1979; Grigoryan et al., 1983; Solovov, 1985; Solovov et al., 1990; Matveev, 2003).

Geochemical anomalies are deviations from the local

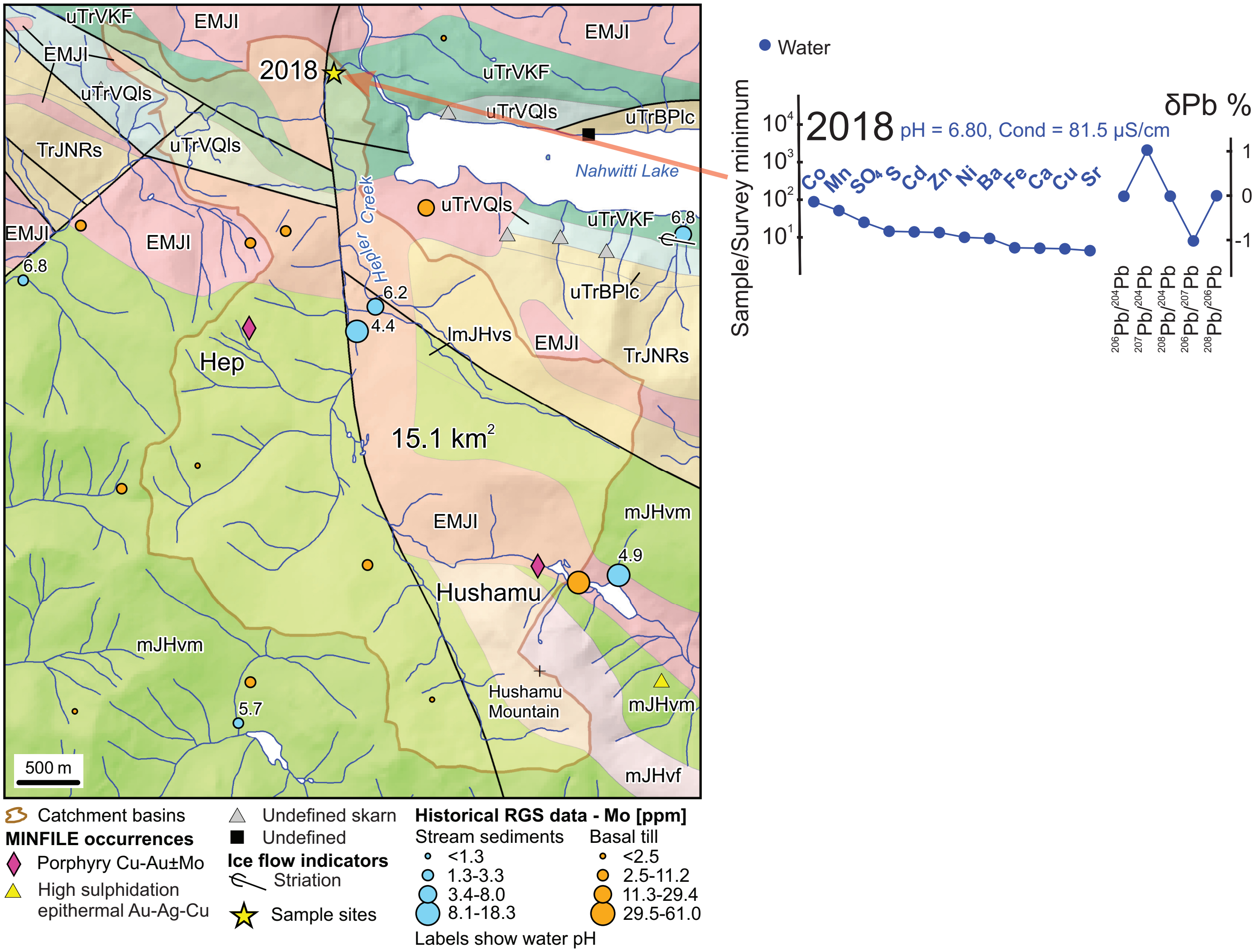

Fig. 14. Hepler Creek basin, northern Vancouver Island, leaders of ranked element contrast relative to survey minimum and δ^{206}Pb/^{204}Pb, δ^{207}Pb/^{204}Pb, δ^{208}Pb/^{204}Pb, δ^{206}Pb/^{207}Pb, and δ^{208}Pb/^{206}Pb pattern (in %) for water sample. δPb (%) values calculated as follows: δ^{20i}Pb/^{20j}Pb (%) = $100\cdot(^{20i}\mathrm{Pb}/^{20j}\mathrm{Pb}_{sample} - {}^{20i}\mathrm{Pb}/^{20j}\mathrm{Pb}_{galena})/\,^{20i}\mathrm{Pb}/^{20j}\mathrm{Pb}_{galena}$, where $^{20i}\mathrm{Pb}/^{20j}\mathrm{Pb}_{galena}$ is the Pb isotopic composition of 2.5N HCl leachate of galena-bearing mineralization (sample 19ARU001; MINFILE 092L 061). Ice-flow indicators after Clague et al. (1982), Kerr (1992), Meldrum and Bobrowsky (1994), Bobrowsky et al. (1995), Bobrowsky (1997), and Bobrowsky and Meldrum (1994a, b). Regional geochemical survey (RGS) data after Matysek and Day (1988), Gravel and Matysek (1989), Matysek et al. (1989), Kerr et al. (1992), Bobrowsky and Sibbick (1996), and Jackaman (2011, 2013a, b, 2014). Bedrock legend as in Figure 3.

geochemical field or background, which is defined as a geological space with variable element concentrations (C_i) above zero in each point in space and time, or

$$C_i = f(x, y, z, T) > 0 \qquad \text{(Eq. 3)}$$

Because elements predominantly occur in a dispersed state rather than forming concentrations, much of the geochemical field has concentrations of ore elements close to their Clarke values (i.e., normal state), which only rarely deviate from this level, i.e., form geochemical anomalies (Solovov et al., 1990). Hence, the local geochemical background (C_b) can be defined as the average (modal) concentration of an element (C_x) in a homogeneous area away from apparent anomalies (Matveev, 2003). Background values of ore elements are lognormally distributed in a normal geochemical field so that 99.86% of background values are less than ($C_x + 3s$), where s is standard deviation. Thus, the threshold of anomalous concentration (C_a) for any single point in a geochemical field is

$$\log C_a = \log C_x + 3s_{\log}, \text{ or } C_a = C\cdot\varepsilon^3, \qquad \text{(Eq. 4)}$$

where C is the geometric average concentration of an element, and ε is standard multiplier

$$\varepsilon = \text{antilog } s_{\log} \qquad \text{(Eq. 5)}$$

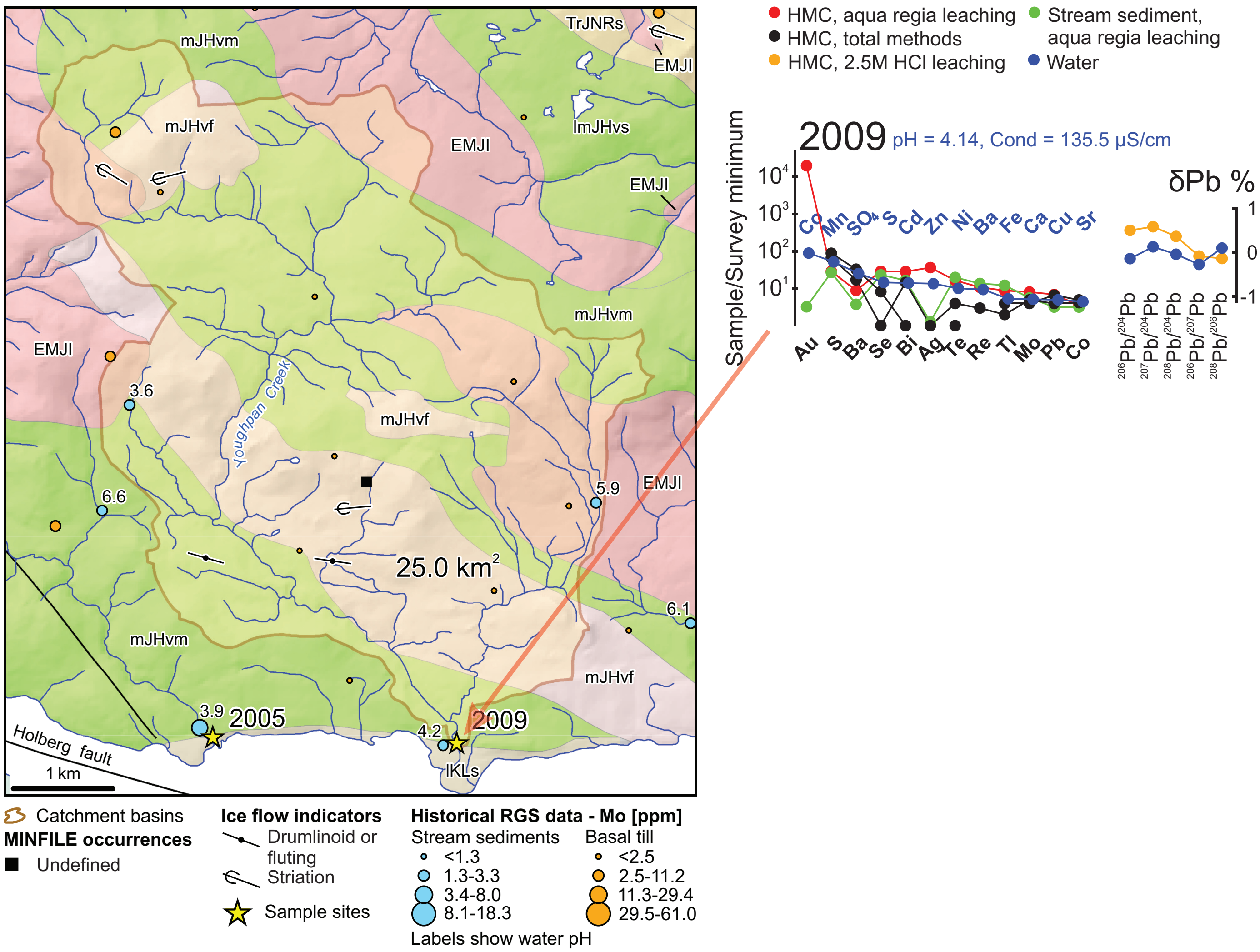

Fig. 15. Youghpan Creek basin, northern Vancouver Island, leaders of ranked element contrast relative to survey minimum and $\delta^{206}Pb/^{204}Pb$, $\delta^{207}Pb/^{204}Pb$, $\delta^{208}Pb/^{204}Pb$, $\delta^{206}Pb/^{207}Pb$, and $\delta^{208}Pb/^{206}Pb$ patterns (in %) for stream sediment, heavy mineral concentrate, and water samples. Water pH, conductivity, and analyte labels shown above patterns. δPb (%) values calculated as follows: $\delta^{20i}Pb/^{20j}Pb$ (%) = $100\cdot(^{20i}Pb/^{20j}Pb_{sample} - {}^{20i}Pb/^{20j}Pb_{galena})/{}^{20i}Pb/^{20j}Pb_{galena}$, where $^{20i}Pb/^{20j}Pb_{galena}$ is the Pb isotopic composition of 2.5N HCl leachate of galena-bearing mineralization (sample 19ARU001; MINFILE 092L 061). Ice-flow indicators from Clague et al. (1982), Kerr (1992), Meldrum and Bobrowsky (1994), Bobrowsky et al. (1995), Bobrowsky (1997), and Bobrowsky and Meldrum (1994a, b). Regional geochemical survey (RGS) data after Matysek and Day (1988), Gravel and Matysek (1989), Matysek et al. (1989), Kerr et al. (1992), Bobrowsky and Sibbick (1996), and Jackaman (2011, 2013a, b, 2014). Bedrock legend as in Figure 3.

For a group of proximal points in a geochemical field having elevated concentrations of an element, the anomaly threshold becomes

$$C_{a(m)} = C\cdot\varepsilon^{3/\sqrt{m}}, \qquad \text{(Eq. 6)}$$

where $m = 2, 3\ldots, 9$ is the number of proximal points with concentrations $C_x \geq C_{a(m)}$, with $m \leq 9$ for any number of points within the anomaly contour. The contrast of a geochemical anomaly (γ) for lognormally distributed elements is the difference between the maximum concentration (C_{max}) above background and its statistical noise (Matveev, 2003):

$$\gamma = (1/\log\varepsilon)\cdot\log(C_{max}/C_b). \qquad \text{(Eq. 7)}$$

6.2. Lithochemical dispersion in a drainage system

Because secondary dispersion halos and related dispersion streams have much larger surficial expression than their primary ore deposit sources, they are readily detectable by regional geochemical surveys. Hydrochemical dispersion of elements is generally subordinate relative to mechanical (i.e., lithochemical) dispersion in drainage systems (Matveev, 2003; Solovov, 1985; Solovov et al., 1990). Hence, ignoring the dispersion of metals dissolved in water, ideal lithochemical dispersion in a drainage system can be applied to interpret stream sediment and HMC geochemical surveys. The total volumetric productivity (P) or quantity of metal above local

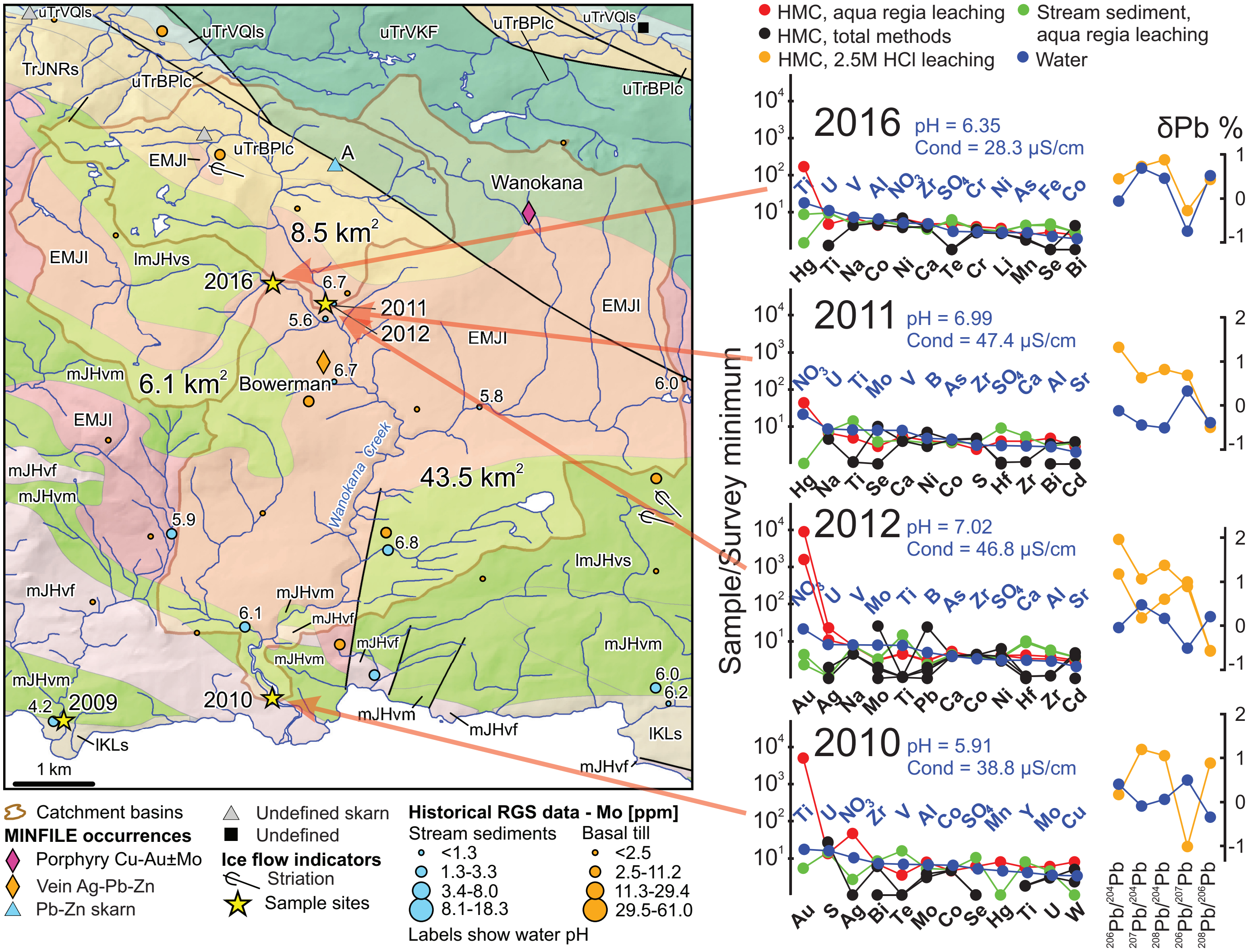

Fig. 16. Wanokana Creek basin, northern Vancouver Island, leaders of ranked element contrast relative to survey minimum and $\delta^{206}Pb/^{204}Pb$, $\delta^{207}Pb/^{204}Pb$, $\delta^{208}Pb/^{204}Pb$, $\delta^{206}Pb/^{207}Pb$, and $\delta^{208}Pb/^{206}Pb$ patterns (in %) for stream sediment, heavy mineral concentrate, and water samples. Water pH, conductivity, and analyte labels shown above patterns. δPb (%) values calculated as follows: $\delta^{20i}Pb/^{20j}Pb$ (%) = $100\cdot(^{20i}Pb/^{20j}Pb_{sample} - {}^{20i}Pb/^{20j}Pb_{galena})/{}^{20i}Pb/^{20j}Pb_{galena}$, where $^{20i}Pb/^{20j}Pb_{galena}$ is the Pb isotopic composition of 2.5N HCl leachate of galena-bearing mineralization (sample 19ARU001; MINFILE 092L 061). Ice-flow indicators from Clague et al. (1982), Kerr (1992), Meldrum and Bobrowsky (1994), Bobrowsky et al. (1995), Bobrowsky (1997), and Bobrowsky and Meldrum (1994a, b). Regional geochemical survey (RGS) data after Matysek and Day (1988), Gravel and Matysek (1989), Matysek et al. (1989), Kerr et al. (1992), Bobrowsky and Sibbick (1996), and Jackaman (2011, 2013a, b, 2014). Bedrock legend as in Figure 3.

background (in tonnes of metal) for n streams draining the secondary dispersion halo of an ore deposit is

$$P = \frac{1}{k'k}\cdot\sum_{i=1}^{n}[S\cdot(C-C_b)]\cdot\frac{1}{40}\cdot H \qquad \text{(Eq. 8)}$$

where S is catchment area of stream basin at the sampling site (in m²), C is the anomalous concentration of element in the sample (in wt.%), C_b is the average local background concentration of an element (in wt.%), $k' <> 1$ is the local proportionality coefficient between the productivity of the dispersion stream and that of the secondary dispersion halo, $k <> 1$ is the residual productivity or proportionality coefficient between the quantity of an element in the secondary dispersion halo and that in the ore body, and H is the calculation depth or probable depth of an ore zone based on geometric and geochemical resemblance of genetically similar deposits. The divider '40' converts m²% into tonnes (after Grigoryan et al., 1983; Solovov, 1985; Solovov et al., 1990; Matveev, 2003).

The values of k' depend on local hydrography and individual properties of elements such as their actual mechanical versus hydrochemical dispersion. The residual productivity (k) also depends on individual properties of elements, morphology of an ore deposit, and local geochemical landscape which was defined by B.B. Polynov in 1956 as an area of uniform migration of elements between the lithosphere, hydrosphere, atmosphere, and biosphere (see Solovov, 1985). Generally, k value changes

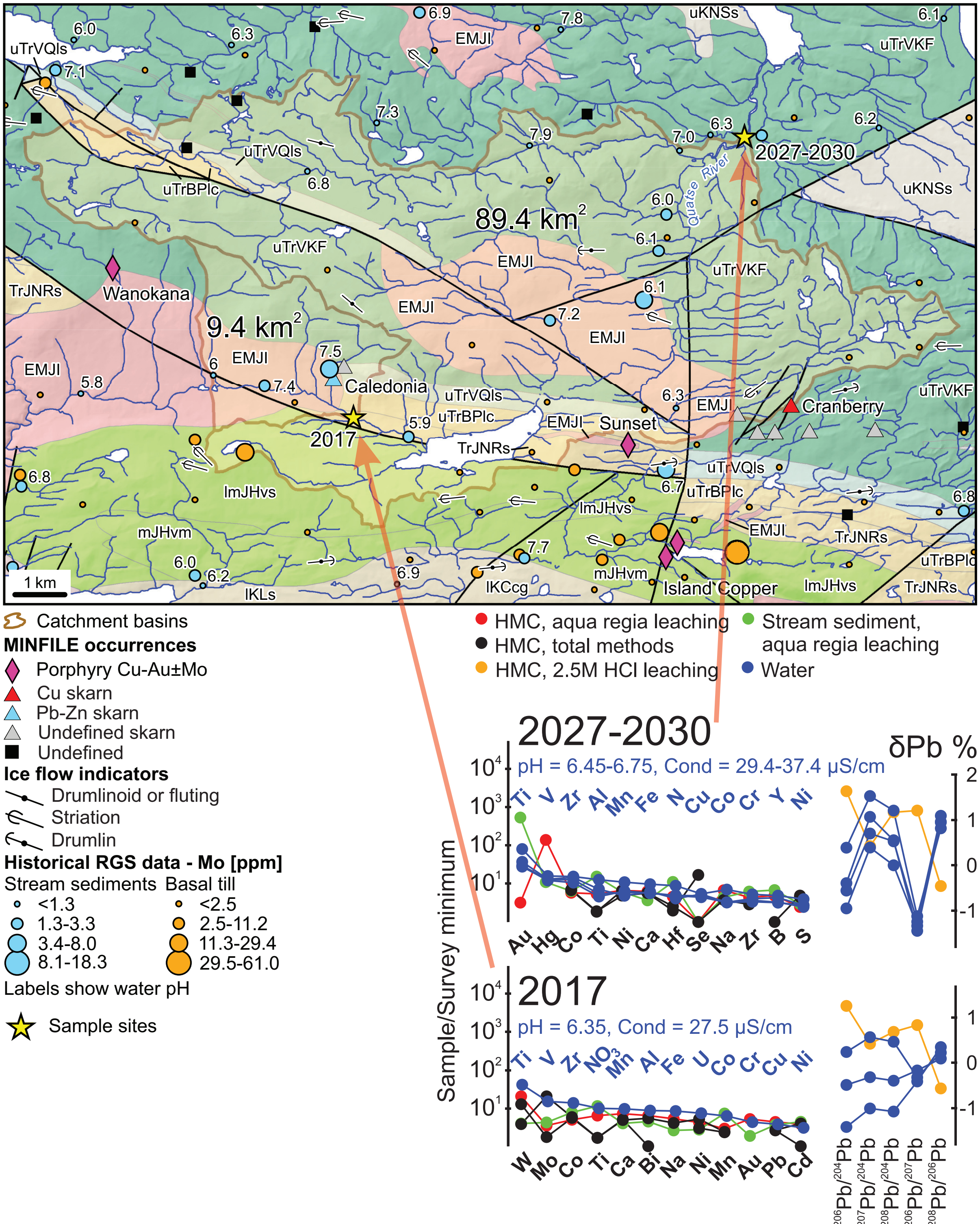

Fig. 17. Leaders of ranked element contrast relative to survey minimum and δ^{206}Pb/^{204}Pb, δ^{207}Pb/^{204}Pb, δ^{208}Pb/^{204}Pb, δ^{206}Pb/^{207}Pb, and δ^{208}Pb/^{206}Pb patterns (in %) for stream sediment, heavy mineral concentrate, and water samples from Quatse River basin, northern Vancouver Island. Water pH, conductivity, and analyte labels shown above patterns. δPb (%) values calculated as follows: $\delta^{20i}\mathrm{Pb}/^{20j}\mathrm{Pb}\ (\%) = 100\cdot(^{20i}\mathrm{Pb}/^{20j}\mathrm{Pb}_{sample} - {}^{20i}\mathrm{Pb}/^{20j}\mathrm{Pb}_{galena})/^{20i}\mathrm{Pb}/^{20j}\mathrm{Pb}_{galena}$, where $^{20i}\mathrm{Pb}/^{20j}\mathrm{Pb}_{galena}$ is the Pb isotopic composition of 2.5N HCl leachate of galena-bearing mineralization (sample 19ARU001; MINFILE 092L 061). Ice flow indicators from Clague et al. (1982), Kerr (1992), Meldrum and Bobrowsky (1994), Bobrowsky et al. (1995), Bobrowsky (1997), and Bobrowsky and Meldrum (1994a, b). Regional geochemical survey (RGS) data after Matysek and Day (1988), Gravel and Matysek (1989), Matysek et al. (1989), Kerr et al. (1992), Bobrowsky and Sibbick (1996), and Jackaman (2011, 2013a, b, 2014). Bedrock legend as in Figure 3.

Fig. 18. Indicator minerals in panned sluice heavy mineral concentrates of alluvium from northern Vancouver Island. **a)** Euhedral magnetite, $Fe^{2+}Fe^{3+}_2O_4$, and spessartine, $(Mn^{2+}, Fe^{2+})_3(Al, Fe^{3+})_2(SiO_4)_3$, at the mouth of Hushamu Creek (sample 2005; 1-2 mm-size fraction). **b)** Almandine fragment, $(Fe^{2+}, Mn^{2+})_3(Al, Fe^{3+})_2(SiO_4)_3$, and euhedral spessartine near the mouth of Quatse River (sample 2027; 0.5-1.0 mm-size fraction).

with depth due to hypergene enrichment ($k > 1$) or leaching ($k < 1$) of ore elements. Based on numerous geochemical surveys in different geochemical landscapes, k values for most ore elements are close to unity for actively eroding mountainous areas (Matveev, 2003). For a detailed discussion of the theory and practice of geochemical exploration and quantitative interpretation of real dispersion streams using differential equations, the reader is referred to Grigoryan et al. (1983), Solovov (1985), Solovov et al. (1990), and Matveev (2003).

6.3. Prognostic geochemical resources based on dispersion streams

The objective of regional geochemical surveys investigating dispersion streams is to find large deposits with economic mineralization close to present erosional levels. Productivity defined above is a parametric and thus objective measure of a geochemical anomaly, which is the basis for identifying prospective areas. Panning of alluvium is the oldest prospecting method for placer gold, diamonds, tin, tungsten, and other commodities. Kukanov et al. (1983), Petrenko et al. (1986), and Kaplenkov (2003, 2006, 2008) collected and analyzed panned HMC samples for many elements in eastern Chukotka and identified several prospective areas; their predictions ultimately led to the discovery of large base and precious metal deposits. We adopted a simplified approach for evaluating drainage lithochemical results in terms of volumetric productivity per element, which is calculated for each stream basin based on the data for near-mouth stream sediment and HMC samples. Assuming $k' = k = 1$ and $H = 1$ m, equation 8 above for productivity of lithochemical anomaly in a drainage system, P (in tonnes per 1 m depth), reduces to

$$P = S\cdot(C - C_b)/40, \qquad \text{(Eq. 9)}$$

where S is the catchment area of stream basin at the sampling site (in m^2), C is the above-background concentration of an element in the stream sediment, moss-mat sediment, or HMC sample (in wt.%), and C_b is the average background concentration of an element (in wt.%). Because our dataset is limited to a few samples, estimating background values as discussed above is not possible. Hence, background per element was calculated as the average of survey values within the range of 10 times the minimum value (e.g., 1.5-15). Although the background values may differ from those based on strict geochemical field theory, this simple approach is similar to the classical ranking for panning of gold (‘nil-trace-counts-weight’) proven by centuries of prospecting. Lithochemical dispersion in high-order streams also significantly differs from ideal dispersion stream, which adequately characterizes only first-order basins. In addition, elements concentrated in heavy minerals (e.g., Au, Pt, Sn, W, Zr, Nb, Ta, REE) will have $k' > 1$, whereas elements migrating in dispersion stream in solution or a non-mineral form, adsorbed on clays and other colloidal particles (e.g., Cu, Mo, Zn, Pb) will have $k' < 1$ in HMC samples. Hence, prognostic geochemical figures based on ideal dispersion stream are intended only for evaluating the survey results and identifying the most prospective basins. Prognostic geochemical resources (P) could be refined by determining local k' and k values for elements of interest, using realistic depth (H) based on the expected geometric and geochemical resemblance to a known deposit, and solving the equation of real dispersion stream (Solovov, 1985; Solovov et al., 1990; Matveev, 2003). If the difference between predicted geochemical resources and observed resources in a partially eroded ore deposit is less than three, they are considered satisfactory (Grigoryan et al., 1983). Well-known geochemical zoning of ore systems (Emmons, 1924) also allows estimating the level of erosion for a predicted ore deposit using multiplicative ratios of highly mobile (e.g., Ag-Hg-Sb) to less mobile (e.g., W-Sn-Bi) ore and indicator elements (Grigoryan et al., 1983; Solovov, 1985; Solovov et al., 1990; Matveev, 2003).

Table 1 lists calculated background values and volumetric productivities (in tonnes per 1 m depth) of the main ore and pathfinder elements for each stream basin based on the stream and moss-mat sediment (<0.18 mm fraction) and HMC (<1 mm fraction) geochemistry. HMC results for 'partial' values (aqua regia digestion–ICP-ES/MS) and 'total' values (fusion–ICP-ES/MS, XRF, and INAA) are given separately. Values for stream and moss-mat sediment samples (bulk sediment) are also 'partial'. Discrepancies between the sample media and different analytical methods reflect different roles of lithochemical (mechanical) and hydrochemical forms of dispersion for individual elements, different mineralogy, and geochemical landscapes even in the northern Vancouver Island study area. Bulk stream and moss-mat sediment samples (<0.18 mm-size, sieved fraction) confidently detect Cu, Mo, Re, Te, Se, Bi, and In, but generally have poor contrast for heavy metals such as Au, Ag, W, and REE, missing even placer Au at Loss Creek. HMC samples (<1 mm-size, 'grey' fraction) greatly enhance the contrast for Mo, Zn, Pb, Au, Ag, W, Sn, Li, Cs, Ge, Be, Y, Sc and REE, with 'total' values yielding greater anomaly contrast for elements hosted in refractory minerals.

Manganese-rich garnet is abundant in the HMC samples at Loss Creek (Fig. 7a). The garnet is the main host of Y, Sc, and heavy rare earth elements (HREE), with their productivities ($n \cdot 10^3$-$n \cdot 10^4$ tonnes/m) indicating a large deposit of these metals, according to Krasnikov's classification of mineral deposits by size (Matveev, 2003). Given that placer garnet is readily concentrated from alluvium, it warrants a metallurgical feasibility study as a potential ore for economic recovery of Y, Sc, and HREE. In addition to Sc, Y, and HREE, Loss Creek basin shows significant prognostic resources ranking from middle- to large-size deposits for Au (confirms placer gold occurrence), Mn (3.1 million tonnes/m), Zn, Li, Cr, Ni, W, Ga, Se, Co, Ge, B, and Cd (Table 1).

As noted above, stream-sediment and HMC samples confirm epithermal Au-Ag-Cu and blind porphyry Cu-Mo-Au deposits at Hushamu. HMC samples greatly enhance the anomaly contrast for Au, Ag, Ba, Sn, Tl, Pb, Zn, and V even many km downstream from the deposit at the Hushamu Creek mouth, where stream-sediment samples did not detect anomalous Au and Ag (Table 1). Productivities of Cu, Mo, Re, Te, Se, Bi, and In based on stream-sediment samples are generally consistent with those based on HMC samples, reflecting predominantly mechanical dispersion of these elements in the drainage system. Volumetric productivities per 1 m depth based on stream-sediment and HMC samples generally confirm the 43-101 resources (Indicated + Inferred) of 131 tonnes Au, 179 tonnes Re, 37619 tonnes Mo, and 1.09 million tonnes Cu for the Hushamu deposit (Tahija et al., 2017). As discussed above, the predicted resources may overestimate Au and other heavy metals concentrated in HMC samples and underestimate metals readily soluble in acidic waters such as Cu and Zn. The subdued Cu geochemical anomaly at Hushamu reflects blind hypogene porphyry Cu-Mo-Au mineralization covered by a thick silica-clay leached cap (Panteleyev and Koyanagi, 1993, 1994; Panteleyev et al., 1995; Tahija et al., 2017). In contrast, the HMC samples confidently detect the epithermal Au-Ag-Cu mineralization and the above-ore primary halo (Ba-Zn-Pb-Sb-Se-Tl) of the deeper porphyry copper system, which generate prominent secondary dispersion in the Hushamu basin. Hence, HMC geochemistry detects even blind porphyry mineralization despite an extensive leached cap and hydrochemical dispersion of metals in highly acidic waters.

Our results also predict significant resources of Ag, Au, Ba, V, Re, Mo, Zn, Pb, Te, Se, Tl, Bi, Sn, In, Zr, and Ga for the Youghpan Creek basin (Table 1). These findings are important because mineral occurrences of these metals are not known in that basin. Prognostic resources for the Wanokana basin confirm known occurrences of porphyry Cu (MINFILE 092L 272), Ag-Pb-Zn±Au vein (MINFILE 092L 131), and Zn-Pb-Cu-Ag±Au skarn (MINFILE 092L 393 and 272) styles of mineralization in that basin. In addition, near-mouth samples predict significant resources of LREE, HREE, Y, Sn, W, Li, and Cs (Table 1). The elevated REE (especially LREE) and Y are accompanied by anomalous (tonnes/m) Mn (38653), Ba (22396), V (20505), Zr (17013), P (14440), Sr (3572), Hf (1227), Nb (497), Ga (301), Ta (42), Th (65), and U (76). An anomalous LREE-Ba-V-Zr-Hf-P-Sr-Nb-Ta-Th-U association suggests carbonatite or alkaline rock-hosted rare-metal mineralization yet to be discovered. This is hardly surprising given the Nb, REE, Y, Zr, Th, U, and fluorite mineralization related to Jurassic to Paleogene peralkaline and carbonatite magmatism in Alaska (e.g., Warner, 1989; Gunter et al., 1993; Thompson, 1997). Nixon et al. (2020) report Late Neogene magmatism (Klaskish Plutonic Suite) associated with porphyry Cu-Mo±Au mineralization immediately south of the Holberg fault on northern Vancouver Island. This young magmatic suite follows along the northeast-trending Brooks Peninsula fault zone, which coincides with the southern limit of Neogene volcanism in the region and marks an extensional regime in the Queen Charlotte basin (Lewis et al., 1997). Hence, the LREE-Ba-V-Zr-Hf-P-Sr-Nb-Ta-Th-U anomaly (Table 1) indicates peralkaline or carbonatite magmatism controlled by major high-angle structures such as Holberg fault and related to the Neogene or older event(s), overprinting the Bonanza magmatic arc on northern Vancouver Island.

The HMC geochemistry from Caledonia Creek indicates significant upstream LREE, Mo, W, Mn, Zr, Ba, Sr, and Hf anomalies. Elevated Pb and Zn also confirm Zn-Pb-Cu skarn mineralization such as the Caledonia developed prospect (MINFILE 092L 061). The geochemistry of a stream-sediment sample near the mouth of Quatse River returned anomalous Au, Ag, Zn, Y, Sc, REE (mainly HREE), Zr, Sr, P, V, Hf, B, and Ga, which indicate rare-metal mineralization in this watershed. However, analysis of the HMC sample at this site does not indicate above-background concentrations of Au, Ag, Zn, and Sc, but shows anomalous Se and W. Both sample media indicate anomalous Cu, Y and REE, reflecting Island Copper

Table 1. Geochemical background and productivity of elements (in tonnes per 1 m depth) in stream basins.

Element	Ag	Au	Cu	Mo	Zn	Pb	Co	Ni	Re	Te	Hg	Sb	Se	Tl	Bi	W	Sn	In	Li	Cs	Ge	Be	Y	Sc	∑HREE	∑LREE
Background (ppm)																										
Bulk sediment	0.093	0.0025	43	1.3	50	6.7	14	18	0.0024	0.064	0.074	0.19	0.59	0.058	0.080	0.16	0.60	0.040	7.1	0.65	0.12	0.26	7.1	6.2	5.2	30
HMC 'partial'	0.036	0.0016	38	0.85	64	5.0	11	20	0.0023	0.043	0.021	0.22	0.28	0.057	0.081	0.24	0.77	0.057	7.4	0.43	0.20	0.24	10	7.4	7.5	30
HMC 'total'	0.18	0.0016	41	0.85	109	3.7	20	38	0.025	0.37	NA	0.68	3.2	0.25	0.11	0.96	2.1	0.093	8.4	0.73	3.3	1.2	20	47	18	82
Productivity (tonnes/m)																										
Loss Creek, near mouth (sample sites 1002 and 1007); catchment area = 68.0 km^2																										
Bulk sediment								2740						9	2	41			1529	81						
HMC 'partial'	85	1025				974		951								1336			500		34		8549	678	4369	
HMC 'total'	78	833	181	8	28724	621	871	2182	1		NA		1532			2568	99		14377		753	57	86132	5553	41516	2873
Hushamu Creek																										
Headwater (sample site 2007); catchment area = 3.82 km^2																										
Bulk sediment	0.2	0.7	430	61		119			0.1	4	0.1	0.1	69	0.3	9		6	1					40		40	102
HMC 'partial'		0.1	144	65		87			0.1	4		0.2	48	0.6	10		9	1								
HMC 'total'	0.2	NA	147	65		213				2	NA	1	120	7	10		75	2	6				14		6	15
Middle course (sample site 2006); catchment area = 12.2 km^2																										
Bulk sediment	4	0.2	131	109	19	129			0.4	28	0.1	6	333	1	17		9	1								
HMC 'partial'	3	2	224	149	270	182	52		0.3	34	9	10	278	1	47		7	1								
HMC 'total'	0.8	NA	130	159	733	214			0.3	25	NA	16	40	2	49		35	1	17	27			5		7	
Near mouth (sample site 2005); catchment area = 20.5 km^2																										
Bulk sediment	3	0.1	428	129		99			0.2	24	0.2	3	316	0.1	17		8	0.8					1	51	12	27
HMC 'partial'	24	315	325	161	1146	180			0.3	18	1	4	190	0.1	18		4	0.2				6			2	60
HMC 'total'		NA	304	151	677	247			0.2	12	NA	6	569	8	16		23	0.3		6			31		35	2
Tributary (sample site 2008); catchment area = 1.86 km^2																										
Bulk sediment				3						0.4	0.2		9	0.1	0.3				7	1		0.2	0.3		2	23
HMC 'partial'				4	40		8			0.5			3		0.5				25	2		0.8				
HMC 'total'		NA		29	236	5					NA		15	0.7	0.3		0.1		26	4						

Table 1. Continued.

Element	Ag	Au	Cu	Mo	Zn	Pb	Co	Ni	Re	Te	Hg	Sb	Se	Tl	Bi	W	Sn	In	Li	Cs	Ge	Be	Y	Sc	∑HREE	∑LREE
Youghpan Creek, near mouth (sample site 2009); catchment area = 25.0 km²																										
Bulk sediment				89		18			0.7	22		4	263	12	16		6	0.6						41	8	91
HMC 'partial'	31	558		142	6716	211	25		0.5	19	1.9	9	170	8	32		2	2				23				20
HMC 'total'		NA		197	17231	314			0.3	27	NA	20	219	9	30		51	0.4				2			0.6	
Wanokana Creek																										
Headwater (sample sites 2011 and 2012); catchment area = 8.47 km²																										
Bulk sediment			1	5	158			34			0.1		5								2	2	32	5	13	79
HMC 'partial'	3	34		7	36		25	46			6					0.6				1					2	36
HMC 'total'		NA		90	60	48					NA		33							3						0.5
Near mouth (sample site 2010); catchment area = 43.5 km²																										
Bulk sediment	4	0.2		134			202		0.2	28			164		10					10		16	109		55	455
HMC 'partial'	69	239		232			403		0.1	3	13		34		6	61	68			13		7	380		310	2825
HMC 'total'		NA		234	1707	13					NA	24			14	118	155	0.7	171	27		4	602		167	2969
Tributary (sample site 2016); catchment area = 6.10 km²																										
Bulk sediment				5			93	89		1	5		6						11	2		0.7				
HMC 'partial'				5			60	247		1	50		0.3						48	3		0.9			0.1	80
HMC 'total'		NA		7	125	10	2	175			NA	6			1			0.1	39	2						14
Caledonia Creek (sample site 2017); catchment area = 9.35 km²																										
Bulk sediment	0.34			17	323	32	254				0.2		0.3		0.2	6	2			0.3		1				
HMC 'partial'				11	177	5	122	51	0.5						1	44	0.7	1				1			0.8	94
HMC 'total'		NA		242	192	32	68				NA	8			3	85		0.2								390
Quatse River, near mouth (sample site 2027); catchment area = 89.4 km²																										
Bulk sediment	10	104	5838		2150		1532	3312			166	60											293	659	146	97
HMC 'partial'			6428				1834	3418			595	13				81								125	43	71
HMC 'total'		NA	5013	11			1803	3241			NA	94	2438			87		2					199		76	60

Table 1. Continued.

Notes: Bulk sediment is <0.18 mm-size, sieved fraction of bulk stream and moss mat-sediment; HMC is heavy mineral concentrate (<1 mm-size, sieved fraction) recovered from <2 mm-size fraction of bulk alluvium (11-16 kg). 'Partial' values based on aqua regia digestion - inductively coupled plasma emission spectrometry (ICP-ES) combined with inductively coupled plasma mass spectrometry (ICP-MS); 'total' values based on lithium borate and sodium peroxide fusion – ICP-ES/MS combined with X-ray fluorescence, and thermal instrumental neutron activation analysis (INAA). ∑HREE = Gd + Tb + Dy + Ho + Er + Tm + Yb + Lu; ∑LREE = La + Ce + Pr + Nd + Sm + Eu. Background is the average of concentration values within the range of 10 times the minimum concentration value per element.

The above-background productivity of element dispersion in a stream system, P (in tonnes per 1 m depth), is calculated as $P = S \cdot (C - C_b)/40$, where S is catchment area at sampling site (in m^2), C is concentration of element above local background value in sample (in wt%), C_b is the local background concentration of element as defined above (in wt%). Divider 40 converts m^2% into tonnes (after Grigoryan et al., 1983; Solovov, 1985; Solovov et al., 1990; Matveev, 2003). See discussion in text for details.

'NA' = not analyzed; blank values indicate background level concentration of element.

In addition, HMC samples at Loss Creek yield (tonnes/m): 3066533 Mn, 38542 Cr, 1640 Ga, 661 B, 613 Cd, 594 Nb, 235 Hf, 207 Th, and 76 Ta, plus 3511 Ba based on bulk sediment analyses. HMC samples at Hushamu Creek yield up to (tonnes/m): 22350 Ba, 4964 V, 4584 Zr, 4050 P, 3063 Mn, 1055 Sr, 408 Hf, 228 B, 35 Nb, 24 Ga, and 13 U; bulk sediments have mostly blank or much lower values for these elements. HMC sample at Youghpan Creek yields (tonnes/m): 329965 Ba, 25339 Mn, 29366 V, 8299 P, 5928 Sr, 5528 Zr, 651 Hf, 117 Ga, and 10 U; bulk sediment sample has much lower values for Ba, Sr, Zr, Hf, and P, and blank for others. HMC samples at Wanokana Creek yield up to (tonnes/m): 38653 Mn, 22396 Ba, 20505 V, 19394 P, 17013 Zr, 3572 Sr, 1227 Hf, 497 Nb, 301 Ga, 76 U, 65 Th, 42 Ta, and 1.8 Cd; bulk sediment samples indicate up to (tonnes/m): 125 Th, 3.4 Cd, and 8.6 B, but much lower or blank values for others. HMC sample at Caledonia Creek yields (tonnes/m): 13334 Mn, 4545 Zr, 1857 Ba, 1364 Sr, 274 Hf, 30 Ga, 22 Nb, 10 B, and 2 Cd; bulk sediment sample yields (tonnes/m): 17195 Mn, 85 V, 34 Ga, 5 Cd, but much lower or blank values for others. HMC sample at Quatse River yields (tonnes/m): 68716 Zr, 19745 Sr, 18501 P, 13488 V, 2868 Hf, 546 B, 238 Ga, 12 Cd; bulk sediment sample yields (tonnes/m): 42828 Mn, 3143 Cr, 1132 B, but much lower or blank values for others.

suite porphyry Cu-Mo occurrences (Perelló et al., 1995) and perhaps garnet as a source of elevated HREE-Y-Sc in the catchment of Quatse River.

6.4. Hydrochemical dispersion

Stream waters draining altered volcanic rocks of the Bonanza Group hosting epithermal Au-Ag-Cu mineralization on northern Vancouver Island exemplify natural acid drainage with pH as low as 2.0, conductivity up to 2400 µS/cm, TDS up to 1190 mg/L, and SO_4^{2-} up to 1300 mg/L (Koyanagi and Panteleyev, 1993, 1994; Sibbick and Laurus, 1995a; Panteleyev et al., 1996b). Waters draining massive sulphide deposits elsewhere have pH values as low as 1.0 and SO_4^{2-} concentration up to 123 g/L (Matveev, 2003). Sulphide minerals are unstable in the hypergene environment and readily oxidize. Free sulphuric acid is generated by the oxidation of pyrite, which is the most common sulphide mineral in the altered rocks (Panteleyev and Koyanagi, 1993, 1994; Panteleyev et al., 1995; Tahija et al., 2017)

$$2FeS_2 + 7O_2 + 2H_2O \rightarrow 2FeSO_4 + 2H_2SO_4 \quad \text{(Eq. 10)}$$

In the presence of free oxygen, ferrous iron sulphate is unstable and oxidizes to ferric iron sulphate according to

$$4FeSO_4 + 2H_2SO_4 + O_2 \rightarrow 2Fe_2(SO_4)_3 + 2H_2O \quad \text{(Eq. 11)}$$

Hydrolysis of $Fe_2(SO_4)_3$ in weakly acidic waters liberates sulphuric acid

$$Fe_2(SO_4)_3 + 6H_2O \rightarrow 2Fe(OH)_3 + 3H_2SO_4 \quad \text{(Eq. 12)}$$

Ferric iron hydroxide precipitates from solution and forms stable limonite $Fe_2O_3 \cdot nH_2O$ (Fig. 19). Both ferric iron sulphate $Fe_2(SO_4)_3$ and sulphuric acid oxidize and facilitate dissolution of other sulphides, the oxidation of which in turn generates sulphuric acid (Matveev, 2003). Cation-deficient, altered volcanic rocks cannot neutralize acidic waters, which results in natural H_2SO_4 drainage at Hushamu. Sulphates of ore metals formed by oxidation of hypogene sulphides are soluble in acidic waters, which favour hydrochemical dispersion of most metals, including Fe, Al, Cu, Zn, Cd, Ni, Fe, Mn, and Pb. However, most metals precipitate from solution as hydroxides at a pH of about 5.5 (Grigoryan et al., 1983; Solovov, 1990).

The solubility of iron in the presence of Cu^{2+} (0.005-0.011 mg/L) is a function of dissolved oxygen activity at different pH, such as for waters of the Hushamu and Youghpan creeks (Fig. 20). Precipitation of Fe^{2+} and Cu^{2+} cations begins in weakly acidic waters forming $CuFeO_2$, which is predominant in neutral water. A plot of the copper-iron-sulphur system versus pH and dissolved oxygen activity for waters from Hushamu and Youghpan creeks (Fig. 21) provides further insight into hypergene processes and mineralogy of the secondary dispersal halo at Hushamu. Assuming oxygen activity constrained by SO_4^{2+}/HS^- equilibrium, these waters are in equilibrium with

Fig. 19. Brown limonite ($Fe_2O_3 \cdot nH_2O$) precipitate in highly acidic Hushamu Creek, which drains an epithermal Au-Ag-Cu and a blind porphyry Cu-Mo-Au system.

covellite, chalcocite, bornite, elemental sulphur, Fe^{2+} and SO_4^{2-} ions at pH values between 3.8 and 5.9. The observed mineralogy of the clay-quartz leached cap and oxidation zone of hypogene ore at Hushamu (Panteleyev, 1992; Panteleyev and Koyanagi, 1993, 1994; Panteleyev et al., 1995; Tahija et al., 2017) confirms the equilibrium assemblage modelled here based on the stream water chemistry.

In contrast, weakly acidic to neutral waters of Loss, Wanokana, and Caledonia creeks and Quatse River are less favourable for hydrochemical dispersion of most elements. Metals form soluble bicarbonates and complexes with organic acids in such waters. Most metals precipitate as hydroxides, carbonate minerals and other salts from neutral and alkalic waters, except for anion-forming Si, Al, Ge, As, V, U, and Mo, and carbonate complexes of Cu, Sc, Y, and Zr, which are soluble in these waters (Grigoryan et al., 1983; Solovov, 1990).

6.5. Lead isotopes as tracers of dispersion in streams

Unlike concentrations of elements, Pb isotopic ratios fingerprint distinct sources making them more efficient tracers of ore fluids and dispersion processes. The application of Pb isotopes in surficial sediments is a well-established method in mineral exploration (e.g., Gulson, 1986; Bell and Franklin, 1993; Bell and Murton, 1995; Simonetti et al., 1996; Hussein et al., 2003; Rukhlov and Ferbey, 2015). Rukhlov and Ferbey (2015) first tested a simplified method of using Pb isotopic ratios measured by ICP-MS in the 2.5N HCl leachate of the <0.063 mm fraction of till samples for mineral exploration of Jurassic VMS deposits in the Canadian Cordillera. The method is based on the Pb isotopic contrast generated between a Pb-rich, U-Th-poor ore (e.g., galena having Th/Pb and U/Pb ~0) and Pb-poor, U-Th-rich host rocks (e.g., intermediate-felsic rocks having high Th/Pb and U/Pb) due to the in situ decay of U and Th isotopes, thereby increasing the $^{206}Pb/^{204}Pb$, $^{207}Pb/^{204}Pb$ and $^{208}Pb/^{204}Pb$ with time in the country rocks but not

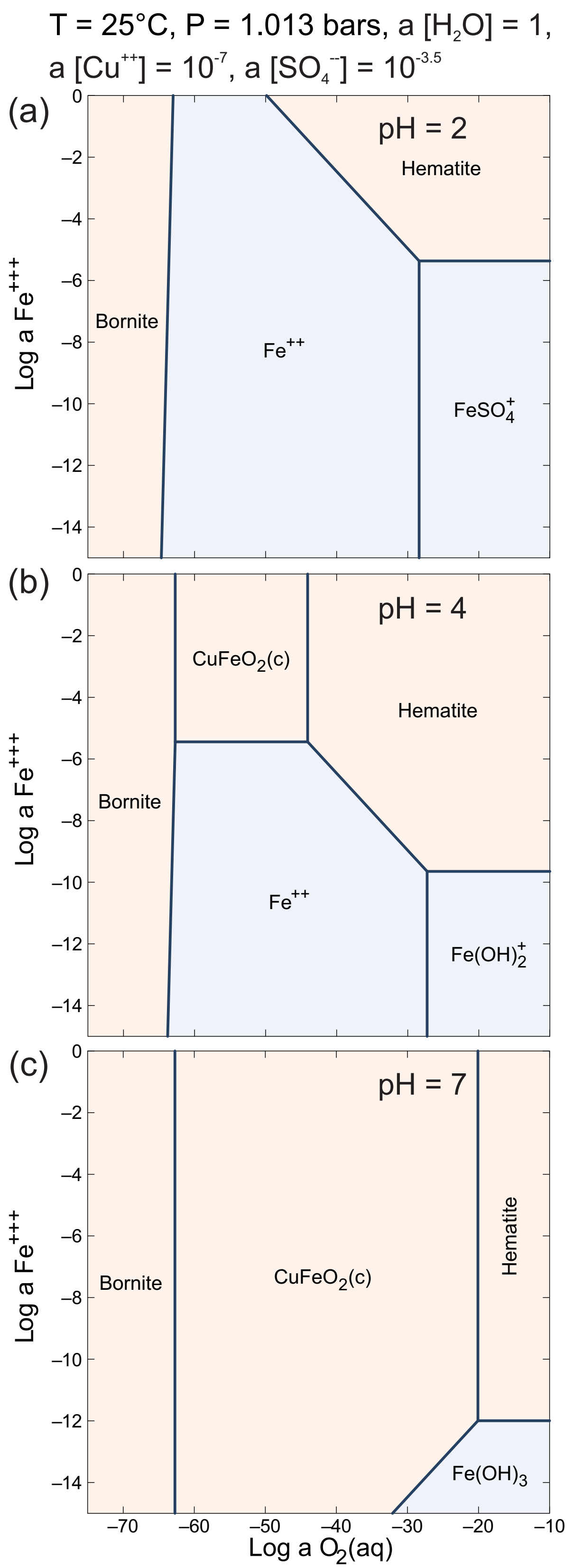

Fig. 20. Solubility of Fe^{3+} and mineral stability fields versus Log a O_2(aq) for water from Hushamu and Youghpan creeks at T = 25°C, P = 1.013 bars, a $[Cu^{2+}] = 10^{-7}$, a $[H_2O] = 1$, a $[SO_4^{2-}] = 10^{-3.5}$, and fixed pH: (a) pH = 2; (b) pH = 4; and (c) pH = 7.

in the ore. The isotopic contrast could also be a primary feature of mineralization. The weak acid extraction targeting labile Pb, as opposed to the total digestion of sample, enhances the isotopic contrast. Mixing between the isotopically distinct end members such as the unradiogenic Pb in ore and the radiogenic Pb in host rock occurs during lithochemical (mechanical), hydrochemical, and biochemical dispersion and is the basis for using Pb isotopes in mineral exploration.

Lead isotopic compositions of stream waters and 2.5N HCl leachates of stream and moss-mat sediment (<0.18 mm fraction), HMC (<1 mm fraction), and mineralized rock samples from Vancouver Island along with tills and a VMS ore from Rukhlov and Ferbey (2015), and Vancouver Island galenas from Godwin et al. (1988) form a linear array on $^{206}Pb/^{207}Pb$ vs. $^{208}Pb/^{206}Pb$ diagram (Fig. 22). The array also extends a linear trend defined by the analyses of honey from Vancouver area and environs, which have higher $^{208}Pb/^{206}Pb$ and lower $^{206}Pb/^{207}Pb$ values (Smith et al., 2019). Analyzed for the first time, stream waters show a wide range of Pb isotopic compositions and overlap that of stream sediments, HMCs, and the ores. The hyperbolic trends defined by tills, VMS ore, and country rock on the Pb concentration versus Pb isotopic ratio diagrams reflect mechanical mixing between the isotopically distinct VMS ore and country rocks during glacial dispersion (Figs. 22c and d; Rukhlov and Ferbey, 2015). Most of the data from this study also follow the same mixing trend. Stream waters and honey have much lower Pb contents and plot outside of the mixing trend (note the logarithmic scale for x-axis in Figs. 22c and d).

We recast Pb isotopic ratios as δ values (in %) relative to a local ore isotopic composition, which in the case of a Pb-rich ore will have the minimum $^{206}Pb/^{204}Pb$, $^{207}Pb/^{204}Pb$, and $^{208}Pb/^{204}Pb$ ratios:

(Eq. 13)

$$\delta^{20i}Pb/^{20j}Pb\ (\%) = 10^2 \cdot \frac{(^{20i}Pb/^{20j}Pb_{sample} - ^{20i}Pb/^{20j}Pb_{ore})}{^{20i}Pb/^{20j}Pb_{ore}}$$

where $^{20i}Pb/^{20j}Pb_{sample}$ is Pb isotopic ratio in sample, and $^{20i}Pb/^{20j}Pb_{ore}$ is the Pb isotopic ratio of galena-bearing ore at Caledonia developed prospect (MINFILE 092L 061). Hence, the Pb isotopic composition of a sample that is identical to the reference ore translates into a δPb (%) value of zero. Samples having less radiogenic Pb isotopic compositions will have negative δPb (%) values, and those with more radiogenic Pb ratios such as country rocks will have positive δPb (%) values. A simple linear plot of δPb (%) values calculated for $^{206}Pb/^{204}Pb$, $^{207}Pb/^{204}Pb$, $^{208}Pb/^{204}Pb$, $^{206}Pb/^{207}Pb$, and $^{208}Pb/^{206}Pb$ ratios thus defines the Pb isotopic signature of a sample, which fingerprints mixing between the isotopically distinct end members such as Pb-rich ore and country rocks. As discussed above, both lithochemical and hydrochemical dispersion streams from porphyry Cu-Mo±Au and epithermal Au-Ag-Cu deposits in Hushamu and Youghpan creek basins have distinct δPb (%) isotopic signatures close to zero, which approximates the Pb isotopic composition of Caledonia Zn-Pb-Cu-Ag skarn (MINFILE 092L 061). Our results demonstrate the efficiency

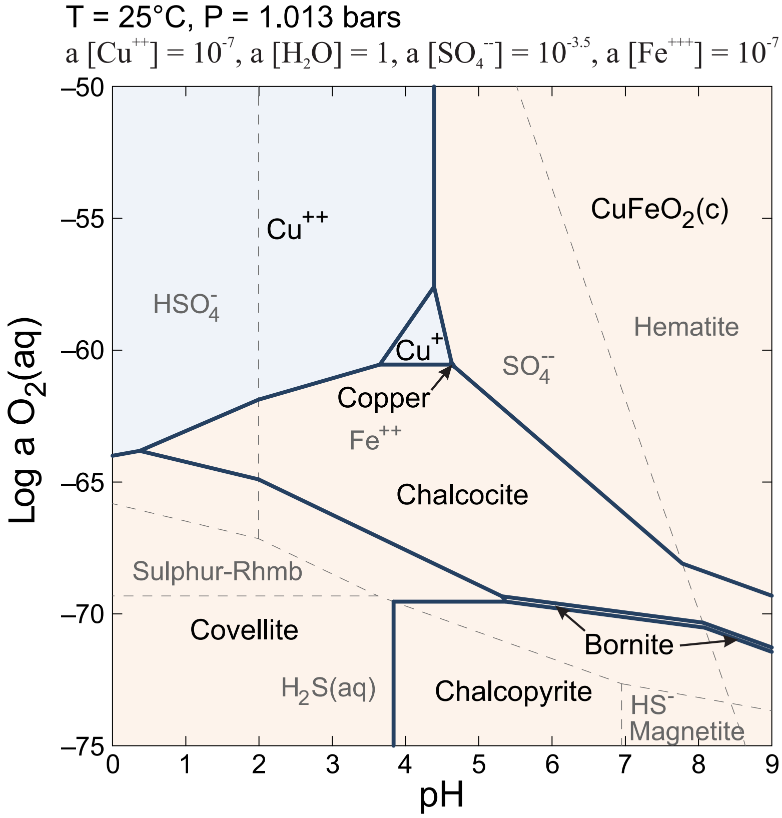

Fig. 21. Copper-iron-sulphur system versus pH and Log a O_2(aq) for water from Hushamu and Youghpan creeks at T = 25°C, P = 1.013 bars, a [Cu^{2+}] = 10^{-7}, a [H_2O] = 1, a [SO_4^{2-}] = $10^{-3.5}$, and a [Fe^{3+}] = 10^{-7}. Broken lines are boundaries for iron and sulphur species: Fe^{2+}, magnetite ($Fe^{2+}Fe_2^{3+}O_4$), hematite (Fe_2O_3), HSO_4^-, SO_4^{2-}, elemental sulphur (sulphur-rhmb), H_2S(aq), and HS^-.

of Pb isotopic tracing in mineral exploration and environmental applications (e.g., Smith et al., 2019). Affordable HR-ICP-MS analysis of stream waters and 2.5N HCl leachates of sediments and rocks provides enough precision to resolve the natural Pb isotopic variability.

7. Conclusions

We have tested stream water, stream and moss-captured sediment, and alluvial HMC samples collected from several drainages on Vancouver Island and analyzed by different methods for a wide range of elements and Pb isotopic compositions. Panned sluice HMC samples (<1 mm-size, 'grey' fraction) of bulk alluvium greatly enhanced the geochemical anomaly contrast, even at mouth of high-order streams, many km downstream from known mineralization. In contrast, less representative, low-volume, bulk stream and moss-captured sediment samples (<0.18 mm fraction) commonly failed to detect even proximal mineralization. Water chemistry provides important information on hydrochemical dispersion of elements in the streams and constrains equilibrium ore mineral assemblages. Lead isotopic ratios in stream water and 2.5N HCl leachates of bedload sediments and HMC measured by inexpensive ICP-MS are sufficiently precise to fingerprint isotopically distinct end-members such as Pb-bearing ore, country rocks, and anthropogenic pollution in the dispersion system. Quantified geochemical resources based on dispersion streams in terms of volumetric productivity (in tonnes per 1 m depth) are parametric and thus an objective measure of the geochemical anomaly.

We propose a three-fold drainage geochemical survey program that consists of reconnaissance, exploration, and detailed stages. The objective of the reconnaissance stage is to identify prospective areas based on collecting one near-mouth HMC sample (200-400 g) per stream (3rd or higher order) at 1:200,000 to 1:500,000 scale. 'Grey' HMC samples, recovered by panning or sluicing 10-20 kg of the <2 mm fraction of bulk alluvium in the field, should retain sulphides and other indicator minerals such as garnet as opposed to hard-panned 'black sand' with a specific gravity >5 g/cm^3. HMC samples must be analyzed for as many elements as possible and with the lowest minimum detection limits per analyte to recognize subtle geochemical anomalies and non-traditional types of economic deposits. Ranking analytical results normalized to minimum values per element reveals contrast leaders of a dispersion stream, which identify the type of ore deposit in the catchment basin. Multiplicative ratios of highly mobile (e.g., Ag-Hg-Sb) to less mobile (e.g., W-Sn-Bi) ore and indicator elements indicate level of erosion for the predicted ore system. Mineralogical analysis of anomalous HMC samples not only identifies commodities such as gold, diamonds, and other

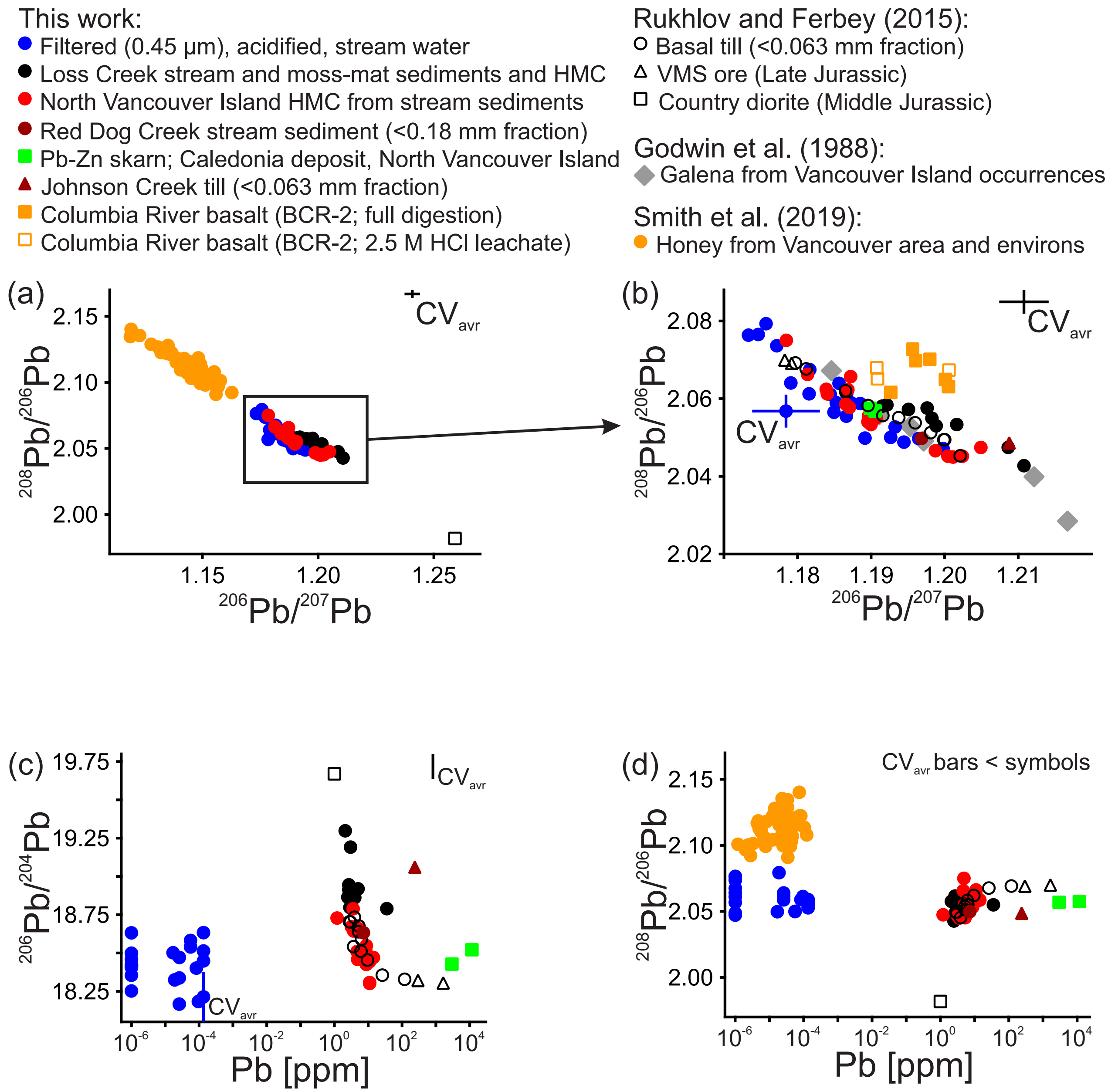

Fig. 22. a) and inset **b)** $^{206}Pb/^{207}Pb$ vs. $^{208}Pb/^{206}$ plots for stream waters and 2.5N HCl leachates of stream sediment, moss-mat sediment, heavy mineral concentrate (HMC), rock, and reference samples analyzed in this study. **c)** Pb [ppm] vs. $^{206}Pb/^{204}Pb$. **d)** Pb [ppm] vs. $^{208}Pb/^{206}Pb$. Compiled data from Godwin et al. (1988), Rukhlov and Ferbey (2015), and Smith et al. (2019). Uncertainties in terms of average coefficient of variation (CV_{avr}) based on at least 6 duplicate pairs (after Abzalov, 2008).

indicator minerals, but also provides additional control of the geochemical data. In the second stage, one near-mouth HMC sample is taken from each tributary of the prospective basin and the adjacent watersheds identified during reconnaissance. The purpose of this stage is to identify the area for the final, detailed study of the ore field, deposit, or ore body. Depending on physiography and geochemical landscape, geochemical methods at this stage may include lithochemical, hydrochemical, atmochemical (e.g., soil and above-ground SO_2, CO_2, O_2, CH_4, H_2S, and Hg vapour surveys), and biochemical surveys of the secondary and primary dispersion halos, accompanied by geophysical surveys, detailed mapping, and excavation.

Acknowledgments

We thank Stephen Cook (Independent Consultant), Wayne Jackaman (Noble Exploration Services Ltd.), and Gene Dodd (Billiken Gold Ltd.) for discussions of drainage sampling procedures and equipment. Wayne Jackaman also helped R.E.L. and A.R. in the field in April. We acknowledge Don Harrison (Senior Inspector of Mines Permitting, British

Columbia Ministry of Energy, Mines and Petroleum Resources) for approving our use of a sluice in the field. Bruce Northcote (British Columbia Geological Survey), John McClintock (Northisle Copper & Gold Inc.), and Western Forest Products Inc. are thanked for discussions about access in the northern Vancouver Island area. Commercial laboratories are thanked for quality and timely analyses. We thank Jeffrey R. Chiarenzelli (St. Lawrence University) and Lawrence B. Aspler (British Columbia Geological Survey) for thorough reviews and constructive comments.

References cited

Abzalov, M.Z., 2008. Quality control of assay data: A review of procedures for measuring and monitoring precision and accuracy. Exploration and Mining Geology, 17, 1-14.

Archibald, D.A., and Nixon, G.T., 1995. $^{40}Ar/^{39}Ar$ geochronometry of igneous rocks in the Quatsino-Port McNeill map area, northern Vancouver Island. In: Geological Fieldwork 1994, British Columbia Ministry of Energy, Mines, and Petroleum Resources, British Columbia Geological Survey Paper 1995-1, pp. 49-59.

Arne, D., and Brown, O., 2015. Catchment analysis applied to the interpretation of new stream sediment data, northern Vancouver Island (NTS 102I and 92L). Geoscience BC Report 2015-04, 41 p.

Bell, K., and Franklin, J.M., 1993. Application of lead isotopes to mineral exploration in glaciated terrains. Geology 21, 1143-1146.

Bell, K., and Murton, J.B., 1995. A new indicator of glacial dispersal: lead isotopes. Quaternary Science Reviews 14, 275-287.

Bobrowsky, P.T., 1997. Surficial geology of northern Vancouver Island area (NTS 92L/5, 6, 11, 12). British Columbia Ministry of Employment and Investment, British Columbia Geological Survey Open File 1997-08, scale 1:100,000.

Bobrowsky, P.T., and Meldrum, D.G., 1994a. Surficial geology of the Port McNeill area (NTS 92L/11). British Columbia Ministry of Energy, Mines and Petroleum Resources, British Columbia Geological Survey Open File 1994-04, scale 1:50,000.

Bobrowsky, P.T., and Meldrum, D., 1994b. Preliminary drift exploration studies, northern Vancouver Island (92L/6, 92L/11). In: Geological Fieldwork 1993, British Columbia Ministry of Energy, Mines and Petroleum Resources, British Columbia Geological Survey Paper 1994-1, pp. 87-99.

Bobrowsky, P.T., and Sibbick, S.J., 1996. Till geochemistry of northern Vancouver Island area (NTS 92L/5, 6W, 11W, 12). British Columbia Ministry of Energy, Mines and Petroleum Resources, British Columbia Geological Survey Open File 1996-07, 25 p.

Bobrowsky, P.T., Best, M., Dunn, C.E., Huntley, D.H., Lowe, C., Roberts, M.C., Seemann, D.A., and Sibbick, S.J., 1995. Integrated drift exploration studies on northern Vancouver Island. In: Geological Fieldwork 1994, British Columbia Ministry of Energy, Mines and Petroleum Resources, British Columbia Geological Survey Paper 1995-1, pp. 23-33.

Clague, J.J., Fulton, R.J., and Ryder, J.M., 1982. Surficial geology, Vancouver Island and adjacent mainland, British Columbia, map. Geological Survey of Canada, Open File 837, scale 1:1,000,000.

Dawson, G.M., 1887a. Geological map of the northern part of Vancouver Island and adjacent coasts, British Columbia. Geological Survey of Canada, Multicoloured Geological Map 247, scale 1:506,880.

Dawson, G.M., 1887b. Report on a geological examination of the northern part of Vancouver Island and adjacent coasts. Geological Survey of Canada, Annual Report 1886, Part B, 129 p.

DeBari, S.M., Anderson, R.G., and Mortensen, J.K., 1999. Correlation amongst lower to upper crustal components in an island arc: the Jurassic Bonanza arc, Vancouver Island, Canada. Canadian Journal of Earth Sciences, 36, 1371-1413.

Emmons, W.H., 1924. Primary downward changes in ore deposits. Transactions of the American Institute of Mining Engineers LXX, 964-997.

Gabrielse, H., Monger, J.W.H., Wheeler, J.O., and Yorath, C.J., 1991. Morphogeological belts, tectonic assemblages, and terranes. In: Gabrielse, H. and Yorath, C.J., (Eds.), Geology of the Cordilleran Orogen in Canada, Geological Survey of Canada, Geology of Canada, vol. 4, pp. 15-59 (also Geological Society of America, The Geology of North America, v. G-2).

Godwin, C.I., Gabites, J.E., and Andrew, A., 1988. Lead table: a galena lead isotope database for the Canadian Cordillera, with a guide to its use by explorationists. British Columbia Ministry of Energy, Mines and Petroleum Resources, British Columbia Geological Survey Paper 1988-4, 187 p.

Gravel, J.L., and Matysek, P.F., 1989. 1988 regional geochemical survey, northern Vancouver Island and adjacent mainland (092E, 092K, 092L, 102I). In: Geological Fieldwork 1988, British Columbia Ministry of Energy, Mines and Petroleum Resources, British Columbia Geological Survey Paper 1989-1, pp. 585-591.

Grigoryan, S.V., Solovov, A.P., and Kuvin, M.F., 1983. Инструкция по геохимическим методам поисков рудных месторождений. М-во геологии СССР. - М.: Недра [Manual on Geochemical Methods of Exploration for Ore Deposits. USSR Ministry of Geology. Nedra, Moscow], 191 p.

Gulson, B.L., 1986. Lead Isotopes in Mineral Exploration. Developments in Economic Geology 23, Elsevier, Amsterdam, 245 p.

Gunter, M.E., Johnson, N.E., Knowles, C.R., and Solie, D.N., 1993. Optical, x-ray, and chemical analyses of four eudialytes from Alaska. Mineralogical Magazine 57, 743-744.

Hammack, J.L., Nixon, G.T., Koyanagi, V.M., Payie, G.J., Panteleyev, A., Massey, N.W.D., Hamilton, J.V., and Haggart, J.W., 1994. Preliminary geology of the Quatsino - Port McNeill area, northern Vancouver Island (NTS 92L/12, 11W). British Columbia Ministry of Energy, Mines and Petroleum Resources, British Columbia Geological Survey Open File 1994-26, scale 1:50,000.

Hammack, J.L., Nixon, G.T., Payie, G.J., Snyder, L.D., Haggart, J.W., Massey, N.W.D., and Barron, D., 1995. Preliminary geology of the Quatsino - Cape Scott area, northern Vancouver Island (NTS 92L/12W; 102I/8, 9). British Columbia Ministry of Energy, Mines and Petroleum Resources, British Columbia Geological Survey Open File 1995-09, scale 1:50,000.

Hawkes, H.E., 1976. The downstream dilution of stream sediment anomalies. Journal of Geochemical Exploration 6, 345-358.

Holland, S.S., 1976. Landforms of British Columbia. British Columbia Ministry of Energy, Mines and Petroleum Resources, British Columbia Geological Survey Bulletin 48, 138 p.

Hussein, A.A., Lochner, C., and Bell, K., 2003. Application of Pb isotopes to mineral exploration in the Halfmile Lake area, Bathurst, New Brunswick. In: Massive Sulfide Deposits of the Bathurst Mining Camp, New Brunswick, and Northern Maine, W.D. Goodfellow, S.R. McCutcheon and J.M. Peter (Eds.), Economic Geology Monographs 11, pp. 679-688.

Jackaman, W., 2011. Regional stream sediment and water geochemical data, Vancouver Island, British Columbia (NTS 92B, C, E, F, G, K, L &102I). Geoscience BC Report 2011-04, 5 p.

Jackaman, W., 2013a. Regional stream sediment and water geochemical data, northern Vancouver Island, British Columbia. Geoscience BC Report 2013-11, 7 p.

Jackaman, W., 2013b. Northern Vancouver Island till sample reanalysis (ICP-MS). Geoscience BC Report 2013-12, 8 p.

Jackaman, W., 2014. Regional stream sediment geochemical data, sample reanalysis (INAA), northern Vancouver Island, British Columbia. Geoscience BC Report 2014-03, 4 p.

Jeffrey, W.G., 1962. Preliminary geological map, Alice Lake-Benson Lake. British Columbia Department of Mines and Petroleum

Resources, British Columbia Geological Survey Preliminary Map 1962, scale 1:63,360.
Kaplenkov, G.N., 2003. Шлихогеохимический метод поисков: новые аспекты применения и значение. - Материалы VI Международной конференции «Новые идеи в науках о Земле», 8 апреля 2003 г., под редакцией А.М. Кузнецова. Московский государственный геологоразведочный университет имени Серго Орджоникидзе (МГРИ-МГГРУ), Москва [Heavy mineral concentrate geochemical exploration method: new application aspects and significance. In: New Ideas in the Earth Sciences, Kuznetsov, A.M., (Ed.), Proceedings of the VI International Conference, April 8, 2003, Moscow State Geological Exploration University (MGRI-MGGRU), Moscow], p. 48.
Kaplenkov, G.N., 2006. Проспекторская геология. - Государственное Управление Ресурсами, Министерство природных ресурсов Российской Федерации, № 5, Москва [Prospecting geology. In: State Resource Management, Ministry of Natural Resources of Russian Federation, 5, Moscow], pp. 38-48.
Kaplenkov, G.N., 2008. Опытные геолого-проспекторские поиски. - Тезисы научно-практической конференции «Прогноз, поиски, оценка рудных и нерудных месторождений-достижения и перспективы», 20-21 мая 2008 г. Федеральное агентство по недропользованию (Роснедра), Российское геологическое общество (Росгео), Российская Академия естественных наук (РАЕН), Международная Академия минеральных ресурсов, Центральный научно-исследовательский геологоразведочный институт цветных и благородных металлов (ЦНИГРИ), Москва. [Orientation geological prospecting. In: Forecast, Exploration, and Evaluation of Ore and Non-Metallic Deposits - Achievements and Prospects, Abstracts of the Applied Science Conference, May 20-21, 2008, Federal Agency for Subsoil Management, the Russian Geological Society, the Russian Academy of Natural Sciences, the International Academy of Mineral Resources, and Central Research Institute of Geological Prospecting for Base and Precious Metals, Moscow], p. 114.
Kerr, D.E., 1992. Surficial geology of the Quatsino area, NTS 092L/12. British Columbia Ministry of Energy, Mines and Petroleum Resources, British Columbia Geological Survey Open File 1992-06, scale 1: 50,000.
Kerr, D.E., Sibbick, S.J., and Jackaman, W., 1992. Till geochemistry of the Quatsino map area (NTS 92L/12). British Columbia Ministry of Energy, Mines and Petroleum Resources, British Columbia Geological Survey Open File 1992-21, 14 p.
Koyanagi, V.M., and Panteleyev, A., 1993. Natural acid-drainage in the Mount McIntosh - Pernbenon Hills area, northern Vancouver Island (92L/12). In: Geological Fieldwork 1992, British Columbia Ministry of Energy, Mines and Petroleum Resources, British Columbia Geological Survey Paper 1993-1, pp. 445-450.
Koyanagi, V.M., and Panteleyev, A., 1994. Natural acid rock-drainage in the Red Dog - Hushamu - Pemberton Hills area, northern Vancouver Island. In: Geological Fieldwork 1993, British Columbia Ministry of Energy, Mines and Petroleum Resources, British Columbia Geological Survey Paper 1994-1, pp. 119-125.
Kukanov, A.B., Kaplenkov, G.N., et al., 1980. Отчет о региональной групповой геологической съемке масштаба 1:50000 в верховьях р.Тнеквеема, листы Q-60-57-АБ и ВГ, Q-60-58-АБ и Q-60-69-АБ и ВГ, Тэркэнейвеемский отряд, 1976-1980 гг., Восточно-Чукотская геологоразведочная экспедиция, № 2628, Эгвекинот [Report on regional geological mapping in the Tnekveem River headwaters, map sheets Q-60-57-AB and VG, Q-60-58-AB, and Q-60-69-AB and VG, Terkeneyveem party, 1976-1980. East Chukotka Exploration Expedition, No. 2628, Egvekinot], scale 1:50,000.
Lett, R.E., 2008. A multi-media analysis of stream geochemistry on Vancouver Island, British Columbia: Implications for mineral exploration. British Columbia Ministry of Energy and Mines, British Columbia Geological Survey, GeoFile 2008-08, 92 p.
Lett, R., and Rukhlov, A.S., 2017. A review of analytical methods for regional geochemical survey (RGS) programs in the Canadian Cordillera. In: Ferbey, T., Plouffe, A., and Hickin, A.S., (Eds.), Indicator Minerals in Till and Stream Sediments of the Canadian Cordillera. Geological Association of Canada Special Paper Volume 50, and Mineralogical Association of Canada Topics in Mineral Sciences Volume 47, pp. 53-108.
Lewis, T.J., Lowe, C., and Hamilton, T.S., 1997. Continental signature of a ridge-trench-triple junction: northern Vancouver Island. Journal of Geophysical Research 102, 7767-7781.
Massey, N.W.D., and Melville, D.M., 1991. Quatsino sound project. In: Geological Fieldwork, British Columbia Ministry of Energy, Mines and Petroleum Resources, British Columbia Geological Survey Paper 1991-1, pp. 85-88.
Matveev, A.A., 2003. Геохимические поиски месторождений полезных ископаемых (краткий курс лекций). - М.: Изд-во Московского университета [Geochemical Exploration of Ore Deposits, Lecture Course Notes. Moscow State University Press, Moscow], 110 p.
Matysek, P.F., and Day, S.J., 1988. Geochemical orientation surveys: northern Vancouver Island fieldwork and preliminary results. In: Geological Fieldwork 1987, British Columbia Ministry of Energy, Mines and Petroleum Resources, British Columbia Geological Survey Paper 1988-1, pp. 493-502.
Matysek, P.F., Gravel, J.L., and Jackaman, W., 1989. British Columbia regional geochemical survey, Alert Bay and Cape Scott (NTS 92L and 102I). Geological Survey of Canada, Open File 2040, and British Columbia Ministry of Energy, Mines and Petroleum Resources, British Columbia Geological Survey, Regional Geochemical Survey (RGS) 23, 154 p.
Meldrum, D.G., and Bobrowsky, P.T., 1994. Drift exploration potential of the Port McNeill area (NTS 92L/11). British Columbia Ministry of Energy, Mines and Petroleum Resources, British Columbia Geological Survey Open File 1994-11, scale 1:50,000.
Monger, J.W.H., 2014, Seeking the suture: The Coast-Cascade conundrum: Geoscience Canada, 41, 379-398.
Monger, J.W.H., and Hutchison, W.W., 1971. Metamorphic map of the Canadian cordillera. Geological Survey of Canada, Paper 70-33, 71 p.
Muller, J.E., 1977. Geology of Vancouver Island. Geological Association of Canada, Mineralogical Association of Canada, Joint Annual Meeting 1977, Field Trip 7, April 21-24, Guidebook, 54 p.
Muller, J.E., 1980. Geology-Victoria map area, Vancouver Island and Gulf islands, British Columbia. Ceological Survey of Canada, Open File 701, scale 1:100,000.
Muller, J.E., 1982. Geology of Nitinat Lake map area. Geological Survey of Canada, Open File 821, scale 1:125,000.
Muller, J.E., and Roddick, J.A.,1983. Geology, Alert Bay-Cape Scott, British Columbia. Geological Survey of Canada, Map 1552A, scale 1:250,000.
Muller, J.E., Northcote, K.E., and Carlisle, D., 1974. Geology and mineral deposits of Alert - Cape Scott map-area (92L-102I), Vancouver Island, British Columbia. Geological Survey of Canada, Paper 74-8, includes Map 4-1974, scale 1:250,000.
Nelson, J.L., Colpron, M., and Israel, S., 2013. The Cordillera of British Columbia, Yukon and Alaska: tectonics and metallogeny. In: Colpron, M., Bissig, T., Rusk, B.G., and Thompson, F.H., (Eds.), Tectonics, Metallogeny, and Discovery: The North American Cordillera and Similar Accretionary Settings. Society of Economic Geologists, Inc. Special Publication 17, pp. 53-109.
Nixon, G.T., and Orr, A.J., 2007. Recent revisions to the Early Mesozoic stratigraphy of northern Vancouver Island and metallogenic implications. British Columbia Ministry of Energy, Mines and Petroleum Resources, British Columbia Geological Survey Paper 2007-1, pp. 163-178.
Nixon, G.T., Hammack, J.L., Koyanagi, V.M., Payie, G.J.,

Panteleyev, A., Massey, N.W.D., Hamilton, J.V., and Haggart, J.W., 1994. Preliminary geology of the Quatsino-Port McNeill map areas, northern Vancouver Island. In: Geological Fieldwork 1993, British Columbia Ministry of Energy, Mines, and Petroleum Resources, British Columbia Geological Survey Paper 1994-1, pp. 63-85.

Nixon, G.T., Hammack, J.L., Koyanagi, V.M., Payie, G.J., Haggart, J.W., Orchard, M.J., Tozer, T., Archibald, D.A., Friedman, R.M., Palfy, J., and Cordey, F., 2000. Geology of the Quatsino-Port MacNeill area, northern Vancouver Island (draft). British Columbia Ministry of Energy, Mines, and Petroleum Resources, British Columbia Geological Survey Geoscience Map 2000-6, scale 1:50,000.

Nixon, G.T., Hammack, J.L., Payie, G.J., Snyder, L.D., Archibald, D.A., and Barron, D.J., 1995. Quatsino-San Josef map area, northern Vancouver Island: Geological overview. In: Geological Fieldwork 1994, British Columbia Ministry of Energy, Mines, and Petroleum Resources, British Columbia Geological Survey Paper 1995-1, pp. 9-21.

Nixon, G.T., Hammack, J.L., Payie, G.J., Snyder, L.D., Koyanagi, V.M., Hamilton, J.V., Panteleyev, A., Massey, N.W.D., Haggart, J.W., and Archibald, D.A., 1997. Geology of northern Vancouver Island: preliminary compilation (NTS 92L/5, 6, 11, 12; 102I/8, 9). British Columbia Ministry of Energy, Mines and Petroleum Resources, British Columbia Geological Survey Open File 1997-13, scale 1:100,000.

Nixon, G.T., Hammack, J.L., Koyanagi, V.M., Payie, G.J., Haggart, J.W., Orchard, M.J., Tozer, T., Archibald, D.A., Friedman, R.M., Palfy, J., and Cordey, F., 2006a. Geology of the Quatsino - Port McNeill area, northern Vancouver Island (NTS 92L/11, 12E). British Columbia Ministry of Energy, Mines and Petroleum Resources, British Columbia Geological Survey Geoscience Map 2006-02, scale 1:50,000.

Nixon, G.T., Hammack, J.L., Koyanagi, V.M., Payie, G.J., Snyder, L.D., Panteleyev, A., Massey, N.W.D., Archibald, D.A., Haggart, J.W., Orchard, M.J., Friedman, R.M., Tozer, T., Tipper, H.W., Poulton, T.P., Palfy, J., Cordey, F., and Barron, D.J., 2006b. Geology of the Holberg - Winter Harbour Area, Northern Vancouver Island (NTS 92L/12W, 102I/8, 9). British Columbia Ministry of Energy, Mines and Petroleum Resources, British Columbia Geological Survey Geoscience Map 2006-03, scale 1:50,000.

Nixon, G.T., Larocque, J., Pals, A., Styan, J., Greene, A.R., and Scoates, J.S., 2008. High-Mg lavas in the Karmutsen fl ood basalts, northern Vancouver Island (NTS 092L): stratigraphic setting and metallogenic significance. British Columbia Ministry of Energy, Mines and Petroleum Resources, British Columbia Geological Survey Paper 2008-1, pp. 175-190.

Nixon, G.T., Hammack, J.L., Koyanagi, V.M., Payie, G.J., Orr, A.J., Haggart, J.W., Orchard, M.J., Tozer, E.T., Friedman, R.M., Archibald, D.A., Palfy, J., and Cordey, F., 2011a. Geology, geochronology, lithogeochemistry and metamorphism of the Quatsino-Port McNeill area, northern Vancouver Island (NTS 92L/11, and parts of 92L/05, 12 and 13). British Columbia Ministry of Energy and Mines, British Columbia Geological Survey Geoscience Map 2011-02, scale 1:50,000.

Nixon, G.T., Hammack, J.L., Koyanagi, V.M., Snyder, L.D., Payie, G.J., Panteleyev, A., Massey, N.W.D., Hamilton, J.V., Orr, A.J., Friedman, R.M., Archibald, D.A., Haggart, J.W., Orchard, M.J., Tozer, E.T., Tipper, H.W., Poulton, T.P., Palfy, J., and Cordey, F., 2011b. Geology, geochronology, lithogeochemistry and metamorphism of the Holberg-Winter harbour area, northern Vancouver Island (parts of NTS 92L/05, 12, 13; 102I/08, 09 and 16). British Columbia Ministry of Energy and Mines, British Columbia Geological Survey Geoscience Map 2011-01, scale 1:50,000.

Nixon, G.T., Friedman, R.M., and Creaser, R.A., 2020. Late Neogene porphyry Cu-Mo(±Au-Ag) mineralization in British Columbia: the Klaskish Plutonic Suite, northern Vancouver Island. In: Geological Fieldwork 2019, British Columbia Ministry of Energy, Mines and Petroleum Resources, British Columbia Geological Survey Paper 2020-1 (this volume).

Northcote, K.E., 1969. Geology of the Port Hardy-Coal Harbour area. In: British Columbia Department of Mines Annual Report on Lode Metals, 1968, pp. 84-87.

Northcote, K.E., 1971. Rupert Inlet-Cape Scott map area. In: Geology, Exploration and Mining in B.C. 1970, British Columbia Ministry of Energy, Mines and Petroleum Resources, pp. 254-258.

Northcote, K.E., and Muller, J.E., 1972. Volcanism, plutonism, and mineralization: Vancouver Island. Canadian Institute of Mining, Metallurgy and Petroleum, Bulletin 65, 49-57.

Panteleyev, A., 1992. Copper-gold-silver deposits transitional between subvolcanic porphyry and epithermal environments. In: Geological Fieldwork 1991, British Columbia Ministry of Energy, Mines and Petroleum Resources, British Columbia Geological Survey Paper 1992-1, pp. 231-234.

Panteleyev, A. and Koyanagi, V.M., 1993. Advanced argillic alteration in Bonanza volcanic rocks, northern Vancouver Island - transitions between porphyry copper and epithermal environments. In: Geological Fieldwork 1992, British Columbia Ministry of Energy, Mines and Petroleum Resources, British Columbia Geological Survey Paper 1993-1, pp. 287-298.

Panteleyev, A., and Koyanagi, V.M., 1994. Advanced argillic alteration in Bonanza volcanic rocks, northern Vancouver Island-lithologic and permeability controls. In: Geological Fieldwork 1993, British Columbia Ministry of Energy, Mines and Petroleum Resources, British Columbia Geological Survey Paper 1994-1, pp. 101-110.

Panteleyev, A., Reynolds, P.H., and Koyanagi, V.M., 1995. $^{40}Ar/^{39}Ar$ ages of hydrothermal minerals in acid sulphate-altered Bonanza volcanics, northern Vancouver Island. In: Geological Fieldwork 1994, British Columbia Ministry of Energy, Mines and Petroleum Resources, British Columbia Geological Survey Paper 1996-1, pp. 61-65.

Panteleyev, A., Bobrowsky, P.T., Nixon, G.T., and Sibbick, S.J., 1996a. Northern Vancouver Island integrated project. In: Geological Fieldwork 1995, British Columbia Ministry of Energy, Mines and Petroleum Resources, British Columbia Geological Survey Paper 1996-1, pp. 57-59.

Panteleyev, A., Sibbick, S.J., and Koyanagi, V.M., 1996b. Natural acid rock-drainage in northern Vancouver Island - its place in geoenvironmental ore deposits models. In: Geological Fieldwork 1995, British Columbia Ministry of Energy, Mines and Petroleum Resources, British Columbia Geological Survey Paper 1996-1, pp. 61-66.

Perelló, J., Fleming, J.A., O'Kane, K.P., Burt, P.D., Clarke, G.A., Himes, M.D., and Reeves, A.T., 1995. Porphyry copper-gold-molybdenum deposits in the Island Copper cluster, northern Vancouver Island, British Columbia. In: Schroeter, T.G., (Ed.), Porphyry Deposits of the Northwest Cordillera of North America, Canadian Institute of Mining, Metallurgy and Petroleum, Special Volume 46, pp. 214-238.

Petrenko, E.E., Kozlov, G.P., and Kaplenkov, G.N., 1986. Отчет о региональной групповой геологической съемке масштаба 1:50000 на левобережье среднего течения р. Амгуэмы, листы Q-1-13-Г, Q-1-14-ВГ, Q-1-15-В, Q-1-25-БГ, Q-1-26-АБ и Q-1-27-АБ, Мараваамский отряд, 1981-1986 гг., Восточно-Чукотская геологоразведочная экспедиция, № 2827, Эгвекинот [Report on regional geological mapping on left bank of the middle course of Amguema River, map sheets Q-1-13-G, Q-1-14-VG, Q-1-15-V, Q-1-25-BG, Q-1-26-AB и Q-1-27-AB, Maravaam party, 1981-1986. East Chukotka Exploration Expedition, No. 2827, Egvekinot], scale 1:50,000.

Read, P.B., Woodsworth, G.J., Greenwood, H.J., Ghent, E.D., and Evenchick, C.A., 1991. Metamorphic map of the Canadian Cordillera. Geological Survey of Canada, Map 1714A, scale 1:2,000,000.

Rose, A.W., Hawkes, H.E., and Webb, J.S., 1979. Geochemistry in Mineral Exploration. London Academic Press, London, United Kingdom, 657 p.

Rukhlov, A.S., and Ferbey, T., 2015. Applications of lead isotopes in till for mineral exploration: a simplified method using ICP-MS. British Columbia Ministry of Energy and Mines, British Columbia Geological Survey, Paper 2015-2, 93 p.

Rukhlov, A.S., and Gorham, J., 2007. Commerce Resources Corp. 2006 diamond drilling and exploration at the Blue River Property, north of Blue River, British Columbia. British Columbia Ministry of Energy, Mines and Petroleum Resources, British Columbia Geological Survey, Assessment Report 29024, 41 p., 16 appendices.

Rukhlov, A.S., Mao, M., and Rippon, C., 2018. Rapid identification of sand-size mineral grains using portable XRF: A new method for indicator mineral surveys. In: Geological Fieldwork 2017, British Columbia Ministry of Energy, Mines and Petroleum Resources, British Columbia Geological Survey Paper 2018-1, pp. 167-182.

Rukhlov, A.S., Fortin, G., Kaplenkov, G.N., Lett, R.E., Lai, V. W.-M., and Weis, D., 2019. Supplementary data for multi-media geochemical and Pb isotopic evaluation of modern drainages on Vancouver Island. British Columbia Ministry of Energy, Mines and Petroleum Resources, British Columbia Geological Survey GeoFile 2019-14, 1 p.

Safronov, N.I., 1971. Основы геохимических методов поисков рудных месторождений. - Л.: Недра [Fundamentals of Geochemical Methods of Exploration for Ore Deposits, Nedra, Leningrad], 216 p.

Sibbick, S.J., 1994. Preliminary report on the application of catchment basin analysis to regional geochemical survey data, northern Vancouver Island (NTS 92L/03,04,05 and 06). In: Geological Fieldwork 1993, British Columbia Ministry of Energy, Mines and Petroleum Resources, British Columbia Geological Survey Paper 1994-1, pp. 111-117.

Sibbick, S.J., and Laurus, K.A., 1995a. Investigation of a natural acid rock drainage and an anomalous mercury-bearing stream, northern Vancouver Island. In: Geological Fieldwork 1994, British Columbia Ministry of Energy, Mines and Petroleum Resources, British Columbia Geological Survey Paper 1995-1, pp. 67-70.

Sibbick, S.J., and Laurus, K.A., 1995b. Integrated geological and geochemical map for the prediction of intrusion-related mineralization, northern Vancouver Island. British Columbia Ministry of Energy, Mines and Petroleum Resources, British Columbia Geological Survey Open File 1995-12, scale 1:250,000.

Simonetti, A., Bell, K., and Hall, G.E.M., 1996. Pb isotopic ratios and elemental abundances for selective leachates from near-surface till: implications for mineral exploration. Applied Geochemistry 11, 721-734.

Smith, K.E., Weis, D., Amini, M., Shiel, A.E., Lai, V.W.-M., and Gordon, K., 2019. Honey as a biomonitor for a changing world. Nature Sustainability 2, 223-232.

Solovov, A.P., 1985. Геохимические методы поисков месторождений полезных ископаемых: Учебник для вузов. - М.: Недра [Methods of Geochemical Exploration for Ore Deposits: Textbook. Nedra, Moscow], 294 p.

Solovov, A.P., Arhipov, A.Ya., Bugrov, V.A., Vorobiev, D.M., Gershman, D.M., Grigoryan, C.V., Kvyatkovsky, E.M., Matveev, A.A., Milyaev, C.A., Nikolaev, V.A., Perelman, A.I., Shvarov, Yu.V., Yufa, B.A., and Yaroshevsky, A.A., 1990. Справочник по геохимическим поискам полезных ископаемых. - М.: Недра [Handbook on Geochemical Exploration of Ore Deposits. Nedra, Moscow], 335 p.

Tahija, L., Roth, D., Game, B., Shouldice, T., Burt, P., Nilsson, J., and Wickland, B., 2017. North Island copper and gold project, preliminary economic assessment, NI 43-101 Technical Report, 174 p.

Thompson, T.B., 1997. Uranium, thorium, and rare metal deposits of Alaska. In: Mineral Deposits of Alaska, Goldfarb, R.J. and Miller, L.D., (Eds.), Economic Geology Monograph 9, pp. 466-482.

Warner, J.D., 1989. Columbium-, rare-earth element-, and thorium-bearing veins near Salmon Bay, southeastern Alaska. United States Bureau of Mines, Open File Report 6-89, 25 p.

Weis, D., Kieffer, B., Maerschalk, C., Barling, J., De Jong, J., Williams, G., Hanano, D., Pretorius, W., Mattielli, N., Scoates, J.S., Goolaerts, A., Friedman, R., and Mahoney, J.B., 2006. High-precision isotopic characterization of USGS reference materials by TIMS and MC-ICP-MS. Geochemistry, Geophysics, Geosystems 7 (8), Q08006, doi:10.1029/2006GC001283.

Detecting porphyry Cu-Mo mineralization using major oxides and pathfinder elements in subglacial till, Highland Valley mine area, south-central British Columbia

Cassandra Shewchuk[1], Travis Ferbey[2, a], and Olav B. Lian[1]

[1] Department of Geography and the Environment, University of the Fraser Valley, Abbotsford, BC, V2S 7M8
[2] British Columbia Geological Survey, Ministry of Energy, Mines and Petroleum Resources, Victoria, BC, V8W 9N3
[a] corresponding author: Travis.Ferbey@gov.bc.ca

Recommended citation: Shewchuk, C., Ferbey, T., and Lian, O.B., 2020. Detecting porphyry Cu-Mo mineralization using major oxides and pathfinder elements in subglacial till, Highland Valley mine area, south-central British Columbia. In: Geological Fieldwork 2019, British Columbia Ministry of Energy, Mines and Petroleum Resources, British Columbia Geological Survey Paper 2020-01, pp. 169-187.

Abstract

Major oxides and pathfinder elements are not typical analytes used in drift prospecting. Testing these analytes by applying principal component analysis to published data from the silt-plus-clay (<0.063 mm) fraction of subglacial tills near the Highland Valley mine, we find that the major oxides Al_2O_3 Fe_2O_3, K_2O, and Na_2O can detect drift-covered porphyry alteration and Cu-Mo mineralization. In addition, the pathfinder elements Pb, Zn, As, and Sb can also identify local dispersal from drift-covered porphyry Cu-Mo (and related) mineralization, and CaO and Ni are linked to peripheral mafic phases of the Guichon Creek batholith (Late Triassic) and regional-scale basalt flows of the Kamloops Group (Eocene). However, Ag, Hg, and Mn values in till do not reliably detect porphyry mineralization, nor do they have a coherent signal that can be related to a specific bedrock unit.

Keywords: Till geochemistry, calc-alkaline porphyry, major oxide, pathfinder element, drift prospecting, Highland Valley mine, Guichon Creek batholith

1. Introduction

Calc-alkaline Cu-Mo and alkalic Cu-Au porphyries are common mineral exploration targets in British Columbia, and many have been developed into producing mines (Fig. 1; e.g., Gibraltar, Mount Polley, New Afton, Copper Mountain, and Highland Valley). Although continuous bedrock outcrops are rare because of extensive and commonly thick (>2 m) Quaternary drift deposits, the Interior Plateau is underlain by rocks of the Quesnel and Stikine terranes, which have high potential to host buried porphyry deposits. New buried discoveries will likely rely on surface sediment geochemistry and mineralogy to see through the glacial sediment cover. Drift prospecting can be used to assess the mineral potential of glaciated terrain and is ideally suited to explore for porphyry mineralization in the Interior Plateau. The British Columbia Geological Survey (BCGS) and Geological Survey of Canada (GSC) have been developing drift prospecting in the province for decades and have built up a catalogue of case studies that demonstrate its effectiveness (Bustard and Ferbey, 2017). Most of these studies focus on commodity and pathfinder element determinations on the matrix of subglacial tills (e.g., Plouffe and Ballantyne, 1993; Levson et al., 1994; Plouffe and Williams, 1998; Levson, 2002; Ferbey, 2011). More recent work has focussed on indicator mineral grain abundances in subglacial tills (e.g., Hashmi et al., 2015; Ferbey et al., 2016; Plouffe et al., 2016).

With notable exceptions (e.g., Cook and Fletcher, 1993), the effectiveness of major element oxides at detecting dispersal from buried mineralized bedrock sources has not been examined. The present study complements previous work in the Highland Valley mine area (Ferbey et al., 2016) and uses analytical data from this work. We look for statistically significant correlations between commodity elements (Cu, Mo) and major oxides (Al_2O_3, CaO, Fe_2O_3, K_2O, Na_2O) and pathfinder elements (Ag, As, Hg, Mn, Ni, Pb, Sb, Zn) in subglacial till and assess their spatial distribution to determine if they can detect porphyry Cu-Mo mineralization at the Highland Valley mine.

2. Background

2.1. Porphyry deposits

Porphyry systems are generated mainly in magmatic arcs where metal-rich hydrothermal fluids move through, and interact with, batholith-scale bodies and adjacent country rock to form mineral deposits (Sinclair, 2007; Berger et al., 2008; Sillitoe, 2010). Undeformed porphyry deposits display concentric alteration zones where the primary dispersion of major elements is predominantly controlled by hydrothermal alteration and mineralization processes (Fig. 2; Olade, 1977; Sillitoe, 2010). Mineralogical variation in these zones, some of which is common to all porphyry systems, is generally predictable. However, mineralogical details can vary from deposit to deposit and depend on the composition of the

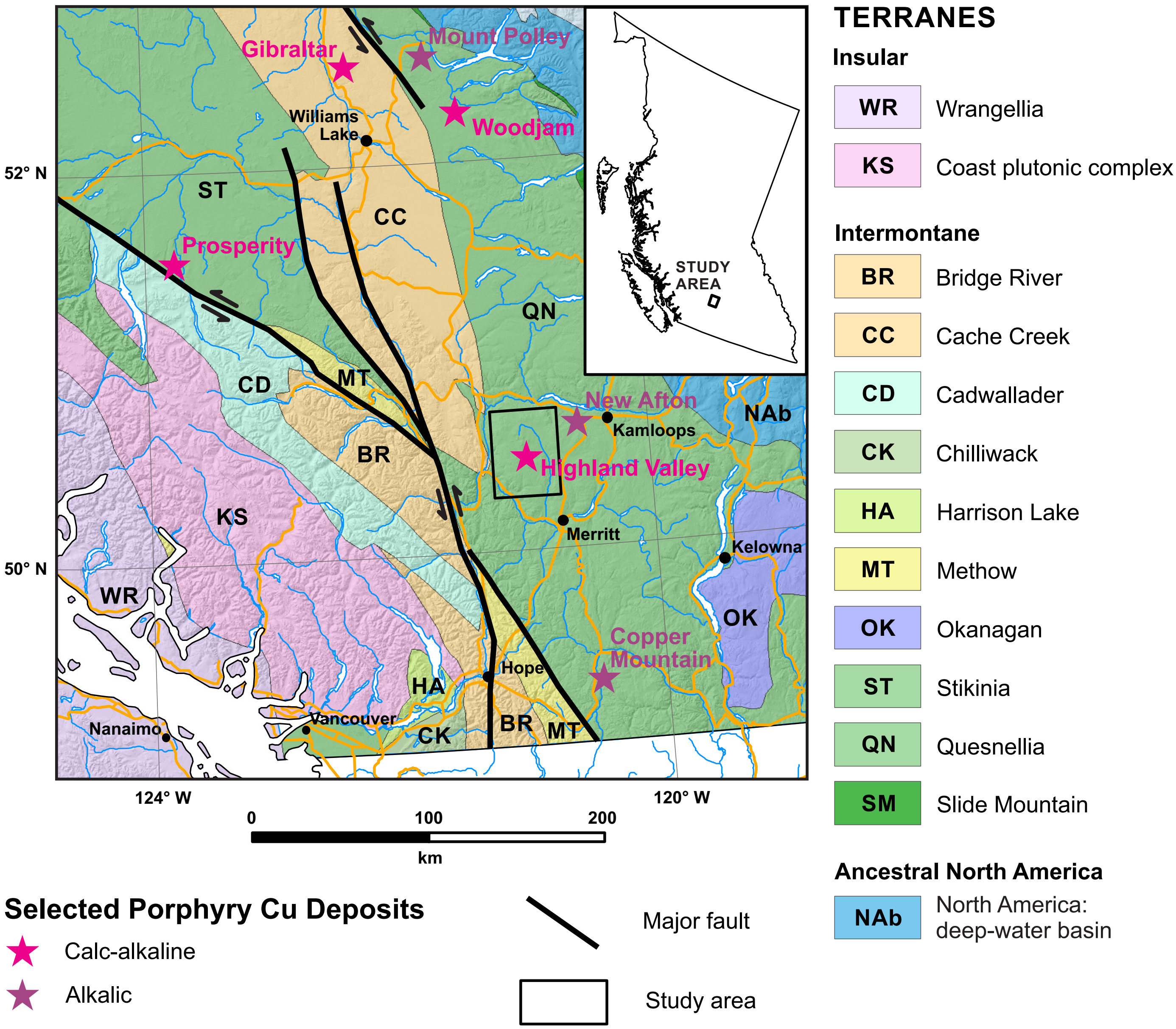

Fig. 1. Location of study area (modified from Ferbey et al., 2016). Terranes of the southern Canadian Cordillera after Nelson et al. (2013).

intrusion and the country rocks, the temperature and chemistry of the hydrothermal fluids, and the interaction between these fluids and ambient water (Byrne et al., 2013; Sillitoe, 2010).

2.2. Drift prospecting

Drift prospecting is a geochemical exploration method used to assess mineral potential in glaciated terrain (Fig. 3; e.g., Levson, 2001; Lian and Hickin, 2017). The elemental and mineralogical composition of a subglacial till is dependent on the material exposed at surface to glacial erosion. Minerals like apatite, epidote, jarosite, and chalcopyrite (recovered from the 0.25 mm to 0.5 mm fraction of subglacial till matrix) can be indicators of porphyry mineralization (Kelley et al., 2011, Mao et al., 2016, 2017; Plouffe and Ferbey, 2017). Determinations on the <0.063 mm size fractions for commodity elements, pathfinder elements and, potentially, major element oxides, can also be used to explore for mineralized bedrock subcrop (Levson, 2001). A detailed multi-element-mineral assemblage investigation on subglacial till matrix can potentially be used to identify the porphyry system zones that were eroded and incorporated into subglacial tills because of the mineralogical variability in each (Fig. 2; Plouffe and Ferbey, 2017).

2.3. Principal component analysis

Principal component analysis (PCA) is a multivariate statistical technique that is used to reduce multi-dimensional datasets (Gazley et al., 2015). It is ideally suited for exploring large geochemical datasets consisting of many samples

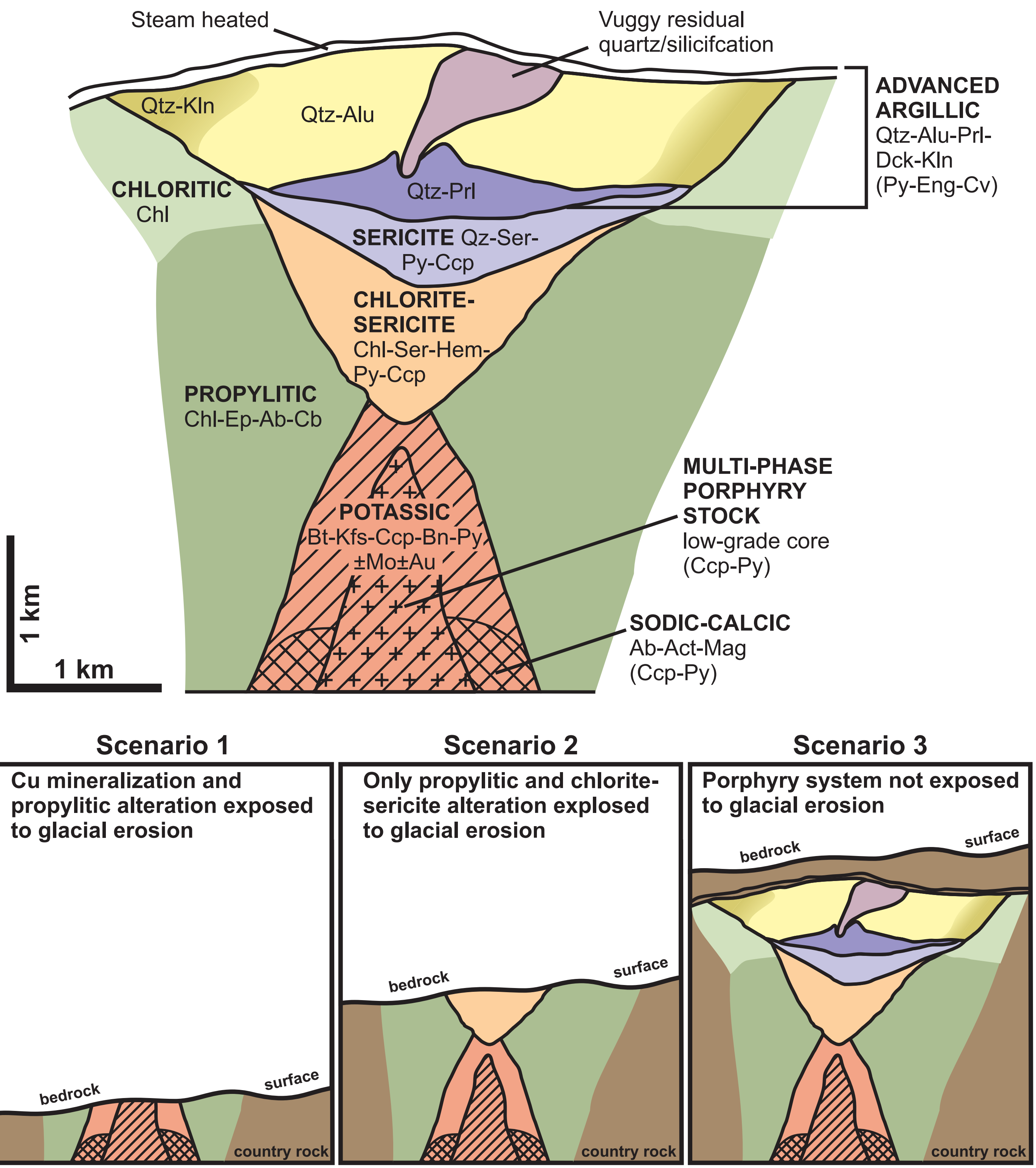

Fig. 2. Porphyry system zonation and mineralogy (modified from Sillitoe, 2010). Mineral abbreviations: ab=albite, act=actinolite, alu=alunite, au=gold, bn=bornite, bt=biotite, cb=carbonate, ccp=chalcopyrite, chl=chlorite, cv=covellite, dck=dickite, eng=enargite, ep=epidote, hem=hematite, kfs=potassium feldspar, kln=kaolinite, mag=magnetite, mo=molybdenite, prl=pyrophyllite, py=pyrite, qz=quartz, ser=sericite. Three scenarios showing different levels of erosion, where mineral contribution to subglacial till composition depends on the porphyry zone(s), if any, exposed to glacial erosion (from Plouffe and Ferbey, 2017).

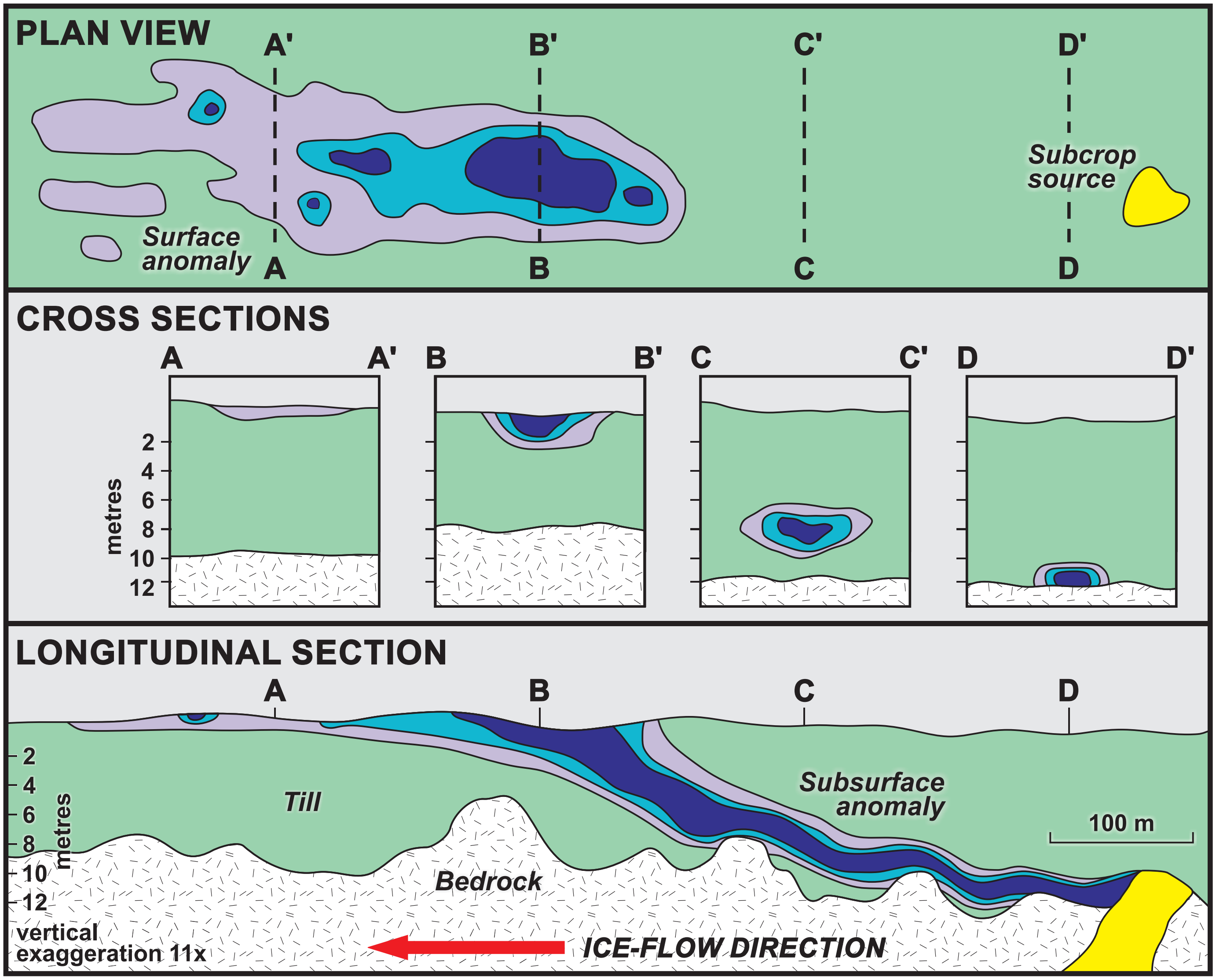

Fig. 3. Drift prospecting dispersal model (modified after Miller, 1984). Deeper blue shades indicate greater element and indicator mineral values.

with determinations for many analytes (Chen et al., 2019). Principal component analysis concentrates on variance, but also considers covariance and correlations (Jolliffe, 2011) and, in the case of geochemistry, calculates which analytes best summarize the variation of the dataset (Abdi and Williams, 2010). Eigenvectors can also be included in PCA plots, with their length proportional to the analyte's influence on data set variance, and their direction indicating covariance with other analytes. Eigenvector angles of less than 90° between analytes indicate a positive correlation, an angle of 90° indicates zero correlation, and angles greater than 90° signify a negative correlation.

3. Study area

The Guichon Creek batholith (Fig. 1) hosts the porphyry Cu-Mo deposits at the Highland Valley mine (Byrne et al., 2013). Quaternary sediments generally cover bedrock. Where the cover is thick (> 2m), bedrock is exposed at the stoss ends of crag and tails and in deeper road cuts. Where the cover is thin, bedrock is commonly exposed as discontinuous outcrop (Ferbey et al., 2016).

3.1. Regional bedrock geology

The study area is in the Quesnel terrane, which includes richly endowed Triassic and Jurassic island arc volcanosedimentary and intrusive rocks (McMillan et al., 2009; Logan and Mihalynuk, 2014). The Guichon Creek batholith (Late Triassic) is a large calc-alkaline body, 30 km wide and 70 km long (Roy and Clowes, 2000). It is zoned, with a mafic facies on its margins and a younger more felsic facies in its interior (Casselman et al., 1995; McMillan et al., 2009; Byrne et al., 2013; Lesage et al., 2019; Fig. 4). The porphyry deposits at the Highland Valley mine (Bethlehem, Valley, Lornex, Highmont, and JA) are hosted in the younger, more felsic rocks of the Bethlehem and Bethsaida phases (Fig. 4; Byrne et al., 2013).

Mineralization occurs as vein fills, disseminations in veins,

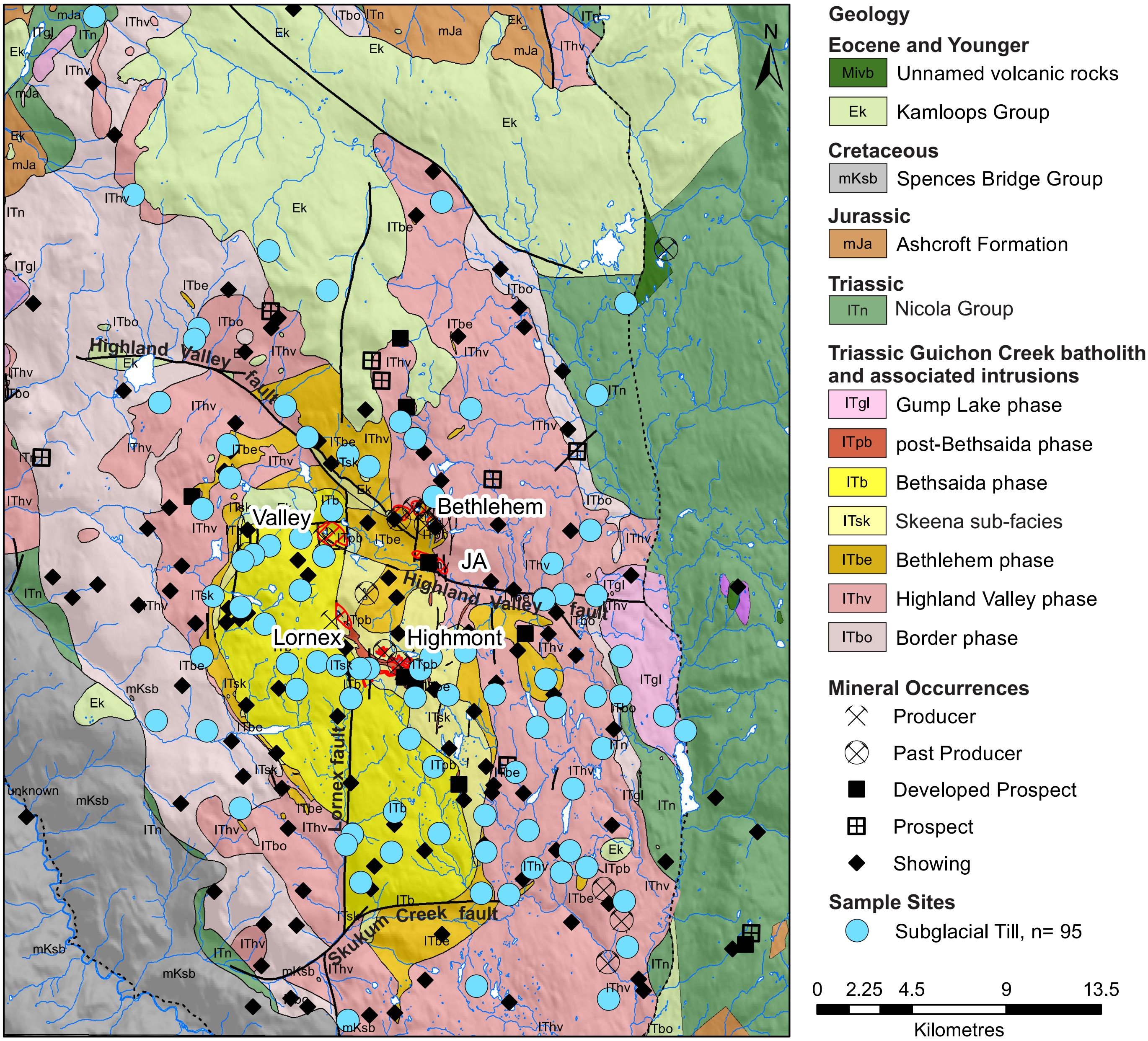

Fig. 4. Bedrock geology of the Guichon Creek batholith and Highland Valley mine area (McMillan et al., 2009; Cui et al., 2017) with subglacial till sample locations. Highland Valley mine porphyry centres are shown with hatched red and labeled.

fracture halos, breccia infills and disseminations, and along faults (Byrne et al., 2013), and includes chalcopyrite, bornite, and molybdenite (Casselman et al., 1995). The deposits contain a bornite-rich core, which transitions outwards into chalcopyrite-rich domains. Alteration minerals include quartz, potassium feldspar, sericite, biotite, anhydrite, magnetite, calcite, hematite, kaolinite, chlorite, epidote, and fluorite; propylitic alteration (sericite, chlorite, epidote) extends outwards up to 15 km from the main deposits (Casselman et al., 1995; Byrne et al., 2013; Lesage et al., 2019). At the Bethlehem, JA and Valley deposits, K_2O and K_2O/Na_2O ratios decrease away from the inner zones of intense hydrothermal alteration and mineralization, whereas concentrations of Na_2O, CaO, MgO and total Fe (as Fe_2O_3) increase (Olade, 1977).

3.2. Quaternary geology

The Highland Valley mine area was covered by the Cordilleran ice sheet during the Late Wisconsinan glaciation (Clague and Ward, 2011 Atkinson et al., 2016). Except for JA, the deposits at Highland Valley mine were at least partially exposed to glacial erosion during the Late Wisconsinan and then covered by glacial sediments (Bobrowsky et al., 1993; Byrne et al., 2013). JA is overlain by Tertiary sedimentary bedrock, which protected it from glacial erosion during the Quaternary (Lesage et al., 2019).

Glaciers advanced out of accumulation areas to the east and west of the study area at the onset of glaciation, coming together to form an ice divide north of the study area (~52° north) during the Late Wisconsinan glacial maximum (Clague and Ward, 2011; Bobrowsky et al., 1993; Ferbey et al., 2016). Based on multi-scale ice-flow indicators, regional ice flow was initially to the south-southeast, but was later to the southeast (Fig. 5; Bobrowsky et al., 1993; Ferbey et al., 2016; Plouffe and Ferbey, 2018).

4. Methods

We chose the major oxides Al_2O_3, CaO, Fe_2O_3, K_2O, Na_2O, and pathfinder elements Ag, As, Hg, Mn, Ni, Pb, Sb, and Zn, from the silt plus clay-size till fraction (<0.063 mm) for statistical analysis because they are in calc-alkaline porphyry systems and can be linked to the mineralogy of specific alteration zones in these systems (Olade, 1977; Panteleyev, 1995; Sillitoe, 2010). We compared the concentrations of these oxides and elements to Cu and Mo, which have been demonstrated to detect porphyry Cu-Mo mineralization at Highland Valley mine (Ferbey et al., 2016). The following summarizes the geochemical datasets and the statistical and spatial analyses we used to assess if major oxides and pathfinder elements in till can detect covered bedrock mineralization.

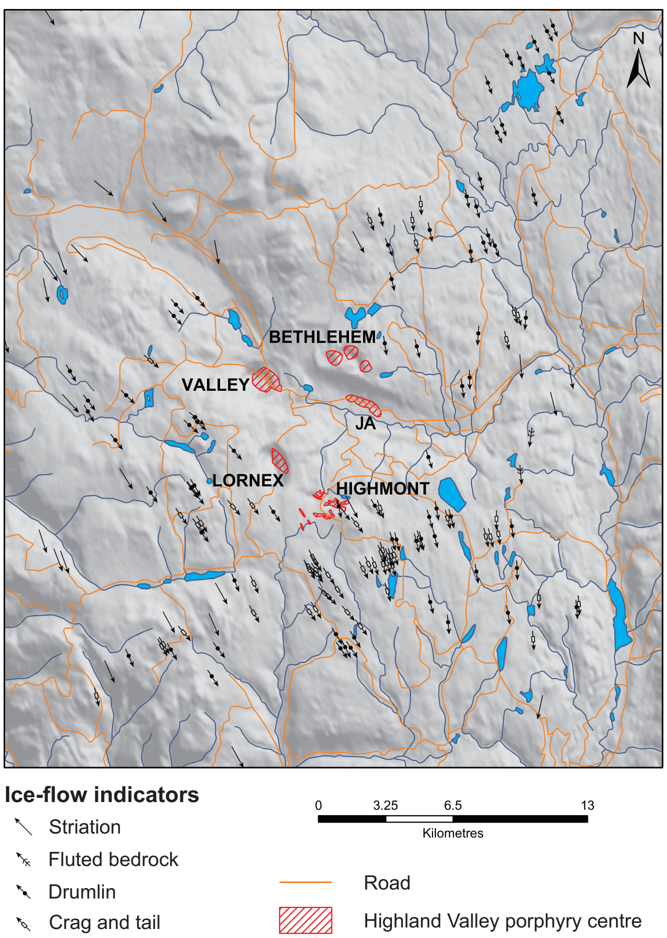

Fig. 5. Ice-flow indicators of the Highland Valley mine area (after Ferbey et al., 2013).

4.1. Till geochemical data

Existing geochemical data from 95 subglacial till samples, originally reported by Ferbey et al. (2016), were used for this study. Samples were collected from 130 to 150 cm below surface at road and stream cuts largely within the confines of the Guichon Creek batholith, including exposures at the Highland Valley mine (Fig. 4). These 1 to 2 kg samples were dry sieved at the Sedimentology Laboratory of the GSC (Ottawa, ON) to produce a silt plus clay-sized pulp (<0.063 mm). All analytical procedures were conducted at Bureau Veritas Commodities Canada Ltd. (Vancouver, BC); these are detailed in Ferbey et al. (2016) and summarized here. Sample aliquots of 0.2 g were analyzed for major elements by lithium metaborate/ tetraborate fusion and inductively coupled plasma emission spectrometry (ICP-ES; laboratory code LF200). Aliquots of 30 g were analyzed for trace elements by modified aqua regia inductively coupled plasma mass spectrometry (ICP-MS; laboratory code AQ252_EXT_REE). In the total fusion method the sample material is totally decomposed, whereas with aqua regia digestion some of the sample may remain, depending on the element and the mineral phase (e.g., sulphide minerals are soluble in aqua regia but silicate minerals are not). Total trace element data were not used here. Blanks, analytical duplicates and field duplicates were inserted into the sample sequence to assess precision and accuracy (Spirito et al., 2011; McClenaghan et al., 2013; Ferbey et al., 2016). Stated analytical detection limits, and the decomposition and analytical methods used for each analyte are presented in Table 1.

4.2. Statistical data analysis

Log-transformed data were used to produce a correlation matrix, which was then used to calculate principal components and generate principal component plots using R (R Core Team, 2019). Graduated symbols were used to compare the spatial distribution of element concentrations at till sample locations. The commodity elements Cu and Mo reliably identify mineralized bedrock at Highland Valley mine (Ferbey et al., 2016), differentiating this bedrock source from other potential sources in the Guichon Creek batholith. The analyte plots were compared to Cu and Mo plots to see if they follow a similar spatial trend, with higher values near porphyry sources at Highland Valley mine that decrease in the down-ice direction.

5. Results

Summary statistics for the elements and oxides we consider are presented in Table 2. Percentile class breaks (≤50, >50-70, >70-90, >90-95, >95) are used in proportional symbol plots to categorize data because they do not bias the classification

Table 1. Detection limits, units, and analytical methods.

Analyte	Detection limit	Unit	Analytical method
Ag	2	ppb	AR ICP-MS
As	0.1	ppm	AR ICP-MS
Cu	0.01	ppm	AR ICP-MS
Hg	5	ppb	AR ICP-MS
Mn	1	ppm	AR ICP-MS
Mo	0.01	ppm	AR ICP-MS
Ni	0.1	ppm	AR ICP-MS
Pb	0.01	ppm	AR ICP-MS
Sb	0.02	ppm	AR ICP-MS
Zn	0.1	ppm	AR ICP-MS
Al_2O_3	0.01	%	Li fusion ICP-ES
CaO	0.01	%	Li fusion ICP-ES
Fe_2O_3	0.01	%	Li fusion ICP-ES
K_2O	0.01	%	Li fusion ICP-ES
Na_2O	0.01	%	Li fusion ICP-ES

Table 2. Summary statistics for silt plus clay-sized fraction (<0.063 mm) of till samples (n=95).

Analyte	AR ICP-MS	Minimum	Mean	Median	95th percentile	Maximum
Ag (ppb)	AR ICP-MS	4	59	39	115	559
As (ppm)	AR ICP-MS	1.2	4.4	3.7	8.6	39.4
Cu (ppm)	AR ICP-MS	37.04	243.50	178.13	611.42	1706.97
Hg (ppb)	AR ICP-MS	2.5	40.7	32.0	100	211.0
Mn (ppm)	AR ICP-MS	227	529	527	766	1251
Mo (ppm)	AR ICP-MS	0.48	2.23	1.13	8.14	28.87
Ni (ppm)	AR ICP-MS	5.1	22.2	21.1	39.3	55.6
Pb (ppm)	AR ICP-MS	1.65	5.93	3.33	7.62	216.20
Sb (ppm)	AR ICP-MS	0.11	0.35	0.30	0.59	0.98
Zn (ppm)	AR ICP-MS	18.1	50.59	49.8	78.2	122.40
Al_2O_3 (%)	Li fusion ICP-ES	13.20	15.63	15.62	17.06	17.70
CaO (%)	Li fusion ICP-ES	2.51	4.95	4.72	7.36	10.71
Fe_2O_3 (%)	Li fusion ICP-ES	3.64	6.12	6.32	7.60	8.19
K_2O (%)	Li fusion ICP-ES	1.39	1.79	1.79	2.08	2.46
Na_2O (%)	Li fusion ICP-ES	2.70	3.60	3.55	4.29	4.92

(Levson, 2001). For the discussion that follows, background concentrations are defined as the mean for a given element; >95th percentile concentrations are considered elevated. Analytes discussed here roughly conform to a log-normal distribution.

5.1. Statistical analysis

Correlation values with respect to Cu in a log-transformed correlation matrix (Table 3) were used to assess the effectiveness of selected analytes at detecting porphyry mineralization. A higher value indicates a stronger positive or negative correlation with Cu values. Ideally, the correlation would be positive and closer to 1, although a strong negative correlation could also be meaningful. The analytes Ag, Mo, Ni, Al_2O_3, CaO, K_2O, and Fe_2O_3 have a statistically significant correlation with Cu at $P_{0.05}$, but the analytes As, Hg, Mn, Pb, Sb, Zn, and Na_2O do not (Table 3).

The first three principal components account for 77.0% of the variability within the dataset and so were chosen for analysis. Principal component plots (PC1 versus PC2, PC1 versus PC3, and PC2 versus PC3) visually illustrate the statistical correlation between analytes and commodity elements. In all

Table 3. Pearson correlation matrix of log-transformed data. Bold type values are statistically significant correlations with Cu at $P_{0.05}$ (n=95).

	Ag	As	Cu	Hg	Mn	Mo	Ni	Pb	Sb	Zn	Al_2O_3	CaO	Fe_2O_3	K_2O	Na_2O
Ag	1.000														
As	0.468	1.000													
Cu	**0.289**	0.187	1.000												
Hg	0.436	0.511	-0.044	1.000											
Mn	0.412	0.503	-0.038	0.426	1.000										
Mo	0.494	0.472	**0.736**	0.134	0.167	1.000									
Ni	0.267	0.331	**-0.373**	0.437	0.588	-0.172	1.000								
Pb	0.156	0.406	0.052	0.208	0.496	0.162	0.243	1.000							
Sb	0.314	0.714	0.125	0.525	0.453	0.311	0.113	0.456	1.000						
Zn	0.419	0.654	0.162	0.364	0.770	0.302	0.499	0.735	0.573	1.000					
Al_2O_3	0.041	0.022	**0.526**	-0.201	0.058	0.592	-0.278	0.306	-0.006	0.283	1.000				
CaO	0.271	0.117	**-0.455**	0.349	0.271	-0.388	0.526	-0.135	0.084	0.067	-0.739	1.000			
Fe_2O_3	0.148	0.326	**-0.368**	0.404	0.353	-0.328	0.792	0.143	0.158	0.300	-0.459	0.535	1.000		
K_2O	0.226	0.062	**0.328**	0.125	0.111	0.225	0.112	0.189	-0.147	0.235	0.260	-0.193	0.027	1.000	
Na_2O	-0.327	-.0462	0.128	-0.568	-0.656	0.105	-0.726	-0.283	-0.306	-0.544	0.315	-0.484	-0.759	-0.239	1.000

three plots, Mo, Al_2O_3, and K_2O are positively correlated to Cu (Figs. 6-8) and Ni, Fe_2O_3, and CaO are negatively correlated (Figs. 6-8). This element assemblage (minus Ni) might be expected from a calc-alkaline porphyry Cu-Mo system when element signatures from the mineralized core and peripheral hydrothermal alteration are accounted for (Panteleyev et al., 1995). These relationships with Cu are stronger than those of As, Ag, Hg, Sb, Zn, and Na_2O, which are only positively correlated in two plots, PC1 versus PC2 (Fig. 6) and PC1 versus PC3 (Fig. 7). Mn and Pb have a variable and weak correlation with Cu (Figs. 6-8). These relationships support the correlation values to Cu presented in Table 3 with one exception. It is unknown why Ag is not positively correlated to Cu in all three plots (Figs. 6-8) given its statistically significant correlation value to Cu is 0.289, higher than As is to Cu (Table 3).

5.2. Spatial analysis

Copper shows a general trend of elevated values near the Highland Valley mine that decrease to the southeast, down ice-flow direction (Fig. 9). This plot, along with the one for Mo (Fig. 10), supports the notion that porphyry mineralization can be detected using the spatial distribution of elevated commodity element values in subglacial tills. The absence of Mo in till down ice-flow direction from Bethlehem reflects the lack of molybdenite in the deposit.

Some of the major oxide and pathfinder element concentrations follow the same trend as those of Cu and Mo. For example, Al_2O_3 is elevated within 3 km of the Valley, Lornex and Highmont porphyry deposits (Fig. 11). Locally, >90th percentile values of K_2O can occur down-ice of Valley and Highmont, but they are also in a group of samples along the eastern margin of the Guichon Creek batholith (Fig. 12). Here, Cu and Mo values range from 90th percentile (locally) down to background. Fe_2O_3, CaO, and Ni have an almost inverse spatial distribution to that of Cu and Mo (Figs. 13-15). In general, samples elevated in Fe_2O_3, CaO, and Ni are near the periphery of the Guichon Creek batholith, not near the core as with Cu and Mo. All >90th percentile values of Na_2O are in the southern part of the study area (Fig. 16), south of Lornex and Highmont, where K_2O, Fe_2O_3, CaO, and Ni are at low to background values. In this cluster, northern samples can have >90th percentile values of Cu and Mo, although most samples have <90th percentile concentrations.

The spatial agreement between elevated Pb, Zn, As, and Sb values, and Cu, is less robust (Figs. 17-20). A group of samples west, and immediately down-ice, of Valley and Lornex deposits have >90th percentile values of Pb, Zn, and As. Down-ice of Lornex is one sample with >95th percentile Sb. Some of these same samples, or neighbouring samples, can also have above background Cu and Mo values. The elements Ag, Hg, and Mn have spatial distributions that do not follow that of Cu and Mo; they are more diffuse regionally and are not shown here. They could still be related to mineralized sources hosted by the Guichon Creek batholith (indicating dispersal that is local and short), but do not have the same response as Cu and Mo to known sources of mineralization at Highland Valley mine.

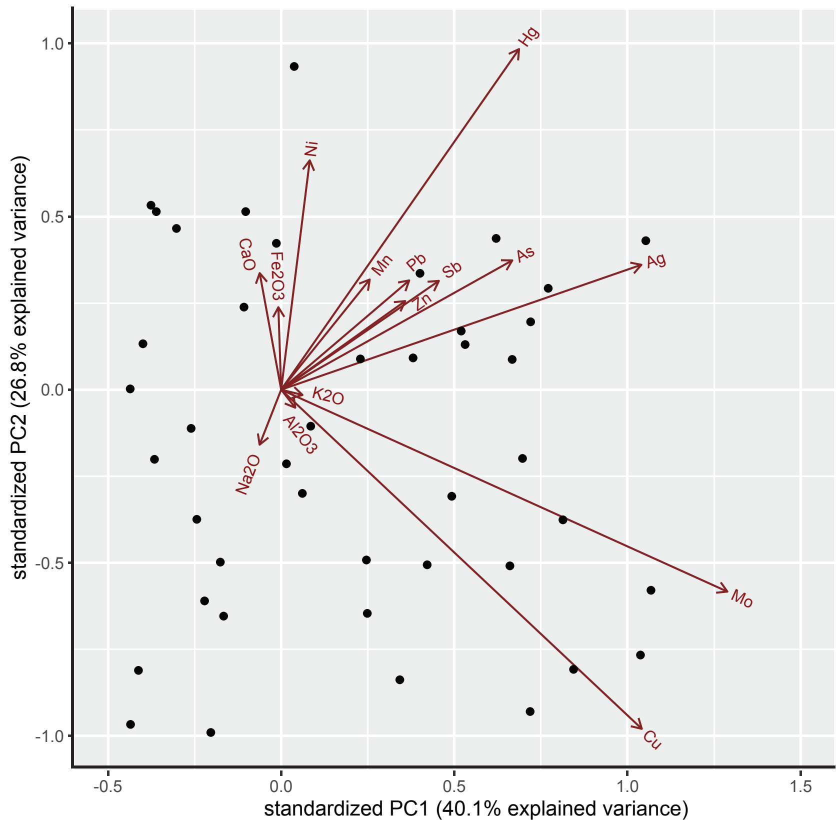

Fig. 6. Principal component analysis results for PC1 and PC2.

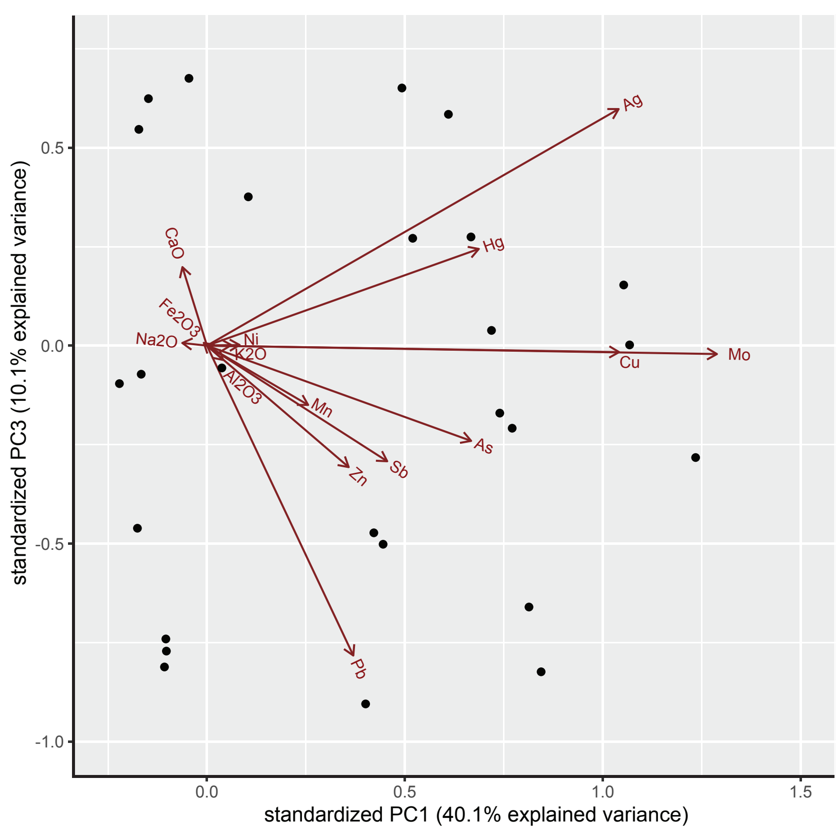

Fig. 7. Principal component analysis results for PC1 and PC3.

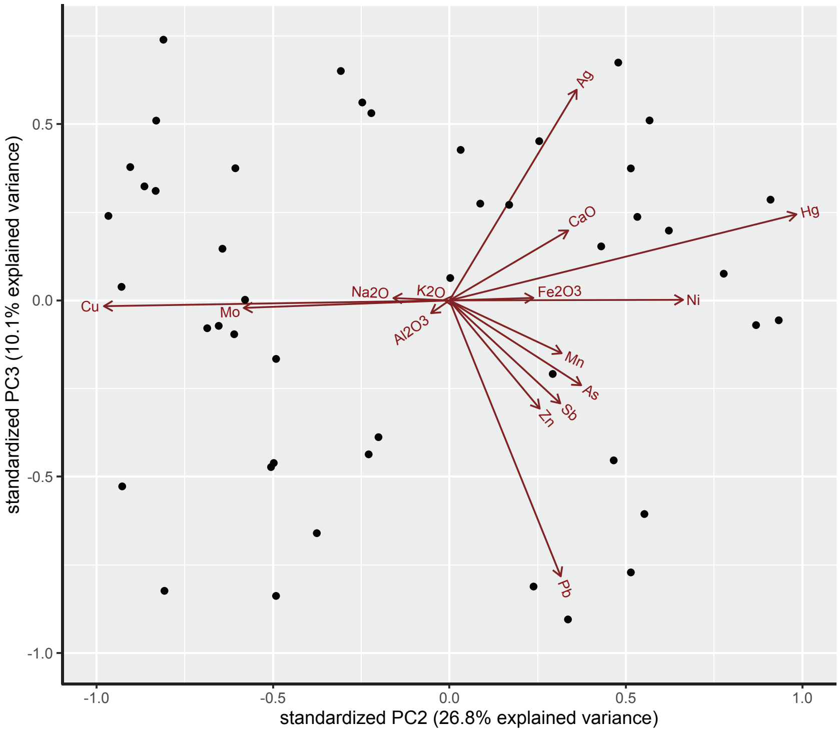

Fig. 8. Principal component analysis results for PC2 and PC3.

6. Discussion

This study shows that major oxides measured in subglacial till samples have the potential to detect porphyry mineralization and alteration associated with emplacement of the Guichon Creek batholith. This conclusion is supported by the calculated correlation matrix (Table 3), visual correlations with commodity elements shown in PCA plots (Figs. 6-8), and by the spatial distribution of elevated values relative to known sources of bedrock mineralization and hydrothermal alteration (Figs. 9-20). This study also shows that major oxide and pathfinder element concentrations can differentiate other rock types at the batholith and regional scales.

6.1. Al_2O_3 and K_2O

Al_2O_3 and K_2O concentrations in till can detect covered mineralized porphyry systems at the Highland Valley mine. Both have a statistically significant positive correlation to Cu values, and Al_2O_3 has a similar spatial distribution to samples elevated in Cu and Mo. Elevated Al_2O_3 could be related to biotite in zones of potassic alteration and/or other mainly phyllosilicate alteration zones that are more central to a porphyry system that also contain Cu-bearing minerals (Fig. 2, e.g., chlorite-sericite, sericite, advanced argillic). K_2O concentrations are spatially coincident with higher Cu and Mo values, but not as strongly as Al_2O_3. They are also elevated in a group of till samples along the eastern margin of the Guichon Creek batholith, where <90th percentile Cu and Mo values (down to background) can occur. The Highmont deposit is the nearest know altered source for K_2O, but potassic alteration is only weakly developed there (Byrne et al., 2013) and it is located ~10 km up-ice from these 95th percentile K_2O values. Although the Highland Valley phase granodiorites have upwards of 13% primary K-feldspar (Byrne et al., 2013), this is likely not enough to account for the >2% K_2O found in tills there. These tills may have been derived from potassically altered rocks from a porphyry system southeast of Highmont. Olade (1977) found a positive correlation between K_2O and Cu values in porphyry deposits of the Guichon Creek batholith. It is worth noting that maximum till values of Al_2O_3 (17.8%) and K_2O (2.5%) are equal to or exceed the average compositions of intrusions in the Highland valley mine area (Al_2O_3=16.7%, K_2O=2.5%; Byrne et al., 2013), and average continental crust (Al_2O_3=15.0%, K_2O=2.6%; Wedepohl, 1995). Given that the geochemical signature of till is inherently diluted relative to its bedrock source, these tills appear to have been derived from bedrock with even greater values of Al_2O_3 and K_2O.

6.2. Na_2O

Rocks in the central part of the Guichon Creek batholith seem to be responsible for the Na_2O response in tills there. These elevated values could be related to high-temperature sodic-calcic alteration (representing the deepest part of a porphyry system; Fig. 2). This agrees with the idea that the Valley deposit has been deeply eroded, exposing the lowermost phases of that porphyry system (Byrne et al., 2013). Byrne et al. (2017) mapped domains of sodic-calcic alteration up to 3 km west of Lornex and upwards of 6 km southeast of Highmont. The group of samples elevated in Na_2O are in this same area and

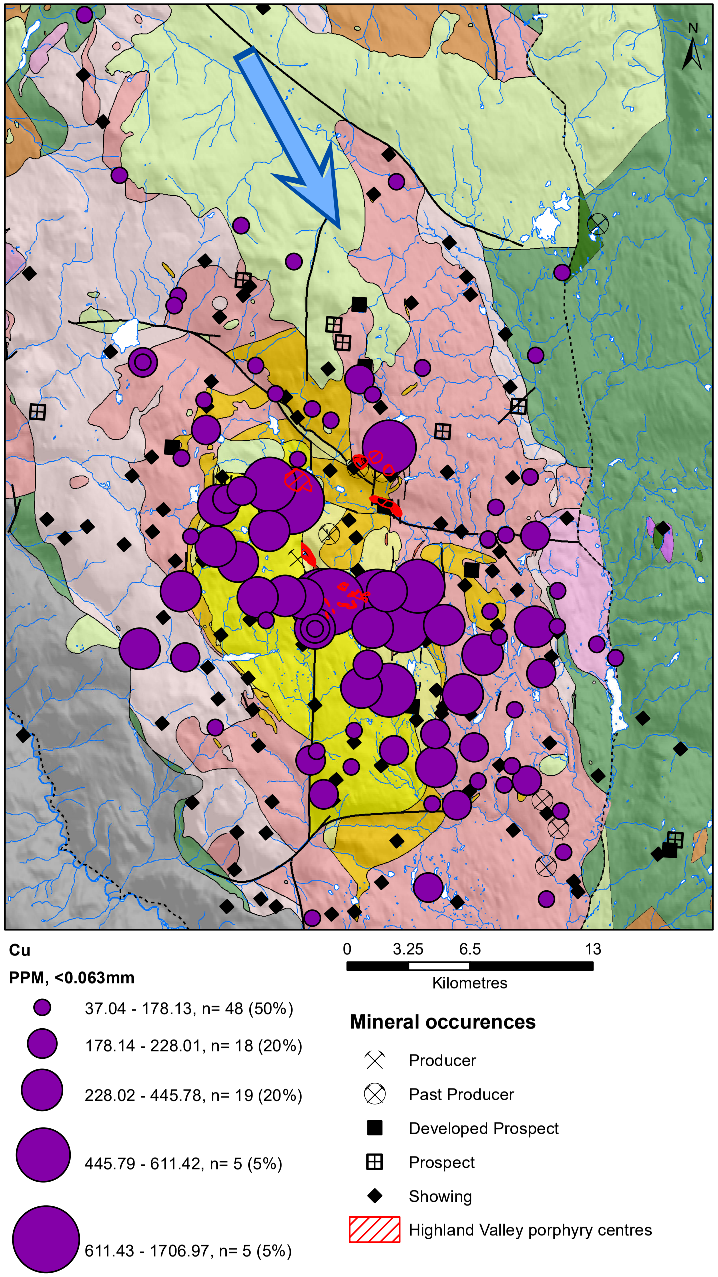

Fig. 9. The spatial distribution of Cu in the silt plus clay-sized fraction (<0.063 mm) of subglacial till. Ice flow direction indicated with blue arrow. Refer to Fig. 4 for bedrock geology legend.

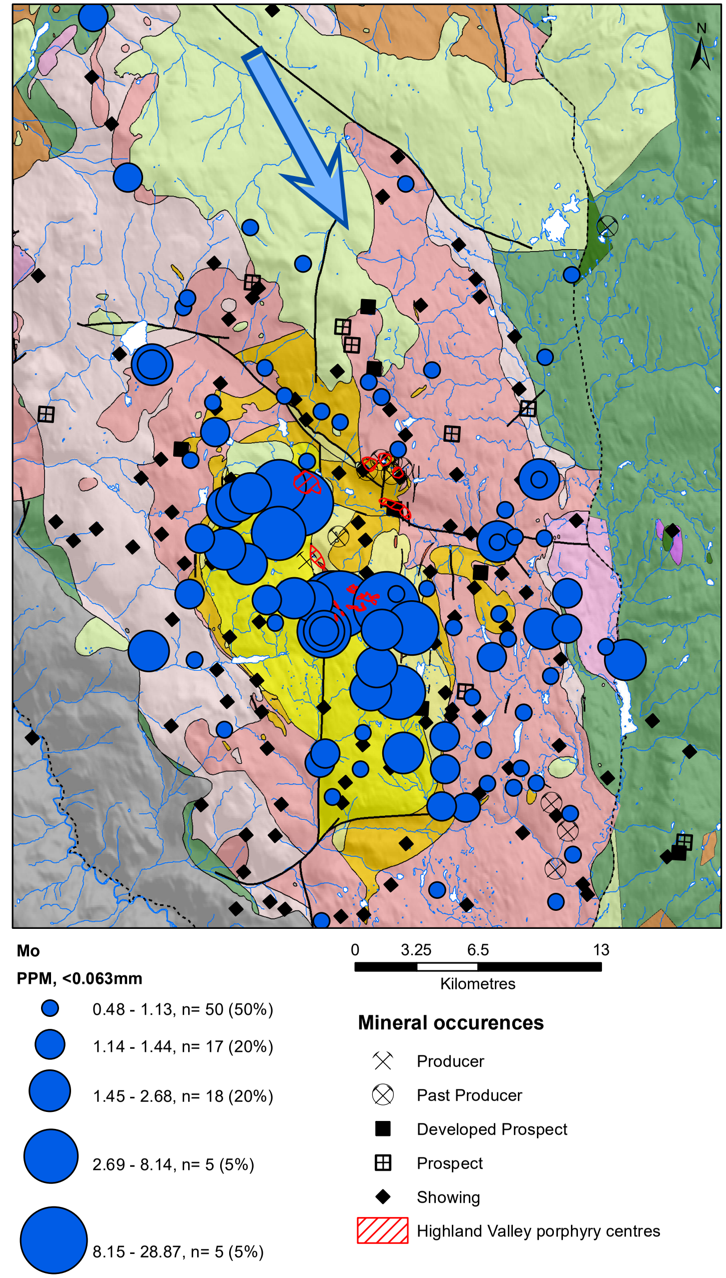

Fig. 10. The spatial distribution of Mo in the silt plus clay-sized fraction (<0.063 mm) of subglacial till. Ice flow direction indicated with blue arrow. Refer to Fig. 4 for bedrock geology legend.

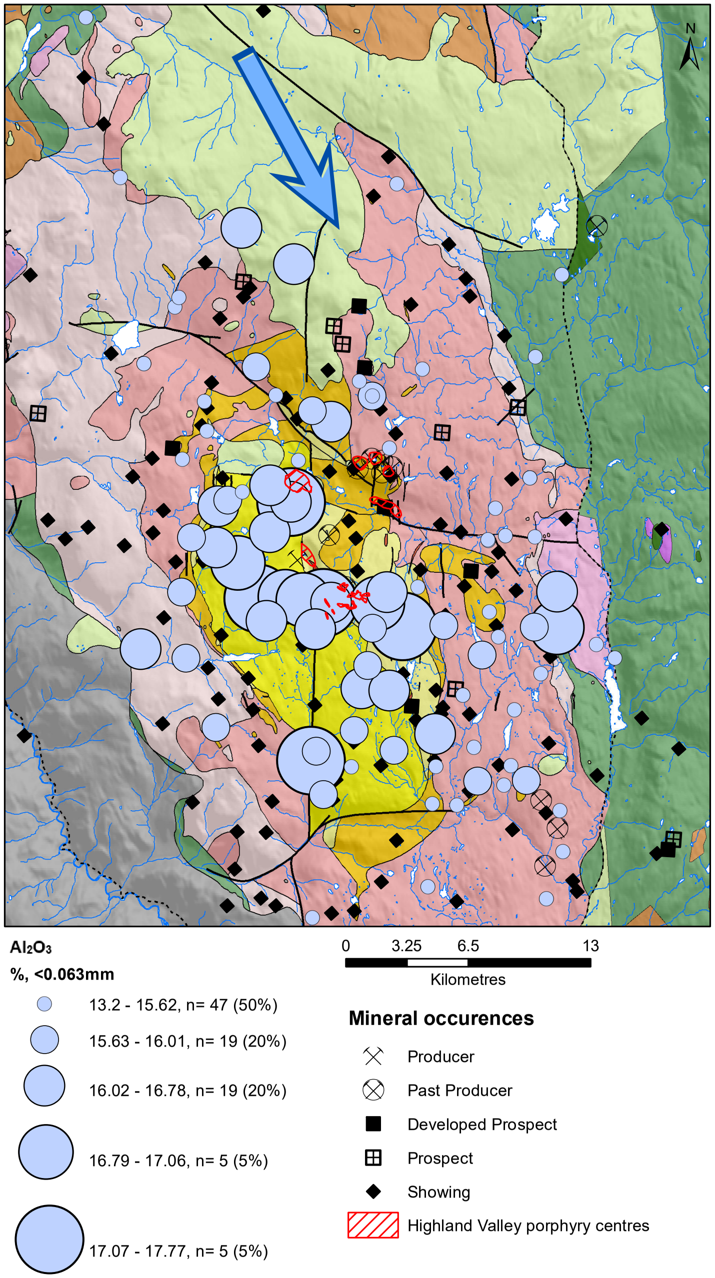

Fig. 11. The spatial distribution of Al_2O_3 in the silt plus clay-sized fraction (<0.063 mm) of subglacial till. Ice flow direction indicated with blue arrow. Refer to Fig. 4 for bedrock geology legend.

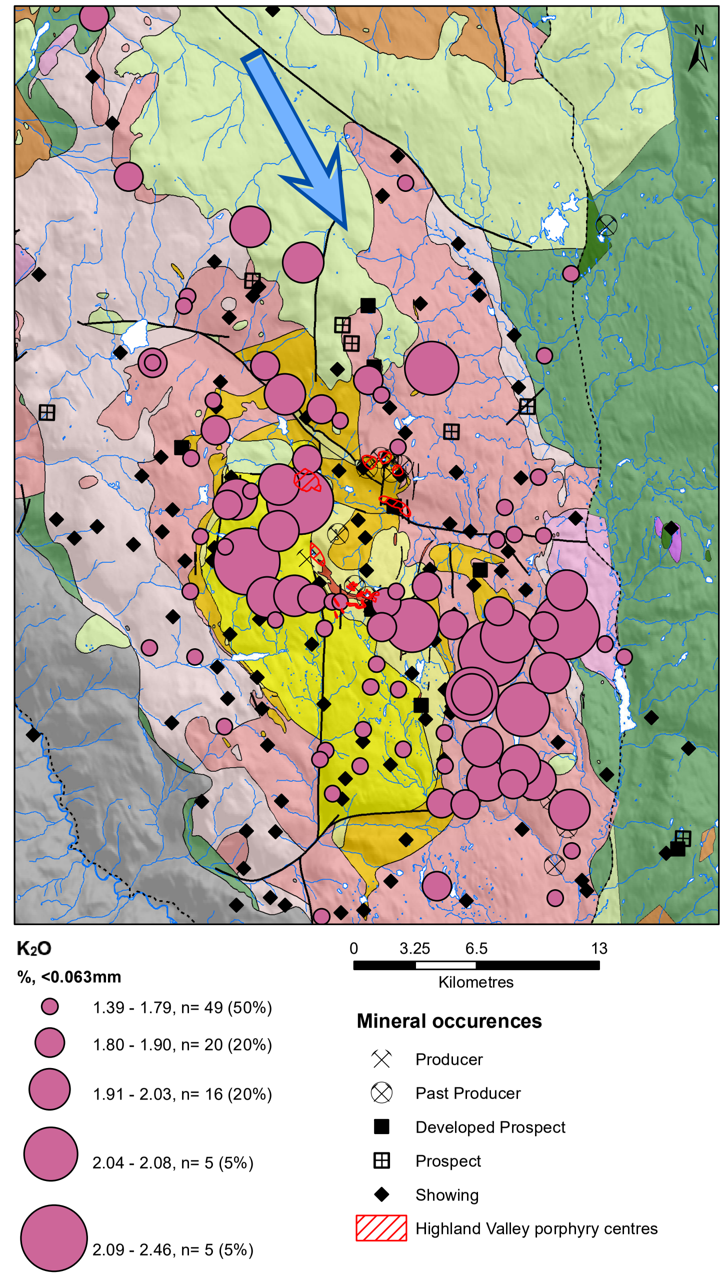

Fig. 12. The spatial distribution of K_2O in the silt plus clay-sized fraction (<0.063 mm) of subglacial till. Ice flow direction indicated with blue arrow. Refer to Fig. 4 for bedrock geology legend.

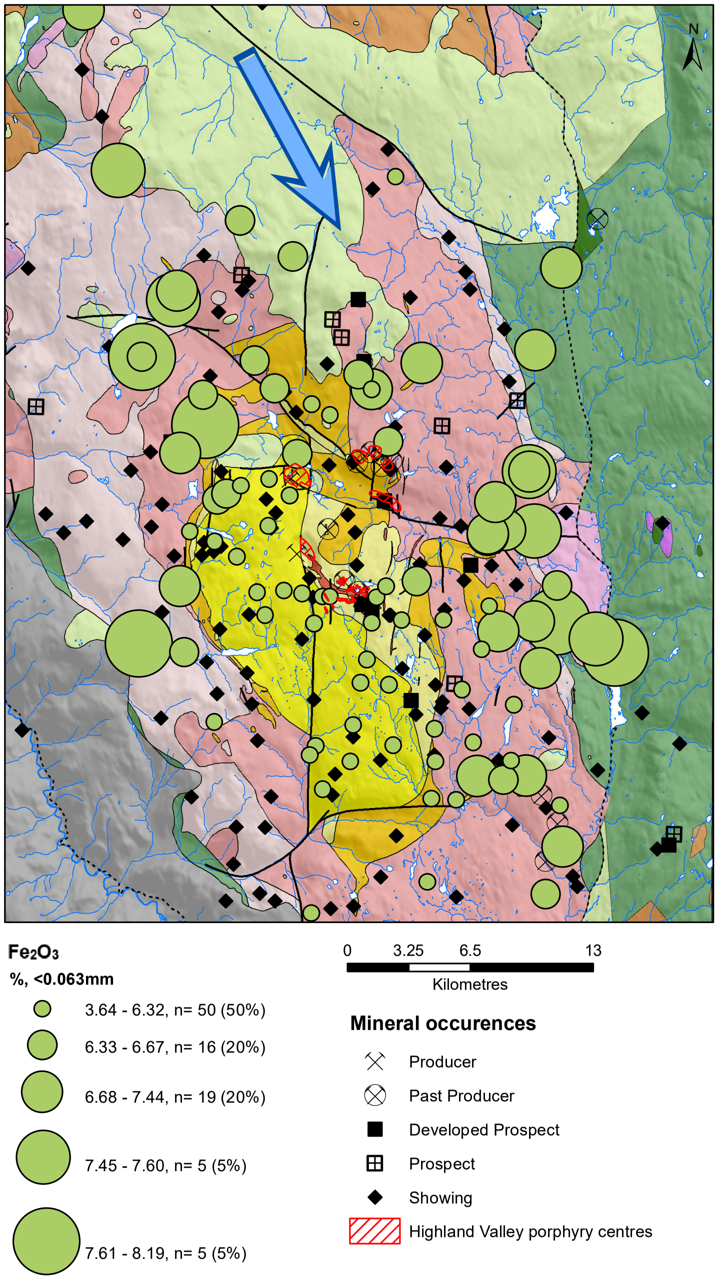

Fig. 13. The spatial distribution of Fe_2O_3 in the silt plus clay-sized fraction (<0.063 mm) of subglacial till. Ice flow direction indicated with blue arrow. Refer to Fig. 4 for bedrock geology legend.

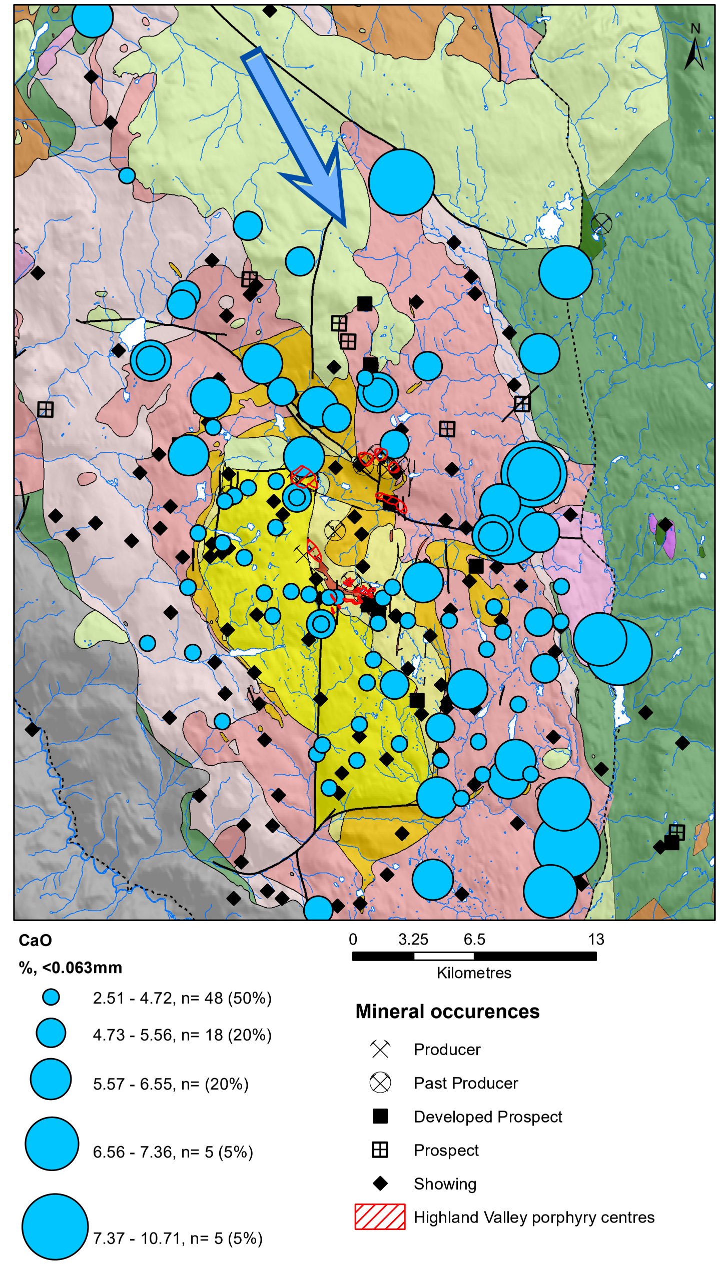

Fig. 14. The spatial distribution of CaO in the silt plus clay-sized fraction (<0.063 mm) of subglacial till. Ice flow direction indicated with blue arrow. Refer to Fig. 4 for bedrock geology legend.

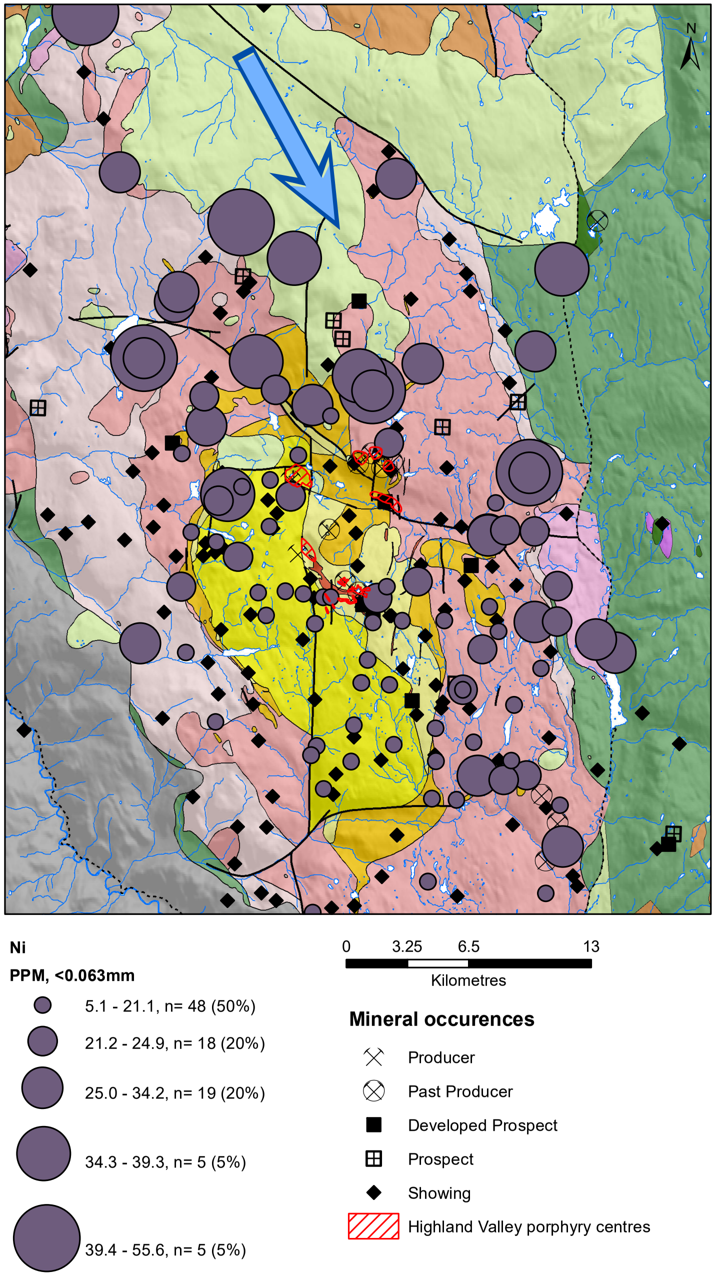

Fig. 15. The spatial distribution of Ni in the silt plus clay-sized fraction (<0.063 mm) of subglacial till. Ice flow direction indicated with blue arrow. Refer to Fig. 4 for bedrock geology legend.

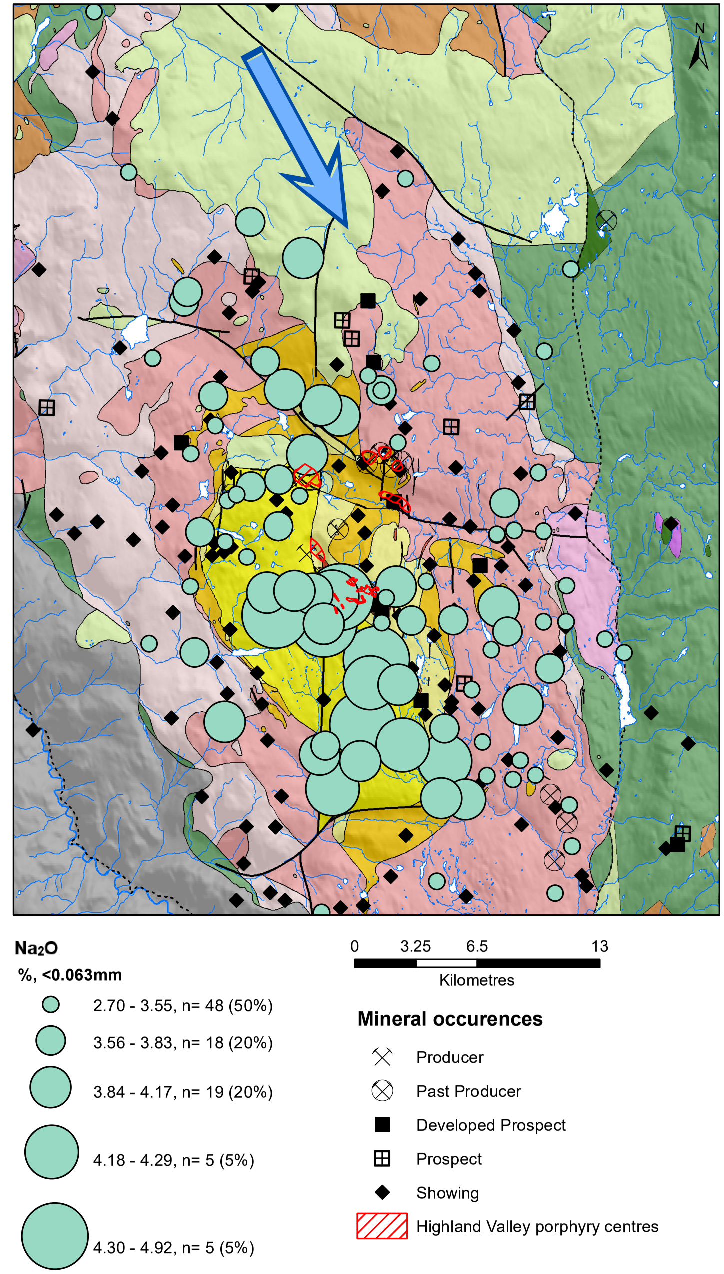

Fig. 16. The spatial distribution of Na_2O in the silt plus clay-sized fraction (<0.063 mm) of subglacial till. Ice flow direction indicated with blue arrow. Refer to Fig. 4 for bedrock geology legend.

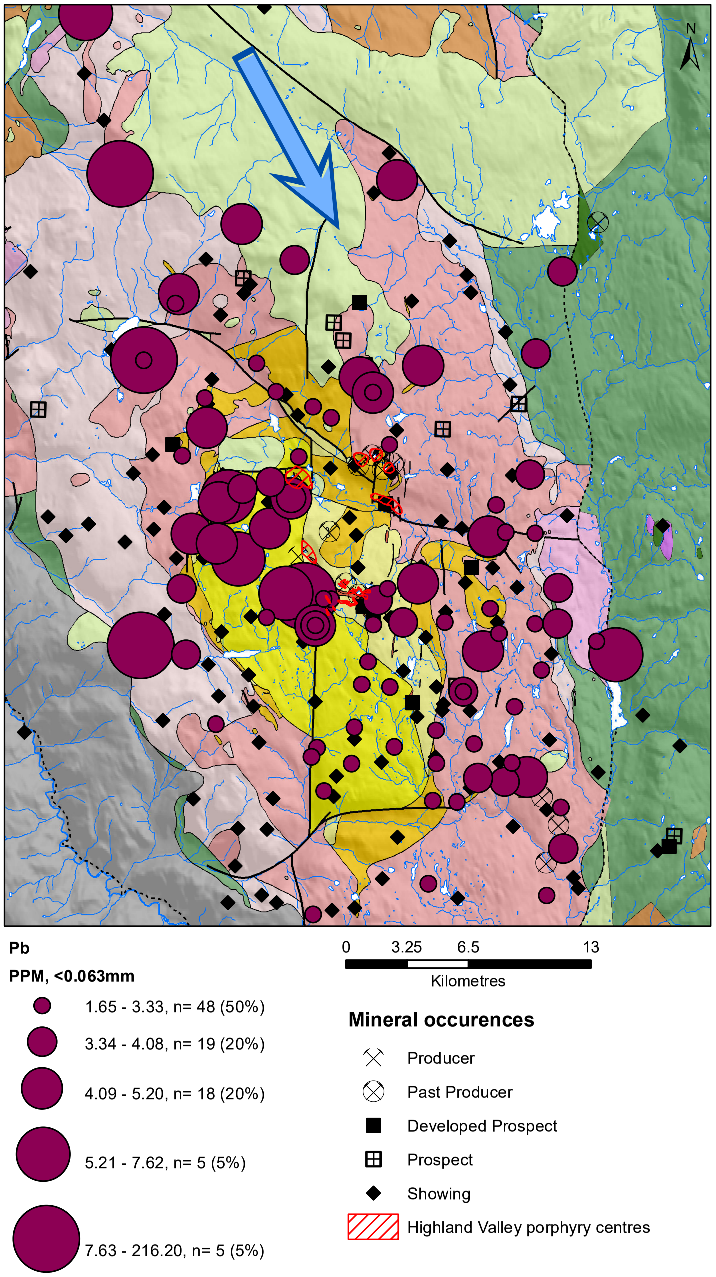

Fig. 17. The spatial distribution of Pb in the silt plus clay-sized fraction (<0.063 mm) of subglacial till. Ice flow direction indicated with blue arrow. Refer to Fig. 4 for bedrock geology legend.

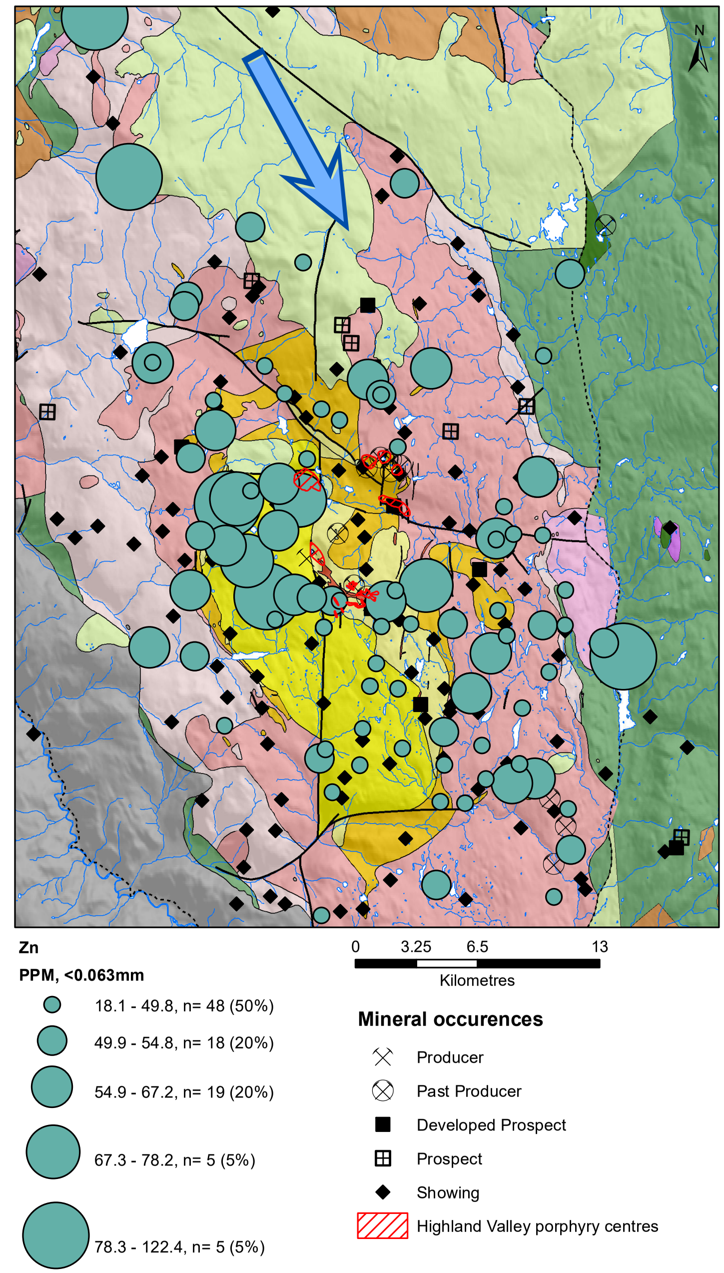

Fig. 18. The spatial distribution of Zn in the silt plus clay-sized fraction (<0.063 mm) of subglacial till. Ice flow direction indicated with blue arrow. Refer to Fig. 4 for bedrock geology legend.

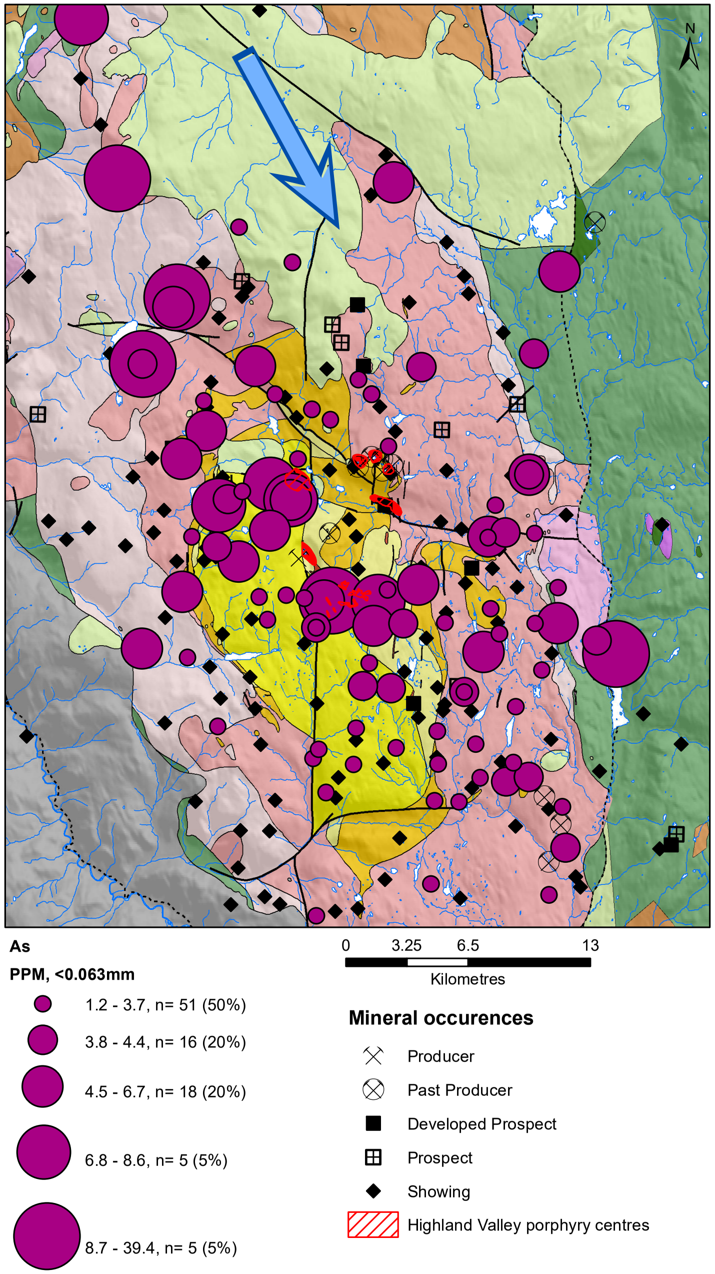

Fig. 19. The spatial distribution of As in the silt plus clay-sized fraction (<0.063 mm) of subglacial till. Ice flow direction indicated with blue arrow. Refer to Fig. 4 for bedrock geology legend.

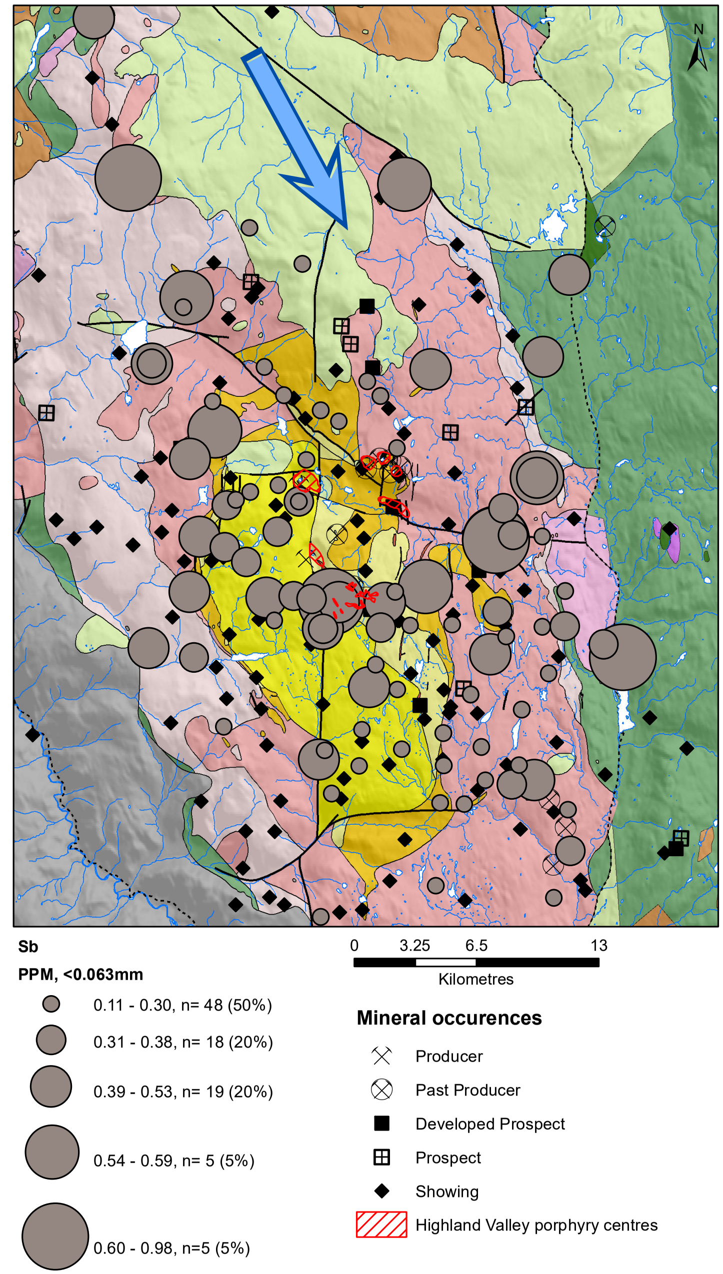

Fig. 20. The spatial distribution of Sb in the silt plus clay-sized fraction (<0.063 mm) of subglacial till. Ice flow direction indicated with blue arrow. Refer to Fig. 4 for bedrock geology legend.

we attribute their more diffuse spatial distribution (relative to the mapped bedrock domains) to glacial transport. A magmatic source of elevated Na_2O can be ruled out because porphyry deposits at Highland Valley mine are calc-alkaline, not alkalic.

6.3. Fe_2O_3, CaO, and Ni

Elevated Fe_2O_3, CaO, and Ni concentrations in till are peripheral to the central phases of the Guichon Creek batholith. They have statistically significant negative correlations to Cu values, and have an almost inverse spatial distribution to that of samples elevated in Cu and Mo. We rule out a relationship between Fe_2O_3 and distal pyrite alteration given that pyrite is only a minor constituent of the Highland Valley porphyry deposits (Byrne et al., 2013) and that elevated Fe_2O_3 (up to 8%) is distributed at the batholith scale. Elevated Fe_2O_3 in bedrock and in till could be related to propylitic alteration, given the size and fertility of the Guichon Creek batholith and that propylitic alteration can extend 10 to 15 km out from Highland Valley mine deposits (Fig. 4; Casselman et al., 1995; Byrne et al., 2013). Olade (1977) observed a similar relationship in bedrock where Fe_2O_3 and CaO values near the Bethlehem, JA, and Valley porphyry deposits increased outwards from the central mineralized core. Tills elevated in Ni and CaO values were likely derived from the more mafic intrusive phases along the batholith's periphery (e.g., Border phase, Fig. 4; Byrne et al., 2013) and/or from up-ice basalt flows of the Kamloops Group (Fig. 4, Ewing, 1981; Schiarizza and Preto, 1987). These mafic units could also be responsible for elevated Fe_2O_3 in tills, but a hydrothermal source seems more likely given that it is more widely distributed than CaO.

6.4. Pb, Zn, As, and Sb

These elements lack a statistically significant correlation with Cu values in till, but can locally have a similar spatial distribution to samples elevated in Cu and Mo. The group of samples with >90th percentile Pb and Zn values west of the Valley and Lornex porphyry deposits could reflect polymetallic vein mineralization. Till samples elevated in As and Sb are widely distributed (i.e., not clustered) and probably reflect dispersal from isolated bedrock sources.

6.5. Ag, Hg, and Mn

Ag, Hg, and Mn values in till do not reliably detect porphyry mineralization hosted by the Guichon Creek batholith. They are not statistically correlated to Cu values in till (except for Ag) and they have a diffuse or heterogeneous spatial distribution relative to Cu or Mo.

7. Summary and conclusions

Major oxide (Al_2O_3, CaO, Fe_2O_3, K_2O, Na_2O) and pathfinder element (Ag, As, Hg, Mn, Ni, Pb, Sb, Zn) determinations on the silt plus clay sized fraction of subglacial tills were analyzed statistically and spatially to assess their ability to detect porphyry Cu-Mo mineralization at the Highland Valley mine. A correlation matrix and PCA plots were produced to statistically compare their response with that of Cu in till, which is known to reflect the presence of buried mineralized bedrock. Sample locations and concentrations were plotted to assess the spatial relationship of elevated values with locations of known sources of porphyry mineralization at the Highland Valley mine and elevated concentrations of commodity elements in till (Cu and Mo).

The major oxides Al_2O_3, Fe_2O_3, K_2O, and Na_2O in till can detect drift-covered porphyry alteration and Cu-Mo mineralization hosted at the Highland Valley mine. Elevated Al_2O_3 and K_2O values in till could be related to zones of potassic alteration and/or to other mainly phyllosilicate alteration zones (e.g., chlorite-sericite, sericite, advanced argillic) that are more central to a porphyry system that also contain Cu-bearing minerals. Likewise, elevated Na_2O in till could be sourced from sodic-calcic alteration, derived from the deeper, higher-temperature porphyry system core at the Valley and Lornex deposits. Elevated Fe_2O_3 values in till are probably related to extensive propylitic alteration.

Pathfinder element concentrations in till can identify drift-covered porphyry Cu-Mo mineralization at the Highland Valley mine. The Valley deposit can be detected by till samples elevated in Pb, Zn, and As values, and the Lornex deposit by elevated Pb, Zn, As, and Sb values. Elevated Pb and Zn values occur in a cluster of samples west of these porphyry deposits and might record polymetallic vein mineralization.

Elevated CaO and Ni values in till could be related to different batholith phases or regional-scale bedrock units. They are likely derived from the more mafic margins of the Guichon Creek batholith (e.g., Border phase) and/or from basalt flows of the Kamloops Group exposed up ice-flow direction. Ag, Hg, and Mn values in till do not reliably detect large-scale porphyry mineralization hosted by the Guichon Creek batholith, nor do they have a coherent signal that can be related to a specific mapped bedrock unit.

Acknowledgments

We thank an anonymous reviewer for providing comments and suggestions that improved the manuscript. C. Shewchuk was supported by an Undergraduate Student Research Award from the Natural Sciences and Engineering Research Council (NSERC) of Canada and O.B Lian acknowledges support from an NSERC Discovery Grant.

References cited

Abdi, H., and Williams, L.J., 2010. Principal component analysis. Wiley Interdisciplinary Reviews: Computational Statistics, 2, 433-459.

Atkinson, N., Pawley, S., and Utting, D.J., 2016. Flow-pattern evolution of the Laurentide and Cordilleran ice sheets across west-central Alberta, Canada: implications for ice sheet growth, retreat and dynamics during the last glacial cycle. Journal of Quaternary Science, 31, 753-768.

Berger, B.R., Ayuso, R.A., Wynn, J.C., and Seal, R.R., 2008. Preliminary model of porphyry copper deposits. US Geological Survey Open-file Report, 1321, 55 p.

Bobrowsky, P.T., Kerr, D.E., Sibbick, S.J., and Newman, K., 1993.

Drift exploration studies, Valley copper pit, Highland Valley copper mine, British Columbia: Stratigraphy and sedimentology. In: Geological Fieldwork 1992, British Columbia Ministry of Energy, Mines and Petroleum Resources, British Columbia Geological Survey Paper 1993-01, pp. 427-438.

Bustard, A.L., and Ferbey, T., 2017. An index of base and precious metal regional-to property-scale subglacial till geochemical and mineralogical surveys in British Columbia. British Columbia Ministry of Energy, Mines and Petroleum Resources, British Columbia Geological Survey Open File 2016-2, scale 1:2,250,000.

Byrne, K., Stock, E., Ryan, J., Johnson, C., Nisenson, J., Alva Jimenez, T., Lapointe, M., Stewart, H., Grubisa, G., and Syroka, S., 2013. Porphyry Cu-(Mo) deposits in the Highland Valley district, south-central British Columbia. In: Logan, J.M., and Schroeter, T.G., (Eds.) Porphyry systems of central and southern British Columbia: Tour of central British Columbia porphyry deposits from Prince George to Princeton. Society of Economic Geologists, Field Trip Guidebook, Series 43, pp. 99-116.

Byrne, K., Lesage, G, Gleeson, S.A., and Lee, R.G., 2017. Large-scale sodic-calcic alteration around porphyry copper systems: examples from the Highland Valley Copper district, Guichon batholith, south-central British Columbia. In: Geoscience BC Summary of Activities 2016, Geoscience BC Report 2017-1, pp. 213–222.

Casselman, M.J., McMillan, W.J., and Newman, K.M., 1995. Highland Valley porphyry copper deposits near Kamloops, British Columbia: A review and update with emphasis on the Valley deposit. Canadian Institute of Mining, Metallurgy and Petroleum, 46, 142-158.

Chen, S., Plouffe, A., and Hattori, K., 2019. A multivariate statistical approach identifying the areas underlain by potential porphyry-style Cu mineralization, south-central British Columbia, Canada. Journal of Geochemical Exploration, 202, 13-26.

Clague, J.J., and Ward, B.C., 2011. Pleistocene glaciation of British Columbia. In: Ehlers, J., Gibbard, P.L., and Hughes, P.D., (Eds), Quaternary Glaciations–extent and chronology. Developments in Quaternary Sciences, 15, 563-573.

Cook, S.J., and Fletcher, W.K., 1993. Distribution and behaviour of platinum in soils, sediments and waters of the Tulameen ultramafic complex, southern British Columbia, Canada. Journal of Geochemical Exploration, 46, 279-308.

Cui, Y., Miller, D., Schiarizza, P., and Diakow, L.J., 2017. British Columbia digital geology. British Columbia Ministry of Energy, Mines and Petroleum Resources, British Columbia Geological Survey Open File 2017-8, 9 p. Data version 2018-04-05.

Ewing, T.E., 1981. Petrology and geochemistry of the Kamloops Group volcanics, British Columbia. Canadian Journal of Earth Sciences, 18, 1478-1491.

Ferbey, T., 2011. Till geochemistry of the Colleymount map area (093l/01), west-central British Columbia. British Columbia Ministry of Energy, Mines and Petroleum Resources, British Columbia Geological Survey Open File 2011-6, 51 p.

Ferbey, T., Arnold, H., and Hickin, A.S., 2013. Ice-flow indicator compilation, British Columbia. British Columbia Ministry of Energy, Mines and Petroleum Resources, British Columbia Geological Survey Open File 2013-06, scale 1:1,650,000.

Ferbey, T., Plouffe, A., and Bustard, A.L., 2016. Geochemical, mineralogical, and textural data from tills in the Highland Valley Copper mine area, south-central British Columbia. British Columbia Ministry of Energy, Mines and Petroleum Resources, British Columbia Geological Survey GeoFile 2016-11, 15 p.

Gazley, M.F., Collins, K.S., Roberston, J., Hines, B.R., Fisher, L.A., and McFarlane, A., 2015. Application of principal component analysis and cluster analysis to mineral exploration and mine geology. In: AusIMM New Zealand Branch Annual Conference, Dunedin New Zealand, 2015, pp. 131-139.

Hashmi, S., Ward, B.C., Plouffe, A., Leybourne, M.I., and Ferbey, T., 2015. Geochemical and mineralogical dispersal in till from the Mount Polley Cu-Au porphyry deposit, central British Columbia, Canada. Geochemistry: Exploration, Environment, Analysis, 15, 234-249.

Jolliffe, I., 2011. Principal component analysis. In: Lovric, M., (Ed.), International Encyclopedia of Statistical Science. Springer Berlin Heidelberg, pp. 1094-1096.

Kelley, K.D., Eppinger, R.G., Lang, J., Smith, S.M., and Fey, D.L., 2011. Porphyry Cu indicator minerals in till as an exploration tool: example from the giant Pebble porphyry Cu-Au-Mo deposit, Alaska, USA. Geochemistry Exploration Environment Analysis, 11, 321-334.

Lesage, G., Byrne, K., Morris, W.A., Enkin, R.J., Lee, R.G., Mir, R., and Hart, C.J., 2019. Interpreting regional 3D fault networks from integrated geological and geophysical data sets: An example from the Guichon Creek batholith, British Columbia. Journal of Structural Geology, 119, 93-106.

Levson, V.M., 2001. Regional till geochemical surveys in the Canadian Cordillera: sample media, methods and anomaly evaluation. In: McClenaghan, M.B, Bobrowsky, P.T., Hall, G.E.M. and Cook, S.J., (Eds.), Drift Exploration in Glaciated Terrain. The Geological Society, Special Publication 185, pp. 45-68.

Levson, V.M., 2002: Quaternary geology and till geochemistry of the Babine Porphyry Copper Belt, British Columbia (NTS 93 L/9,16, M/1, 2, 7, 8); British Columbia Ministry of Energy, Mines and Petroleum Resources, British Columbia Geological Survey Bulletin 110, 278 p.

Levson, V.M., Giles, T.R., Cook, S.J., and Jackaman, W., 1994. Till geochemistry of the Fawnie Creek map area (93F/03). British Columbia Ministry of Energy, Mines and Petroleum Resources, British Columbia Geological Survey Open File 1994-18, 173 p.

Lian, O.B., and Hickin, A.S., 2017. Origin and character of till and other diamictons and their applicability to mineral prospecting. In: Ferbey, T., Plouffe, A., and Hickin, A.S., (Eds.), Indicator Minerals in Till and Stream Sediments of the Canadian Cordillera. Geological Association of Canada Special Paper Volume 50, and Mineralogical Association of Canada Topics in Mineral Sciences, 47, pp. 109-127.

Logan, J.M., and Mihalynuk, M.G., 2014. Tectonic controls on Early Mesozoic paired alkaline porphyry deposit belts (Cu-Au ± Ag-Pt-Pd-Mo) within the Canadian Cordillera. Economic Geology, 109, 827-858.

Mao, M., Rukhlov, A.S., Rowins, S.M., Spence, J., and Coogan, L.A., 2016. Apatite trace element compositions: A robust new tool for mineral exploration. Economic Geology, 111, 1187-1222.

Mao, M., Rukhlov, A.S., Rowins, S.M., Hickin, A.S., Ferbey, T., Bustard, A., Spence, J., and Coogan, L.A., 2017. A novel approach using detrital apatite and till geochemistry to identify covered mineralization in the TREK area of the Nechako Plateau, British Columbia. In: Ferbey, T., Plouffe, A., and Hickin, A.S., (Eds.), Indicator Minerals in Till and Stream Sediments of the Canadian Cordillera. Geological Association of Canada Special Paper Volume 50, and Mineralogical Association of Canada Topics in Mineral Sciences Volume 47, pp. 191-243.

McClenaghan, M.B., Plouffe, A., McMartin, I., Campbell, J.E., Spirito, W.A., Paulen, R.C., Garrett, R.G., and Hall, G.E.M., 2013. Till sampling and geochemical analytical protocols used by the Geological Survey of Canada. Geochemistry: Exploration, Environment, Analysis, 13, 285-301.

McMillan, W.J., Anderson, R.G., Chan, R., and Chow, W., 2009. Geology and Mineral Occurrences (minfile), Guichon Creek Batholith and Highland Valley porphyry copper district, British Columbia. Geological Survey of Canada, Open File 6079, scale 1:100,000 and 1:150,000.

Miller, J.K., 1984. Model for clastic indicator trains in till. In: Prospecting in Areas of Glaciated Terrain, Institute of Mining and Metallurgy, London, pp. 69-77.
Nelson, J., Colpron, M., and Israel, S., 2013. The Cordillera of British Columbia, Yukon and Alaska: tectonics and metallogeny. In: Colpron, M., Bissig, T., Rusk, B., and Thompson, J.F.H., (Eds.), Tectonics, Metallogeny, and Discovery-the North American Cordillera and similar accretionary settings. Society of Economic Geologists, Special Publication 17, 53-109.
Olade, M.A., 1977. Major element halos in granitic wall rocks of porphyry copper deposits, Guichon Creek batholith, British Columbia. Journal of Geochemical Exploration, 7, 59-71.
Panteleyev, A., 1995. Porphyry Cu+/-Mo+/-Au. In: Lefebure, D.V., and Ray, G.E., (Eds.), Selected British Columbia Mineral Deposit Profiles, Volume 1-Metallics and Coal. British Columbia Ministry of Employment and Investment, British Columbia Geological Survey Open File 1995-20, pp. 87-92.
Plouffe, A., and Ballantyne, S.B., 1993. Regional till geochemistry, Manson River and Fort Fraser area, British Columbia (93K, 93N), silt plus clay and clay size fractions. Geological Survey of Canada, Open File 2593, 210 p.
Plouffe, A., and Williams, S.P., 1998. Regional till geochemistry, gold and pathfinder elements, northern Nechako River, British Columbia. Geological Survey of Canada, Open File 3687, scale 1:400,000.
Plouffe, A., and Ferbey, T., 2017. Porphyry Cu indicator minerals in till: A method to discover buried mineralization. In: Ferbey, T., Plouffe, A., and Hickin, A.S., (Eds.), Indicator Minerals in Till and Stream Sediments of the Canadian Cordillera. Geological Association of Canada Special Paper Volume 50, and Mineralogical Association of Canada Topics in Mineral Sciences Volume 47, pp. 129-159.
Plouffe, A., and Ferbey, T., 2018. Surficial geology of the Highland Valley copper mine area (Parts of NTS 092I/06, 7, 10 and 11), British Columbia. British Columbia Ministry of Energy, Mines and Petroleum Resources, British Columbia Geological Survey Geoscience Map 2018-01, scale 1:50,000.
Plouffe, A., Ferbey, T., Hashmi, S., and Ward, B.C., 2016. Till geochemistry and mineralogy: vectoring towards Cu porphyry deposits in British Columbia, Canada. Geochemistry: Exploration, Environment, Analysis, 16, 213-232.
R Core Team, 2019. R: A Language and Environment for Statistical Computing. R Foundation for Statistical Computing, https://www.R-project.org/. Last accessed September 2019.
Roy, B., and Clowes, R.M., 2000. Seismic and potential-field imaging of the Guichon Creek batholith, British Columbia, Canada, to delineate structures hosting porphyry copper deposits. Geophysics, 65, 1418-1434.
Schiarizza, P., and Preto, V.A., 1987. Geology of the Adams Plateau-Clearwater-Vavenby area. British Columbia Ministry of Energy, Mines and Petroleum Resources, British Columbia Geological Survey Paper 1987-2, 89 p.
Sillitoe, R.H., 2010. Porphyry copper systems. Economic Geology, 105, 3-41.
Sinclair, W.D., 2007. Porphyry deposits. In: Goodfellow, W.D., (Ed.), Mineral Deposits of Canada: A Synthesis of Major Deposit-Types, District Metallogeny, the Evolution of Geological Provinces, and Exploration Methods. Geological Association of Canada, Mineral Deposits Division, Special Publication No. 5, pp. 223-243.
Spirito, W., McClenaghan, M.B., Plouffe, A., McMartin, I., Campbell, J.E., Paulen, R.C., Garrett, R.G., and Hall, G.E.M., 2011. Till sampling and analytical protocols for GEM projects: from field to archive. Geological Survey of Canada, Open File 6850, 83 p.
Wedepohl, K.H., 1995. The composition of the continental crust. Geochimica et Cosmochimica Acta, 59, 1217-1232.

Generating photogrammetric DEMs in the field from remotely piloted aircraft systems

Easton A. Elia[1] and Travis Ferbey[1, a]

[1] British Columbia Geological Survey, Ministry of Energy, Mines and Petroleum Resources, Victoria, BC, V8W 9N3
[a] corresponding author: Travis.Ferbey@gov.bc.ca

Recommended citation: Elia, E.A., and Ferbey, T., 2020. Generating photogrammetric DEMs in the field from remotely piloted aircraft systems. In: Geological Fieldwork 2019, British Columbia Ministry of Energy, Mines and Petroleum Resources, British Columbia Geological Survey Paper 2020-01, pp. 189-200.

Abstract

Remotely piloted aircraft systems (RPAS) can be used in the field to acquire air photos which can subsequently be used to produce digital elevation models (DEM) and orthomosaics. In this study, we examined if field-generated photogrammetric DEMs in a remote, sparsely vegetated mountainous region of north-central British Columbia are of adequate resolution to guide surficial geology mapping. Using a quadcopter RPAS with real-time kinematic (RTK) positioning, we conducted 16 flights (more than 150 line-km), taking photographs with a visible-light RGB digital camera equipped with a 1-inch CMOS sensor and mechanical shutter. Once programmed using flight-planning software, the aircraft flew itself although, as required by federal regulations, we maintained continuous visual line-of-sight. The aircraft flew at a speed of 4 m/s, at heights of less than 120 m above ground, and with a line spacing that gave 70% horizontal overlap (side lap) and 80% vertical overlap (end lap). We processed the air photos in the field using structure from motion (SfM) photogrammetry to create topographic DEMs. With resolutions of <10 cm/pixel, these DEMs rival those produced using lidar in unvegetated areas. Easy to acquire, affordable, and immediately accessible, the DEMs provided details in near real-time about surficial deposits that field crews would not otherwise have gained. Not only did the DEMs help us better define deposit types, they enabled us to gather data on movement of glaciers during the Late Wisconsinan by highlighting landform-scale streamlined features that could not be identified on air photos nor measured on the ground.

Keywords: Remotely Piloted Aircraft System (RPAS), Unmanned Aerial Vehicle (UAV), drone, photogrammetry, Digital Elevation Model (DEM), Agisoft Metashape Professional, DJI Phantom 4 Pro, Real-time Kinematic, surficial geology

1. Introduction

Remotely piloted aircrafts (RPAs) are defined as any navigable aircraft where a pilot is not onboard (Transport Canada, 1996). More commonly, RPAs are referred to as drones, unmanned aerial vehicles (UAV), or unmanned aircraft systems (UAS; Carrivick et al., 2013; Niedzielski, 2018). In the last five years, remotely piloted aircraft system (RPAS) technology has progressed to a level where publication-quality data can be captured by small, commercially available systems (Chabot, 2018). The use of RPASs in the field has become more common as user-friendly, commercially available aircraft systems and high-performance portable computers have become available. RPAS and photogrammetric technology can now be used as a complete, self-supported package, deployable using small, one- or two-person crews. Current photogrammetry software does not require the use of internet or office resources, a prerequisite to any technology that is to be used in the field. High processing speeds allow dense photogrammetry datasets to be obtained and processed in near-real time. By incorporating RPAS technology in a field program, scientists can access more information in remote locations.

In this study, we test if field-generated photogrammetric DEMs in a remote, sparsely vegetated mountainous region are of adequate resolution to guide geologic mapping. To support ongoing surficial and bedrock (Ootes et al., 2019, 2020) mapping projects, in the Hogem batholith area of north-central British Columbia (Fig. 1), we flew 16 RPAS surveys, testing if the constructed DEMs provided significant insights that otherwise might have been missed. Herein we report on two of these surveys focussed on surficial deposits. Not only, in both cases, did the DEMs help us better define deposit types, in one case they enabled us to gather data on movement of the Late Wisconsinan Cordilleran Ice Sheet by highlighting streamlined features that could not be identified on air photos nor measured on the ground.

2. Background

2.1. Remotely Piloted Aircraft Systems (RPAS)

Rapid advancement in RPAS and payload technology is contributing to dramatic changes in field-based remote sensing. Satellites and piloted aerial surveys have been major contributors to imagery for geological mapping since the late 1950s (Hansman and Ring, 2019). Although these methods produce high-quality imagery, they are time consuming or expensive (Hansman and Ring, 2019). Miniaturization of aircraft and sensors has led to small, affordable, and commercially available RPASs becoming more common as tools in scientific research and industry activity (Chabot, 2018). Early versions of RPA have wing spans of several metres and require a highly trained pilot to fly. Today, RPA pilots can fit

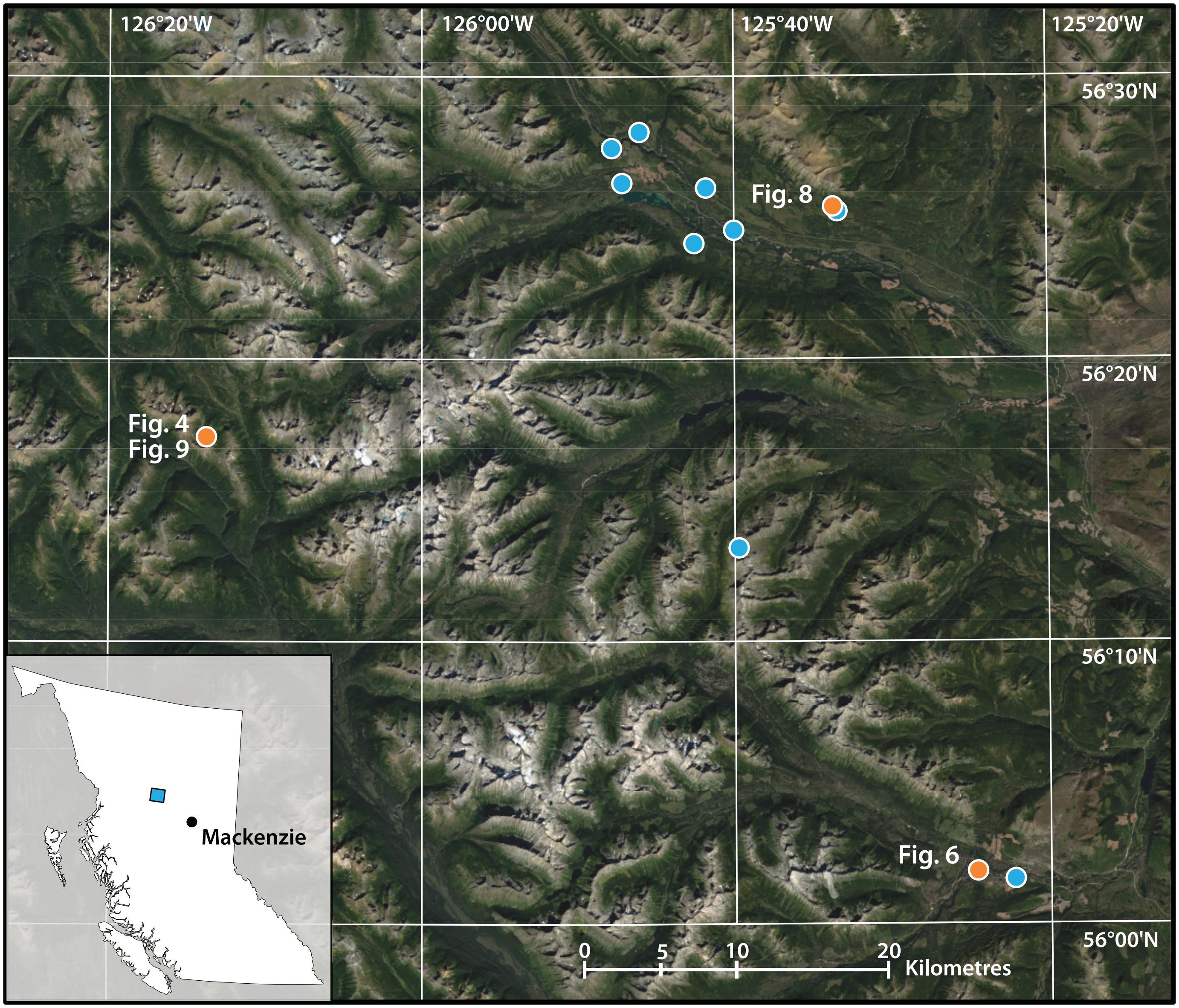

Fig. 1. Remotely piloted aircraft system flights conducted in the Hogem batholith region. Location of RPAS air photo flights are shown with blue points. Locations of case study flights are shown with orange points. Multiple flights conducted from the same take off location are represented by a single point.

an aircraft into their backpack and fly the machine with little training. Images acquired by an RPA are more affordable then most aerial imaging techniques and the time required for planning, capturing, and processing is faster than most traditional methods (Carrivick et al., 2013). An inexpensive RPA equipped with an RGB camera can be used to provide a new aerial perspective to geologists and access places that are impossible or unsafe to reach by foot. Areas like cliff faces and steep ridges can be safely and easily accessed, acquiring images within metres of the ground without the interference caused by downwash of conventional helicopter rotors. Images captured by an RPAS can be used as stand-alone products, viewed in stereo, or can be manipulated using photogrammetry software.

Multiple rotor RPASs constitute the latest advances in remotely piloted aircraft. With four rotors providing effective lift and maneuverability, quadcopters have many advantages over other RPAs including their ability to carry heavy payloads, hover in position through heavy winds, complete a vertical take off and landing (VTOL), and produce high-quality, precisely located aerial photos (Carrivick et al., 2013). Quadcopter RPAs also contain an onboard computer used for autopilot capabilities, allowing the RPA to take off, fly, and land with little input from the pilot (Carrivick et al., 2013). Onboard flight assistance systems help maintain stable flight and avoid collisions with the ground and other static objects. Using flight-planning software, specific survey grids can be constructed, and an area can be flown on autopilot following a designed flight path. However, quadcopters are not the only RPASs capable of remote sensing and photogrammetry. A range of single propeller, multirotor (e.g., octocopter) and glider RPAs are also available.

All RPASs used for conducting aerial surveys are equipped with GPS receivers that collect spatial information associated for each photograph. Real-time kinematic (RTK) positioning is a method used to enhance the precision of data collected from Global Navigation Satellite System (GNSS), a satellite-based system with global coverage. The USA's GPS GNSS is the most known, but Russia (GLOSNASS), the European Union (Galileo), and other countries have deployed and maintain their own GNSS. The satellites in each of these systems form an Earth-orbit constellation, allowing multiple satellites to be in range of a receiver at all times, thereby increasing accuracy and reliability. An RTK base station receives spatial data from GNSS satellites, calculates positional corrections based on carrier wave phase, and forwards corrections wirelessly to the RPA in real-time. The RPA uses these corrections to improve in-air positioning. Because of this, each RPA photo has a very precise 3-dimensional coordinate associated with it. Another benefit of using RTK technology is that, in specific situations, it eliminates the need for ground control points (GCPs), which are targets placed throughout the survey area to provide accurate positional information. Eliminating GCPs reduces the amount of set-up time for each survey, as well as time required for post-processing.

RPASs can provide high-quality, cost-effective, imagery ideally suited to multitemporal surveys in regions undergoing continuous changes that require monitoring by repeated surveys. For example, the Newfoundland Geological Survey has been using RPASs for several years to assess coastline stability and hazards (Irvine et al., 2018). Other examples include monitoring rock glacier movement (Kaufmann et al., 2018), investigating landslide topography (Niethammer et al., 2010), repeat characterization of landslide-prone areas (Rossi et al., 2018) and soil erosion studies (D'Oleire-Oltmanns et al., 2012). RPAs can also be used to construct digital bedrock outcrop models, extracting structural information, allowing the configuration of dipping rock units to be assessed and measured in the digital environment (Zahm et al., 2016). Some of the challenges around RPAS use in the field include: the limited number of sensors and aircrafts available on the market; country-specific above ground level (AGL) and visual line-of-sight regulations; and field logistics related to recharging multiple, high-capacity batteries.

2.2. Photogrammetric DEMs

Standard photographs acquired by an RPAS can be uploaded onto a high-performance computer to generate a photogrammetric digital elevation model (DEM), which is a representation of a surface created by processing multiple overlapping RGB photographs. Photogrammetry software extracts a large amount of information per image to place and orient topographical data in real space, producing a DEM (Hansman and Ring, 2019). The photogrammetric process begins with the identification of key points in each uploaded photo. These key points can number in the 10,000s per image and are placed in locations that can be recognized in each overlapping photograph (Hansman and Ring, 2019). Modern photogrammetry software calculates key points by a structure from motion (SfM) algorithm. SfM photogrammetry uses images taken at varying distances and angles to construct models, as apposed to a systematic grid required for traditional photogrammetry (Johnson et al., 2014; Hansman and Ring, 2019). Images acquired with RTK positioning provide SfM photogrammetry software accurate photograph locations, allowing models to be produced faster and more accurately. The position of overlapping key points is triangulated in multiple photographs to create a single tie point, stitching the photographs together. The photogrammetry software identifies an x-y-z coordinate for each tie point and places it into real space. Once a large number of tie points are positioned, a manipulatable point cloud model representing the geometry of the captured scene is created (Hansman and Ring, 2019). Spaces between tie points can be interpolated, leading to the generation of a DEM. The resultant DEM can be manipulated in a geographic information system (GIS) to produce hill-shaded models and a range of other products.

Digital elevation models can be produced using other methods and sensors including light detection and ranging (lidar). Lidar is an active, aircraft mounted sensor that emits a laser pulse (upwards of 50,000 Hz) and records the laser's reflected travel times. Last returns in a lidar point cloud can represent laser light reflected off the Earth's surface, beneath vegetation or tree canopies. These last returns are used to produce a bare-Earth DEM, or a model of the Earth's surface without vegetation. In contrast, photogrammetric DEMs are produced using reflected, visible light photography and cannot produce a bare-Earth model in fully treed areas. However, in areas of sparse ground cover, photogrammetric DEMs can rival lidar-generated DEMs (Johnson et al., 2014). Some SfM photogrammetry software can recognize trees and eliminate them from the final DEM. This is useful for regions with sparse tree cover. When producing models of heavily forested regions, so little of the ground is imaged that large holes exist in the DEM where the forest canopy once was. For this reason, bare-Earth photogrammetric DEMs can only be produced in regions with low levels of vegetation.

3. Geologic setting

In the Hogem ranges of north-central British Columbia, about 200 km northwest of Mackenzie (Fig. 1), our study area is a steep mountainous terrain with northward facing cirques and deep U-shaped valleys (Holland, 1976). The area is remote and road access is limited to larger valleys with a history of logging activity. Valley bottoms commonly contain thick and laterally extensive glaciofluvial deposits, and hummocky deposits that range in height from 1-10 m and extend for 100s of metres. Undulating and streamlined till, and colluvial aprons and fans, with sparse bedrock outcrop, are common on valley sides adjacent to glaciofluvial deposits. Cirques and arêtes are predominant in alpine regions, locally containing remnant ice, with intervening low-gradient slopes or plateaus consisting of felsenmeer. Although bedrock outcrop is exposed continuously in these high elevation settings, it is difficult to find glacially polished or striated outcrop used to reconstruct ice flow history.

The Hogem batholith is a composite intrusive body consisting mainly of felsic to mafic plutonic rocks that show significant local variation (for details see Ootes et al., 2019; Ootes et al., 2020). The batholith has high potential to host syngenetic porphyry-style Cu (±Au, Ag, Mo) mineralization and quartz vein-hosted concentrations of precious and base-metals. Northwest of the study area (70 km) is the past producing Kemess mine (calc-alkaline porphyry Cu-Mo-Au) and to the south (10 km) the Lorraine developed prospect (porphyry alkalic Cu-Au).

Air photo surveys were flown in areas of sparse to no vegetation such as cut blocks, cirques, mountain tops, and areas with burned or disease-infected trees. Recent, unplanted, cut blocks are ideal to conduct an RPAS survey due to their lack of vegetation, allowing clearer photos to be taken of the ground surface, but also because they allow a large area to be covered while maintaining visual line-of-sight (VLOS) with the aircraft.

4. Methods

4.1. Air photo acquisition

A DJI Phantom 4 Pro RTK RPAS was used to conduct each survey (Fig. 2). This RPAS is equipped with a fixed payload RGB camera that has a 20 mega-pixel, 1-inch CMOS sensor, and a mechanical shutter. A mechanical shutter does not produce wobble associated with a rolling shutter, commonly known in photogrammetry as the ‘jello effect’. The camera is attached to the airframe by a three-axis gimbal, which provides image stability and allows for in-flight adjustment of camera angle. Practical flight time for the Phantom 4 Pro RTK is approximately 25 minutes per battery. Ground control points were not used during our surveys. The positional accuracy of the Phantom 4 Pro RTK, as stated by the manufacturer, is approximately 2.00 cm vertically and 1.20 cm horizontally, when flying at 33 m above ground level.

All survey areas were accessed by truck or helicopter. We selected sites that had a surficial or bedrock geology unit of interest, lacked trees, and permitted us to maintain VLOS while flying within 120 m above ground level. The outer bounds of the survey area were first flown without using autopilot. The track recorded in DJI GS RTK flight-planning software was then used to design the survey, which was flown using the autopilot function (Fig. 3). Missions were flown between 50 m and 100 m AGL, with 70% horizontal overlap (side lap) and 80% vertical overlap (end lap). Aircraft speed was maintained at 4.0 m/s to minimize distortion caused by a moving camera. Survey flight times ranged from 20 to 60 minutes, including initial set up, mission design, and completion. Surveyed areas ranged from 15,810 to 424,251 m^2. Precautions were not taken for light conditions or sun altitude.

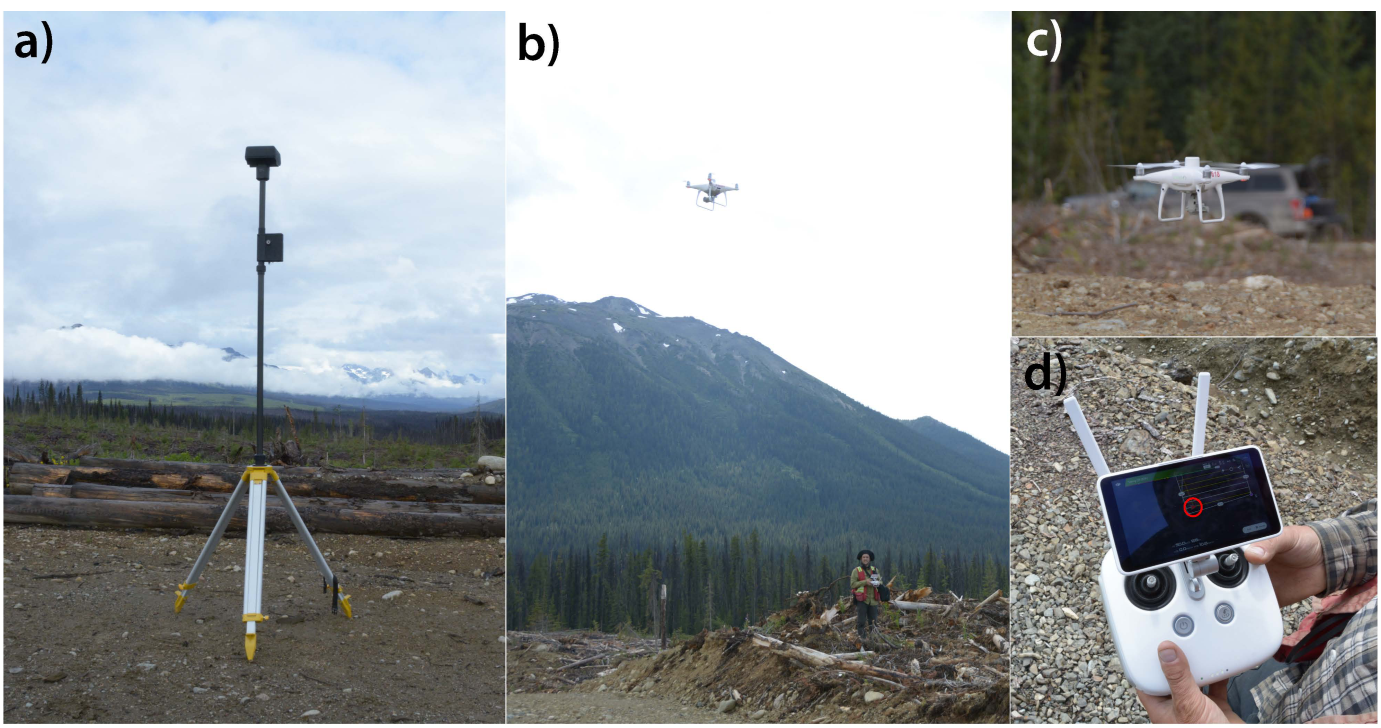

Fig. 2. Equipment used in the field that makes up the RPAS. **a)** RTK mobile base station. **b)** DJI Phantom 4 Pro RTK being operated remotely by pilot on-ground. **c)** DJI Phantom 4 Pro RTK in flight with the camera facing away from the viewer. **d)** DJI Remote control, with DJI flight-planning software DJI GS RTK on screen, showing location of RPAS (red circle) while conducting an air photo mission autonomously in auto pilot mode following pre-planned flight lines.

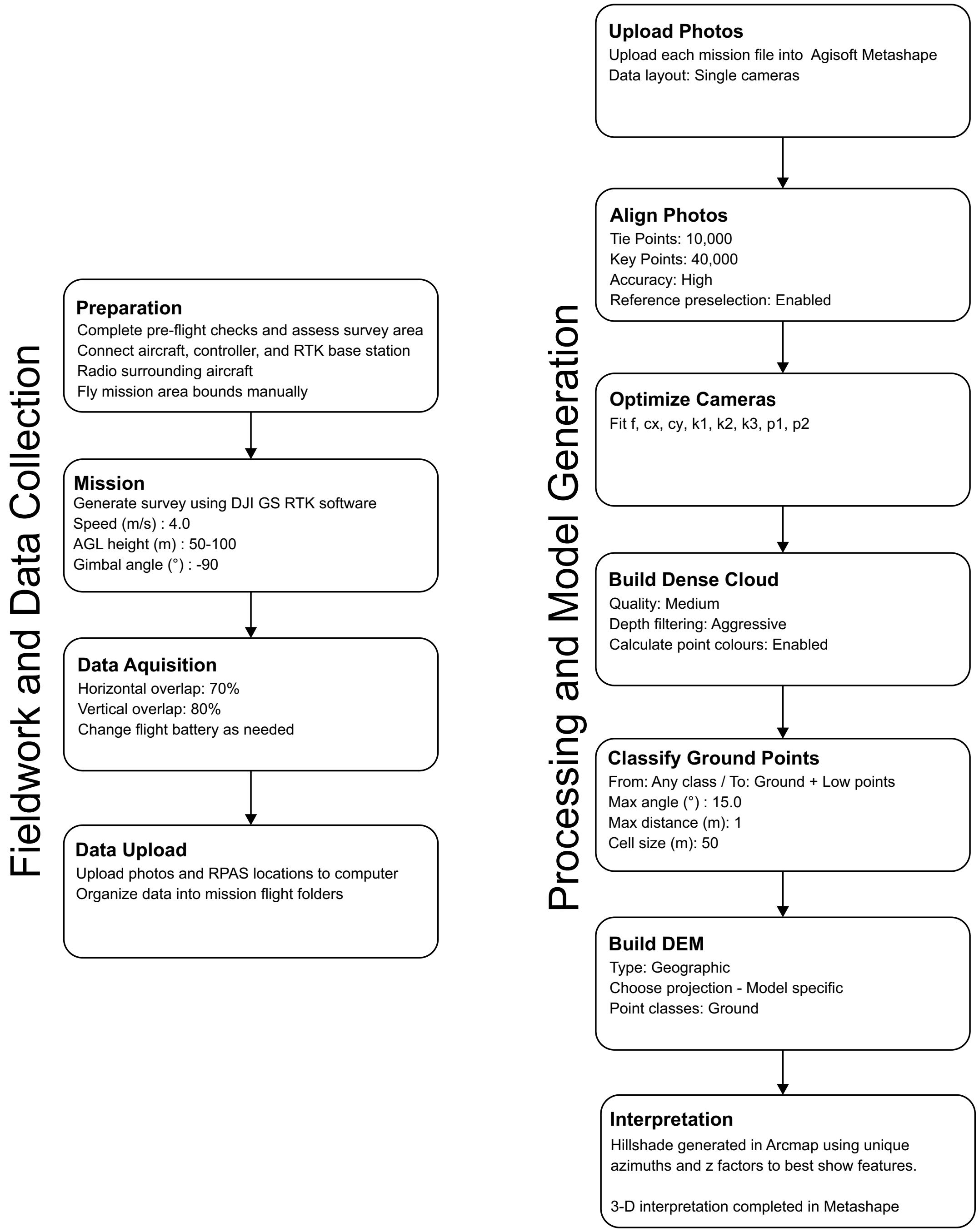

Fig. 3. Flight and data workflow for typical generation of photogrammetric DEMs.

4.2. Data processing

Agisoft Metashape Professional was used in the field to produce photogrammetric DEMs from air photos acquired by the RPAS. Metashape is a simple, yet powerful, application intended for a variety of 3D modelling purposes and is not limited to constructing DEMs. One advantage of Metashape for remote field work, is that it is not built on cloud processing; all processing is done locally on a personal computer running the software. Metashape is also considered a complete package, allowing a DEM to be generated solely using a single application. Other DEM production software requires switching between multiple programs for each step in the generation process (Johnson et al., 2014). Metashape's batch processing feature allows parameters for each step to be specified beforehand. Using this feature, a product is generated from start to finish without requiring the user to watch over the process.

Metashape works efficiently with RTK data, importing all metadata associated with RPA position, pitch, roll, and yaw for each captured photograph. Processing was completed on a laptop running a 2.2 GHz Intel Core i7 CPU, 32 GB RAM, and an NVIDIA Quadro P3200 graphics card. Processing a survey with 300 individual photographs, 4.5 x 10^5 sparse points, and 4.0 x 10^7 dense points at a high-resolution takes approximately 3 hours. Eight years ago, a survey with a similar number of dense points would take 7 to 56 hours on a high-end desktop computer using similar SfM processing techniques (Westoby et al., 2012).

When working to generate a photogrammetric DEM, three other products are produced: a dense point cloud, textured mesh, and orthomosaic. A dense point cloud is created from further interpolation of each photo, adding more calculated points to the sparse point cloud model. This produces a dynamic, three-dimensional model constructed from millions of individual points, each with an assigned RGB colour. A dense point cloud can be manipulated in 3D space and viewed from any perspective (Fig. 4). Although a dense point cloud does not replace a true 3-dimensional model, it can be generated very quickly to gain a rudimentary understanding of topography. An orthomosaic is a geometrically rectified compilation of aerial images that allows measurements to be taken directly from the image in real-world units. High-resolution orthomosaics are an ideal base layer for mapping large-scale geologic features. A textured mesh is a true 3-dimensional model, with a triangulated network of points and a solid coloured surface. The solid surface fills the holes produced in point cloud models.

5. Results

We conducted 16 individual surveys using the Phantom 4 Pro RTK RPAS to capture high-resolution, nadir imagery. The resultant images were processed in the field, producing photogrammetric DEMs and point cloud models for each mission. Below we present the results from two of these missions. One was flown over hummocky terrain, the other over glacially streamlined terrain (Table 1).

Table 1. Summary of RPAS air photo survey parameters.

	Hummocky terrain	Glacially streamlined terrain
Flight time	50 min	30 min
Processing time	4 hr	2 hr
Area	386,100 m^2	11,500 m^2
Photos	676	277
DEM resolution	9.66 cm/pixel	9.09 cm/pixel

5.1. Hummocky terrain

In this terrain, hummocks that are 1-10 m high extend for 100s of metres and are mantled by large (up to 1 m) boulders (Fig. 5). On the basis of roadside exposure, we originally considered that these are stagnant ice glaciofluvial sand and gravel deposits. Most of the standing trees in the area were recently burned and lack foliage.

We created a photo density map (Fig. 6a) showing the RPA path (northeast-southwest) and the degree of redundancy in image collection. Each black point represents the location of an image and the colour ramp shows the number of adjacent overlapping photos. The density of photos corresponds to point density in cloud models (Johnson et al., 2014). A greater point density results in higher resolution models, and more redundancy in the data allows positions to be more accurately represented. For nearly the entire extent of the surveyed area, >9 overlapping photos were used to create the dense point cloud.

Metashape's 'classify points' function was applied to the dense point cloud to identify low-lying points and ground points, based on maximum slope of changing terrain, distance between points, and cell size of classified features. Unclassified and low-lying point classes were subtracted from the dense point cloud and the resultant photogrammetric DEM represents a pseudo bare-earth model, consisting of solely ground points (Figs. 6b, c). The central portion of the DEM, shown in detail in Figure 6b, is clean where vegetation consists of standing dead and fallen trees. The regional DEM has a rougher texture where low-lying vegetation or trees could not be completely removed from the dense point cloud (e.g., northeast and southeast corners) and is overly smoothed where bare earth could not be imaged over entire regions of dense forest (e.g., east margin). This is due to the software building a DEM with very few remaining points. Without many points to reference, the software produces a low-resolution, smoothed model.

The photogrammetric DEM extended ground observations to a much larger area and it also allowed us to recognize a second deposit type. Using the DEM, we found that the hummocky glaciofluvial sands and gravels we considered stagnant ice deposits at road exposures extend northeast for >500 m and southwest for >200 m. In addition however, in the western part of the photogrammetric DEM are features with a channel-like geometry that were not observed from the road. These are likely glaciofluvial sediments that were deposited by meltwater systems. Thus, based on the DEM, we now recognize that the survey area includes two genetically distinct deposits, stagnant ice hummocky drift and a glaciofluvial blanket.

5.2. Glacially streamlined terrain

This survey was conducted in a recent forestry cut block underlain by till that we originally considered a veneer or blanket deposit, and local bedrock outcrop. Most of the timber left from logging is stacked in slash piles along the cut-block periphery. Nonetheless, the cut-block floor is still obscured by stumps, leftover woody debris, and saplings (Fig. 7a). Although topographic relief is subtle (<1 m), discontinuous positive linear features extend through the cut block. Because of scale and tree cover, these features cannot be recognized in 1:40,000-scale black and white air photographs (Fig. 7b). Furthermore, because of their low relief, the geometry and orientation of the features are difficult to establish on the ground. We flew the survey to investigate these features and combined the survey with ground observations, particularly near small (~2 m^2) bedrock outcrops.

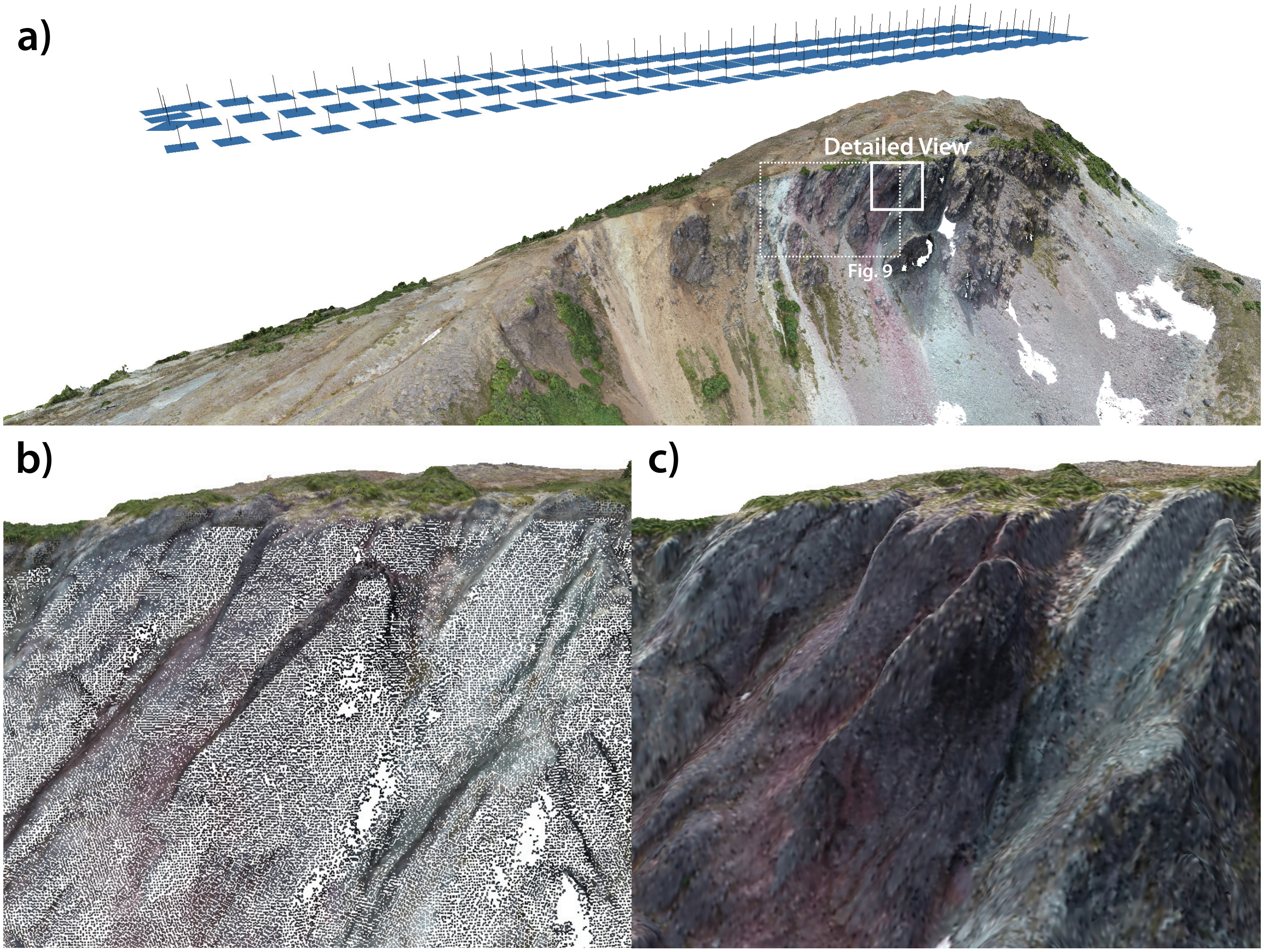

Fig. 4. Point cloud and textured model of a bedrock ridge. **a)** Dense point cloud model. Blue rectangles over ridge represent air photo locations, with black vertical lines oriented normal to the image plane. **b)** Detailed view of dense point cloud model. Each point has an x,y, and z coordinate and is coloured based on RPAS air photos. **c)** Detailed view of textured mesh model. This image covers the same area represented in b), but here the dense point cloud model is draped with a raster image, thereby removing empty spaces between points. See Figure 1 for location.

Fig. 5. Oblique photograph of hummocky terrain in RPAS survey area. Photo taken from RPA.

The dense point cloud was classified into ground points, low points, and unclassified points using Metashape. The unclassified points and low points were not used to produce the final DEM surface (Fig. 8). The area to the north and south of the DEM was cropped due to being heavily forested and at a poor resolution. The DEM was then imported into ArcMap, where a hillshade model was created using a unique azimuth and altitude to best display the streamlined terrain.

The photogrammetric DEM produced for this region shows that the discontinuous positive linear features identified on the ground, are fully continuous for up to 75 m, approximately 10 m wide and 1 m high (Fig. 8). Highlighted in the central part of the DEM (Fig. 8), parallel ridges are organized en echelon, oriented east-southeast, and can have bedrock outcropping on their western ends. In plan view, these features have longitudinal asymmetry, tapering from outcropping bedrock on their stoss

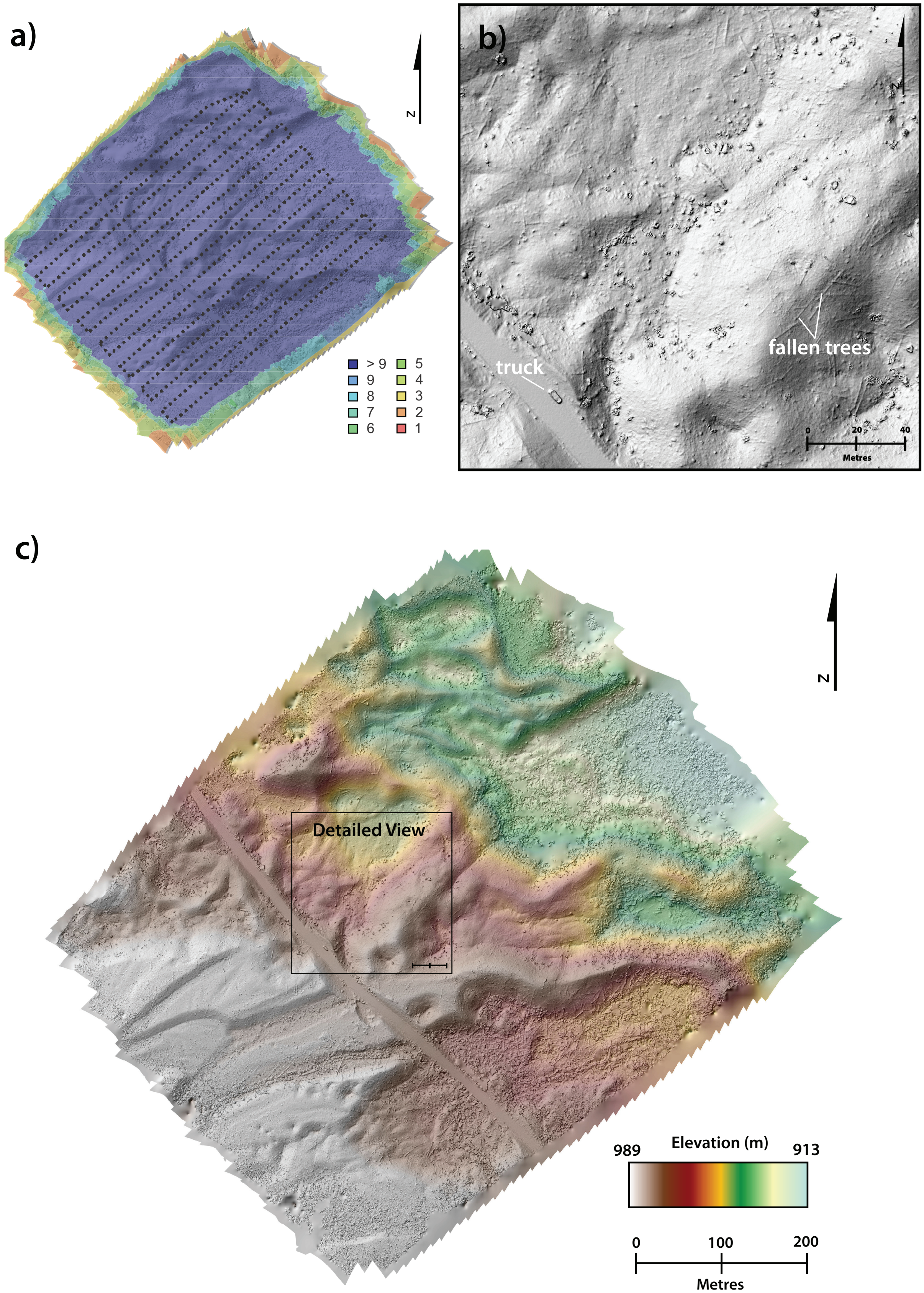

Fig. 6. Hummocky terrain survey area. **a)** Photo density model. Each point represents a RPAS air photo location, with each colour representing the number of overlapping photos used to create the photogrammetric DEM. See Figure 1 for location. **b)** Detailed view of survey area. Fallen trees are represented by linear, criss-crossing objects. **c)** Photogrammetric DEM of ice contact and channelized glaciofluvial sediments.

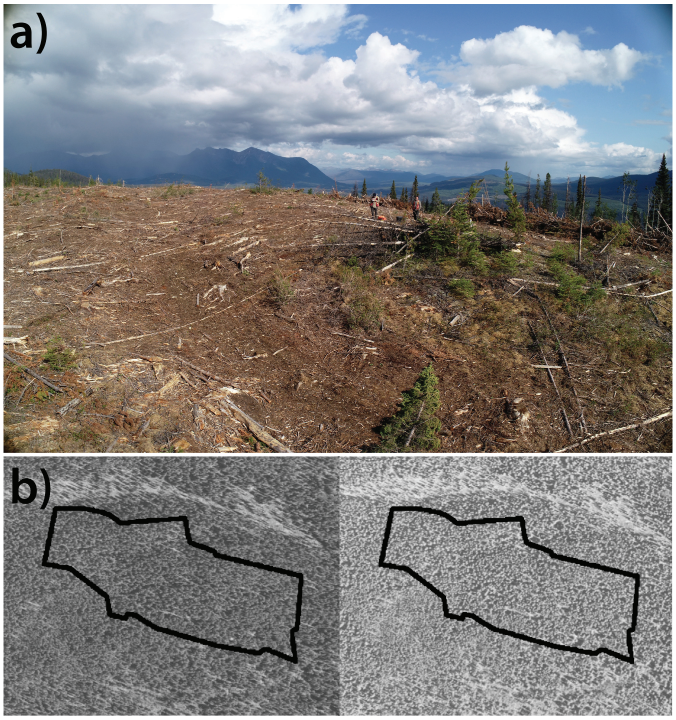

Fig. 7. a) Oblique photograph of glacially streamlined terrain. Photograph taken from RPA. **b)** Black and white, 1:40,000-scale air photo stereopair of same area. Tree canopy masks subtle streamlined features observable in photogrammetric DEM.

end to their leeward side composed of a diamicton. Crag and tail ridges are unidirectional, glacially streamlined landforms created by the deposition of sediments on the lee side of an eroded bedrock obstacle. Although the features seen in the DEM are low relief, they are interpreted as small crag and tail ridges and their orientations indicate east-southeast movement of glaciers through the region during the Late Wisconsinan. These small crag and tail features sit on a larger bedrock high that itself is streamlined in the same direction (see red to white elevations, Fig. 8). A smaller streamlined ridge, just north of this larger feature, indicates more easterly flow. This could be a product of ice deflecting around the larger topographic high.

The photogrammetric DEM showed us that deposits in the clear cut are not part of a till blanket or veneer as we previously thought, but rather part of a glacially streamlined terrain with ice-flow direction significance. This conclusion prompted us to fly another RPAS survey in similar terrain that also resulted in a change in deposit type designation from till blanket to streamlined till. Although the crag-and-tail streamlined features are rare in the Hogem batholith area, they can guide bedrock mappers to isolated exposures in largely drift-covered areas because outcrops are likely at or close to surface at their stoss ends.

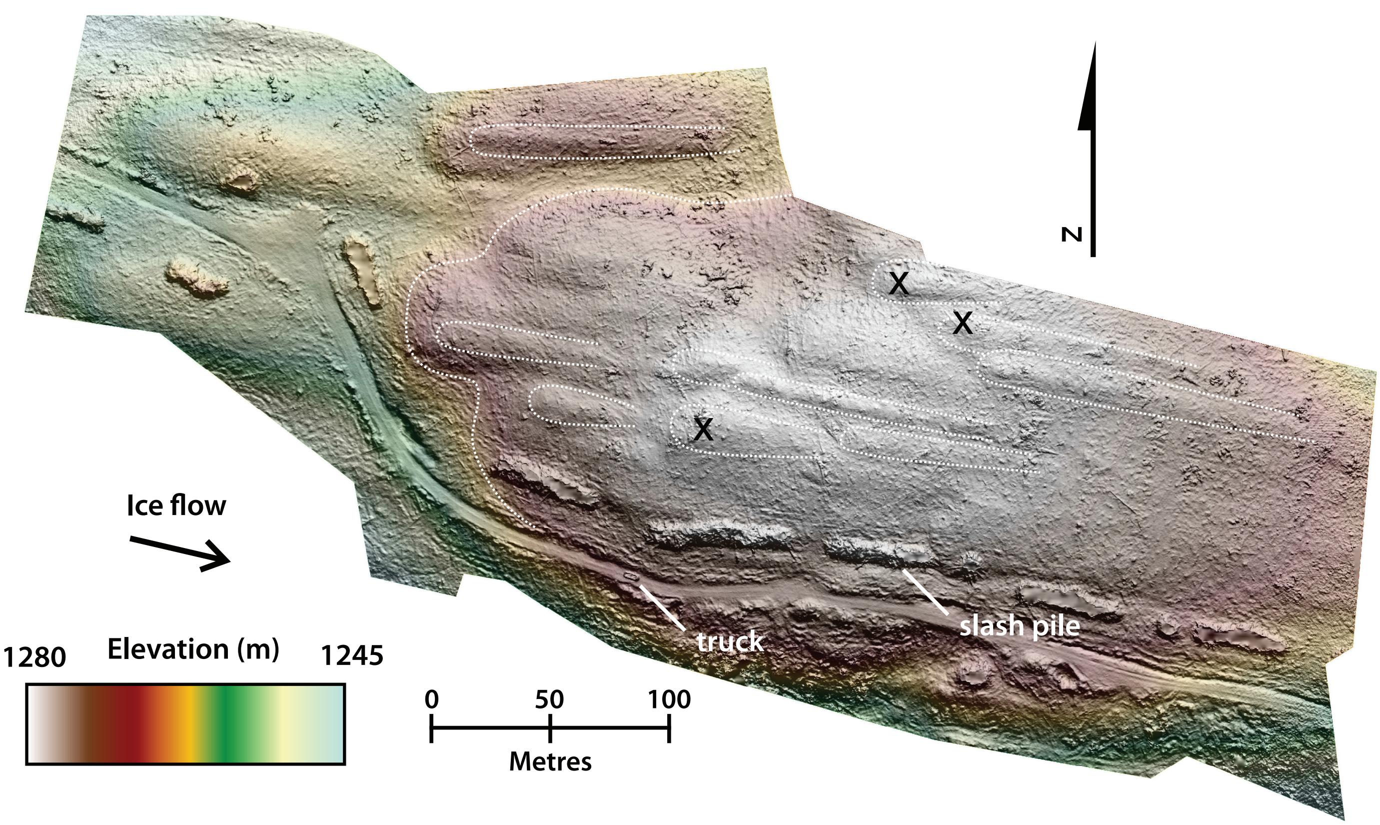

Fig. 8. Photogrammetric DEM of glacially streamlined terrain created from RPAS-acquired air photos. Outlined crag and tail features indicate ice flow towards the east-southeast. Bedrock outcrops represented by xs. See Figure 1 for location.

6. Discussion

6.1. Surficial geology and bedrock mapping

Remotely piloted aircraft system (RPAS) imagery, and derived photogrammetric digital elevation models (DEM), occupy a resolution between traditional, smaller-scale air photos and ground observations. Practical hardware design limitations (e.g., battery capacity) and flight regulations (altitude above ground; within visual line-of-sight; and others, see below) mean that at present RPAS cannot cover the same large areas that a piloted fixed-wing aircraft can. However, RPAS missions can be planned spontaneously to take advantage of exposure or access opportunities presented in the field. A high resolution (<10 cm/pixel), vertical perspective, photogrammetric DEM for sparsely vegetated to unvegetated terrain provides surficial geology mappers with additional context, or detail, on surficial material types and their surface expression. This is particularly true for areas where traditional datasets are lacking, and for newly logged or fire-burned areas where trees and vegetation have been removed.

The two RPAS missions presented here demonstrate how traditional fieldwork can be expanded. The photogrammetric DEMs changed how we mapped the survey areas. They also provide insight into glacial processes. For example, the survey over glacially streamlined terrain documented the eastward movement of the glaciers through the area during the Late Wisconsinan. This has immediate applications because, knowing ice-flow direction is key to finding the bedrock source of tills anomalous in commodity element concentrations or mineral grain counts (Levson, 2001). For the survey conducted over the hummocky terrain, differentiating between stagnant ice versus fluvial deposition can help predict aggregate quality. Although both surficial material types have high aggregate potential, the channelized areas are more likely to be composed of better sorted sands and gravels with lower silt-clay content; material appropriate for a gravel road running surface (Smith et al., 2005).

The same RPAS air photo methods used to map surficial geology can also be used to map bedrock lithology and structure (Nesbit et al., 2018). These systematic surveys, the acquired images, and derived geometrically rectified orthomosaics and DEMs, provide bedrock geologists perspectives that are difficult to obtain in the field, particularly in high-relief terrain. High-resolution orthoimages can be created within hours of completing an RPAS air photo survey and geologists can map directly onto these images using a standard field tablet. An RPAS survey was flown west of Hogem batholith, over a ridge consisting of rhyolitic tuffs and lesser andesite-basalt of the Asitka Group (Permian). The rhyolites weather maroon (oxidized) and white (reduced) and the andesite-basalt is darker green-black. The resultant colour orthomosaic has a resolution of 2.9 cm/pixel and oxidized (maroon) versus reduced (buff white) rhyolites can be identified on the northwestern cliff face (Fig. 9).

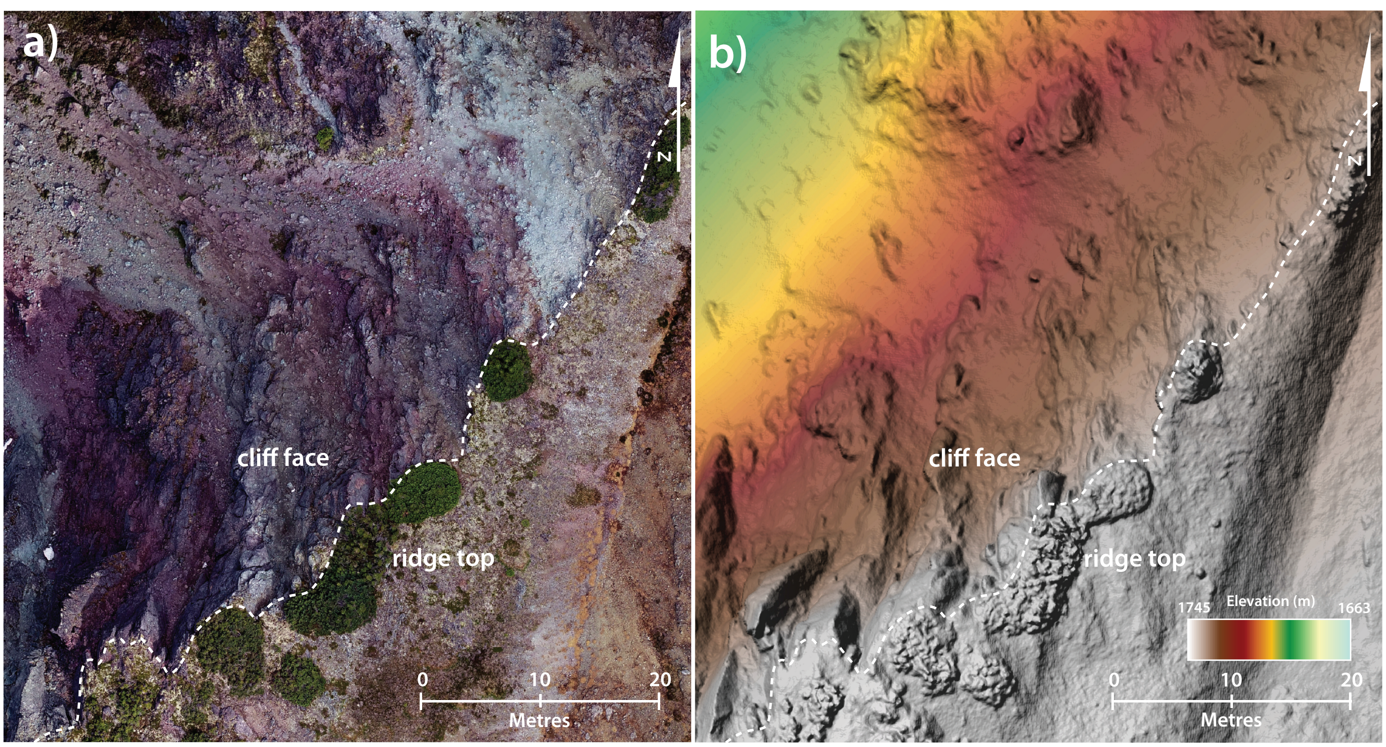

Fig. 9. a) Orthomosaic of bedrock ridge created from RPAS-acquired air photos. It is possible to identify and differentiate oxidized maroon rhyolites and reduced buff-white rhyolites on the northwestern cliff face. This orthomosaic is high-resolution (~3 cm/pixel) and can be used as a base map for fine-scale geologic mapping. **b)** Photogrammetric DEM produced for the same region. For general location see Figure 1, for specific location and perspective, see Figure 4.

6.2. Challenges

Jordan (2015) categorized the challenges of using RPAs in geoscience into natural, technological, and legal groupings; we experienced examples of each. The most significant natural challenge we encountered was tree cover. Tree canopies add noise and decrease resolution of photogrammetric DEMs and can also prevent visual line-of-sight between pilot and RPA. Precipitation and wind also proved challenging. All RPA have a wind speed resistance rating (DJI Phantom 4 Pro RTK is 10 m/s). Exceeding this rating will deplete batteries faster as the RPA works harder to maintain stability or a heading and can result in loss of RPA control. Some of our air photo missions had to be temporarily postponed due to wind or rain. The autopilot function in DJI GS RTK flight planning software made this easy to deal with. The survey can be paused and, once the poor weather passes, the mission can be invoked again and the RPA resumes the exactly where it left off.

A significant technology challenge to our survey was the need to log into DJI servers every 10 days to use the flight-planning software. We were unaware of this requirement until fieldwork began and, because our remote location, we had no internet access. Thus, the RPA was unflyable until a successful login was completed. Another technology challenge, inherent to all RPAS, is field repairs. Simple repairs like propeller replacement are straightforward and can be done in the field, but most other repairs require expensive replacement parts on hand and a clean workspace protected from weather.

In Canada and many other countries, regulations exist governing the registration of RPAS, certification of RPAS pilots, and where RPA can be flown given its weight, mission, and airspace classifications. Most existing literature regarding RPAS survey techniques and workflows unintentionally violate current Transport Canada regulations and cannot be directly followed. Current regulations should be reviewed and understood, in the context of a given application, before an RPAS is purchased. Some regulations can affect how a survey is conducted or dictate if it can be run at all.

6.3. The future?

Exchangeable-payload RPAS are the future for baseline and exploration geoscience applications. Today, RPAS-ready lidar, gamma ray spectrometers, magnetometers, hyperspectral, and VLF sensors are commercially available, with synthetic aperture radar expected soon. Each of these sensors could be used to infill, at an intermediate-scale, between traditional aerial and ground-based surveys, just as RPAS photogrammetric DEMs have. Although these sensors are expensive, some can be rented and fit on an RPAS system. Along with the instrument, software for each application needs to be considered prior to purchase. Not only does the ability to change payloads provide more versatility to the types of data the aircraft can collect, it also 'future-proofs' an RPAS program. Miniaturization of sensors and improvements to RPASs is being driven by advances in technology, and an exchangeable-payload approach is modular. Aircrafts or sensors can be switched in and out of an RPAS program so that updated technology can be incorporated when necessary.

7. Conclusion

We completed 16 RPAS air photo surveys in the Hogem batholith area using a DJI Phantom Pro 4 RTK. The RPAS acquired air photos automatically, following survey parameters set in DJI GS RTK flight-planning software. A dense point cloud and photogrammetric DEM were produced in the field for each survey area. The surveys were flown in areas with sparse vegetation, where high-resolution (<10 cm/pixel) photogrammetric DEMs rival lidar DEMs, gaining detail and insight on surficial materials and their morphology. Field-generated photogrammetric DEMs, produced in near real time, extended traditional point-based field observations (e.g., conducted at a road cut or soil pit) to observations of areas up to ~0.5 km^2. These observations improved our understanding of the surficial geology of the Hogem batholith area, resulting in more accurate mapping. They also helped guide the field program by providing insight and detail that otherwise could not be gained.

Exchangeable payload RPASs, and commercially available geophysical and imaging sensors further broaden the application of RPAS in geoscience. As with RPAS photogrammetric surveys, these sensors fill a niche between the scale of traditional airborne surveys (e.g., aeromagnetic) and outcrop-scale measurements (e.g., magnetic susceptibility). The miniaturization of traditional airborne sensors to a size that is RPAS mountable is technology driven. Many sensors like gamma ray spectrometers, VLF, hyperspectral, lidar are already commercially available. Others like electromagnetic sensors currently are not available but are likely to be so soon.

Acknowledgments

We thank Inge Baggaley (Silver King Helicopters) for her assistance with keeping the RPAS program running. Thank you to Ian Grady (IGI Consulting Ltd.), Bill Lakeland (Spexi Geospatial), and Ryan Preston (Golder Associates Ltd.) for RPAS advice. Matt Sakals and James Thompson (British Columbia Forests, Lands, Natural Resource Operations and Rural Development) are thanked for instruction and debugging support. Matt Sakals is also thanked for his review of the manuscript.

References cited

Carrivick, J.L., Smith, M.W., Quincey, D.J., and Carver, S.J., 2013. Developments in budget remote sensing for the geosciences. In: Geology Today. The Geologists' Association & The Geological Society of London 29, pp. 138-143.

Chabot, D., 2018. Journal of Unmanned Vehicle Systems turns five. Journal of Unmanned Vehicle Systems, 6, vi-xv.

D'Oleire-Oltmanns, S., Marzolff, I., Peter, K.D., and Ries, J.B., 2012. Unmanned aerial vehicle (UAV) for monitoring soil erosion in Morocco. Remote Sensing, 4, 3390-3416.

Hansman, R.J., and Ring, U., 2019. Workflow: From photo-based 3-D reconstruction of remotely piloted aircraft images to a 3-D

geological model. Geosphere, 15, 1393-1408.
Holland, S.S., 1976. Landforms of British Columbia: a physiographic outline. In: British Columbia Ministry of Energy and Mines, and Petroleum Resources Bulletin 48, 138 p.
Irvine, M., Roberts, G., and Oldham, L., 2018. (Uav) Data in environmental monitoring of coastal environments: St. David's, Newfoundland. In: Current Research, Newfoundland and Labrador Department of Natural Resources Geological Survey 18, pp. 15-30.
Johnson, K., Nissen, E., Saripalli, S., Arrowsmith, J.R., McGarey, P., Scharer, K., Williams, P., and Blisniuk, K., 2014. Rapid mapping of ultrafine fault zone topography with structure from motion. Geosphere, 10, 969-986.
Jordan, B.R., 2015. A bird's-eye view of geology: The use of micro drones/UAVs in geologic fieldwork and education. GSA Today, 25, 50-52.
Kaufmann, V., Seier, G., Sulzer, W., Wecht, M., Liu, Q., Lauk, G., and Maurer, M., 2018. Rock glacier monitoring using aerial photographs: Conventional vs. UAV-based mapping - A comparative study. International Archives of the Photogrammetry, Remote Sensing and Spatial Information Sciences, 42, 239-246.
Levson, V.M., 2001 Regional till geochemical surveys in the Canadian Cordillera: sample media, methods, and anomaly evaluation. In: McClenaghan, M.B., Brorowsky, P., Hall, G.E.M. and Cook, S.J., (Eds.), Drift Exploration in Glaciated Terrain. Geological Society of London Special Publication 185, pp. 45-68.
Nesbit, P.R., Durkin, P.R., Hugenholtz, C.H., Hubbard, S.H., and Kucharczyk, M., 2018. 3-D stratigraphic mapping using a digital outcrop model derived from UAV images and structure-from-motion photogrammetry. Geosphere, 14, 2469-2486.
Niedzielski, T., 2018. Applications of unmanned aerial vehicles in geosciences: Introduction. Pure and Applied Geophysics, 175, 3141-3144.
Niethammer, U., Rothmund, S., James, M.R., Travelletti, J., and Joswig, M., 2010. Uav-based remote sensing of landslides. International Archives of Photogrammetry, Remote Sensing and Spatial Information Sciences, 38, 496-501.
Ootes, L., Bergen, A., Milidragovic, D., Graham, B., and Simmonds, R., 2019. Preliminary geology of northern Hogem batholith, Quesnel terrane, north-central British Columbia. In: Geological Fieldwork 2018, British Columbia Ministry of Energy, Mines and Petroleum Resources, British Columbia Geological Survey Paper 2019-01, pp. 31-53.
Ootes, L., Bergen, A.L., Milidragovic, D., Jones, G.O., Camacho, A., and Friedman, R., 2020. An update on the geology of northern Hogem batholith and its surroundings, north-central British Columbia In: Geological Fieldwork 2019, British Columbia Ministry of Energy, Mines and Petroleum Resources, British Columbia Geological Survey Paper 2020-01, pp. 25-47.
Rossi, G., Tanteri, L., Tofani, V., Vannocci, P., Moretti, S., and Casagli, N., 2018. Multitemporal UAV surveys for landslide mapping and characterization. Landslides, 15, 1045-1052.
Smith, I.R., Paulen, R., Plouffe, A., Kowalchuk, C. and Peterson, R., 2005. Surficial mapping and granular aggregate resource assessment in northwest Alberta. In: Summary of Activities, British Columbia Ministry of Energy and Mines, pp. 80-95.
Transport Canada., 1996. Canadian Aviation Regulations (SOR/96-433), 989 p.
Westoby, M.J., Brasington, J., Glasser, N.F., Hambrey, M.J., and Reynolds, J.M., 2012. "Structure-from-Motion" photogrammetry: A low-cost, effective tool for geoscience applications. Geomorphology, 179, 300-314.
Zahm, C., Lambert, J., and Kerans, C., 2016. Use of Unmanned Aerial Vehicles (UAVs) to create digital outcrop models; an example from the Cretaceous Cow Creek Formation, Central Texas. In: Gulf Coast Association of Geological Societies Journal, 5, 180-188.

Appendix: British Columbia Geological Survey publications and peer-reviewed journal papers authored by BCGS staff and released in 2019

All BCGS publications are available for download, free of charge, from
https://www2.gov.bc.ca/gov/content/industry/mineral-exploration-mining/british-columbia-geological-survey/publications

To receive notification of our latest releases email
Geological.Survey@gov.bc.ca

Papers

Paper 2019-01
Geological fieldwork 2018, a summary of field activities and current research, 140 p.

Ferri, F., Jones, L.D., and Clarke, G., 2019. British Columbia Geological Survey annual program review 2018-2019. In: Geological Fieldwork 2018, British Columbia Ministry of Energy, Mines and Petroleum Resources, British Columbia Geological Survey Paper 2019-01, pp. 1-14.

Schiarizza, P., 2019. Geology of the Nicola Group in the Bridge Lake – Quesnel River area, south-central British Columbia. In: Geological Fieldwork 2018, British Columbia Ministry of Energy, Mines and Petroleum Resources, British Columbia Geological Survey Paper 2019-01, pp. 15-30.

Ootes, L., Bergen, A., Milidragovic, D., Graham, B., Simmonds, R., 2019. Preliminary geology of northern Hogem batholith, Quesnel terrane, north-central British Columbia. In: Geological Fieldwork 2018, British Columbia Ministry of Energy, Mines and Petroleum Resources, British Columbia Geological Survey Paper 2019-01, pp. 31-53.

Milidragovic, D., and Grundy, R., 2019. Geochemistry and petrology of rocks in the Decar area, central British Columbia: Petrologically constrained subdivision of the Cache Creek complex. In: Geological Fieldwork 2018, British Columbia Ministry of Energy, Mines and Petroleum Resources, British Columbia Geological Survey Paper 2019-01, pp. 55-77.

van Straaten, B.I., and Wearmouth, C., 2019. Geology of the Latham and Pallen Creek area, northwestern British Columbia: Distinguishing the Tsaybahe group, Stuhini Group, and Hazelton Group, and the onset of Triassic arc volcanism in northern Stikinia. In: Geological Fieldwork 2018, British Columbia Ministry of Energy, Mines and Petroleum Resources, British Columbia Geological Survey Paper 2019-01, pp. 79-96.

Mihalynuk, M.G., Zagorevski, A., Logan, J.M., Friedman, R.M., and Johnston, S.T., 2019. Age constraints for rocks hosting massive sulphide mineralization at Rock and Roll and Granduc deposits between Iskut and Stewart, British Columbia. In: Geological Fieldwork 2018, British Columbia Ministry of Energy, Mines and Petroleum Resources, British Columbia Geological Survey Paper 2019-01, pp. 97-111.

Simandl, G.J., Petrus, J.A., Matthew I., Leybourne, M.I., Suzanne Paradis, S., and Akam, C., 2019. Characterization of primary fersmite from the Mount Brussilof magnesite deposit, southeastern British Columbia, Canada. In: Geological Fieldwork 2018, British Columbia Ministry of Energy, Mines and Petroleum Resources, British Columbia Geological Survey Paper 2019-01, pp. 113-123.

Han, T., Rukhlov, A.S., Riddell, J.M., and Ferbey, T., 2019. A skeleton data model for geochemical databases at the British Columbia Geological Survey. In: Geological Fieldwork 2018, British Columbia Ministry of Energy, Mines and Petroleum Resources, British Columbia Geological Survey Paper 2019-01, pp. 125-135.

Appendix: British Columbia Geological Survey publications and peer-reviewed journal papers authored by BCGS staff and released in 2018, pp. 137-140.

Open Files

OF 2019-01
Clarke, G., Northcote, B., Katay, F., and DeGrace, J.R., 2019. Mines, mine development, selected proposed mines, and selected exploration projects in British Columbia, 2018. British Columbia Ministry of Energy, Mines and Petroleum Resources, British Columbia Geological Survey Open File 2019-01.

OF 2019-02
Ootes, L., Bergen, A.L., Milidragovic, D., and Graham, B., 2019. Preliminary geology of Notch Peak and Ogden Creek (parts of NTS 094C/04 and 093N/13), northern Hogem batholith, Quesnel terrane, north-central British Columbia. British Columbia Ministry of Energy, Mines and Petroleum Resources, British Columbia Geological Survey Open File 2019-02, 1:50,000 scale.

OF 2019-03
Arnold, H., and Ferbey, T., 2019. British Columbia surficial geology map index. British Columbia Ministry of Energy, Mines and Petroleum Resources, British Columbia Geological Survey Open File 2019-03.

OF 2019-04
Bustard, A.L., Ferbey, T., and Arnold, H., 2019. Regional- to property-scale till geochemical and mineralogical surveys in British Columbia for base and precious metals. British Columbia Ministry of Energy, Mines and Petroleum Resources, British Columbia Geological Survey Open File 2019-04.

OF 2019-05
van Straaten, B.I., and Wearmouth, C.D., 2019. Preliminary bedrock geology of the Latham and Pallen Creek area. British Columbia Ministry of Energy, Mines and Petroleum Resources, British Columbia Geological Survey Open File 2019-05, 1:50,000 scale.

OF 2019-06
Milidragovic, D., 2019. Geology of the Cache Creek terrane north of Trembleur Lake, parts of NTS 93K/14. British Columbia Ministry of Energy, Mines and Petroleum Resources, British Columbia Geological Survey Open File 2019-06, 1:50,000 scale.

OF 2019-07
Angen, J.J., Rahimi, M., Nelson, J.L., and Hart, C.J.R., 2019. Bedrock geology, Search phase 1 project area, western Skeena arch, west-central British Columbia. British Columbia Ministry of Energy, Mines and Petroleum Resources, British Columbia Geological Survey Open File 2019-07, 1:150,000 scale. Also published as Geoscience BC Map 2019-03-01 and MDRU Map 17-2018.

OF 2019-08
Angen, J.J., Rahimi, M., Nelson, J.L., and Hart, C.J.R., 2019. Aeromagnetic correlation with bedrock geology, Search phase 1 project area, western Skeena arch, west-central British Columbia. British Columbia Ministry of Energy, Mines and Petroleum Resources, British Columbia Geological Survey Open File 2019-08, 1:150,000 scale. Also published as Geoscience BC Map 2019-03-02 and MDRU Map 18-2018.

OF 2019-10
Plouffe, A., and Ferbey, T., 2019. Indicator-mineral content of bedrock and till at the Gibraltar porphyry Cu-Mo deposit and the Woodjam porphyry Cu-Au-Mo prospect, south-central British Columbia. British Columbia Ministry of Energy, Mines and Petroleum Resources, British Columbia Geological Survey Open File 2019-10, 33 p. Also published as Geological Survey of Canada Open File 8580. https://doi.org/10.4095/315647.

GeoFiles

GF 2019-01
Mihalynuk, M.G., Friedman, R.M., and Logan, J.M., 2019. Laser ablation ICP-MS geochronologic data from Granduc and Rock and Roll deposits, northwest British Columbia. British Columbia Ministry of Energy, Mines and Petroleum Resources, British Columbia Geological Survey GeoFile 2019-01, 5 p.

GF 2019-02
Nelson, J.L., 2019. Iskut region geological compilation: Supporting data and working files. British Columbia Ministry of Energy, Mines and Petroleum Resource, British Columbia Geological Survey GeoFile, 2019-02, 2 p.

GF 2019-03
Febbo, G.E., Friedman, R.M., Kennedy, L.A., and Nelson, J.L., 2019. U-Pb geochronology of the Mitchell deposit, northwestern British Columbia. British Columbia Ministry of Energy, Mines and Petroleum Resources, British Columbia Geological Survey GeoFile, 2019-03, 8 p.

GF 2019-04
Norris, J., and Fortin, G., 2019. Assessment report-sourced surface sediment geochemical database: Development and initial data release from the Interior Plateau. British Columbia Ministry of Energy, Mines and Petroleum Resources, British Columbia Geological Survey GeoFile 2019-04, 10 p.

GF2019-05
Simandl, G.J., Akam, C., Yakimoski, M., Richardson, D., Teucher, A., Cui, Y., Paradis, S., McPhail, S., and Ferri, F., 2019. Potential recovery of Ca, K, Mg, Br, I, B, and Li from produced water at oil and gas fields, British Columbia. British Columbia Ministry of Energy, Mines and Petroleum Resources, British Columbia Geological Survey GeoFile 2019-05 (Poster).

GF2019-06
Simandl, G.J., Petrus, J.A., Leybourne, M.I., Paradis, S., and Akam, C., 2019. Primary fersmite and direct indicator mineral concept, Mount Brussilof, British Columbia. British Columbia Ministry of Energy, Mines and Petroleum Resources, British Columbia Geological Survey GeoFile 2019-06 (Poster).

GF2019-07
Simandl, G.J., Kon, Y., Paradis, S., Hoshino, M., Akam, C., Miller, D., Araoka, D., and Kodama, S., 2019. Geochemistry of the Rock Canyon Creek REE-F-Ba deposit, British Columbia, Canada. British Columbia Ministry of Energy, Mines and Petroleum Resources, British Columbia Geological Survey GeoFile 2019-07 (Poster).

GF2019-08
Rukhlov, A.S., Aspler, L.B., and Gabites, J., 2019. Are Cordilleran carbonatite hosts of Ta, Nb and REE from the deep mantle? British Columbia Ministry of Energy, Mines and Petroleum Resources, British Columbia Geological Survey GeoFile 2019-08 (Poster).

GF2019-09
Cui, Y., Diakow, L.J., and Miller, D., 2019. Toward international geoscience standards and interoperable web services for British Columbia geology and mineral resources. British Columbia Ministry of Energy, Mines and Petroleum Resources, British Columbia Geological Survey GeoFile 2019-09 (Poster).

GF2019-10
Ferri, F., and Reyes, J., 2019. Rock-Eval, lithogeochemistry, gamma ray spectrometry, vitrine reflectance, and X-ray diffraction analysis of the Besa River Formation in the Rocky Mountains of northeastern British Columbia. British Columbia Ministry of Energy, Mines and Petroleum Resources, British Columbia Geological Survey GeoFile 2019-10, 3 p.

GF2019-11
Ferri, F., and Reyes, J., 2019. Rock-Eval, lithogeochemistry, gamma ray spectrometry, thermal maturity, X-ray diffraction analysis, and organic carbon isotope geochemistry of the Besa River Formation, west-central Liard Basin, British Columbia (94N/14). British Columbia Ministry of Energy, Mines and Petroleum Resources, British Columbia Geological Survey GeoFile 2019-11, 5 p.

GF2019-12
Ferri, F., Golding, M., and Reyes, J., 2019. Rock-Eval, lithogeochemistry, gamma ray spectrometry, thermal maturity, and X-ray diffraction analysis of the Grayling and Toad formations (Montney and Doig formations equivalent), Halfway River map area (94B/14). British Columbia Ministry of Energy, Mines and Petroleum Resources, British Columbia Geological Survey GeoFile 2019-12, 5 p.

GF2019-13
Mihalynuk, M.G., 2019. Reconnaissance mapping in the Lardeau Group, southeastern British Columbia, with implications for Outokumpu-style deposits and high-technology battery metals, Ni and Co. British Columbia Ministry of Energy, Mines and Petroleum Resources, British Columbia Geological Survey GeoFile 2019-13 (Poster).

GF2019-14
Rukhlov, A.S., Fortin, G., Kaplenkov, G.N., Lett, R.E., Lai, V. W.-M., and Weis, D., 2019. Supplementary data for multi-media geochemical and Pb isotopic evaluation of modern drainages on Vancouver Island. British Columbia Ministry of Energy, Mines and Petroleum Resources, British Columbia Geological Survey GeoFile 2019-14, 1 p.

Information Circulars

IC 2019-01
Provincial overview of exploration and mining in British Columbia, 2018. British Columbia Ministry of Energy, Mines and Petroleum Resources, British Columbia Geological Survey, Information Circular 2019-01, 133 p.

Clarke, G., Northcote, B., Katay, F., and DeGrace, J.R., 2019. Exploration and mining in British Columbia, 2018: A summary. In: Provincial Overview of Exploration and Mining in British Columbia, 2018. British Columbia Ministry of Energy, Mines and Petroleum Resources, British Columbia Geological Survey, Information Circular 2019-01, pp. 1-37.

DeGrace, J.R., 2019: Exploration and mining in the North Central and Northeast regions, British Columbia. In: Provincial Overview of Exploration and Mining in British Columbia, 2018. British Columbia Ministry of Energy, Mines and Petroleum Resources, British Columbia Geological Survey, Information Circular 2019-01, pp. 39-56.

Katay, F., 2019. Exploration and mining in the Southeast Region, British Columbia. In: Provincial Overview of Exploration and Mining in British Columbia, 2018. British Columbia Ministry of Energy, Mines and Petroleum Resources British Columbia Geological Survey, Information Circular 2019-01, pp. 57-82.

Northcote, B., 2019. Exploration and mining in the South Central Region, British Columbia. In: Provincial Overview of Exploration and Mining in British Columbia, 2018. British Columbia Ministry of Energy, Mines and Petroleum Resources, British Columbia Geological Survey, Information Circular 2019-01, pp. 83-99.

Northcote, B., 2019. Exploration and mining in the Southwest Region, British Columbia. In: Provincial Overview of Exploration and Mining in British Columbia, 2018. British Columbia Ministry of Energy, Mines and Petroleum Resources British Columbia Geological Survey, Information Circular 2019-01, pp. 101-113.

Clarke, G., 2019. Exploration and mining in the Northwest Region, British Columbia. In: Provincial Overview of Exploration and Mining in British Columbia, 2018. British Columbia Ministry of Energy, Mines and Petroleum Resources, British Columbia Geological Survey, Information Circular 2019-01, pp. 115-133.

IC 2019-02
British Columbia Geological Survey, 2019. British Columbia coal industry overview 2018. British Columbia Ministry of Energy, Mines and Petroleum Resources, British Columbia Geological Survey Information Circular 2019-02, 13 p.

Peer-reviewed journal publications

Akam, C., Simandl, G.J., Let, R., Paradis, P., Hoshino, M., Kon,Y., Araoka, D., Green, C., Kodama, S., Takagi, T., and Chaudhry, M., 2019. Comparison of methods for the geochemical determination of rare earth elements: Rock Canyon Creek REE–F–Ba deposit case study, SE British Columbia, Canada. Geochemistry: Exploration, Environment, Analysis 19, 414-430. https://doi.org/10.1144/geochem2018-044.

Febbo, G.E., Kennedy, L.A., Nelson, J.L., Savell, M.J., Campbell, M.E., Creaser, R.A., Friedman, R.M., van Straaten, B.I., and Stein, H.J., 2019. The evolution and structural modification of the supergiant Mitchell Au-Cu porphyry, northwestern British Columbia. Economic Geology 114, 303-324. https://doi:10.5382/econgeo.2019.4632.

Hickin, A.S., Best, M.E., and Levson, V.M., 2019. Electromagnetic resistivity anisotropy in till from the Kiskatinaw streamlined landform field, northeastern British Columbia, Canada. Geomorphology, 335, 14-27. https://doi.org/10.1016/j.geomorph.2019.03.011.

Ootes, L., Sandeman, H., Cousens, B.L., Luo, Y., Pearson, D.G., and Jackson, V.A., 2019. Pyroxenitic magma conduits (ca. 1.86 Ga) in Wopmay orogen and Slave craton: Petrogenetic constraints from whole rock and mineral chemistry. Lithos, in press. https://doi.org/10.1016/j.lithos.2019.105220.

Sheen, A., Heaman, L.M., Kjarsgaard, B., Ootes, L., Pearson, D.G., and Creaser, R.A., 2019. Athapuscow aulacogen revisited: geochronology and geochemistry of the 2046 Ma Union Island Group mafic magmatism, East Arm of Great Slave Lake, Northwest Territories, Canada. Precambrian Research, 321, 85-102. https://doi.org/10.1016/j.precamres.2018.11.012.

Toma J., Holmden C., Shakotko, L., Pan Y., and Ootes L., 2019. Cr isotopic insights into oxidative weathering of the continents at 1.9 Ga utilizing the Beaverlodge Lake paleosol, Northwest Territories, Canada. Geobiology, 17, 467-489. https://doi.org/10.1111/gbi.12342.

Contributions to partner publications

Miller, E.A., Kennedy, L., and van Straaten, B.I., 2019. Preliminary field results from Kinskuch Lake, northwestern British Columbia(NTS 103P/11): a study of the boundary between the Stuhini and Hazelton groups. In: Geoscience BC Summary of Activities 2018: Minerals and Mining, Geoscience BC, Report 2019-1, pp. 75-86.

Nixon, G.T., Milidragovic, D., and Scoates, J.S., 2019. Convergent margin Ni-Cu-PGE-Cr ore systems: temporal and magmatic evolution. In: Targeted Geoscience Initiative 5, Grant Program Interim Reports 2018-2019. Geological Survey of Canada Open File 8620, pp. 49-61. https://doi.org/10.4095/314997.

Ootes, L., Castonguay, S., Friedman, R., and Devine, F., 2019. Superimposed auriferous structural events along the Llewellyn-Tally Ho deformation corridor in southern Yukon and northwest British Columbia. In: Rogers, N., (Ed.), Targeted Geoscience Initiative: 2018 Report of Activities, Geological Survey of Canada Open File 8549, pp. 49-58.

Paradis, S., and Simandl, G.J., 2019. Preliminary carbon and oxygen isotope analyses of hydrothermal carbonates from Mississippi Valley-type and REE-F-Ba deposits of the southern Canadian Rocky Mountains–a comparison. In: Rogers, N., (Ed.), Targeted Geoscience Initiative: 2018 Report of Activities, Geological Survey of Canada Open File 8549, pp. 205-216. https://doi.org/10.4095/313652.

Plouffe, A., Kjarsgaard, I.M., Kobylinski, C.H., Hattori, K., Petts, D.C., Venance, K.E., and Ferbey, T., 2019. Discovering the next generation of copper porphyry deposits using mineral markers. In: Rogers, N., (Ed.), Targeted Geoscience Initiative: 2018 Report of Activities, Geological Survey of Canada Open File 8549, pp. 321-331. https://doi.org/10.4095/313666.

The British Columbia Geological Survey is celebrating its 125th anniversary in 2020. Each year it publishes Geological Fieldwork, a Summary of Fieldwork and Current Research (this volume), the Provincial Overview of Mining and Exploration in British Columbia, and the British Columbia Coal Industry Overview. All British Columbia Geological Survey publications can be downloaded, at no cost, from www.BCGeologicalSurvey.ca

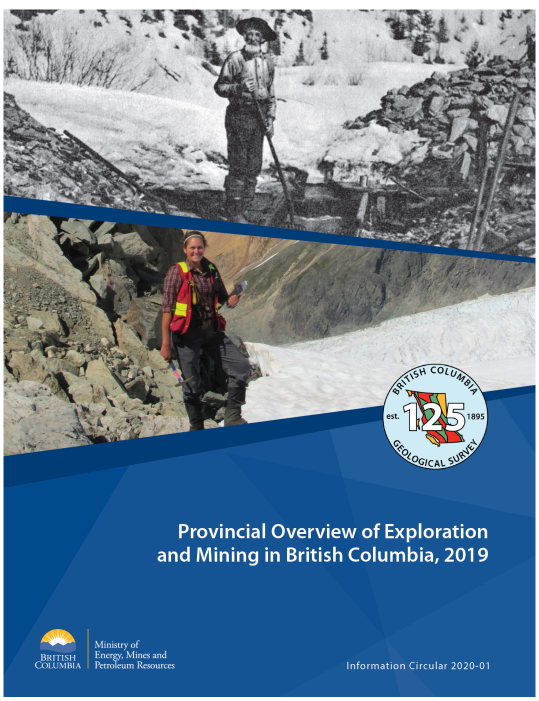

Provincial Overview of Mining and Exploration in British Columbia volume, Information Circular 2020-01. Top photo of a "forty-niner" tending a dumpbox, Lightning Creek, South Central Region circa 1860, from Royal BC Museum Archives. Bottom photo of British Columbia Geological Survey field assistant mapping in the Golden Triangle, Northwest Region by JoAnne Nelson.

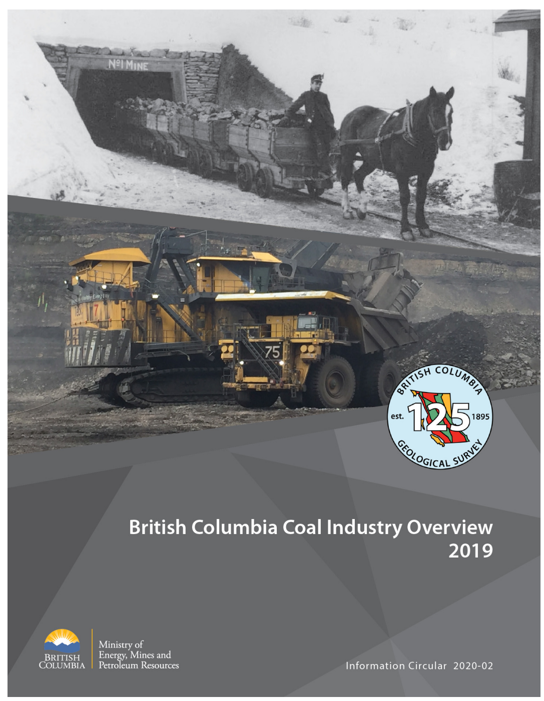

British Columbia Coal Industry Overview volume, Information Circular 2020-02. Top photo of the entrance to the No.1 mine of the Nicola Coal and Coke Company at Merritt in 1908, from Royal BC Museum Archives. Bottom photo of shovel and truck operations at Fording River, Kootenay coalfields, southeastern British Columbia by Fiona Katay.